Interpreting dyke propagation and emplacement dynamics using crystal and vesicle textures

CERI ALLGOOD

Interpreting dyke propagation and emplacement dynamics using crystal and vesicle textures

Ceri Allgood

Abstract

The textures of crystals and vesicles within volcanic rocks are a product of cooling and flow conditions within the volcanic system. This thesis concerns the textures within basaltic dykes, which are the planar conduits that feed fissure eruptions, which produce more magma than any other type of eruption on Earth. Fissure eruptions pose a hazard to life by emitting toxic gases, and pose a hazard to infrastructure by releasing voluminous lava flows. Understanding dyke emplacement is integral to forecasting the likelihood, location and longevity of potential eruptions. However, our means of monitoring dyke emplacement are limited. We can interpret the earthquakes and surface deformation generated by magma fracturing through the crust, but these cannot provide a complete image of dyke structure or flow dynamics. As such, the textures captured within exposed, solidified dykes provide a valuable insight into the flow and cooling conditions that existed while the dyke was active.

In this thesis, dyke emplacement processes are inferred from crystal and vesicle textures. Analogue experiments are used to demonstrate the potential for crystal alignment and vesicle shapes to be read as a record of flow history. A key concept underpinning much of the work in this thesis is that dyke textures should be read as a time-series. Dykes solidify progressively inwards from their margins, so marginal textures record early-stage processes in the dyke tip, whereas central textures record late-stage processes as the dyke is sealing shut. A conceptual model of dyke emplacement is developed by interpreting textures across the widths of dykes at numerous locations within the exposed dyke system, combining field study and petrographic analysis. Textures suggest that cooling and solidification play a significant role in mediating magma flow, and that dykes develop preferential flow pathways. The conceptual model challenges the common conception of dykes as simple, planar fractures, and highlights the importance of thermal processes, which should be included in future models that aim to capture the dynamics of dyke propagation and emplacement.

Interpreting dyke propagation and emplacement dynamics using crystal and vesicle textures

Ceri Allgood

Thesis submitted in fulfilment of the requirements for the degree of Doctor of Philosophy

Department of Earth Sciences, Durham University

2024

Contents

List of figures

Declaration

I declare that this thesis, which I submit for the degree of Doctor of Philosophy at Durham University, is my own work, and not substantially the same as any which has been submitted previously at this or any other university.

This work was funded by the Natural Environment Research Council (NERC) [NE/S007431/1].

Statement of copyright

Acknowledgements

I would like to thank my supervisors, Ed Llewellin, Madeleine Humphreys, Rich Brown and Charlotte Vye-Brown, who came up with the original idea for this project, and who have provided me with guidance and encouragement for the last three and a half years. This project has let me pursue various avenues of enquiry, to the point where this thesis now explores processes at every scale within the dyke system, and I could not have done it without their help. Particular thanks go to Ed for all the discussions we had on volcanic processes, experiment design, and writing papers. I feel much more confident voicing my thoughts now than when I first arrived in Durham.

For the fieldwork aspect of this project, I am hugely grateful to Ariane Loisel. Not only was she an enthusiastic fieldwork companion, helping with taking photos and collecting samples, but she very literally came to the rescue when disaster struck. I genuinely don't know what would have happened had she not been there when I fell and fractured my ribs. Thanks for patching me up, carrying all of our stuff down from the ridge, insisting that I go to hospital, driving me to said hospital, then arguing in Spanish with the airport staff to get me on the flight back home. I also want to thank Alexis Schwartz for helping Ariane in the field for the last two days when I couldn't be there.

For the laboratory parts of this thesis, I am very grateful to Ian Chaplin and Sophie Edwards for making thin sections following my complicated instructions. Huge thanks go to Neil Tunstall in Geography for running x-ray CT scans on my analogue sugar samples, which underpin half the work in this thesis. He pushed the scanner to its limits to get such high resolution images, and the results are incredible. I am also very grateful to Eloise Bretagne for teaching me how to use Avizo to analyse the scan data, and I want to thank Leon Bowen for training me on the SEM.

I also want to thank Simon Mathias for helping me develop a 1D conduction model for dykes that incorporates latent heat release on solidification. This model is central to much of the analysis in this thesis, allowing me to predict the thermal evolution of dykes and the surrounding host rock. I am also incredibly grateful to Fabian Wadsworth for helping differentiate a horrible equation in Chapter 4.

Finally, I want to thank everyone in the volcanology group at Durham who provided feedback and advice on writing and presenting at the weekly VolcCoffee meetings. We have such a supportive group in Durham, and I know that my work, and the way that I perceive my work, has benefitted so much from our discussions. I also want to thank Becca Winstanley for getting us to the IAVCEI conference in New Zealand by car, boat, bus, and propeller-plane after our flight was diverted to the wrong island. I definitely wouldn't have made it there without her. Last but certainly not least, I want to thank Janina Gillies for putting up with all the rambling discussions and silly questions that came from sitting next to me for three years. She is always so cheerful, and she made the office somewhere that I wanted to be.

Chapter 1

Introduction

1.1. Basaltic dykes and fissure eruptions

Basaltic fissure eruptions are the most common form of volcanism on Earth, and produce the greatest volume of lava out of any eruption type (Sigurdsson, 2000). These fissure eruptions pose a hazard to life through their emission of toxic gases such as sulphur dioxide, and they also pose a significant hazard to property and essential infrastructure via the emission of voluminous, long-lasting lava flows, as demonstrated by recent eruptions on the Reykjanes Peninsula in Iceland. Basaltic fissures can reach several kilometres in length (e.g., Richter et al., 1970; Neal et al., 2019; Carracedo et al., 2022), and these fissures are fed by planar conduits known as dykes.

Dykes are the primary pathway for magma transport through the crust (Taisne and Gonnermann, 2015). Understanding the fracturing and flow processes guiding their propagation would allow us to forecast potential eruption sites more effectively, and understanding the flow dynamics within the plumbing system feeding an eruption would allow us to make better predictions for eruption duration and behaviour. However, our means of monitoring dyke emplacement are limited. Active dyke intrusions are monitored by interpreting the seismicity and ground deformation generated by magma fracturing its way through the crust (e.g., White et al., 2011; Woods et al., 2019; Fischer et al., 2022). Interpretations of these geophysical signals rely on our concept of dyke structure and fracturing processes, which is largely based on field observations of solidified dykes exposed by erosion.

The behaviour of a basaltic fissure eruption is partly controlled by the structure and flow dynamics of the feeder dyke (e.g., Menand and Phillips, 2007; Jones and Llewellin, 2021). Once an eruption is underway, activity typically localises from a long fissure into discrete vents, which then become the source for long-lasting lava flows (e.g., Richter et al., 1970; Thorarinsson et al., 1973). These vents may display unique styles of activity, such as the differences in lava and ash emissions from neighbouring vents in the La Palma eruption (e.g., Carracedo et al., 2022). A better understanding of the structure and dynamics of the plumbing system would therefore aid efforts to mitigate the damage posed by lava flows or gas emissions (Figure 1.1).

Our current understanding of dyke propagation and internal flow processes comes from a combination of field observations, theoretical and numerical models, and analogue experiments. The large-scale morphology of exposed, solidified dykes provides evidence for propagation processes, including flow directions (e.g., Pollard et al., 1975; Baer and Reches, 1987), whether a dyke propagated in a brittle or non-brittle manner (e.g., Kjøll et al., 2019), and whether it was guided by host rock weaknesses or by

regional stresses (e.g., Magee et al., 2019). Internal textures, such as the orientations of crystals and vesicles, are commonly used to infer flow directions (e.g., Coward, 1980; Wada, 1992), whereas textural layers are commonly interpreted as records of multiple magma injections or flow episodes (e.g., Gudmundsson, 1984; Platten, 2000).

Theoretical and numerical models commonly operate within the framework of linear elastic fracture mechanics (LEFM), and focus on the effects of regional stress fields and lithologic discontinuities (e.g., Maccaferri et al., 2011). These models are supported by analogue experiments, where a fluid (typically air or water) is injected into gelatin, an elastic solid (e.g., Kavanagh et al., 2018). However, far fewer models account for non-brittle deformation processes or cooling effects.

To create the next generation of dyke propagation models for forecasting transport pathways and potential eruption sites, we need a comprehensive picture of dyke emplacement. This includes the nature of interactions between magma and host rock, the development of dyke segments, the evolution of flow pathways, and the links with eruptive activity should the dyke reach the surface. In this thesis, we will use crystal and vesicle textures within exposed, solidified dykes to infer flow dynamics within the context of large-scale dyke morphology. Three key themes are explored: the development of rock textures in flowing magma, the effects of cooling and solidification on dyke dynamics, and the nature of dyke propagation. This introductory chapter presents an overview of these themes, starting at a large scale (dyke propagation) and moving to the small scale (texture development), providing a broad picture of the concepts central to this thesis.

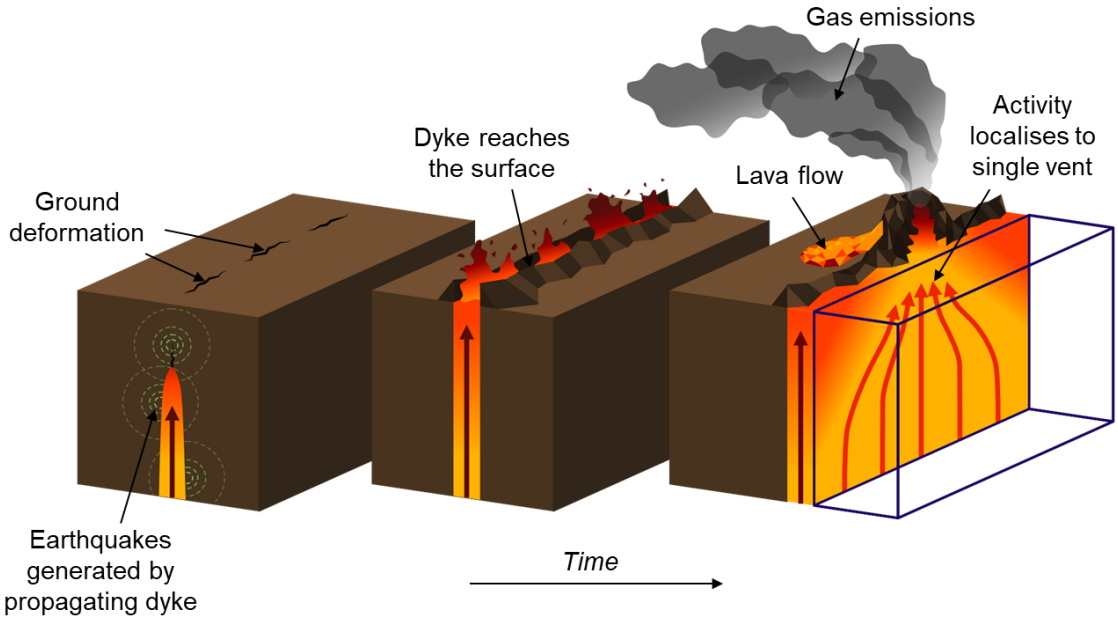

Figure 1.1 Dyke reaching the surface and feeding a fissure eruption. A propagating dyke produces earthquakes as it fractures through the host rock, and leads to ground deformation. If the dyke reaches the surface, it produces a fissure eruption. Over time, eruptive activity along the fissure localises into a small number of discrete vents. The main hazards from basaltic fissure eruptions are lava flows and gas emissions.

1.2. Dyke propagation: transporting magma towards the surface

1.2.1 The nature of dyke propagation

Dykes are magma-filled cracks that propagate by fracturing their way through the crust. However, there is no single mechanism governing this process, and there are several schools of thought regarding dyke propagation models. Most models are based in the framework of linear elastic fracture mechanics (LEFM), where a dyke is assumed to be a pressurised crack with pointed tips that concentrate stress and fracture the host rock (Taisne and Gonnermann, 2015; Rivalta et al., 2015). A common analogue experiment for this type of fracture is the injection of fluids such as water or air into blocks of gelatin (e.g., Menand and Tait, 2002; Kavanagh et al., 2018). However, other models incorporate ductile deformation, where dykes intrude by melting, folding, or fluidising the host rock. Analogues in this regime include intrusion of oil into granular materials (e.g., Galland et al., 2006; Mathieu et al., 2008).

Several key questions remain to be answered by existing propagation models. Numerical and analogue models using LEFM cannot currently explain field observations such as dyke segmentation, which is now viewed as being universal to all dykes (e.g., Pollard et al., 1975; Jolly and Sanderson, 1995). They also cannot explain seismic evidence for propagation occurring in bursts (e.g., White et al., 2011; Woods et al., 2019). Another key uncertainty is the shape of the active dyke tip, which has a significant impact on fracturing dynamics. The dyke tip is where stress is exerted on the host rock, but a rift has emerged between field observations, which include a range of blunted, pointed, or branching dyke tip morphologies (e.g., Harker, 1904; Stephens et al., 2017; Magee et al., 2019) (Figure 1.2), and numerical and analogue models which assume simple elliptical cracks (e.g., Menand and Tait, 2002; Maccaferri et al., 2010). The role of solidification is commonly overlooked, despite multiple theoretical studies emphasizing its crucial role in mediating propagation (Bolchover and Lister, 1999), and despite the seismic evidence for episodic solidification and refracturing (e.g., Hayashi and Morita, 2003; White et al., 2011).

1.2.2 LEFM models: fracture toughness vs. viscous losses

In the framework of LEFM, a dyke is a crack containing a pressurised fluid. The stress exerted on the host rock is a product of the fluid pressure and the crack length, with stress concentrated around the crack tips. When this stress exceeds the fracture toughness of the host rock, the crack propagates (Taisne and Gonnermann, 2015). The fracture toughness is thought to be an intrinsic material property, although estimates from lab experiments (e.g., Atkinson, 1984; Atkinson and Meredith, 1987) and field observations (e.g., Delaney and Pollard, 1981; Olson, 2003; Daniels et al., 2012) differ by several orders of magnitude, suggesting that there is some crucial element of dyke fracturing that is yet to be understood.

LEFM models may be divided into two types: in type I models, propagation is limited by fracture toughness of the host rock, and in type II models, propagation is limited by viscous losses within the flowing magma (Rivalta et al., 2015). Type I models take a quasi-static approach and omit fluid flow within the crack. A dyke has "buoyancy" arising from the difference in lithostatic pressure between the top and bottom of the crack, and once the crack reaches the critical length needed to overcome the fracture toughness of the host rock, this "buoyancy" causes the magma pocket to rise upwards, fracturing at its upper tip and sealing shut at its lower tip, disconnecting itself from the magma source (e.g., Maccaferri et al., 2010; Davis et al., 2021). Type II models are similar to those used in the fracking industry, and incorporate fluid flow through the crack, driven by pressure from a source region (e.g., Spence and Turcotte, 1985; Lister, 1990; Roper and Lister, 2007). The dyke remains attached to the source, and as the crack gets longer, the stress at its tip increases, so propagation cannot be limited by the fracture toughness of the host. Instead, propagation is limited by viscous losses within the fluid, causing a reduction in fluid pressure with increasing distance from the source. The key differences in structure between these two model types are outlined in Figure 1.3.

Both model types have strengths and weaknesses. Type I models are useful for predicting how propagation paths are influenced by tectonic or topographic stresses (e.g., Maccaferri et al., 2011), but without accounting for fluid flow, they cannot make estimates of propagation speeds. Additionally, it is hard to reconcile observations of fissure eruptions lasting weeks or months (e.g., Richter et al., 1970; Muñoz et al., 2022) with models that involve a rising magma pocket detaching from its source. Type II models are useful because they can predict propagation speeds (e.g., Roper and Lister, 2007; Taisne and Jaupart, 2009), but they give the strength of the host rock only secondary importance, which does not agree with observations of dykes terminating at lithological boundaries or following faults (e.g., Baer and Reches, 1987; Galindo and Gudmundsson, 2012).

There has been only a limited effort to create models that account for both host rock strength and fluid flow (e.g., Dahm, 2000). Instead, these two model types appear to have become entrenched and detached from field observations. These model types are now available in 3D (e.g., Zia and Lecampion, 2020; Davis et al., 2021), perpetuating the simple assumptions made in 2D. Although type I 3D models have allowed convoluted propagation paths to be reconstructed based on regional stresses, these models cannot reproduce complex dyke morphologies such as segmentation, or make predictions of eruption likelihood or dyke stalling.

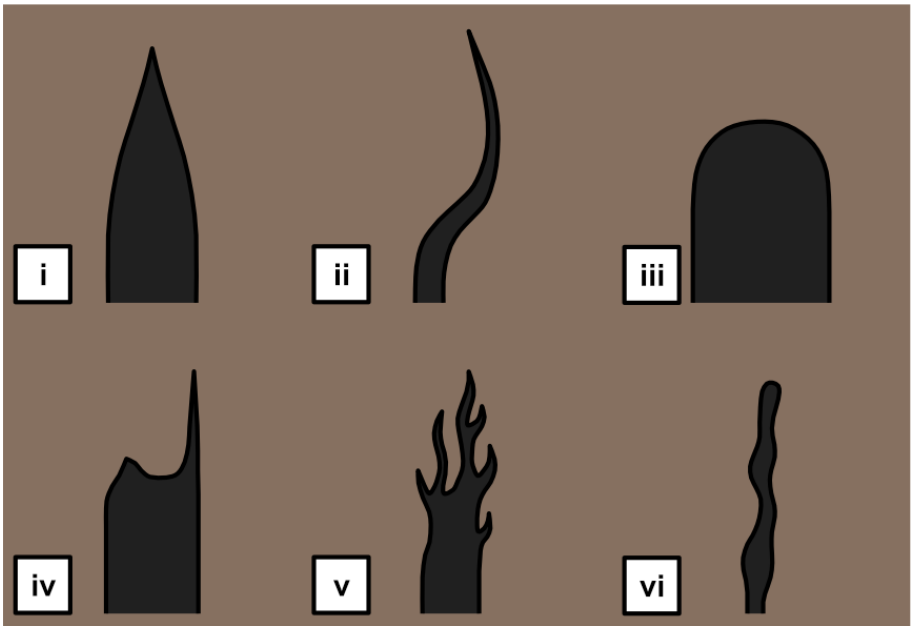

Figure 1.2 Cartoon schematics of dyke tip morphologies: i) classic tapered (Gudmundsson et al., 1999; Clemente et al., 2007); ii) irregular tapered (Marinoni and Gudmundsson, 2000); iii) blunt (Pollard et al., 1975; Stephens et al., 2017); iv) blunt with offshoots (Currie and Furgusson, 1970; Pollard, 1973); v) branching (Kjøll et al., 2019; Magee et al., 2019); vi) irregular (Airoldi et al., 2011).

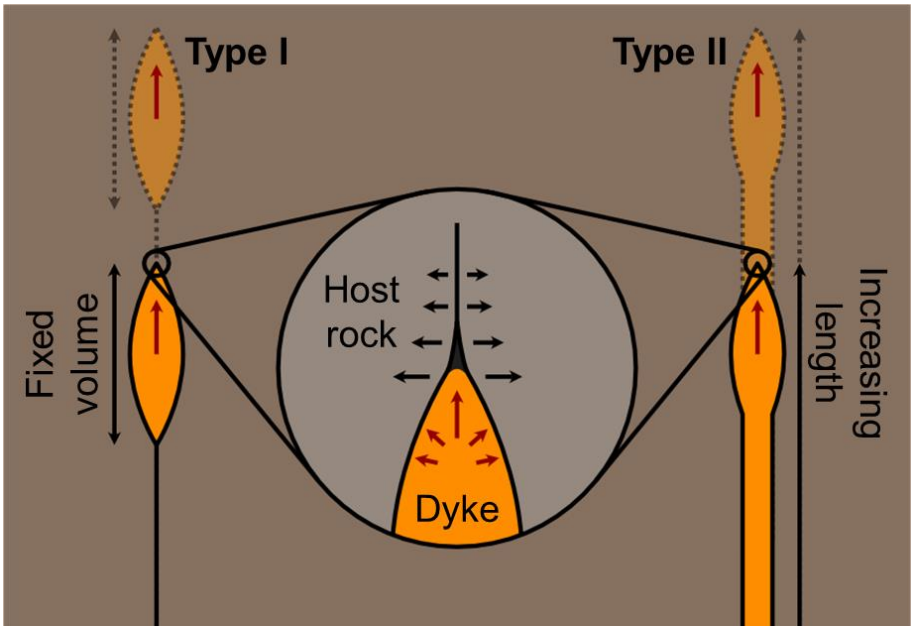

Figure 1.3 Two main types of propagation models: type I (left), with a fixed volume of magma rising through buoyancy, limited by fracture toughness of the host rock; and type II (right), connected back to a pressurised magma source, growing longer, limited by viscous losses within the magma. Both model types require a tapering dyke tip to instigate fracturing.

Another issue is lateral dyke propagation. If dykes are predominantly buoyancy-driven, what could possibly drive them to travel hundreds of miles laterally from their source, such as the giant solitary dykes across northern Britain (MacDonald et al., 1988), or the Mackenzie swarm in Canada (Ernst and Baragar, 1992)? Existing models for lateral propagation assume a level of neutral buoyancy halting upwards propagation and forcing a crack to expand laterally (e.g., Pinel and Jaupart, 2004; Townsend et al., 2017). Again, these models cannot reproduce complex dyke morphology, despite the evidence for segmentation on giant lateral dykes.

The most glaring omission from most propagation models is cooling and solidification. This omission is justified by comparing propagation speeds inferred from seismicity, which are typically a few km per hour, to the time taken to cool a molten slab, which is several hours to days for most dykes (Rivalta et al., 2015). However, this justification is ill-posed. Most models require dykes to have a tapering tip to instigate fracturing, and this narrow tip region will cool rapidly. Even if the main body of the dyke remains molten, its propagation front will be subjected to rapid heat loss, and this is the region that transmits pressures to the host rock, determines the dyke's propagation pathway and structure, and influences the likelihood of stalling versus eruption.

Numerical models incorporating heat loss have shown that it has a pronounced effect in 2D, able to halt propagation (e.g., Lister, 1994a; 1994b; Bolchover and Lister, 1999). Analogue models that intrude solidifying waxes into gelatin have reproduced stepwise propagation (Taisne and Tait, 2011) and segmentation (Chanceaux and Menand, 2014). The viscosity of magma is strongly temperature dependent, and this has been used to explain the localisation of fissure eruptions within feeder dykes (e.g., Bruce and Huppert, 1990; Wylie et al., 1999). However, a similar analysis has never been applied to dykes in their propagation phase, despite the same thermal feedback being present throughout the plumbing system. Models that omit cooling can never fully capture the dynamics of dyke emplacement.

1.2.3 Non-brittle propagation

The shapes of exposed solidified dykes show great variation. Intrusion tips may be tapered, blunt, rounded, or branching (e.g., Harker, 1904; Stephens et al., 2017), and their leading edge may consist of fingers of material, not consistent with LEFM (e.g., Pollard et al., 1975). Faced with these observations, field geologists often infer non-brittle propagation processes, including the fluidisation of unconsolidated host rocks, folding, or melting (e.g., Schofield et al., 2012; Magee et al., 2019). These non-brittle processes have been reproduced in analogue experiments. Intrusions of oil into granular materials such as sand or flour produce complex dyke morphologies that more closely resemble those seen in the field (e.g., Mathieu et al., 2008; Galland et al., 2014).

In summary, it is clear that while LEFM models are getting increasingly complicated and expanding into 3D, they are overlooking two key aspects of dyke propagation: cooling and solidification, and non-brittle emplacement mechanisms.

1.3. Cooling, solidification and flow localisation

1.3.1 Cooling via conduction

Dykes cool by transferring heat via conduction into their surroundings. This is described by Fourier's Law, where the rate of heat flow at a given position depends on the thermal gradient. Positions with a steeper thermal gradient will change temperature faster, which is why the margins of dykes are fine-grained or glassy. The thermal gradient is steepest when the magma first makes contact with the host rock, and so magma at this contact cools rapidly. This is described by the heat equation:

$$\frac{\partial T}{\partial t} = \alpha \frac{\partial^2 T}{\partial x^2} \qquad \text{Eq. 1.1}$$

where T is temperature, t is time, and x is position. The rate of temperature change $\partial T/\partial t$ not only depends on the thermal gradient, but on the thermal diffusivity α of the host rock. This is an intrinsic physical property which combines specific heat capacity c (J kg^{-1} K^{-1}), density ρ (kg m^{-3}) and thermal conductivity k (W m^{-1} K^{-1}), so that $\alpha = k/c\rho$. The heat equation can only be solved numerically. We use it throughout this thesis to model the conductive cooling of dykes, and the derivation of the heat equation and the methods we use to solve it are outlined in Section 1.6.

As the dyke loses heat to its surroundings, its thermal profile relaxes from a step into a curve (Figure 1.4). At any given position, the magma temperature decreases over time, eventually leading to crystal growth and solidification. A solidification front, i.e., an isotherm at the solidus temperature, moves inwards from the margins towards the dyke centre. This solidification front migrates fastest at the margins, where thermal gradients are steepest.

The inwards migration of the solidification front is a concept that underpins much of the work in this thesis. Material at the margins solidifies first, and material in the dyke centre solidifies last, creating a textural time-series across the half-width of the dyke. To interpret this time-series, we must understand the rate of dyke cooling and solidification. However, estimating the thermal evolution of dykes using conduction models such as those presented in Section 1.6 is often an oversimplification. This is because the magma in dykes is flowing, leading to advective heat transfer in competition with conductive heat transfer.

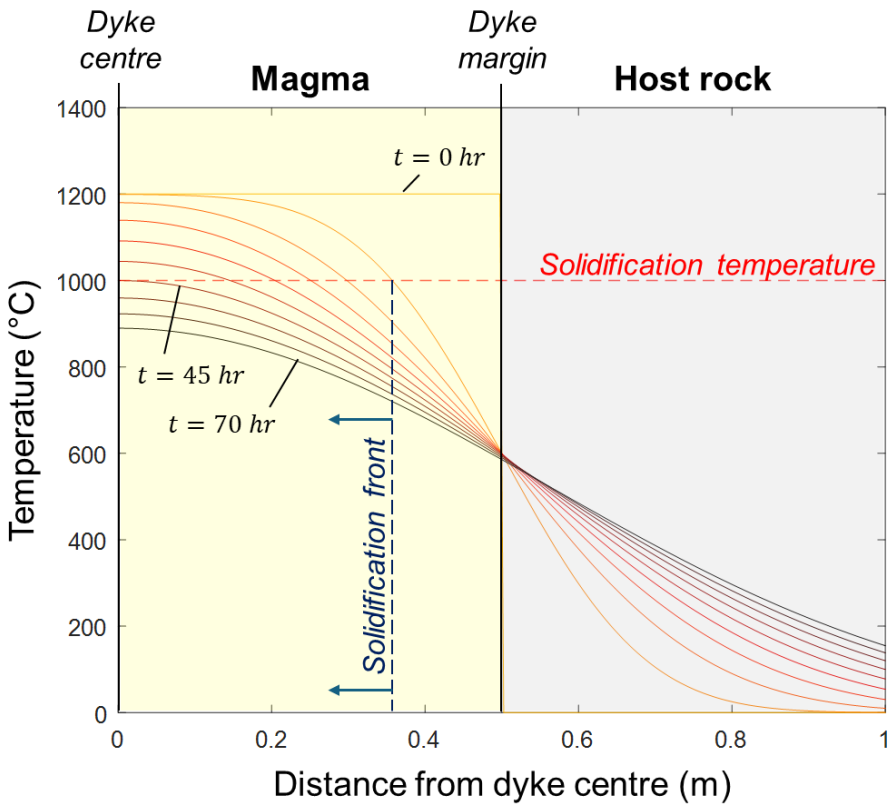

Figure 1.4 Conductive cooling of a 1-m-wide basaltic dyke. Thermal profiles are recorded at ten equal intervals between t = 0 hours (the instant that the dyke is emplaced) and t = 70 hours. The intersection between the thermal profile and the solidification temperature marks the position of the solidification front, which moves towards the dyke centre over time. The dyke has fully solidified after approximately 45 hours. Details of the model used to create this figure are presented in Section 1.6.

1.3.2 Effect of advection

A key implicit assumption of using conduction models for estimating dyke cooling histories is that the magma is stationary. If the dyke is flowing, then heat is also being transferred through advection, with cooler magma in the dyke centre being continuously replenished by hotter magma from upstream (Figure 1.5). Advection can increase cooling times significantly (Delaney and Pollard, 1982; Fialko and Rubin, 1999; Petcovic and Dufek, 2005). In fact, if the dyke is sufficiently wide, or with a high enough flow rate, it cannot solidify shut, and will instead thermally erode the host rock and widen the channel. The tipping point between these solidifying or eroding regimes is described by three dimensionless numbers: firstly, the dimensionless solidification temperature:

$$\theta = \frac{T_S - T_0}{T_M - T_0}, \qquad \text{Eq. 1.2}$$

which gives the solidification temperature T_S as a fraction of the range between the host rock temperature T_0 and initial magma temperature T_M; secondly, the Stefan number:

$$S = \frac{L}{c(T_M - T_0)}, \qquad \text{Eq. 1.3}$$

which gives a ratio of the latent heat L to the sensible heat within the system, indicating the impact of latent heat release; and finally, the Peclet number:

$$Pe = \frac{\Delta P w_0^4}{\alpha \mu H^2}, \qquad \text{Eq. 1.4}$$

which is a ratio of the advective transport rate to the diffusive transport rate, where ΔP is the pressure difference between the start and end of a semi-infinite channel with rectangular cross section, w_0 is the initial half-width of this channel, μ is the viscosity of the fluid and H is the height of the channel (the along-flow distance). Lister and Dellar (1996) present critical Peclet numbers for any combination of θ and S. By rearranging Eq. 1.4 it is possible to express the critical Peclet number Pe_{crit} as a critical initial half-width $w_{0,crit}$, based on the pressure drop and length of the channel:

$$w_{0,crit} = \left(Pe_{crit} \frac{\alpha \mu H^2}{\Delta P} \right)^{1/4}. \qquad \text{Eq. 1.5}$$

Any dyke narrower than this critical width will solidify shut as it is flowing. Otherwise, the dyke will widen by thermally eroding its surroundings, and will only solidfy shut when the flow rate declines. Of course, the approximation as a rectangular channel does not capture the dynamics of the propagation phase, where the dyke has a tapering tip that makes some regions more prone to cooling and solidification than others.

1.3.3 Thermal feedback

The solidification of dykes depends on the balance between conduction and advection, which is highly sensitive to the width of the channel (Eq. 1.5). A compounding factor is the temperature-dependent viscosity of the magma, which leads to thermal feedback that can amplify minor perturbations. A dyke will vary in width perpendicular to the flow plane, and narrower sections will flow more slowly and have a lower advective flux. As such, narrow sections will cool faster and increase in viscosity, causing them to flow more slowly, which reduces the advective flux further. This positive feedback amplifies the effects of width variations by stifling magma flow in narrow sections, and focussing it into wider, faster-flowing regions (Baer and Reches, 1987).

This cooling-driven localisation of flow has been explored extensively in the context of dykes feeding fissure eruptions, where activity progressively localises from continuous eruptions along the fissure to a series of discrete vents. Theoretical models investigated the effects of solidification (Delaney and Pollard, 1982; Bruce and Huppert, 1989; 1990), then viscosity (Helfrich, 1995; Wylie et al., 1999), finding it to be a viable mechanism for fissure localisation. However, this type of analysis has never been applied to dykes in their propagating phase. It seems likely that the narrow, leading edge of the dyke would be highly prone to cooling and thermal feedback, which will influence propagation dynamics. The planar structure favoured by fracturing is not thermally efficient, and magma flow should be expected to localise (Figure 1.6).

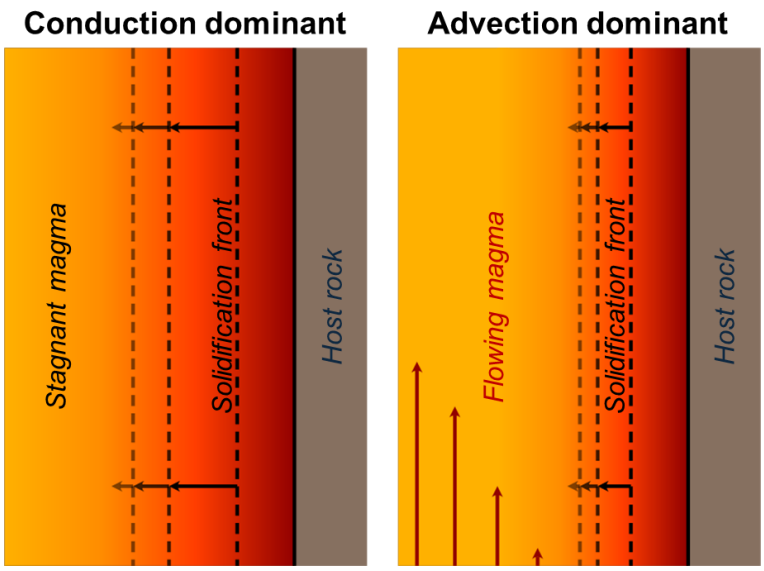

Figure 1.5 Competing effects of conduction and advection within cooling dykes. When the magma is stationary (left), conduction is the only heat transfer mechanism, and the solidification front migrates inwards from the margins as shown in Figure 1.4. When magma is flowing (right), heat is also transferred via advection, and cooler magma is continuously replenished by hotter magma, causing the solidification front to migrate inwards at a slower rate, so the dyke stays hotter for longer.

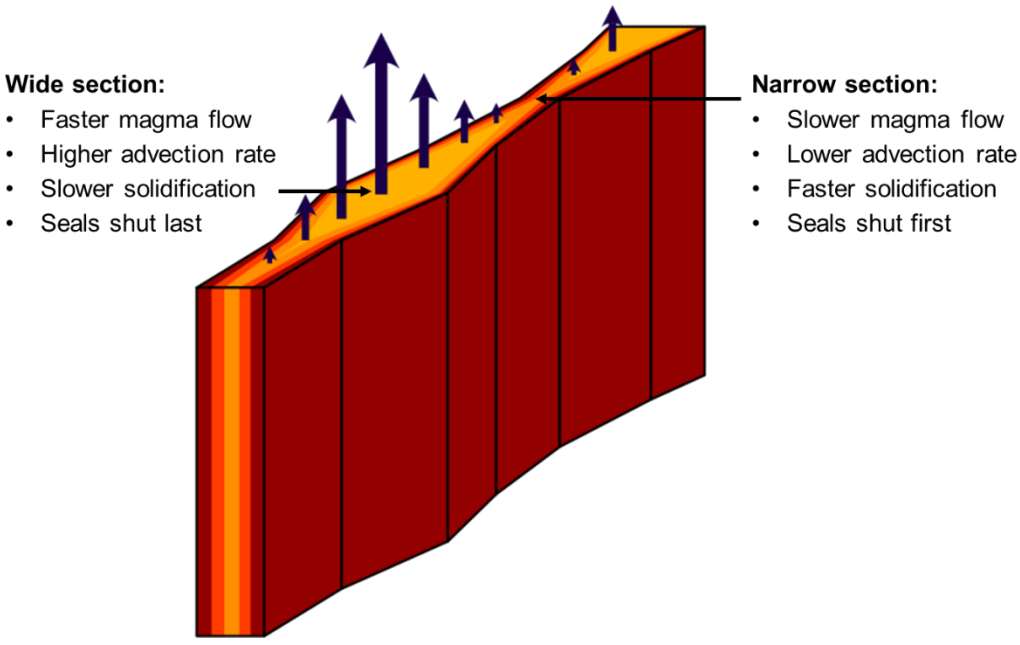

Figure 1.6 Flow localisation within a channel of varying width, driven by thermal feedback. Wide sections flow faster, have a higher advection rate and solidify shut more slowly, causing them to become long-lived preferential flow pathways.

1.4. Using textures to infer flow processes

1.4.1 Textural time-series

As established in Section 1.3, dykes cool and solidify progressively inwards from their margins. The term "texture" refers to the size, abundance, and orientations of phenocrysts, microlites and vesicles, which are a product of flow, cooling and pressure histories captured at the point of solidification at that position within the dyke system. The margins are the first material to solidify, so they capture textures produced in the earliest stages of dyke emplacement, in the propagating tip of the dyke. Moving inwards, textures get progressively younger. Textures in the dyke centre are captured as the dyke seals shut. We can therefore read the textures from margins to centre as a time-series, recording flow processes throughout dyke emplacement at a given position. This textural time-series concept underpins most of the work in this thesis.

However, the textural time-series is not linear. As demonstrated by the conduction model in Figure 1.4, the solidification front advances at a variable rate. This is further complicated by advection, with fluctuations in magma flow rate and channel width causing further variability in the rate of solidification. One of the key textures used to infer timescales are chilled margins. These exist at the outer edges of intrusions, where magma has solidified rapidly against the host rock, leading to a fine-grained texture, or a glass if cooling is sufficiently rapid (Huppert and Sparks, 1989). If a dyke contains an internal chilled margin, seen as a sudden drop in grain size moving towards the centre, this implies that the outer region was allowed to cool significantly before the inner region was emplaced. In other words, there was a significant time gap between consecutive magma pulses through the conduit (Figure 1.7).

Many dykes consist of multiple layers, defined by different compositions (e.g., Eriksson et al., 2011), textures (e.g., Platten, 2000), cooling joints (e.g., Wada, 1992), or internal chilled margins (e.g., Hintz and Valentine, 2012; Munteanu et al., 2017). These are known as composite dykes, and they occur as a result of multiple magma pulses using the same conduit, intruding through the warm, weak centre of a previous pulse (Gudmundsson, 1984; Pansino et al., 2019). Sometimes, however, dykes may display variations in texture that fall short of being defined as individual layers, either because the drop in grain size is relatively minor (e.g., Brouxel, 1991), or because the change in texture is relatively diffuse (e.g., Platten, 2000). However, these "sub-layers" are also likely to result from variations in magma flow rate, and this raises an interesting question regarding timescales.

What constitutes a magma pulse? What distinguishes separate injection episodes from fluctuations in flow rate during a single intrusion event? A simple answer would be that an injection event consists of a batch of material being released from the source. However, thermal feedback can create fluctuating flow rates within a single batch even if the pressure at the source is constant (Whitehead and Helfrich, 1991). Determining whether magma pulses were driven by external dynamics from the source, or

whether they were driven by internal dynamics within the dyke plumbing system, is a difficult task, and magma pulse timescales have received little attention in the literature.

A prevalent assumption in the analysis of dykes (as well as sills and lava flows) is that the textures across their width reflect conditions that existed across the channel while it was flowing. For example, arcs of vesicles and phenocryst distributions have been read as velocity profiles (e.g., Komar, 1976; Coward, 1980), and marginal textures are assumed to represent the high strain rates at the edge of a flowing channel (e.g., Varga et al. 1998; Cañón-Tapia, 2004). In other words, across-width textures are often viewed as a "snapshot" of active dyke flow. This assumption contradicts the fact that dykes solidify progressively inwards from their margins, and that conditions such as flow rate and channel width vary throughout emplacement.

For the "snapshot" approach to work, the dyke must either have solidified near-instantaneously (which may be true for centimetre-wide intrusions), or it must have developed textures during flow, stopped flowing, then maintained those textures as it solidified. This assumes no change in channel width, no backflow or convection, and that bubbles hold their form rather than returning to spheres (a highly unlikely scenario, discussed further in Section 1.4.3). Such assumptions may be valid in some cases, but they are often made implicitly, without justification. Particularly egregious cases occur in studies of the anisotropy of magnetic susceptibility (AMS), used as a proxy for crystal alignment; for example, taking samples at uneven distances from dyke margins, or from a limited number of localities (or a single locality) along the length of a dyke (e.g., Ernst and Baragar, 1992; Staudigel et al., 1999; Raposo et al., 2020). These approaches fail to account for magma flow directions changing over time and with position within the dyke.

Although the "snapshot" assumption is ill-posed, it is still possible for across-width dyke textures to capture textural patterns that existed within the channel while it was flowing. For example, it is a relatively common observation that phenocrysts are concentrated in dyke centres and depleted at their margins (Bhattacharji and Smith, 1964; Komar, 1972; Ross, 1983; Munteanu et al., 2017). This is often interpreted as a result of flow differentiation, where suspended particles migrate away from the high velocity gradients at the edges of a channel (Bagnold, 1954; Baragar, 1960; Bhattacharji, 1967; Yamato et al., 2012). Reading the textures as a time-series, we could infer that the phenocryst concentration within the magma increased over time. However, flow differentiation operates at the same time as progressive inwards solidification, and if the rate of inwards crystal migration exceeds the rate of advance of the solidification front, the margins will end up depleted in phenocrysts. The time-series approach is still valid, but interpretations of textures should also consider the role of active flow processes, such as the redistribution of phenocrysts.

To gain the greatest insight into dyke emplacement processes, the time-series approach should be used at multiple locations within the dyke system. By establishing flow histories at different positions, it is

possible to infer which regions were flowing for the longest, and whether flow localised over time. This provides an insight into the dynamics of the dyke system, which can complement interpretations of migrating seismicity during active dyke emplacement, and constrain numerical and analogue models of dyke propagation.

1.4.2 Crystal alignment

Phenocrysts and microlites within dykes are aligned by the flow of magma. Any elongated particle suspended in simple shear flow will rotate within the velocity gradient, as one side always travels faster than the other (Jeffery, 1922). The particle rotates most slowly when its long axis is parallel with the flow direction, and so it is most likely to be observed at this orientation. However, the crystals within dykes are not rotating in isolation; collisions between neighbouring crystals cause them to stack like fallen dominoes in the direction of flow (Figure 1.7), and crystal imbrication is a useful flow direction indicator (Knight and Walker, 1988; Arbaret et al., 1996).

Crystal alignment may be observed by eye in the field if crystals are large enough, or in thin section under the microscope (e.g., Shelley, 1985; Wada, 1992). The AMS of samples is commonly used as a proxy for crystal alignment, as it is faster to measure (e.g., Cañón-Tapia, 2004), and the imbrication of the maximum susceptibility axis is used to infer flow direction (Knight and Walker, 1988).

However, there is significant uncertainty in using AMS as a proxy for crystal alignment. The AMS is a product of the crystal lattice orientations, shapes, and distributions of all the magnetic grains within a sample (Hargraves et al., 1991). Magnetic phases are some of the last to crystallise, and their growth within the flow-aligned groundmass is poorly understood. Rapid cooling can inhibit the growth of magnetic phases (Cañón-Tapia and Pinkerton, 2000), different phases can produce different AMS responses (Kissel et al., 2010), and magnetic minerals can be modified by later recrystallisation and hydrothermal interactions (Cañón-Tapia, 2004; Hrouda et al., 2020). The AMS is significantly impacted by cooling rate, with magnetic fabrics dependent on distance from the margin and dyke width (Féménias et al., 2004; Kissel et al., 2010; Magee et al., 2016). Some studies have found good agreement between AMS and magmatic fabric (Knight and Walker, 1988; Varga et al., 1998; Aubourg et al., 2008; Montalbano et al., 2016), but in other cases, the relationship is weak or non-existent (Philpotts and Philpotts, 2007; Soriano et al., 2016). Many studies rely on AMS alone, but without validating the results against other flow indicators, it is difficult to trust AMS as a proxy.

It is relatively common to find imbricated phenocrysts or AMS fabrics within dykes, indicating the magma flow direction (e.g., Coward, 1980; Shelley, 1985; Wada, 1992). However, there are also cases of phenocrysts aligning parallel with the dyke margins, without imbrication (Varga et al., 1998; Aubourg et al., 2008). The highest degree of phenocryst and/or microlite alignment often occurs at the margins of dykes (e.g., Coward, 1980; Shelley, 1985; Hastie et al., 2011; Montalbano et al., 2016). This trend is reflected by AMS measurements, with the degree of anisotropy typically highest at the

margins and lowest in the centre (Silva et al., 2010; Raposo et al., 2020). In the few cases where the angle of imbrication has been measured systematically across the widths of dykes, it increases towards the dyke centre (Shelley, 1985; Ross, 1986; Silva et al., 2010; Montalbano et al., 2016).

The pattern of crystal alignment across dykes is often related to the number of magma pulses responsible for their creation. Narrow dykes are more likely to show a high degree of alignment at the margins and a low degree in the centre, whereas wider dykes (and thicker lavas and sills) contain complex and repeating trends, likely to have resulted from multiple injections (Cañón-Tapia and Coe, 2002; Féménias et al., 2004; Hrouda et al., 2019). The degree of crystal alignment varies as a result of cooling and flow rates, but the precise controls over the degree and direction of crystal alignment have never been thoroughly explored.

One of the biggest obstacles to understanding crystal alignment is the lack of studies that consider textures across the entire widths of intrusions. In AMS studies, samples are commonly taken only from within 10 cm of the dyke margin (e.g., Ernst and Baragar, 1992; Varga et al., 1998; Staudigel et al., 1999; Hastie et al., 2013; Hoyer and Watkeys, 2017). This method captures only the initial flow direction, but the margins are targeted as they are believed to capture the steepest velocity gradients and therefore hold the greatest degree of crystal alignment (Tauxe et al., 1998). Few studies focus on exploring textural changes across the widths of intrusions, and those that do sometimes take a "snapshot" approach (e.g., Coward, 1980; Ross, 1986), rather than viewing textures as a time-series (e.g., Wada, 1992; Varga et al., 1998; Platten, 2000; Cañón-Tapia and Coe, 2002; Liss et al., 2002; Féménias et al., 2004; Philpotts and Philpotts, 2007; Wadsworth et al., 2015; Martin et al., 2019).

Currently, crystal interactions within dykes are poorly understood. Collisions are more prevalent at higher crystal concentrations, leading to a lower degree of alignment (Arbaret et al., 2007). At very high concentrations, crystals lock up and only accommodate strain in localised shear planes, and sometimes, collisions cause "reverse imbrication", where crystals stack in a manner indicating the opposite flow direction (Ildefonse et al., 1992; Cañón-Tapia and Chávez-Álvarez, 2004; Mulchrone et al., 2005). Interactions between smaller, younger crystals and larger, older crystals that aligned earlier are particularly complicated (Launeau and Cruden, 1998). Phenocryst alignment dynamics are different to those of microlites, which have a higher likelihood of collisions due to the proximity of neighbouring crystals, and experience a different balance between cooling and strain rates.

Crystal imbrication angles have obvious potential as indicators of strain rates. The increase in imbrication angle towards dyke centres (e.g., Shelley, 1985; Ross, 1986) implies that the balance between cooling and strain rates is having an effect, as does Knight and Walker's (1988) observation that AMS imbrication angles are generally higher in wider dykes. However, the controls on imbrication angle, which potentially include crystal collisions or progressive inwards solidification, are currently poorly understood.

1.4.3 Vesicle textures

Vesicles are captured bubbles that existed within magma as volatiles. These bubbles are deformed by the flow before it solidifies, and the captured shapes and orientations of vesicles are used in a similar way to crystal imbrication to infer flow directions (Figure 1.7). The flow of magma stretches out bubbles at an angle to the channel margin, pointing downstream, making it a reliable flow direction indicator (e.g., Knight and Walker, 1988; Cañón-Tapia and Coe, 2002; Liss et al., 2002; Geshi, 2008; Soriano et al., 2016; Hoyer and Watkeys, 2017; Martin et al., 2019).

The deformation of bubbles in simple shear flow is well understood, and an empirical relationship exists to predict the equilibrium bubble shape from a given strain rate, bubble size and surface tension (Rust and Manga, 2002). However, the link between vesicle shapes and magma flow rates remains poorly understood. Bubbles take time to attain their equilibrium deformation, and this time is proportional to viscosity, provided that bubble size and surface tension remain constant. If strain rates are changing faster than a bubble can attain equilibrium, the bubble shape will not reflect the flow conditions (Llewellin et al., 2002). So, as magma cools and its viscosity increases, bubbles will eventually fall out of equilibrium with flow conditions, and it is these non-equilibrium shapes that are recorded as vesicles.

Few studies have focussed on investigating the shapes of vesicles across the widths of dykes. Generally, it is observed that vesicles are more elongated at dyke margins and more spherical in dyke centres (Coward, 1980; Varga et al., 1998; Geshi, 2008). However, this is not a universal trend. Philpotts and Philpotts (2007) report a dyke where vesicles have a broadly consistent orientation from margins to centre, and Lanzafame et al. (2017) report a dyke where vesicles display no trend in orientation across its width.

Some authors take the “snapshot” approach in interpreting vesicle trends; for example, Coward (1980) interprets a parabolic arc traced out by deformed vesicles as representing the velocity profile that existed across the flowing channel, and Lanzafame et al. (2017) interpret the lack of any trend across their dyke as indicating turbulent flow. By contrast, Philpotts and Philpotts (2007) take a time-series approach, and assume that the constant orientation of vesicles across their dyke has resulted from a balance between strain rates and capture times ahead of an inwards-migrating solidification front. Vesicles have obvious potential as strain rate indicators, if the link between active deformation and captured product can be established.

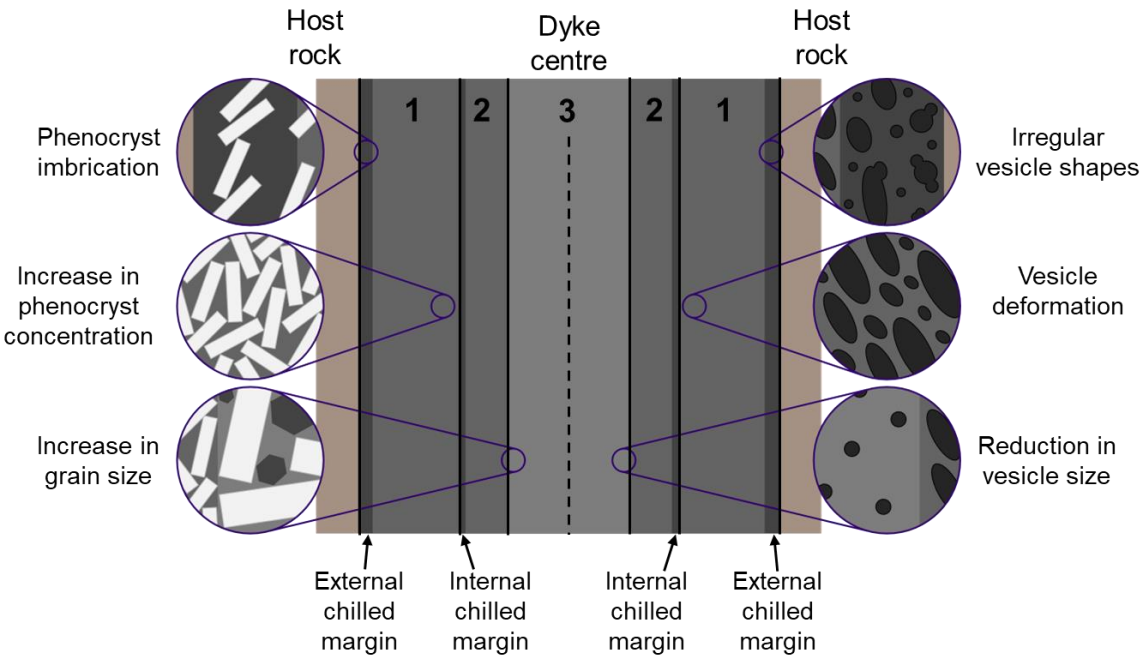

Figure 1.7. Example of phenocryst (left) and vesicle (right) textures across the width of a dyke. The presence of abrupt textural changes suggest that the dyke formed through three distinct magma injection events. Phenocryst imbrication and elongated vesicles indicate an upwards flow direction in the first injection. An internal chilled margin suggests a significant time gap between the first and second injections. An abrupt inwards increase in phenocryst size, coupled with a decrease in bubble concentration and size, suggests a change of composition in the third injection, without a significant time gap. The central layer has no preferred orientations of phenocrysts or vesicles, suggesting that the magma in the third injection stopped flowing long before it solidified.

1.5. Numerical methods used throughout this thesis

Much of the interpretations in this thesis rely on estimates of dyke cooling times and thermal histories. As discussed in Section 1.3, dyke cooling is influenced by the magma flow rate, which determines the amount of heat transferred by advection along the channel. However, for very narrow dykes that solidify rapidly, and for wide dykes that have stagnated in the final stages of emplacement, we can use simple 1D conduction models to estimate cooling times. This section introduces the numerical cooling models that are used throughout this thesis, not only for the cooling of magma within dykes, but for the cooling of sugar used in analogue experiments.

1.5.1 Deriving the heat equation

As established in Section 1.3, molten dykes lose heat to their surroundings via conduction. This is described by Fourier's Law:

$$q = -k\frac{\partial T}{\partial x} \qquad \text{Eq. 1.6}$$

where q is the heat flux density in W m^{-2}, k is the thermal conductivity of the material in W m^{-1} K^{-1}, and $\partial T/\partial x$ is the thermal gradient in K m^{-1}. If there is no heat generation in the system, then at any

position x within the dyke, the rate of change in heat energy Q is proportional to the rate of change in temperature, so $\partial Q/\partial t = (c\rho)\,\partial T/\partial t$, where c is the specific heat capacity in J kg^{-1} K^{-1} and ρ is the mass density in kg m^{-3}. The rate at which heat accumulates at any position is given by the derivative of heat flow at that point, so $\partial Q/\partial t = -\partial q/\partial x$. It follows that

$$\frac{\partial T}{\partial t} = -\frac{1}{c\rho}\frac{\partial q}{\partial x} = -\frac{1}{c\rho}\frac{\partial}{\partial x}\left(-k\frac{\partial T}{\partial x}\right) \qquad \text{Eq. 1.7}$$

which leads us to the heat equation:

$$\frac{\partial T}{\partial t} = \alpha\frac{\partial^2 T}{\partial x^2} \qquad \text{Eq. 1.8}$$

where α is the thermal diffusivity in m^2 s^{-1}, a combination of specific heat capacity, density and thermal conductivity, so that $\alpha = k/c\rho$. We can calculate the time required for a slab of magma to solidify by solving the heat equation numerically, using a finite difference method. This is the method we use in Chapter 2 to estimate the thermal evolution of solidifying sugar in analogue experiments. However, the finite difference approach cannot account for the release of latent heat upon crystallisation, which is a significant heat source within dykes (Bruce and Huppert, 1990; Turcotte and Schubert, 2002). So, to model dyke cooling and solidification, we must reframe the heat equation to include latent heat.

1.5.2 1D conduction model including latent heat

The following method was written by Simon Mathias from the Department of Engineering, Durham University. I have modified it to handle dyke intrusions into cold host rock by choosing appropriate boundary conditions and initial conditions, and ensuring that the fixed boundary (the far-field temperature) is far enough from the dyke to avoid being warmed by the intrusion. This basic model will be used throughout the thesis to predict cooling times in a variety of scenarios.

The model operates as follows. A specified half-width w of molten material with uniform temperature T_M is emplaced instantaneously into host rock of uniform temperature T_0. We assume that the magma and host rock have the same thermal conductivity, which is reasonable for a basaltic dyke intruding layered basaltic lava flows. The model boundary condition is that the host rock is fixed at temperature T_0 at a distance ten times the half-width of the dyke, far from the warming effect induced by its emplacement. The total width of the model is $W = 10w$.

Assuming the magma to be incompressible, the following energy conservation equation applies:

$$\rho\frac{\partial h}{\partial t} = k\frac{\partial^2 T}{\partial x^2} \qquad \text{Eq. 1.9}$$

where ρ is mass density (kg m^{-3}), h is enthalpy per unit mass (J kg^{-1}), t is time after emplacement (s), k is the thermal conductivity (W m^{-1} K^{-1}), T is temperature within the magma (K), x is distance from

the centre of the dyke normal to the dyke plane (m), T_M is the temperature of the magma pulse (K), and T_0 is the temperature of the host rock (K).

Assuming that magma and host rock have the same specific heat capacity, the relationship between temperature and enthalpy takes the form

$$T = \begin{cases} \frac{h}{c} & h < cT_S \\ T_S & cT_S \leq h \leq cT_S + L \\ \frac{h-L}{c} & h > cT_S + L \end{cases} \quad \text{Eq. 1.10}$$

where T_S is the solidification temperature (K), c is the specific heat capacity (J kg^{-1} K^{-1}), and L is latent heat (J kg^{-1}). Solidification has occurred where $T < T_S$. Latent heat is released when $T = T_S$.

A numerical solution is achieved by discretising Eq. 1.10 in space using finite differences and solving the resulting set of ordinary differential equations (ODE) with respect to time using MATLAB's stiff ODE solver, ODE15s (Shampine and Reichelt, 1997; Shampine and Thompson, 2001).

We take a density of ρ = 2700 kg m^{-3} for the liquid and solidified magma (Lesher and Spera, 2015), a thermal conductivity of k = 1.3 W m^{-1} K^{-1} (Sehlke et al., 2020), a specific heat capacity of c = 1200 J kg^{-1} K^{-1} (Turcotte and Schubert, 2002; Mollo et al., 2011), and a latent heat L of 4 x 10^5 J kg^{-1} (Bruce and Huppert, 1990; Turcotte and Schubert, 2002). The initial magma temperature T_M is taken to be 1200 °C, which is the eruption temperature measured in the 2021 La Palma eruption (Carracedo et al., 2022; Castro and Feisel, 2022). We use an approximate solidification temperature T_S of 1000 °C, and a host rock temperature T_0 of 0 °C.

The release of latent heat has a significant impact on dyke cooling. By running the model for a dyke 1 m wide, both with and without latent heat, we see that solidification is delayed by 12 hours when latent heat is included (Figure 1.8). The decision of whether or not to include latent heat depends on the setting; for example, if a dyke is sufficiently narrow that it will cool rapidly and form a glass, there will be no crystallisation, and no latent heat release. This concept is visited again in Chapter 4.

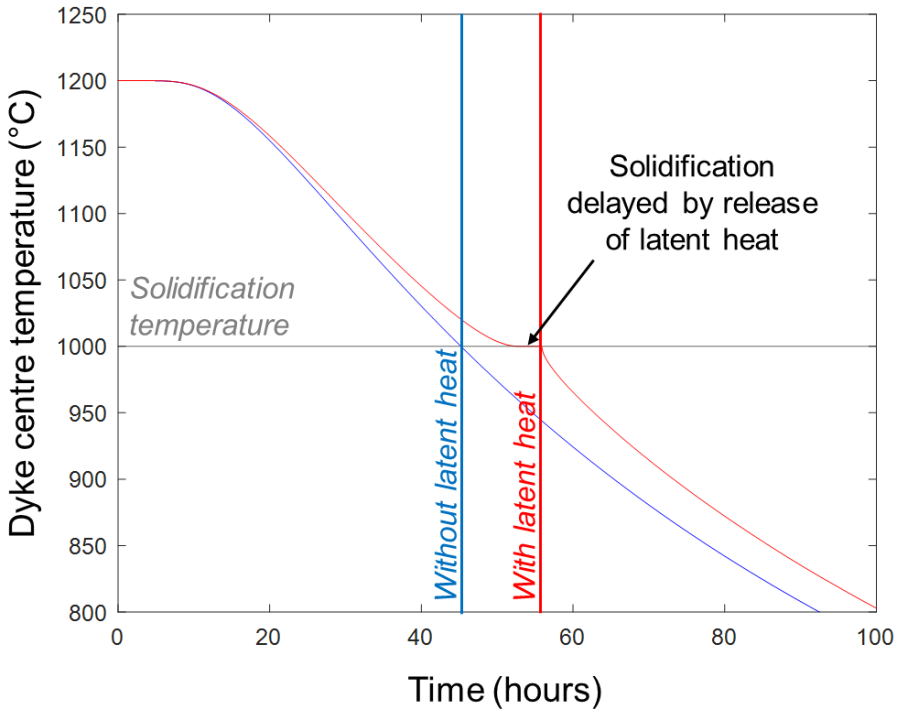

Figure 1.8. Temperature of the dyke centre over time, with and without latent heat (red and blue curves respectively). When latent heat is included, the dyke takes approximately 12 hours longer to solidify.

1.6. Aims and scope of this thesis

This thesis will examine evidence for dyke flow processes at a range of scales, building towards a conceptual model of dyke emplacement. The key aim is to gain a better understanding of the development of dyke textures, and how these can be interpreted in the context of their position within the larger dyke plumbing system to provide insight into emplacement dynamics. The four results chapters (Chapters 2-5) demonstrate that crystal and vesicle textures provide crucial evidence for dyke flow processes, such as the effects of cooling and flow localisation. These textures therefore provide constraints for numerical and analogue models of dyke propagation, and context for the interpretation of seismicity during active intrusion events.

Chapters 2 and 3 present the results of analogue experiments investigating the development of phenocryst and vesicle textures respectively. These experiments use molten sugar to explore the effects of progressive inwards solidification on the alignment of isolated particles and on the shapes of isolated bubbles. The analogue textures are imaged using x-ray CT and reconstructed in Avizo.

Chapter 2 introduces the Jeffery equations for describing particle motions in simple shear flow, and implements the Jeffery equations in MATLAB to model the development of stable alignment in a particle population. By comparing the model and experiments, it is shown that progressive inwards solidification leads to a higher degree of particle alignment than can be produced in an isothermal fluid. The amount of additional alignment caused by solidification depends on the balance between

the advance rate of the solidification front and the strain rate within the fluid. The chapter ends with a conceptual model for particle alignment ahead of a solidification front, which explains the results of the analogue experiments, and also suggests a link between strain rates and imbrication angles.

Chapter 3 starts with a review of bubble deformation in simple shear. The vesicles captured in analogue experiments have shapes which are highly dependent on flow history. In samples where strain rates decrease ahead of the solidification front, bubbles have time to return to spheres before capture, whereas samples with increasing strain rates produce highly elongated vesicles. There follows a discussion on the complexities involved in interpreting vesicles across dykes, and the potential of this method for understanding the links between flow processes and final products.

Chapter 4 presents an investigation into banded textures at the margins of dykes, using samples from the Teno Massif, Tenerife (Spain) and from the Columbia River Basalt Province (USA). Marginal textures form within the tip of the dyke, so they record processes associated with propagation. The bands are interpreted as a time-series, moving inwards from the margins, and the cyclic variations in phenocryst and vesicle concentrations are read as a record of cyclic fluctuations in flow rates and pressures in the dyke tip. Marginal bands suggest that propagation occurs in a stepwise manner, and demonstrate that solidification has a significant impact on magma flow within the narrow dyke tip.

Chapter 5 examines textures across the widths of dykes in the Teno Massif in relation to the larger-scale dyke morphology, particularly segmentation. Various dykes contain evidence of multiple magma pulses, flow localisation, and late-stage convection currents. A conceptual model for dyke emplacement is developed, where segmentation is driven by host rock heterogeneities and amplified by thermal feedbacks, and where propagation occurs on multiple competing fronts, leading to flow localisation. By including the effects of cooling and host rock weaknesses, the conceptual model addresses several key aspects overlooked by current numerical and analogue models.

The main findings of this thesis are summarised in Chapter 6. The work in Chapter 4 has been published as a paper on marginal bands and pulsatory dyke propagation (Allgood et al., 2024), which is presented in Appendix B, and a paper on flow localisation within dykes, as discussed in Chapter 5, is in review.

Chapter 2

The effect of cooling rate and strain rate on particle alignment in solidifying flows

---

Aims of this chapter:

We use analogue experiments to explore how the balance between cooling rate and strain rate influences the degree and direction of particle alignment in progressively solidifying dykes. Particle motions and the development of preferred orientations are well understood for simple shear flow in isothermal fluids, but as we established in Section 1.3, dykes are not isothermal environments. Magma has a temperature dependent viscosity, and steep viscosity gradients are likely to develop at the dyke margins, which are the regions most often sampled in efforts to establish flow directions. Our analogue experiments allow us to investigate particle alignment in a fluid experiencing simultaneous shearing and progressive inwards solidification.

Our experiments use a low concentration of particles in order to limit interactions and collisions between neighbours, allowing us to focus exclusively on the effects of cooling and solidification. We find that the degree of particle alignment is related to the strain that accumulates in the fluid immediately before it solidifies, and that alignment is enhanced beyond what would be expected in an isothermal fluid due to the presence of a migrating solidification front. Our conceptual model suggests that the migration rate of the solidification front, and the strain rates ahead of it, should influence the degree and (potentially) the direction of particle alignment. This could help explain why the degree of crystal alignment and angle of imbrication are often seen to vary across the widths of intrusions.

2.1. Introduction

Crystal textures preserved in solidified dykes are a product of processes that operated while they were molten and flowing. The alignment of crystals is commonly used to interpret the direction of magma flow, either by measuring the alignment of crystals in thin sections (e.g., Shelley, 1985; Wada, 1992), or by using the anisotropy of magnetic susceptibility (AMS) as a proxy for crystal alignment (e.g., Knight and Walker, 1988; Tauxe et al., 1998; Martin et al., 2019). Flow directions are inferred from crystals which have aligned at an angle to the margin, producing an imbricated texture. This texture is thought to result from crystals colliding, causing them to stack like dominoes pointing downstream, and it is a quick and intuitive way to ascertain magma flow directions (Blanchard et al., 1979; Benn and Allard, 1989; Philpotts and Asher, 1994). However, the processes controlling the degree and direction of crystal alignment in dykes are not well understood.

The rotations of particles suspended in simple shear flows are described by the Jeffery equations (Jeffery, 1922), which have been experimentally verified for a range of particle shapes and sizes relevant to crystals in magma (e.g., Ildefonse and Fernandez, 1988; Arbaret et al., 1996). However, these equations and experiments all assume that the suspending fluid is isothermal, with a constant viscosity. This is problematic when interpreting the textures within dykes, which did not form in isothermal environments but in flowing magma that cooled and solidified progressively inwards from its edges. As such, the Jeffery equations and isothermal analogue experiments have limited applicability when interpreting crystal textures in dykes, especially at the margins, which are the regions most often sampled in efforts to determine flow directions (e.g., Tauxe et al., 1998). The margins solidified rapidly, and would have hosted steep viscosity gradients.

Both the degree and direction of crystal alignment can vary across the widths and along the lengths of dykes, but the reasons for this are not well understood. For example, many authors report a lower degree or total lack of alignment in the centres of intrusions (e.g., Shelley, 1985), which is often attributed to low strain rates or stagnant magma (Knight and Walker, 1988; Holness and Humphreys, 2003). The imbrication angle can also vary across dykes, generally increasing away from the margins, although there are few systematic studies of this (e.g., Blanchard et al., 1979; Shelley, 1985). Clearly, the degree and direction of crystal alignment are a product of flow conditions, but to our knowledge, no attempt has been made to explore the effects of progressive inwards cooling and solidification.

We propose that the degree and direction of crystal alignment can be used to infer more than basic flow directions, and that changes in crystal textures across the widths of solidified intrusions and lavas can be used to infer relative changes in cooling and strain rates throughout their emplacement. To demonstrate this, we have devised a series of analogue experiments to explore the development of particle alignment within samples that cool and solidify progressively inwards from their edges, mimicking the conditions found in dyke margins.

2.2. Background: particle motions in isothermal fluids

2.2.1 Jeffery equations and coordinate system

Jeffery (1922) derived equations describing the rotation of an isolated, rigid ellipsoid in a viscous fluid undergoing simple shear. The Jeffery equations assume that the motion of the suspended particle is controlled only by the motion of the surrounding fluid, and because one side is always moving faster than the other, the particle will continuously rotate.

Jeffery defines the axes x', y' and z' as fixed in direction, with the components of fluid velocity u', v' and w' parallel to these axes. Laminar flow is defined by $u' = v' = 0$, and $w' = \dot{\gamma}y'$, with $\dot{\gamma}$ being strain rate. This setup is outlined in Figure 2.1. The particle orientation is defined by axes x, y and z, centred on the same origin as the fixed axes, and particle dimensions are a, b, and c respective to its orientation axes. In the case where $b = c$, the ellipsoidal particle is axisymmetric around the x-axis, creating a special type of ellipsoid known as a spheroid. Jeffery defines three Euler angles that describe particle rotation: θ, the angle between the x and x' axes; ϕ, the angle between the planes $x'y'$ and $x'x$; and ψ, the angle between the planes $x'x$ and xy (Figure 2.1). For spheroids, the final rotation by ψ around the x-axis makes no difference, as dimensions b and c are equal.

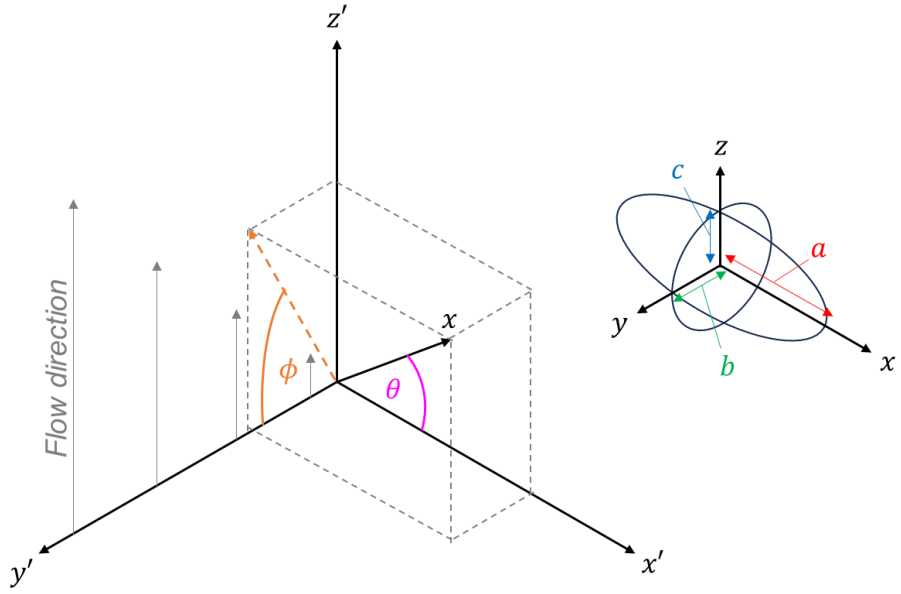

Figure 2.1. The axes and flow direction defined by Jeffery (1922), also showing the dimensions of a prolate spheroid ($a > b = c$), and the Euler angles θ and ϕ measured from the x-axis, which is a spheroid's axis of rotational symmetry.

Jeffery derived three equations to describe the motions of the ellipsoid, where θ and ϕ are initially zero. These original equations have since been modified by Stover et al. (1992) to create a more general solution allowing any initial angles for θ and ϕ. The general equations are as follows:

$$\dot{\theta} = \frac{\dot{\gamma}(r_e^2 - 1)}{(r_e^2 + 1)} \sin\theta \cos\theta \sin\phi \cos\phi, \quad \text{Eq. 2.1}$$

$$\dot{\phi} = \frac{\dot{\gamma}}{(r_e^2 + 1)} (r_e^2 \cos^2\phi + \sin^2\phi), \quad \text{Eq. 2.2}$$

$$\tan\theta = \frac{C\, r_e}{(r_e^2 \cos^2\phi + \sin^2\phi)^{1/2}}, \quad \text{Eq. 2.3}$$

and

$$\tan\phi = r_e \tan\left(\frac{2\pi t}{T} + \kappa\right), \quad \text{Eq. 2.4}$$

where $\dot{\theta}$ and $\dot{\phi}$ are the rates of rotation for the θ and ϕ angles respectively, r_e is the effective aspect ratio, and t is time. For spheroids, the effective aspect ratio is simply the aspect ratio, a/b. Other shapes must have their effective aspect ratio determined experimentally, so that they can be approximated as spheroids (Bretherton, 1962). The constants C and κ are calculated from initial conditions using Eqs. 2.3 and 2.4, and T is the period of rotation, where

$$T = \frac{2\pi(r_e + r_e^{-1})}{\dot{\gamma}}. \quad \text{Eq. 2.5}$$

The period of rotation can also be expressed in terms of strain γ_T by multiplying T by the strain rate. From here, Eqs. 2.1-2.5 will be referred to as "the Jeffery equations".

The Jeffery equations predict periodic rotations for a spheroidal particle in simple shear flow. The nature of these rotations depends on the initial orientation of the particle. At one extreme, the x-axis can be locked in place over the x'-axis at $\theta = 0°$, and the particle undergoes a constant rolling motion. In this scenario, it is impossible to define the ϕ angle, and the ψ rotation rate is constant. The other extreme is where the x-axis is perpendicular to the x'-axis, locked in place at $\theta = 90°$. In this scenario, the particle experiences a tumbling motion, with the x-axis tracing a perfect circle on the $y'z'$ plane. Between these extremes lie an infinite number of potential rotation paths, known as Jeffery orbits, determined by the particle's initial orientation (Figure 2.2).

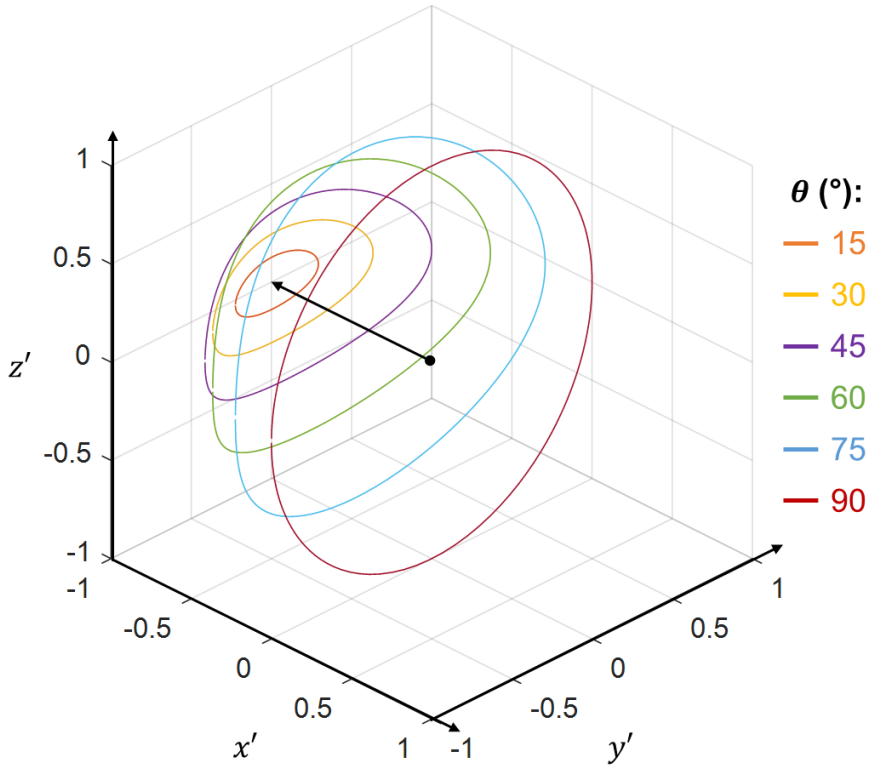

Figure 2.2. The Jeffery orbits for a spheroid of aspect ratio 5, for a variety of initial θ values between 0° (aligned with x'-axis) and 90° (perpendicular to x'-axis).

2.2.2 Particle alignment and strain dependence

A key prediction of the Jeffery equations is a periodic variation in rotation rates (Eqs. 2.1 and 2.2). ϕ rotation rates are fastest when the particle long-axis is perpendicular to the flow direction, and slowest whenever the long-axis is parallel with the flow. Therefore, any spheroidal particle will spend most of its time in close alignment with the flow. An oblate spheroid ($a < b = c$), spends most of its time close to $\phi = 0°$, and if we extrapolate this behaviour to a population of identical oblate spheroids, most of them will be aligned with orientations close to $\phi = 0°$ at any given moment. As such, the population has a preferred orientation while the particles are in motion.

The direction of preferred orientation has two modes, determined by the value of r_e being more or less than one. For oblate spheroids ($a < b = c, r_e < 1$), the direction of preferred orientation is $\phi = 0°$, and for prolate spheroids ($a > b = c, r_e > 1$), the direction of preferred orientation is $\phi = 90°$ (Figure 2.3). Prolate spheroids align with their long axis parallel with the flow direction, while oblate spheroids align their long axes within the flow plane.

The degree of particle alignment is determined by the aspect ratio of the particles, which controls the variation in rotation rate. For example, if the rotation rate is constant, each particle is equally likely to be found at any orientation, and there will be no alignment. Particles with r_e further from one spend an increasing proportion of each rotation close to their preferred orientation, and will display a greater degree of alignment.

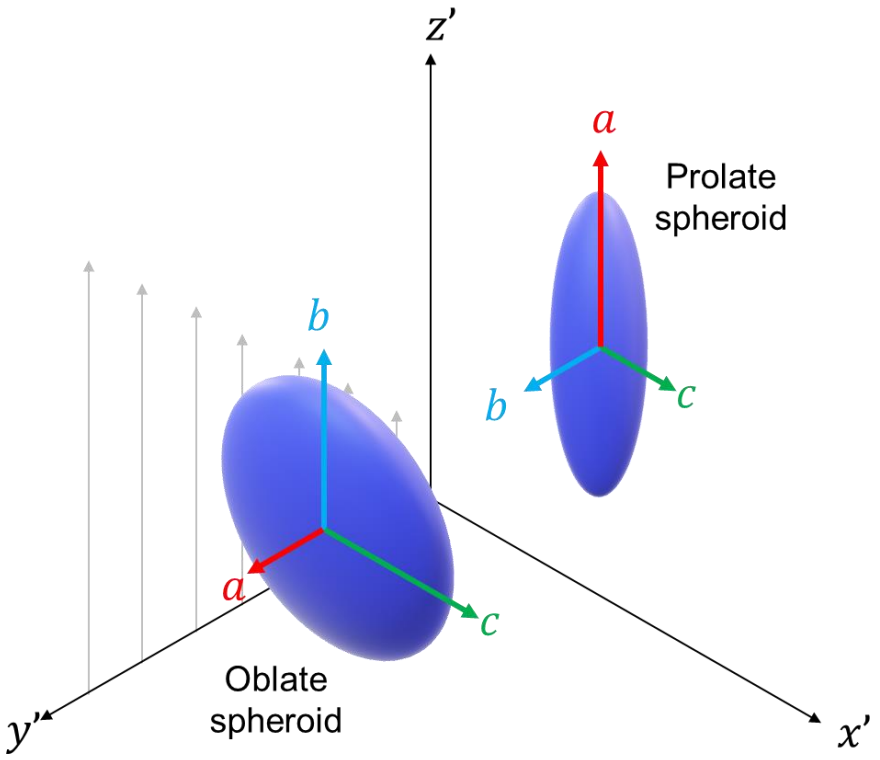

Figure 2.3. Preferred orientations of prolate and oblate spheroids in the Jeffery coordinate system. Preferred orientations are at ϕ = 90° for prolate spheroids and ϕ = 0° for oblate spheroids.

For a population of identical particles, the direction and degree of preferred orientation is periodic. Each particle has the same rotation period T, so the population returns to its starting conditions every T seconds (Ildefonse et al., 1992; Ildefonse et al., 1997; Mueller et al., 2010). However, such cyclicity is unlikely to arise in nature. Magma within dykes carries phenocrysts with a range of shapes and aspect ratios, all of which will have different rotation periods. As such, crystal alignment within dykes cannot be expected to be periodic. If there are multiple sub-populations of crystals present, these will each oscillate according to their own rotation periods (e.g., Willis, 1977; Arbaret et al., 1996); however, this is still a simplification. It is more likely that a crystal population will contain a continuous range in r_e, and this leads to the development of a stable particle alignment.

If a population contains a range of r_e, each particle will have a slightly different value for T. Every particle will rotate out of sync, resulting in a preferred orientation that stays approximately constant. However, it takes a critical amount of strain for this stability to emerge. If there is a low standard deviation in r_e, the first few particle rotations will be almost synchronised. As strain increases, this synchronicity will decay, and eventually the alignment of the population will appear stable (Mueller et al., 2010). As such, we expect crystals within magma to attain a stable degree of alignment after a critical amount of strain.

2.2.3 Limitations in magmatic settings

The Jeffery equations provide the theoretical basis for interpreting flow conditions from crystal alignment. Some authors have tried to infer total strain by assuming that the degree of alignment will increase and the direction of alignment will approach the flow direction as strain increases towards $\gamma_T/2$ (e.g., Ildefonse and Fernandez, 1988; Fernandez and Laporte, 1991). However, it is difficult to justify this approach for dyke textures, where crystals have been transported considerable distances and are likely to have experienced multiple rotations by the time they are solidified in place. It is therefore impossible to estimate strain from crystal orientations because we cannot assume their starting conditions or the window over which their alignment evolved.

Numerous authors have verified the Jeffery equations experimentally by tracing the motions of particles within flows (e.g., Willis, 1977; Ildefonse and Fernandez, 1988; Stover et al., 1992; Arbaret et al., 1996). Further theoretical investigations have shown that the Jeffery equations describe the motions of almost any axisymmetric body (Bretherton, 1962), and that complex shapes can also be approximated as ellipsoids (Arbaret et al., 2001). However, applying the Jeffery equations to geological settings remains questionable due to one key violation of the initial assumptions. Crystals suspended in melts do not always rotate in isolation. In many cases, crystal volume fractions are high enough that collisions and interactions are inevitable, and as such, the Jeffery equations cannot reasonably be applied.

Crystal interactions impact texture development in several ways. Firstly, the creation of particle clusters leads to erroneous orientations, as the cluster rotates as a single object (Arbaret et al., 2019). Even if only two crystals are involved in a collision, they can align in a way that implies the opposite flow direction (Mulchrone et al., 2005). At higher volume fractions, fluid can be channelled through the gaps between clusters, causing localised alignment (Arbaret et al., 2019), and at the highest volume fractions, the suspension starts locking up, leading to narrow shear bands with localised crystal alignment (Picard et al., 2011). Even at particle volume fractions of 0.1-0.2, collisions between crystals interrupt cyclic rotations and cause imbrication, resulting in a stable particle alignment at an angle to the flow (Arbaret et al., 2007; Arbaret et al., 2013). However, the processes controlling the magnitude of this imbrication angle are not well understood (Rees, 1968).

The other key limitation of the Jeffery equations in magmatic settings is that they apply only to fluids with a constant viscosity. Dykes cool and solidify progressively inwards from their edges, capturing crystal textures immediately ahead of an inwards-migrating solidification front. Viscosity gradients are to be expected, especially at the fast-cooling margins, and the Jeffery equations cannot describe particle motions in these conditions. Crystals will rotate as they are being captured, but to our knowledge, we are the first to explore the impact of this process on crystal textures.

2.3. Methods

2.3.1 Experimental procedure

Our analogue experiments are designed to simulate the progressive inwards cooling and solidification experienced at the margins of magmatic intrusions. We use sugar as an analogue for magma, and mica flakes as an analogue for suspended tabular phenocrysts. The molten sugar cools to form a glass, capturing the textures of the particles inside, and we shear each sample to explore the relationship between cooling rates and strain rates.

Molten sugar containing < 5 wt.% water is a low-viscosity liquid at 140-150 °C, but cools to an amorphous solid at room temperature. The precise melting point of sucrose, which forms the majority of our sugar mixture, is debated (Lee et al., 2011). Confectionary sugar glass is typically created by making an aqueous sugar solution and then boiling off the water, before allowing the molten sugar to cool rapidly. Adding water stops the sugar burning and caramelising in the pan, which makes the procedure safer, and also allows more consistency between batches, because the manufacturing process is slower and allows changes in rheology and water content to be monitored more easily. Boiling the sugar solution at 140-150 °C, referred to as the "hard crack stage" by confectioners, reduces the water concentration to < 5 wt.%, which in turn raises the glass transition temperature of the mixture, so that it forms a glass at room temperature (Hartel et al., 2011).

The viscosity of our molten sugar mixture is highly temperature dependent. We measured the viscosities of three batches at a range of temperatures between 60 and 135 °C in an Anton-Paar MCR702 rheometer, using a narrow gap concentric cylinder apparatus. By running flow curves at a range of strain rates, we established that the molten sugar is Newtonian, as shear stress is directly proportional to strain rate. As there is no way to measure the temperature within the cylinder directly, we ran flow curves until the viscosity plateaued out to a stable value, indicating that the sample had reached the target temperature. We then took the average of the plateaued viscosity values over a range of strain rates, and the results are shown in Figure 2.4. For temperatures ≥100 °C, we used strain rates between 0.1 and 100 s^{-1}, but for the lower temperatures a range of 0.01 to 1 s^{-1} was used to avoid shear-induced crystallisation. We use the power law fitted by the trendline function in Microsoft Excel, and find that

$$\mu = 10^{22.00} T^{-10.37} \qquad \text{Eq. 2.6}$$

where μ is viscosity in Pa s, and T is temperature in °C. The sugar solidifies at 60 °C. It can be sheared at this temperature long enough to measure the viscosity, but then the mixture locks up within a few minutes, even at the lowest strain rates.

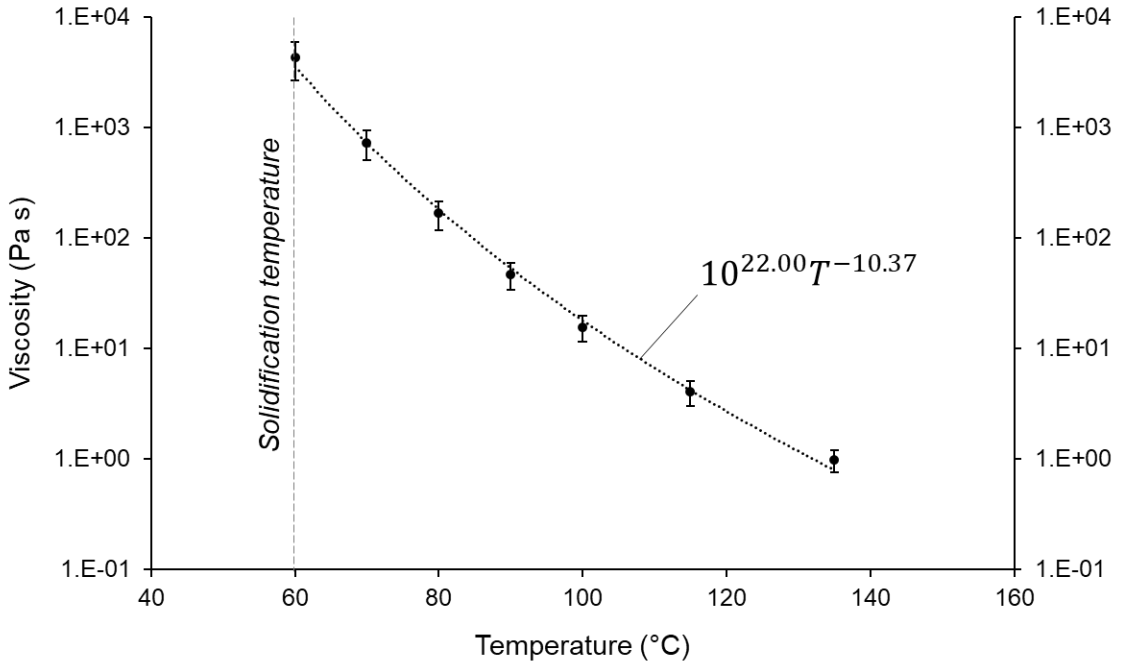

Figure 2.4. Viscosity of molten sugar against temperature. A constant viscosity could be measured at 60 °C, but after a few minutes, the molten sugar suddenly locked up and became solid. As such, we define 60 °C as the approximate solidification temperature.

Each batch of sugar glass in our experiments started as a sugar solution containing 170 g caster sugar (sucrose), 70 g glucose syrup, and 50 g water. We used a high-sided pan on a hot plate in the lab, but the process is the same as making confectionary sugar glass in a pan on the hob. We found that adding glucose syrup reduced crystallisation and burning within the pan. The sugar and syrup were allowed to fully dissolve in the water, keeping the solution at a low-medium temperature (~80 °C) without bubbling or boiling. Once all the sugar crystals had dissolved, the suspension was brought to a high temperature to boil off the water. The temperature of the solution in the pan increased as the water was boiled off.

The solution was raised to 145 °C to ensure that water concentrations were < 5 wt.% (Hartel et al., 2011). However, due to temperature differences across the pan, ascertaining a representative temperature with a thermometer is difficult. A more reliable test for water concentration is the "drop test", where a teaspoon of stirred sugar solution is taken straight from the pan and dropped into cold water. If the sugar instantly solidifies (impossible to deform under pressure, snapping rather than bending), it has reached the "hard crack" stage. We used same test with the same sized drop each time. Other indications of water concentration include the amount of bubbling within the pan, which decreases over time, and the colour of the sugar, which starts caramelising at temperatures >145 °C, leading to a golden-brown colour. We therefore used multiple lines of evidence to ensure consistency between our samples.

Once the “hard crack” stage was reached, the sugar solution was taken off the heat and allowed to rest. At this stage, bubbles would nucleate in the solution if it was disturbed. Dragging a stirrer through the solution resulted in a chain of bubbles nucleating and growing in its wake. This behaviour became less pronounced as the solution cooled. After two to three minutes, bubbles no longer nucleated when the solution was stirred, and this was when particles were added. We added the particles late so that they didn’t act as sites for bubble nucleation or crystallisation. It should be noted that our final sugar samples contained some steam bubbles, but these were small and sparse enough that they did not significantly influence the particle textures.

Our particles are flakes of biotite mica, sieved to be within the size range 0.25-0.50 mm. These were gently mixed into the molten sugar as quickly and efficiently as possible, because stirring the sugar solution excessively at this stage causes shear-induced crystallisation. The sugar-mica suspension was then poured into plastic cups and placed into the rheometer, all within three minutes of leaving the hot plate. We measured the sugar at this stage to be around 135 °C. Subsequent x-ray scans of the sample reveal that the particle volume fraction is < 0.01.

The Peltier cooling unit in the rheometer was set to a fixed temperature of 5 °C, so each sample solidified at the same rate. However, when a hot sample entered the rheometer, the cooling system temperature rose to around 15 °C in response, and there was a lag of 11 minutes before it returned to the specified temperature. As such, the wall temperature of the sample was not a consistent 5 °C, but the variation in wall temperature was consistent between samples.

Once in the rheometer, the stirring rod was introduced to the sugar. We used a wooden rod to minimise the conduction of heat from the sample, and to provide a suitable density contrast in the subsequent x-ray CT scans. The rod was lowered until there was 10 mm of clearance in the base of the cup, and then stirring commenced. The cup and stirring rod are shown in Figure 2.5. Most samples were either sheared at a constant rotation rate or a constant shear stress. One sample remained unstirred, to provide a baseline against which stirred samples could be compared. This is because some degree of particle alignment occurred as the sample was being poured into the cup, and subtracting the alignment of the unstirred sample from the stirred samples allows us to isolate the effects of cooling and stirring rates. Another sample remained unstirred until 12 minutes, before stirring commenced at a fixed rate, and another sample was stirred at a fixed rate, but had the stirring direction reversed at 12 minutes. Finally, an additional sample was created with a particle volume fraction of approximately 0.1, to explore the effects of particle collisions. A list of experimental parameters is given in Table 1.

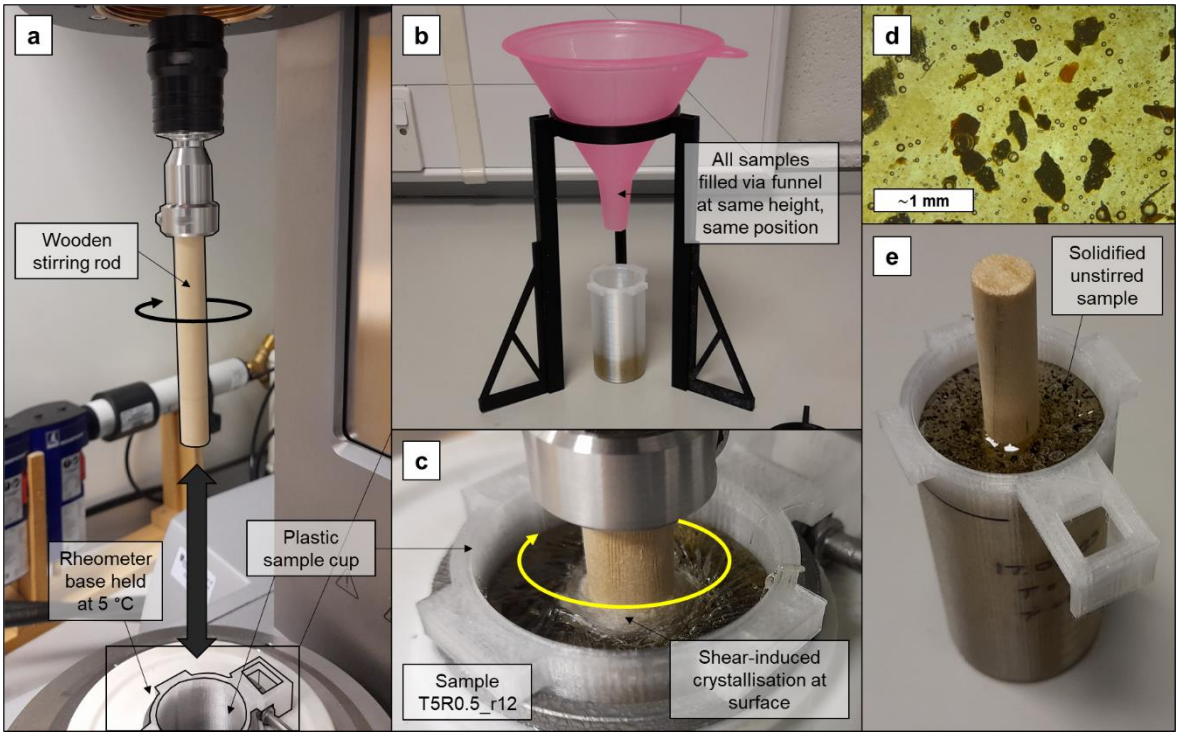

Figure 2.5. Summary of the process used to create sugar glass samples: a) rheometer setup with stirring rod and plastic sample cup; b) sample filling procedure; c) closer view of sample being stirred; d) sugar sample under the microscope; e) solidified sample removed from the rheometer.

Table 1. List of experiment names and parameters.

Name	Temp. [°C]	Constant stir rate [rad/s]	Constant shear stress [Pa]	Additional notes
T5-R0	5	0	n/a	Unstirred sample
T5-R0.1	5	0.0334	n/a	
T5-R1	5	0.334	n/a	
T5-R10	5	3.34	n/a	
T5-S1	5	n/a	1	
T5-S10	5	n/a	10	
T5-S100	5	n/a	100	
T5-R1-p12	5	0.334	n/a	Stirring started at 12 min
T5-R0.5-r12	5	0.167	n/a	Stir direction reversed at 12 min
T5-R1-pvf0.1	5	0.334	n/a	High particle volume fraction

We ended stirring once the sample solidified. This was determined either when the rod detached from the solid sugar, leading to zero torque being measured, or when the sugar became so solid that the rheometer could no longer turn the rod. We note that the surface of the sample cooled faster than its interior, and so the development of a solid skin could lock the stirring rod in place while deeper regions of the sample remained molten. However, the surface cooled at a similar rate between all samples, so this end condition was broadly consistent between them. Only in sample T5-R10 ($\omega = 3.34\ rad/s$) did we end stirring early due to shear-induced crystallisation.

Samples were left in the rheometer at 5 °C for 20 minutes once stirring ended, to ensure that they were fully solid before being removed. Extracted samples were then scanned by Neil Tunstall at the Geography Department at Durham University (Geotek Vertical X-ray CT System, Thermo Kevex PsX10-65W x-ray generator, 100 kV x-ray voltage, 500 μA current). We stored samples in an air-tight container with silica gel to absorb moisture, but the surface of the sugar still reacted with water in the air. Water lowers the glass transition temperature of the surface layer, prompting crystallisation that spreads deeper into the sample. As such, all samples were scanned within six weeks of being made, to avoid crystallisation or dissolution modifying their textures.

2.3.2 Scaling considerations

Our experiments are designed to explore the effects of progressive inwards cooling on particle alignment, and so they do not need to scale perfectly with conditions in magmatic dykes. What matters most is not the absolute viscosity of the sugar, but the balance between cooling rates and strain rates, and the ratio of the viscosity gradients relative to the size of the particles. Viscosity gradients vary spatially and temporally within dykes, so the conditions within our sugar sample will relate to some time or position within a dyke containing phenocrysts of a given size. However, the aim of our experiments is not to simulate a specific part of the dyke system, but to demonstrate how the balance between cooling rates and strain rates influences particle textures.

It should also be noted that the cylindrical geometry of our samples influences the conditions of shear. The velocity profile across the radius of the molten sample follows the equation

$$v(r) = \omega\, R_i \left(\frac{\frac{R_o}{r} - \frac{r}{R_o}}{\frac{R_o}{R_i} - \frac{R_i}{R_o}} \right), \qquad \text{Eq. 2.7}$$

where v is velocity, r is radial position, ω is the rotation rate of the stirring rod in rad/s, R_i is the radius of the stirring rod (inner cylinder), and R_o is the internal radius of the sample cup (outer cylinder). The derivation of this equation is outlined in Appendix A. The molten sugar within the sample is therefore not undergoing simple shear (Figure 2.6). However, on the 0.25-0.50 mm length scale of individual particles, this slight curve in the velocity profile should be insignificant, especially when the greater modification to the velocity gradient comes from cooling and solidification.

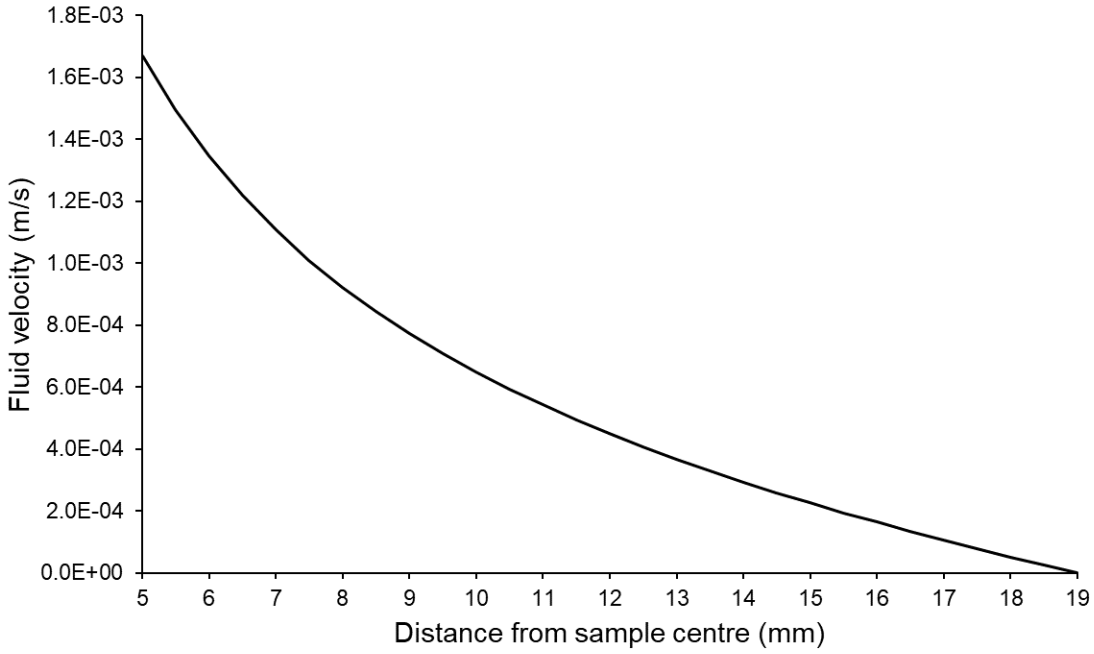

Figure 2.6. Velocity profile across the radius of the sample at a constant stirring rate of 0.334 rad/s.

2.3.3 Particle analysis

X-ray CT scans of each sample have a voxel resolution of 0.0272 mm, which is around a tenth of the smallest particle diameter (0.25 mm). The mica has a much higher density ($\sim$3 g cm^{-3}) than the sugar ($\sim$1.6 g cm^{-3}), and so distinguishing mica, sugar and air bubbles is straightforward based on brightness thresholds within the x-ray images. We used Avizo (ver. 2022.1, ThermoFisher Scientific) to reconstruct and analyse particle volumes (Figure 2.7). Measurements of centroid position, orientation, volume, and surface area were exported from Avizo for further analysis in MATLAB (ver. 9.9.0 (R2020b), MathWorks).

We also collected images of the reconstructed particles in each sample, viewed from above, as well as cross-section images through the sample centre, taken in the $x_A z_A$ plane and the $y_A z_A$ plane. Here, we introduce the axes x_A, y_A and z_A as the global axes used in Avizo, where z_A is vertical, and x_A and y_A are perpendicular on the horizontal plane with arbitrary directions. The cross-sections allow us to measure the orientations of the stirring rod and cup walls, which in turn allow us to correct the orientation of the sample (Figure 2.8), which was rarely perfectly upright within the scanner. We had to correct particle positions and orientations so that the stirring rod axis was vertical, allowing us to convert global orientations measured in Avizo to local orientations in the Jeffery coordinate system.

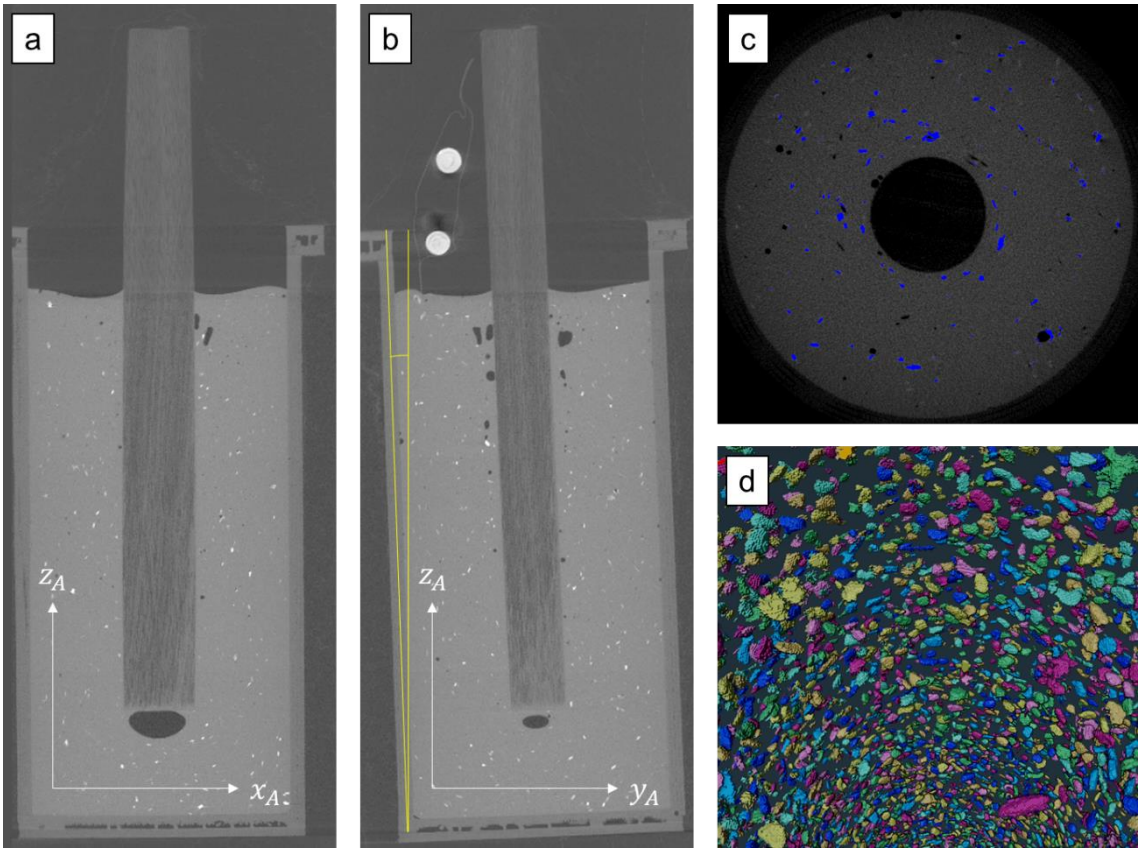

Figure 2.7. Summarising the process of extracting particle data from x-ray CT images: a) and b) vertical cross-sections showing the slight misalignment of the sample inside the scanner; c) example of thresholding the sample by brightness to isolate the mica flakes; d) volume rendering of isolated mica flakes within Avizo (voxel dimensions 0.0272 mm, particle size 0.25-0.50 mm).

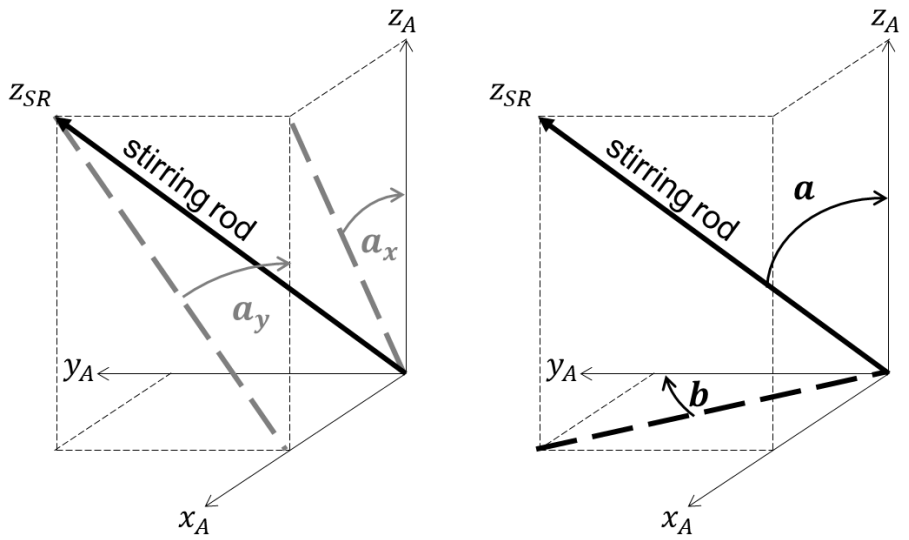

Figure 2.8. Exaggerated schematic showing the correction process to put the stirring rod in a vertical position. Angles a_x and a_y are measured from cross-sections in the $x_A z_A$ and $y_A z_A$ planes respectively (left). The correction involves rotating the sample by two angles, a and b (right).

The correction procedure is as follows. We first define the stirring rod axis as the z_{SR}-axis. The sample starts in a position where the z_{SR}-axis is at an angle to the vertical z_A-axis. We rotate all particle positions and orientations by correction angle b around the z_A-axis until the z_{SR}-axis lies within the $y_A z_A$-plane (global north-vertical). All particle positions and orientations are then rotated by correction angle a around the x_A-axis (global east), until the z_{SR}-axis aligns with the z_A-axis. This is shown schematically in Figure 2.8, and with real data from sample T5R1 in Figure 2.9.

Correction angles a and b are calculated from angles a_x and a_y, which are the angles of the cup walls/stirring rod measured from the vertical in the $x_A z_A$ and $x_A y_A$ plane respectively. The correction angles are calculated as

$$b = \text{atan}\left(\frac{\tan(a_x)}{\tan(a_y)}\right), \quad \text{Eq. 2.8}$$

and

$$a = \text{atan}\left(\sqrt{\tan^2(a_x) + \tan^2(a_y)}\right). \quad \text{Eq. 2.9}$$

The uncorrected particle orientations measured in Avizo are described by two Euler angles, θ_{SR} and ϕ_{SR}, measured from the x_{SR}-axis and z_{SR}-axis respectively. To correct these particle orientations to be measured from the x_A and z_A axes instead, we convert the Euler angles into points on a unit sphere, defined by coordinates (x_a, y_a, z_a). These coordinates are calculated as follows:

$$x_a = \cos(\theta_A)\sin(\phi_A), \quad \text{Eq. 2.10}$$

$$y_a = \sin(\theta_A)\sin(\phi_A), \quad \text{Eq. 2.11}$$

and

$$z_a = \cos(\phi_A). \quad \text{Eq. 2.12}$$

These points are then rotated using the same process used for the particle positions. Once the new, rotated points have been found, the corrected Euler angles θ_A and ϕ_A are calculated using Eqs. 2.10-2.12.

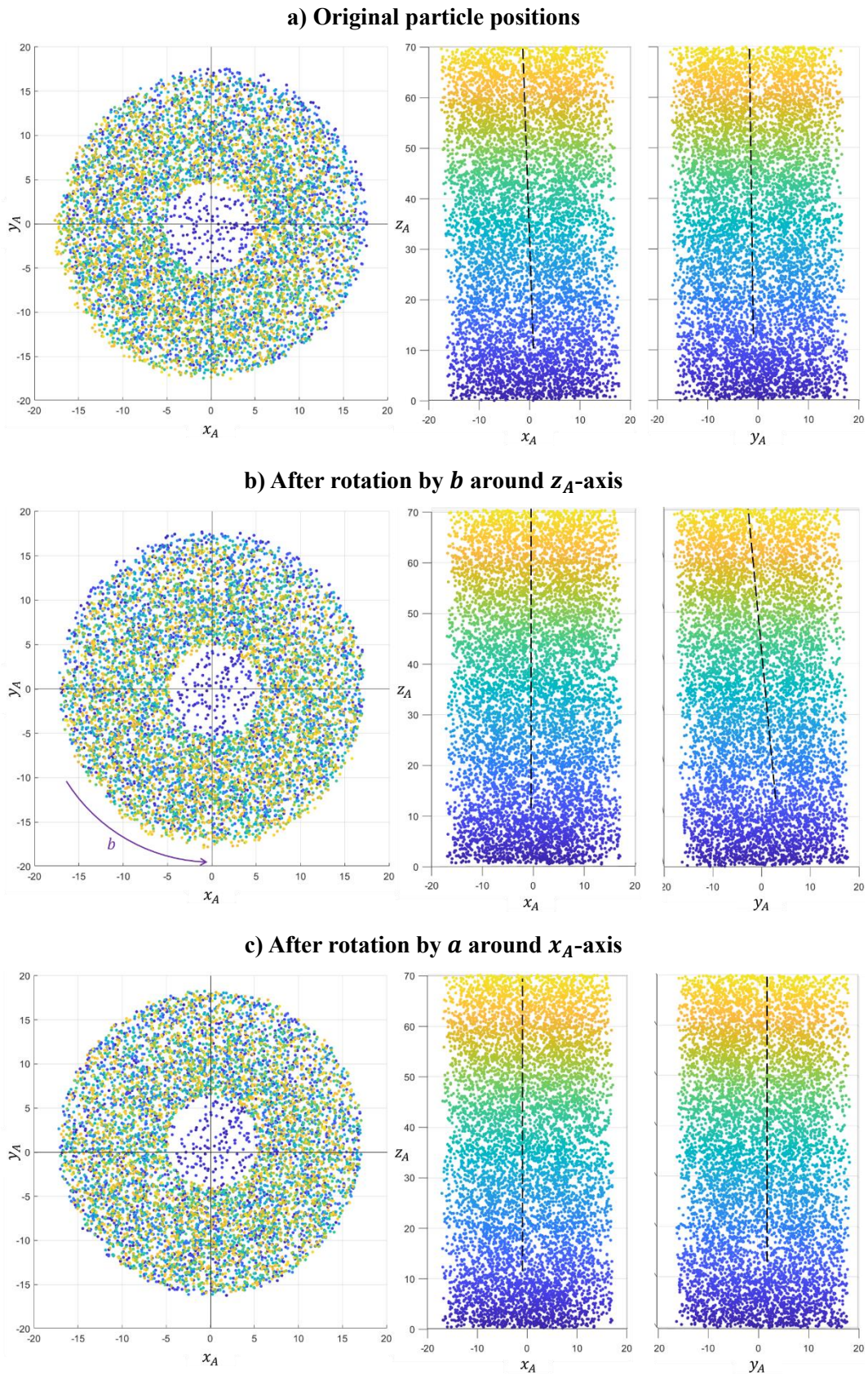

Figure 2.9. Correcting the orientation of sample T5R1, showing the centroid positions of particles measured in Avizo, where colour indicates particle height to give a sense of depth: a) original orientations, with the rod at an angle; b) particle positions after rotating around the vertical axis by angle b; c) final position, after rotating by angle a around the x_A-axis, resulting in the rod being completely vertical.

The rest of the particle shape analysis was conducted within MATLAB. Here, particle data was filtered by volume to exclude artefacts and particle clusters. The modal particle length measured in Avizo is 0.65 mm, and the modal particle thickness is 0.25 mm. If we approximate the particles as tabular cuboids, their modal volume should be in the range 0.021-0.055 mm^3. As such, the maximum volume included in the analysis was 0.0825 mm^3, 50% larger than 0.055 mm^3, to exclude most particle pairs or clusters. The minimum volume included in the analysis was 0.002 mm^3 (~100 voxels). Volumes smaller than this have missing or unreliable orientation measurements. Particles positioned beneath the depth of the stirring rod were excluded, as were particles within 5 mm of the surface, which would have been impacted by significant vertical thermal gradients, as well as the accumulation of large bubbles and later crystallisation.

We note that the sizes of particles measured in Avizo are larger than expected, as the particles were sieved to be within the range 0.25-0.50 mm. This is likely due to brightness shadows around the particles in the scans, resulting in an overestimate of their size when brightness thresholds are applied. This will have no significant impact on the measured orientations of particles; however, aspect ratios calculated from measured dimensions are likely to be closer to one than in reality. We also note that the brightness and contrast is different in each scan, and so each image required a different threshold to isolate the particles. Although this adds some additional uncertainty to the measured dimensions of particles, it does not impact measured orientations.

The most meaningful orientation measurement for particles is the orientation of their minor axis. The thickness of particles is their most consistent dimension, and so the minor axis is the most robust measure of particle orientation. Additionally, we can approximate the mica flakes as oblate spheroids, so the orientation of their minor axis is directly comparable with the rotational axis in the Jeffery equations (Section 2.2).

To compare our experimental results with theory, we convert our measurements to use the coordinate system of the Jeffery equations. Jeffery angles θ and ϕ (Section 2.2.1) are measured relative to the flow directions, but within our samples, flow direction is always perpendicular to the cup radius, so varies with position. The process by which we convert the particle orientations measured in Avizo to local orientations is outlined in Figure 2.10.

Orientations measured in Avizo are defined by two angles. θ_A is the angle from the x_A-axis (east), and ϕ_A is the angle from the z_A-axis (vertical). The Jeffery angles, to which we now add subscript "J", define θ_J as the angle from the x'-axis, and ϕ_J as the angle between the $x'x$ plane and the $y'z'$ plane (Figure 2.1). A comparison of the global and local coordinate systems reveals that $\theta_J = \phi_A$. However, finding ϕ_J requires the bearing b of the particle, relative to the global axis y_A (north), to provide the orientations of the y'- and z'- axes. We calculate ϕ_J as $\theta_y - b$, where $\theta_y = 90 - \theta_A$.

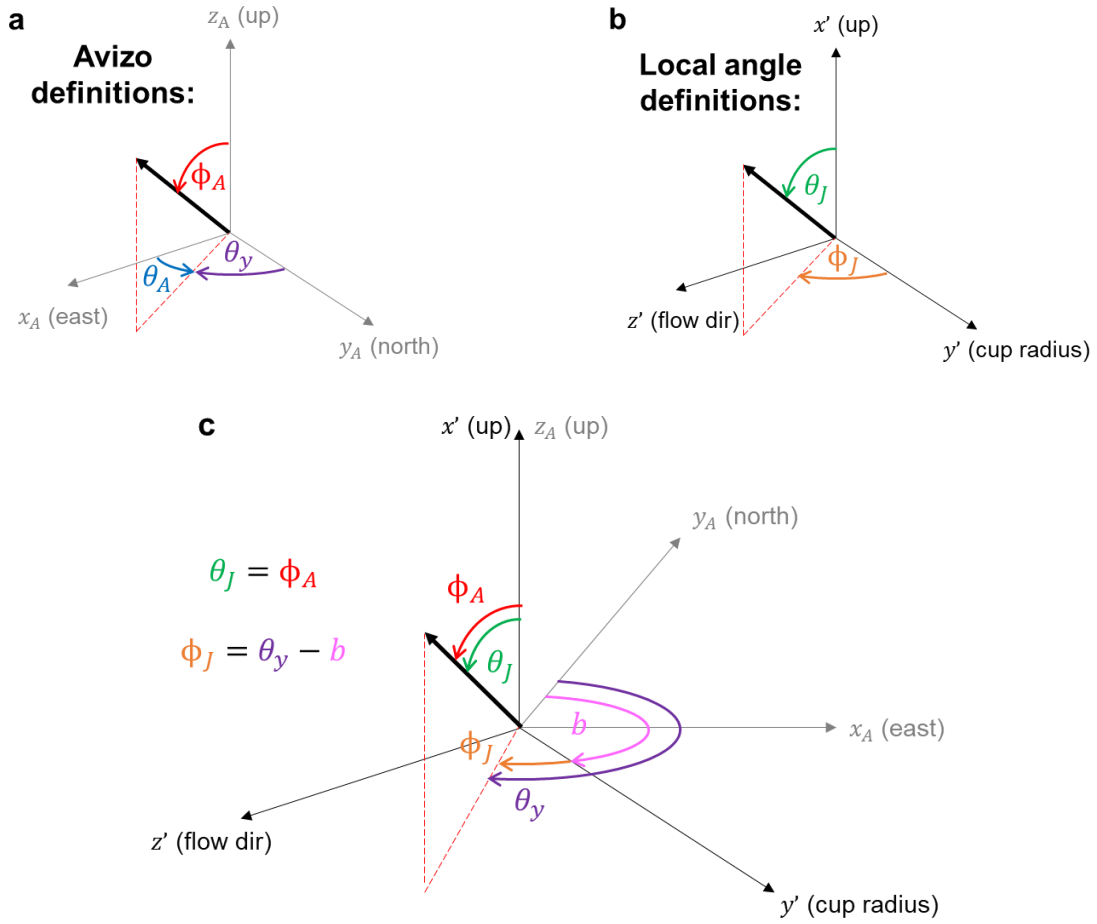

Figure 2.10. Angle conversions between orientations measured in Avizo from global axes (subscript *A*), to local orientations given relative to the flow direction, using the conventions of Jeffery (1922) (subscript *J*). Global, fixed axes are shown in grey, while local, position-dependent axes are shown in black. Particle orientation is shown by a thick black arrow. The bearing b and the angle θ_y, measured from the y_A axis (north), are required to convert between the coordinate systems.

The next step in our particle analysis is to quantify the degree of local orientation, and to explore how this varies between the stirring rod and the cup wall. We have found that a tensor approach is the most robust measure of preferred orientation in three dimensions, which involves finding the ratios of the principal eigenvectors for a distribution of orientations (Woodcock, 1977). The tensor approach accounts for the three-dimensional nature of orientations without considering θ_J and ϕ_J separately, as would be the case with circular means (Jammalamadaka and SenGupta, 2001).

We calculate the direction and degree of particle alignment as follows. Each particle orientation may be expressed as three angles from the x', y' and z' axes, the cosines of which are l, m and n respectively. These cosines are used to construct a 3x3 matrix, α, where

$$\alpha = \begin{bmatrix} \sum l^2 & \sum lm & \sum ln \\ \sum ml & \sum m^2 & \sum mn \\ \sum nl & \sum nm & \sum n^2 \end{bmatrix}. \quad \text{Eq. 2.13}$$

This matrix α has three eigenvectors, v_1, v_2 and v_3, and three corresponding eigenvalues, λ_1, λ_2 and λ_3, which we calculate in MATLAB using the *eig* function (MathWorks, 2024). The principal eigenvector v_1 gives the direction of particle alignment, and the degree of alignment is quantified by ratios between the three eigenvalues. Normalised eigenvalues s_1, s_2 and s_3 are created by dividing original eigenvalues by the number of particles.

The shape of the distribution of particle alignment is described by parameter K, where

$$K = \frac{\ln (s_1/s_2)}{\ln (s_2/s_3)}. \quad \text{Eq. 2.14}$$

If we visualise particle orientations as points on a unit sphere, these points may be uniformly distributed over the sphere surface, clustered at one position, or spread as a girdle around a plane through the sphere. Parameter K describes this distribution. A cluster is when $s_1 \gg s_2 > s_3$, resulting in values of $K < 1$, and a girdle is when $s_1 > s_2 \gg s_3$, resulting in values of $K > 1$.

The degree of particle alignment is given by parameter C, where

$$C = \ln(s_1/s_3). \quad \text{Eq. 2.15}$$

These parameters are a robust measure of the degree of particle alignment, as they are not sensitive to the population size.

However, the tensor method only works on unimodal distributions. Our particle orientations have a symmetrical bimodal distribution, i.e., a particle with an orientation of $\theta_J = 90°, \phi_J = 0°$ appears identical in orientation to a particle at $\theta_J = 90°, \phi_J = 180°$. While a true circular distribution wraps

from $0° - 360°$, our distribution wraps from $0° - 180°$, and so a natural distribution of aligned particles will have symmetrical peaks at both $\phi_J = 0°$ and $\phi_J = 180°$. As such, we cannot apply our tensor method to the raw data, as these peaks would cancel each other and result in an erroneous preferred orientation, or lack thereof.

To overcome this issue, we present all particle orientations in a form where $0° < \phi_J < 180°$, and then we double these angle values, so that they wrap from $0° - 360°$. This can be envisaged as taking a hemisphere of datapoints and stretching it around the z'-axis to cover an entire sphere. This results in a unimodal transformed distribution, and from here, the tensor method can be used as described; the only difference is that the calculated directions of alignment must be halved, to convert back to real space.

2.4. Results and interpretation

2.4.1 Degree of particle alignment

Images of the particles in Avizo show that the stirred samples have a significantly higher degree of particle alignment than the unstirred sample (Figure 2.11). This is captured by the variation in C across the radius of samples, measured in a 2-mm-wide window at 1 mm radial intervals. For the samples stirred at a constant rate, C values are higher than or equal to the unstirred sample (Figure 2.12a).

A total lack of particle alignment would yield a C value of zero. However, even the unstirred sample displays a level of particle alignment (Figure 2.12a). This is produced when the suspension is poured into the cup, and when the rod is inserted into the sample centre. We take the unstirred sample to represent the initial state of all samples. Based on this, we calculate a new C relative to the unstirred sample, to show the additional alignment that has resulted from stirring (Figure 2.12b).

Constant shear rate

For the samples stirred at a constant rate, we find that the maximum degree of particle alignment depends on the stirring rate used, with faster stirring rates generally resulting in higher degrees of alignment. The degree of alignment is broadly consistent across the width of the unstirred sample, slightly higher at the edges due to particles aligning against the cup walls. In fact, an uptick in particle alignment at the cup walls is seen in all samples (Figure 2.12a). Generally, there is an increase in particle alignment away from the walls, which is clearer in the relative C values that capture only the alignment introduced by shearing. We also find that the sample stirred at the slowest rate shows a greater variation in particle alignment across the sheared region, while the samples stirred faster have C values that increase away from the sample walls, which reach constant, relatively higher values in the half of the sheared region closest to the stirring rod (Figure 2.12b).

Constant shear stress

For the samples stirred at a constant shear stress, the stirring rate declined as the sample cooled and its viscosity increased. For these samples, the degree of particle alignment is generally lower compared to the samples stirred at a constant rate, but still generally higher than the unstirred sample (Figure 2.13). However, the sample stirred with the lowest shear stress of 1 Pa shows considerable overlap in C values with the unstirred sample in its outer half, and so we infer that this region was not sheared enough to produce particle alignment (Figure 2.14a). In the samples stirred at constant shear stresses of 10 and 100 Pa, C values peak halfway across the stirred region, then decline towards the centre. This reduction in alignment can also be seen in the Avizo images, close to the central stirring rod (Figure 2.13).

Sudden change in shear conditions

We also produced two additional samples where the stirring conditions changed partway through the experiment: one where the stirring rate was constant, but the stirring direction was instantaneously reversed after 12 minutes of stirring, and one where the sample remained unstirred for 12 minutes, before stirring started at a constant rate. The degree of alignment is generally lower in these samples (Figure 2.15). Nearer the cup edge, their C values are slightly lower than the unstirred sample, showing that no additional alignment has been produced by shear in this region (Figure 2.16).

In the sample where stirring started after 12 minutes, we see a sharp increase in the degree of particle alignment around 12 mm from the cup centre, moving inwards, where C values start to exceed those from the unstirred sample. Particles within 12 mm of the cup centre were aligned by shear before the sample solidified, implying that the solidification front, separating solid and liquid regions of the sample, was approaching 12 mm after 12 minutes. Small vesicles captured within the sugar also allow the position of the solidification front to be inferred. These vesicles formed from steam bubbles trapped in the molten sugar, and are discussed in detail in the Chapter 3. Vesicles beyond 14 mm from the cup centre are spherical, while those closer to the centre are deformed, suggesting that the outer 14 mm of the sample had solidified after 12 minutes of cooling (Figure 2.17).

For the sample where stirring was at a constant rate of 0.167 rad/s, but direction was reversed at 12 minutes, the degree of alignment is consistent and generally low across the radius of the sample, similar to the sample stirred at a constant 0.0334 rad/s. Based on our findings from the previous sample, we know that the solidification front is 14 mm away from the cup centre after 12 minutes of cooling. Therefore, the solidification front in this sample would have been at 14 mm when the flow direction was reversed. However, we see no significant changes in the degree of alignment at this position; C values remain generally low towards the centre.

High particle volume fraction

For the sample with a particle volume fraction of 0.1, we expect widespread particle interactions to interfere with particle rotation and alignment (Section 2.2.3). Indeed, the degree of alignment is significantly lower compared to the unstirred sample (Figure 2.15; Figure 2.16a). It peaks in the immediate vicinity of the cup edges and the stirring rod, suggesting that most of the width of the sample experienced minor shearing, and that this was concentrated at the edges of the flow. This is also evidenced by the vesicle textures, as vesicles in the intermediate regions of this sample remain largely undeformed. We cannot calculate relative C for this sample because we cannot assume that the unsheared sample at low particle volume fraction represents its initial state.

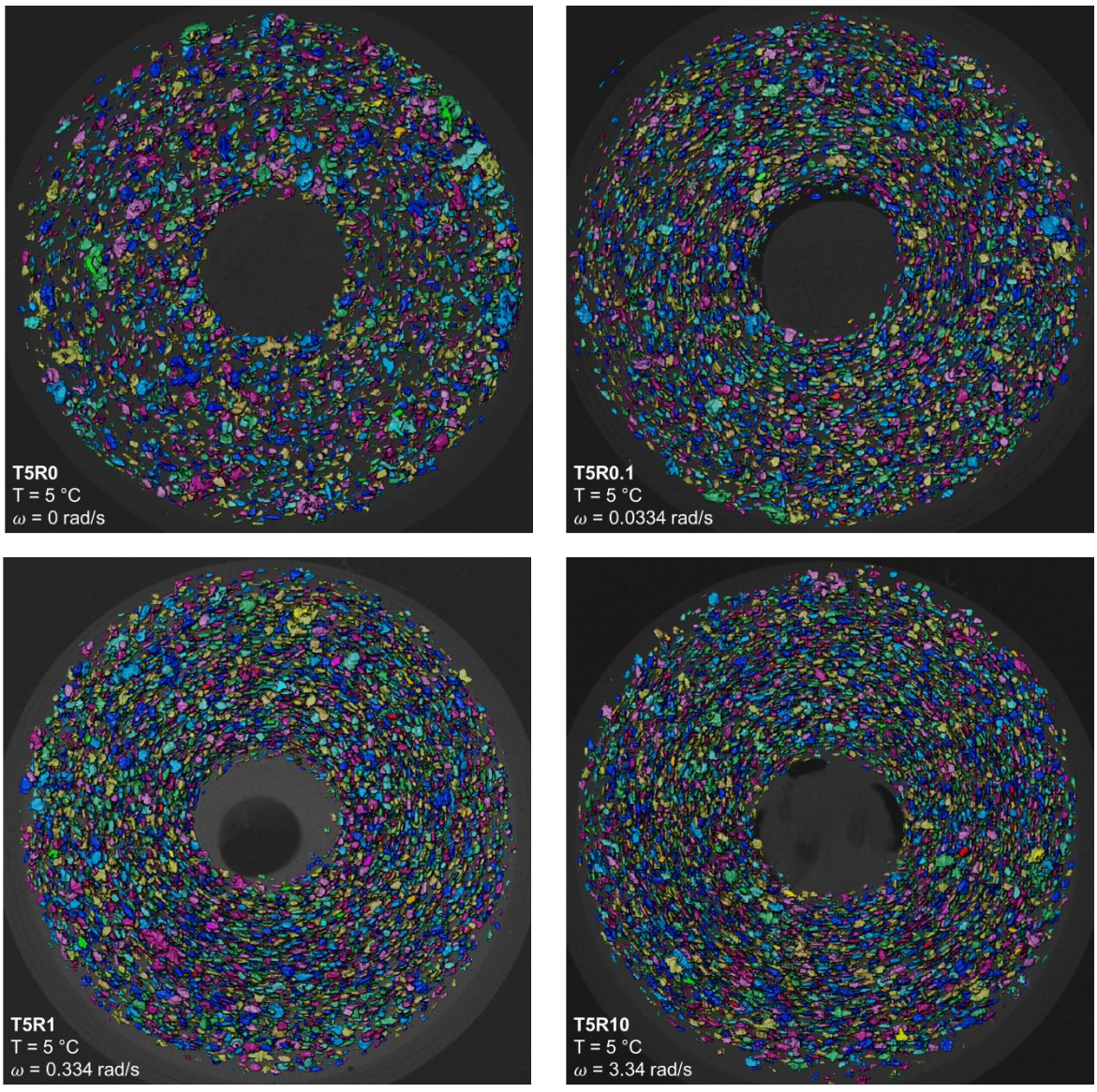

Figure 2.11. Particles in the samples with a constant stirring rate, viewed from above. The stirred samples are noticeably more aligned than the unstirred sample (top left). Note that these images from Avizo have not accounted for the slight misorientation of the sample in the scanner, and as such, the central gap marking the position of the stirring rod is not always perfectly circular.

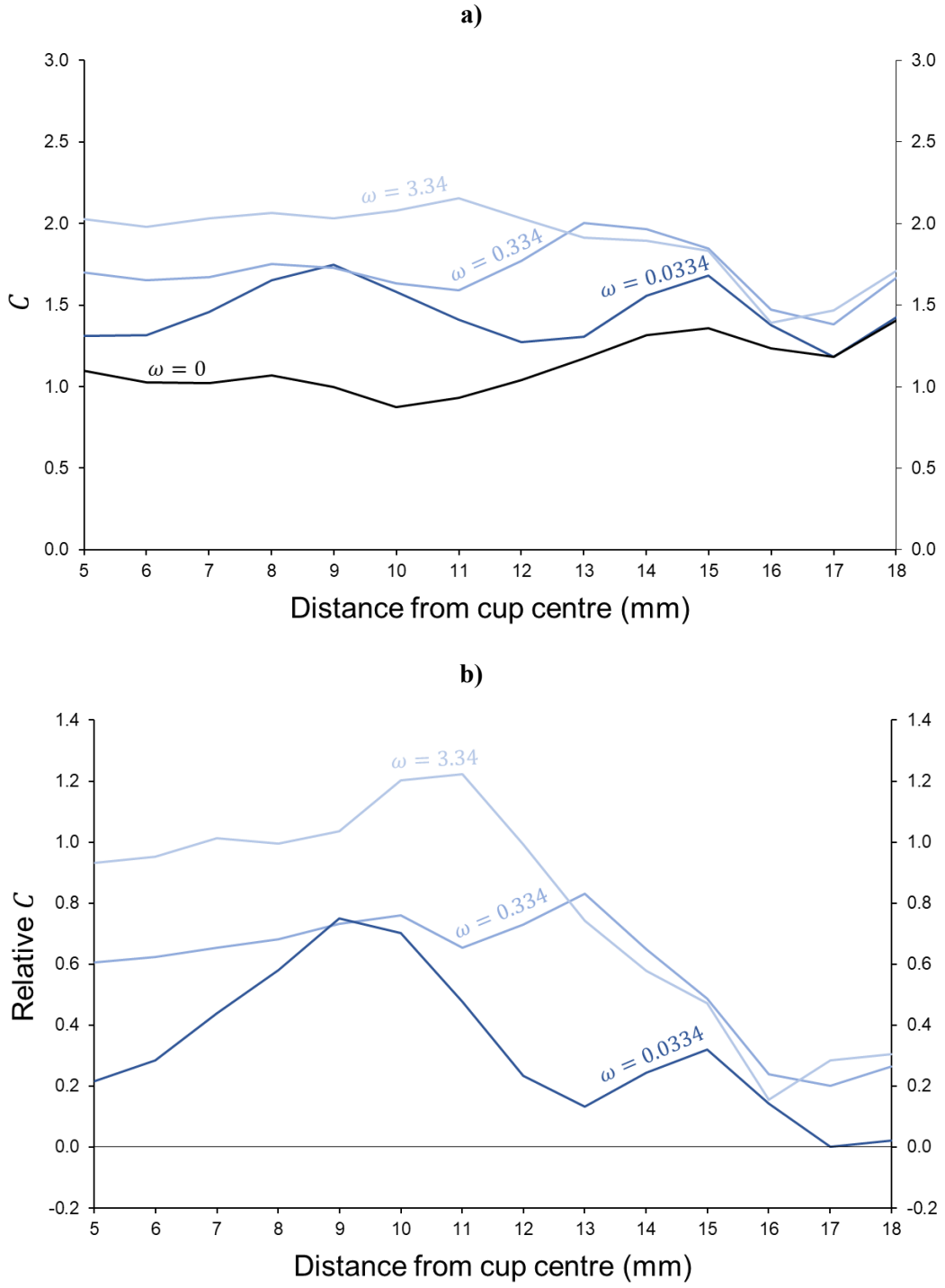

Figure 2.12. a) Variation in the degree of preferred orientation C across the radius of samples stirred at a constant rate (ω is rotation rate in rad/s), and with the same cooling rate; b) variation in relative C, calculated by subtracting the C values of the unstirred sample from the stirred samples.

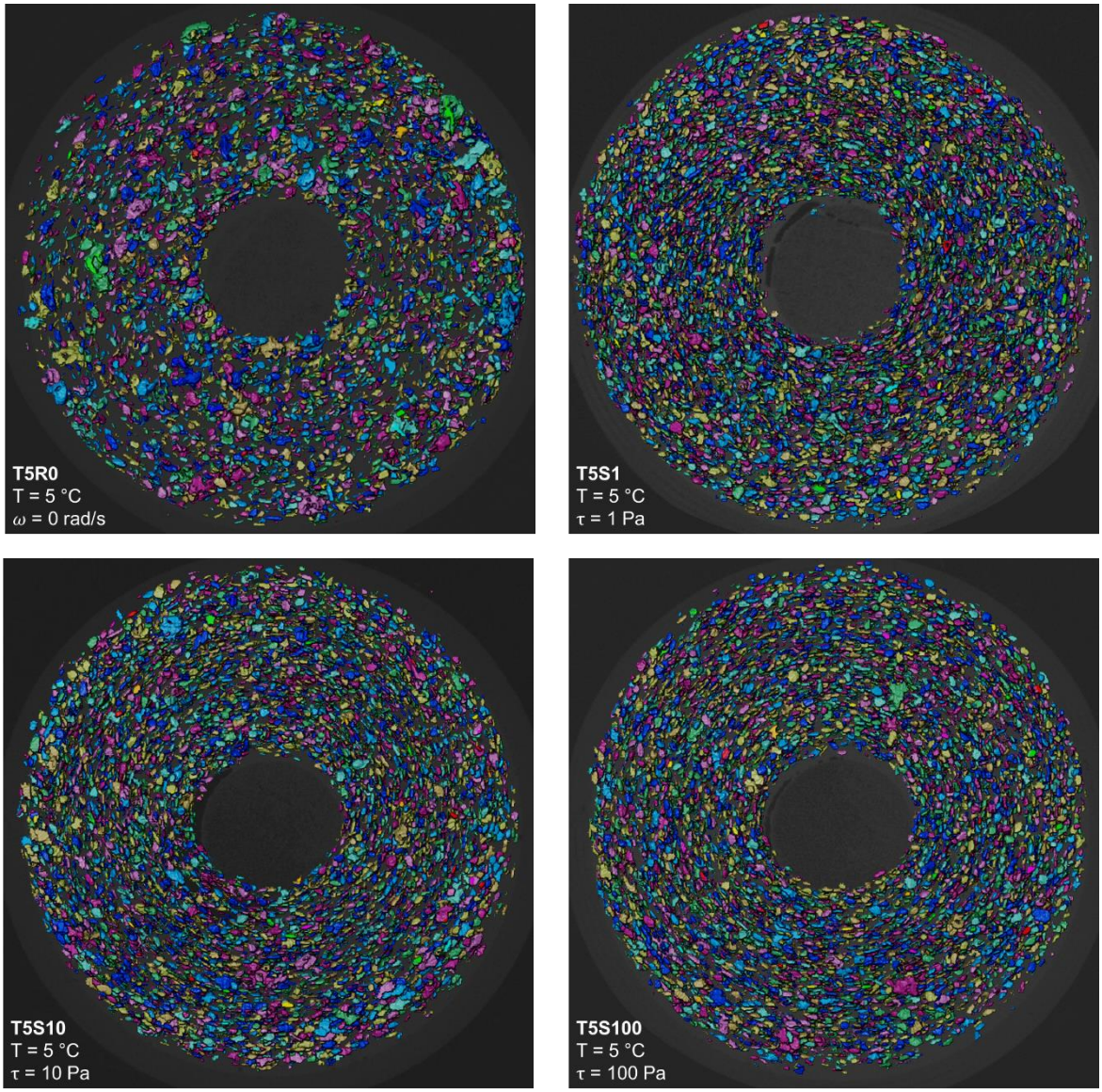

Figure 2.13. Particles in the samples stirred with a constant shear stress, viewed from above. The stirred samples are more aligned than the unstirred sample (top left), but less aligned than the samples stirred at a constant rate (Figure 2.11). Note that these images from Avizo have not accounted for the slight misorientation of the sample in the scanner, and as such, the central gap marking the position of the stirring rod is not always perfectly circular.

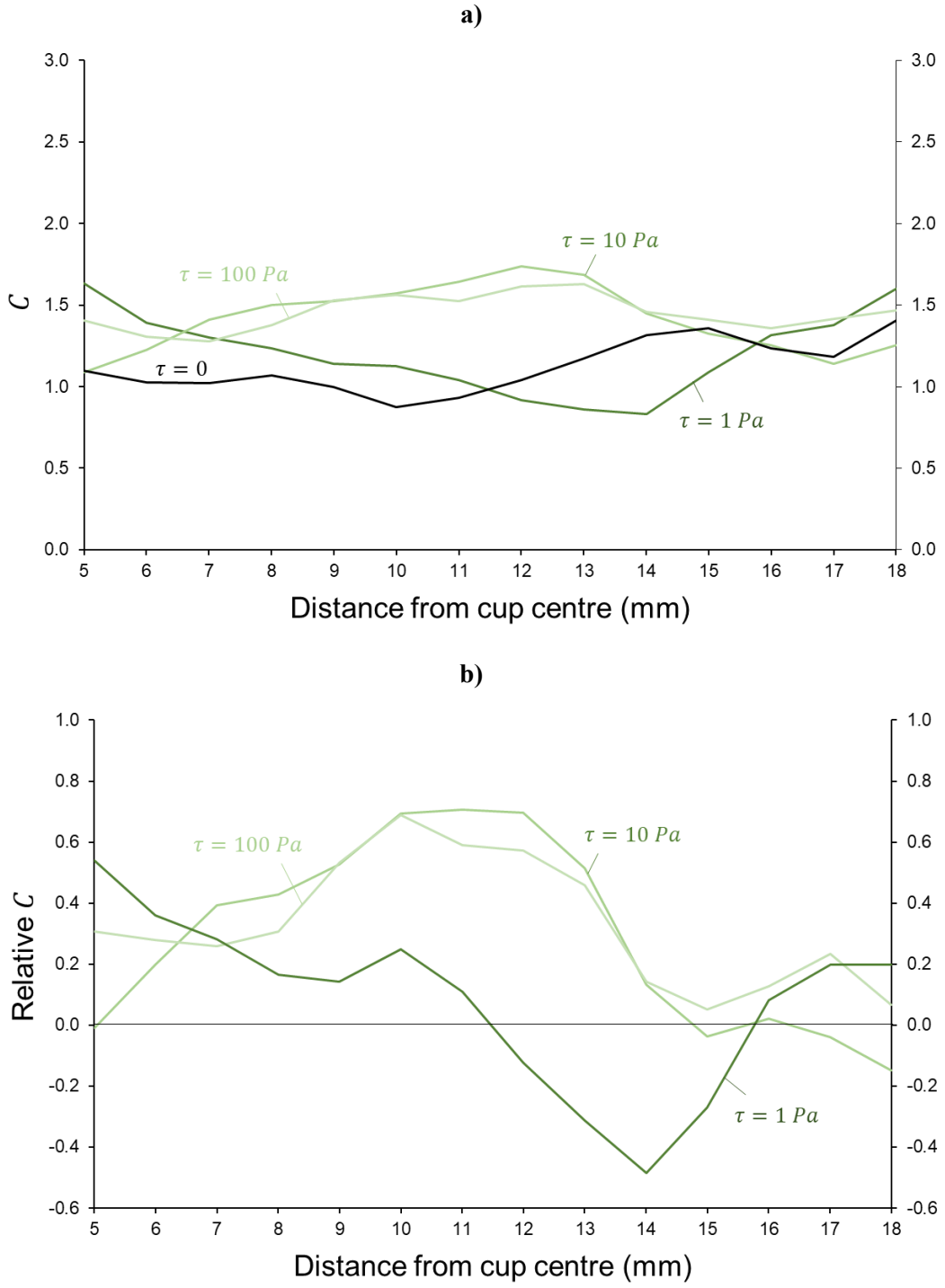

Figure 2.14. a) Variation in the degree of preferred orientation C across the radius of samples stirred at a constant shear stress τ, and cooled at the same rate; b) variation in relative C, calculated by subtracting the C values of the unstirred sample.

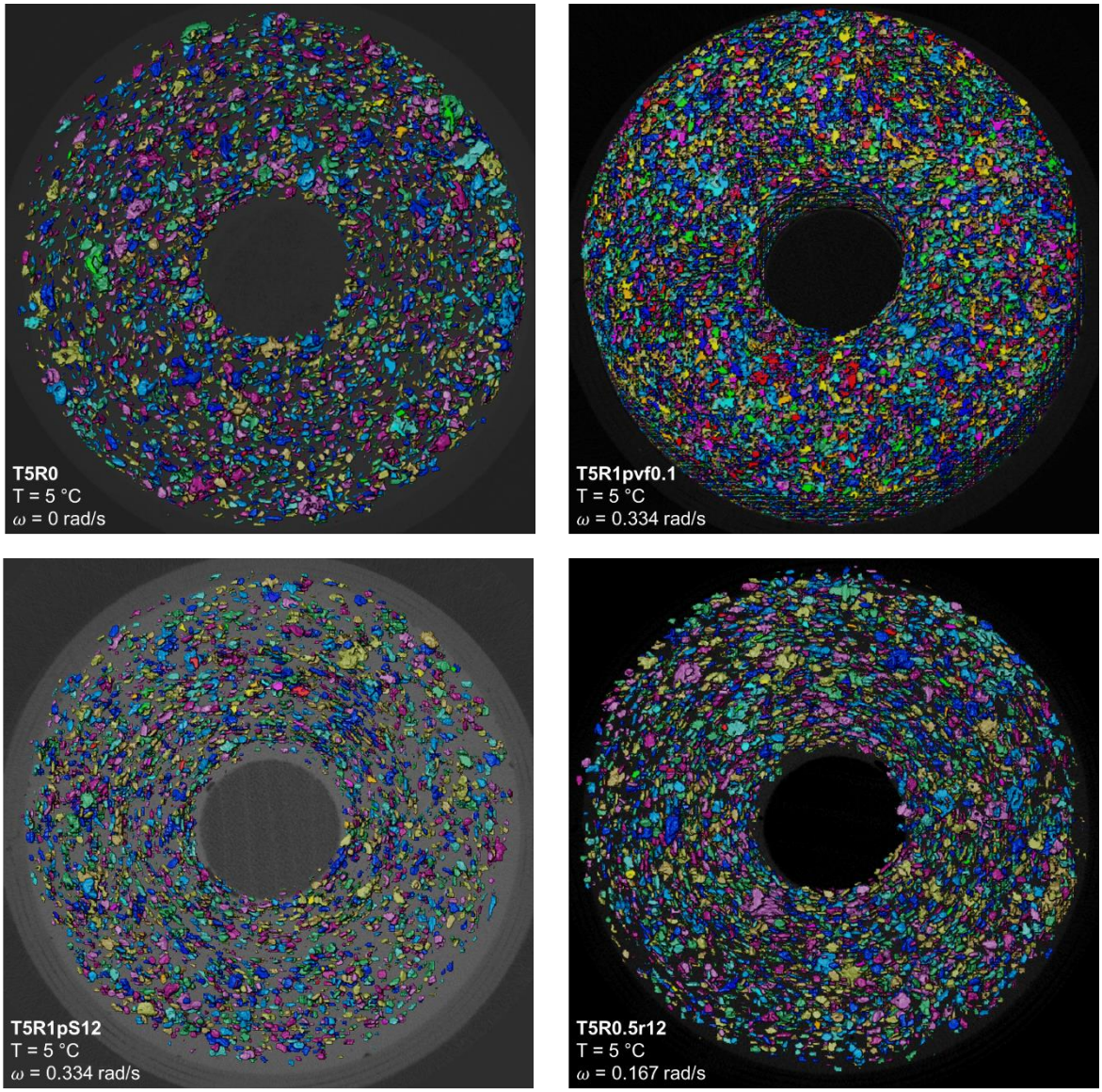

Figure 2.15. Particles in the samples with unique stirring conditions, viewed from above. Unstirred sample is at top left for comparison. Top right: particle volume fraction of 0.1, stirred at a constant rate; bottom left: stirring started after 12 minutes of solidification; bottom right: stirring direction instantaneously reversed at 12 minutes. Stir rate ω is in rad/s. Note that these images from Avizo have not accounted for the slight misorientation of the sample in the scanner, and as such, the central gap marking the position of the stirring rod is not always perfectly circular.

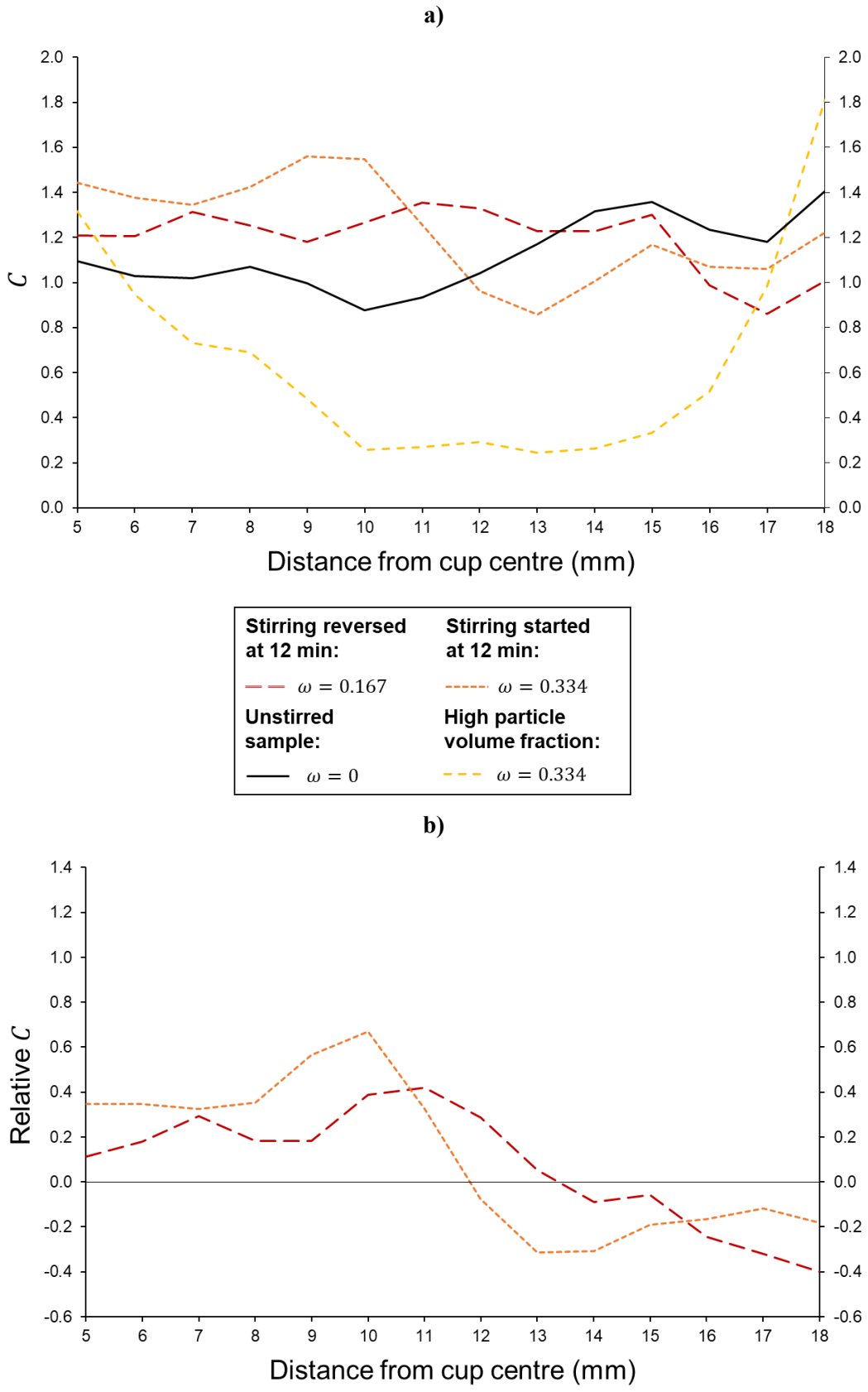

Figure 2.16. a) Variation in the degree of preferred orientation C across the radius of samples with unique stirring conditions, which cooled at the same rate; b) variation in relative C, calculated by subtracting the C values of the unstirred sample. There is no relative C for the high particle volume fraction sample as we cannot assume the unstirred sample to represent its initial state.

2.4.2 Form of particle alignment

The degree of particle alignment can also be described in terms of the shape of the minor axis distribution using parameter K (Section 2.3.3). The Jeffery equations predict oblate spheroids to align with a girdle distribution, so that most x-axes align on the $x'y'$-plane, at $\phi_J = 0°$, but θ_J angles can show more variation around their modal value of $\theta_J = 90°$. For example, particles with an initial orientation of $\theta_J = 0°$ or $\theta_J = 90°$ will remain locked in position, so we should expect a range of θ_J between these extremes. However, if particles have aligned in response to pure shear, in the vicinity of a wall or compressive flow, they will align more strongly, with a cluster distribution. Therefore, we can use K values to show whether alignment is in response to simple shear from stirring, or pure shear from pouring and wall effects.

We find that most stirred samples have girdle distributions with values of $K > 1$, excluding the 2 mm near the cup wall (Figure 2.18). The unstirred sample mostly has clustered distributions with values of $K < 1$, meaning that the particles have aligned due to pure shear as the suspension was poured into the cup. The sample in which stirring only started after 12 minutes shows a transition of K values from below to above one around 12 mm, which is just ahead of where we inferred the solidification front to have been when stirring started. Finally, it is worth noting that the sample with high particle volume fraction shows no preference for cluster or girdle distributions, as the degree of preferred orientation is consistently low. As such, the K values give us confidence that most particle alignment in our stirred samples is shear-induced.

2.4.3 Direction of particle alignment

The direction of particle alignment is described by the two Euler angles θ_J and ϕ_J, the same as for individual particles (Section 2.2.1). Our particles are approximated as oblate spheroids, and the Jeffery equations predict a preferred orientation of $\theta_J = 90°, \phi_J = 0°$. The preferred orientations of particles within our samples generally match these predictions within 10° (Figure 2.19). No sample shows a significant change in the direction of particle alignment across its radius, and no sample shows significant imbrication. Several samples show a greater variation in θ_J close to the cup wall, but this is likely in response to lower degrees of alignment generally. If the degree of alignment is low, then the direction becomes less reliable.

Two samples are worth noting for their direction of particle alignment. Firstly, the sample where stirring started after 12 minutes shows the greatest variation in alignment direction, although the average direction is still $\theta_J = 90°, \phi_J = 0°$. Secondly, the sample with a particle volume fraction of 0.1 shows an increase in θ_J up to 160° in the centre of the stirred region, where the degree of alignment is the lowest (Figure 2.16). In this latter case, low degrees of alignment have likely resulted in less reliable, and less meaningful, directions of alignment.

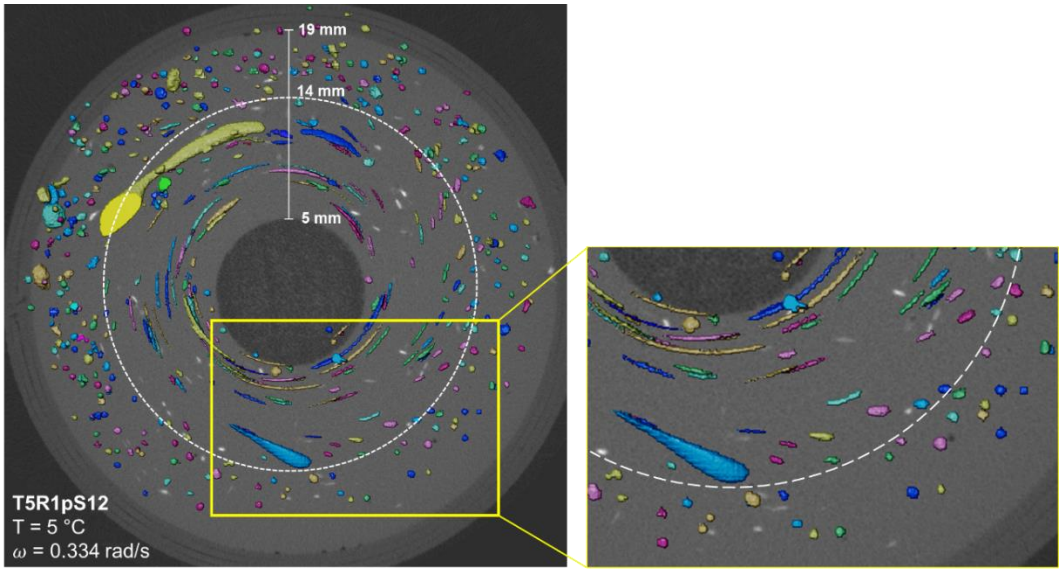

Figure 2.17. Vesicle textures within the sample where stirring started after 12 minutes of cooling and solidification, viewed from above. Constant stirring rate ω is in rad/s. Vesicles beyond 14 mm from the sample centre remain spherical, but closer to the centre, they are deformed. This helps to demonstrate how much of the sample had solidified after 12 minutes. See Chapter 3 for vesicle analysis.

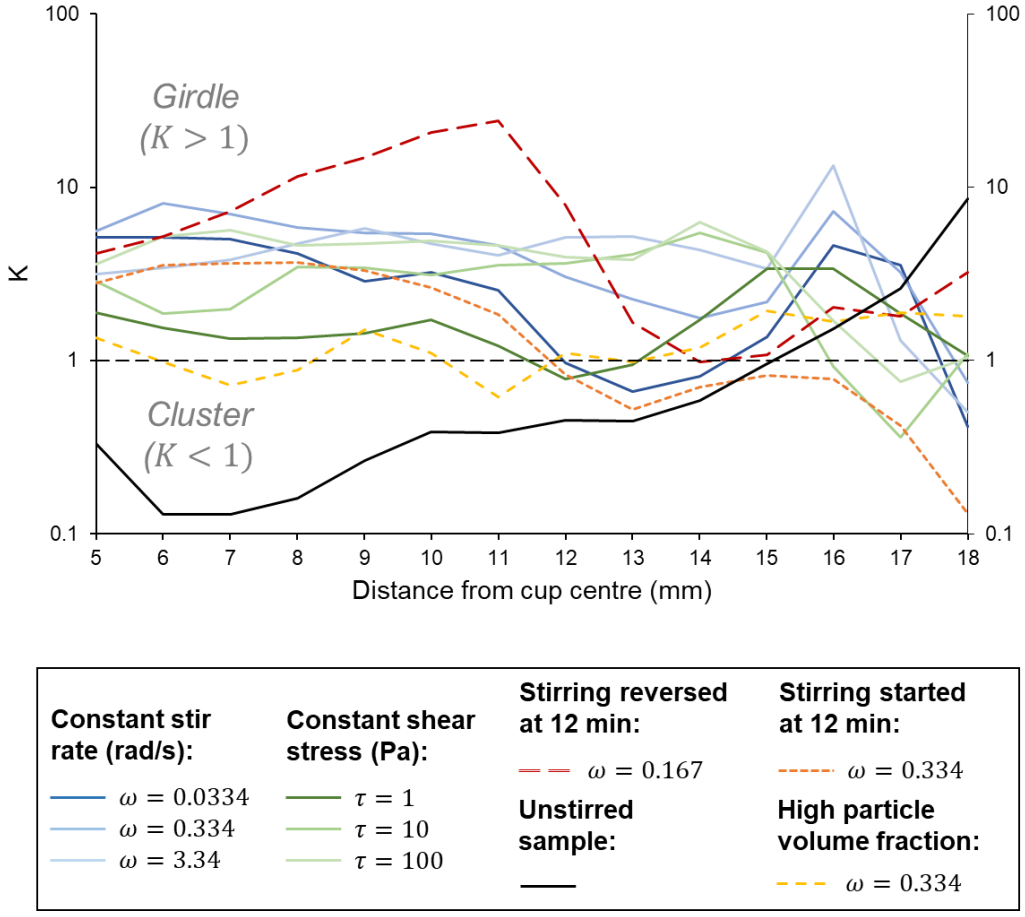

Figure 2.18. Variation in the distribution shape of the preferred orientation K across the radius of samples. Each sample cooled at the same rate (rheometer temperature 5 °C). ω is a constant stirring rate in rad/s, and τ is a constant shear stress in Pa.

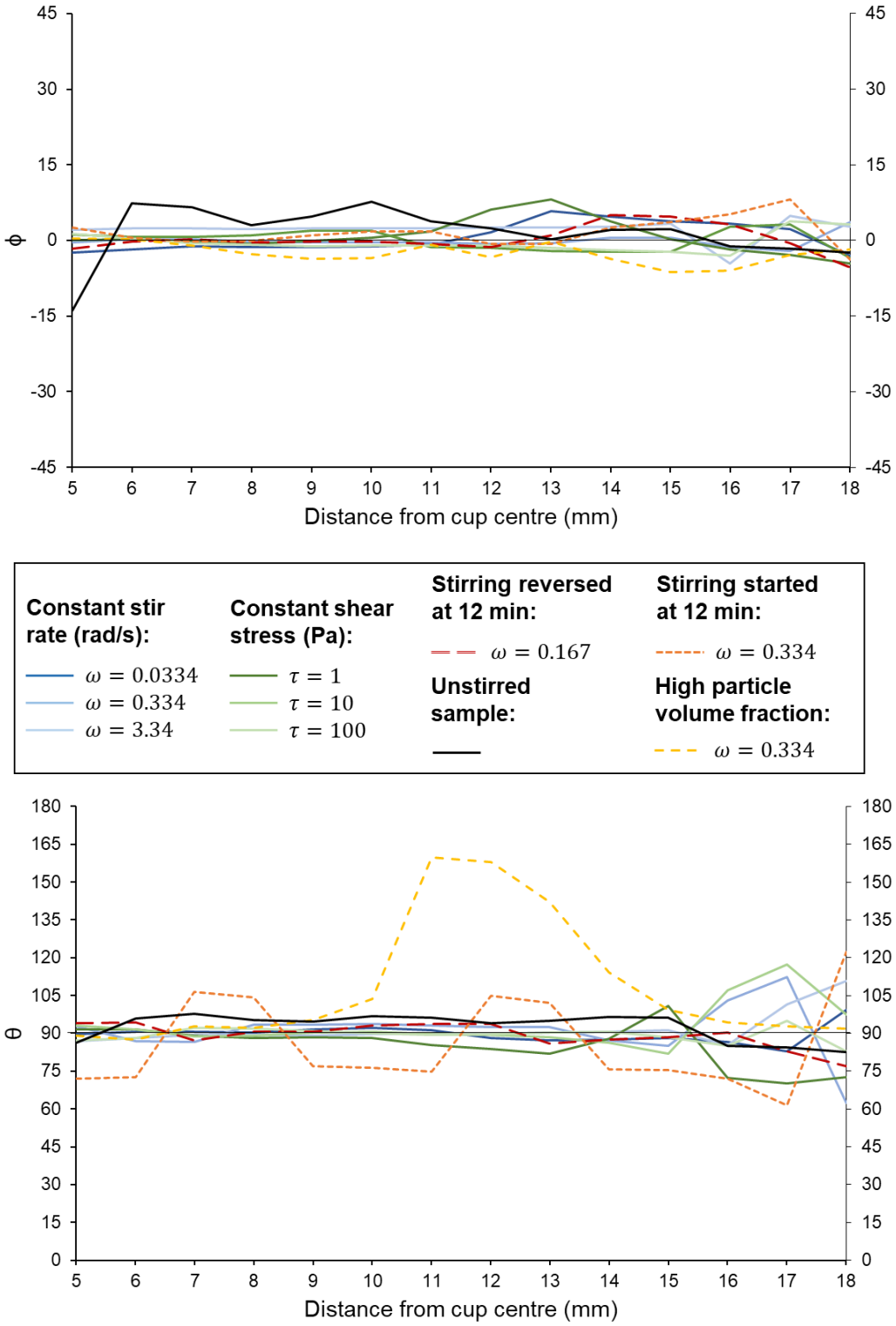

Figure 2.19. Variation in the direction of particle alignment across the width of each sample, described by Euler angles θ and ϕ (for details see Section 2.2.1). Constant stirring rates ω are in rad/s, and constant shear stress τ is in Pa.

2.4.4 Effect of particle shape

Another prediction of the Jeffery equations is that the degree of particle alignment is higher for particles with high aspect ratio (Section 2.2.2). This is true for our samples. For example, in the samples with the constant stirring rate, we find that particle aspect ratio has a stronger influence on the mean degree of alignment than the stirring rate (Figure 2.20a). Particle length, however, shows no significant relationship with the degree of alignment (Figure 2.20b).

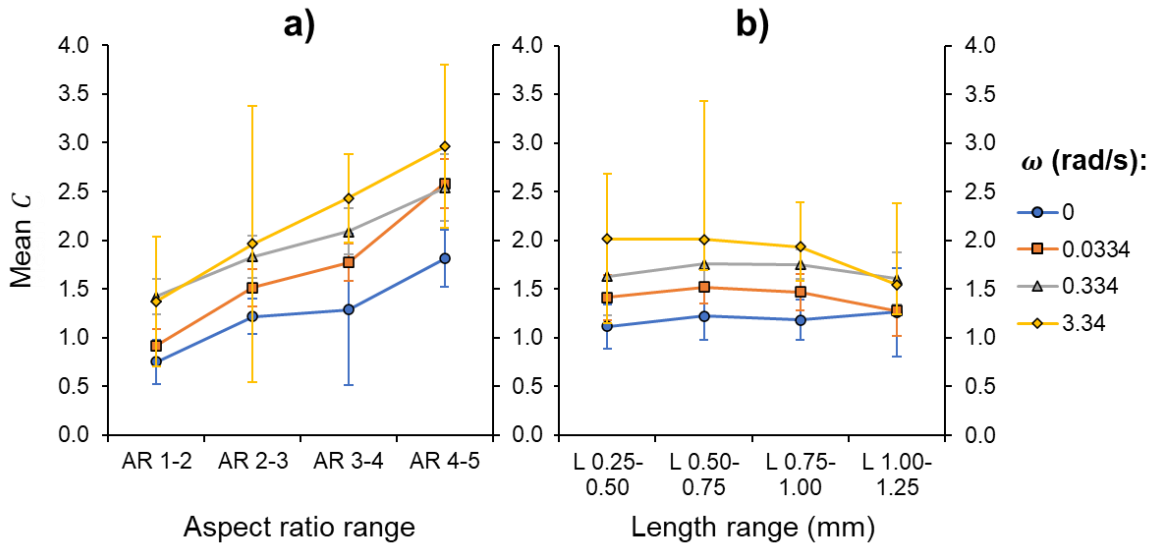

Figure 2.20. Mean degree of particle alignment C across the width of each sample stirred at a constant rate ω, separated by particle aspect ratio (a) and particle length (b). Error bars show one standard deviation.

2.5. Discussion

2.5.1 Effect of strain

In the samples stirred at a constant rate, the degree of alignment shows a general increase towards the centre. This partially reflects the total strain that has accumulated within different regions of the sample, as the central region is the last to solidify and is therefore sheared for longer. In Section 2.2.2, we established that it takes a critical amount of strain for a population of particles to develop a stable preferred orientation, if there are a range of aspect ratios present. It could be inferred that the low degrees of alignment at the cup edge are a result of the particles being captured rapidly, before they had the opportunity to align with the flow; however, this is an oversimplification. Before the critical amount of strain is attained, the degree of alignment will oscillate from high to low values, and so low degrees of strain will not necessarily yield low degrees of particle alignment.

We demonstrate the effect of strain on the degree of particle alignment by simulating the rotations of a large population of particles. Our particle rotation model implements the Jeffery equations presented in Section 2.2.1 in MATLAB. The first step is to define the aspect ratios r_e for a population of n

particles. Aspect ratios may be set to a single value, a range of values, or a measured set of values. Each particle has an initial orientation at time $t = 0$, given by $\theta_{t=0}$ and $\phi_{t=0}$. If initial orientations are random, they are calculated via

$$\theta_{t=0} = \text{acos}(2v - 1) \quad \text{Eq. 2.16}$$

and

$$\phi_{t=0} = 2\pi u, \quad \text{Eq. 2.17}$$

where v and u are random numbers between 0 and 1. This results in a series of polar coordinates that are uniformly distributed over the surface of a unit sphere (Weisstein, 2023). Alternatively, initial orientations can be set manually to match measured orientations.

The original Jeffery equations are set up to calculate θ and ϕ at any time t, based on parameters C and κ, and rotation period T, all of which are calculated from initial conditions. However, we find that it is more informative to calculate orientations with strain rather than time. Inspection of Eq. 2.4 shows that ϕ depends on the ratio t/T, which is a fraction of progress through one rotation. This is equivalent to γ/γ_T, where γ_T is the rotation period expressed as strain rather than time. We calculate γ_T by rearranging Eq. 2.5, so that

$$\gamma_T = T\dot{\gamma} = 2\pi(r_e + r_e^{-1}). \quad \text{Eq. 2.18}$$

We can then calculate θ and ϕ for each particle in the population, for any specified value of strain, by replacing t/T in Eq. 2.4 with γ/γ_T.

However, due to the tan function in Eq. 2.4, calculated ϕ values wrap from 0 to π (180°). Full particle rotations can only be simulated by extending ϕ values from 0 to 2π (360°). To address this issue, we keep two parallel sets of ϕ values: original values ϕ_1 from 0 to π, and modified values $\phi_2 = \phi_1 + \pi$. We then monitor the differences between iterative values of ϕ_1, and create a switch that flips whenever ϕ_1 jumps from $\sim\pi$ to ~ 0 in one step. When the switch is off, $\phi = \phi_1$, and when the switch is on, $\phi = \phi_2$. This method works well provided that strain iterations are sufficiently closely spaced to capture the jump from $\sim\pi$ to ~ 0.

When we use 10,000 particles with entirely random start orientations, we find that a strain of ~25 is required to attain a stable degree of alignment (Figure 2.21). The mean C beyond 25 strain is 0.49 ±0.02. However, if we set our initial orientations to match the orientations measured in the unstirred sample, (thereby limiting the simulated population size to 5038 particles) we find that oscillations in C are dampened. A stable alignment is attained around a lower strain of 10, and the degree of alignment is higher, with a mean C value of 1.18 ±0.01 beyond 10 strain. This latter case is more likely to reflect the starting conditions of our samples, where particles had been pre-aligned by pouring the suspension into the cup.

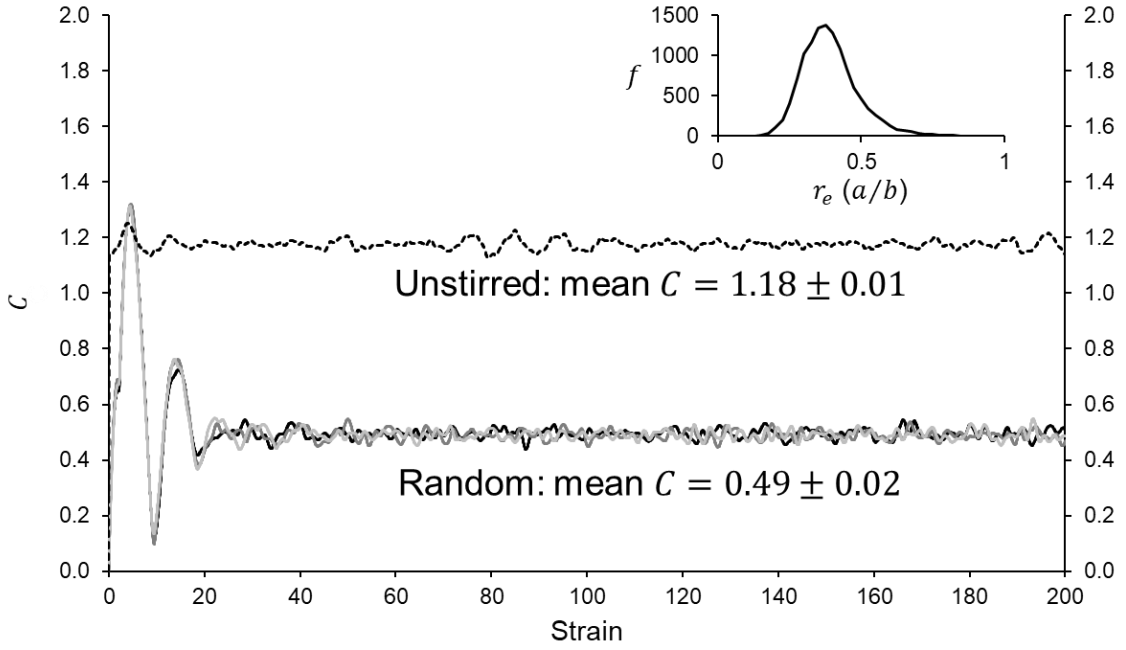

Figure 2.21. Degree of alignment in a population of simulated particles with aspect ratios randomly selected from our dataset of measured particle dimensions. Solid curves show simulations of 10,000 particles with random initial orientations, with three shades of grey showing three model runs from different random starting conditions. Dashed curve shows simulations of 5038 particles with initial orientations matching the measured orientations from the unstirred sample. Inset figure shows distribution of aspect ratios measured in Avizo.

To determine whether our samples reached the critical strain to develop a stable particle alignment, we use a simple 1D conduction model to estimate their solidification history.

The general form of the heat equation (Section 1.6.1) in cylindrical coordinates is

$$\frac{1}{r}\frac{\partial}{\partial r}\left(kr\frac{\partial T}{\partial r}\right)+\left[\frac{1}{r^2}\frac{\partial}{\partial \phi_c}\left(k\frac{\partial T}{\partial \phi_c}\right)+\frac{\partial}{\partial z}\left(k\frac{\partial T}{\partial z}\right)\right]=\rho c\frac{\partial T}{\partial t} \qquad \text{Eq. 2.19}$$

where r is radial position, k is thermal conductivity, T is temperature, ϕ_c is circumferential position, z is vertical position, ρ is density, c is specific heat capacity and t is time (Forsberg, 2020). We assume that there is no heat transfer in the ϕ_c or z directions; therefore, the section of Eq. 2.19 in square brackets can be ignored. Given that thermal diffusivity $\alpha = k/\rho c$, we can express the heat equation for our cylindrical samples as

$$\frac{\partial T}{\partial t}=\alpha\left(\frac{\partial^2 T}{\partial r^2}+\frac{1}{r}\frac{\partial T}{\partial r}\right), \qquad \text{Eq. 2.20}$$

and we solve this equation numerically using a basic finite difference scheme in MATLAB.

We use an array of temperatures $T(i)$ at radial intervals dr, and for a series of timesteps $t(n)$ at time intervals dt, we calculate

$$\frac{dT}{dt}(i,n) = \alpha\left(\frac{T_{i-1} - 2T_i + T_{i+1}}{dr^2} + \frac{1}{r_i}\left(\frac{T_{i+1} - T_{i-1}}{2dr}\right)\right), \quad \text{Eq. 2.21}$$

and

$$T(i,n) = T_{n-1} + dt\frac{dT}{dt}(i,n). \quad \text{Eq. 2.22}$$

For our sample size and thermal diffusivity, we find that the numerical solution is stable using intervals of $dr = 0.01 \times 10^{-3}\ m$ and $dt = 0.1 \times 10^{-3}\ s$. Our model includes an inner cylinder of wood and an outer cylinder of sugar. The boundary conditions are that the outer wall is fixed at 5 °C, but the central temperature is allowed to vary. We calculate the central temperature using the symmetry of the system, because the temperatures on either side of the centre ($i = 0$) should be equal, so Eq. 2.21 simplifies to

$$\frac{dT}{dt}(0,n) = \alpha\left(\frac{2T_{i=1} - 2T_{i=0}}{dr^2}\right). \quad \text{Eq. 2.23}$$

Our initial conditions are that the sugar is set to a uniform 135 °C, as measured in the lab, and the wooden rod is set to a uniform 20 °C, to match the ambient lab temperature. The model is reasonably sensitive to the thermal diffusivity of the sugar, and much less sensitive to the thermal diffusivity of the wood. The thermal diffusivity of pure sucrose is of the order 0.01×10^{-6} m^2 s^{-1} (MacCarthy and Fabre, 1989); however, the thermal diffusivity of saturated aqueous sucrose solutions is an order of magnitude higher, around $0.15—0.30 \times 10^{-6}$ m^2 s^{-1} (temperature dependent), due to the presence of water (Martins et al., 2021). The precise water content of our sugar is unknown, although extended boiling at 145 °C should reduce it to <5 wt.% (Hartel et al., 2011). Based on the time taken for our sugar to solidify, we estimate its thermal diffusivity to be between $0.04—0.06 \times 10^{-6}$ m^2 s^{-1}, with cooling times of 18.17—26.83 minutes respectively. The thermal diffusivity of wood is of the order of 10^{-7} m^2 s^{-1} (Hrčka and Babiak, 2017; Maeda et al., 2021).

We assume that the sugar solidifies at 60 °C, as indicated by our viscosity measurements (Section 2.3.1), and define the solidification front as the 60 °C isotherm, which moves inwards over time (Figure 2.22). Using Eq. 2.7, we calculate the velocity profile across the molten region of the sample, assuming the solidification front to be the effective inner radius of the cylinder, and assuming the molten region to have a constant viscosity. From these velocity profiles, we calculate strain rates and the strain accumulated with each timestep.

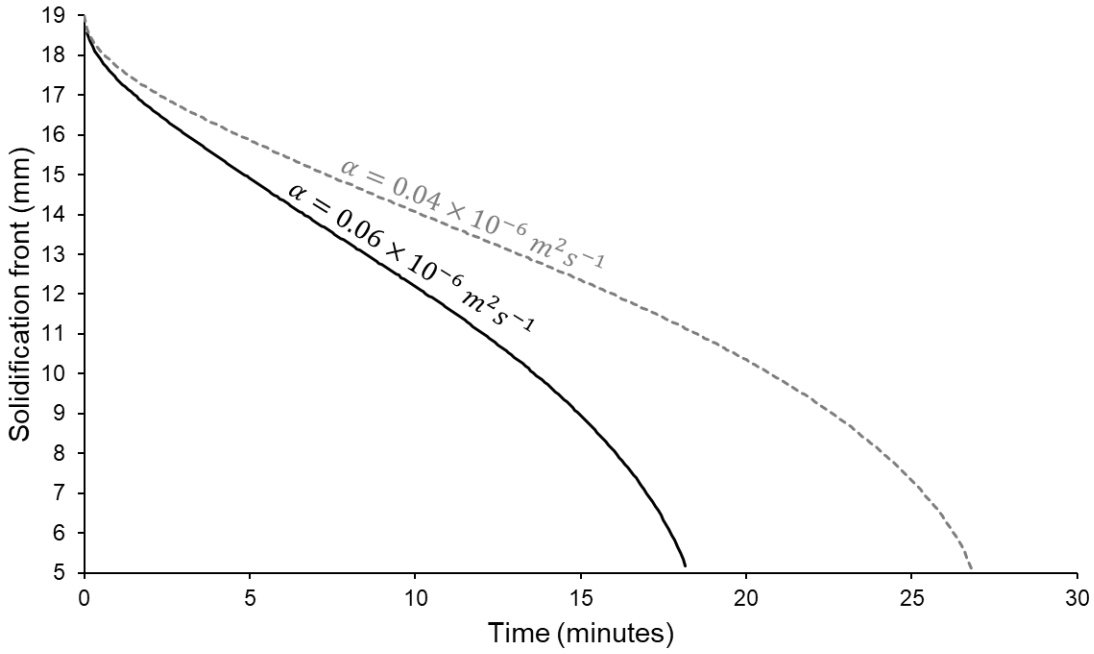

Figure 2.22. Position of the solidification front over time, defined as the 60 °C isotherm. Upper and lower estimates are generated based on a likely range of thermal diffusivities α for molten sugar.

We find that the samples stirred at a constant rate of $\omega = 0.334\ rad/s$ and $\omega = 3.34\ rad/s$ exceed the critical strain across the majority of their widths; however, the sample stirred at $\omega = 0.0334\ rad/s$ is not expected to exceed the critical strain (Figure 2.23). This partly explains the greater variability in C across the $\omega = 0.0334$ sample, which likely captured particles that were still in their oscillating regime rather than steady alignment (Figure 2.21).

Our particle rotation simulations show that the initial state of particles impacts the degree of stable alignment. The particles in our samples, which have been aligned by pure shear before being further aligned by simple shear, are expected to attain a higher degree of alignment than if they had started from random orientations. However, the degree of alignment in our samples is still significantly higher than our simulations predict (compare Figure 2.12 and Figure 2.21).

One potential reason for this is that the size of particles has been inflated in the x-ray images. This is likely to have occurred to an equal extent in all dimensions, resulting in aspect ratios being overestimated (i.e., closer to one) which will result in a lower simulated degree of alignment (Section 2.2.2). However, this overestimation will be consistent across all samples, and our samples show systematically higher degrees of alignment for higher stirring rates (Figure 2.12). Therefore, we propose that there is another process acting to increase the degree of particle alignment, involving the balance between cooling rates and strain rates.

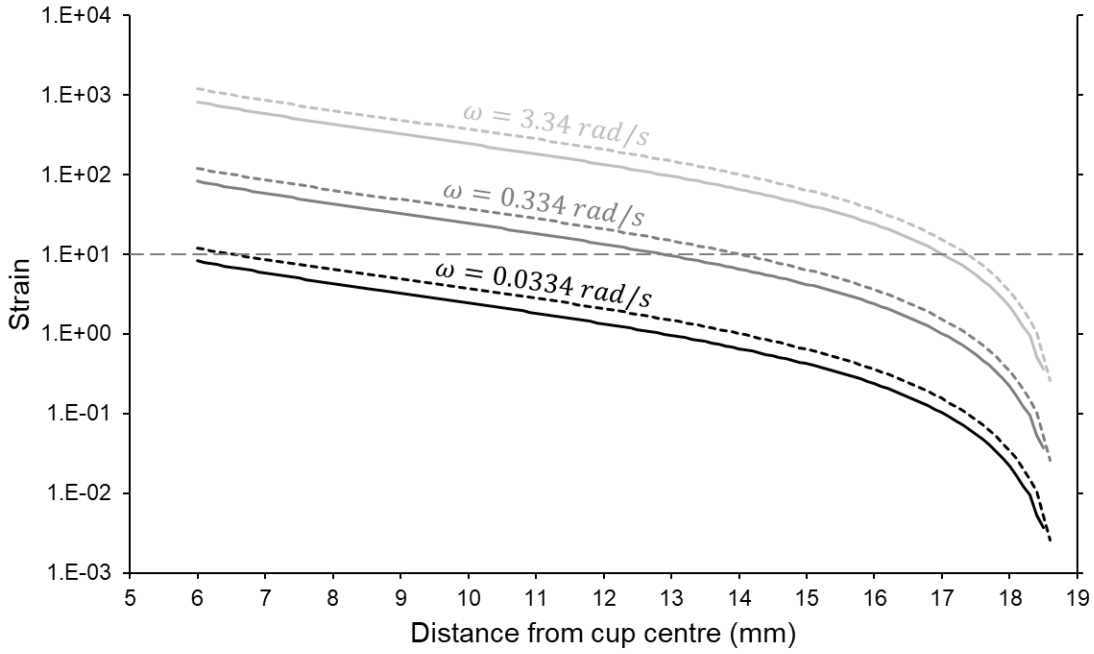

Figure 2.23. Total strain accumulated in each sample, estimated based on the position of the solidification front (Figure 2.22). ω is the constant rotation rate. A horizontal dashed line marks a strain of 10, which we estimate to be the critical strain for a stable particle alignment. Solid lines are minimum estimates, using thermal diffusivity $\alpha = 0.06 \times 10^{-6} m^2\, s^{-1}$, and small dashed lines are maximum estimates using $\alpha = 0.04 \times 10^{-6} m^2\, s^{-1}$.

2.5.2 Effect of progressive inwards solidification

Creating a complete fluid dynamical model for particle motions within a viscosity gradient or across a solidification front is beyond the scope of this study, but here we present a conceptual model that demonstrates how viscosity gradients and solidification will impact particle rotation and alignment. Our samples display higher degrees of particle alignment than predicted for an isothermal fluid, and this has likely arisen due to progressive inwards cooling.

To demonstrate the effects of progressive inwards solidification, we present an extreme example in which the solidification front has just reached a particle (Figure 2.24). Here, one side of the particle is trapped within surroundings that are essentially solid, while the other side remains within flowing, low-viscosity fluid. The trapped side acts as a pivot around which the particle will rotate as it is pushed by the flow. This results in a levering motion, as the particle will rotate faster when it protrudes at a high angle, placing it in the path of faster-flowing fluid (Figure 2.24a). The rotation rate will decrease as the particle becomes more aligned with the flow. If the particle is already aligned when the solidification front arrives (Figure 2.24b), this levering motion will be insignificant, and so the particle has no impetus to rotate. As such, the presence of the solidification front enhances the degree of particle alignment beyond what would be expected in an isothermal fluid.

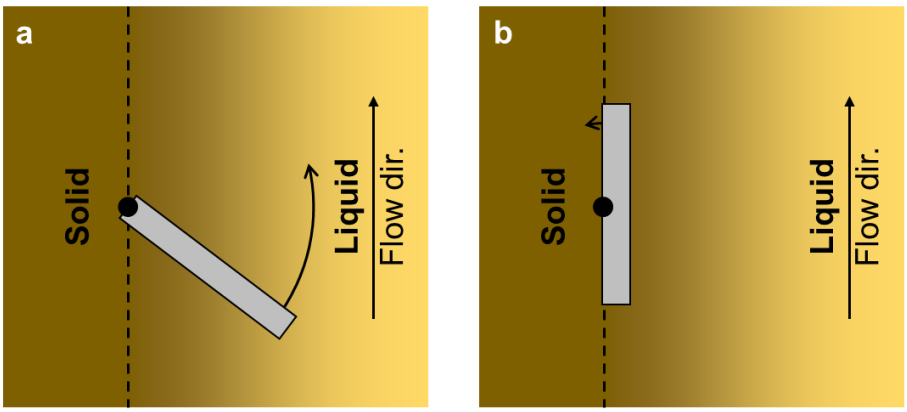

Figure 2.24. Schematic cartoon displaying the effect of the solidification front on particle rotation, where one end of the particle is trapped in fluid so viscous that it is essentially solid, creating a pivot point (black dot). In scenario a (left), the particle protrudes at a high angle to the solidification front, and will be dragged around its pivot towards alignment with the flow. In scenario b (right), the particle is already aligned, and so the torque it experiences is lower, meaning that it remains in place against the solidification front.

2.5.3 Balance between cooling rate and strain rate

The effect of progressive inwards solidification on particle alignment explains why our measured values of C are higher than those predicted by theory. However, the magnitude of this effect depends on two key factors: cooling rate and strain rate. The strain rate $\dot{\gamma}$ determines the rate at which a particle rotates towards alignment with the flow. The cooling rate, which may be viewed as the advance rate of the solidification front v_s, limits the amount of rotation possible before the particle is frozen in place. As such, the final degree of particle alignment is determined by the balance between cooling rate and strain rate (Figure 2.25).

This balance may be quantified as follows. The maximum time to capture a particle of length L is L/v_s, assuming that the particle is oriented perpendicular to the solidification front. Within this time, the amount of strain in the fluid surrounding the particle is determined by the strain rate $\dot{\gamma}$. We therefore define a characteristic strain

$$\gamma_c = \frac{L\dot{\gamma}}{v_s}, \qquad \text{Eq. 2.24}$$

which is a dimensionless parameter relating particle size, cooling rate and strain rate. This is a simplification, as the strain rate within the fluid will change as the solidification front advances, and the solidification front will typically advance at a decreasing rate. However, γ_c provides a simple means to quantify the balance between cooling and strain rate, with higher values indicating a greater amount of additional particle rotation and a higher degree of particle alignment.

Using our cooling and velocity model (Section 2.5.1), we estimate the flow velocity one particle length ahead of the solidification front (0.25—0.50 mm), and divide this by the particle length to estimate the strain rate $\dot{\gamma}$. We approximate v_s as the distance travelled by solidification front between

timesteps, divided by the timestep interval. We find that γ_c is lowest at the sample edge and increases towards the centre (Figure 2.26), which is concordant with our observations of particle alignment (Figure 2.12). Particles near the cup edge experienced lower strain rates and rapid solidification, so they were captured without significant alignment in the viscosity gradient (Figure 2.25c). Particles near the stirring rod experienced higher strain rates and slow solidification, leading to significant further alignment (Figure 2.25b).

We find that the greatest influence on γ_c in our experiments is the stirring rate, which is again concordant with our observations that faster stirring rates produced higher degrees of alignment. The length of particles has a much lesser effect within our experiments, which again agrees with our observations (Figure 2.20). When we plot γ_c against relative C measured at the same position within the sample, we find a positive relationship (Figure 2.27), showing that the degree of alignment is influenced by the balance between cooling rate and strain rate.

This relationship between γ_c and C can also explain the trends in our other samples. In the samples stirred at a constant shear stress, the stirring rate decreased over time, as the sample cooled and its viscosity increased. We expect that γ_c initially increased as v_s decreased, but the reduction in stirring rate gradually reduced $\dot{\gamma}$ ahead of the solidification front, which eventually caused a decrease in γ_c, resulting in lower values of C towards the sample centre (Figure 2.14).

In the sample where stirring direction reversed at 12 minutes, the balance between cooling rate and strain rate determined the window over which particles could re-align with the new flow direction. Particles already parallel with the flow would have no impetus to rotate when the flow direction was reversed; only those protruding at an angle would have been levered back the opposite way. If they were protruding at a high angle upstream, as in Figure 2.24a, they would have rotated rapidly. So, providing that v_s was sufficiently low or $\dot{\gamma}$ was sufficiently high, they could have re-aligned with the new flow direction before being captured. This explains why we see no change in the degree or direction of alignment across the 14-12 mm threshold, where we expect the solidification front to have been at 12 minutes.

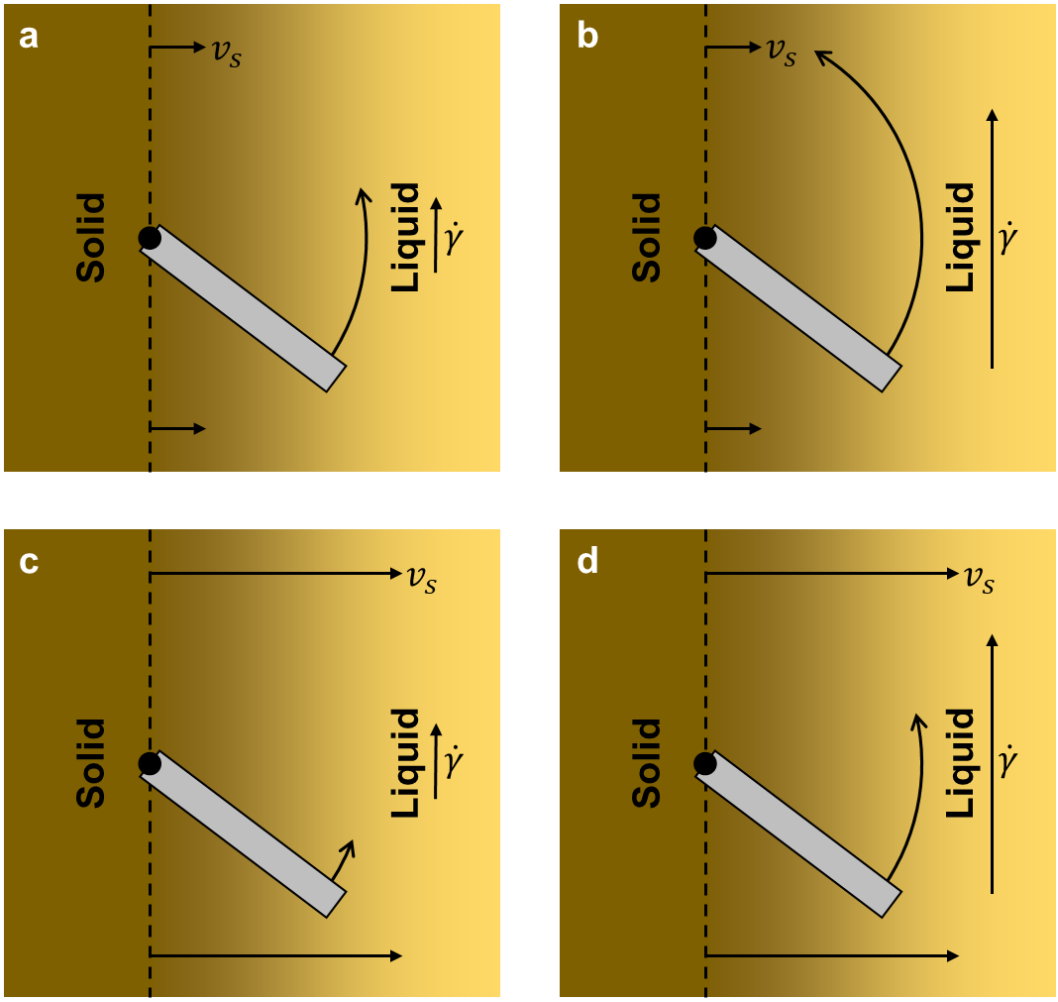

Figure 2.25. Balance between cooling rate (velocity of the solidification front v_s) and strain rate $\dot{\gamma}$ influences the time available for particles to rotate and the rate at which they rotate. Curved arrows show the amount of rotation expected before particles are frozen in place. Maximum rotation is produced by low v_s and high $\dot{\gamma}$ (b), and minimum rotation is produced by high v_s and low $\dot{\gamma}$ (c).

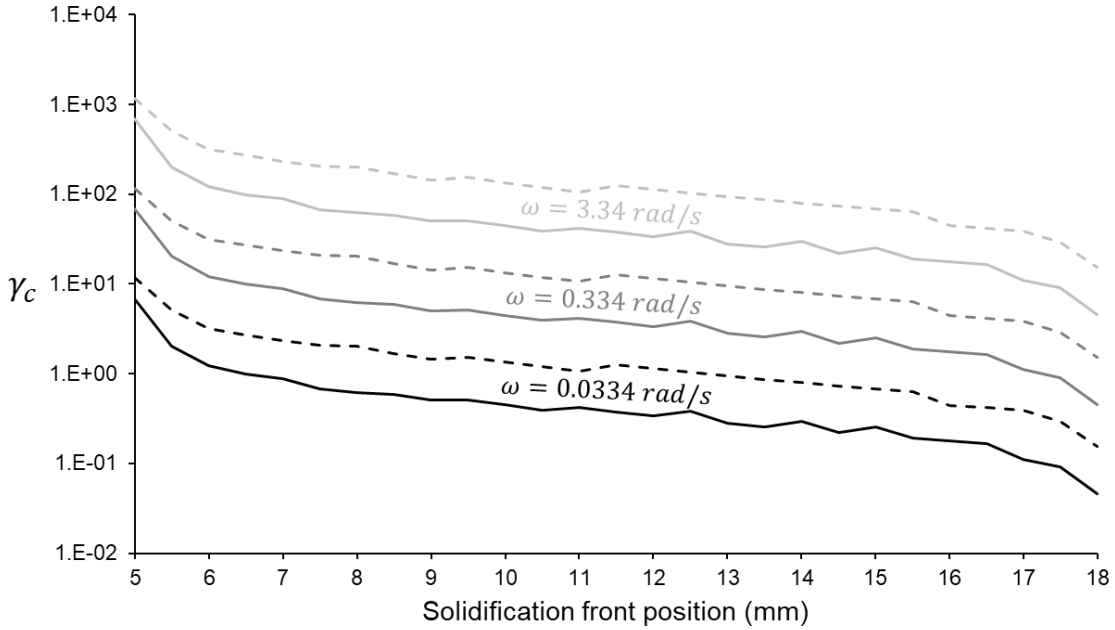

Figure 2.26. Characteristic strain γ_c ahead of the solidification front, calculated across the radius of each sample stirred at a constant rate ω. Minimum values for γ_c are shown as solid curves, calculated with particle length $L = 0.25\ mm$ and thermal diffusivity $\alpha = 0.6 \times 10^{-7}\ m^2\ s^{-1}$. Maximum values are shown with dashed curves, with $L = 0.50\ mm$ and $\alpha = 0.4 \times 10^{-7}\ m^2\ s^{-1}$.

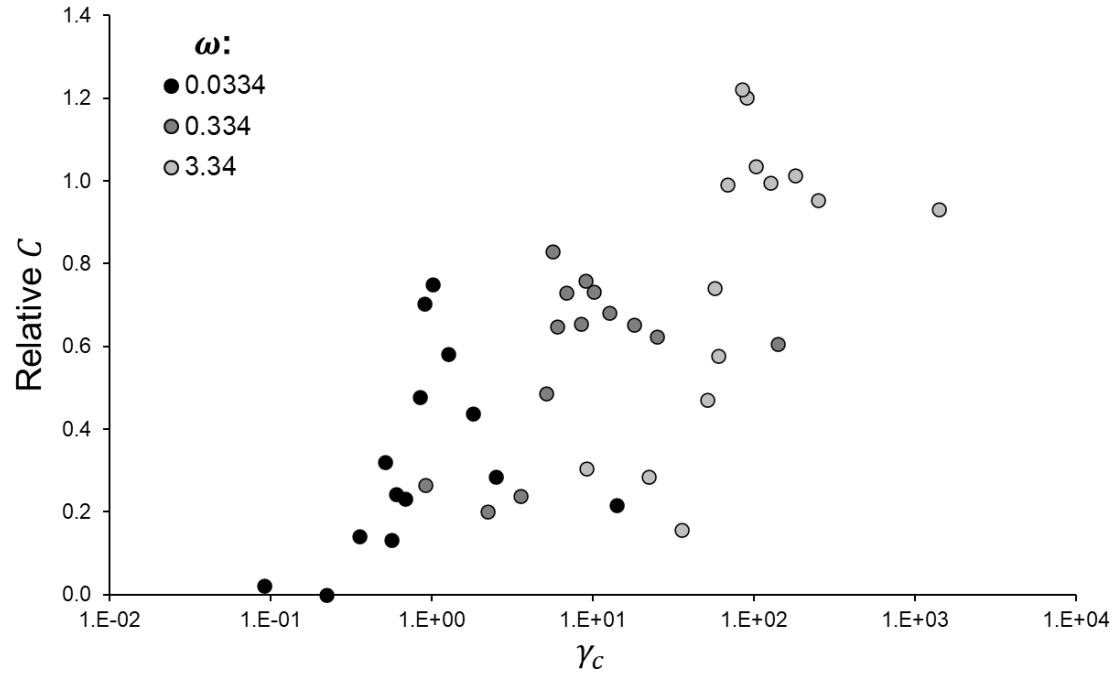

Figure 2.27. Characteristic strain γ_c against degree of particle alignment C relative to the unstirred sample, taken from the same position across the radius of a sample stirred at constant rate ω (rad/s). γ_c values assume a particle length $L = 0.25\ mm$ and thermal diffusivity $\alpha = 0.6 \times 10^{-7}\ m^2\ s^{-1}$.

2.5.4 Effect of a viscosity gradient

We note that the characteristic strain presented in Eq. 2.24 does not entirely capture the effect of the viscosity gradient ahead of the solidification front. Specifically, it does not capture the effect of the steepness of this gradient. The rate of advance of the solidification front depends on the steepness of the thermal gradient, in accordance with the heat equation (Eq. 2.20); however, the steepness of the viscosity gradient depends on the temperature-viscosity relationship for that particular fluid, so the characteristic strain and the steepness of the viscosity gradient are only indirectly related. We acknowledge that the viscosity gradient will have some impact; for example, it seems intuitive that a steep viscosity gradient will lead to a higher degree of particle alignment than a shallow viscosity gradient, which would cause more particles to be captured at an oblique angle.

The viscosity gradient in our samples does not appear to have influenced the direction of particle alignment (Figure 2.19), even though our conceptual model predicts a breakdown of cyclical rotations. We expect particles that are already aligned with the flow to remain in this position, whereas protruding particles should rotate towards alignment, leading to a skewed distribution of particle orientations (Figure 2.24). This skew would produce a texture similar to the imbrication of crystals, with the angle of imbrication dependent on the balance between cooling rates and strain rates, without the need for particle collisions. The amount of imbrication would partly depend on the steepness of the viscosity gradient immediately ahead of the solidification front. In the context of dykes, this gradient would be steepest at the margins, and would become shallower as the solidification front moved inwards, causing imbrication angles to increase towards the dyke centre.

However, our samples show no evidence of progressive inwards cooling modifying the direction of particle alignment. We suspect that this may be related to the length of particles used compared to the viscosity gradients that developed, and due to the pre-existing alignment caused by pure shear. Further experiments or numerical models are needed to explore this concept, with the aim of establishing a link between cooling rates, strain rates and the angle of crystals to intrusion margins.

2.5.5 High particle volume fraction

Our final sample contained a higher volume fraction of particles of 0.1. We expected systematic imbrication of particles due to collisions within the flow, as seen in experiments by previous authors (e.g., Arbaret et al., 2007; Picard et al., 2011; Arbaret et al., 2013), and within dykes (e.g., Shelley, 1985). However, the particles in our samples show no alignment, except in the immediate vicinity of the stirring rod and the walls. In horizontal cross-sections through our sample, we can pick out narrow bands of crystal alignment by eye, forming arcs across the stirred region, but these are too localised and with too few particles to be quantified. It appears that the sample flowed in a complex manner, beyond the scope of this investigation, and we cannot confirm if this was due to progressive inwards cooling, widespread particle interactions, or the shape of the velocity profile in our cylinder geometry.

2.6. Implications

Our analogue experiments show that progressive inwards cooling increases the degree of particle alignment beyond what would be predicted under isothermal conditions. This has implications for the textures of crystals used to infer flow conditions within dykes. Most studies of dyke textures use the imbrication of crystals at the margins to infer initial flow directions, either by measuring crystal orientations in thin section (e.g., Shelley, 1985; Wada, 1992), or by using the anisotropy of magnetic susceptibility as a proxy (e.g., Knight and Walker, 1988; Martin et al., 2019). A high degree of crystal alignment increases the statistical significance of any preferred orientation and makes the direction of alignment easier to determine; however, neither the degree of alignment nor the magnitude of the imbrication angle is needed to infer flow directions. Even so, we believe that the current tendency to ignore the degree of crystal alignment has led to valuable information on flow conditions being overlooked.

Given that the degree of alignment depends on a balance between cooling rate and strain rate, any variation in the degree of alignment across the width of an intrusion can be read as a change in strain rates and cooling rates with time. It is a relatively common observation that the degree of groundmass or phenocryst alignment is higher at intrusion margins, and either lower (e.g., Blanchard et al., 1979; Shelley, 1985; Holness and Humphreys, 2003) or absent (Knight and Walker, 1988) in the dyke centre. Based on our analogue experiments, such a pattern is likely to develop in response to γ_c declining over time (Eq. 2.24). We expect v_s to decrease as the solidification front approaches the dyke centre, and so the reduction in the degree of alignment is most likely caused by a significant decrease in strain rates, which is to be expected if the pressure driving magma flow reduces over time. Additionally, our conceptual model predicts that the shallowing of viscosity gradients ahead of the inwards-migrating solidification front will reduce the degree of alignment and increase the imbrication angle towards the dyke centre, although our experiments did not capture this behaviour.

However, the trend of strong alignment at the margins and weak alignment in the centre is by no means ubiquitous within dykes. If a dyke has been emplaced by multiple magma pulses, each of these may result in different textures; for example, Wada (1992) reports that only the central layer of a composite basaltic dyke shows any groundmass alignment. Furthermore, the width of an intrusion may impact its textures. Holness and Humphreys (2003) report that narrower sections of a dolerite sill show a high degree of crystal alignment in their centres because they solidified while the magma was still flowing, compared to thicker sections which only solidified once the magma was stagnant. Our experiments support such interpretations, and show that variations in the degree of crystal alignment across the width of intrusions, combined with estimates of an intrusion's cooling history, can be used to infer variations in strain rate throughout its emplacement.

We also note that many authors have observed a systematic variation in the direction of crystal alignment across the widths of intrusions. It is a relatively common observation that the angle of groundmass alignment (e.g., Blanchard et al., 1979; Shelley, 1985) and the orientation of the AMS (e.g., Féménias et al., 2004) is sub-parallel near the margins, but the magnitude of this angle increases towards the intrusion centre. Previous authors have suggested that this reflects strain rate profiles across intrusions, with higher strain rates at the margins promoting closer alignment with the flow (Blanchard et al., 1979; Shelley, 1985); however, they do not present a mechanism to explain this. Imbrication is widely assumed to result from collisions between suspended crystals, with the oblique angle of alignment being a stable configuration to minimise momentum transfer (Rees, 1968), or merely due to the particles stacking like fallen dominoes in the direction of flow (Blanchard et al., 1979; Knight and Walker, 1988). There is currently no theory to explain the magnitudes of imbrication angles.

While we found no evidence in our experiments of a systematic variation in alignment direction with strain rate, our conceptual model suggests that progressive inwards cooling could result in crystals aligning at an oblique angle to the flow direction in the absence of collisions. The amount of additional rotation within a viscosity gradient depends on γ_c (Eq. 2.24) and the steepness of this gradient, with low γ_c values and shallower gradients leaving a greater number of particles at a higher angle to the flow. This produces a lower degree of alignment, but also skews the direction of alignment to higher angles. As such, an increase in imbrication angles across the width of an intrusion is unlikely to reflect the velocity gradients that existed across its molten width, but the declining strain rates that existed immediately ahead of the inwards-migrating solidification front.

Finally, we note that the implications of our experimental findings are limited by additional complications present in magmatic intrusions, mainly particle collisions. In our experiments, we kept particle volume fraction low to avoid particle interactions and focus entirely on the effects of cooling; however, the crystal volume fraction of magma is likely to be much higher, and so interactions will play a major role in modifying crystal fabrics. The crystals within magmatic intrusions are also expected to grow and change shape, leading to a change in their rotation behaviour over time. Crystal volume fractions and aspect ratios captured in the final rock texture may not reflect the conditions responsible for its formation (Shelley, 1985; Benn and Allard, 1989). Further experiments are needed to explore the effect of crystal interactions within the context of progressive inwards cooling and solidification.

2.7. Conclusion

Our experiments demonstrate that a balance between cooling rate and strain rate controls the degree of particle alignment in flows which solidify inwards from their edges. This finding is particularly relevant to intrusion margins, where the degree of crystal alignment is likely to be enhanced by high strain rates and rapid inwards migration of the solidification front. Our findings in no way undermine inferences of flow direction from imbricated crystals; however, our experiments highlight an opportunity to use crystal textures to infer relative strain rates when the cooling history of the intrusion can be estimated. Low degrees of alignment may reflect very rapid cooling, but are more likely to reflect low strain rates immediately ahead of the solidification front, which is why the degree of crystal alignment is often found to decrease towards intrusion centres. Our conceptual model also raises the possibility that the direction of alignment, often measured as an imbrication angle within intrusions, may be controlled by the balance between cooling and strain rates, although further work is needed to explore this effect. Comparing the degree and direction of crystal alignment along the lengths or across the widths of dykes can yield more than just magma flow directions; the textures can reveal spatial and temporal variations in strain rates throughout their emplacement.

Chapter 3

Inferring dyke flow histories from vesicle shapes using analogue experiments

---

Aims of this chapter:

The orientations of deformed vesicles are commonly used to infer flow directions within dykes and lavas. However, vesicles remain underutilised as a means for interpreting flow histories, even though their shape is largely a product of strain rate. The deformation of bubbles within isothermal fluids is well understood. Bubbles attain a steady-state shape and orientation for any given viscosity and strain rate, quantified by the capillary number Ca, a ratio of the viscous stress acting to deform the bubble and the surface tension stress acting to keep the bubble spherical. Dykes are not isothermal environments, so the straightforward relationships between bubble orientation and strain rate cannot be applied. Viscosities and strain rates change as the dyke cools and solidifies progressively inwards from its margins, and the extent to which a bubble can respond to these changes depends on the balance between the rate of change in strain rate, and the bubble response time, which depends on viscosity, bubble radius and surface tension. When a deformed bubble is finally captured as a vesicle, it is always out of equilibrium. If we are to use vesicle shapes to infer flow conditions, we need to know whether these shapes more closely reflect conditions in the molten channel, or conditions at the solidification front.

Here, we present analogue experiments that produce vesicle shapes from a range of shear conditions and solidification rates. Just like the previous chapter, we use samples of molten sugar that solidify progressively inwards from their edges as they are stirred, capturing deformed steam bubbles. We find that final vesicle shape depends on a balance between cooling rate and deformation conditions. The strain rates ahead of the solidification front determine the equilibrium shape for a bubble to attain, but its final shape is determined by its response time versus the time available for deformation before the surrounding fluid solidifies. We propose that vesicle shapes across the widths of dykes can be used to make qualitative interpretations of dyke flow history when their thermal evolution is considered.

3.1. Introduction

The orientations of elongated vesicles are commonly used to infer magma flow directions in dykes, sills and lavas. Suspended bubbles of exsolved volatiles are deformed within the flowing magma, then captured as elongated vesicles when the melt solidifies. These elongated vesicles are a reliable indicator of flow direction (e.g., Coward, 1980; Philpotts and Philpotts, 2007), but they remain underutilised as a means for inferring strain rates and flow histories. The deformation of bubbles in simple shear is well understood, but relating vesicles to strain rates is not straightforward due to the effects of progressive inwards cooling and solidification. Vesicle shapes are a result of bubbles responding dynamically to changing flow conditions, and reflect the balance between strain rates, viscosities, and the rate of vesicle capture. In this chapter, we use analogue experiments to explore the effects of simultaneous deformation and solidification on the vesicle shapes, then discuss the implications in the context of progressively solidifying basaltic dykes.

The deformation of bubbles in isothermal fluids undergoing simple shear is well understood, and has been measured in numerous laboratory experiments (e.g., Taylor, 1934; Rust and Manga, 2002). A bubble in simple shear will progressively elongate and decrease its angle to the flow until it reaches an equilibrium deformation, a stable shape where further viscous deformation is resisted by surface tension. This seemingly straightforward relationship between strain rate and bubble shape has led some authors to infer magmatic strain rates from vesicles, assuming them to have maintained their equilibrium deformation during capture (e.g., Rust and Cashman, 2007). This would be a particularly useful tool in the context of dykes, where changes in vesicle orientation from margins to centre could be read as changes in magma flow rates through time. However, there are numerous complications to this approach, as the majority of bubbles will not have been captured as vesicles at equilibrium.

Many authors report a decrease in vesicle elongation towards the dyke centre, with vesicle orientations becoming more oblique to the flow direction (e.g., Coward, 1980; Shelley, 1985; Varga et al., 1998; Hintz and Valentine, 2012). Some authors have interpreted vesicle shape profiles to reflect the flow profiles of the active channel (e.g., Coward, 1980; Lanzafame et al., 2017), by which they make the implicit assumption that bubbles maintained the shapes that they attained during active flow until the dyke solidified. Such interpretations are very much at odds with the way that dykes solidify progressively inwards from their margins. Vesicles at the dyke margins are captured earlier than those in the centre, which makes it highly unlikely that a vesicle shape profile across the width of a basaltic dyke reflects the velocity profile of the active channel. Instead, any change in vesicle shapes from the margins inwards is likely to reflect changes in flow conditions over time; for example, some authors have used changes in vesicle orientations across the widths of dykes to infer a reversal in flow direction (Philpotts and Philpotts, 2007; Wadsworth et al., 2015).

There is a stark difference between studies that interpret vesicle profiles as a record of active velocity profiles, and studies that interpret vesicle profiles as a record of changes in flow throughout dyke emplacement. A similar division exists in the literature on lavas, where some authors interpret vesicle shapes and orientations to reflect flow profiles (e.g., Cañón-Tapia et al., 1996), whereas others interpret vesicle textures as a time series captured by progressive inwards solidification (e.g., Aubele et al., 1988). In the former case, there is a general lack of consideration for solidification processes, or for changes in flow conditions that occur throughout emplacement. The response time of bubbles is rarely compared to the time taken for their surroundings to solidify, and the implicit assumption that bubbles hold their shapes throughout solidification is often unjustified. Studies that take a time-series approach are also held back from interpreting dyke emplacement histories, due to the current lack of understanding around the transition from active flows to solidified textures.

In this chapter, we present analogue experiments exploring the simultaneous deformation and capture of gas bubbles held within a viscous, progressively solidifying melt. The experiments are the same as those presented in the previous chapter, and were originally designed to explore the alignment of particles. The inclusion of steam bubbles was unintended but unavoidable during sugar production, and yet their existence has allowed us to investigate the shapes of vesicles within samples deformed under various conditions. Here, we take the first steps in understanding the balance between cooling rates and strain rates, and the effect on vesicle shape.

3.2. Background

3.2.1 Bubble deformation in simple shear

The deformation of bubbles within isothermal, iso-viscous fluids undergoing simple shear is well understood. Two opposing forces act to modify bubble shape. Viscous forces in the surrounding fluid act to stretch the bubble, whereas surface tension acts to make the bubble spherical. The balance between these competing forces is described by the capillary number

$$Ca = \frac{r_b \mu \dot{\gamma}}{\Gamma}, \qquad \text{Eq. 3.1}$$

where r_b is the radius of the bubble, μ is the fluid viscosity, $\dot{\gamma}$ is strain rate and Γ is surface tension. A bubble in simple shear becomes increasingly elongated until it reaches its equilibrium deformation, where viscous forces are matched by surface tension forces (Taylor, 1934; Rust and Manga, 2002). The bubble will remain in this shape and orientation until conditions change. There is also a critical Ca beyond which the bubble will break up, which depends on the viscosity contrast between the bubbles and suspending fluid. The large viscosity contrast between gaseous bubbles and silicic melt means that bubbles in basaltic dykes require values of $Ca > 10^2$ to be broken up (Grace, 1982;

Rallison, 1984; Müller-Fischer et al., 2008). This suggests that most bubbles in dykes are unlikely to break up, unless conditions have produced particularly large bubbles or high strain rates.

Bubbles take time to reach their equilibrium deformation. The rate at which bubbles respond to changes in flow conditions is described by a characteristic relaxation time, or response time,

$$\lambda = \frac{r_b \mu}{\Gamma}. \quad \text{Eq. 3.2}$$

If strain rates are changing, the response time of bubbles determines whether they can maintain their equilibrium deformation. If strain rates are changing quickly with respect to the bubble response time, the bubble shape will be increasingly further from equilibrium. This balance is quantified by the dynamic capillary number

$$Cd = \lambda \frac{\ddot{\gamma}}{\dot{\gamma}}, \quad \text{Eq. 3.3}$$

where $\ddot{\gamma}$ is the rate of change in strain rate (Llewellin et al., 2002). When $Cd \ll 1$, bubbles respond to changes relatively quickly, and so vesicles that are captured in this state are a reliable record of strain rates at the point of solidification. When $Cd \gg 1$, bubbles are relatively slow to respond and will be far from their equilibrium deformation, so when they are captured as vesicles, their shape will not reflect the strain rates at the time of capture.

The extent of bubble deformation is typically quantified by the dimensionless parameter

$$D_b = \frac{l - b}{l + b}, \quad \text{Eq. 3.4}$$

where l is the length of the bubble semi-major axis, and b is the semi-minor axis (Taylor, 1934; Rust and Manga, 2002). Deformation may also be described by the angle θ_b between the bubble long axis and the flow direction. The relationship between Ca, D_b and θ_b has been investigated theoretically (e.g., Hinch and Acrivos, 1980; Rallison, 1981) and experimentally (e.g., Guido et al., 1999); however, the most comprehensive experimental study, covering the wide range of Ca present in volcanic systems, is from Rust and Manga (2002). They find that, for $Ca > 0.5$, bubble orientation is described well by

$$\theta_b = \operatorname{atan}\left(0.359\, Ca^{3/4}\right). \quad \text{Eq. 3.5}$$

3.2.2 Application to magmatic vesicles

The orientation of elongated vesicles is a reliable and commonly used indicator of magma flow directions within dykes (e.g., Coward, 1980; Shelley, 1985; Wada, 1992; Varga et al., 1998; Philpotts and Philpotts, 2007). It is intuitive that a bubble will be stretched out at an angle to the dyke margin, because magma in the dyke centre flows faster. However, the role of solidification versus strain rate in determining the shapes and orientations of vesicles is rarely considered.

The study of Coward (1980) focusses solely on interpreting dyke flow conditions from vesicles. Vesicle shapes are used to infer components of simple and pure shear, from which the author estimates finite strains across the width of the dyke, and infers a velocity profile for the flowing magma. However, there are two problems with this approach. Firstly, there is no accounting for surface tension, which modifies bubble shapes in a manner that undermines this analysis. Secondly, the progressive inwards cooling of the dyke is ignored.

The effect of progressive inwards solidification on vesicle textures is addressed by Philpotts and Philpotts (2007), who propose that vesicles are a product of conditions within the boundary layer ahead of the solidification front. They suggest that vesicle shapes reflect a balance between the strain rate and the time available for the bubble to accumulate strain before capture. They present a camptonite lamprophyre dyke in which vesicle orientations are broadly consistent from the margins to centre, at odds with the parabolic profile presented by Coward (1980). Such consistent vesicle orientations cannot be read as a parabolic velocity profile, and the authors interpret the vesicles as a time series showing a reduction in strain rates over time (Philpotts and Philpotts, 2007).

In other volcanic settings, authors have inferred magmatic strain rates from the shapes and orientations of vesicles in basaltic glass, obsidian and rhyolite (e.g., Burnard, 1999; Rust et al., 2003; Rust and Cashman, 2007). These bubbles are likely to have maintained their shapes before being solidified in place, either as a result of high viscosity magma increasing the bubble response time, or due to solidification being rapid. However, these conditions cannot be applied to basaltic dykes, where viscosities are significantly lower than in silicic melts, and where solidification is relatively slow (except for the margins). In basaltic dykes, vesicles are very likely to have been captured out of equilibrium with their surroundings.

It is relatively straightforward to determine whether a vesicle was captured at its equilibrium deformation, as its orientation and elongation should fit the empirical relationship presented by Rust and Manga (2002). A vesicle can also be compared to its neighbours, which should have all deformed under the same strain rate, viscosity and surface tension conditions. This means that, for neighbouring vesicles, plotting r_b against θ_b (Eq. 3.5) should result in points falling on one curve.

Ohashi et al. (2018) present a numerical model of bubble deformation, where θ_b decreases with increasing strain. If it can be established that vesicles were captured at equilibrium, this model allows an estimate of the minimum strain required to make them this shape. If the vesicles are not indicative of equilibrium conditions, then the strain rate can be estimated by comparing neighbouring vesicles, which have all experienced an equal amount of strain (Ohashi et al., 2018). However, this approach has not been tested for fluids with a changing viscosity, or with steep viscosity gradients.

When interpreting vesicle textures within dykes, the effect of progressive inwards cooling cannot be overlooked. Vesicle textures are captured as a time series from margins to centre, allowing them to be viewed as a record of changing flow conditions, related to changing magma flow rates or a changing channel width. The balance between strain rates, bubble response times, and the velocity of the solidification front is key for determining the amount of bubble deformation that occurred before vesicles were captured, and this is what we explore with our analogue experiments.

3.3. Methods

3.3.1 Experimental procedure

This analysis is based on the vesicles that were unavoidably captured in experiments designed to investigate the alignment of particles. These experiments used samples of molten sugar that solidified progressively inwards from their edges while being sheared. Full details of the experimental method and sugar properties can be found in Chapter 2 (Section 2.3). We note that these experiments were not designed with the express intention of analysing bubbles, but for investigating particle alignment; however, the particle volume fraction was sufficiently low (< 0.01) that we assume the molten sugar to be Newtonian.

The steam bubbles come from the water used in making sugar glass, which involves the creation of a high concentration sucrose solution before boiling off the water. By taking the mixture up to 145 °C, we are confident that the water content was < 5 wt.%, but the small amount of water remaining in the samples formed steam bubbles. Almost all the bubbles are less than 0.5 mm in diameter. They are present throughout the sample, although their concentration shows a slight increase towards the centre, as the stirring rod appears to have acted as a surface on which bubbles nucleated. We know from monitoring sugar in the pan that no bubbles nucleate or show significant growth once the sugar is < 120 °C; as such, bubbles could only have nucleated and grown significantly within the first few minutes of the experiment. The largest bubbles (> 0.5 mm diameter) showed some amount of buoyant rise within the sugar, but most of this occurred within the first few minutes of the experiment, before the viscosity greatly increased. The majority of bubbles were too small to experience any buoyant rise, but where it occurred for the largest bubbles, it is unlikely to have significantly impacted the elongation parallel to the shear direction.

We have analysed the vesicles in eight samples, listed in Table 1 (Chapter 2). Three were stirred at a constant rate throughout their solidification (0.0334, 0.334 and 3.34 rad/s), and three were stirred at a constant shear stress (1, 10 and 100 Pa). Two additional samples investigated the effects of changing stirring conditions partway through solidification. The first was stirred at a constant rate of 0.167 rad/s, but the stir direction was instantaneously reversed after 12 minutes of cooling. The second was left unstirred for 12 minutes, before stirring commenced at a steady rate of 0.334 rad/s.

3.3.2 Vesicle analysis

The solidified samples were scanned in the x-ray CT scanner, as outlined in the previous chapter, at a resolution of 0.0272 mm. Three-dimensional reconstructions of void spaces within the sample were reconstructed using Avizo (ver. 2022.1, ThermoFisher Scientific), allowing us to measure the position, volume, surface area and bounding box coordinates of every vesicle (Figure 3.1). The brightness contrasts were different for every scan, and so the appropriate brightness threshold for extracting void spaces was determined manually for each sample.

In Avizo, the measurements we could take from the vesicles are limited by the cylindrical geometry of our sample. We decided to conduct most of the analysis in MATLAB, where we could correct the orientation of the sample in the same way we corrected the particle data (see Section 2.3.3) and develop unique measurement methods to handle the curved vesicle shapes (Figure 3.1a). We are most interested in the deformation caused by the flow within the sample, rather than by any minor amount of bubble rise, and so we take horizontal, two-dimensional slices through the centre of each bubble volume (Figure 3.2). These two-dimensional shapes are then used to measure vesicle area, perimeter and equivalent radius (radius for a circle of the same area), and a best-fit ellipse was used to estimate orientation (Figure 3.3).

Vesicles were measured via the following steps. In Avizo, we extracted measurements of vesicle centre coordinates, bounding box coordinates and vesicle volume. We then used MATLAB to process the x-ray images further. For each vesicle, we use the bounding box coordinates measured in Avizo to select the horizontal x-ray image slice positioned at its centre (Figure 3.2a). We then crop this image using the width and depth of the bounding box, so that it fits the size of the vesicle plus a border of one pixel, ensuring that the vesicle does not touch the image edges. Each cropped image is then binarized using the same brightness thresholds used in Avizo. We use MATLAB's Image Processing Toolbox to identify contiguous regions within each image, which often captures portions of neighbouring vesicles or the wooden stirring rod (Figure 3.2b). These infringing regions are removed from the cropped image by identifying that portions of their perimeter exist on the edges of the image (red lines in Figure 3.2b), whereas the target vesicle does not touch the image edges.

Once the vesicle shape has been extracted, we save the coordinates of its edge points for further analysis, rather than continuing to work with large, memory-intensive x-ray images. We then correct

all vesicle edge coordinates in the same manner used for the particles (Section 2.3.3). By using the particles as a baseline for the corrections, all positions from the bubble and particle analysis are directly comparable.

We use the corrected vesicle edge coordinates to measure vesicle cross-section area and perimeter, and we generate a best-fit ellipse for each shape using MATLAB's image processing toolbox, allowing us to estimate the orientation of each vesicle. This works well for the vesicles in the outer portions of each sample, as they have suffered only minor deformation. However, the best-fit ellipse cannot approximate the highly curved, elongated vesicles nearer the centre of the sample. Here, the ellipse orientation appears to align with the tangent of the vesicle curvature at its centre of mass. This doesn't truly capture the shape of the vesicle, but it provides some indication of flow alignment.

Ellipse orientations are initially expressed in the global coordinate system, so we convert them to local orientations relative to the flow direction at that position within the cup. This is achieved by subtracting the global orientation from the angle of flow at that point, which depends only on the radial position of the vesicle. Negative values of local orientation show bubbles angled in the direction of clockwise flow (Figure 3.3).

The main obstacle to describing vesicle shapes is that they have been deformed in a curvilinear fashion. The largest vesicles, close to the sample centre, are curled around the stirring rod, with curved central axes. It is impossible to define the orientation of a curved axis in a manner comparable to the bubble angles measured by Rust and Manga (2002). The curved axis also makes it difficult to measure the length of the deformed vesicle. We take a numerical approach and divide the vesicle outline into sections, allowing us to trace a line through its centre.

Our method for tracing the centreline of curved vesicles is as follows. The vesicle outline is defined by a series of coordinates, and for each of these coordinates (x, y) we calculate the distance to the sample centre r and a bearing b from arbitrary "north". The centreline through the bubble starts at the point with the minimum bearing b_{min}, and ends at the point with the maximum bearing b_{max} (Figure 3.4a). We split the vesicle edge into radial slices (b_1, b_2, b_3, …) at a fixed angular interval so that the centreline is divided into sections approximately 0.1 mm long (Figure 3.4b). To calculate the fixed angular interval, we first estimate L_{arc}, the length of the arc passing through the centre of the vesicle, from b_{min} to b_{max}. We calculate this as

$$L_{arc} = (b_{max} - b_{min})\left(\frac{r_{max} - r_{min}}{2}\right). \quad \text{Eq. 3.6}$$

By dividing L_{arc} by 0.1 mm, we find the number of required intervals n. We then find the angular interval by dividing $(b_{max} - b_{min})$ by n.

Once the intervals have been determined, we split the vesicle outline coordinates into two groups, which we call "left" and "right", on either side of the start and end points. We then move through each angular interval, finding all the points within this interval and calculating the mean radial positions of the points on the "left" and then on the "right". By using these means, we smooth out any irregularities in the bubble outline arising from the resolution of the x-ray images. We then calculate the radial position halfway between the "left" and "right" mean positions, and use this to define the midpoint within the centre of that interval (Figure 3.4c). Finally, we define the centreline of the vesicle by tracing a line through the interval midpoints, connecting the start and end of the vesicle (Figure 3.4d).

The length of the vesicle L is the sum of the lengths of lines connecting the interval midpoints. We also measure the radial extent of the vesicle Δr as $r_{max} - r_{min}$, the range in radial positions of the edge coordinates. For an undeformed vesicle, $\Delta r = L = D_V$, the spherical diameter of the vesicle. We calculate D_V based on the vesicle volumes measured in Avizo. By taking a ratio L/D_V, we quantify the extent of bubble deformation, and by taking a ratio $\Delta r/D_V$, we quantify the degree that the bubble has "flattened" perpendicular to the flow direction (Figure 3.5).

3.3.3 Scaling considerations

As expressed in the previous chapter, our experiments do not need to scale perfectly with conditions in magmatic dykes, as we are exploring the balance between cooling rates and strain rates, which vary spatially and temporally during dyke emplacement (Section 2.3.2). Our aim is not to simulate a specific part of the dyke system, but to demonstrate how the balance between cooling rates and strain rates influences vesicle textures. However, the cylindrical geometry of our samples means that the molten sugar is not strictly undergoing simple shear, as might be expected in flowing magma. Instead, the velocity profile is slightly curved, following Eq. 2.7 (Figure 2.6). Approximately 75% of vesicles are < 0.5 mm in spherical diameter, and over this length scale, the departure from simple shear is unlikely to have impacted bubble shapes greatly.

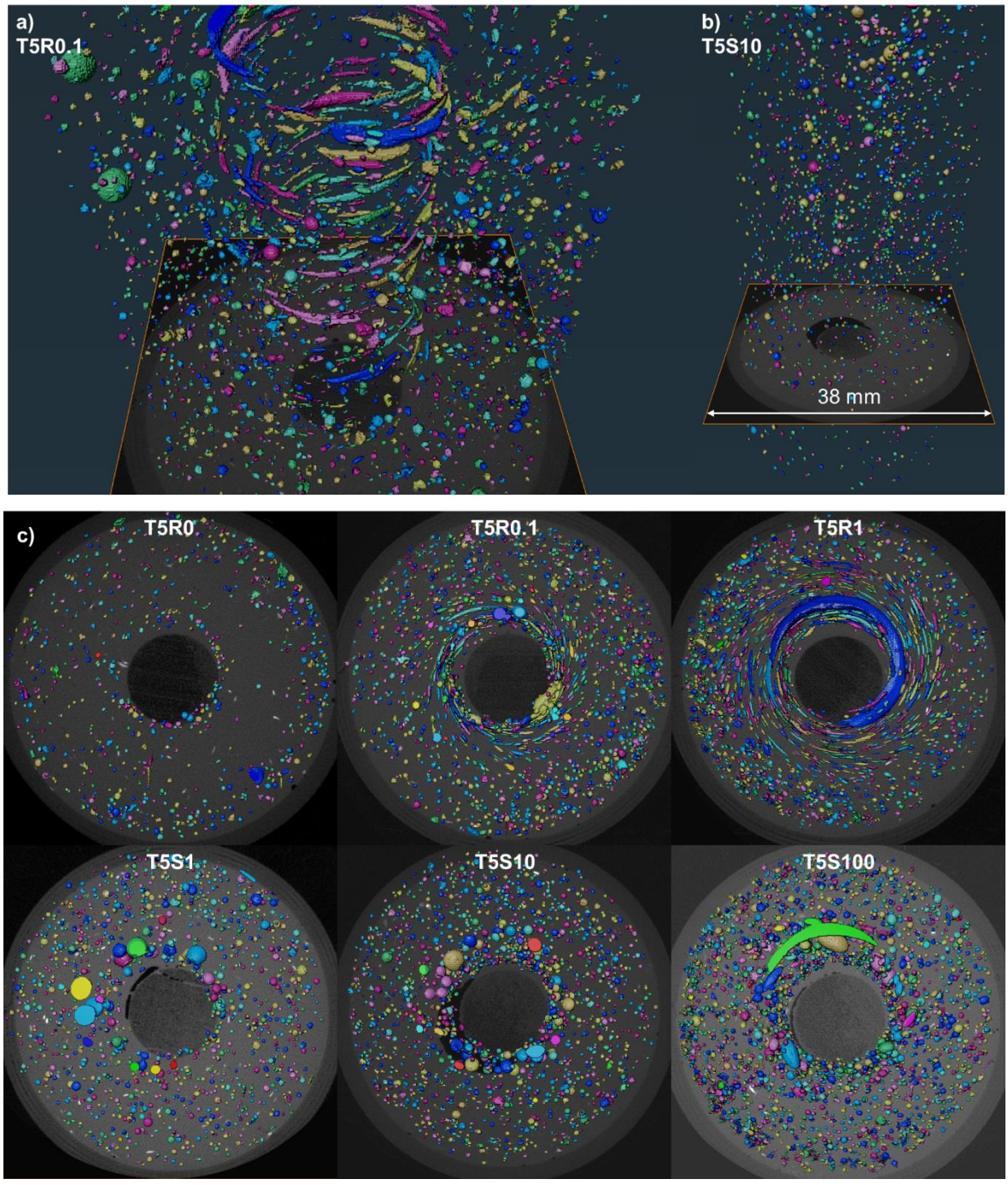

Figure 3.1. Vesicle reconstructions in Avizo: a) sample with deformed vesicles stirred at constant rate of 0.334 rad/s, looking diagonally down; b) looking diagonally down at a sample with spherical vesicles stirred at constant shear stress of 10 Pa, with larger vesicles concentrated towards the stirring rod and towards the top of the sample; c) collection of examples looking down from above, showing range in vesicle concentrations and distributions. The unstirred sample T5R0 has the fewest and smallest vesicles, but the sizes and distributions in stirred samples is broadly consistent, with larger vesicles in the centre and typically within the top 10 mm of the sample.

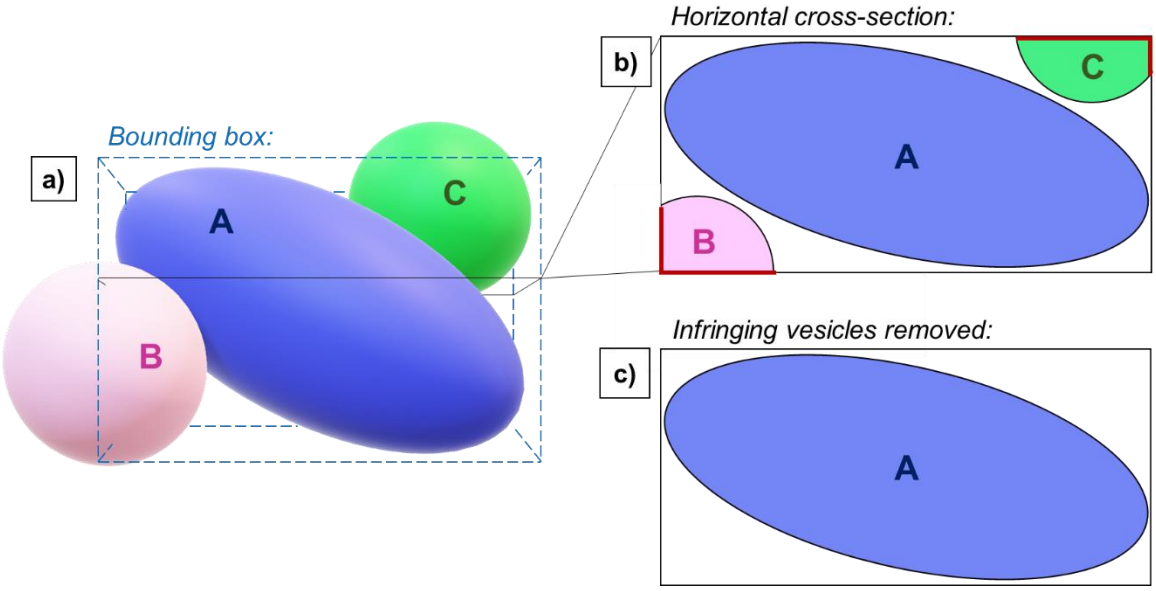

Figure 3.2. Schematic showing the process of extracting vesicle cross-sections: a) using the 3D bounding box for each vesicle to extract a cropped horizontal cross-section through its centre; b) the cross-section may contain parts of neighbouring vesicles; c) infringing vesicles are removed based on the large proportion of their perimeter coinciding with the image edge (highlighted in red), as the target vesicle does not touch the image edges.

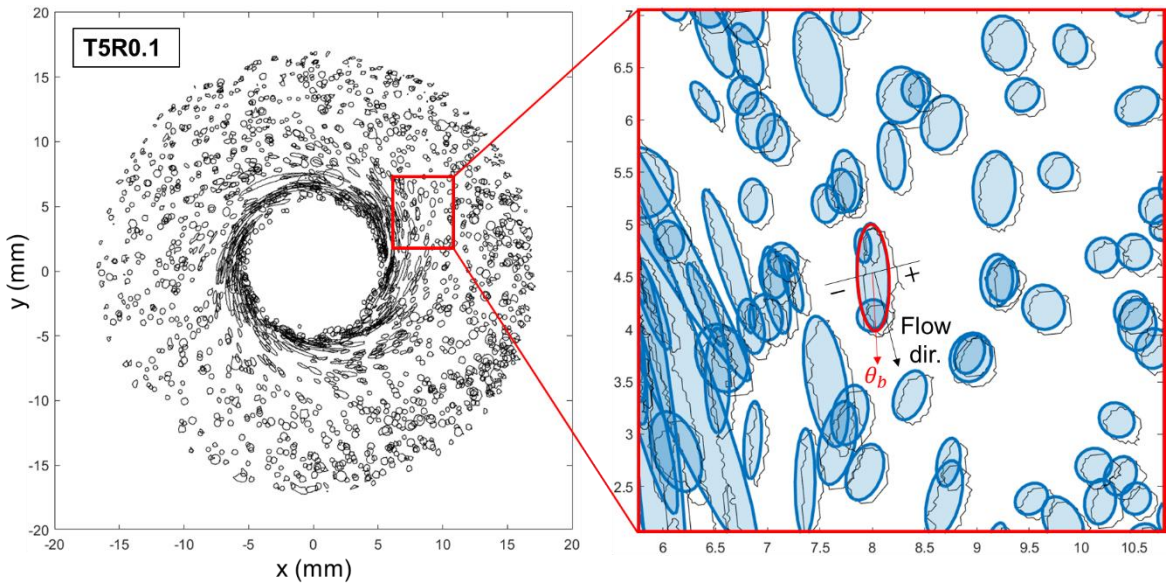

Figure 3.3. Extracted vesicle cross-sections in sample T5R0.1, with sample orientation corrected to ensure a vertical stirring rod. Vesicle cross-sections are approximated using the best-fit ellipse function in MATLAB, allowing orientations and long axes to be measured. Orientations are given relative to the flow direction at that position, with negative angles indicating a clockwise stirring direction.

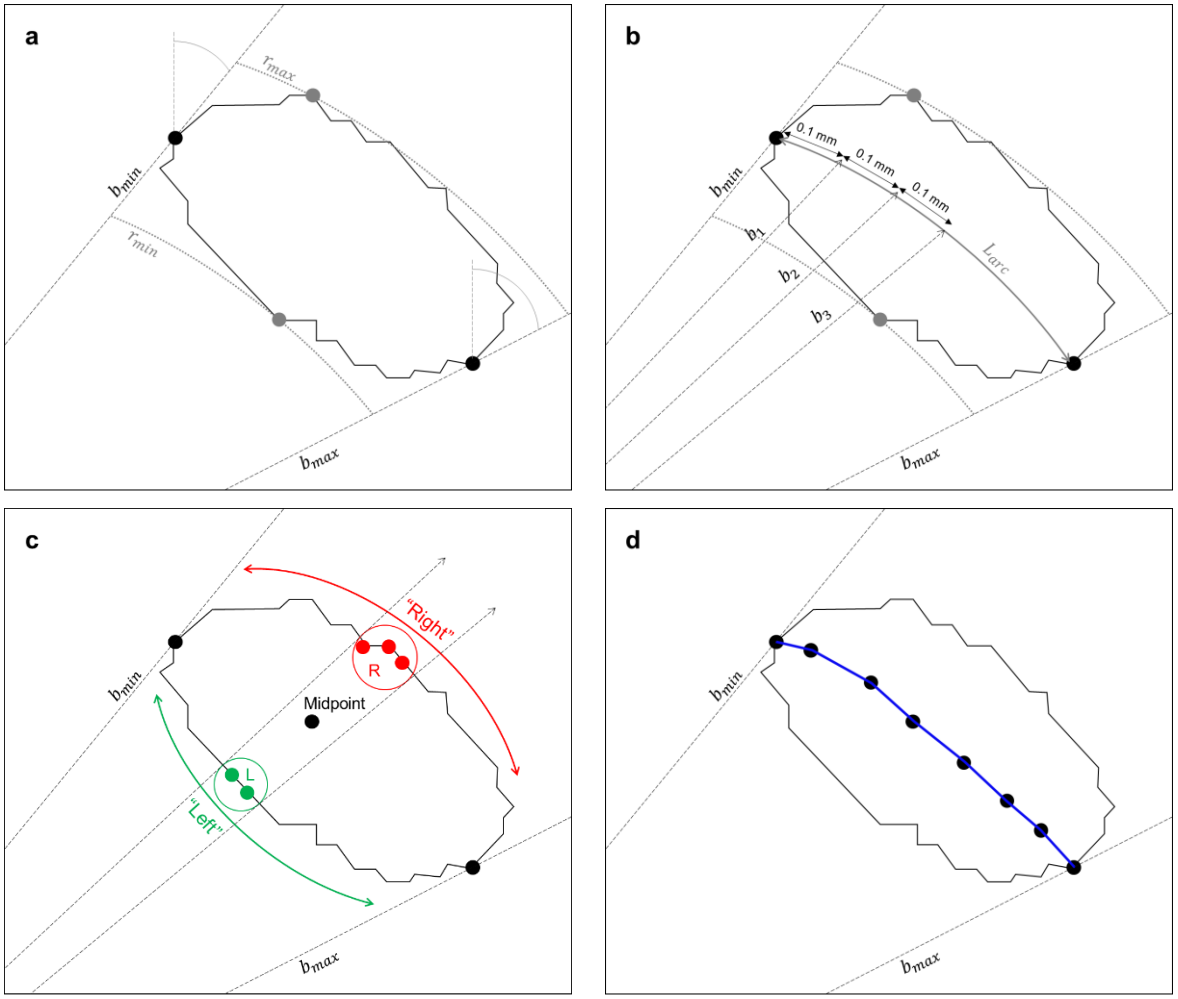

Figure 3.4. Measuring vesicle length L: a) finding edge points with the minimum and maximum bearing, and with the minimum and maximum radial distance; b) calculating intervals through the vesicle; c) dividing the vesicle outline into "left" and "right" halves, and calculating the midpoint between the "left" and "right" edge points within every interval; d) connecting the midpoints from each interval to create the vesicle centreline.

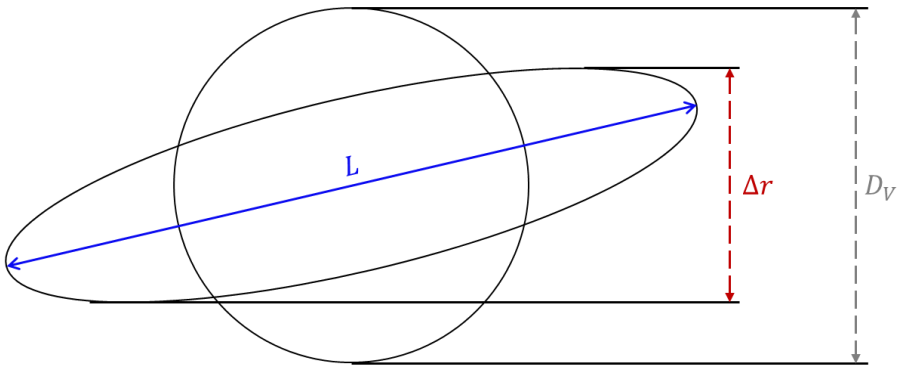

Figure 3.5. Schematic representation of measured vesicle dimensions: L centreline length from extreme ends of vesicle defined by bearings, Δr radial extent of vesicle calculated from distance to sample centre, and D_V the original spherical diameter of the vesicle calculated from its volume.

3.4. Results and interpretation

3.4.1 Constant stirring rate

The three samples stirred at a constant rate show a marked difference in vesicle shape depending on distance from the sample centre and the stirring rate used (Figure 3.6). Vesicles at the edges of the samples are spherical, but become progressively more elongated and parallel to the flow with distance towards the sample centre. This is captured by the deformation ratio L/D_V, where a vesicle with $L/D_V = 1$ is spherical, and a vesicle with $L/D_V > 1$ has been stretched by the flow. Within each sample, the deformation ratio shows a sudden increase at a critical radial distance moving inwards from the sample edges. This critical distance depends on the stirring rate used, with the highest stirring rate displaying vesicle deformation close to the cup edge, and the lowest stirring rate only containing deformed vesicles within 10 mm of the stirring rod (Figure 3.7).

In the sample stirred at 3.34 rad/s, there are spherical vesicles close to the stirring rod (Figure 3.6c). This is because we ended stirring early to avoid shear-induced crystallisation. As such, the bubbles near the very centre of this sample had time to relax back to spheres before they were captured. However, this was not the case for the other two samples, or for the more central regions of the 3.34 rad/s sample, which were sheared until they solidified.

We use the ratio $\Delta r/D_V$ to quantify the extent that bubbles have flattened perpendicular to the flow direction, comparing their radial extent Δr to their spherical diameter. For an undeformed vesicle, $\Delta r/D_V = 1$, whereas for a bubble that has flattened perpendicular to the flow, $\Delta r/D_V < 1$. Where flattening has occurred, the bubble walls have moved perpendicular to the flow direction, rather than being translated purely in parallel with the flow. The flattening ratio is constant across the radius of the sample stirred at the slowest rate, indicating that bubbles did not experience significant flattening (Figure 3.8a). However, the samples stirred at 0.334 and 3.34 rad/s both show some amount of flattening, with ratios starting to decrease beyond a critical distance away from the sample wall. This critical distance is closer to the wall in the 3.34 rad/s sample.

This flattening of bubble shapes towards the sample centre is not unexpected. Photos from laboratory experiments show that bubbles at equilibrium deformation become more flattened with increasing Ca, although this flattening has never been measured explicitly (Rust and Manga, 2002; Müller-Fischer et al., 2008). We might also expect some degree of flattening due to interaction with other bubbles, which becomes more likely as bubbles stretch out over a wider area, and also due to shear-induced crystallisation moving outwards from the stirring rod, providing a compressive radial force. These factors would be more pronounced at higher stirring rates. However, it seems likely that bubble flattening is a natural result of higher Ca towards the stirring rods in the sample centres, rather than additional compressive effects from neighbouring bubbles or the solidification front.

Vesicle orientations also capture the effects of cooling versus strain rates (Figure 3.9). There is no preferred orientation near the edges of the samples, because when bubbles are close to spherical, the orientations of the best-fit ellipse are highly unreliable. Moving in towards the centre, the standard deviation of angles decreases, as vesicles start to become elongated and inclined to the flow. In each sample, there is a sharp transition from randomly-distributed orientations at the sample edge, where vesicles are near-spherical, to a clear preferred orientation moving towards the sample centre, where vesicles are deformed. The highest angle to the flow occurs at the transition from random to preferred orientations. From there, vesicle orientation decreases towards the sample centre, as vesicles become increasingly parallel with the flow.

3.4.2 Constant shear stress

Vesicles within the samples stirred at constant shear stress look very different from those stirred at a constant stir rate. Virtually all the vesicles within the constant shear stress samples are spherical (Figure 3.10). There are no trends in bubble deformation or orientation moving radially across the samples. However, it is infeasible that the bubbles remained spherical while the sample was being stirred. The constant shear stress samples started with stirring rates similar to the samples that used a constant stirring rate (Figure 3.11); in fact, the sample at 100 Pa spent nearly eight minutes being stirred at faster rates than the sample stirred constantly at 0.0334 rad/s, and yet it contains almost no elongated vesicles.

a) T5R0.1

($\omega = 0.0334\ rad/s$)

b) T5R1

($\omega = 0.334\ rad/s$)

c) T5R10

($\omega = 3.34\ rad/s$)

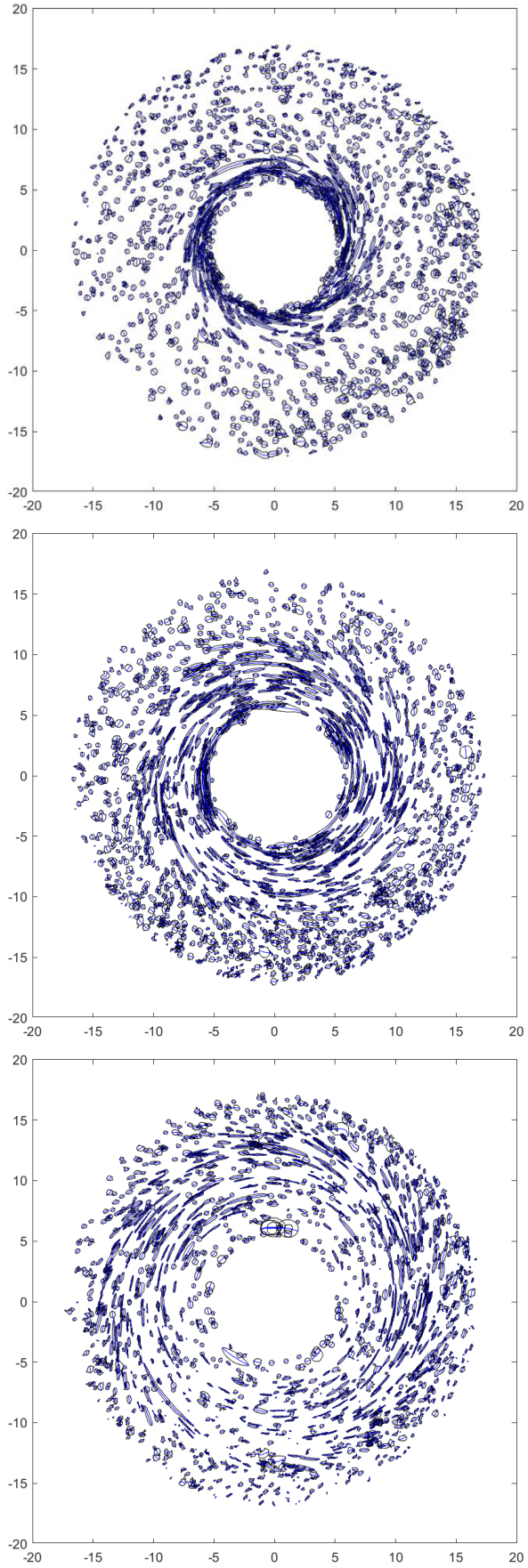

Figure 3.6. Vesicle cross-section outlines viewed from above, in the three samples that were stirred at constant rates ω. Calculated vesicle centrelines are shown in blue.

a) T5R0.1

($\omega = 0.0334\ rad/s$)

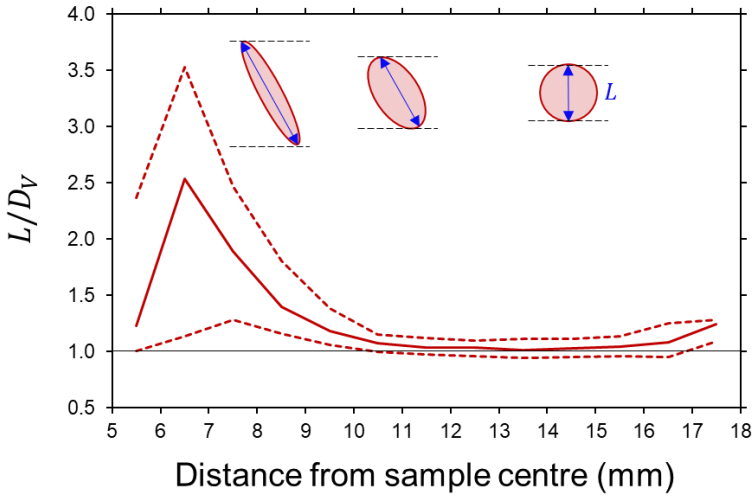

b) T5R1

($\omega = 0.334\ rad/s$)

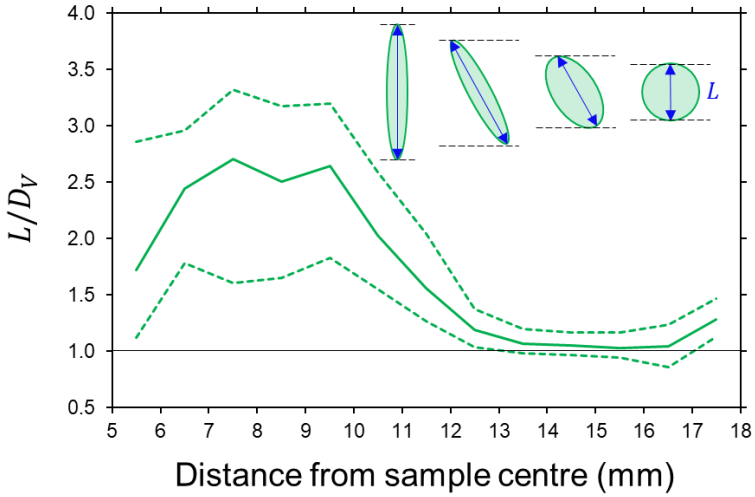

c) T5R10

($\omega = 3.34\ rad/s$)

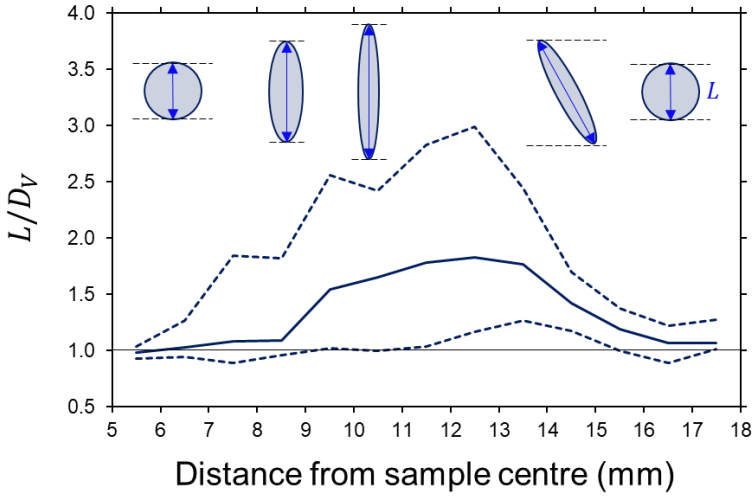

Figure 3.7. Vesicle deformation ratio across the widths of samples stirred at a constant rate. Solid lines show median values, and dashed lines show the interquartile range. The stirring rod has a radius of 5 mm, and the cup edge is approximately 18 mm from the sample centre. Also shown are schematic cartoons of bubble deformation, demonstrating the change in vesicle shape and orientation, D_V and L towards the sample centre.

a) T5R0.1

($\omega = 0.0334\ rad/s$)

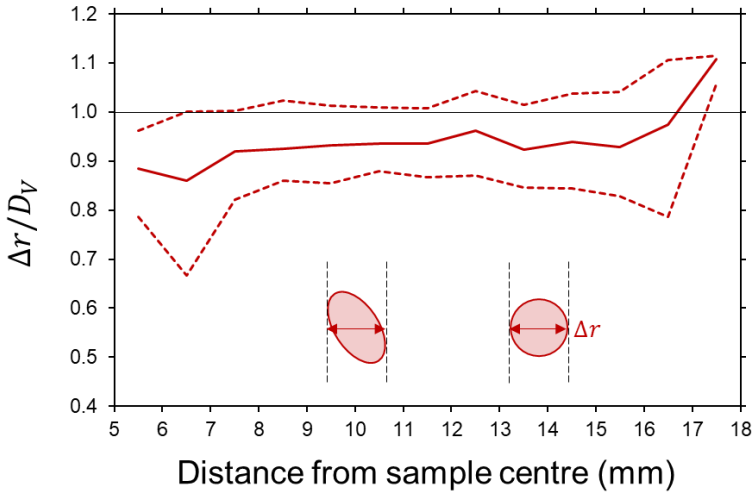

b) T5R1

($\omega = 0.334\ rad/s$)

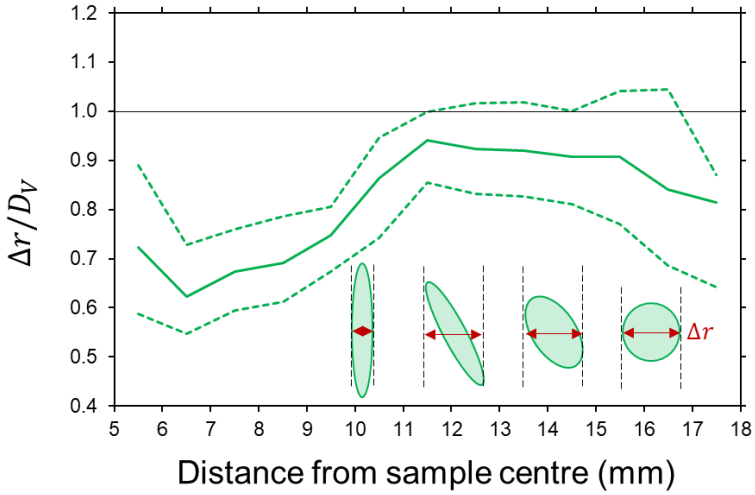

c) T5R10

($\omega = 3.34\ rad/s$)

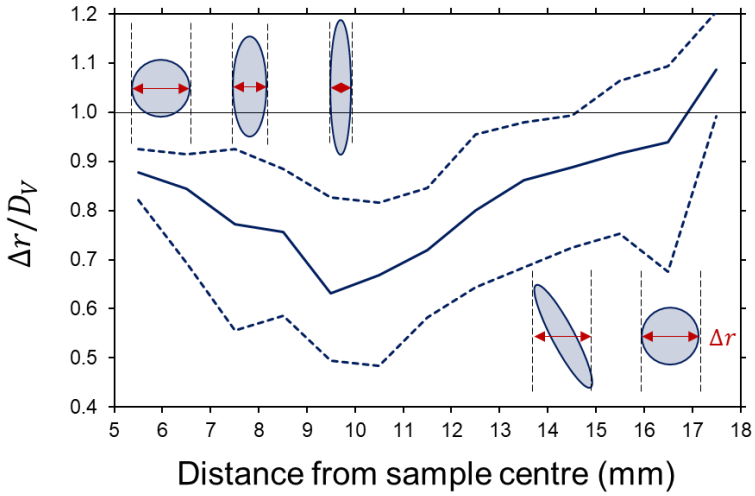

Figure 3.8. Vesicle flattening ratio across the widths of samples stirred at a constant rate. Solid lines show median values, and dashed lines show the interquartile range. The stirring rod has a radius of 5 mm, and the cup edge is approximately 18 mm from the sample centre. Schematic cartoons demonstrate how bubble orientation and Δr changes towards the sample centre.

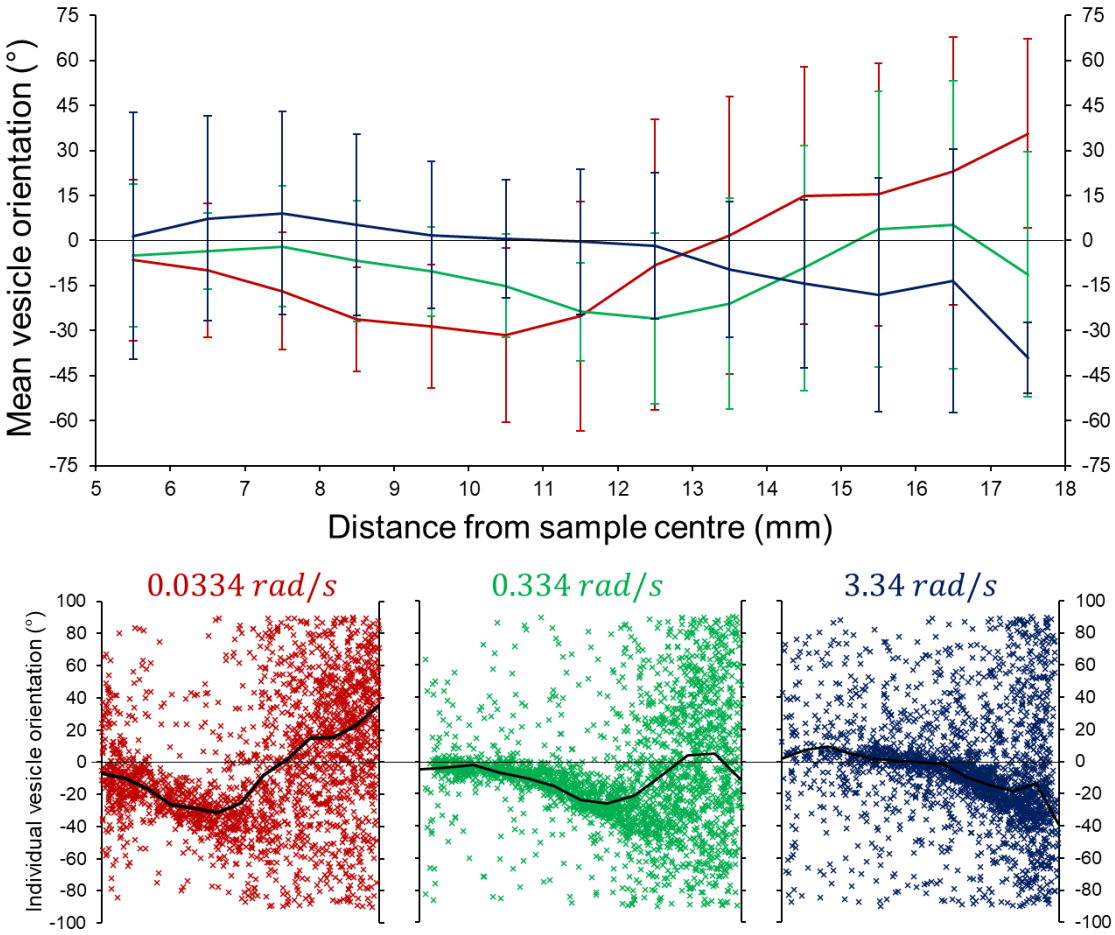

Figure 3.9. Vesicle cross-section orientations, as measured from best-fit ellipses, across the width of each sample stirred at a constant rate. Error bars show one circular standard deviation. Sub-plots show all vesicle orientations in each sample, with a black line tracing the circular mean.

a) T5S1

($\tau = 1\ Pa$)

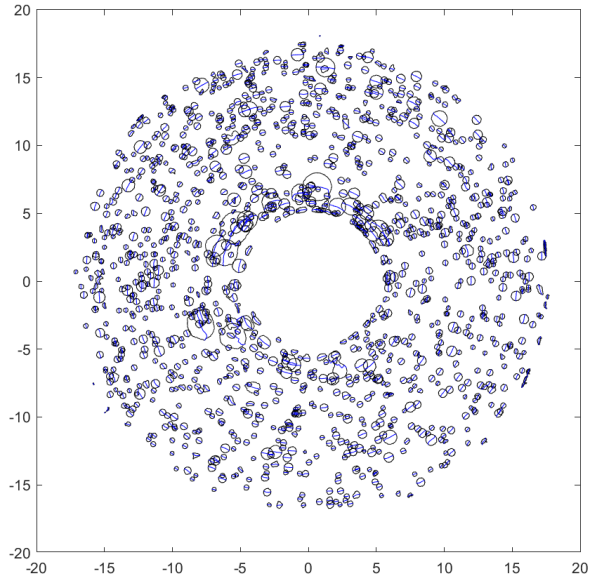

b) T5S10

($\tau = 10\ Pa$)

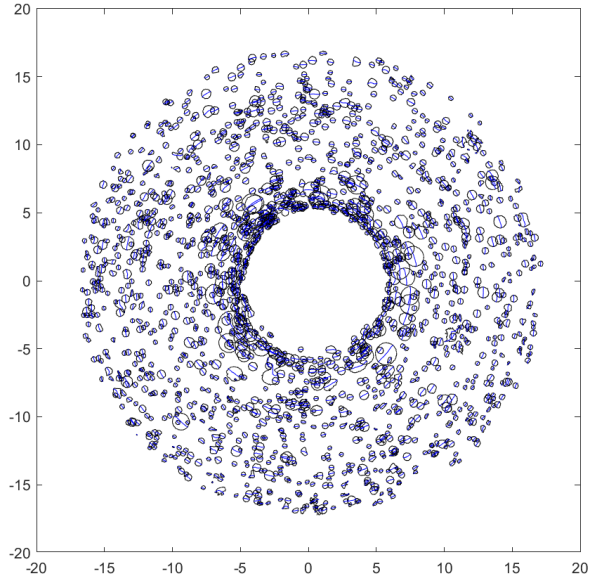

c) T5S100

($\tau = 100\ Pa$)

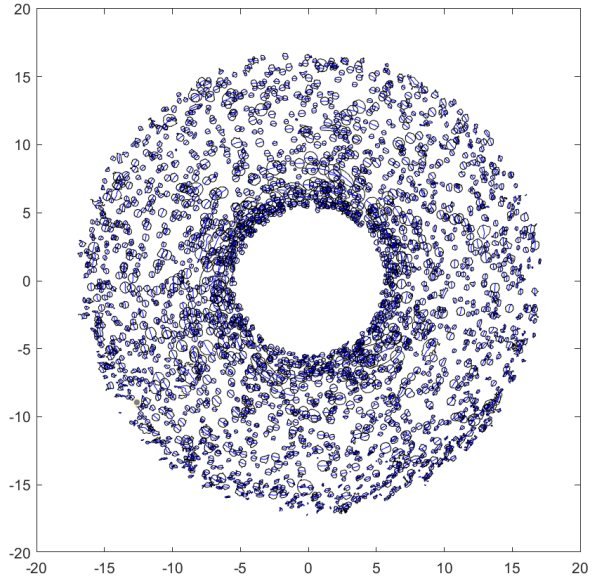

Figure 3.10. Vesicle cross-section outlines viewed from above, in the three samples that were stirred at constant shear stress τ. Calculated vesicle centrelines are shown in blue.

3.4.3 Solidification behaviour

Figure 3.11 also reveals some interesting trends regarding the solidification of each experiment. The initial temperature and viscosity of each sample was kept constant between experimental runs (for details see Section 2.3), and yet some samples appear to solidify faster than others. For the sample stirred at 3.34 rad/s, we deliberately ended stirring before complete solidification to avoid shear-induced crystallisation disrupting the textures, but for the other samples, stirring ended when the stirring rod detached from the solidified sugar, or when the mixture became too solid for the rheometer motor to continue stirring. As such, the ends of the curves in Figure 3.11 provide an insight into the solidification times of each sample, excluding the one stirred at 3.34 rad/s.

For the constant shear stress samples, the sugar took longer to solidify at higher shear stress. In the samples stirred at a constant rate, faster stirring resulted in shorter solidification times. We note that most of the sugar in our samples forms a glass rather than a crystalline solid, which makes determining the "solidification point" challenging. By comparing the apparent viscosities measured throughout each experiment, we see that the samples stirred at a constant rate follow a different solidification behaviour to those stirred at a constant shear stress (Figure 3.12). Each sample cooled under the same conditions, meaning that viscosity gradients should be broadly consistent between them, and we established in Chapter 2 that molten sugar above 60 °C is Newtonian. The only reason for such a significant divergence in apparent viscosity is that the stirring conditions have influenced the solidification of the sample.

There are several reasons that stirring rate might impact solidification: firstly, stirring adds heat to the sample via friction, so faster stirring may keep the sample warmer for longer. This may modify the cooling rate, and alter the rate at which the sample becomes glass. Secondly, stirring promotes crystallisation, and crystallised sugar will solidify in a different manner to glass. Crystallisation will also release latent heat that could further modify the sample. Establishing the effects of shearing on glass formation and solidification is beyond the scope of this investigation; however, we want to highlight the discrepancy between the two sets of samples, because the differences in viscosities may have impacted bubble relaxation, equilibrium deformation and final bubble textures.

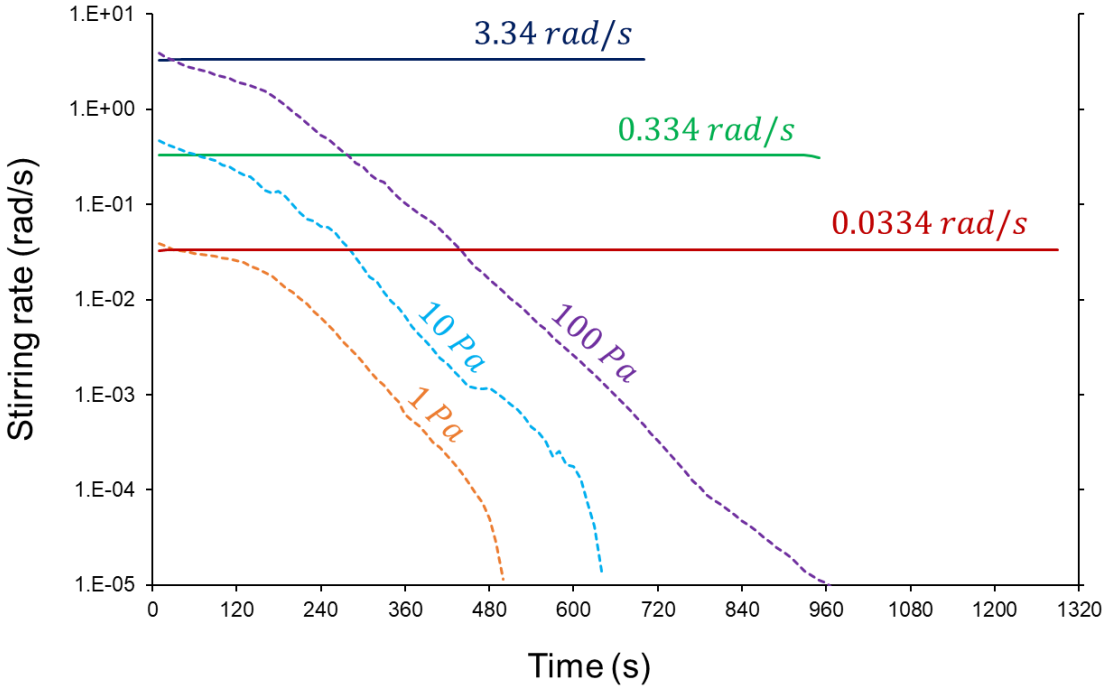

Figure 3.11. Stirring rates in the samples stirred at constant rate (solid lines) and at constant shear stress (dashed lines). The samples started at similar stirring rates, but the constant shear stress samples experienced a decrease in stirring rate over time.

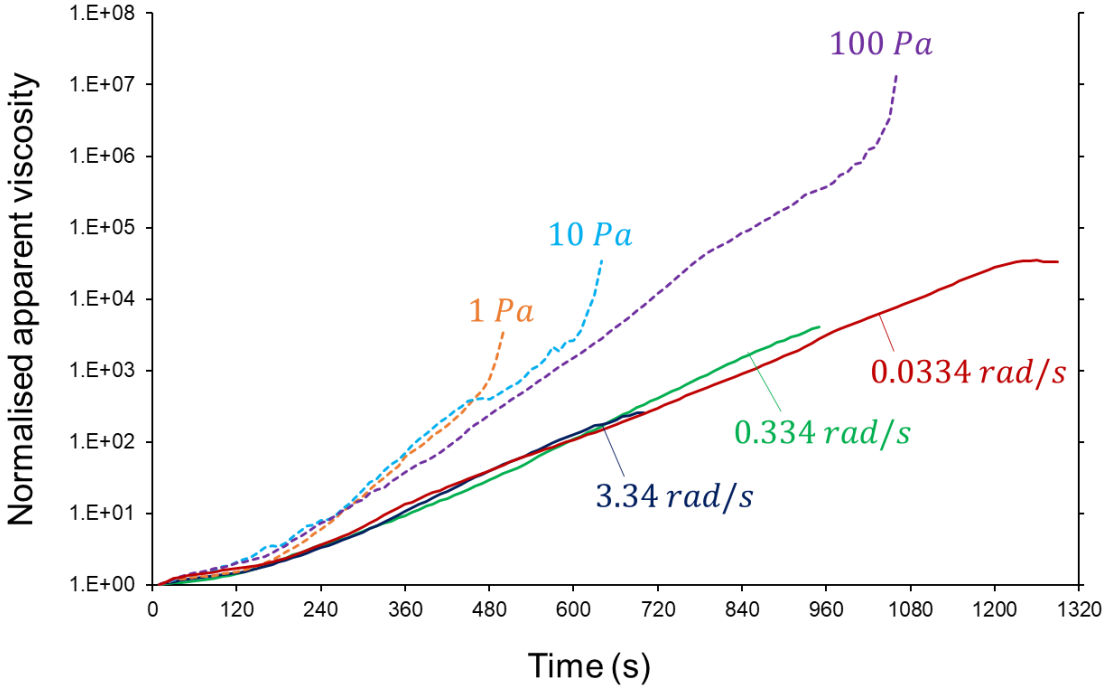

Figure 3.12. Apparent viscosity measured throughout the solidification of each sample, normalised against the initial apparent viscosity. Samples stirred at a constant rate (solid lines) follow a different path compared to samples stirred at a constant shear stress (dashed lines). With the exception of the 3.34 rad/s sample, the end of the curves indicates the time at which the sample solidified.

3.4.4 Changing flow conditions during solidification

Two of our experiments were designed to investigate the impact of changing flow conditions midway through the solidification of the sample. The first sample was stirred at a constant rate of 0.167 rad/s, and after 12 minutes of cooling, the stirring direction was reversed instantaneously. This resulted in vesicles in the outer portion of the sample being elongated in the opposite direction to those in the inner portion of the sample (Figure 3.13a). The clockwise to anticlockwise transition occurs at around 10-11 mm from the sample centre. However, the transition region is not always clear, and there appears to be some overlap between bubbles oriented clockwise and anticlockwise (Figure 3.14). This overlap is caused by vertical differences through the sample. Vesicles higher up in the sample transition from clockwise to anticlockwise orientations closer to the sample centre, compared to vesicles lower in the sample.

Vertical position influences the radial position of the textural reversal due to differences in cooling rate. The surface of the sample was open to the air, leading to the development of vertical as well as radial thermal gradients. The surface of the sample solidified sooner than the interior, and so vesicles near the surface were captured sooner than those at depth. As such, vesicles higher in the sample had a shorter window to respond to the change in flow direction compared to vesicles lower in the sample. This vertical thermal gradient is significantly weaker than the one imposed by the rheometer cooling system, but the sample is also much taller than it is wide (approximately 70 mm tall, but only 19 mm in radius), so the differences in capture times vertically are less pronounced than differences radially. However, sudden changes in stirring conditions have stronger signatures than gradual changes, and so they are apparent in the vertical dimension.

The second experiment with a change in flow conditions was left undisturbed for 12 minutes, then stirred at a constant rate of 0.334 rad/s until it solidified. The most striking feature of this sample is the large vesicle with one rounded side and one pointed side, which appears to have only partly solidified before stirring commenced (Figure 3.13b). The outer part of the vesicle is rounded, suggesting that it solidified in place while the sugar was stationary, whereas the inner part of the vesicle is stretched out, and has been significantly deformed by the flow before being captured. Pointed shapes like this one are only seen in the largest vesicles. Due to the thermal gradients present within the sample, smaller vesicles were less likely to be caught with one side solid and one side molten, and so they retain broadly elliptical shapes.

A comparison between the textures in samples where conditions were constant and where conditions changed partway through solidification reveals very few differences, aside from the switch from clockwise to anticlockwise orientations in the sample where flow direction was reversed. The vesicle deformation ratio and flattening ratio for the $\omega = 0.167\ rad/s$ sample falls almost exactly between the $\omega = 0.0334\ rad/s$ and $\omega = 0.334\ rad/s$ samples (Figure 3.15a, 3.15b), as would have been

expected under constant conditions. Likewise, the $\omega = 0.334\ rad/s$ sample in which stirring started at 12 minutes shows very similar trends to the $\omega = 0.334\ rad/s$ sample in which stirring was constant throughout (green curves, Figure 3.15). These similarities suggest that the final shape of vesicles is determined late in the solidification process. The vesicles captured in the samples stirred continuously are no more deformed than the vesicles in samples in which stirring started or reversed after 12 minutes.

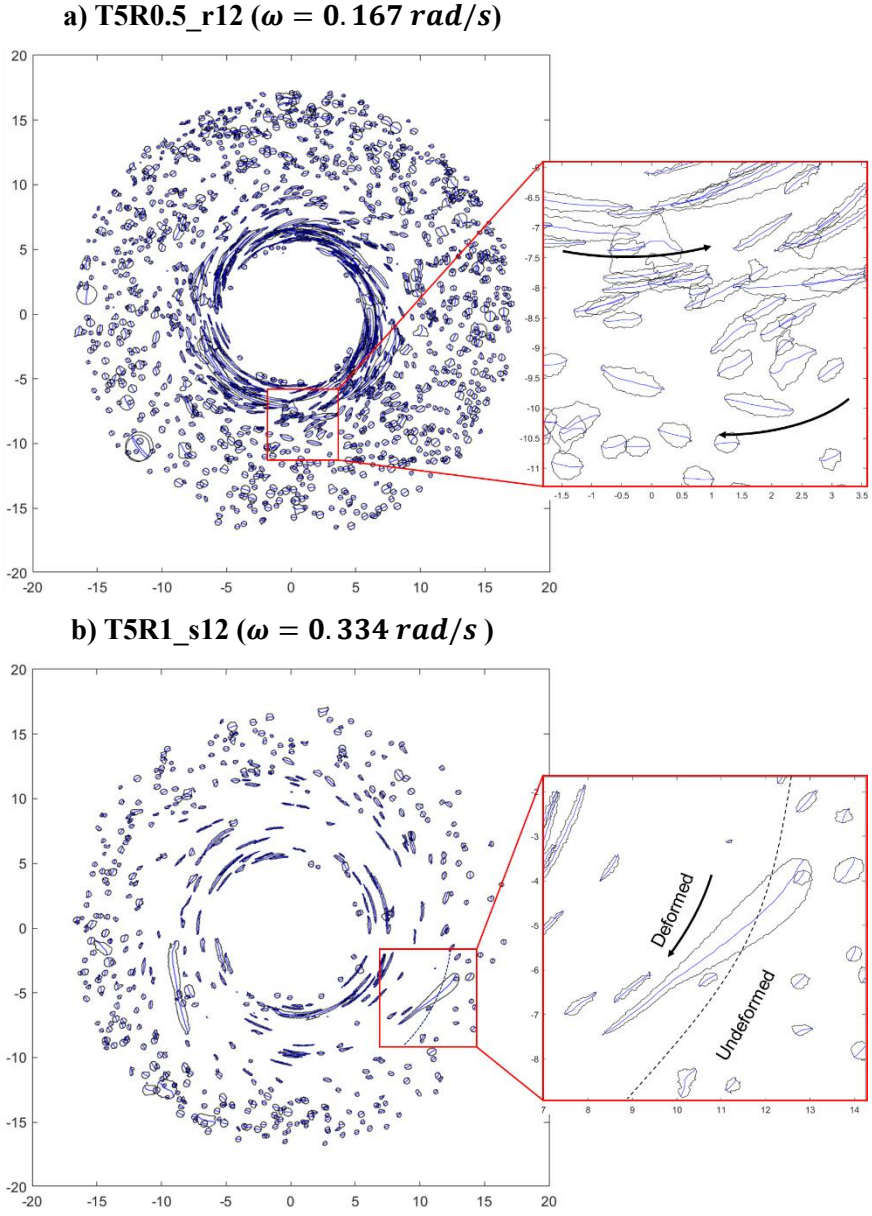

Figure 3.13. Vesicle cross-section outlines viewed from above, in the two samples where stirring conditions changed partway through their solidification: a) sample stirred at a constant rate ω, where the stir direction was reversed from clockwise to anticlockwise at 12 minutes, causing a reversal in the orientation of elongated vesicles; b) sample left undisturbed for 12 minutes, before being stirred at a constant rate. Calculated vesicle centrelines are shown in blue.

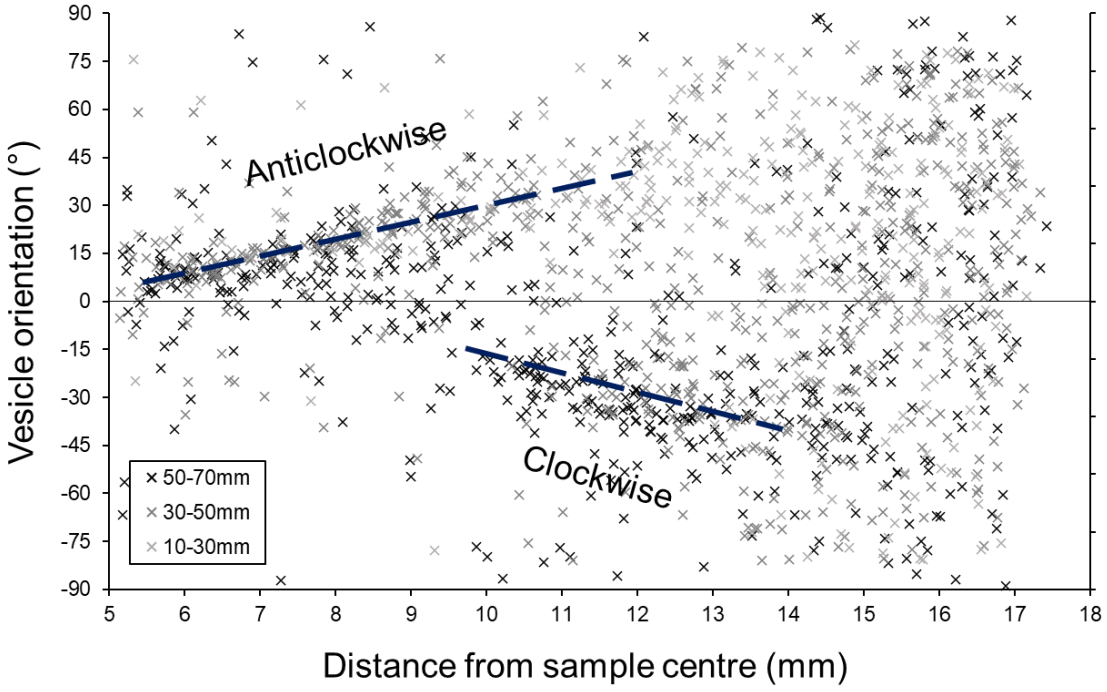

Figure 3.14. Vesicle orientations in the sample where stirring direction was reversed after 12 minutes, with bubble vertical position indicated by marker colour. There is an overlap between the trends of clockwise and anticlockwise bubble elongation, related to bubble vertical position. Bubbles higher up in the sample transition from clockwise to anticlockwise orientations closer to the sample centre.

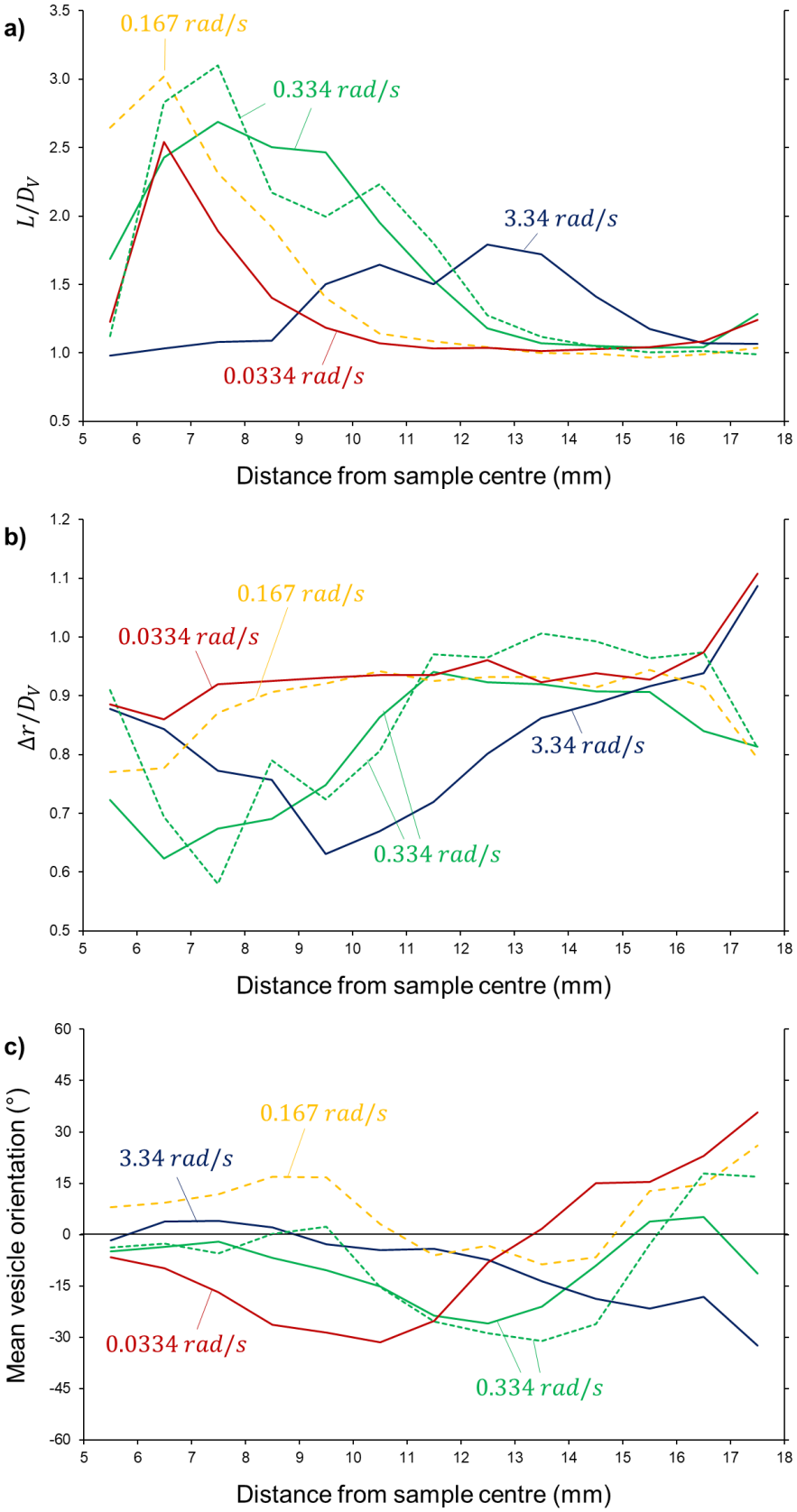

Figure 3.15. Comparison of vesicle textures between samples stirred under constant conditions (solid lines) and samples that witnessed a change in stirring conditions partway through solidification (small dashed lines = stirring commenced at 12 minutes; long dashed lines = stirring direction reversed at 12 minutes).

3.5. Discussion

3.5.1 Constant stirring rate vs. constant shear stress

The vesicles within samples stirred at a constant rate look very different to those stirred at constant shear stress, where the stirring rate decreased over time. Vesicles in the constant shear stress samples are spherical, and yet the bubbles must have been deformed at some point during the sample lifetime, as they started with similar stirring rates to the samples in which stirring rate was kept constant. In fact, the 100 Pa sample started with a stirring rate 100 times greater than the 0.0334 rad/s sample, and had a stirring rate > 0.0334 rad/s for almost eight minutes, during which time the bubbles must have deformed (Figure 3.11). We therefore infer that bubbles in the constant shear stress samples had the opportunity to relax back to spheres before they were captured as vesicles, but bubbles within the samples stirred at a constant rate did not have this opportunity.

By comparing our samples, we see that vesicle shapes are determined late in the solidification history. Vesicles in the constant shear stress samples record no evidence of stirring, and vesicles in the sample where stirring started after 12 minutes record no evidence of having been stationary. The final shape of vesicles appears to depend on a balance between bubble relaxation time, the rate of change in equilibrium deformation, and the migration rate of the solidification front. This balance is easiest to imagine if we consider the evolution of the velocity profile within the samples. Here we present a conceptual model in which we treat the solidification front as a sharp boundary between solid and molten sugar, and treat the molten region as if it had a constant viscosity. The velocity profile within the molten sugar is a function of radial position r and the stirring rate ω, as given by Eq. 2.7 (Section 2.3.2).

Over time, the solidification front moves inwards and the molten region grows narrower. If the stirring rate is kept constant, we see an increase in strain rates across the molten region, and the strain rates ahead of the solidification front increase over time. If the shear stress is kept constant and the stirring rate declines, strain rates ahead of the solidification front decrease over time. This is presented in Figure 3.16, where velocity gradients are calculated for values of R_o of 19, 15 and 10 mm. For the samples stirred at a constant rate, we simply solve Eq. 2.7 for specified values of R_o. For samples stirred at a constant shear stress, we use the thermal model presented in Chapter 2 (Section 2.5) to estimate the times at which the solidification front was at 15 and 10 mm. We then find the stirring rates that the rheometer recorded at these times, and use these to estimate the velocity profile. We assume a thermal diffusivity for the sugar of $\alpha = 0.06 \times 10^{-6}\ m^2 s^{-1}$. This simple model does not account for the viscosity gradient across the molten region; however, it serves to demonstrate the general change in strain rates ahead of the solidification front for constant stirring rates and constant shear stress.

In the constant stirring rate samples, bubbles are never given an opportunity to relax, and so captured vesicles have deformed shapes. Strain rates ahead of the solidification front are always increasing, and so the equilibrium deformation of any bubble becomes increasingly elongated over time, at any position within the sample. Bubbles are in a constant state of being elongated, right up until the moment that they are captured as vesicles. This is in contrast to the constant shear stress samples, where strain rates ahead of the solidification front are always decreasing, meaning that the equilibrium deformation of bubbles becomes increasingly spherical over time. In this case, bubbles are in a constant state of relaxing up until the moment they are captured, and in our samples, all bubbles appear to have returned to spheres. This shows that the relaxation time of the bubbles was sufficiently short for them to respond to changes in the shearing environment before the solidification front arrived.

This balance between bubble relaxation times and the rate of solidification implies the existence of a threshold for the creation of elongated vesicles. If bubble relaxation times had been longer, or the solidification front had progressed inwards faster, then deformed bubbles in our constant shear stress samples would not have been able to return to spheres before being captured. Clearly, this threshold is greater than 100 Pa for the cooling rate we used. However, it is likely that elongated vesicles could be captured within constant shear stress samples if either the shear stress or the cooling rate was higher.

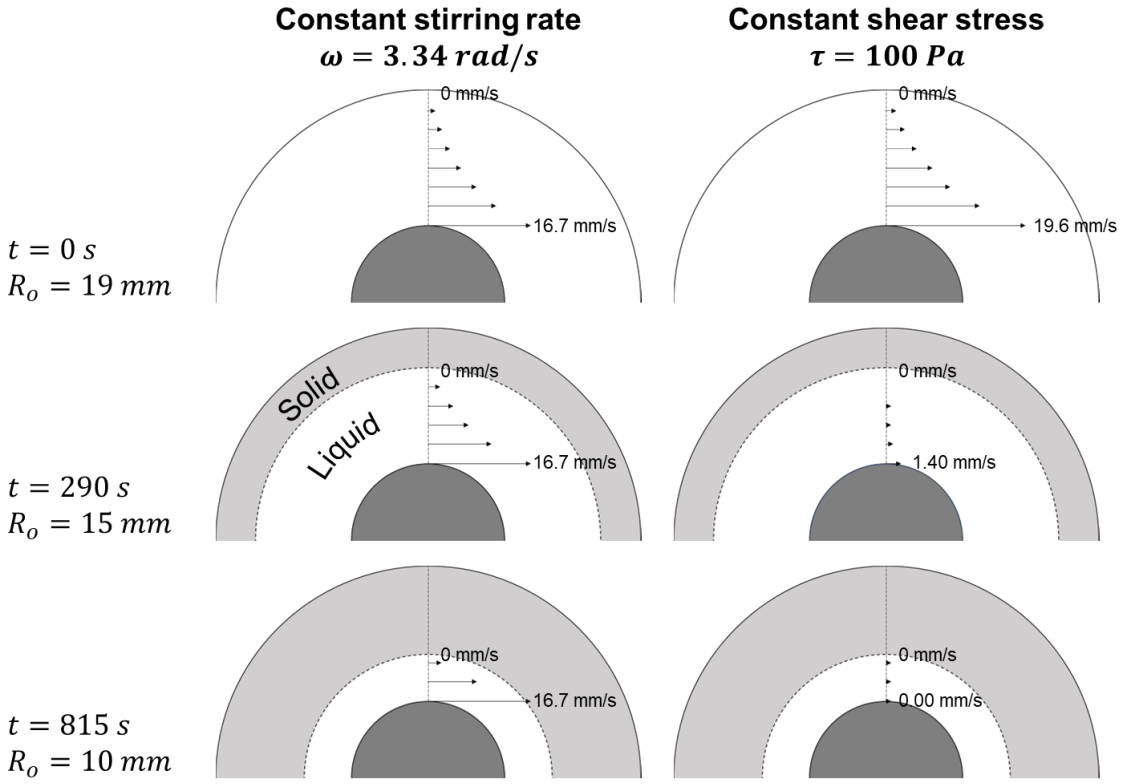

Figure 3.16. Evolution of velocity profiles within samples stirred at constant rate and at constant shear stress. The solidification front is marked by a dotted line, separating solid regions (grey) and liquid regions of a constant viscosity (white). The stirring rod is dark grey.

3.5.2 Changing flow conditions

For the sample where stirring direction was instantaneously reversed after 12 minutes, we see a sharp transition in vesicle orientation from clockwise to anticlockwise. This sharp transition reflects the width of the solidification front, and suggests the presence of a steep viscosity gradient between liquid and solid regions of the sample. Had the front been more diffuse, with a gentle viscosity gradient between liquid and solid regions, we would have expected a wider transition zone in vesicle orientations, with some vesicles caught in the process of "unwinding" in response to the change in flow direction. This is because high viscosities increase the response time of bubbles, and so a viscosity gradient manifests as a gradient in response times, with the potential to capture vesicles caught in various stages of adapting to the change in flow conditions. Instead, the sharp transition from clockwise to anticlockwise vesicles shows that bubbles immediately ahead of the solidification front adapted rapidly to the change in flow conditions, suggesting a sharp boundary between solid and liquid regions.

In the sample where stirring started after 12 minutes of cooling, the largest vesicles are teardrop shaped, in that they are rounded on their outer edge and pointed on their inner edge. This shape has formed due to their outer walls already being solidified when stirring began. Smaller bubbles rarely show this texture, and this is due to a balance between viscosity gradients and bubble size. If bubbles are small in relation to the viscosity gradient, their walls are likely to be deforming under broadly uniform conditions, whereas if bubbles are large in relation to the viscosity gradient, their walls will exist across a range of viscosities, deforming at different rates, potentially even having some sections that have solidified while others remain molten and mobile.

The final shape of vesicles also depends on the migration rate of the solidification front. If the vesicle is large enough to exist across the solid-liquid boundary, then the rate at which this boundary traverses the diameter of the bubble will determine the time available for deformation. We explore this relationship using a simple simulation in MATLAB. We deform a circle of points with a diameter of 1 mm in simple shear at a strain rate of 0.01. A solidification front moves inwards at a given rate, perpendicular to the flow direction, and points which lie on the solid side of this boundary are fixed in place, while points on the liquid side remain free to deform. The flow velocity is always 0 m/s at the solidification front. The simulation does not account for surface tension; however, the effect of surface tension should be minimal in the high-viscosity fluid ahead of a solidification front.

The simulation produces a variety of vesicle shapes (Figure 3.17). Simulated vesicles are rounded on the side which solidified first, and pointed on the side which solidified last, similar to the large, pointed vesicles seen in the sample where stirring started after 12 minutes. The angularity of simulated vesicles depends on the velocity of the solidification front. A slower-moving front allows the inner bubble walls to deform into a longer point before the bubble solidifies.

Our modelling suggests that vesicle shape may not be a simple reflection of flow conditions frozen in time, as this shape may be modified during capture. Such modifications will be more pronounced for bubbles which are large in relation to the viscosity gradient, and when the solidification front migrates rapidly in relation to the strain rate.

Finally, in both samples where stirring conditions changed partway through the experiment, final vesicle textures are broadly in line with the samples where stirring was constant throughout solidification (Figure 3.15). Just as we saw in the constant shear stress samples, this similarity suggests that vesicle shape is not heavily dependent on the early deformation history of the bubble. It appears that final vesicle shape is dominantly controlled by shear conditions immediately ahead of the solidification front, and that bubbles reacted quickly to changes, such as the sudden change from a stagnant to a stirred environment, or the sudden change in flow direction. We note that the vesicles captured within the stirred region of the sample in which stirring started after 12 minutes are near identical to the vesicles in the sample which had been stirred from the start at the same rate. This strongly suggests that the bubble shapes reached equilibrium quickly when stirring started at 12 minutes, and that the subsequent vesicle shapes reflect conditions at the solidification front.

Our experiments involving sudden changes in stirring conditions highlight the balance between the response time of bubbles and the velocity of the solidification front. If the front moves quickly in relation to the response time of bubbles, it will capture bubbles in various stages of responding to the change in flow environment. When the front moves slowly in relation to bubble response times, as appears to be the case in our samples, the dynamic response is not captured, and the change in textures occurs suddenly, over a short distance.

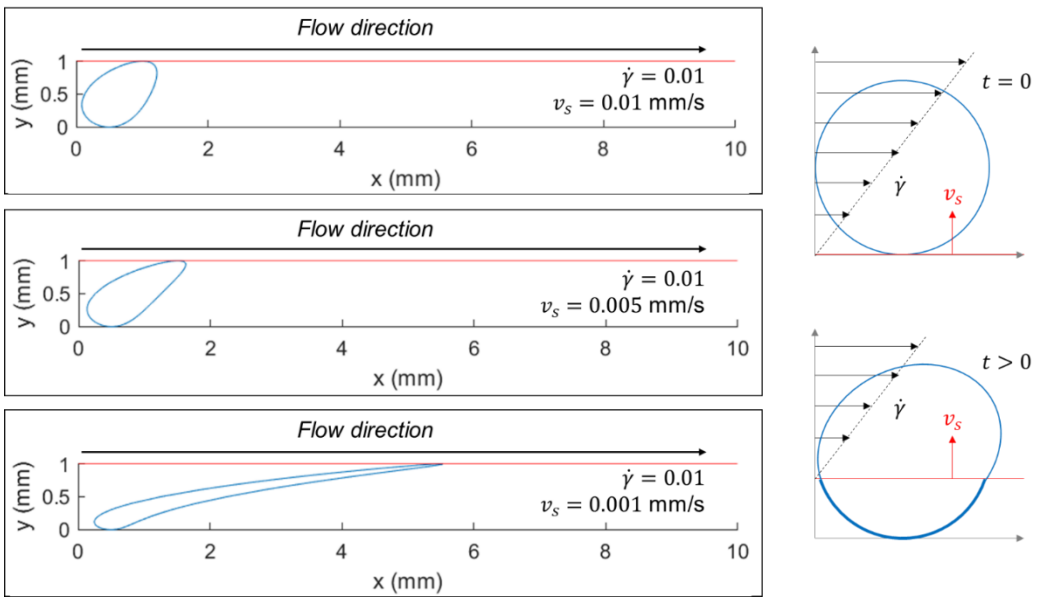

Figure 3.17. Modelled vesicle shapes with progressive inwards solidification in simple shear. Bubbles start spherical. The solidification front (red line) moves upwards, perpendicular to the flow direction, at a rate v_s. Flow velocity is zero at the solidification front. Sections of the bubble wall in the liquid region deform in response to flow, while sections in the solid region are fixed in place.

3.6. Implications: application to real vesicles

3.6.1 Vesicles as a time series

The first step in interpreting vesicle textures within dykes and lava flows is to ascertain when they were captured. Dykes solidify progressively inwards from their margins, and so all textures may be read as a time series with the youngest material in the centre. However, the solidification front does not advance towards the centre at a constant rate. Its advance is controlled by the balance between conduction and advection, and as such, the cooling history of a dyke is strongly dependent on channel width and magma driving pressures, and how these varied over time.

The first factor to consider is the dyke width. This has a significant impact on solidification history, because the channel width influences the volumetric flux of magma and therefore the amount of advection within the system. Advection counteracts the effects of conduction by continuously replacing cooled magma with fresh, hot magma. In fact, if a dyke is sufficiently wide, or if the pressure driving magma flow is sufficiently high, advection can produce runaway thermal erosion. A critical Peclet number determines whether a dyke will solidify shut or thermally erode (Lister and Dellar, 1996), and for a given channel length and driving pressure, this may be expressed as a critical initial half-width (Section 1.3.2).

Many dykes in the field display chilled margins, suggesting that they did not experience runaway thermal erosion during their emplacement (Huppert and Sparks, 1989). However, it would be incorrect to assume that their final, solidified width equals their initial width, because all dykes experience some amount of inflation during their emplacement. Dyke tips are narrow and tapering to instigate fracture (Rivalta et al., 2015), and so the initial stage of intrusion always involves the channel widening. Inflation occurs simultaneously with progressive inwards solidification, so in the absence of any evidence for thermal erosion, it is highly unlikely that the entire width of solid dyke was ever molten. This is a key reason that vesicle profiles across the widths of dykes are highly unlikely to capture an active velocity profile.

In the initial stages of dyke emplacement, the channel is narrow, advection is minimal, and conduction is dominant, leading to relatively rapid inwards solidification. Vesicles are captured quickly, with little chance to reach their equilibrium deformations. Even if they experience some deformation before capture, this deformation will reflect conditions in the narrow, early channel. As such, marginal vesicles are likely to be irregularly shaped, and if they are deformed, these deformations should not be interpreted as having formed at the edges of a channel as wide as the solidified dyke.

During the middle stages of emplacement, the dyke will inflate. Advection becomes more pronounced as the flow rate increases, and so the solidification front advances at a slower rate. Advection increases thermal gradients ahead of the solidification front, narrowing the transition region between bubbles and vesicles. If the molten channel is sufficiently wide, or driving pressures are sufficiently

high, solidification will progress slowly, and the dyke will enter a quasi-steady state of flow. These conditions may persist for most of the active lifetime of the dyke, but few vesicles will be captured in this time.

In the late stages of emplacement, flow rates will decrease, either due to a decrease in pressure at the source, or due to blockages downstream. Advection will be reduced, and so the solidification front will advance at a faster rate towards the dyke centre. The vesicles in the centres of dykes are therefore likely to represent conditions at the very end of its active lifetime. There may be a relatively sharp transition between marginal, early-emplacement vesicles and central, late-emplacement vesicles, because slow solidification rates during the steady, high-flux conditions mid-emplacement could lead to very few vesicles being captured (Figure 3.18a).

Finally, it is worth considering the balance between dyke inflation and progressive inwards solidification. If the rate of inwards solidification matches the rate of inflation in the mid stages of dyke emplacement, then the molten channel width will remain constant while the width of solidified material increases (Figure 3.18b). If the width of the molten channel is constant and driving pressures are constant, then the strain rates and thermal profile ahead of the solidification front will also be constant, and all vesicles captured at the solidification front can be expected to have the same shapes and orientations. In this scenario, the region representing the mid stages of dyke emplacement may have a significant width, and vesicle textures will be unchanging across this width.

3.6.2 Conditions captured by vesicles

The next step in interpreting vesicles textures is to determine the extent to which they were in equilibrium when they were captured. While it may be tempting to interpret an arc of deformed vesicles across the widths of dykes as a reflection of the velocity profile across an active channel, the response time of bubbles and the velocity of the solidification front must be considered, as well as any additional deformation caused by the front itself. The only way for vesicles to capture an active velocity profile is if the response times of all bubbles, across the entire width of the dyke, is significantly greater than the rate of solidification. However, the critical balance between response rates and capture rates is frequently overlooked when interpreting vesicle profiles (e.g., Coward, 1980; Lanzafame et al., 2017).

Our analysis in Section 3.5.2 suggests that shorter bubble response times produce vesicles that more closely reflect shear conditions at the solidification front, whereas longer bubble response times produce vesicles that more closely reflect the initial velocity profile. In basaltic magma, surface tension does not vary significantly with temperature (Colucci et al., 2016), so if bubbles remain a constant size, their response time is directly proportional to viscosity (Eq. 3.2), which is temperature dependent. As the solidification front approaches a bubble, viscosities and response times increase by orders of magnitude. At the same time, strain rates are likely to decline. The balance between response

time and the change in strain rate is quantified by Cd (Eq. 3.3), which indicates whether a bubble can remain in equilibrium with the flow conditions. As such, we can use Cd to gauge whether vesicle shapes more closely reflect conditions at the solidification front, or initial conditions.

Our constant shear rate samples represent a scenario where bubbles remained at equilibrium as local viscosities increased and local strain rates decreased to zero. This resulted in spherical vesicles. A similar reduction in local strain rates can be expected within dykes, due to the increase in viscosity ahead of the solidification front. If Cd is sufficiently low, bubbles could return to spheres before being captured as vesicles, but if Cd is sufficiently high, bubbles will be captured before they can respond, and vesicles will reflect the flow conditions of the molten channel. Between these extremes are a range of vesicle shapes resulting from some amount of re-equilibration to suit the changing conditions.

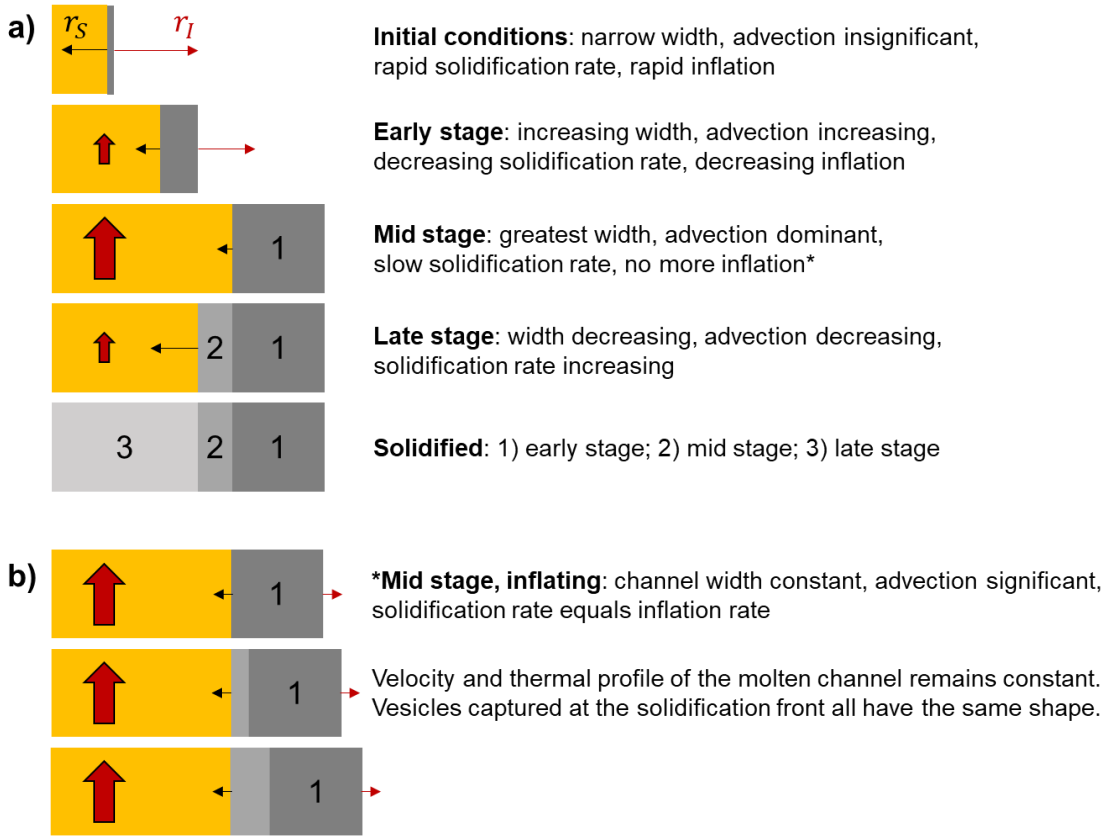

Figure 3.18. Schematic representation of progressive dyke solidification controlled by the balance between conduction, advection and inflation: a) a dyke inflates to a given width, then stops inflating; b) during steady flow, mid emplacement, the rate of inwards solidification r_S matches the rate of inflation r_I, leading to the molten channel remaining the same width, with the same flow conditions, while material continues to accrete to the margin.

Let us consider a typical vesicle profile, with vesicles showing the greatest elongation at the margins and becoming more spherical towards the dyke centre (e.g., Coward, 1980; Shelley, 1985; Varga et al., 1998; Hintz and Valentine, 2012). We view these vesicle textures as a time series, showing changing flow conditions throughout dyke emplacement. At the dyke margin, vesicles are captured near instantaneously. Strain rates are high, and so the equilibrium deformation is highly elongated, but solidification is so rapid that bubbles cannot attain equilibrium before they are captured (Figure 3.19). Marginal vesicles are therefore approximately spherical, just as we see at the edges of our sugar samples (Figure 3.6).

Moving inwards, the rate of advance of the solidification front r_S decreases, and so t_c increases. Bubbles have time to deform before they are captured, and so vesicles become more elongated, just as we see moving towards the centre of our sugar samples. Continuing towards the dyke centre, t_c will eventually exceed λ, allowing bubbles to attain their equilibrium deformation before capture. However, bubbles may not remain in equilibrium when strain rates decrease and viscosities increase by orders of magnitude ahead of the solidification front. If Cd remains sufficiently low, then vesicles represent conditions immediately before solidification. If Cd is high, vesicles will reflect the strain rates that existed within the molten channel.

Variations in Cd depend strongly on the thermal gradient ahead of the solidification front, which determines the increase in response times and the decrease in strain rates (Section 3.6.1). Calculating the response of vesicles to changing flow conditions is beyond the scope of this thesis, as it requires numerical solutions involving conduction and advection (e.g., Lister and Dellar, 1996), and bubble deformation (e.g., Ohashi et al., 2018). However, we can make some generalisations. If we assume a constant driving pressure through our dyke, then as the magma solidifies and the channel grows narrower, we expect strain rates to decrease. Therefore, by the time the solidification front reaches a bubble, equilibrium deformations will be less elongated than when the molten channel was first established. Vesicle shapes will be somewhere in between the initial and final equilibrium deformations. The only bubbles that remain the same shape throughout emplacement are those in the centre of the channel, which are always spherical. This is shown schematically in Figure 3.19, but this is purely conceptual. We now take a more quantified approach for predicting final vesicle shapes by considering the evolution of temperatures, viscosities and strain rates across the width of a dyke.

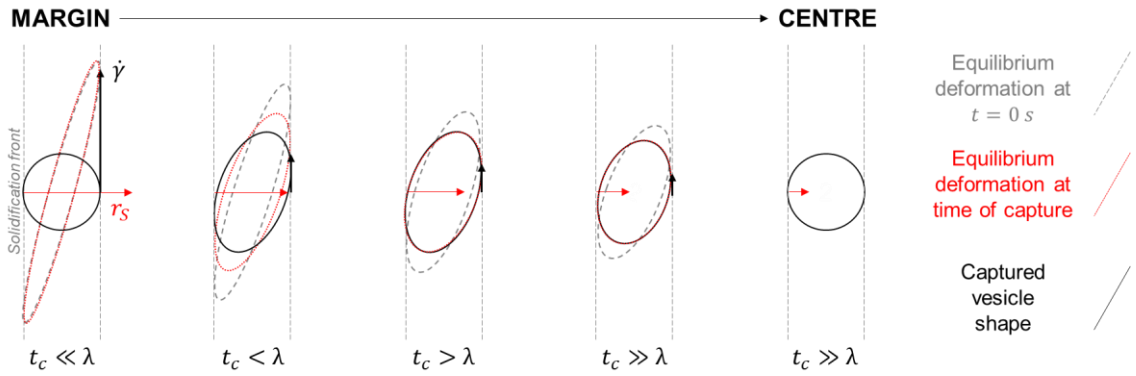

Figure 3.19. Schematic representation of bubble shapes and captured vesicles across the half-width of a dyke. Grey dashed outlines show equilibrium bubble deformations when the channel is first established at time $t = 0\ s$. Red dotted outlines show equilibrium bubble deformations at the time of capture. Black solid outlines show the captured vesicle shapes, which depend on the balance between the time to capture the vesicle t_c and the bubble response time λ. The solidification front moves inwards at rate r_S, and the flow has strain rate $\dot{\gamma}$, which decreases over time at each position.

3.6.3 Evolution of Ca and λ within dykes

In this section, we use a simple 1D conduction model to estimate thermal profiles across a dyke 1 m wide. We calculate a viscosity profile based on temperatures, and use the viscosity profile to estimate strain rates based on a given pressure gradient. Our model is not a realistic reflection of dyke solidification as it omits advection (Section 1.3); instead, we intend this model to be a thought experiment, to demonstrate how changes in temperature influence strain rates and resulting bubble shapes within dykes. Details of the thermal model are presented in Section 1.6.

We start with a molten channel with a half-width of 0.5 m, filled with magma at 1200 °C, which is the approximate temperature reported in the 2021 La Palma eruption (Carracedo et al., 2022; Castro and Feisel, 2022). We assume that the magma solidifies at 1000 °C, and that the host rock is 0 °C, fixed at this temperature beyond the reach of warming effects. We use a specific heat capacity of c = 1200 J kg^{-1} K^{-1} (Turcotte and Schubert, 2002), and a latent heat of L = 4 x 10^5 J kg^{-1} (Bruce and Huppert, 1990; Turcotte and Schubert, 2002). Our 1D conduction model calculates the thermal evolution of the dyke, and we then convert temperatures to viscosities using the model of Giordano et al. (2008) with an alkali basalt composition from the Teno Massif reported by Thirlwall et al. (2000).

Once we have viscosities, we calculate strain rates within the solidifying dyke. We assume laminar flow within the channel, which we define as the molten region bounded by the solidification front, which we take to be the 1000 °C isotherm. Our boundary conditions are that the flow has zero velocity v at the channel walls, and zero shear stress σ in the centre. The equation for a velocity profile across a slot of fixed width and infinite extent is

$$v = \frac{1}{2\mu}\frac{\Delta P}{L}\left(x^2 - \frac{w^2}{4}\right), \qquad \text{Eq. 3.7}$$

where $\Delta P/L$ is the pressure gradient, w is the half-width of the channel and x is distance from the channel centre. We differentiate Eq. 3.7 to find the equation for strain rates across the channel, so

$$\frac{dv}{dx} = \frac{1}{\mu}\frac{\Delta P}{L}x = \dot{\gamma}, \qquad \text{Eq. 3.8}$$

meaning that strain rates are a result of the viscosities calculated from our thermal model, the pressure gradient, and position. We then calculate Ca profiles across the dyke (Eq. 3.1), using the viscosities and calculated strain rates from our numerical model, and a surface tension of 0.2 N/m (Colucci et al., 2016). We use a bubble radius of 0.5 mm. By assuming that neither the surface tension nor bubble size is temperature dependent, Ca is directly proportional to the shear stress,

$$\sigma = \mu\dot{\gamma} = \frac{\Delta P}{L}x. \qquad \text{Eq. 3.9}$$

Therefore, the Ca profile is linear across the dyke at any moment in time.

We calculate strain rate profiles for three scenarios: 1) where $\Delta P/L$ is constant throughout solidification; 2) where $\Delta P/L$ declines linearly; and 3) where $\Delta P/L$ declines exponentially (Figure 3.20a). For the first scenario, the Ca profile always follows the same linear trend across the channel, even as the solidification front moves inwards. For the second and third scenarios, the reduction in the pressure gradient over time causes Ca values to decrease at every position across the dyke (Figure 3.20b). The equilibrium deformations of bubbles are directly related to Ca (Section 3.2.1), and any reduction in Ca results in a more spherical equilibrium deformation. In dykes where the pressure gradient is decreasing, bubbles will always be relaxing, but whether they remain in equilibrium depends on Cd.

We calculate Cd profiles for the three scenarios by considering the rate of change in strain rate at each position, calculated between each iteration in the model. For the scenarios with decreasing pressure gradient, Cd values fluctuate over time, starting low, rising, falling, then rising again in response to the balance between strain rate and viscosity. The values for Cd are generally high (> 100), meaning that bubbles are always out of equilibrium, and with the added fluctuation driven by cooling, our model suggests that the final shape of vesicles will neither reflect solidification front conditions nor the initial velocity profile.

The final point of interest from our simple model comes from the first scenario, where the pressure gradient remains constant. The fact that the Ca profile remains unchanged means that equilibrium bubble deformations remain constant throughout solidification. In other words, the final vesicle profile will match the initial velocity profile, which will result in an arc of vesicle shapes across the dyke. Such a pattern is unlikely to arise in nature, because driving pressures are likely to vary, and are especially likely to decline towards the end of dyke emplacement. Also, bubbles in the centres of dykes are likely to grow due to coalescence, and so their Ca and equilibrium deformations will

change. However, under certain conditions (e.g., if the dyke is part of a larger system and solidifies before there are significant reductions in pressure at the source), a balance between rapid solidification and constant driving pressures may allow parabolic vesicle profiles to be captured, such as the one presented by Coward (1980).

3.6.4 Interpreting vesicle profiles

In this section, we will discuss three examples of vesicle profiles: the parabolic arc of vesicles reported by Coward (1980), the consistent vesicle orientations reported by Philpotts and Philpotts (2007) and our own vesicle data from a basaltic dyke in Tenerife. Unfortunately, few studies provide detailed records of vesicle shapes and positions, because many focus exclusively on marginal vesicles as flow direction indicators (e.g., Delcamp et al., 2012; Geshi and Neri, 2014). As such, it is difficult to ascertain if there are any general vesicle trends that hold true for all basaltic dykes, related to dyke widths and cooling times.

The vesicles reported by Coward (1980) exist within the central 30 cm of a basaltic dyke 1 m wide. Vesicles are highly elongated at the edges of this zone, at a low angle to the flow direction, and moving towards the dyke centre, vesicles become less elongated and at higher angles to the flow (Figure 3.21). In the dyke centre, vesicles are either spherical or elongated perpendicular to the flow, as if they have been compressed in the flow direction. The pattern of vesicles across the central zone appears to be parabolic. However, vesicles in the outer, marginal regions are noted to be relatively undeformed. The author infers that the central vesicles represent the velocity profile from the late stages of flow, when the marginal regions had already solidified.

Viewing these vesicles in the context of progressive inwards solidification, the change in vesicle shape and orientation towards the centre is likely to reflect changes in flow conditions over time. The vesicles in the marginal region were presumably captured rapidly, faster than the time taken for bubbles to respond to flow conditions, which is why they are relatively undeformed. By contrast, the vesicles at the edge of the central zone mark the earliest position at which solidification was slow enough for bubbles to attain elongated shapes before capture. Vesicles in the central zone are therefore likely to have attained equilibrium deformations while it was molten. As discussed in Section 3.6.2, a dyke may fail to accrete much material while it is flowing at its fastest rate, due to the effects of advection. This might explain the relatively sharp contact between the marginal and central regions, and the distinct difference in vesicle shapes.

It is likely that the bubbles in the central region of the dyke attained equilibrium deformations while it was molten. However, whether their final shapes reflect the velocity profile that existed during steady flow depends on the balance between changing viscosities and strain rates. The central region is only likely to have solidified once flow rates declined, reducing the impact of advection. A sudden drop to a new, lower pressure gradient would allow bubbles to adjust quickly, before viscosity increased

significantly. If the new pressure gradient was sufficiently low, conduction would become dominant and the channel would start to solidify. Providing that this new pressure gradient remained constant, Ca values and bubble shapes would also remain constant, and so captured vesicles would match the final velocity profile (Section 3.6.2). The compressed vesicles in the very centre are of interest, as they suggest that the dyke was flowing right up until it solidified, and that flow was halted by a blockage downstream, rather than a declining in pressure from the source.

The vesicles reported by Philpotts and Philpotts (2007) are in a camptonite lamprophyre dyke 1.6 m wide, which has narrow marginal regions 20 cm wide that record upwards magma flow, and a main central region recording downwards flow (Figure 3.22). The transition between these regions is only a few millimetres wide. Throughout the central region, vesicle orientations are consistent, only transitioning towards spherical forms within several centimetres of the dyke centre. The authors infer that the vesicles record the strain that accumulated in the boundary layer ahead of the solidification front. They infer that the time required to capture a vesicle increases towards the dyke centre, and so the consistent orientations indicate a reduction in strain rate within the boundary layer, as would be expected when the dyke solidifies.

However, this interpretation overlooks the shape of bubbles prior to the arrival of the solidification front. The authors seem to make the implicit assumption that bubbles are spherical when they enter the boundary layer, allowing their final deformation to be related to the stain accumulated during capture. In reality, the bubbles will be starting from an elongated state when the solidification front arrives, having been suspended in flowing magma for some time.

Based on the sharp transition between the marginal and central zones, we infer that bubbles responded to the change in flow conditions at a faster rate than they were being captured by the solidification front, the same as in our analogue experiments (Section 3.4.4). This rapid response implies that bubbles were attaining equilibrium deformations at some point before capture. The fact that vesicle orientations are constant across the width of the dyke implies that conditions ahead of the solidification front remained constant, and that the bubbles had sufficient time to respond to these conditions.

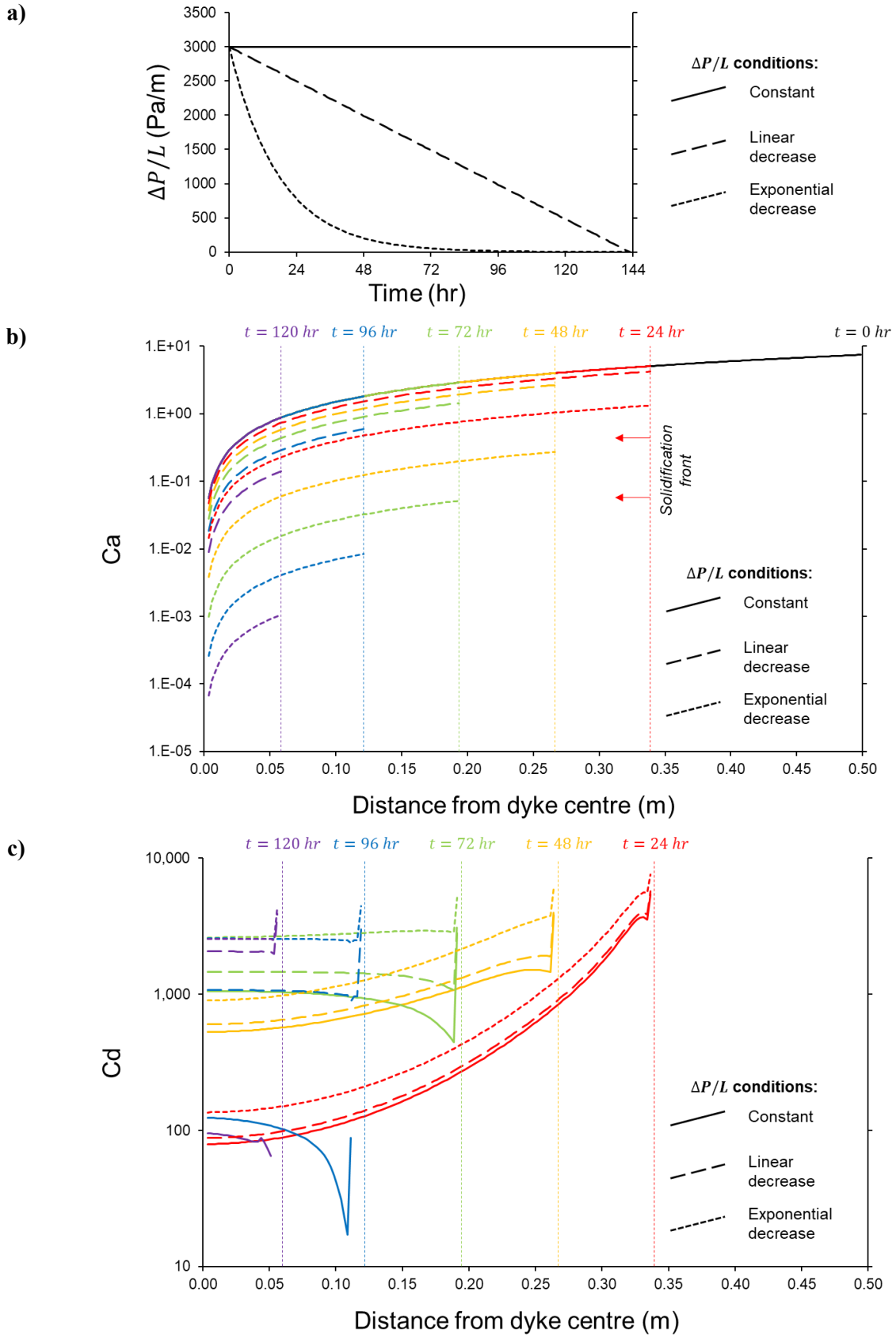

Figure 3.20. a) Variation in $\Delta P/L$ over time for three different pressure scenarios; b) Ca profiles during dyke solidification, for three pressure scenarios; c) Cd profiles during dyke solidification. Vertical dashed lines show the position of the solidification front at time t.

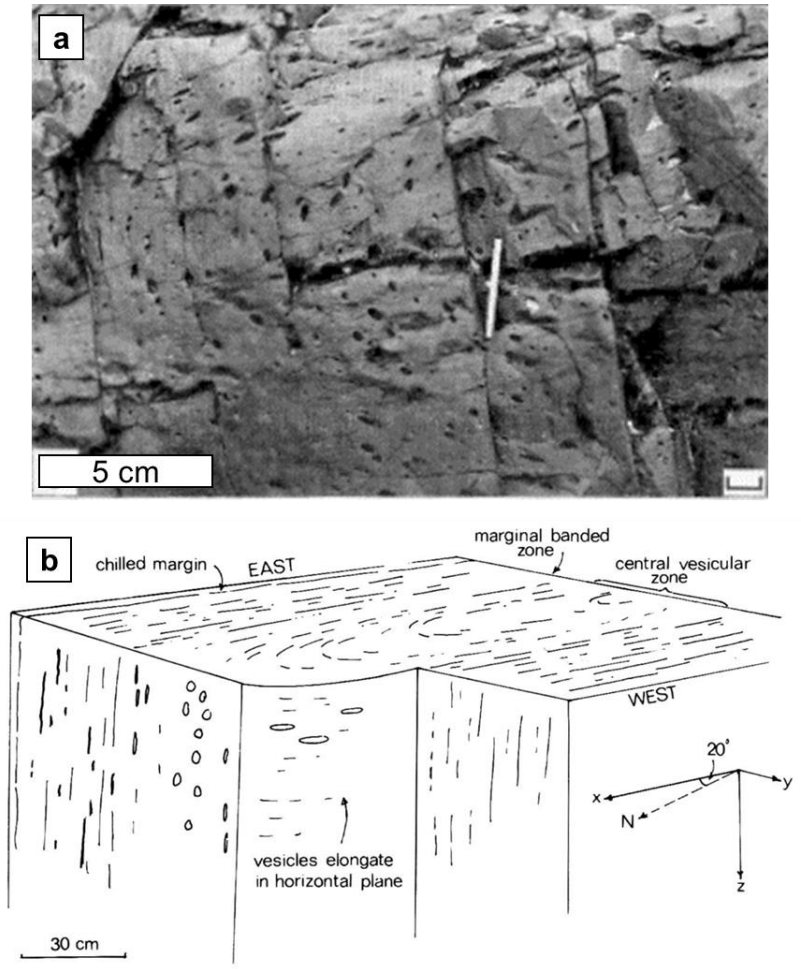

Figure 3.21. Figures reproduced from Coward (1980): a) elongated vesicles tracing a U-shape pointing to the left; b) schematic representation of the dyke, showing vesicle orientations.

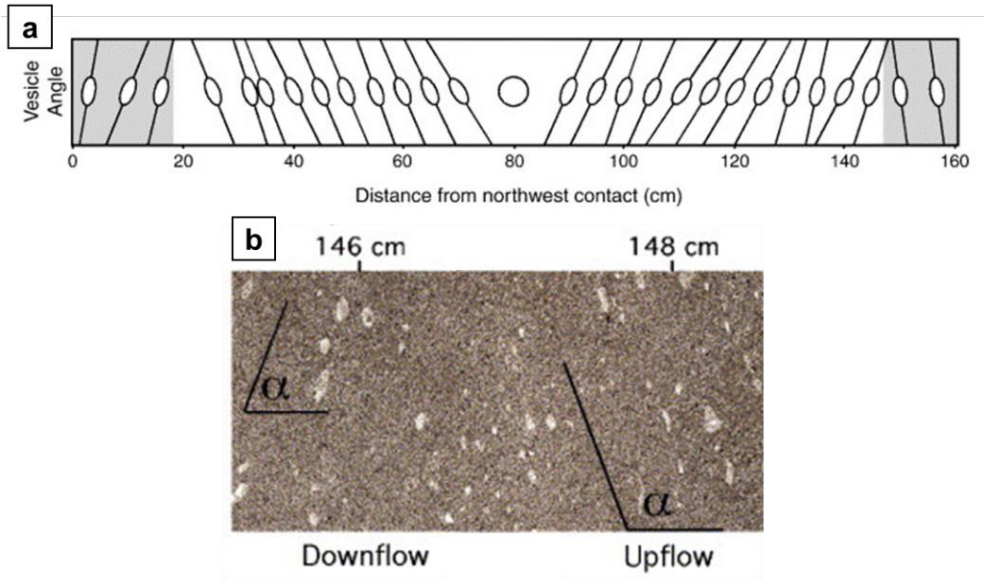

Figure 3.22. Figures reproduced from Philpotts and Philpotts (2007): a) mean vesicle orientations across the dyke; b) thin section photograph with the margin to the right (positions indicated), showing transition in vesicle orientations, showing a change from upflow to downflow.

One way for conditions to remain constant at the solidification front is if the width of the molten channel remains constant. As discussed in Section 3.6.1, this can occur if the dyke is inflating at the same rate that it is solidifying. Under these conditions, the solidification front is always advancing into a region with the same deformation rate, which exists at the edge of a channel of fixed width. It is likely that a dyke 1.6 m wide inflated during its lifetime. If the channel remained flowing for long enough, under roughly constant conditions, the dyke may have accreted a significant portion of its width in this manner, capturing consistent vesicle textures across this width.

Finally, our own vesicle data come from a basaltic dyke in the Teno Massif, NW Tenerife (see description of D3, Section 5.4.3). We focus on one section of a 60-cm-wide dyke, the northern half of which contains hundreds of well-preserved vesicles, which we measure from margin to centre. Vesicles in the outermost 12 cm of the dyke are sub-millimetre in diameter with irregular shapes, showing no clear preferred orientation, but in the central region, 36 cm wide, vesicles are larger and show obvious deformation from magma flow. We measure the central vesicles in ImageJ (Schindelin et al., 2012), approximating them with best-fit ellipses from their outlines. We measure orientations and vesicle length L from the ellipse major axis, and we calculate their undeformed, spherical diameter D from the area A of the outlined vesicle, where $D = 2\sqrt{A/\pi}$. We then calculate the deformation ratio L/D, comparable to the deformation ratios measured in our sugar samples.

The central vesicles range in size from sub-millimetre to over 30 mm in diameter, and they display remarkably consistent orientations across the width of the central region. Only the vesicles within a few centimetres of the dyke centre have spherical shapes, and the rest show a pronounced preferred orientation (Figure 3.23). Although the southern half of the dyke is more weathered and fewer vesicles are visible, the dyke appears to show symmetry down its centre, with reflected preferred orientations indicating a lateral flow component to the SW. The average orientation on the northern side is a constant -20° within 15 cm of the dyke centre. The average deformation ratio shows a slight linear increase across this distance from 1.2 to 1.53, indicating that bubbles further from the dyke centre are slightly more elongated. There is no relationship between vesicle size and orientation, and the vesicles do not fit the relationship between shape and orientation measured by Rust and Manga (2002), showing that these vesicles were not captured at equilibrium.

However, the high vesicularity in this dyke means that equilibrium deformations were unlikely to be attained, as bubbles would have been interacting during flow. Many of the vesicles have irregular rather than elliptical shapes, and in some cases, this appears to have resulted from bubble coalescence, as some vesicles clearly comprise two connected volumes. The fact that these coalescence textures have been preserved shows that viscosities were high enough to restrict bubbles from relaxing back to ellipsoids. Many bubbles have angular, pointed shapes (Figure 3.23c and d), which implies that the

nature of bubble deformation was not simple, probably due to interactions between bubbles, or due to highly localised deformation in magma that was almost solid.

We infer that the central vesicles record the late stages of flow, once advection rates declined. It appears that magma flow persisted while the dyke centre was solidifying, but the result is entirely different from the vesicle arc reported by Coward (1980). The high vesicularity is the complicating factor here, with bubble interactions occurring within a high viscosity environment.

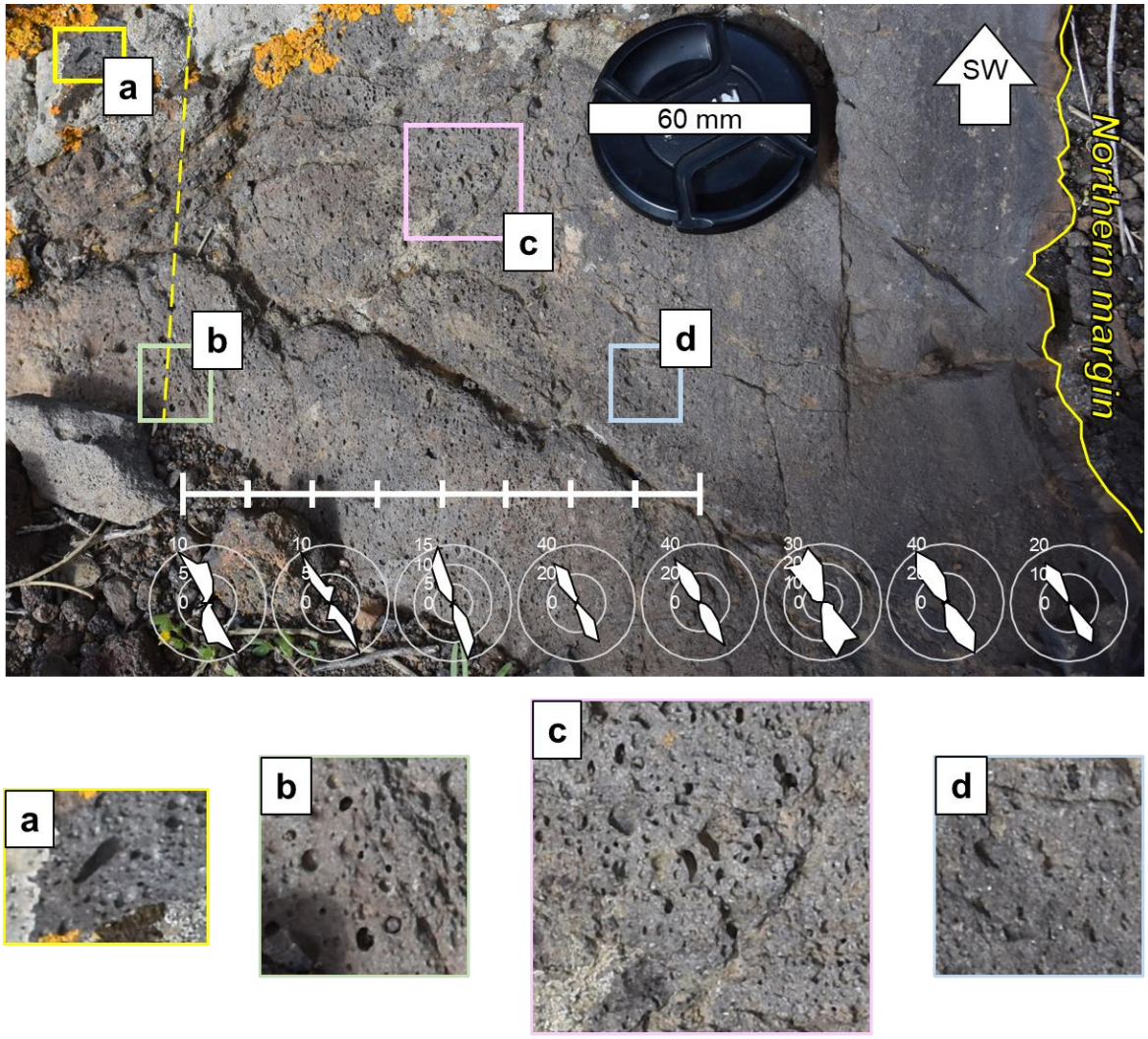

Figure 3.23. Vesicular dyke in the Teno Massif, photographed on a horizontal surface, facing SW. The northern margin is visible, but the southern half of the dyke has weathered away. A dashed yellow line shows the approximate dyke centre, based on the symmetry of elongated vesicles. Rose diagrams of vesicle orientations are from the regions indicated by the white bar. Image a) shows a vesicle in the southern half; b) spherical vesicles at dyke centre; c and d) elongated vesicles in the northern half.

3.7. Conclusion

The orientations of deformed vesicles within dykes and lava flows have been widely used as a flow direction indicator, being more reliable and intuitive than crystal alignment and AMS. However, vesicle shapes have been underutilised as a means for establishing magma strain rates. Our analogue experiments in solidifying sugar have revealed the complexities involved in deciphering flow conditions from vesicles. Although equilibrium bubble deformations can be reliably predicted based on capillary number Ca, the time taken to achieve this equilibrium is key, with bubbles soon falling out of equilibrium as magma viscosity increases. The final shape of a vesicle depends on the extent to which a bubble can attain or remain in equilibrium as the magma solidifies around it. Marginal vesicles are captured so quickly that they are unlikely to have ever attained equilibrium shapes. Towards the dyke centre, bubbles are likely to have attained equilibrium at some point during dyke emplacement, but their captured shape depends on the balance between their response time and capture time. If bubble response times are long, vesicles will more closely represent initial flow conditions across the molten channel. If response times are short, vesicles will represent conditions at the solidification front.

In order to interpret vesicle shape profiles as records of changing magma strain rates, the thermal evolution of the dyke must be considered. The inwards migration of the solidification front determines the time available for bubbles to deform before they are captured, and it also determines the flow conditions under which the bubbles deformed. Careful consideration of dyke widths and internal textures allow qualitative inferences of changing magma flow rates, channel widths and pressure gradients throughout dyke emplacement. Detailed measurements of vesicle shapes across the widths of dykes would be required for a more quantitative analysis, as well as further analogue experiments in a greater range of flow conditions.

Chapter 4

Banding in the margins of basaltic dykes indicates pulsatory propagation during emplacement

---

Aims of this chapter:

Having investigated the development of crystal and vesicle textures in laboratory experiments, we now apply these findings to textures at the margins of basaltic dykes in the Teno Massif (Tenerife, Spain) and the Columbia River Basalt Province (USA). These dyke margins contain banding features millimetres to centimetres wide, and similar marginal banding features have been reported in numerous localities around the world. Marginal textures are key to understanding dyke emplacement, as they are the first material to solidify against the host rock in the tip of the dyke, meaning that they record valuable information about dyke propagation. We find that the bands get wider and less distinct towards the dyke centre, and that they are defined by cyclic variations in phenocryst concentration and vesicularity. We infer that these cyclic textures are a product of cyclic variations in magma flow rates and pressures within the dyke tip, which suggests that dyke emplacement occurs in pulses, with propagation repeatedly hindered by the rapid solidification at the narrow leading edge. Using a simple 1D conduction model, we estimate the time taken for each band to cool and solidify, which provides a timescale of tens of minutes for the magma pulses. The occurrence of similar bands in various volcanic settings suggests that pulsatory propagation is a common, if not ubiquitous, process associated with dyke emplacement.

4.1. Introduction

In this chapter, we explore the development of crystal and vesicle textures in the margins of dykes, which originate in the earliest stages of dyke emplacement. Dyke margins are the first material to solidify against the host rock, so they form at the leading edge of the dyke as it propagates through the crust. Marginal textures are therefore intrinsically related to dyke propagation, and provide a record from initial crack formation towards sustained magma flow within the dyke. Understanding dyke tip processes is crucial for modelling dyke propagation, and for interpreting the seismic signals associated with dyke emplacement.

Currently, our understanding of dyke propagation comes from analogue experiments, numerical models, field observations, and seismic data. However, the geometry of exposed, solidified dykes provides only a limited insight into propagation processes, because the final width of a dyke may not resemble its active, molten width. Subsurface flow cannot be observed directly, so we do not have a clear picture of the geometry of propagating dyke tips, or the processes operating within them. We do, however, have some idea of the rates and overall direction of dyke propagation, inferred from the migration of seismic activity to be around tens of centimetres per second (e.g., Einarsson and Brandsdóttir, 1980; White et al., 2011; Woods et al., 2019). Rock textures and magnetic fabrics in solidified dykes have been used to infer propagation directions (e.g., Baer and Reches, 1987; Wada, 1992; Philpotts and Asher, 1994; Philpotts and Philpotts, 2007; Staudigel et al., 1999); however, we believe we are the first to use marginal textures to infer dyke tip processes and relate them to propagation dynamics.

There is currently limited evidence for the geometry of propagating dyke tips, and for the behaviour of magma within the narrow tip region. Numerical dyke propagation models, whether 2D (e.g., Taisne and Jaupart, 2009; Maccaferri et al. 2010) or 3D (e.g., Zia and Lecampion, 2020; Davis et al., 2021), operate within the framework of linear elastic fracture mechanics (LEFM), where propagation is controlled by the geometry of the dyke tip, and by either the fracture toughness of the medium, or viscous losses from the fluid (Taisne and Gonnermann, 2015). LEFM models require a tapering dyke tip geometry to concentrate stress and instigate fracture; however, most models overlook the role of cooling and solidification, even though the narrow tip must be prone to rapid heat loss. Marginal textures provide information about the role of cooling and solidification at the tip of a propagating dyke, and about the geometry of the tip itself. These textures therefore provide additional constraints to analogue and numerical models of dyke propagation.

In this chapter we present two marginal dyke samples which display banded textures: one from the Teno Massif (Tenerife, Spain) and one from the Columbia River Basalt Province (CRBP) (USA). We view these textures as a time series, with the oldest material at the dyke wall, and progressively younger material towards the dyke centre. The samples therefore provide a record from initial

propagation to sustained magma flow, from which we interpret the dyke tip processes responsible for the banding. This allows us to construct a conceptual model for dyke propagation.

4.2. Background

4.2.1 Examples of marginal banding

Banded textures have been found at the margins of basaltic dykes in numerous settings, including the Canary Islands (Delcamp et al., 2012; Thiele et al., 2021), the CRBP (Thordarson and Self, 1996), Paleogene dykes and sills in northwest Scotland (Drever and Johnston, 1959; Roberts and Sanderson, 1971; Kile, 1993; Platten, 2000; Holness and Humphreys, 2003), the Karoo dyke swarm in Namibia (Coward, 1980), American Samoa (Walker and Eyre, 1995), Koolau Volcano, Hawaii (Walker, 1987), and the San Rafael subvolcanic field in Utah (Kavanagh et al., 2018). The unifying characteristic of these marginal bands (Figures 4.1, 4.2, 4.3) is a general trend of bands getting wider and less distinct towards the intrusion centre, typically starting at widths of only a few millimetres, and attaining maximum widths of up to several centimetres before becoming indistinct (Walker and Eyre, 1995; Thordarson and Self, 1996; Kavanagh et al., 2018; Thiele et al., 2021).

By eye, the marginal bands are distinguished through variations in groundmass grain size, phenocryst concentration, and/or vesicularity. Bands defined by groundmass grain size appear as a series of discontinuities, involving a sharp drop in grain size moving towards the dyke centre (Holness and Humphreys, 2003). Where bands are defined by phenocryst concentration, they can appear as porphyritic and non-porphyritic zones, sometimes associated with a gradation in phenocryst size (Drever and Johnston, 1959). In cases where bands are defined by variations in vesicularity, they appear as by narrow, highly vesicular or amygdaloidal regions running parallel to the dyke margins (Walker and Eyre, 1995; Thordarson and Self, 1996; Kile, 1993; Platten, 2000; Delcamp et al., 2012; Galindo and Gudmundsson, 2012; Kavanagh et al., 2018; Thiele et al., 2021). Other authors describe banded margins with colour variations and platy textures, the cause of which is uncertain (Roberts and Sanderson, 1971; Coward, 1980; Healy et al., 2018).

Marginal bands are typically found within approximately 15 cm of the dyke margin. This is especially the case for bands defined by groundmass variations and phenocrysts (e.g., Drever and Johnston, 1959; Holness and Humphreys, 2003). By contrast, vesicle bands have been observed to extend further towards intrusion centres, such as in dykes in the CRBP, where highly vesicular bands may be present all the way to the dyke centre, increasing from 1 to 10 cm in width (Thordarson and Self, 1996). Vesicle bands have also been observed to extend across the entire width of dykes in American Samoa (Walker and Eyre, 1995). A key aim of this work is to establish whether the bands defined by groundmass, phenocrysts and vesicles are caused by the same process within the dyke tip, and to determine why most cases of banding are limited to the dyke margins.

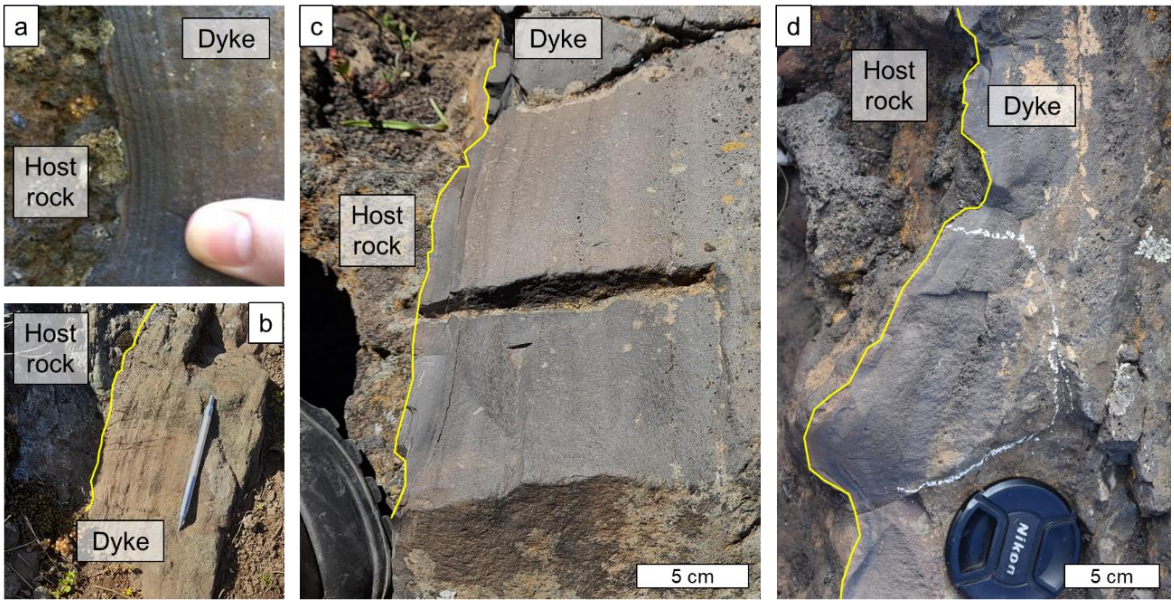

Figure 4.1. Examples of marginal banding from dykes in the Teno Massif, NW Tenerife. Bands can be found as weathered ridges (a and b), or defined by variation in colour and vesicularity (c and d).

4.2.2 Formation of bands and layers within dykes

Dykes often contain large-scale layering, several centimetres to metres wide, defined by jointing patterns (Gudmundsson, 1984; Ray et al., 2007), distinct compositions (Eriksson et al., 2011) or textural changes such as internal chilled margins (e.g., Brouxel, 1991; Platten, 2000) or melt-back margins (Huppert and Sparks, 1989; Svenningsen, 1994). Internal margins are indicative of a substantial time gap between the magma injections that formed the layers, and so each layer is taken to represent a discrete injection episode. This is especially clear where there is a change of composition between layers; for example, where felsic magma has been injected into the centre of a pre-existing basaltic dyke (e.g., Eriksson et al., 2011; Tomé et al., 2020). The large-scale layering within a dyke is therefore a product of a unique emplacement history comprising a sequence of distinct injection events. This is in contrast to the marginal bands, which always show a general trend of widening and becoming less distinct towards the dyke centre, wherever they are found. The consistency in banded marginal textures implies that they are not merely small-scale versions of a composite dyke; instead, they are indicative of a common, if not ubiquitous, dyke tip process.

Several explanations have been proposed for marginal banding described in the literature. The most common interpretation is that the bands represent variations in magma flow rates, attributed to repeated injections of magma (Drever and Johnston, 1959; Platten, 2000). Another explanation is that each layer represents a plane of movement in the high shear stresses at the margins of the active intrusion (Roberts and Sanderson, 1971). For the cases where bands are defined by vesicles alone, the variation in vesicularity has been interpreted as a product of pressure fluctuations and temporal variations in flow, captured by progressive inwards solidification (Kile, 1993; Walker and Eyre, 1995;

Kavanagh et al., 2018; Thiele et al., 2021), or due to preferential degassing pathways developing within the active conduit (Delcamp et al., 2012).

Unlike the large-scale layering within dykes, very few reports of marginal bands have included observations of internal chilled margins. In fact, their absence has been noted (Platten, 2000), and the few reported drops in grain size are not deemed to be true internal margins (Platten, 2000; Holness and Humphreys, 2003). It appears that band formation is too rapid to permit long cooling intervals between their emplacements. However, most interpretations of the bands involve fluctuations in flow conditions. Our aim is to determine the timings and cause of these fluctuations, and to relate them to processes operating within the propagating dyke tip.

4.3. Field sites and samples

We have two samples that display marginal bands: one from the Teno Massif (Tenerife, Spain), collected by Professor Ed Llewellin of Durham University, and one from the CRBP (USA), collected by Dr Rich Brown, Durham University. From here, we will refer to these samples as the "Teno sample" and the "CRB sample" respectively.

4.3.1 Teno Sample

This sample comes from the Teno Massif in NW Tenerife, which is the eroded remains of a basaltic shield volcano that was active from 6.3 to 5.0 Ma (Leonhardt and Soffel, 2006; Longpré et al., 2009). A brief geological history of this region is presented in Section 5.2. The Teno sample comprises the outermost 10 cm of a 0.5-m-wide dyke (Figure 4.2), and six bands are recognisable by eye. Several dykes in the immediate area also displayed bands at their margins, usually defined by a dark-to-light colour variation, often paired with a variation in vesicularity (Figure 4.1). The majority of dykes in this region are single intrusions, but multiple and composite intrusions are relatively common, displaying large-scale layers defined by distinct compositions and chilled margins. It is common to see dyke tips, which typically have a tapering, crack-like geometry (Chapter 5; Marinoni and Gudmundsson, 2000).

4.3.2 CRB Sample

The CRB sample is from the outermost 12 cm of a 0.95-m-wide basaltic dyke in SE Washington State, and it contains nine bands distinguishable by eye (Figure 4.3). The dyke is one of many that fed the Roza lava flow, which was emplaced over at least 14 years around 14.7 Ma, covering an area of 40,300 km^2 (Thordarson and Self, 1998). Rich Brown inferred an emplacement depth of around 500 m. He reports that many dykes in the area, feeding the Roza flow, display bands of vesicles at their margins. Some display up to 18 bands, symmetrical on either side of the dyke.

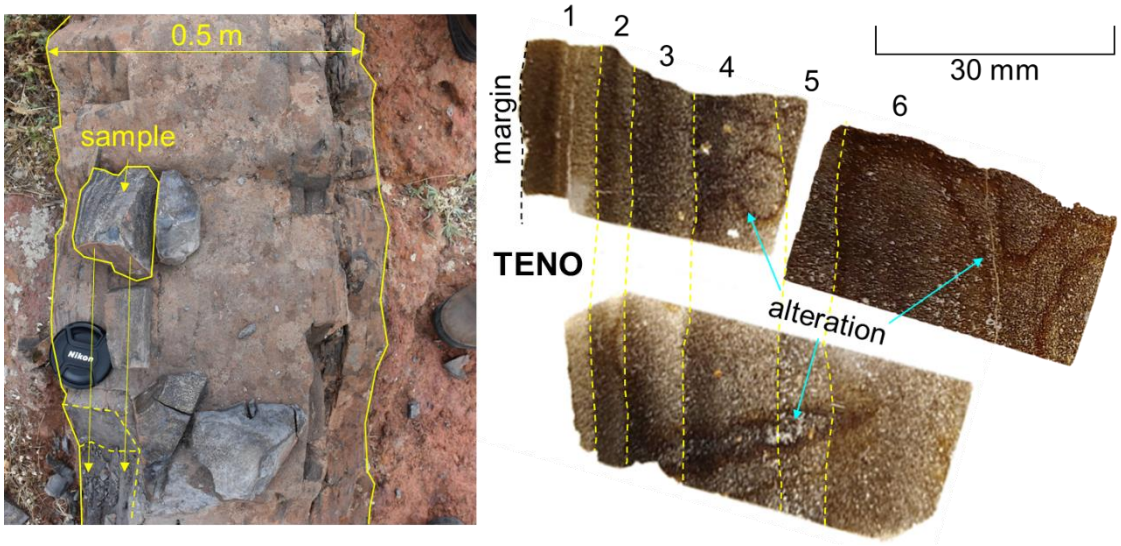

Figure 4.2. (Left) Origin of the Teno sample in the margins of a 0.5-m-wide dyke; (Right) three aligned thin sections taken from the sample, showing the first six bands. Heavily altered streaks through the sample are highlighted.

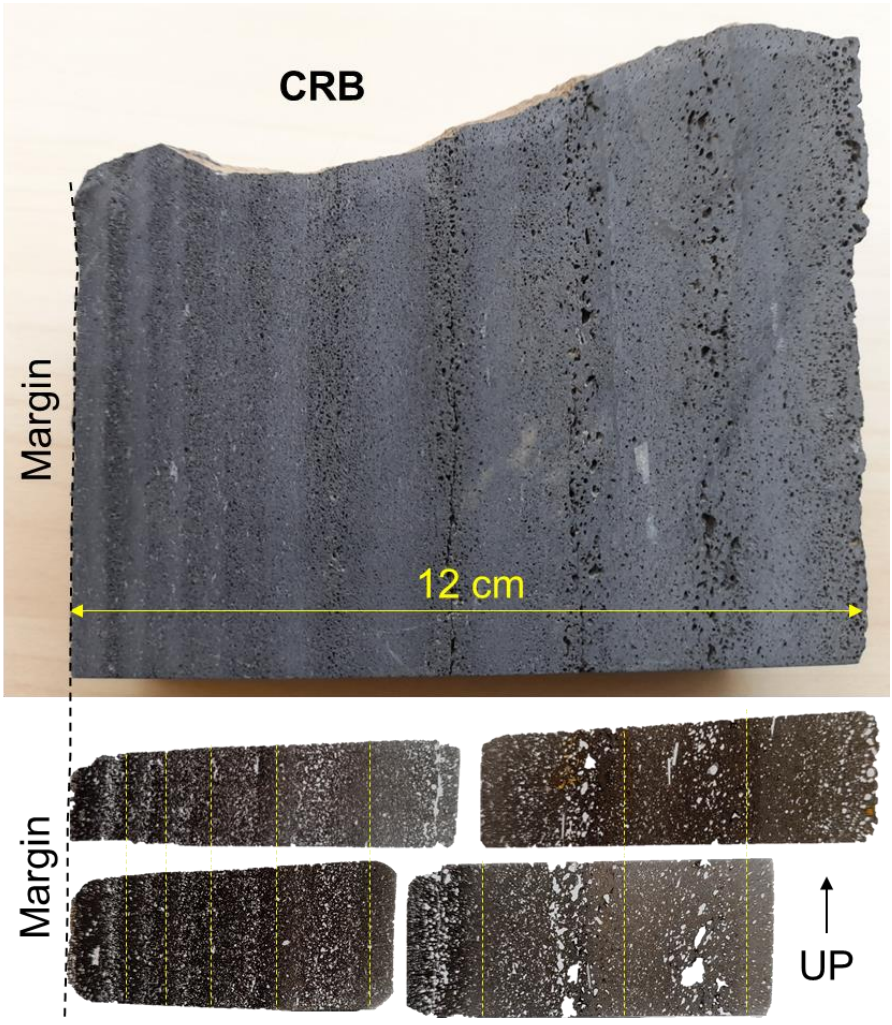

Figure 4.3. The CRB sample, from the margins of a feeder dyke to the Roza lava flow, with four aligned thin sections taken from the sample in the vertical plane, perpendicular to the margin. Dashed yellow lines on the thin sections show the positions of minimum vesicularity, used to define the bands.

4.4. Methods

The banded textures in both samples were analysed from the margins inwards in order to read them as a time series. Thin sections were taken perpendicular to the margin, and in the CRB sample, where the orientation was known, thin sections were taken in the vertical plane. Multiple thin sections were required to cover the full width of each sample, and these were cut so that there was some overlap between them, allowing the textures to be aligned and positioned correctly (Figure 4.3). Images were collected at x5 magnification under the petrological microscope, then stitched together in Inkscape to create continuous swaths across the width of each thin section. These swaths were then aligned using the bands as a guide (Figures 4.2 and 4.3), allowing all subsequent measurements of phenocrysts and vesicles to be located with positions relative to the dyke margin.

The phenocrysts and vesicles in each image swath were outlined manually in ImageJ (Schindelin et al., 2012). Using ImageJ's measurement functions, we found the centroid position, area and maximum diameter of each outline, and by approximating the shape with a best-fit ellipse, we found major and minor axes lengths, aspect ratio, and orientation. Centroid positions were corrected to give the distance from the dyke margin. For the Teno sample, where thin sections were taken at an angle to the margin and to the banding (Figure 4.2), all positions were rotated to correct this misalignment. We then used the outlines to create two binary images from each swath: one containing phenocrysts, and one containing vesicles (Figure 4.4). These binary images were then imported into MATLAB for further analysis.

In MATLAB, we took moving averages across each sample, moving perpendicularly inwards from the dyke margin. Both the raw data (area, major axis etc.) and binary images were analysed in bins 1080 pixels (1 mm) wide. We chose this bin width because it is wider than the largest vesicles, captures enough phenocrysts and vesicles to calculate reliable means, and is narrow enough to show changes within the bands themselves, which are each several millimetres wide.

Raw data for phenocryst and vesicle area, maximum diameter, aspect ratio, and circularity were quantified using medians and interquartile ranges, which account for the skewed distribution towards smaller objects. Circular statistical methods were used on orientation data to find means and standard deviations (Jammalamadaka and SenGupta, 2001). We define aspect ratio as the major axis over the minor axis.

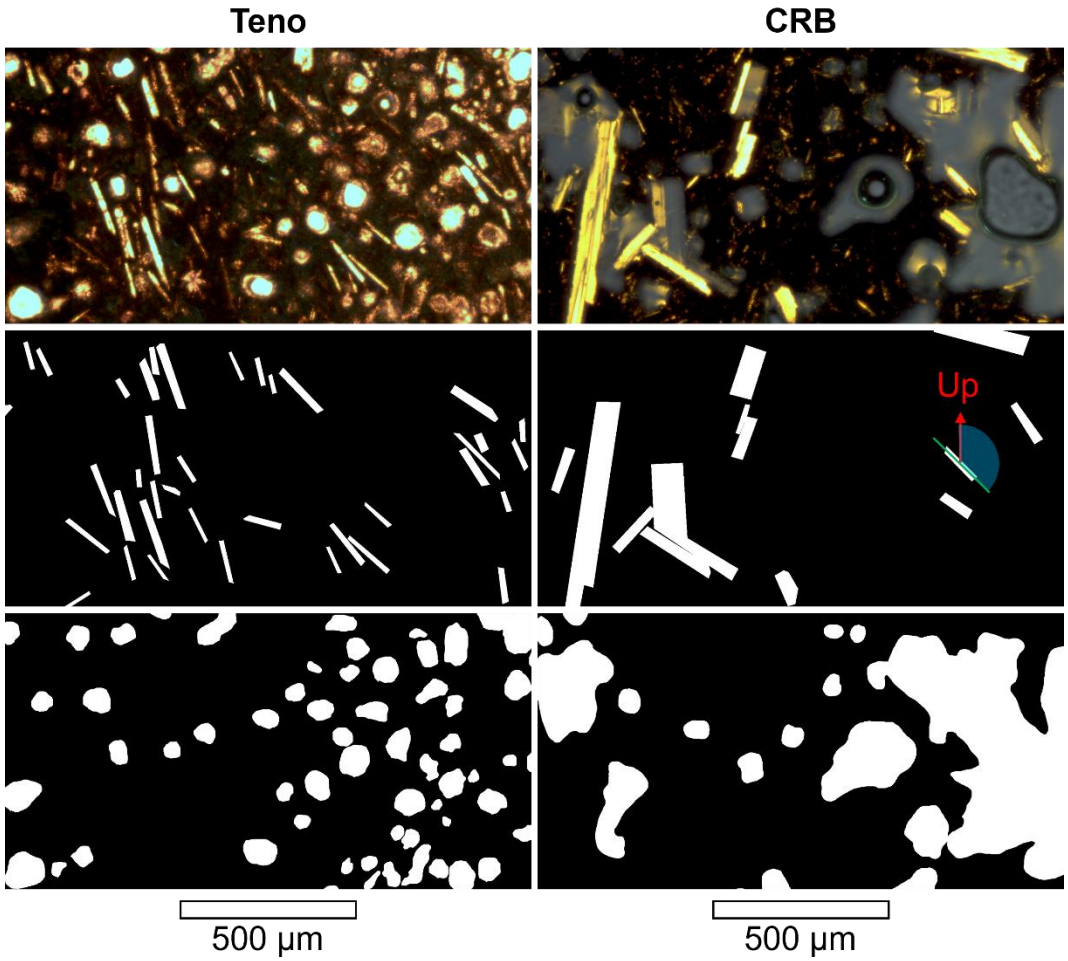

Figure 4.4. Examples of binary images created from Teno (top left, plane-polarised light) and CRB (top right, cross-polarised light) microscope images. Binary phenocryst images (middle row) and binary vesicle images (bottom row) are created from manual outlines. Angle measurements from the vertical are demonstrated on the CRB phenocrysts. Margin is to the left in both images.

The binary images allowed us to find phenocryst and vesicle area fractions and number densities, moving across the samples away from the dyke margins. Area fractions were generated from the proportions of white pixels within each 1080 px strip, and number densities were generated by counting the number of independent white areas. Vesicle area fraction was calculated as vesicle area / total area, and vesicle number density was calculated as vesicle number / (total area – vesicle area) to consider vesicles nucleating within the melt area before the vesicles grew. Phenocryst area fraction was calculated as phenocryst area / (total area – vesicle area), and phenocryst number density was calculated as phenocryst number / (total area – vesicle area), to exclude vesicles and consider only the melt regions.

In addition to using the petrological microscope, we studied the CRB thin sections using the Zeiss Evo scanning electron microscope with 15.00 kV beam at the GJ Russell Microscopy Facility, Durham University. At x400 magnification, it was not feasible to create continuous image swaths across the sample, and so three rows of isolated images were captured at intervals of 0.5 mm, moving

inwards from the margin to the sixth apparent band. Plagioclase microlites were outlined manually within each SEM image, whereas oxides were captured automatically via thresholding in ImageJ.

The reason for using SEM on the CRB sample was due to a greater range in crystal size. In the Teno sample, phenocrysts are 0.02-0.45 mm long (median 0.10 mm) and are perfectly visible under a petrological microscope. They exist within a dark groundmass, which is glassy at the margin but more crystalline towards the dyke centre. By contrast, the CRB sample contains phenocrysts up to 4.28 mm in length, and microlites that are too small to outline accurately in images from the petrological microscope. We define phenocrysts in the CRB sample as crystals longer than 0.1 mm, and microlites as anything shorter than this. The CRB sample also contains two vesicle populations: large, rounded, primary magmatic vesicles that are easily seen under the petrological microscope, and small, angular diktytaxitic voids, all < 30 μm, only seen under the SEM. These diktytaxitic voids are discussed in more detail later (Section 4.5.2), but they are considered separate to the primary vesicle population. When we use the term “vesicle” or “vesicularity”, we refer to the primary population only.

4.5. Results

4.5.1 Teno Sample

There are six apparent bands within the Teno sample (Figure 4.5). By eye, each band appears to be defined by dark, glassy material on its marginal side, which transitions to lighter-coloured material moving towards the dyke centre, before there is a relatively sharp boundary with the next band (Figure 4.2). The bands become wider and less distinct away from the dyke margin, with their boundaries becoming more diffuse. As such, we focus on the first four bands, which have the most distinct edges.

Teno Phenocrysts

Our binary image analysis reveals that the colour variations defining the bands are caused by variations in the concentration of phenocrysts, which in this sample are dominantly light-coloured plagioclase. On their marginal side, the bands contain fewer phenocrysts, and so they appear darker, but their phenocryst number density increases moving towards the dyke centre, leading to the band transitioning from dark to light in appearance. Across each band, phenocryst number density increases by 30-70 mm^{-2}. The onset of a new band is defined by a sharp drop in phenocryst concentration, captured by drops in both area fraction (Figure 4.6a) and number density (Figure 4.6b).

Phenocrysts show a gradual increase in size moving towards the dyke centre, with median lengths increasing from around 0.10 to 0.15 mm across the region studied. However, phenocryst size shows no relation to the bands (Figure 4.7). The variation in phenocryst area fraction is therefore predominantly controlled by phenocryst concentration, not phenocryst size.

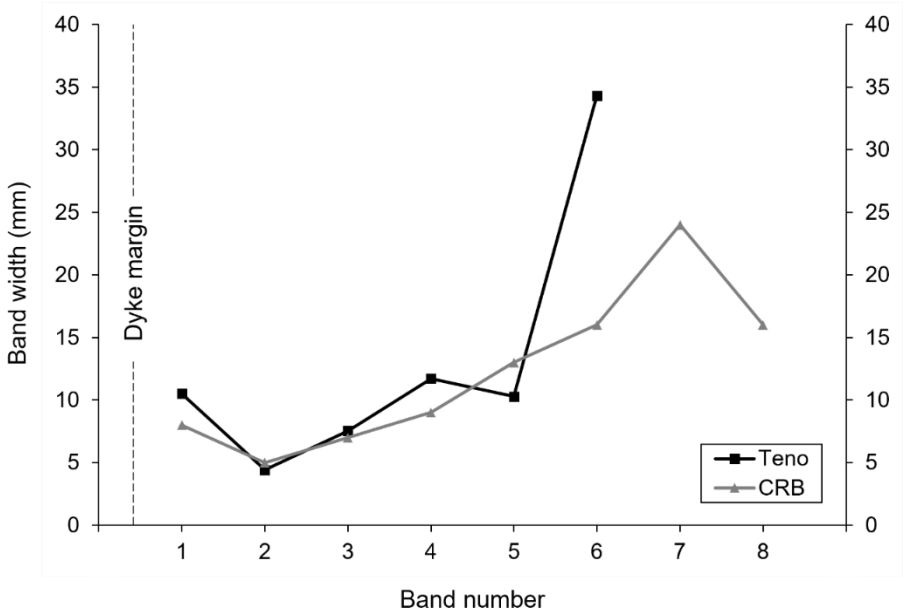

Figure 4.5. Widths of bands in the Teno and CRB samples. Teno bands were measured based on colour variations by eye, later found to be caused by changes in phenocryst concentration. Teno band 6 overran the end of the thin section, making the value plotted a minimum estimate. CRB bands are based on distances between troughs in vesicularity.

The aspect ratio of phenocrysts shows no significant variation towards the dyke centre or across the bands (Figure 4.7). Mean phenocryst orientations are also broadly constant across the sample, and within the bands, remaining at a constant 10°, measured from the dyke margin (note that the orientation of this sample is unknown, so we cannot infer a flow direction). The standard deviation in phenocryst orientations gradually increases from 30 to 50° across the sample, moving towards the dyke centre, showing a reduction in the strength of the preferred orientation.

Teno Vesicles

The bands are not only associated with variations in phenocryst concentration but in vesicularity, with the edges of bands having lower vesicularities than their centres (Figure 4.6a). In the first band, the edges have a vesicle area fraction of 0.05, whereas the peak value of 0.22 occurs within the band. However, peak vesicularities do not fall exactly in band centres; instead, the peak is skewed towards the dyke centre. The variation in vesicularity shows no relationship with vesicle size. There is a gradual increase in vesicle size away from the dyke margin, with median maximum diameters increasing from 0.05 to 0.32 mm across the studied region, but fluctuations in size are not associated with the bands. Across the sample, vesicles have a mean orientation of 10°, the same as the phenocrysts, but with a much greater circular standard deviation of 60°. The relationship between vesicles and phenocrysts is discussed further in Section 4.6.6. Vesicle orientation is also unrelated to the bands.

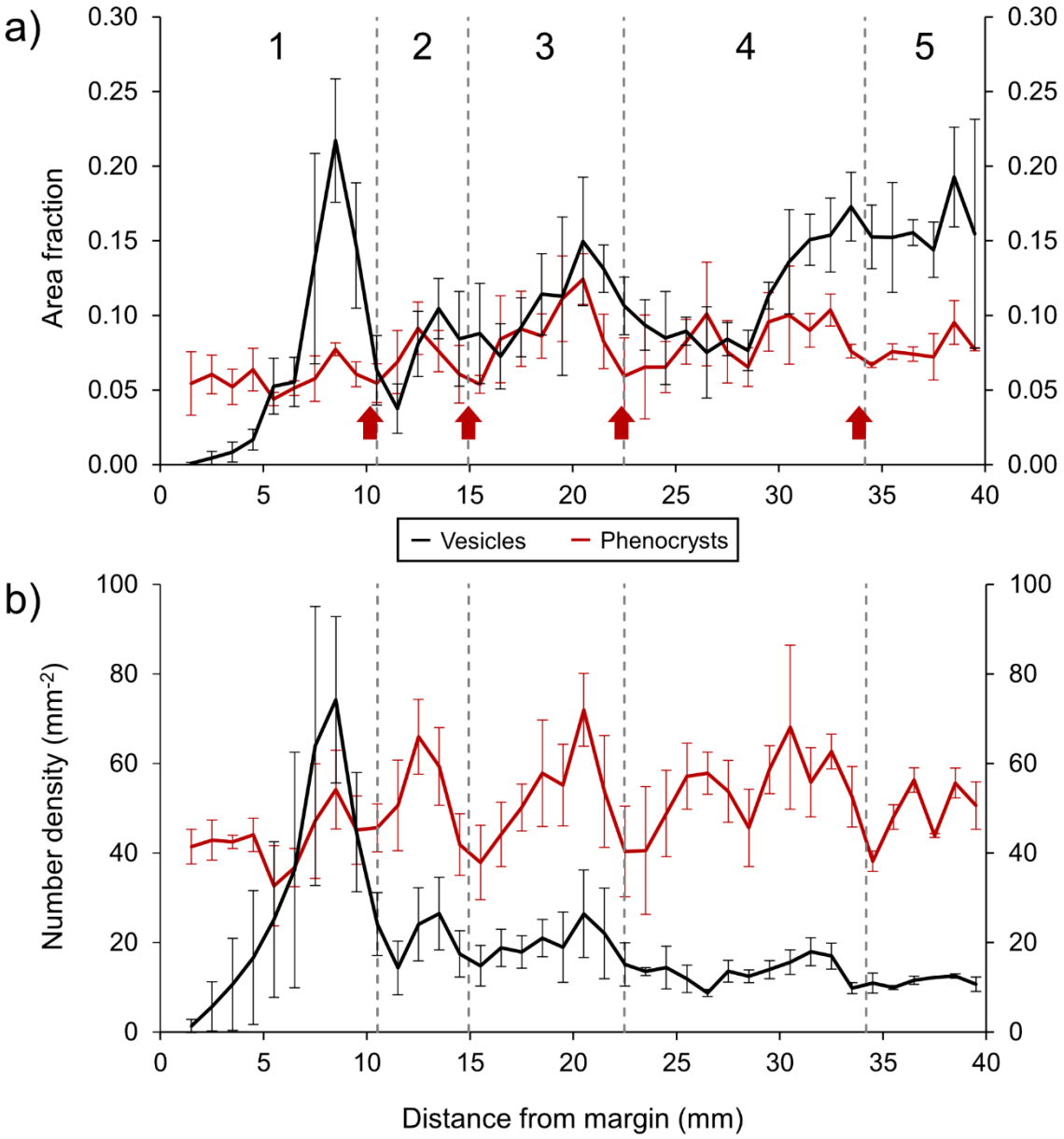

Figure 4.6. a) Variation in vesicularity (vesicle area fraction) and phenocryst area fraction across the Teno sample; b) number densities of vesicles and phenocrysts across the Teno sample. Dashed lines show the positions of the bands determined by eye, based on colour variations. Band edges coincide with drops in the phenocryst area fraction (highlighted with red arrows in a) and number density. Error bars show standard deviation.

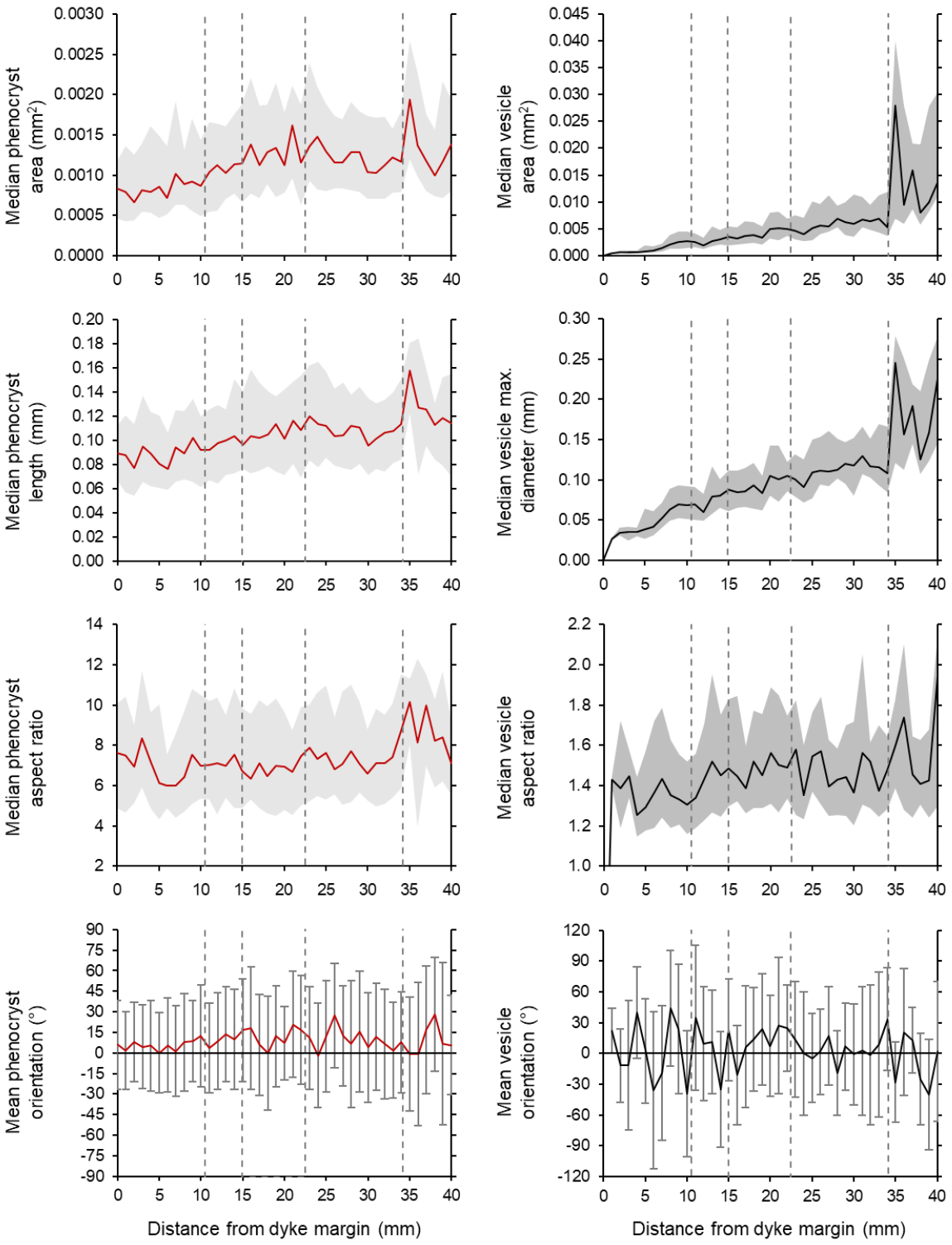

Figure 4.7. Phenocryst (red lines) and vesicle (black lines) shape statistics moving across the Teno sample. In the top three rows, the solid line shows the median and the grey area shows the interquartile range, and in bottom row, the solid line shows the circular mean and bars show standard deviation. Vertical dashed lines show band edges.

4.5.2 CRB Sample

By eye, there appear to be eight bands in the CRB sample (Figure 4.5), defined by a variation in vesicularity, but not by colour. Unlike the Teno sample, there are no clear boundaries between bands defined by light-to-dark transitions. Therefore, to measure the CRB bands we assume that it is analogous to the Teno sample, and define the band edges as the positions with the lowest vesicularity. Just like the Teno sample, the bands get wider and less distinct towards the dyke centre.

CRB Phenocrysts

Analysis of binary images reveals that there is no relationship between the bands and the phenocrysts in the CRB sample. Area fraction is generally low (Figure 4.8), but neither that nor any other measured phenocryst characteristics show any relation to the bands (Figure 4.9). The mean orientation of phenocrysts is a constant 13±41° from the margin in the vertical plane, and this imbrication angle suggests a component of upwards flow (as discussed in Chapter 2).

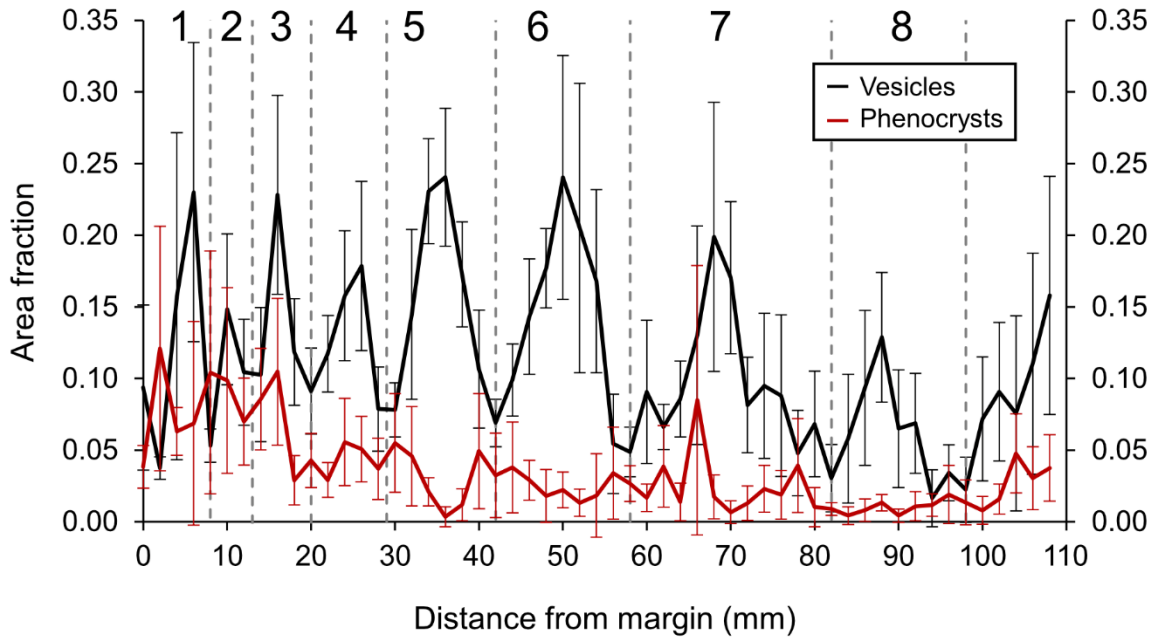

Figure 4.8. Variation in vesicularity (vesicle area fraction) and phenocryst area fraction across the CRB sample. Grey dashed lines have been placed at troughs in vesicularity. Bands are defined purely by variation in vesicularity, and show no relation to the phenocrysts. Error bars show standard deviation.

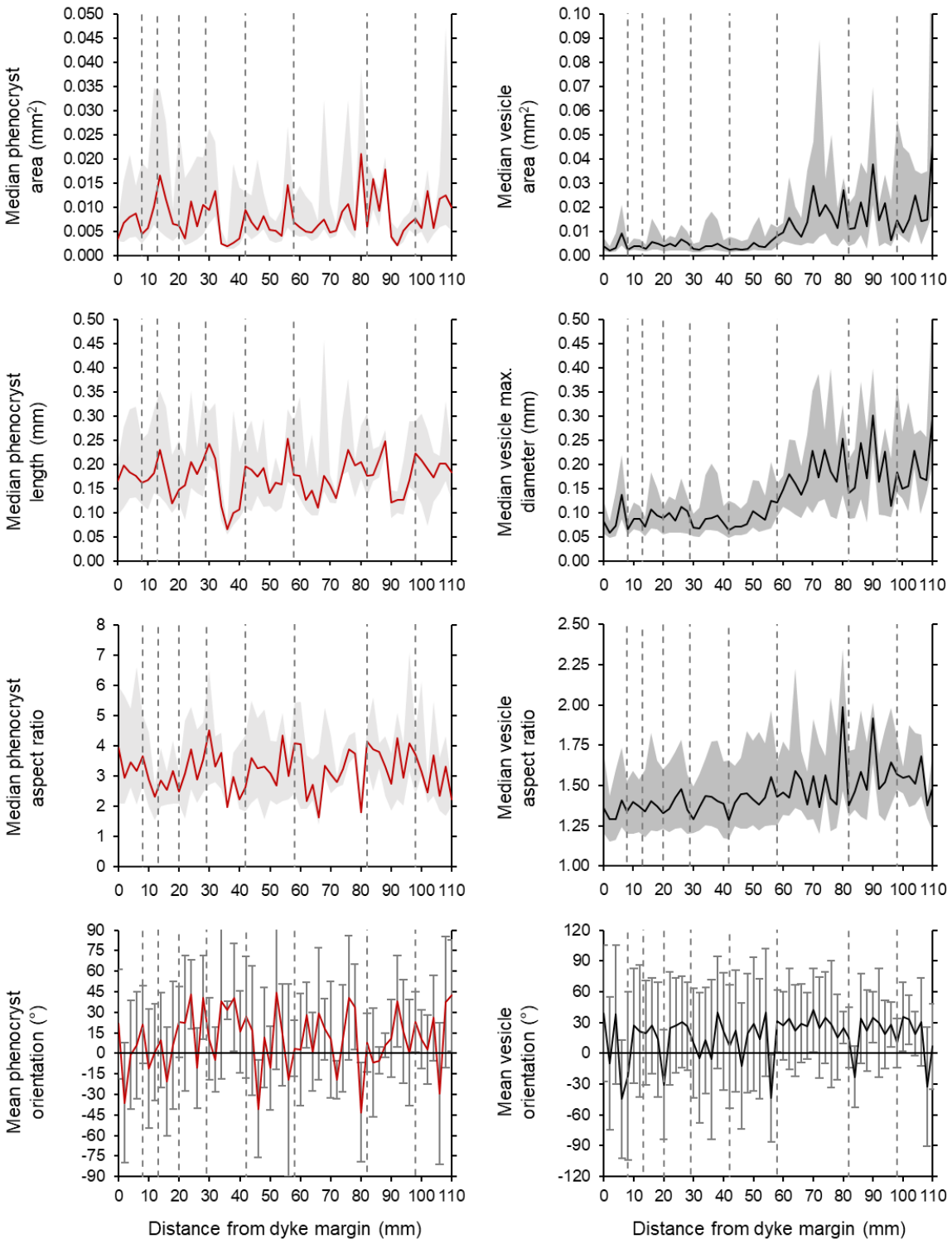

Figure 4.9. Phenocryst (red lines) and vesicle (black lines) shape statistics moving across the CRB sample. In the top three rows, the solid line shows the median and the grey area shows the interquartile range, and in bottom row, the solid line shows the circular mean and bars show standard deviation. Vertical dashed lines show band edges.

CRB Vesicles

Based on the assumption that bands begin and end at the lows in vesicularity, we find that vesicularity peaks near the centre of each band at values between 0.15 and 0.25 (Figure 4.8). Lows in vesicularity are around 0.01 to 0.10. The size of vesicles increases towards the dyke centre, with median maximum diameters increasing from 0.02 to 0.30 mm (Figure 4.9), and unlike in the Teno sample, vesicle size fluctuates within each band, with peaks in vesicle size coinciding with peaks in vesicularity. The vesicles have highly irregular shapes, which suggests rapid solidification before the deformed and coalesced bubbles could relax back to spheres (see discussion in Section 3.5). The mean orientation of vesicles is roughly constant across the sample at 24±55° from the margin, in the vertical plane. This implies the same flow direction as the phenocrysts, although we note that the vesicles have highly irregular forms which has led to a high standard deviation.

There are two populations of vesicles present within the CRB sample. The large, rounded vesicles that we see under the petrological microscope at x5 magnification are primary magmatic vesicles, which we have analysed for vesicle number density and area fraction. However, SEM images of the CRB sample at x400 magnification reveal a second population of diktytaxitic voids, which are all < 30 μm in maximum diameter (Figure 4.10). These small voids are angular, with straight edges aligning with surrounding microlites, and sometimes they fill all the available space between microlites. However, the size distribution from small, diktytaxitic voids to large, rounded vesicles is discontinuous, and nowhere do we see diktytaxitic voids merging with larger, primary magmatic vesicles. As such, we are confident that they are separate populations, likely to have formed at different stages in band formation. All vesicle measurements from the binary image analysis apply only to the larger, primary magmatic vesicle population.

CRB Microlites

Due to the greater range in crystal size within the CRB sample, we used SEM images at x400 magnification to study microlites not visible under the petrological microscope. The microlites are dominantly plagioclase, with a median length of around 20 μm and a modal aspect ratio of 5, both of which are constant across the studied region (Figure 4.11). The size, shape and abundance of plagioclase microlites shows no relation to the bands. We also measured oxide microlites, which show a gradual increase in size across the sample, with maximum diameter increasing from 6 to 10 μm towards the dyke centre. They also display a relatively sharp increase in circularity from 0.3 to 0.5 between 20 and 30 mm from the dyke margin, which is associated with a change from skeletal, dendritic shapes to more equant forms (Figure 4.10). Circularity is the perimeter of each shape divided by the perimeter of a circle with the same area. However, no aspect of the oxide microlites showed any relation to the bands.

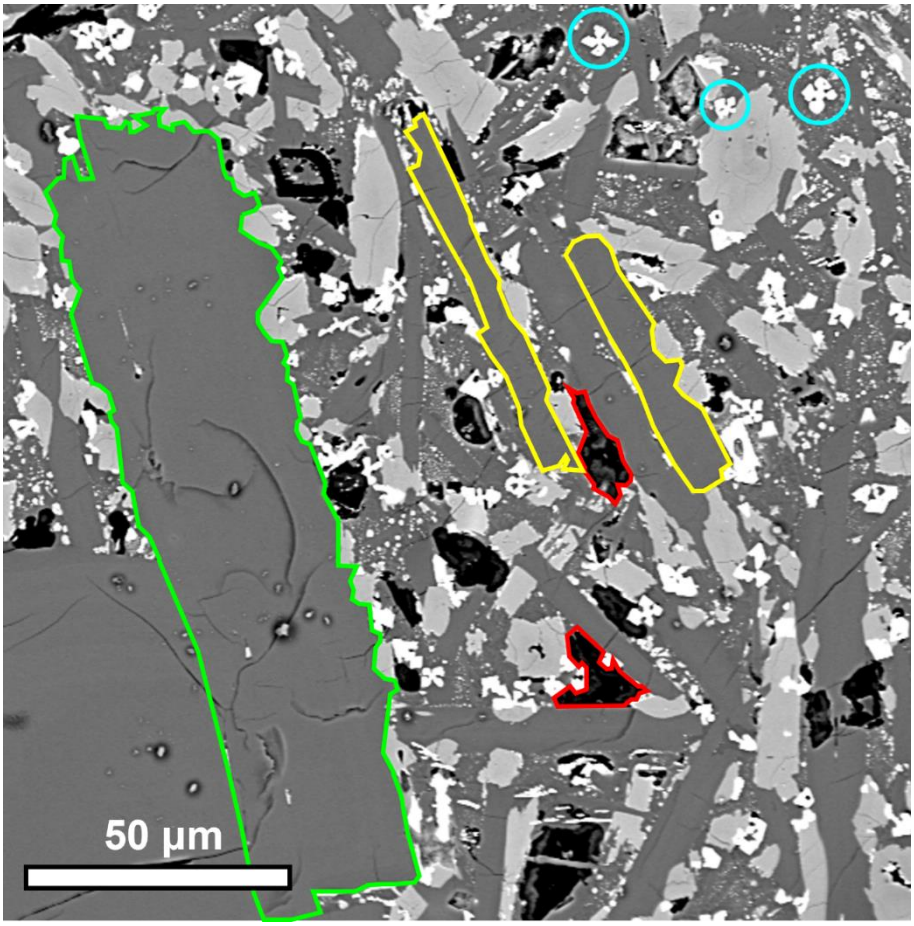

Figure 4.10. SEM image of the CRB sample. Examples of plagioclase microlites are outlined in yellow, diktytaxitic voids in red, and oxide microlites have been circled in cyan. The large plagioclase crystal on the left side of the image, outlined in green, is 0.15 mm in length, so is classed as a phenocryst.

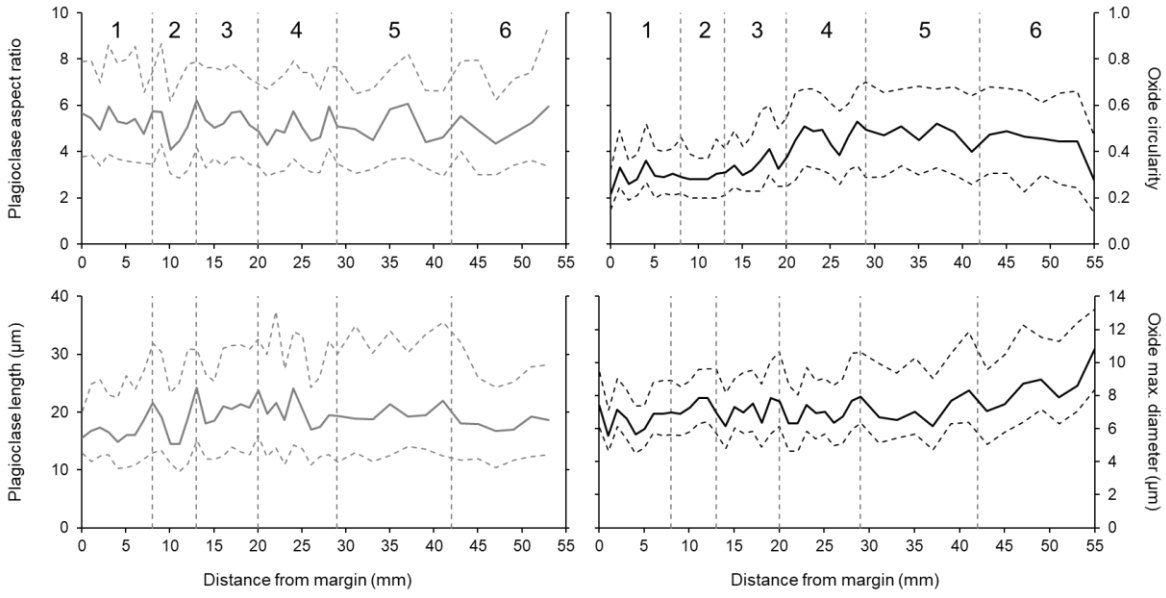

Figure 4.11. Variation in plagioclase microlite length and aspect ratio, and oxide circularity and maximum diameter across the first six bands of the CRB sample. The solid line shows the median value, and the dashed lines show the interquartile range.

4.6. Discussion

4.6.1 Conceptual framework for a band-formation model

Before interpreting the processes responsible for creating the phenocryst and vesicle textures within each band, we outline a conceptual framework for band formation. This framework is based on the key similarities between our two samples, and other examples reported in the literature. The main unifying feature of the bands is their position only at the margins of dykes, their millimetre to centimetre widths, and their tendency to become wider and less distinct towards the dyke centre (Figures 4.1, 4.2, 4.3, 4.5). The Teno sample contains bands defined by variations in phenocryst number density and vesicularity, with vesicularity peaking near band centres. The CRB sample contains bands defined by cyclic variations in vesicularity only, with no variation in phenocrysts. However, the fact that bands become wider and less distinct in all cases suggests that they form via the same process, at the same stage of dyke emplacement.

Marginal banding is defined by cyclic variations in phenocryst number density and vesicularity moving away from the margins, and these repeating textures suggest that the bands are a result of a repetitive process. Given that the margins are the first material to solidify within the fracture, and that they originate at the tip of the dyke, we must therefore infer that a repetitive process is operating within the dyke tip, driving band formation. The prevalence of bands across diverse volcanic settings (Drever and Johnston, 1959; Walker, 1987; Brouxel, 1991; Walker and Eyre, 1995; Thordarson and Self, 1996; Platten, 2000; Holness and Humphreys, 2003; Delcamp et al., 2012; Galindo and Gudmundsson, 2012; Kavanagh et al., 2018; Thiele et al., 2021) suggests that this repetitive dyke tip process is intrinsically related to dyke propagation.

We propose that the most likely cause for band formation is the repeated cooling, solidification and refracturing of magma within the dyke tip. Cooling is ubiquitous within dykes, no matter their volcanic setting, propagation direction, or host rock properties. We interpret the bands to represent sequential pulses of magma through the narrow dyke tip, which will experience rapid heat loss, unlike the wider body of the dyke. Each band represents a magma pulse that propagated the dyke a step further, and which caused widening of the dyke further upstream (Figure 4.12). Wherever bands are found along the length of the dyke, they always show the same increase in width and loss of distinction towards the dyke centre, and the bands themselves are always millimetres to centimetres wide. This suggests that the timescales associated with each magma pulse are roughly constant, resulting in similar banding patterns at any point of observation.

We envisage the accumulation of marginal bands as follows. Imagine a fixed point of observation, initially positioned just ahead of the dyke tip. As the dyke propagates, a crack forms in the host rock, and a thin sheet of magma is emplaced at our point of observation, forming the first band. This is the first magma pulse, and its narrow width means that it solidifies rapidly. This causes a blockage in the

channel, stopping the melt from transmitting pressure to the host rock, and so propagation is temporarily stalled. Pressure builds behind the blockage as magma continues to be supplied from upstream, until the thin sheet ruptures, with a fracture propagating down its centre and into the host rock beyond. The second pulse of magma enters this fracture, and this forms the second band at our point of observation.

The second magma pulse differs from the first in two key ways. Firstly, the magma-filled crack is now wider at our point of observation, as the dyke has a tapering geometry, and the tip is now further away. Secondly, magma has been injected into the centre of the previous band, which is warmer than the host rock. This causes band two to be wider than band one, but to lack a glassy margin. The roughly constant interval between magma pulses is long enough for both bands to solidify fully, despite their different widths.

Bands accumulate as this process repeats. Pulse three cracks through band two, and pulse four cracks through band three, always intruding down the centre of the previous pulse where material is warmest and weakest (Gudmundsson, 1984). The tapered dyke tip propagates progressively further from the point of observation, and so the magma-filled crack gets wider. However, the interval between pulses is still long enough for them to fully solidify before the next arrives. As the tip moves further away, the fluctuations in pressure and flow rate become less pronounced, which leads to the bands becoming less texturally distinct. Eventually, the magma-filled crack at the point of observation will be so wide that it cannot solidify to its centre before the next pulse arrives. From then on, no more bands can be produced at the point of observation. At the dyke tip, magma flow is still pulsatory, but fluctuations in pressure and flow rate are now so distant and so minimal, and cooling rates are so subdued, that these fluctuations will not be recorded. Eventually, the dyke tip will have progressed so far from the point of observation that magma flow becomes steady.

It is worth noting that each magma pulse forms a first band at the dyke tip, a second band immediately upstream from the tip, a third band behind that, and so on. In our conceptual framework, each band could, in principle, be traced to the outermost dyke margin. However, the extremely high aspect ratio of bands (i.e., their length compared to their width), combined with the poor and patchy exposure of dyke margins means that this would be near impossible to test in practise. Additionally, the three-dimensional nature of the dyke tip means that individual pulses may not nest neatly inside one another. The dyke tip is likely split into segments that move at different rates, with complex dynamics driving their coalescence (discussed in depth in Chapter 5). This complexity is one reason why marginal bands may show some variation in width rather than a simple linear increase towards the dyke centre (Figure 4.5).

In the rest of this section, we explore the feasibility of our conceptual model in the context of the data presented in Section 4.5.

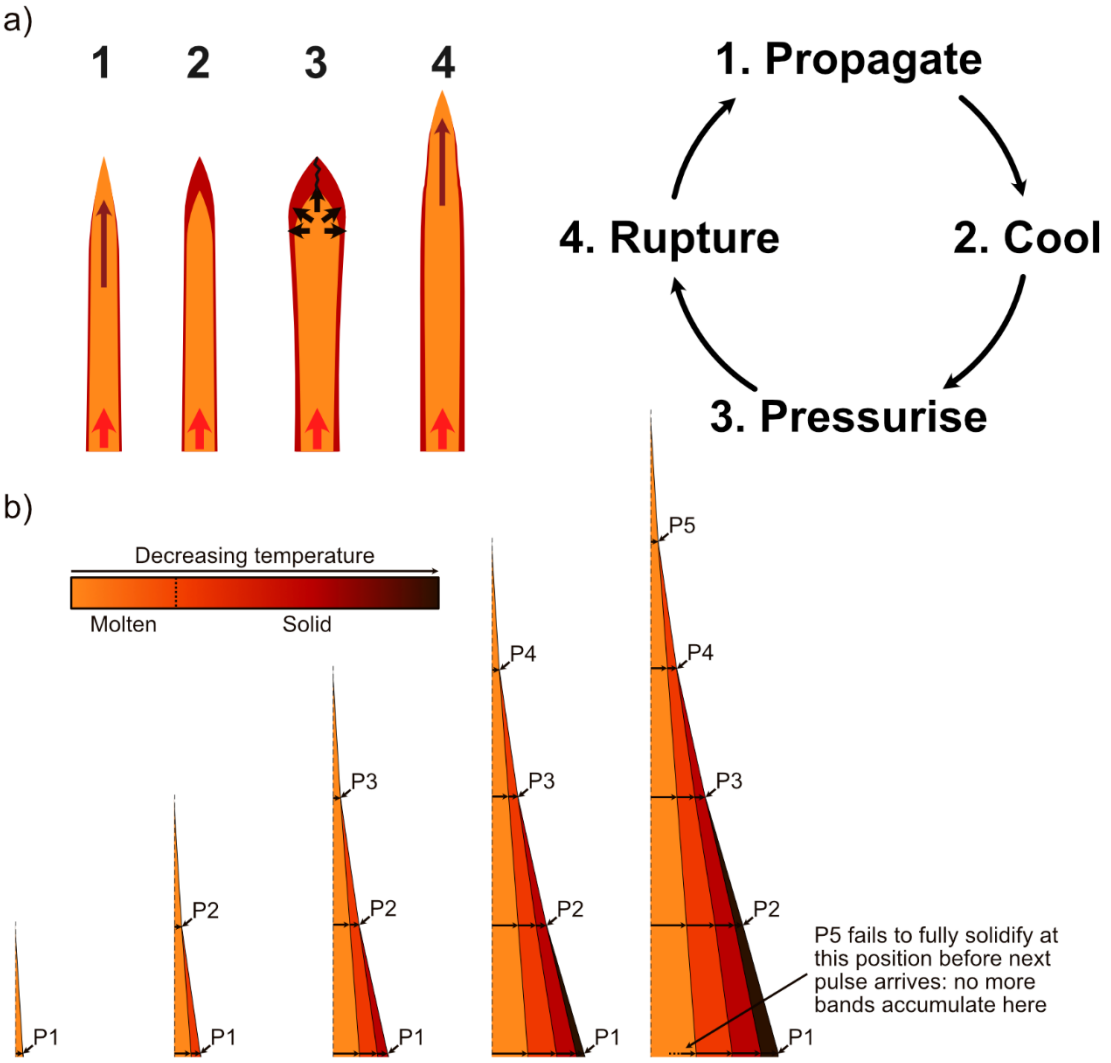

Figure 4.12. Schematic representation of our conceptual framework: a) the cooling-driven cycle that leads to pulsatory propagation of the dyke tip; b) gradual accumulation of bands. Each band represents a pulse of magma through the dyke tip, causing the dyke to propagate a step further, and to inflate further upstream. Note that once a sufficient number of bands have accumulated, a pulse will not fully solidify, causing it to mingle with the next pulse. At this point, the band formation mechanism is lost.

4.6.2 Band widths and dyke geometry

We interpret each band to be a pulse of magma that propagated the dyke one step further, and which had time to fully solidify before the next pulse arrived. The increase in band width towards the dyke centre reflects an increase in the width of the magma-filled crack as the dyke tip moved further beyond the point of observation. In other words, the widths of the marginal bands reveal the geometry of the dyke tip. The increase in band widths towards the dyke centre suggest that the magma-filled crack has a tapering geometry, as has previously been inferred from the geometry of solidified dyke tips (Marinoni and Gudmundsson, 2000; Clemente et al., 2007; Geshi et al., 2010; Stephens et al., 2017; Healy et al., 2018).

The marginal bands are very narrow, implying that the propagating dyke tip was also narrow, at millimetres to centimetres in width. This is feasible, as dykes have been recorded to be less than a few centimetres wide (Jolly and Sanderson, 1995; Marinoni and Gudmundsson, 2000; Stephens et al., 2017). Indeed, several other dykes in the Teno region were found to be only a couple of centimetres wide (Figure 4.13). This is concordant with LEFM models, which require pressurised, fluid-filled cracks to have tapering points, to concentrate stress and instigate fracturing (Rivalta et al., 2015). We note that our model does not require the dyke tip to be a specific shape (i.e., concave or convex), only that it must taper to a point.

We also note that our model involves a constant interval between magma pulses. The increasing width of bands towards the dyke centre reflects the tapering dyke tip geometry, not an increase in duration for each magma pulse. If the interval between magma pulses was to increase over time, we would see an increase in the width of the first band in the direction of dyke propagation. Wherever marginal bands were identified along the same dyke in the Teno region, the outermost band was only a few millimetres wide. Similar initial widths occur in our CRB sample and in the literature. Therefore, the intervals between magma pulses are likely to have been roughly constant.

Figure 4.13. The tapering tip of a dyke in the Teno Massif, Tenerife, which narrows to a width of < 2 cm (lens cap is 6.5 cm in diameter). Such narrow dykes are relatively common in the area, and are assumed to come from the leading edge of a magma pulse, stalled through rapid solidification.

4.6.3 Band emplacement timescales

We now estimate the likely timescales of band emplacement, and the constant interval between cooling-driven magma pulses through the dyke tip. We assume that each band represents the half-width of a molten magma pulse, and we estimate the time required for that pulse to solidify by considering the rate of heat conduction into the adjacent host rock. This analysis utilises the MATLAB model introduced in Section 1.6, which was written by Simon Mathias of the Department of Engineering, Durham University. Here, I adapt this model to handle multiple injections of magma to the centre of the intrusion (Allgood and Mathias, 2023).

The model starts with a width of molten material injected instantaneously into a narrow dyke. The intrusion cools via conduction until its centre reaches a defined final temperature T_f. Upon reaching this temperature, a second pulse of magma is emplaced instantaneously in the dyke centre, shifting the previous temperature profile laterally to accommodate the new material. The system continues to cool until the centre once again reaches T_f, whereupon the process is repeated. The widths of each magma pulse are defined by the measured widths of our bands.

We use the final central temperature T_f to constrain our model in order to explore the relationship between rock textures and temperatures. The bands show no evidence of melt-back or mingling, so we infer that each band had fully solidified by the time the next pulse was emplaced. The cyclic

variations in phenocryst concentration show sharp boundaries (Figure 4.6), which would not exist had the magma pulses mingled, or if the arrival of one pulse had thermally eroded the last. This means that $T_f \leq T_S$ for each band, which places a lower constraint on likely emplacement timescales. Similarly, we do not see any glassy margins on our bands, and this provides an upper constraint on our timescales. Setting T_f rather than defining an injection interval allows us to explore the interaction between sequential pulses based on temperature.

We assume that the magma and host rock have the same density, thermal conductivity and specific heat capacity, which is reasonable for a basalt dyke intruding layered basaltic lava flows. We take a density of ρ = 2700 kg m^{-3} for the liquid and solidified magma (Lesher and Spera, 2015), a thermal conductivity of k = 1.3 W m^{-1} K^{-1} (Sehlke et al., 2020), and a specific heat capacity of c_p = 1200 J kg^{-1} K^{-1} (Turcotte and Schubert, 2002; Mollo et al., 2011).

We run the model twice, both omitting and including the release of latent heat on solidification. This is because the groundmass is glassy in the first band, but becomes more crystalline towards the dyke centre, indicating that the release of latent heat varied over time. We therefore create upper and lower bounds for our estimated emplacement timescales by including and omitting latent heat respectively. When included, we use a latent heat L of 4 x 10^5 J kg^{-1} (Bruce and Huppert, 1990; Turcotte and Schubert, 2002).

The initial magma temperature T_M is taken to be 1200 °C, which is the eruption temperature measured in the 2021 La Palma eruption (Carracedo et al., 2022; Castro and Feisel, 2022). We use an approximate solidification temperature T_S of 1000 °C, and a host rock temperature T_0 of 0 °C. The model boundary condition is that the far-field host rock temperature is fixed at T_0. To ensure that the warming effect does not approach the model boundary, we set the total width of the model W to be ten times the final dyke half-width away from the dyke centre. This approach was tested for each value of T_f, and we find that the warming effect only extends ~0.5 m from the final dyke width. We ran the model for six values of T_f: 1000, 900, 800, 700, 600 and 500 °C. A schematic model setup is shown in Figure 4.14.

In Section 4.6.2 we proposed that the increase in band widths towards the dyke centre reflects the tapered geometry of the dyke tip, and that the interval between each magma pulse is likely to be roughly constant. The narrower, outer bands take the least time to solidify, and so the solidification timescales of the inner bands are the most representative of magma pulse durations. However, we must model the outer bands because they act as insulation for all subsequent magma pulses. We do not intend for the following solidification timescales of sequential bands to imply that magma pulse duration increases over time; instead, the range of timescales for the innermost bands should be taken

as an indicator of pulse durations, and we constrain the model using T_f to relate timescales to observed textures.

Before discussing the model results, we note a key, implicit assumption in our method: that the magma is stationary. The advection of heat driven by magma flow increases cooling times significantly by constantly supplying fresh, uncooled magma to the dyke centre (Fialko and Rubin, 1999; Petcovic and Dufek, 2005). However, in the case of the marginal bands, advection should be insignificant, because the magma pulses are narrow enough that they solidify rapidly, and flow is not constant. The greatest uncertainty in this model is likely to come from our assumed values of thermal conductivity, which is poorly constrained (Clark, 1966; Robertson and Peck, 1974; Hanley et al., 1978; Durham et al., 1987; Mostafa et al., 2004).

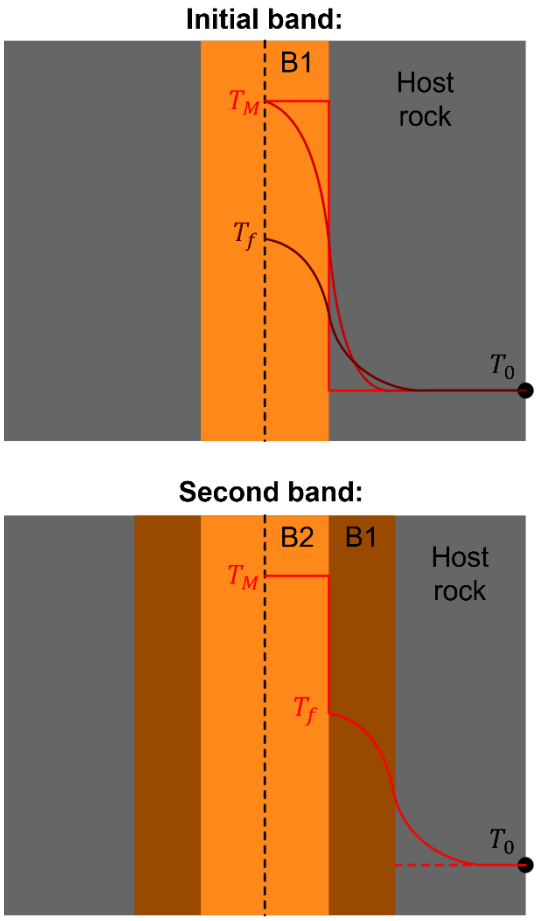

Figure 4.14. Schematic representation of MATLAB cooling model, expanded from the simple version outlined in Section 1.6. A magma pulse is emplaced at T_M in host rock of T_0, and cools following Fourier's law of conduction. When the centre reaches a defined final temperature T_f, a new pulse is injected. Old material is shifted sideways to make way, pushing aside host rock that remains unwarmed by the intrusion. The model boundary is held at T_0.

We track the solidification of each band by monitoring the position of the solidification front (the $T = T_S$ isotherm) through time (Figure 4.15). Given that the Teno and CRB bands are of similar width, we only present the results for the Teno bands. Bands solidify faster when the centre of the previous band is allowed to cool to a lower final temperature T_f. In cases where T_f > 800 °C, the previous band is thermally eroded by the arrival of the next, and the solidification front moves back towards the margin before reverting and moving towards the dyke centre again. Injecting pulses when the centre reaches 1000 °C (i.e., when $T_f = T_S$) can cause up to 80% of the previous band to be thermally eroded, as seen in the yellow curves in Figure 4.15. Given that we see no thermal erosion between the marginal bands, we conclude that each band must have cooled to a maximum temperature of 800 °C before the next pulse arrived. This provides a lower bound for emplacement timescales, of a few tens of minutes.

To find an upper bound for emplacement timescales, we must consider the minimum temperature to which each band cooled before the next pulse arrived. We know that the bands did not cool enough to produce chilled margins on the subsequent band, because we see no chilled margins or variations in groundmass textures between bands. Only the first band at the outermost margin is glassy, so no subsequent bands faced a similar degree of cooling.

To produce a glass, magma must drop below its glass transition temperature, which is usually around 739 °C for a basaltic melt, although this depends on the cooling rate and H_2O concentration (Giordano et al., 2005). When magma makes contact with the host rock, the first response is to cool to a temperature halfway between T_M and T_0. If our initial magma temperature T_M is 1200 °C, the wall must be ≤ 278 °C to induce a glassy chilled margin. As such, we would only expect each marginal band to display a glassy margin if the previous pulse had cooled to 278 °C. This allows us to estimate an upper bound for our emplacement timescales.

We estimate this upper bound by re-running the model for the first three bands, setting T_f to 278 °C. These outer bands would be the most likely to develop glassy margins, because they are emplaced into cooler surroundings, the first band having heated the host rock only slightly. For the Teno sample, we find that the first band must cool for 27-45 minutes to induce a glassy margin on the second band, and the second band must cool for 34-57 minutes to induce a glassy margin on the third band. In the CRB sample, where the bands are slightly narrower, the first band must cool for 15-26 minutes, and the second must cool for 30-50 minutes to induce glassy margins. Even greater cooling intervals would be required to generate glassy margins for subsequent bands, and the fact that we don't see glassy margins on bands two and three strongly suggests that the upper bound for band emplacement timescales is several tens of minutes. This is similar to the time required for the innermost bands to solidify. As such, we conclude that the likely interval between magma pulses is on the scale of tens of minutes.

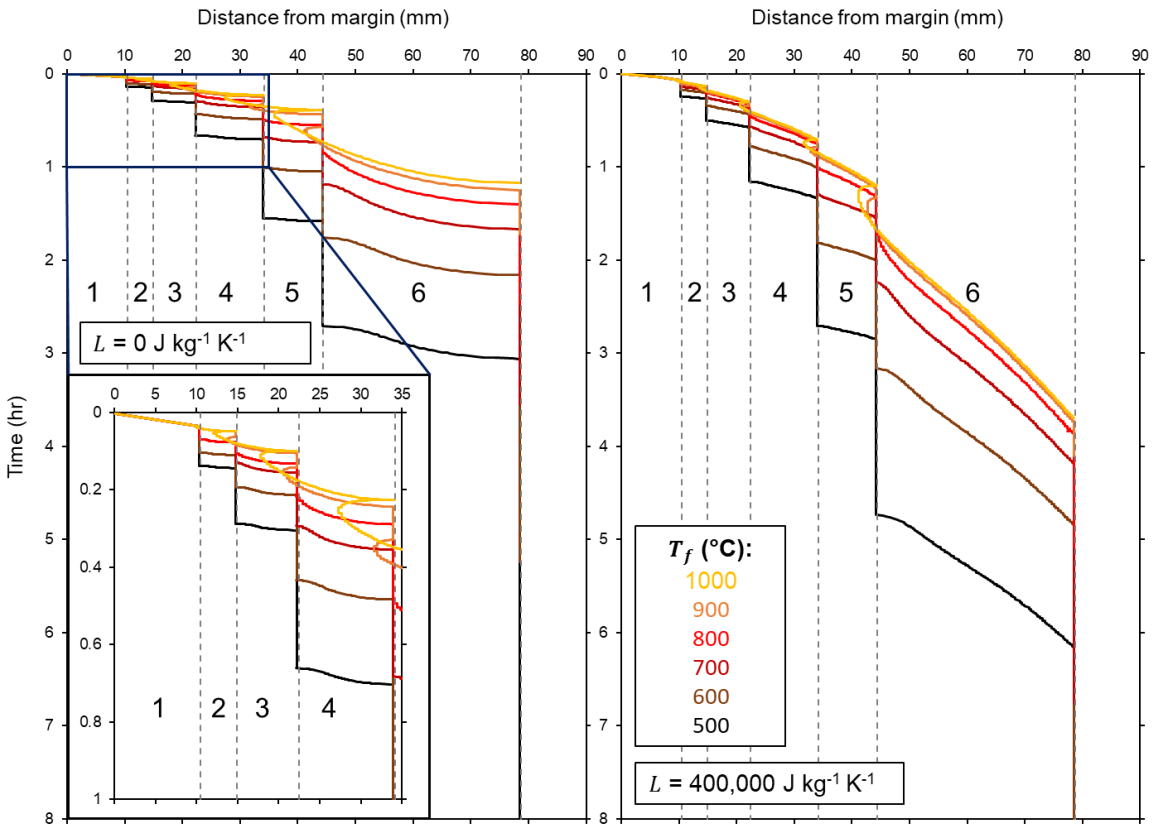

Figure 4.15. The position of the solidification front (the $T = T_S$ isotherm), moving inwards from the margin, based on the widths of the bands in the Teno sample: (left) latent heat release is neglected; (right) latent heat release is included. T_f is the final temperature at the dyke centre before the next magma pulse is emplaced. When the solidification front moves back towards the margin (which is most obvious in the yellow curves), it is melting back previously solidified material.

4.6.4 Vesicles and pressure drops

The bands in both samples are associated with variations in vesicularity. By reading the band textures as a time-series, with the oldest material at the margin, we interpret the variations in vesicularity as a record of fluctuating magma pressures. Vesicularity depends strongly on pressure, so that peaks in vesicularity indicate low pressures, when bubbles expanded, whereas troughs indicate high pressures, when bubbles shrank. In the context of our conceptual framework, these repeated pressure drops are likely associated with the episodic fracturing of the host rock, allowing the dyke tip to propagate a step further (Figure 4.12).

To demonstrate this concept, we draw on previous work regarding bubble growth in magma (Prousevitch et al., 1993) and on LEFM models of pressures within dykes (Menand and Tait, 2002; Rivalta et al., 2015). Specifically, we test whether the pressure drops indicated by the variation in vesicularity are consistent with the pressure drops caused by fracture propagation. We also test whether the time required for bubble growth is sufficient to capture pressure variations within the emplacement timescale of each magma pulse (Section 4.6.3).

In the LEFM framework, a crack will propagate when its geometry and internal pressure produce a stress intensity at its tip that exceeds a critical threshold K_C, the fracture toughness of the host rock. This is taken to be an intrinsic host rock property. For a given crack of length l, the critical internal pressure P_F required for fracture is given by Menand and Tait (2002):

$$P_F = \frac{K_C}{\sqrt{\pi l}}. \quad \text{Eq. 4.1}$$

The buoyancy pressure within a self-propagating dyke is

$$P_B = \Delta\rho g l\,, \quad \text{Eq. 4.2}$$

where $\Delta\rho$ is the density difference between magma and host rock, and g is gravitational acceleration (Menand and Tait, 2002). For self-propagating dykes where buoyancy is the dominant driving pressure, $P_F = P_B$. We can therefore substitute Eq. 4.2 into Eq. 4.1, and rearrange to find an equation for the critical crack length l_C required for fracturing at the tip of buoyancy-driven dykes:

$$l_C = \left(\frac{K_C}{\sqrt{\pi}\Delta\rho g}\right)^{2/3}. \quad \text{Eq. 4.3}$$

We then substitute Eq. 4.3 into Eq. 4.1 and obtain an expression for P_F as a function of the fracture toughness and density difference:

$$P_F = \left(\frac{K_C^2\,\Delta\rho g}{\sqrt{\pi}}\right)^{1/3}. \quad \text{Eq. 4.4}$$

The value for fracture toughness is highly uncertain, with values in the literature ranging from 0 to 10^4 MPa m$^{1/2}$. Laboratory measurements (e.g., Atkinson, 1984; Atkinson and Meredith, 1987; Balme et al., 2004) are several orders of magnitude lower than estimates based on the geometry of dykes measured in the field (e.g., Delaney and Pollard, 1981; Olson, 2003; Daniels et al., 2012). We therefore assume that fracture toughness is in the region of 0-500 MPa m$^{1/2}$, the same as most lab and field values. The density difference between the magma and its surroundings is taken to be 100-500 kg m^{-3}, based on the assumption that pure magma and host rock both have a density of 2700 kg m^{-3}, with the magma containing a bubble volume fraction of up to 0.2. Using these variables, all estimated internal pressures are less than 10 MPa. We therefore take this value as the maximum pressure drop that could occur when a new fracture forms in the tip of a temporarily stalled dyke, leading to a sudden growth in vesicles and a new pulse of magma.

Using this estimated value of P_F, we calculate a characteristic growth timescale t_r for the bubbles within the dyke tip using the model of Prousevitch et al. (1993), in which a bubble of radius r grows at a rate given by

$$\frac{dr}{dt} = \frac{P_F - P_L}{4\eta\left(\frac{1}{r} - \frac{r^2}{S^3}\right)} \quad \text{Eq. 4.5}$$

where $P_L = 2\sigma/r$ is the Laplace pressure arising from surface tension σ for a bubble, η is fluid viscosity, and S is the radius of the melt shell that surrounds the bubble, which is given by

$$S = \left(\frac{r^3}{\phi}\right)^{1/3}. \quad \text{Eq. 4.6}$$

We combine Eq. 4.5 and Eq. 4.6 to give

$$\frac{dr}{dt} = \frac{rP_F}{4\eta(1-\phi)}. \quad \text{Eq. 4.7}$$

Note that we have neglected the Laplace stress. This is because the vesicles in our samples typically have equivalent radii $r \gtrsim 10^{-5}$ m, and surface tension in basaltic melts is typically σ = 0.2 N m^{-1} (Colucci et al., 2016), leading to a Laplace stress of the order 0.1 MPa. This is much smaller than the fracture pressure of 10 MPa, i.e., $P_F \gg 2\sigma/r$. The characteristic growth timescale t_r is therefore given by

$$t_r = \frac{r}{\frac{dr}{dt}} = \frac{4\eta(1-\phi)}{P_F}. \quad \text{Eq. 4.8}$$

We take a typical viscosity for basaltic magma of η = 100 Pa s (Giordano et al., 2008), and using measured values for vesicle area fraction ϕ (Section 4.5) and values for P_F between 1 and 10 MPa, bubble growth timescales from decompression are all less than 4 x 10^{-4} s.

However, bubbles may also grow via diffusion, and so we calculate an additional diffusional growth timescale t_D:

$$t_D = \frac{{L_W}^2}{D_{H2O}}, \quad \text{Eq. 4.9}$$

where L_W is the characteristic thickness of the walls between bubbles, and D_{H2O} is the diffusivity of H_2O in the melt. We estimate diffusivity using the equations of Zhang et al. (2007), which require the initial H_2O concentrations of the magma. For the Teno basalts, we use values between 0.8 and 1.5 wt.%, which are measured values from the neighbouring volcanoes of El Hierro and La Palma, which are in the early stages of basaltic shield evolution, comparable to the origins of the Teno dyke (Weis et al., 2015; Taracsák et al., 2019). For the CRB sample, the initial H_2O concentration is likely to have

been higher, at 1.5—2.0 wt.% (Thordarson and Self, 1996). Using these water contents, we estimate D_{H2O} to be 3.6—5.3^{-10} m^2 s^{-1} for the Teno sample, and 5.3—6.7^{-10} m^2 s^{-1} for the CRB sample.

Based on these estimated H_2O diffusivities, we find that the diffusional timescale for vesicles in both samples is around 20 s, which is significantly shorter than the emplacement timescales of the bands (Section 4.6.3). Based on our estimates of t_R and t_D, we conclude that bubble size is predominantly controlled by and responds quickly to pressure, which makes vesicularity a reliable indicator of pressure fluctuations within the dyke tip.

We now infer pressures from vesicularity using the equation of Shishkina et al. (2010), which relates the solubility of H_2O in basalt to pressure, so that

$$S_{H_2O} = 0.2351\, P^{0.5758}\,, \qquad \text{Eq. 4.10}$$

where S_{H2O} is the solubility in wt.%, and P is pressure in MPa. The saturation pressure (i.e., the pressure below which volatiles start coming out of solution) is when S_{H2O} equals the initial concentration of H_2O in the melt. At pressures below the saturation pressure, we can calculate the total volume of H_2O exsolved per kilogram of magma, then express this as a gas volume fraction.

For any pressure below the saturation pressure, we can calculate the solubility. The difference in wt.% between the initial H_2O content S_0 and the solubility S_P at any given pressure is used to calculate the mass of H_2O exsolved per cubic metre, where

$$m_{H2O} = \rho_m(S_0 - S_P)/100. \qquad \text{Eq. 4.11}$$

We can then convert this mass into a volume using the ideal gas law $PV = nRT$, where P is the pressure in Pa, V is the volume in m^3, n is the number of moles of H_2O exsolved per cubic metre of magma, R is the universal gas constant 8.3145 J mol^{-1} K^{-1}, and T is temperature in K. We then use the volume of exsolved gas to calculate a vesicularity ϕ_V as

$$\phi_V = \frac{V}{V+1}. \qquad \text{Eq. 4.12}$$

This gives us a way to calculate the vesicularity at a given pressure. However, calculating pressure from a given vesicularity means following this process in reverse, which requires a numerical solution. For this, we use the solvers in MATLAB.

To estimate the variations in pressure associated with each magma pulse, we identify regions with the highest and lowest vesicularity within each band. In the Teno sample, the maximum vesicularity is 0.22, the minimum is 0.04, and the mean value for a vesicularity peak is 0.16. In the CRB sample, the maximum is 0.24, the minimum is 0.02, and the mean peak value is 0.20. We use the water concentrations mentioned previously, which leads to saturation pressures of 8.4—25 MPa for the Teno sample, and 25—41 MPa for the CRB sample.

To calculate pressures from vesicularities, we assume a basaltic melt density ρ_m of 2700 kg m^{-3} and a temperature of 1200 °C. Comparing the maximum and minimum vesicularities within the Teno samples yields a maximum pressure drop of 1.5—5.9 MPa and a mean pressure drop of 1.0—1.5 MPa for all the bands, with the ranges caused by the uncertainty around initial H_2O concentration. For the CRB sample, the maximum pressure drop is 7.2—13.4 MPa, whereas the mean pressure drop for all the bands is 6.1—11.4 MPa. The values for both samples are consistent with our ballpark figure for fracture pressure P_F of 10 MPa.

Finally, it is worth mentioning the diktytaxitic voids within the CRB sample (Figure 4.10). These small, angular voids are unlikely to have resulted from decompression-driven growth. Previous instances of this texture in dykes and lava flows have been interpreted to result from crystallisation driving late-stage degassing (Fuller, 1939; Walker, 1989; Rogan et al., 1996; Martin et al., 2006). As discussed in Section 4.5.2, the diktytaxitic voids are separate population to the large, rounded, primary magmatic vesicles, with no evidence of them coalescing. It seems likely that the primary vesicles grew in response to fluctuating pressures, whereas the diktytaxitic voids appeared late in the crystallisation process.

4.6.5 Phenocrysts and flow differentiation

The Teno bands are defined by a cyclic variation in plagioclase phenocryst concentration, starting with a low concentration on their marginal side, which increases towards the dyke centre before a sharp drop in concentration at the onset of the next band (Figure 4.6). This is the cause of the dark-to-light colour variations seen by eye. There is also an associated variation in vesicularity, with peaks in vesicle area fraction skewed slightly towards the dyke centre within each band. The Teno sample is rare in displaying coupled variations in phenocryst and vesicle textures. Most marginal bands in the literature are defined purely by phenocrysts (Drever and Johnston, 1959), groundmass (Brouxel, 1991; Holness and Humphreys, 2003), or vesicles (Walker, 1987; Kile, 1993; Walker and Eyre, 1995; Thordarson and Self, 1996; Platten, 2000; Delcamp et al., 2012; Galindo and Gudmundsson, 2012; Kavanagh et al., 2018; Thiele et al., 2021). By containing coupled variations in both phenocrysts and vesicles, the Teno sample provides a crucial connection between these textures, allowing us to infer that they formed via the same process.

The length of phenocrysts within the Teno sample shows only a slight increase towards the dyke centre, from 0.10 to 0.15 mm, with no relation to the bands. Plagioclase is the dominant crystal species, and we have classified these crystals as phenocrysts because close to the margin, they exist within a glassy groundmass. They are likely to have grown elsewhere in the dyke system before being frozen in place in the tip of the dyke. The gradients in phenocryst concentration within the bands are independent of crystal size, so they cannot be the result of cooling rates. We therefore require a mechanical explanation for the spatial distribution of phenocrysts.

The most likely cause of an increase in phenocryst concentration moving towards the dyke centre is flow differentiation, whereby suspended crystals migrate away from the high velocity gradients near the dyke walls. This phenomenon has been demonstrated in analogue laboratory experiments and has previously been used to explain phenocryst concentrations increasing towards dyke centres (Bhattacharji and Smith, 1964; Bhattacharji, 1967; Gibb, 1968; Komar, 1972; Barrière, 1976). Several mechanisms are known to cause lateral particle migration within flows, including wall effects (Maude and Whitmore, 1956) and the Magnus effect for spinning particles (Komar, 1972). However, the most widely accepted mechanism is flow differentiation, sometimes called the Bagnold effect, which is driven by particle interactions (Bagnold, 1954).

Suspended crystals can migrate away from the dyke walls as follows. When suspended particles collide, they temporarily gain momentum perpendicular to the flow direction. This momentum gain is higher when particles collide with a greater velocity difference, and so lateral motion is enhanced in regions with steep velocity gradients. The result is a net motion away from the edges of flows, causing particles to concentrate in central regions where lateral motion is minimal (Bagnold, 1954; Phillips et al., 1992; Petford and Koenders, 1998). The rate of net migration is dependent on the frequency of particle collisions, which is increased at higher shear rates and higher particle concentrations (Karnis et al., 1963; Leighton and Acrivos, 1987; Abbott et al., 1991).

We can estimate the amount of flow differentiation likely to have occurred within the tip of the Teno dyke by considering the initial volume fraction of phenocrysts, their size, and the width of the channel. We use the method of Lecampion and Garagash (2014) to find a development length L_{dev}, which is the characteristic lengthscale travelled by magma over which particles migrate into a steady-state concentration distribution across the molten channel. This lengthscale depends on the initial, uniform particle fraction within the channel ϕ_0, the spherical particle radius a, and the channel half-width H, so

$$L_{dev} = \frac{H^3}{a^2} \frac{I(\phi_0)\, S(\phi_0)}{\kappa(\phi_0)}, \qquad \text{Eq. 4.13}$$

where I is the dimensionless viscous number, S is the dimensionless inelastic storage coefficient, and κ is the dimensionless permeability. The viscous number depends on the maximum particle volume fraction, ϕ_m, so that

$$I(\phi_0) = \left(\frac{\phi_m}{\phi_0} - 1\right)^2. \qquad \text{Eq. 4.14}$$

The inelastic storage coefficient S is controlled by the dimensionless friction coefficient μ, which can be calculated via

$$\mu = \mu_1 + \frac{\phi_m}{\beta}\left(1 - \frac{\phi}{\phi_m}\right) + \left[I(\phi) + \left(\frac{5}{2}\phi_m + 2\right) I(\phi)^{1/2}\right]\left(1 - \frac{\phi}{\phi_m}\right)^2, \quad \text{Eq. 4.15}$$

where μ_1 is the value of μ at ϕ_m, and β is a dimensionless compressibility coefficient. The value of S can then be calculated using

$$S(\phi_0) = -\frac{\mu}{\phi_0}.\frac{d\phi_0}{d\mu}. \quad \text{Eq. 4.16}$$

By differentiating Eq. 4.15 with respect to ϕ, we find $d\mu/d\phi$, the reciprocal of which is

$$\frac{d\phi}{d\mu} = \left(-\frac{1}{\beta} - I(\phi)\left(\frac{2}{\phi} + \frac{5}{2}\right) - \frac{2}{\phi_m}\left[I(\phi) + \left(\frac{5}{2}\phi_m + 2\right) I(\phi)^{\frac{1}{2}}\right]\left[1 - \frac{\phi}{\phi_m}\right]\right)^{-1} \quad \text{Eq. 4.17}$$

which we can then substitute into Eq. 4.16 to find S. The dimensionless permeability is calculated as

$$\kappa(\phi_0) = \frac{2(1-\phi_0)^\alpha}{9\phi_0}, \quad \text{Eq. 4.18}$$

where α is a constant. The constants used by Lecampion and Garagash (2014) have been experimentally verified for suspensions of hard spheres, but reliable empirical relationships do not exist for tabular shapes. Therefore, we must proceed by treating the phenocrysts as spherical. The constants for spheres are: ϕ_m = 0.585, μ_1 = 0.3, β = 0.158 and α = 5.1.

The development length is then

$$L_{dev} = \frac{H^3}{a^2}\frac{I(\phi_0)S(\phi_0)}{6\kappa(\phi_0)}. \quad \text{Eq. 4.19}$$

For the initial particle volume fraction ϕ_0 we take the total area of phenocrysts within each band, and divide this by the area of that band, excluding vesicles. The mean value across all the bands is 0.07 ±0.01, showing that the initial particle fraction was consistent within each magma pulse. We use a characteristic particle radius a of 0.05 mm, which is half the median phenocryst length. Finally, we take the channel half-width H to be the width of each band (Figure 4.5). Using values for the first four bands, we find that L_{dev} = 1.4 km. This is shorter than the length of most dykes, which implies that flow differentiation can be expected to occur. We also note that flow differentiation is an asymptotic process, meaning that most differentiation occurs before L_{dev} is reached.

Inspection of Eq. 4.19 reveals that the development length depends strongly on the channel half-width, so that $L_{dev} \propto H^3$. This means that flows in narrower channels differentiate over shorter distances; for example, band 2 has a width of 4.44 mm and a development length of only 70 m, whereas band 3 has a width of 18.06 mm and a development length of 3.9 km. This dependence on channel width goes some way to explaining why the initial, narrower bands show steeper phenocryst

concentration gradients, and why bands become less texturally distinct as they get wider towards the dyke centre.

Our analysis indicates that flow differentiation is a viable mechanism for producing gradients in phenocryst concentration within the narrow tips of dykes, and it can explain the textures in the Teno sample. However, the model does not account for the presence of bubbles in the magma, which will likely have some effect on particle migration. In the Teno sample, there is evidence that vesicles mostly grew after flow differentiation had occurred (Section 4.6.6). In the CRB sample, the vesicle fraction of 0.2 greatly exceeds the phenocryst fraction of 0.05, and so we do not attempt to estimate the feasibility of flow differentiation, although we note the lack of evidence for it having occurred.

Finally, we note that the preferred orientation of phenocrysts within the Teno sample shows no variation towards the dyke centre. We cannot infer a flow direction, as the orientation of the sample is unknown, but we can infer that the magma flow direction was the same for each pulse based on the consistent angle of the phenocrysts to the dyke margin (Wada, 1992; Philpotts and Asher, 1994). We also note that the degree of preferred orientation is highest closer to the margins, echoing the results of previous studies (Coward, 1980; Das and Mallik, 2020). This is perhaps due to the increasing crystallinity of the groundmass for later bands, leading to more complex collisions during emplacement. In the CRB sample, there are fewer phenocrysts, but these show a broadly constant direction of preferred orientation moving towards the dyke centre, implying that the flow direction for each magma pulse was consistently upwards.

4.6.6 Relationship between phenocrysts and vesicles

Phenocrysts and vesicles in the Teno sample have almost identical preferred orientations (Figure 4.7), and here we investigate the relationships between them. Many vesicles are flattened against neighbouring phenocrysts, while some even wrap around the ends of phenocrysts (Figure 4.13). These relationships suggest that bubble growth was impeded by the phenocrysts, indicating that the bubbles grew within a pre-existing network of aligned crystals. The bubbles were therefore forced to grow in an elongate manner, aligned with the phenocryst framework, resulting in phenocrysts and vesicles sharing a preferred orientation. Importantly, this shows that the vesicles in the Teno sample grew after the phenocrysts had been emplaced, and after the phenocryst textures had been established by flow differentiation.

Within the CRB sample, vesicles and phenocrysts also show similar preferred orientations (Figure 4.9); however, there is no textural evidence to suggest whether bubbles grew constrained within a pre-existing phenocryst network. There are few flattened vesicle edges in this sample, potentially due to its lower concentration of phenocrysts. It is likely that the similarity in preferred orientation has developed due to crystal rotation and bubble deformation processes explored in Chapters 2 and 3.

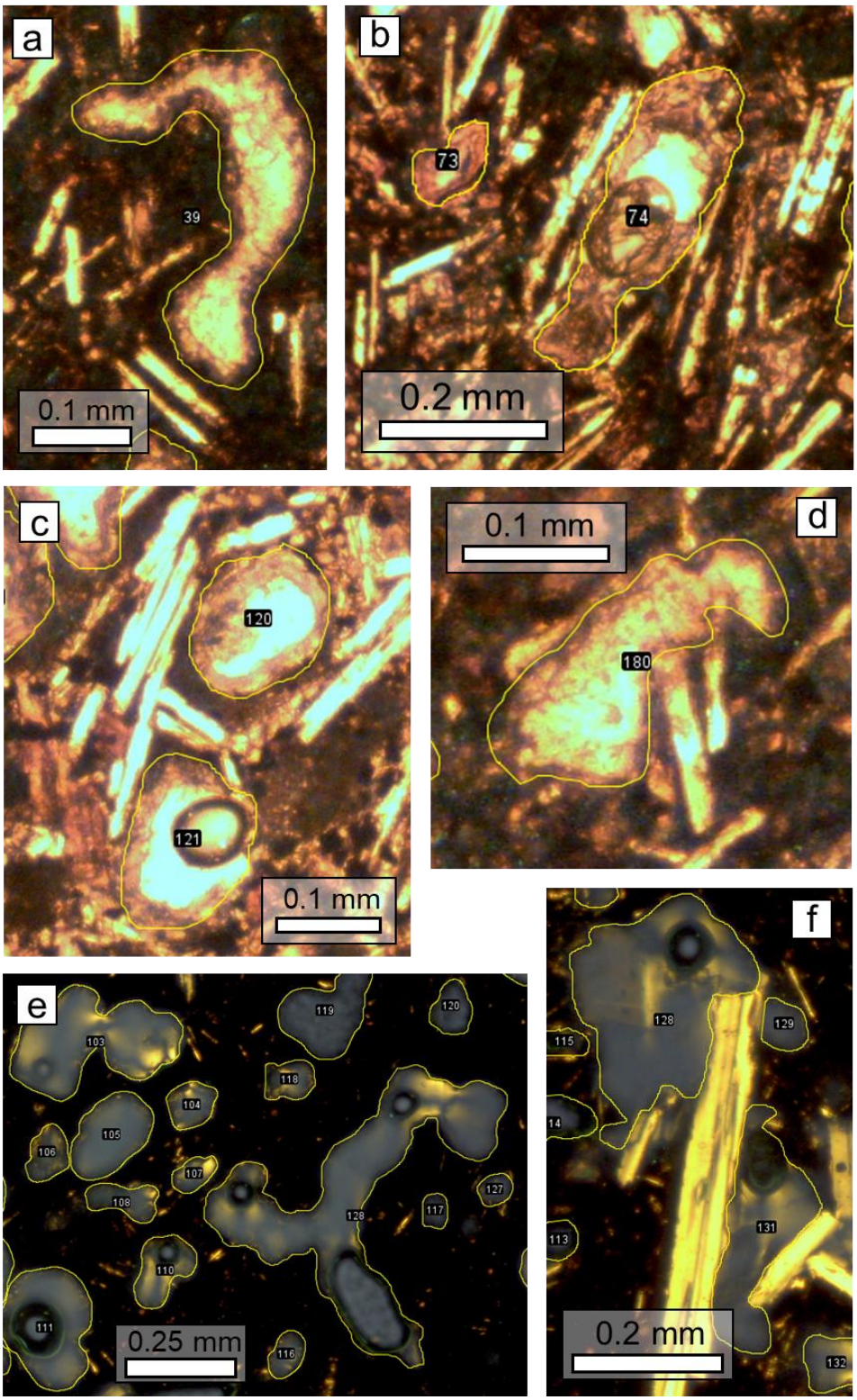

Figure 4.16. Examples of vesicles within the Teno and CRB samples. Teno: a) vesicle showing evidence of coalescence; b and c) vesicle shape and orientation determined by the orientation of surrounding phenocrysts; d) vesicle enveloping ends of phenocrysts. CRB: e) highly irregular vesicle shapes in the first band of the CRB sample caused by coalescence; f) vesicle shapes influenced by neighbouring phenocrysts (note that these are rounded, magmatic vesicles, as opposed to the small, angular, diktytaxitic voids that were found using the SEM, which are a separate population.

Crucially, the relationship between phenocrysts and vesicles in the Teno sample allows us to infer the order of events associated with band formation. The phenocryst textures are established first, resulting from flow differentiation, which is in accordance with our conceptual framework of a magma pulse arriving and filling a crack at the tip of the dyke. The phenocryst gradients are then fixed in place by rapid cooling, which stalls the propagation temporarily. As the stagnant magma in the crack cools over tens of minutes (to temperatures lower than 800 °C but no lower than 278 °C), pressures build up, until a critical fracture pressure is attained and a new fracture forms through the centre of the stalled dyke tip and into the host rock beyond. A pressure drop of up to 10 MPa causes rapid vesicle growth within the stalled magma, which is on the brink of solidifying. Indeed, the margin-side is likely entirely solid, which is why the largest vesicles are captured towards the dyke-centre-side of each band. Bubbles grow within a rigid network of phenocrysts. Finally, as magma intrudes the newly-formed fracture, pressures are restored and bubbles shrink, leading to a reduction in vesicle size at the start of the next band.

4.6.7 Band formation model

We now refine the conceptual framework presented in Section 4.6.1 into a band formation model, based on the analysis presented in Sections 4.6.2-4.6.6. Our model has the following steps:

1. A magma pulse with a tapering geometry propagates through the host rock
2. The narrow tip solidifies rapidly, stalling propagation by creating a blockage at the crack tip
3. Pressure builds behind the blockage until it ruptures
4. A fresh pulse of magma causes the dyke to propagate a step further.

This is a cyclical process, resulting in the progressive accumulation of bands at any fixed point of observation along the dyke (Figure 4.17). Pulsatory magma flow drives episodes of flow differentiation, leading to gradients in phenocryst concentration within each band. The fluctuations in pressure associated with blockages developing and new cracks forming results in a cyclic variation in vesicularity. There is no textural evidence of thermal erosion between bands, or of glassy margins developing, suggesting that the interval between magma pulses is tens of minutes in duration. This must be roughly constant in order to produce a consistent banding pattern at any position along the dyke. The increase in band width reflects the tapering geometry of the dyke tip, with the wider, inner bands having formed furthest from the crack tip, where a greater width of molten material is available for solidification. The loss of textural distinction towards the dyke centre also reflects the increasing distance to the crack tip, as fluctuations in pressure and flow rate are felt less strongly. Eventually, the dyke tip is far enough from the point of observation that pulses cannot fully solidify before the next pulse arrives, which leads to pulses mingling, and so no more bands are recorded. This is why we only see these bands at dyke margins.

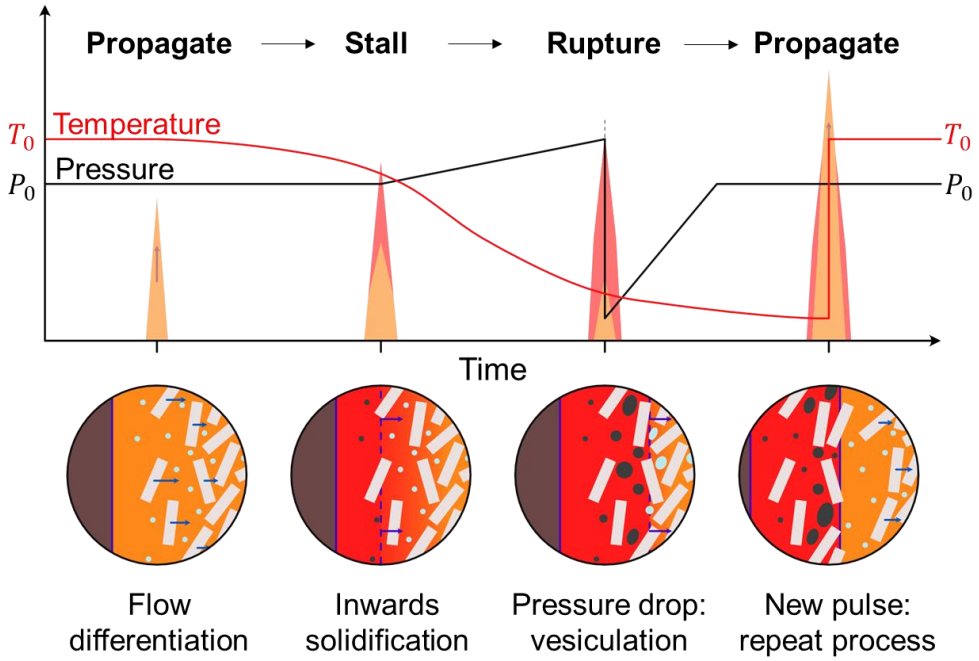

Figure 4.17. Model for band formation. Each band is a pulse of magma which caused the dyke to propagate another step. Each pulse experienced flow differentiation, before cooling and solidifying, capturing the phenocryst gradient. Pressure builds until the dyke tip ruptures, leading to a pressure drop and vesiculation. Propagation resumes with a fresh pulse of magma through the dyke tip.

4.7. Implications

4.7.1 Numerical propagation models

The marginal bands reveal the crucial role of cooling and solidification within the narrow dyke tip, with implications for the efficiency with which magma imparts pressure on the host rock and instigates fracturing. The bands also provide evidence for the geometry of the dyke tip. Both of these inferences are of relevance to numerical dyke propagation models, which forecast the likely pathways for magma ascent.

Generally speaking, dyke propagation models fall into two categories: those in which propagation is limited by fracture toughness, and those in which propagation is limited by viscous resistance (Rivalta et al., 2015). Propagation is initiated when the stress intensity at the dyke tip exceeds the fracture toughness of the host rock (see equations in Section 4.6.4). Models operate in the framework of LEFM, and so dykes are required to have a tapering point to instigate fracturing and support propagation (e.g., Lister and Kerr, 1991). Once the geometry and internal pressure of the crack combine to exceed the fracture toughness of the host, propagation will continue until the dyke enters a material with a higher fracture toughness, or due to viscous resistance within the magma, depending on the model type.

Solidification is almost always neglected in numerical and theoretical models (e.g., Maccaferri et al., 2010; Kavanagh et al., 2006). This is typically justified by comparing the rate of dyke propagation to

the rate of solidification. Propagation rates inferred from seismicity are around 1-2 km/hr (e.g., Einarsson and Brandsdóttir, 1980; White et al., 2011), whereas solidification rates are estimated to be a few days for a molten slab a few metres in width (Rivalta et al., 2015). The argument is that dykes are sufficiently wide that they can travel long distances before their centres solidify, and as such, solidification plays an insignificant role in mediating their progress.

However, our analysis suggests that this argument is ill-posed. Propagation models require dykes to have a tapering tip, and this narrow tip region will be vulnerable to rapid cooling, within several to tens of minutes (Section 4.6.3). Dyke tips seen in the field can be only a few centimetres wide (Figure 4.13), suggesting that the leading edge of any intrusion will be highly susceptible to the effects of cooling. Using the width of solidified dykes is misleading, as they have inflated to this size during their emplacement. Their molten interior must always have been narrower than their final, solidified width, and all dykes must start as narrow cracks. At the dyke tip, we should expect cooling to influence propagation.

Even if the main body of the dyke remains molten, propagation may be stalled by solidification in the dyke tip. This is because the fluid pressures required for host rock fracturing can only be transmitted by molten magma. Once the narrow tip region solidifies, these fluid pressures are imparted on the freshly solidified region instead, which must be repeatedly re-fractured in order for propagation to continue. We conclude that solidification can stall propagation at least temporarily, and we revisit the concept of thermal instabilities and feedbacks in Chapter 5.

The repeated cooling and re-fracturing of the dyke tip also has implications for the nature of host rock fracturing. Fracture toughness is considered to be an intrinsic material property. However, if the connection between fluid pressure and host rock is repeatedly interrupted by the formation of solid or stagnant magma at the point where fractures are instigated, the efficiency with which a dyke can continue to propagate depends not only on the host rock properties, but on the rate of heat loss in the narrow tip region. The physical properties of the host rock, the shape of the magma-filled crack, and the effects of cooling are likely to be interrelated, leading to complex propagation dynamics.

4.7.2 Experimental and field analogues

Analogue models for dyke propagation typically use isothermal fluids injected into gelatin, leading to continuous propagation (e.g., Menand and Tait, 2002; Kavanagh et al., 2018). However, in cases where solidifying fluids are injected, propagation becomes pulsatory. For example, an analogue dyke using paraffin wax was observed to propagate in bursts due to solidification reducing the stress intensity at its tip, which temporarily stalled propagation until the solidified area refractured (Taisne and Tait, 2011). The paraffin wax dyke propagated via a cycle of stalling, inflating, then rupturing, following the same steps that we have inferred from the marginal band textures.

Pulsatory flow has been shown to develop in other flowing fluids undergoing solidification. For example, the pressure-driven flow of syrup through chilled tubes becomes pulsatory due to the balance between cooling, viscosity and local pressures, leading to unstable flow even with a fixed driving pressure (Whitehead and Helfrich, 1991). Pulsatory flow can therefore develop even in the absence of complete solidification, due to the temperature dependence of viscosity.

We also consider pulsatory dyke propagation to be analogous to the emplacement of pahoehoe lava lobes. These propagate via cyclical rupturing, cooling, stalling and inflation (Hon et al., 1994). Lava flows lose heat much more rapidly than dykes, as they cool dominantly via radiation rather than conduction. However, the same thermal instabilities may be expected to occur in both settings, on different lengthscales and timescales. This concept will be revisited in the context of the larger dyke system in Chapter 5.

4.7.3 Dyke propagation inferred from seismicity

The concept of pulsatory dyke propagation is not a new idea. Dyke emplacement is commonly monitored through the migration of seismicity, with volcano-tectonic earthquakes interpreted to originate around the leading edge of the propagating dyke (Einarsson and Brandsdóttir, 1980; White et al., 2011; Woods et al., 2019). Using this method, dyke propagation is observed to happen in bursts at timescales of hours to days, showing that magma transport is not a continuous process, and that it can occur in pulses.

Common interpretations for pulsatory dyke emplacement observed through seismicity include the dyke encountering changes in host rock properties, interacting with faults, experiencing stress changes related to surface topography, or experiencing variations in pressure from the magma source (Rivalta et al., 2015). Examples include the temporary stalling of a dyke ascending beneath Piton de la Fournaise, interpreted to result from a lithological discontinuity (Battaglia et al., 2005), and bursts of dyke propagation in Iceland that have been interpreted to result from caldera subsidence changing magma pressures at the source (Sigmundsson et al., 2015).

Other examples of pulsatory propagation have been attributed to the effects of cooling and solidification. The migration of earthquake foci during the Bárðarbunga–Holuhraun rifting event showed rapid lateral growth interspersed by periods of stalling that lasted hours to days, during which time the earthquake foci moved backwards from the inferred dyke tip, which was inferred to be a result of inflation. The stalling was attributed to changes in topography, host rock properties or source pressure, but with the effects amplified by solidification around the dyke edges (Woods et al., 2019). Other examples of pulsatory propagation have been attributed entirely to solidification and refracturing (Hayashi and Morita, 2003; White et al., 2011).

We note that the dyke propagation pulses observed through seismicity occur on a much larger scale than the pulses we infer from the marginal bands. Temporary halts in propagation last hours or days,

whereas our thermal modelling suggests that the magma pulses forming the bands occur at a scale of tens of minutes (Section 4.6.3). Additionally, these large-scale bursts are related to the unique emplacement history of each dyke, whereas the marginal bands show the same pattern in every setting and must therefore share a ubiquitous formation process. The large bursts in propagation, detected from seismicity, are more likely to form the large-scale textural layers discussed in Section 4.2.2. By contrast, the marginal bands are a product of smaller-scale dyke-tip process driven by cooling effects, which are present in every dyke.

However, our model for pulsatory dyke propagation is consistent with seismic data, in that it provides more evidence for the discrete nature of host rock fracturing and dyke advance. Even when "smooth" dyke propagation is inferred from seismicity, each of the earthquakes around the dyke tip has resulted from a discrete fracturing event. As discussed in Section 4.6.2 regarding band widths, the 2D presentation of our cyclic model is idealised, because in 3D, the dyke tip will consist of discrete segments experiencing complex, dynamic interactions. The leading edge of the dyke will advance through a series of small, repetitive bursts, but their individual signals will be concealed in the noise arising from neighbouring sections, as well as by larger-scale pulses transiting the system.

4.7.4 Relation to dyke arrest or eruption onset

The marginal bands demonstrate that magma flow is impacted by solidification in the narrow dyke tip. We have estimated that the dyke tip may stall for tens of minutes due to solidification; however, it is worth considering the conditions that would be required to stall magma for longer (e.g., low magma flux into the tip, or a highly resistant host rock). The relationships between magma temperature, viscosity and advection rates lead to positive feedback, whereby small-scale perturbations have the potential to cascade into larger events that could impact the main dyke body. It is feasible that some large-scale layering within dykes could arise from thermal feedbacks, such as centimetre- to metre-scale layering marked by internal chilled margins (e.g., Platten, 2000) or differences in columnar jointing structure (e.g., Gudmundsson, 1984; Ray et al., 2007; Das and Mallik, 2020). We will explore the effects of thermal feedbacks on the larger dyke system in Chapter 5, in the context of dyke architecture.

Finally, we note that marginal bands are not found on all dykes, despite us stating that cooling effects are ubiquitous to narrow dyke tips. There are several reasons that bands may not form. Firstly, bands defined by a variation in vesicularity are more likely in magma with a high volatile content, or at shallower depths, which increase the sensitivity to pressure drops (Section 4.6.4). If pressure fluctuations are occurring above the saturation pressure of the magma, there will be no bubble nucleation and growth to capture as vesicles. Similarly, gradients in phenocryst concentration will only form when conditions are suited to flow differentiation, which requires a high volume fraction of phenocrysts of an appropriate size relative to the width of the dyke tip (Section 4.6.5). Finally, it is

likely that bands which form in areas that become long-lived preferential flow pathways may be removed by thermal erosion due to the effects of advection. For the same reason, we would not expect bands in the shallow subsurface immediately below a volcanic vent.

4.8. Conclusion

Marginal bands are a common feature of basaltic dykes in a range of volcanic settings. They may be defined by a variation in the concentration of phenocrysts and/or vesicularity, but in all cases they show a trend of getting wider and less distinct towards the dyke centre. We have interpreted variations in phenocryst concentration to be a product of flow differentiation, whereas variations in vesicularity record fluctuating pressures. Both textures are indicative of pulsatory flow through the dyke tip, implying that dyke propagation is pulsatory. Based on our estimates of cooling times, these pulses occur on timescales of tens of minutes.

Dyke margins are the earliest material to solidify, and therefore originate in the tip of the dyke, making them incredibly valuable for interpreting dyke tip processes. The most likely cause for pulsatory flow is cyclical cooling, stalling and refracturing, which is ubiquitous to all cases of migrating, cooling fluids with a temperature dependent viscosity. The increase in band width is explained by an increasing distance to the dyke tip at the point of observation, which provides evidence for the dyke tip being tapered in form. The narrow dyke tip is highly prone to cooling and thermal feedbacks, which has implications for numerical models handling fracture propagation. Our analysis does not put any particular constraints on the conditions required for pulsatory propagation, and we conclude that it is generally applicable to batches of migrating, cooling fluids, especially impacting those with a narrow leading edge.

This chapter has focussed exclusively on the dyke tip region, where thermal feedbacks operate on relatively small scales. In the next chapter, we expand our investigation to the wider dyke system, and consider the broader impacts of cooling and unsteady flow on dyke architecture, and the development of long-lived preferential flow pathways.

Chapter 5

Relating small-scale dyke textures to large-scale segmentation patterns reveals complex nature of dyke emplacement

---

Aims of this chapter:

Having explored the development of crystal and vesicle textures using analogue experiments, and having interpreted small-scale textures at dyke margins as evidence of pulsatory propagation, we now interpret dyke textures in the context of large-scale dyke morphology, to develop a broader picture of dyke emplacement. Segmentation patterns and internal textural zoning suggest that flow within dykes is constantly localising through thermal feedback processes, leading to the creation of a complex network, broadly planar in shape, with stable conduits and failed branches, analogous to a long-lived lava flow field. We produce a conceptual model for dyke emplacement, in the context of dyke architecture seen in the field and seismic evidence produced during active dyke emplacement.

5.1. Introduction

The textures of crystals and vesicles within dykes record flow conditions, and may be read as a time-series from margins to centre. The margins of a dyke form in the earliest stages of emplacement, and in Chapter 4, we interpreted banded marginal textures as evidence of pulsatory propagation. We now analyse textures within the interiors of dykes, and relate these textures to their position within the dyke and to the geometry of the dyke itself, in order to gain a deeper understanding of flow patterns within the dyke system. Analysing textures from margins to centre reveals how conditions varied throughout dyke emplacement, from initial propagation to the cessation of flow. By examining these textural time series at multiple points along the lengths of dyke segments, we infer the flow history of the larger system and build a conceptual model of dyke emplacement.

In this chapter we focus on dykes in the Teno Massif, northwest Tenerife. This region contains hundreds of exposed basaltic dykes, and provides an excellent opportunity to investigate their textures in relation to their geometry. The aim of this chapter is to understand the links between small-scale dyke textures and larger-scale layering and geometry, in order to understand the processes driving changes in magma flow within the dyke system. This allows us to create a new, conceptual model of dyke emplacement, which will provide context to support the interpretation of seismic signals during dyke propagation, and to inform numerical and analogue models.

5.2. Background

5.2.1 Teno Massif stratigraphy

The Teno massif in northwest Tenerife is the deeply eroded remains of a basaltic shield volcano. Ridges of over 1300 m elevation are interspersed by deep valleys with cliffs a few hundred metres tall, which provide the opportunity to study dykes along their lateral and vertical extents. The Teno volcano was constructed between 6.3 and 5.1 Ma (Leonhardt and Soffel, 2006), when the region contained three separate volcanic islands. These now comprise the three corners of Tenerife: the Teno and Anaga massifs in the northwest and northeast respectively, and the Roque del Conde in the south (Ancochea et al., 1990).

The oldest rocks in the Teno region are a series of thin, layered pahoehoe lavas and basaltic pyroclastics, which are exposed on the southwest and northern coastlines (Guillou et al., 2004). These rocks are named the “Masca Formation”, and they are separated from the rocks above by an angular unconformity that marks a giant landslide event known as the “Masca Collapse” (Walter and Schmincke, 2002). This unconformity defines a horseshoe-shaped trough opening to the northeast. Above it lies a series of sub-horizontal lava flows known as the “Carrizales Formation”, which are then truncated by a second angular unconformity dipping to the northeast, marking a giant landslide

known as the "Carrizales Collapse" (Walter and Schmincke, 2002; Leonhardt and Soffel, 2006). Above this lies another series of sub-horizontal lava flows known as the "El Palmar Formation", and these are overlain by a series of thin pahoehoe lavas known as the "Los Gigantes Formation", likely erupted after a period of erosion or a hiatus in activity (Guillou et al., 2004; Leonhardt and Soffel, 2006).

5.2.2 Field location

Fieldwork took place along the ridge south of the villages of Los Carrizales (Figure 5.1). The eastern end of the ridge contains the "Masca Collapse" unconformity, seen most easily where the southwest-dipping rocks of the ridge contact the thick, sub-horizontal lava flows that form the bulk of the region (Figure 5.2). However, the bedrock of the ridge is unlike anything previously ascribed to the Masca Formation. Rather than the thinly layered pahoehoe flows and basaltic pyroclastics described by previous authors (Walter and Schmincke, 2002; Guillou et al., 2004; Leonhardt and Soffel, 2006), the Carrizales Ridge consists of beds of rounded to sub-angular volcaniclastic material, ranging in size from pebbles up to rounded boulders 40 cm in width. This material can be found along the length of the ridge, and appears to be present in the valley slopes on either side, suggesting that the volcaniclastic deposit is a few hundred metres thick, with a lateral extent of at least 1-2 km^2.

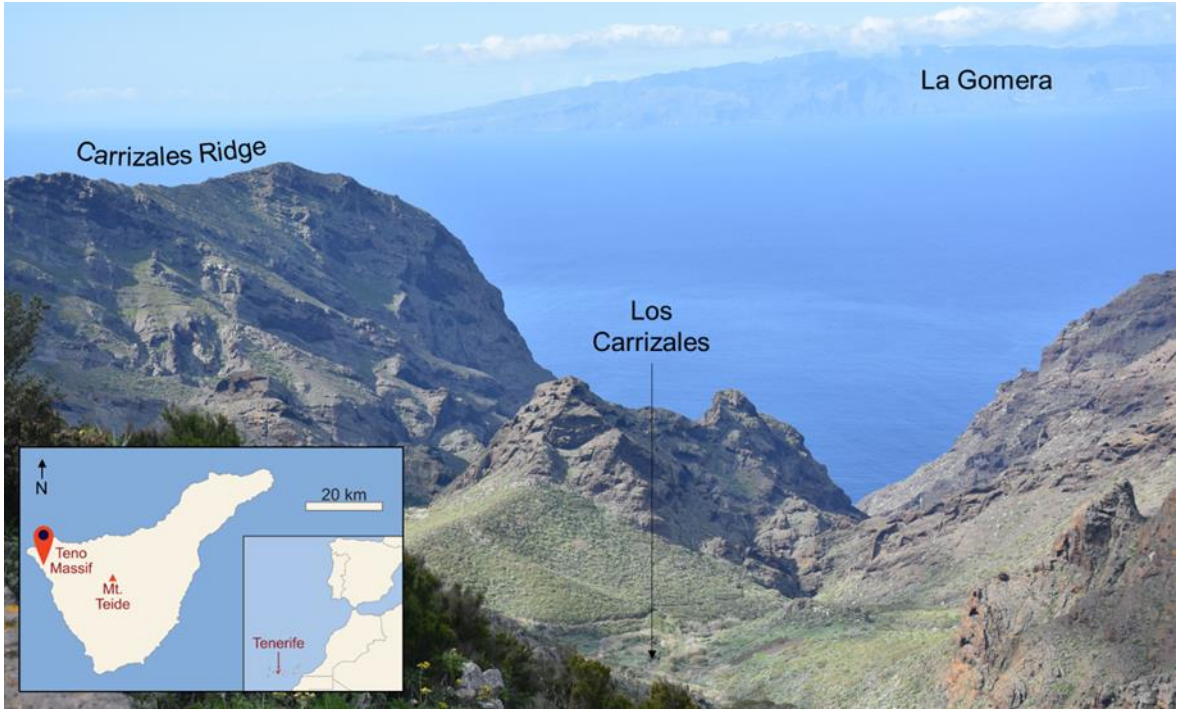

Figure 5.1. View of the Carrizales Ridge, looking southwest towards La Gomera. The ridge is ~700 m above sea level. Inset shows the location of the Teno Massif in NW Tenerife, and the position of Tenerife to the west of north Africa.

The volcaniclastic rocks of the Carrizales Ridge are likely to be part of the Masca Formation, as they exist beneath the Masca Collapse (Figure 5.2); however, their presence has not been documented in the most recent stratigraphies (Walter and Schmincke, 2002; Guillou et al., 2004; Leonhardt and Soffel, 2006). Only a brief mention of volcanic breccias in the lower part of the series is made in earlier works, where it is noted that the origin of these rocks is uncertain (Ancochea et al., 1990). However, the volcaniclastic material on the Carrizales Ridge is similar to descriptions of volcanic breccias on the neighbouring island of La Gomera, where breccias exist within layered pahoehoe flows dipping towards the sea. These breccias can be over 100 m thick, sometimes seen to fill basins or channels (Ancochea et al., 2006). They lie within the oldest part of the edifice, and are taken by Ancochea et al. (2006) to represent landslides, ranging from small and frequent episodes, to giant, destructive events, depending on the thickness of the breccia layer.

The Carrizales Ridge also differs from the surrounding massif due to the strike of its dykes. The main trend of the Teno dyke swarm is generally NW/SE, or N/S south of Masca (Féraud et al., 1985; Walter and Schmincke, 2002). However, many dykes along the ridge strike NE/SW (Figure 5.3), perpendicular to the main swarm. Only a few of these dykes are seen to intersect the Carrizales Formation at the eastern end of the ridge, suggesting that most were truncated by the Masca Collapse, and therefore predate it (Figure 5.2). As such, their intrusion depth cannot be inferred from stratigraphy, as they would have been within the original edifice before it collapsed. No dykes on the ridge are observed to connect to lava flows. However, we infer that these dykes were emplaced at relatively shallow depths, perhaps tens to hundreds of metres beneath the surface, due to the presence of vesicles implying volatile exsolution, and due to the irregular form of the margins, suggesting that the host rock was poorly consolidated when the dykes intruded.

Figure 5.2. View looking northwest from the Carrizales Ridge. The layers of pahoehoe lava and volcaniclastic deposits dipping towards the sea are part of the Masca Formation, but the bulk of the region is comprised of the sub-horizontal lava flows of the Carrizales Formation. These are separated by the Masca Collapse unconformity.

5.2.3 The three main dykes

Three dykes on the ridge were studied in detail (Figure 5.3):

- D1: A 1-m-thick composite dyke containing three layers, the outermost of which shows marginal banding. The intermediate layer contains several planes of large, flattened vesicles running parallel to the margin. The core is non-vesicular and porphyritic, with euhedral clinopyroxene phenocrysts 2-8 mm in diameter.
- D2: A 0.5-m-thick dyke with chilled margins and distinctive cooling joints. It has a uniform composition, but contains cm-scale sub-layers of varying plagioclase phenocryst content.
- D3: A 0.6-m-thick dyke with banded margins and a highly vesicular core. The vesicles are typically elongated, indicating the direction of magma flow.

Other dykes with interesting features will also be discussed, but these could not be followed for significant distances along their length. Although they are useful as supporting evidence for dyke flow processes, their limited extent means they cannot provide a bigger picture of evolving flow patterns within the dyke system.

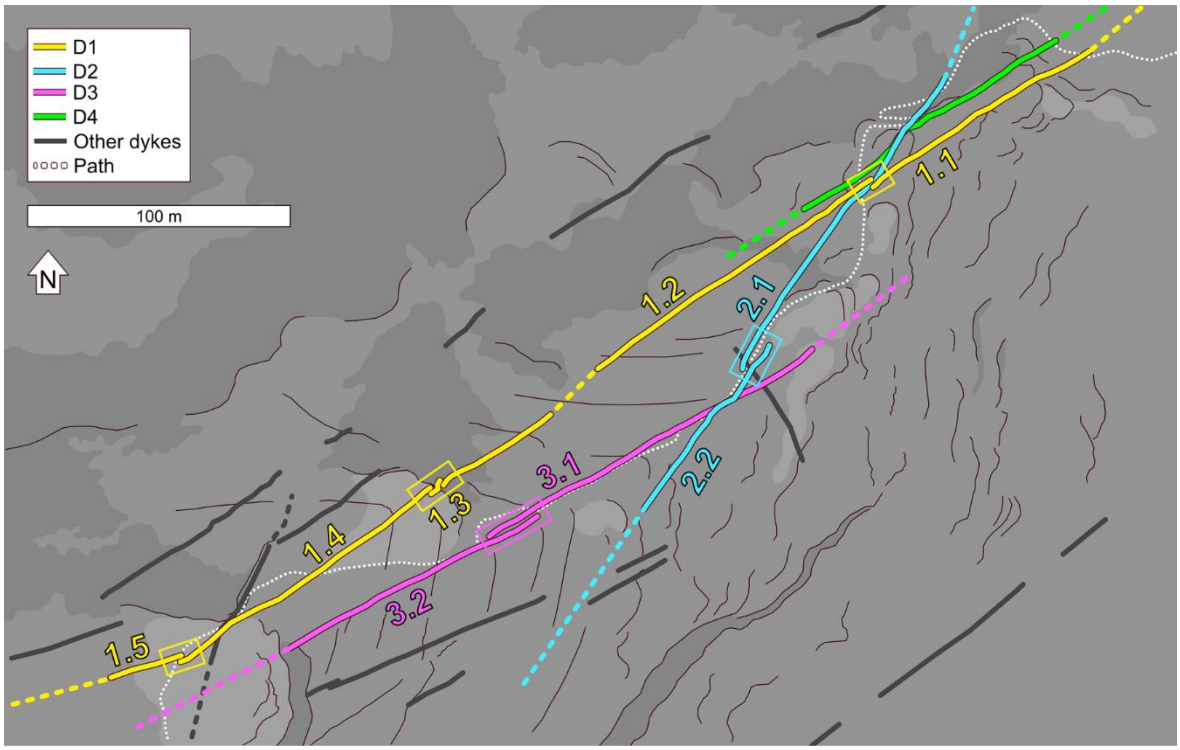

Figure 5.3. Map of the major dykes along the Carrizales Ridge. Relays between dyke segments are outlined in boxes, and segments are numbered. The path along the ridge is shown by a white, dashed line. Shading indicates gradient, with darker colours showing cliffs.

5.3. Methods

5.3.1 Data collection

To relate dyke textures to dyke geometry, we collected data at a range of scales. At the largest scale, dykes were followed along their length, taking measurements of their width, dip, strike, and the widths of their layers. At the macroscopic scale, photos were taken of phenocryst and vesicle textures visible by eye. These photographs were then analysed in ImageJ to quantify the variation in phenocryst and vesicle size, shape and orientation across the width and along the length of the dykes. At the microscopic scale, oriented samples were collected from the dykes, in a line from margin to centre where possible. Thin sections were cut on three orthogonal planes, allowing phenocrysts, microlites and vesicles to be imaged under the microscope and outlined manually in ImageJ, and allowing the true 3D preferred orientation of the crystal population to be calculated. From here onwards, the following names are used for the three orthogonal planes (Figure 5.4):

- Vertical plane – the vertical plane perpendicular to the dyke margin
- Horizontal plane – the horizontal plane perpendicular to the dyke margin
- Parallel plane – the plane parallel to the dyke margin.

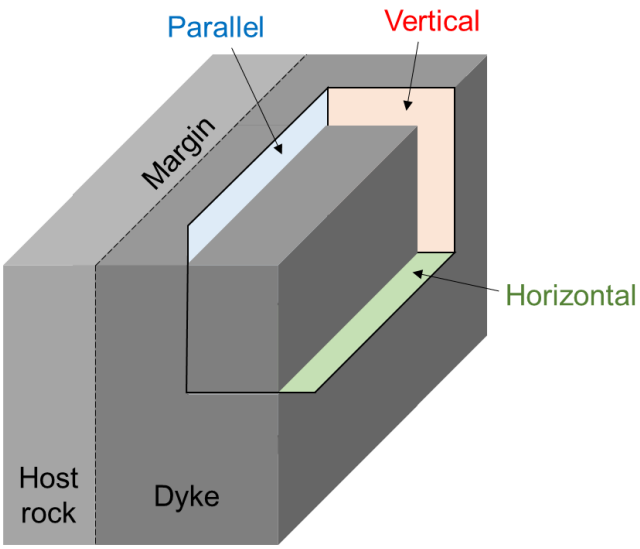

Figure 5.4. Schematic cartoon illustrating three orthogonal planes within the dyke: vertical plane perpendicular to dyke margin, horizontal plane perpendicular to dyke margin, and parallel plane parallel to dyke margin.

5.3.2 Image analysis

Photos and thin section images were analysed in ImageJ (Schindelin et al., 2012). Phenocrysts and vesicles were outlined by hand, and then their 2D area, shape and orientation were measured. ImageJ approximates each shape with a best-fit ellipse, from which it measures the lengths of the major and minor axes, which are used to calculate an aspect ratio (major/minor). Phenocrysts and vesicles can have very irregular shapes (for example, clinopyroxene phenocrysts have cross-sections ranging from triangles to octagons, and vesicles are often coalesced and deformed) and the best-fit ellipse is a robust, repeatable approximation for shape and orientation. The orientations presented here are the orientations of the ellipse major axes, and these values are corrected so that orientations are given relative to the strike of the dyke and its layers.

5.3.3 Terminology

The following terms are used when describing dyke geometry:

- *Segment*: a discrete section along the length the dyke, separated from neighbouring sections by host rock or a chilled margin. Segments are sometimes offset, but they are always sufficiently aligned to indicate that they are part of the same, larger feature, and they contain the same textures and layering.
- *Relay*: the zone on the surface where one segment ends and another begins. Typically, there is some overlap where the segments run parallel, sometimes for several metres.
- *Offshoot*: a narrower section clearly connecting back to a larger dyke. Sometimes, offshoots may also be segmented.
- *Layer*: a textural zone defined by any sharp change across the width of a dyke, such as a chilled margin or a change in composition. These are typically centimetres to metres in width, and are inferred to be the product of distinct magma injection episodes.
- *Sub-layer*: a textural zone defined by a change in phenocryst size, type, or concentration, or a change in vesicularity, without a chilled margin or significant change in composition. By this definition, the marginal bands in Chapter 4 are sub-layers. These are small features, millimetres to centimetres wide, and they are inferred to result from perturbations within the same magma injection episode. We will explore the distinction between layers and sub-layers further in the discussion.

5.4. Results

5.4.1 D1

D1 runs down the centre of the Carrizales Ridge and can be traced for 1500 m, giving it the greatest exposed extent of all the dykes studied (Figure 5.3). Its strike is generally ~060°, and although it is typically vertical, it can dip either north or south locally. It has a consistent width of around one metre, and contains three main layers (Figures 5.5, 5.6 and 5.7): an outer layer with a mean width of 12 cm showing marginal banding; an intermediate layer with a mean width of 12 cm containing planes of large, flattened vesicles; and a central layer with a mean width of 44 cm containing clinopyroxene phenocrysts 2-8 mm in diameter.

D1 segmentation and offshoots

D1 is split into five apparent segments of varying length (Figure 5.3). The shortest (1.3) has a lateral extent of < 10 m, while the longest (1.2) is around 200 m, although parts of this are inaccessible and may contain additional relays. Of the four relays seen, two are on gentle, SW-facing slopes (1.3-1.4 and 1.4-1.5; Figure 5.8), one is on a steep, SW-facing slope (1.1-1.2), and one is on a vertical, NE-facing cliff (1.2-1.3; Figure 5.9). The segments start tapering to narrow points around 3 m from their terminations (Figure 5.8). Within relay zones, segments can run parallel for up to 5 m, either directly in contact (1.3-1.4; Figure 5.8) or separated by a screen of host rock up to 50 cm wide (1.1-1.2, 1.2-1.3; Figure 5.9).

Offshoots are not common along D1. An offshoot near the southern end of 1.3 is around 1 m long and 6 cm wide, tapering to a point (Figure 5.8), and the northern end of 1.2 has several offshoots, giving it a branching appearance in addition to tapering out. All the observed offshoots originate within the marginal layer and appear to share its composition. Additionally, marginal banding can be seen to continue from the outer layer into the offshoots.

D1 layering

Along most of its length, D1 is divided into three obvious layers. In every segment studied, the layers retain a consistent width and are symmetrical about the dyke centre. Even in heavily weathered sections, layer widths can be determined due to the differential weathering between them (e.g., Figure 5.5). However, towards segment tips, the definition of the layers is lost, most probably due to extensive weathering. At the relay between 1.3 and 1.4, the central layer of 1.3 appears to cut across its outer layers, creating a contact between the core of 1.3 and the outermost margin of 1.4 (Figure 5.8). The widths of the three layers were measured along the length of segment 1.4 at 5 m intervals, and at intervals of every metre for one relatively un-weathered 20 m stretch (Figure 5.6). These results are used to generate a 3D model of the dyke and its layers (Figure 5.10).

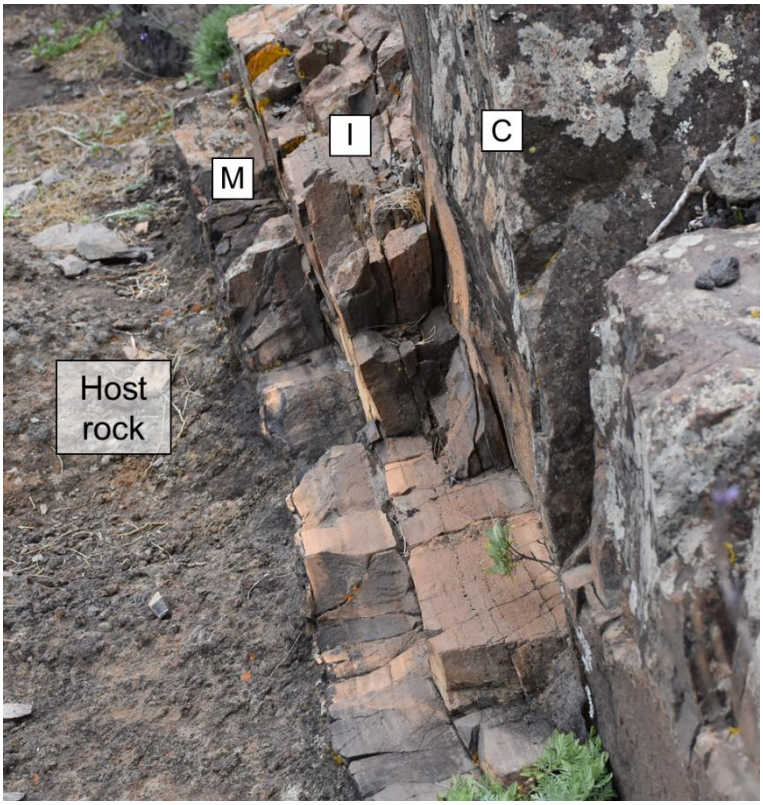

Figure 5.5. Layering within D1: M = margins, containing narrow bands defined by variations in colour and vesicularity (12 cm wide); I = intermediate, containing planes of highly vesicular material (12 cm wide); C = centre, ankaramite with large clinopyroxene phenocrysts and no vesicles.

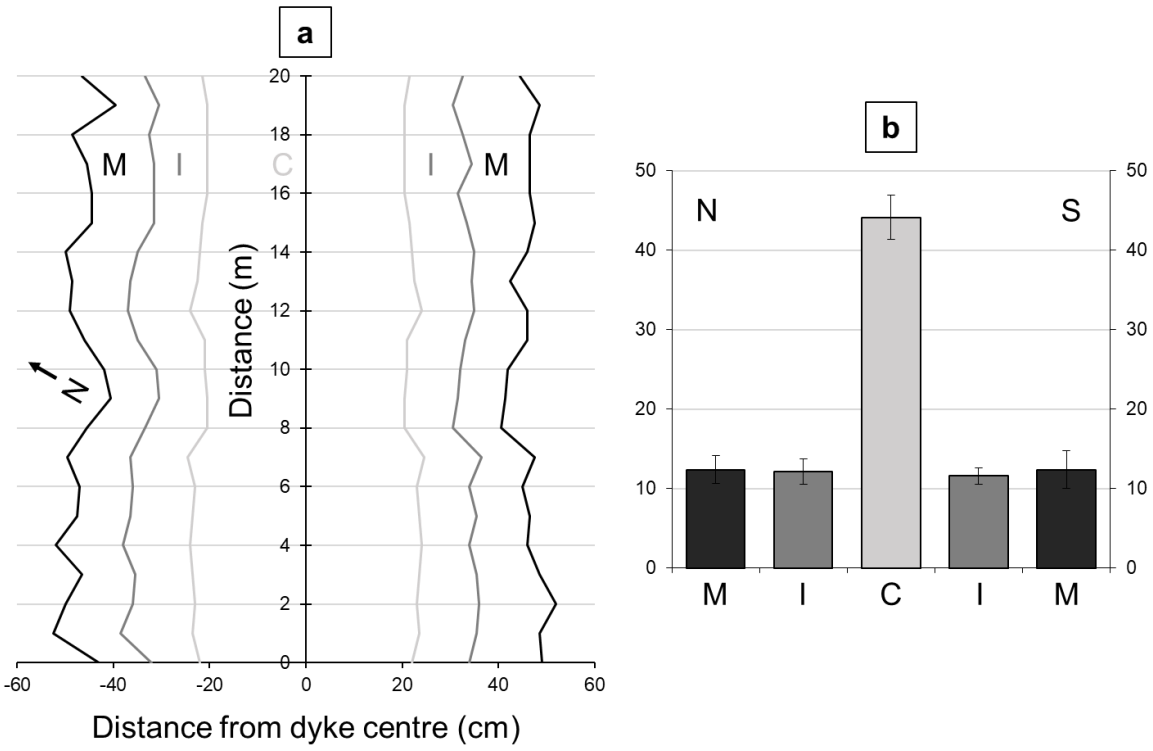

Figure 5.6. Widths of layers within D1, where C = centre, I = intermediate and M = margins: a) widths measured at 1 m intervals along the least weathered stretch of D1, with an arrow pointing north; b) average width of each layer along this distance, with the north and south sides labelled.

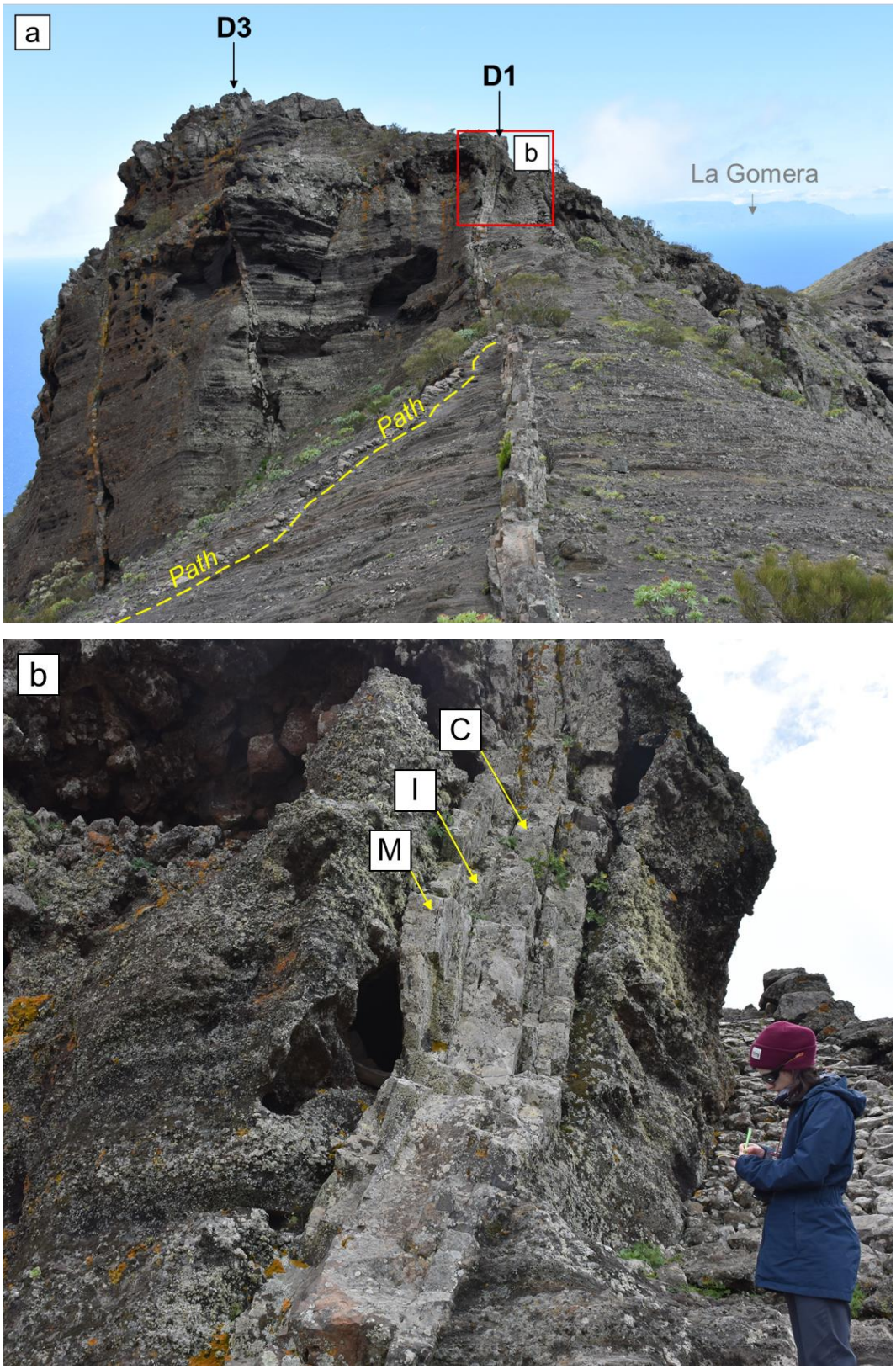

Figure 5.7. a) Segment 1.4 of D1, where the widths of each layer were measured at 1 m intervals. View is southwest, with La Gomera in the distance. D1 is approximately 1 m wide. b) Vertical section of D1, showing the three layers (M = margin, I = intermediate, C = centre).

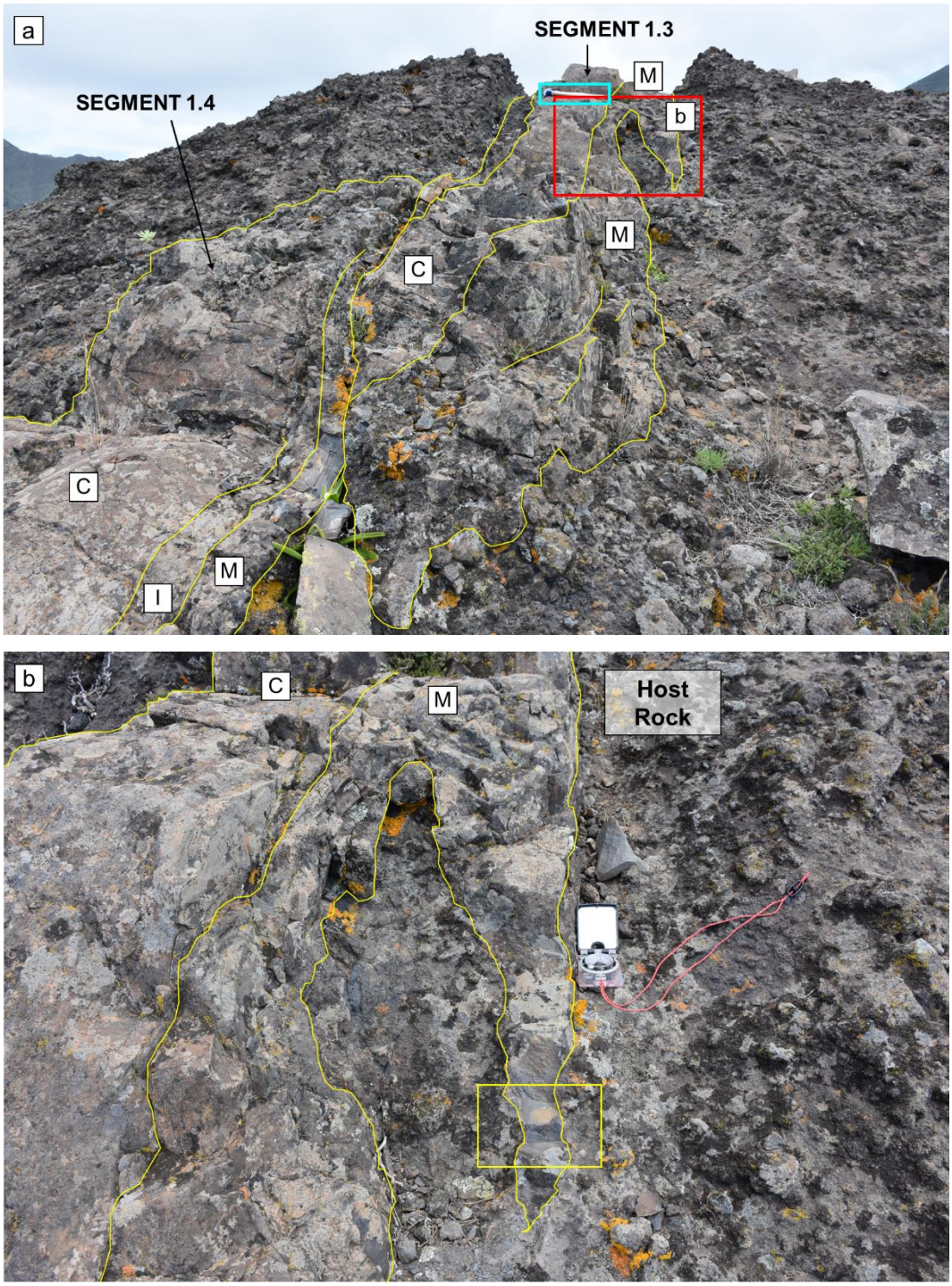

Figure 5.8. a) Relay between segment 1.3 and 1.4 on D1, facing northeast. Both segments are approximately 1 m wide, and the cyan box highlights a 33-cm-long hammer for scale. The central layer of segment 1.3 cuts through the outer layers to make contact with the margin of segment 1.4. b) A closer look at the offshoot from segment 1.3. The offshoot is the same composition as the marginal layer, and tapers to a point. A yellow box shows where a sample was taken.

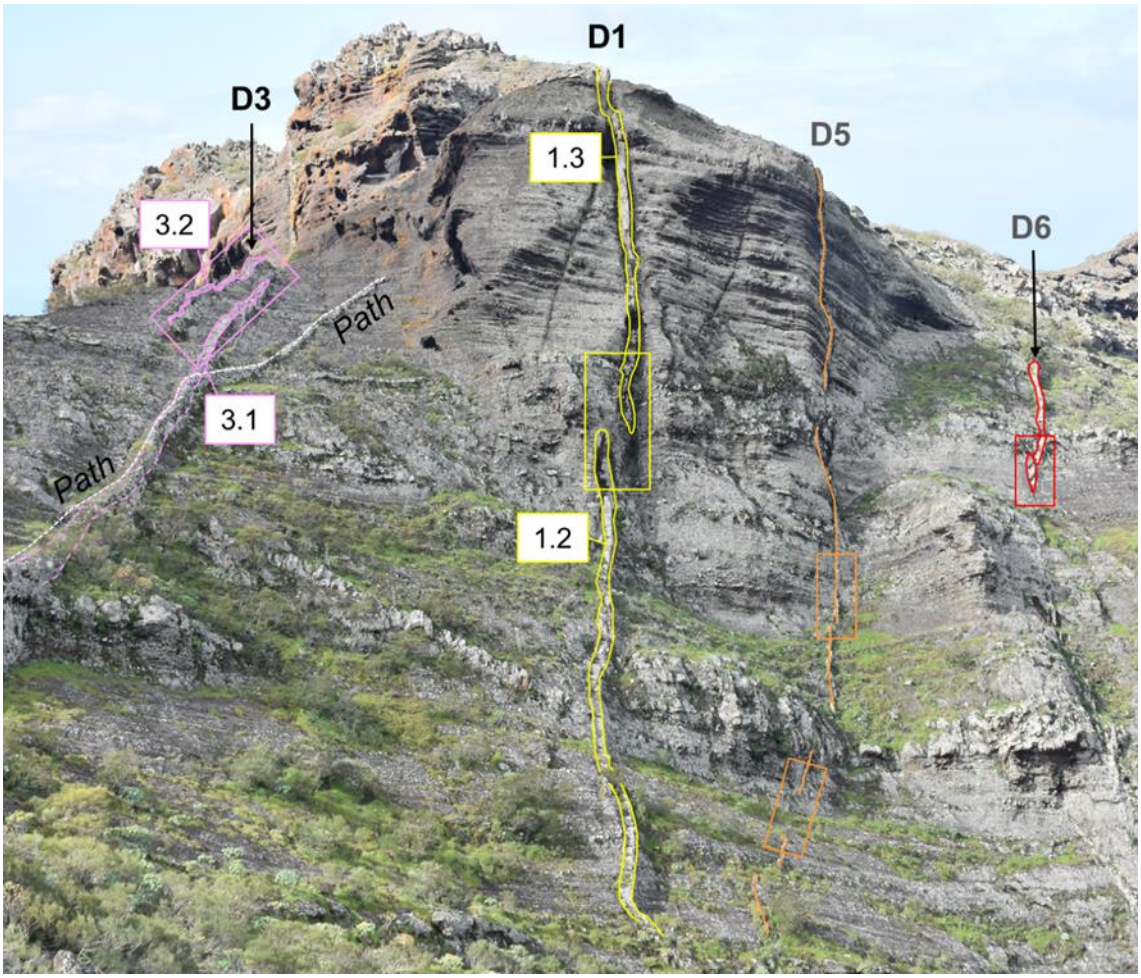

Figure 5.9. View southwest towards the vertical relay between segments 1.2 and 1.3 on D1, which is 1 m wide. The cliff also contains a relay between segments 3.1 and 3.2 on D3, as well as many other segments and relays on neighbouring dykes. D5 and D6 are only exposed for relatively short distances, so were not studied in so much detail, but they both show obvious segmentation.

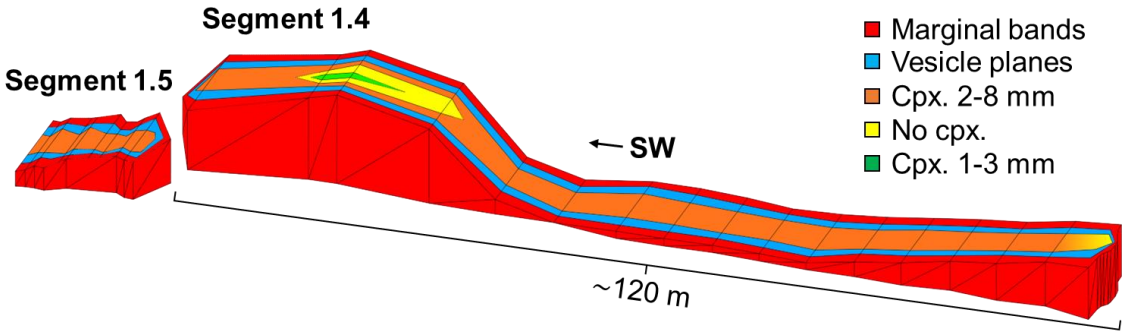

Figure 5.10. Reconstruction of segment 1.4 on D1, with dyke width and elevation change exaggerated by a factor of ten. Segment 1.4 is approximately 120 m long.

D1 macro-textural features

The three layers of D1 are defined not only by differential weathering, but by distinct textures. The outer layer contains marginal banding, characterised by a repetitive dark-to-light colour variation moving inwards from the margin, and the bands become wider and less distinct towards the dyke centre wherever they are seen along the length of the dyke. On less weathered sections, it is apparent that the colour variations are associated with a variation in vesicularity, as seen in previous examples of marginal bands (Chapter 4). The margins are wavy at a very local scale, bending around large clasts within the host rock by up to 5 cm. The outermost marginal bands follow these oscillations closely, but become progressively straighter and more uniform towards the dyke centre.

The intermediate layer of D1 is characterised by planes of large, flattened vesicles running parallel to the margins (Figure 5.11). There is no distinct contact between the outer and intermediate layers of the dyke, but they are typically split apart by differential weathering. In some places, the outer layer has cleaved from the intermediate layer, possibly down one of the planes of vesicles. By eye, the intermediate layer seems compositionally similar to the outer layer, in that the bulk material is fine-grained with a uniform distribution of vesicles < 1 mm in diameter. Towards the central side of the intermediate layer, these small vesicles are often elongated at an angle to the dyke margin. Their elongation is symmetrical around the dyke centre, forming a V-shape pointing southwest.

The vesicle planes of the intermediate layer are narrow regions 2-5 mm wide running parallel to the margin (Figure 5.11). The planes can be followed for a few metres on well-preserved surfaces, but can also be found to split or die out within tens of centimetres. The planes have sharply defined edges, and the largest vesicles are confined strictly within these bounds, giving them a flattened appearance. At the southwest end of segment 1.4, and in the northeast tip of 1.5, the vesicle planes contain clinopyroxene phenocrysts up to 4 mm in diameter, but these always reside solely within the boundaries of the plane, and do not protrude into the bulk material. On the freshest surfaces, the vesicle planes stand out as a different colour to the material either side (Figure 5.11b).

The contact between the intermediate and central layers is marked by a dark band, just over a millimetre wide, running in a straight line parallel with the dyke margin. Black, dendritic crystals grow inwards from this contact for around 10 mm, with some individual crystals reaching several millimetres in length. These dendritic crystals grow nearly perpendicular to the contact between the layers, but on horizontal surfaces they show a distinct inclination to the southwest.

The central layer of D1 typically contains clinopyroxene phenocrysts around 2-8 mm in diameter, except in the outermost 20 mm, which either lacks phenocrysts or contains very few, much smaller clinopyroxene crystals. Aside from this outermost region, however, phenocrysts are typically evenly dispersed across the central layer. Still, although this is the general rule, there is significant variation

in the size and concentration of clinopyroxene phenocrysts depending on elevation and lateral position. Segment 1.4 has the best exposure, and we studied its textures in detail.

At some locations along segment 1.4, the central layer can be further divided into sub-layers based on the size and abundance of clinopyroxene phenocrysts. At the southwest end of this segment, the central layer contains three sub-layers: an outer sub-layer containing 2-8 mm diameter phenocrysts, an intermediate sub-layer containing no phenocrysts, and a central sub-layer containing smaller, 2-4 mm diameter phenocrysts at a much lower concentration. There is no dendrite margin or clear contact separating the outermost central sub-layer from the intermediate layer. However, 10 m further northeast, the outermost sub-layer has larger clinopyroxene phenocrysts, with some that are over 20 mm long (Figure 5.12a). Just 5 m further east and 10 m lower (at Figure 5.7), the centre contains its typical, uniform distribution of phenocrysts, no sub-layering, and an obvious internal chilled margin with the intermediate layer.

Another intriguing variation in the central layer phenocrysts is found at the eastern tip of segment 1.4 (Figure 5.8a). Heading east, the size and concentration of phenocrysts gradually decreases, until 2 m from the segment tip, the central layer becomes entirely devoid of phenocrysts. This variation in phenocryst content and sub-layering is shown in Figure 5.10.

In the field, the clinopyroxene phenocrysts in the central layer did not appear to show any alignment or preferred orientation. However, analysis of crystal outlines in photos shows that nearly every site has a preferred orientation. The preferred orientations are generally at an angle to the dyke margin, and are mirrored around the centre of the dyke to form a V-shape. This V-shape is present at nearly all sites, with the systematic symmetry indicating that these orientations are likely to have developed due to magma flow. The so-called “imbrication” of crystals is often used to infer magma flow direction (Chapters 1 and 2), and in the case of D1, magma appears to have flowed southwest. The only site indicating a northeast flow direction is at the northern tip of segment 1.4, and further investigation would be required to determine if this trend is a highly localised phenomenon, and how far it persists moving SW.

The clinopyroxene phenocrysts are not the only textural feature pointing southwest in the centre of D1. The black, dendritic crystals at the contact between the intermediate and central layers also have a distinct lean to the southwest wherever they are seen on horizontal surfaces. These sorts of crystals are not common flow indicators within dykes, and they are discussed further in Section 5.5.5.

a)

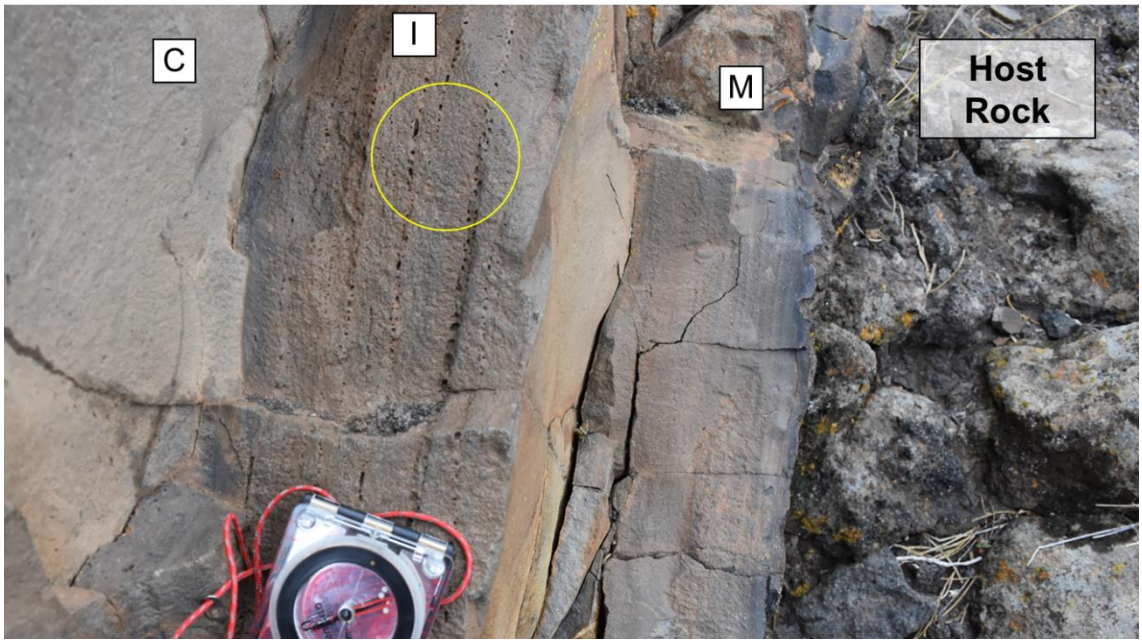

b)

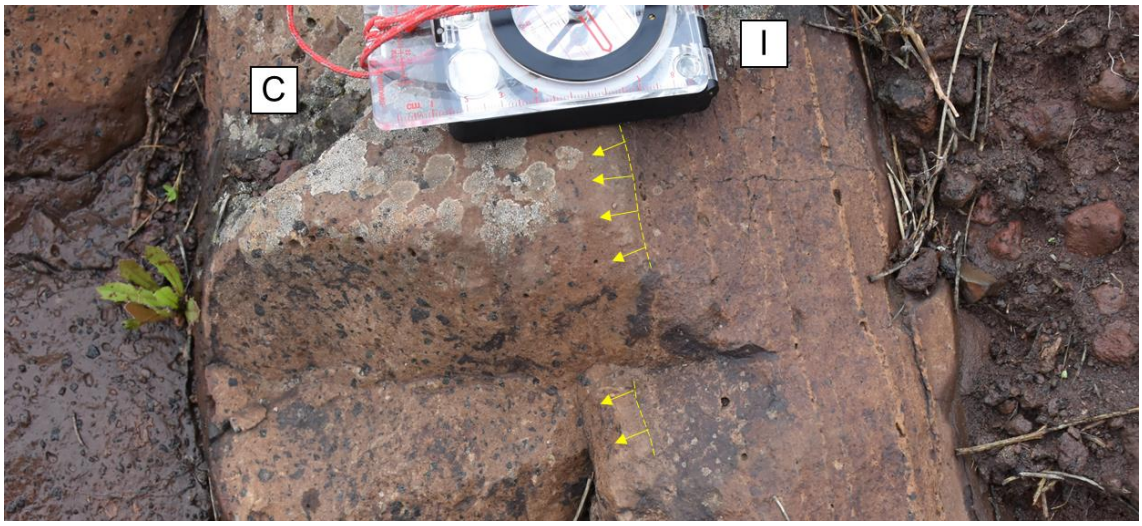

Figure 5.11. Examples of vesicle planes in the intermediate layer of D1: a) segment 1.4, with the yellow circle highlighting the end of a vesicle plane; b) segment 1.5, with the compositional difference of the vesicle planes standing out on the wet surface. Here, the vesicle planes contain small clinopyroxene phenocrysts, similar to the central layer. Yellow dashed lines show the chilled margin, and arrows show the direction of the dendritic crystals along this boundary.

a)

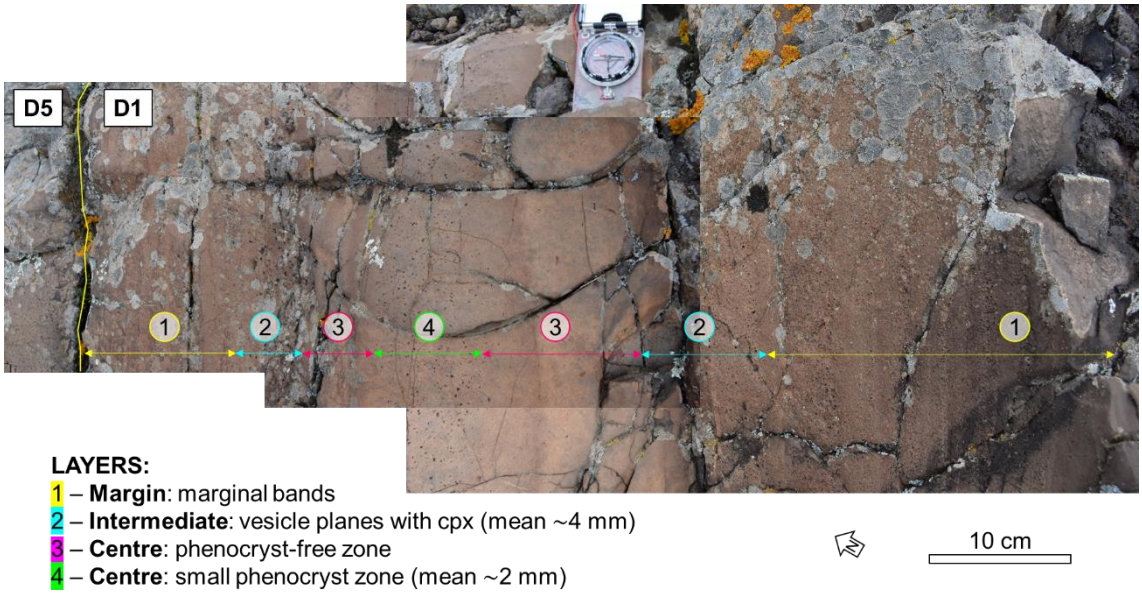

b)

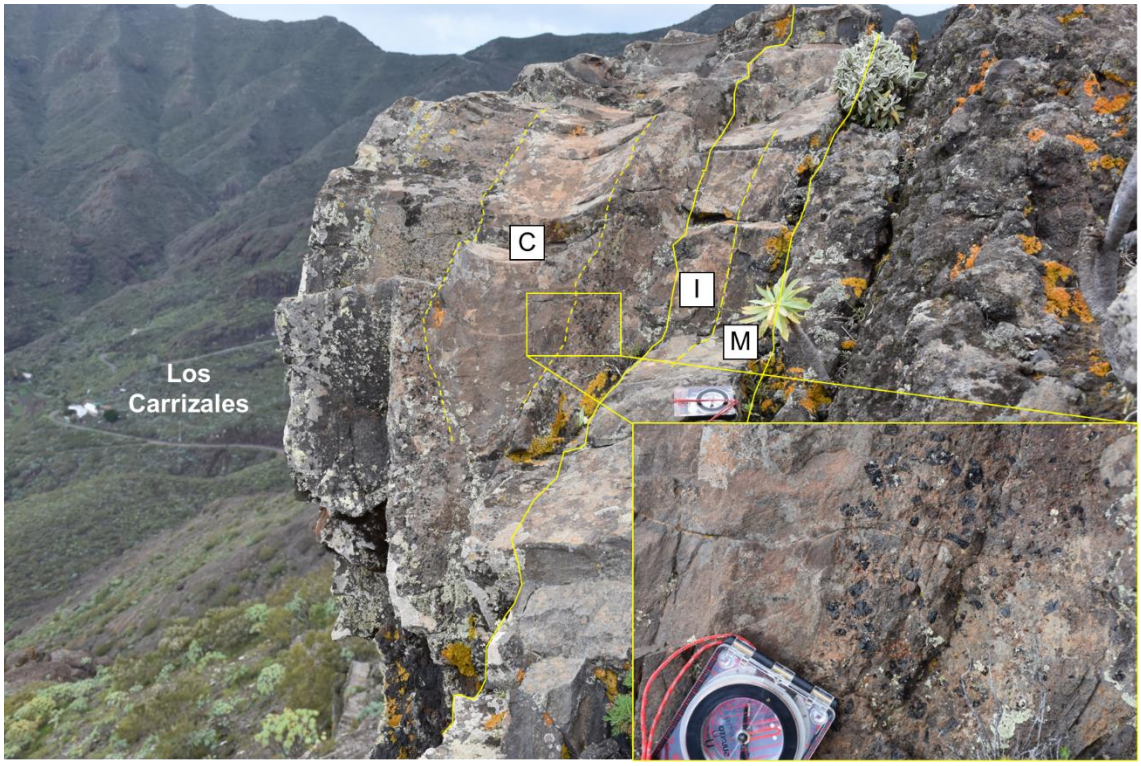

Figure 5.12. Variation in sub-layering in the centre of D1: a) at the southwest end of segment 1.4, where D1 and D5 are in contact, there is no clear boundary between the central and intermediate layers, and the vesicle planes contain clinopyroxene phenocrysts; b) 10 m further north, in the same segment, the centre has a sub-layer rich in clinopyroxene phenocrysts up to 20 mm long, with a relatively sharp contact with a central sub-layer devoid of phenocrysts.

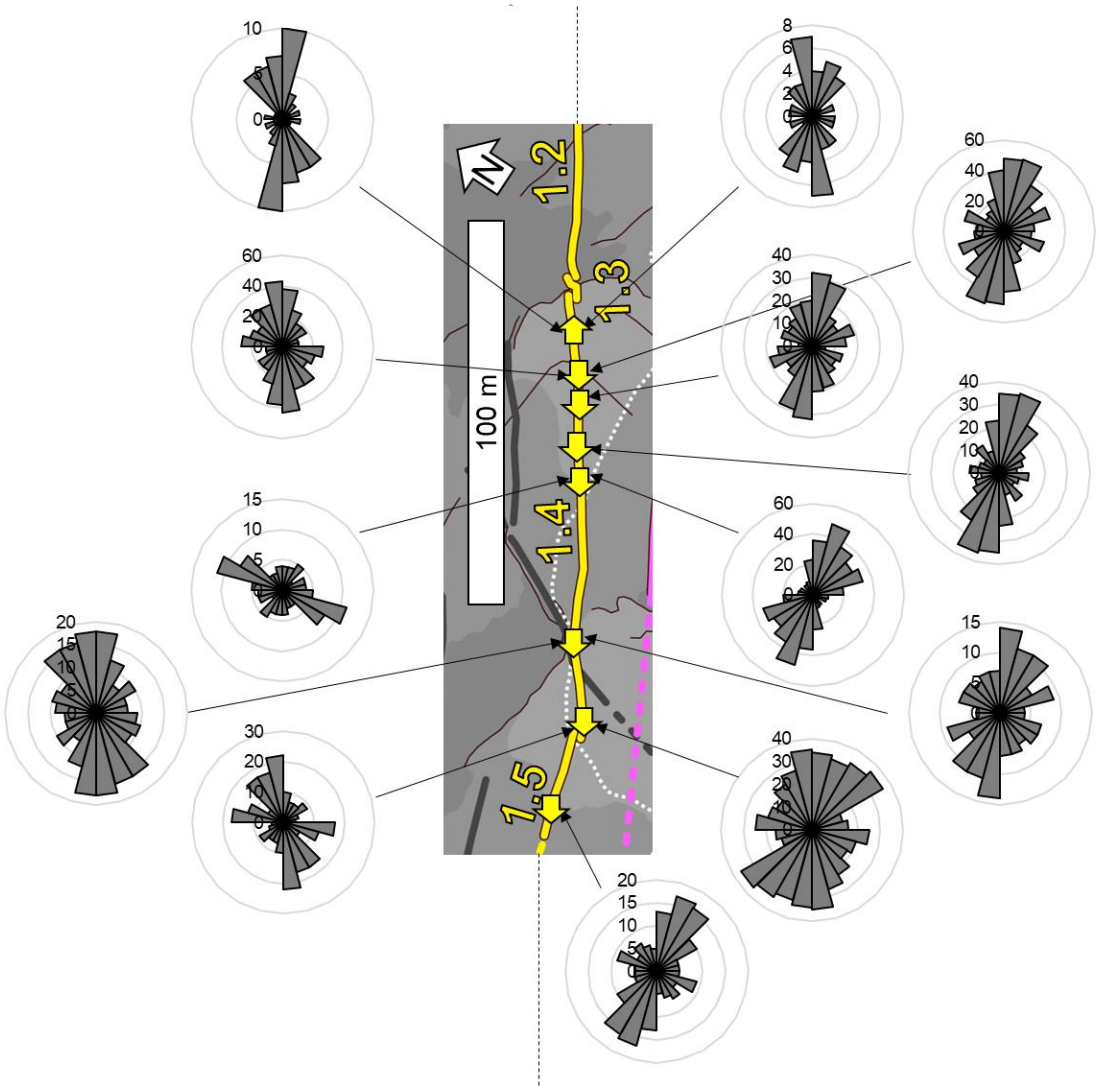

Figure 5.13. Rose diagrams showing the preferred orientation of clinopyroxene phenocrysts at sites along segment 1.4 and 1.5 of D1. Data is split down the centre of the dyke, with the northern half on the left and the southern half on the right. All sites show a preferred orientation at an oblique angle to the orientation of the dyke, indicating a southwest magma flow direction, except for the most northern site, which indicates a northeast flow direction.

D1 micro-textural features

Oriented samples were collected from each of the three layers of D1, and thin sections were taken in three orthogonal planes, aligned with the dyke margin and the vertical. Samples were taken from the middle of segment 1.4, near the intersection with the path (Figure 5.3). The key features of interest are the marginal banding in the outer layer, the vesicle planes in the intermediate layer, the internal chilled margin with dendritic crystals between the intermediate and central layers, and the groundmass of the central layer. In addition, a sample was taken across the width of the offshoot on segment 1.3 (Figure 5.8), with a thin section taken in the vertical plane, to compare textures in the offshoot to those in the margin of the main dyke.

By eye, the marginal bands in the outer layer of D1 are very similar to those seen elsewhere in the Teno region, a detailed analysis and interpretation of which can be found in Chapter 4. Here, we focus instead on the three-dimensional orientation of the micro-phenocrysts in the margins, to get a sense of the flow direction when the dyke was emplaced.

In each of the three layers of D1, the micro-phenocrysts and microlites have similar preferred orientations. The crystals show an imbricated texture, with orientations at an oblique angle to the dyke margin in both the vertical and horizontal planes (Figure 5.14). The parallel plane, on the other hand, does not show a strong preferred orientation in any layer of D1. The long axes of crystals have a similar preferred orientation in the vertical plane of each layer, but there is more variation in the horizontal plane (Table 2). The two-dimensional angles equate to three-dimensional preferred orientations that are broadly similar, although crystals in the central layer are the most heavily inclined away from the margin (Figure 5.15).

Based on imbrication angles, we infer that magma flow was downwards and to the SW in each of the three layers at this locality. The fact that preferred orientations remain constant from the margin to the dyke centre demonstrates that the dyke continued to flow in the same direction throughout its active lifetime at this position, for each magma injection episode.

Table 2. Apparent angles of shape preferred orientation (SPO) in the vertical (a_V) and horizontal (a_H) planes, and calculated three-dimensional orientations θ_A and ϕ_A. Note that these are not the same as Jeffery angles θ and ϕ presented in Chapter 2. The subscript "A" shows that these are apparent flow angles, assuming flow to be directly upwards.

	2D measured SPO		3D calculated SPO	
Layer:	a_V	a_H	θ_A	ϕ_A
Margin	80	70	70	10
Intermediate	80	85	85	10
Centre	70	55	57	20

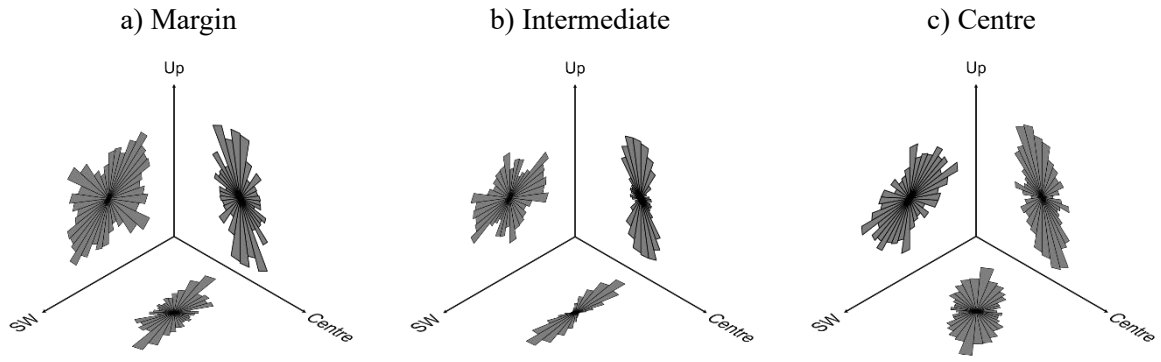

Figure 5.14. Orientations from three orthogonal thin sections for each layer of D1. Imbrication in the vertical plane suggests downwards flow in each layer, whereas imbrication in the horizontal plane suggests SW flow in each layer.

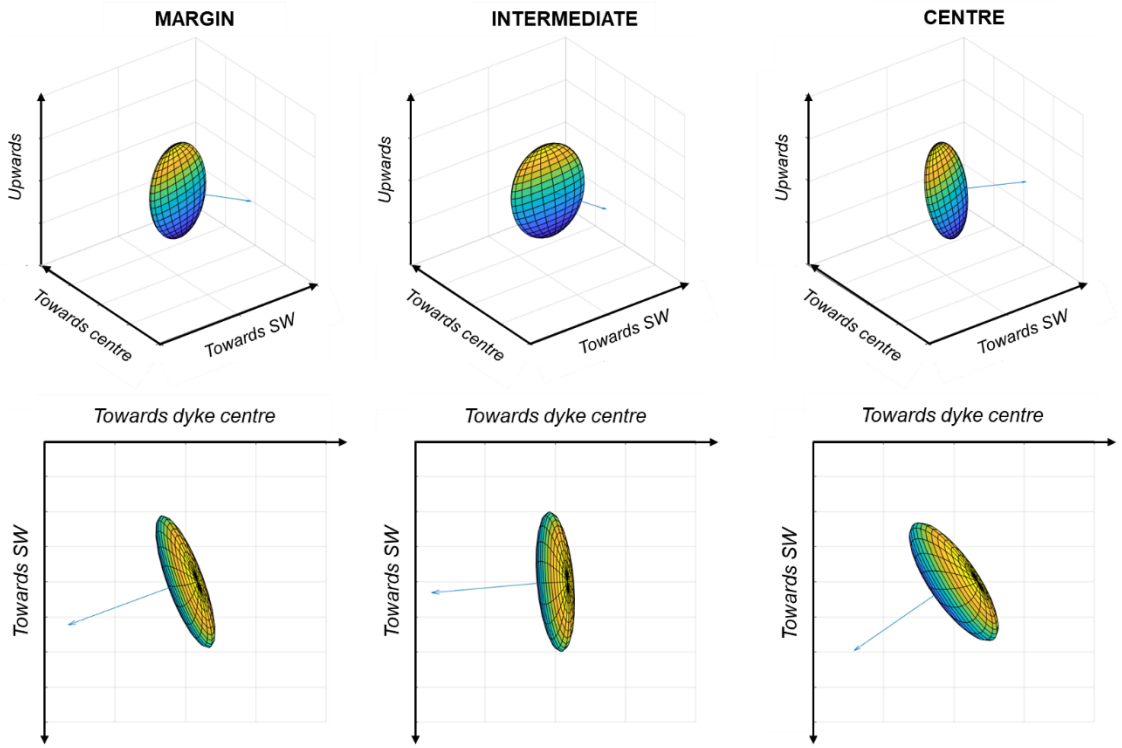

Figure 5.15. Three-dimensional preferred orientations of crystals in each layer of D1. Although they are broadly similar, and all show the same direction of flow downwards and to the SW, crystals in the central layer are inclined more heavily than in the outer layers.

The intermediate layer is distinguished by several highly vesicular planes running parallel to the margin (Figure 5.11). It was observed by eye that the vesicles are elongated and flattened within the planes, but under the microscope, it becomes even more apparent that vesicles are confined, never extending beyond the bounds of the planes, which are much coarser grained and have sharp contacts with the surrounding material (Figure 5.16). The median crystal length in the planes is 2.6x longer than the bulk material (Figure 5.17).

The composition of the vesicular planes and the bulk material appears to be broadly similar (Figure 5.16), and crystals have a similar direction of preferred orientation (Figure 5.17). However, vesicularity in the planes is ~0.35 compared to ~0.15 in the bulk material, and the largest vesicles in the planes are 3.4x times greater in area.

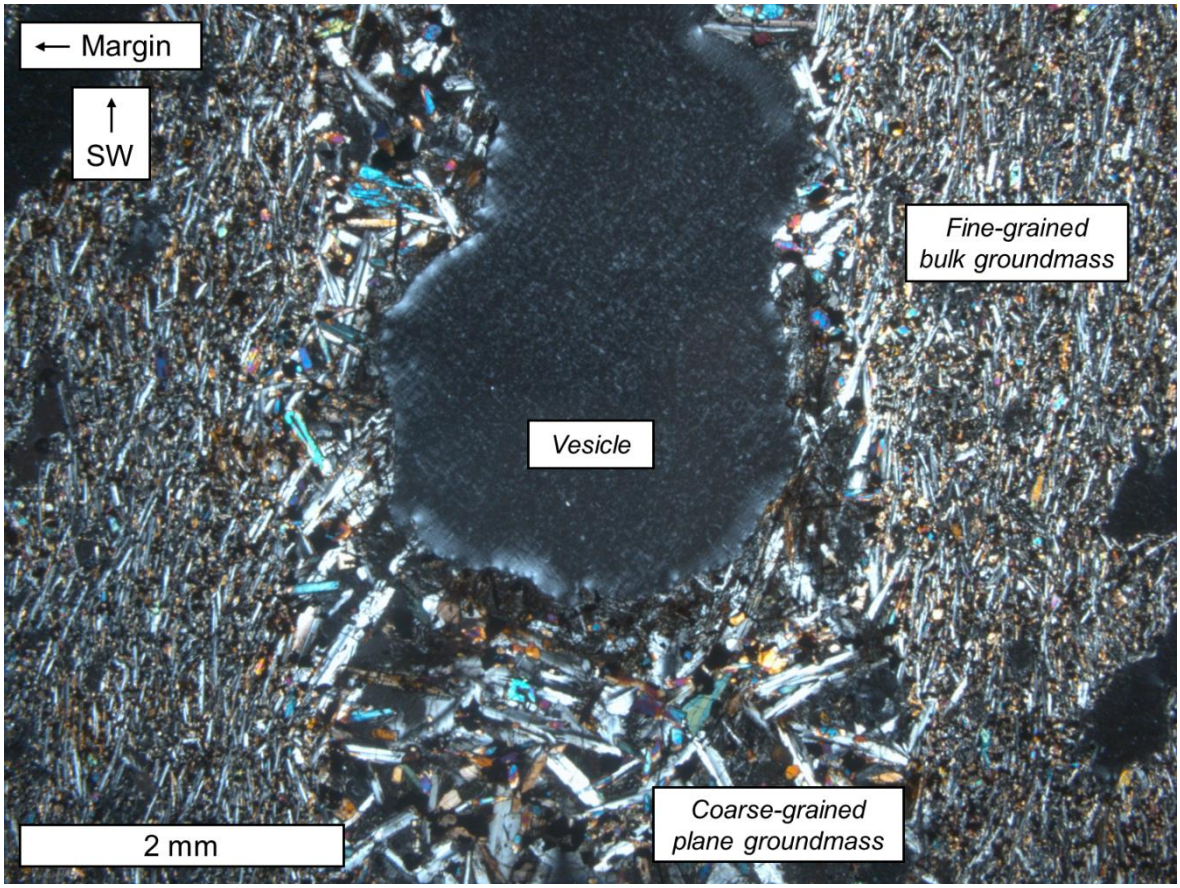

Figure 5.16. A vesicular plane from the intermediate layer of D1, imaged in the horizontal plane, where the dyke margin is to the left and SW is to the top of the image. There is a sharp boundary between the plane and its surroundings, with stark differences in microlite length.

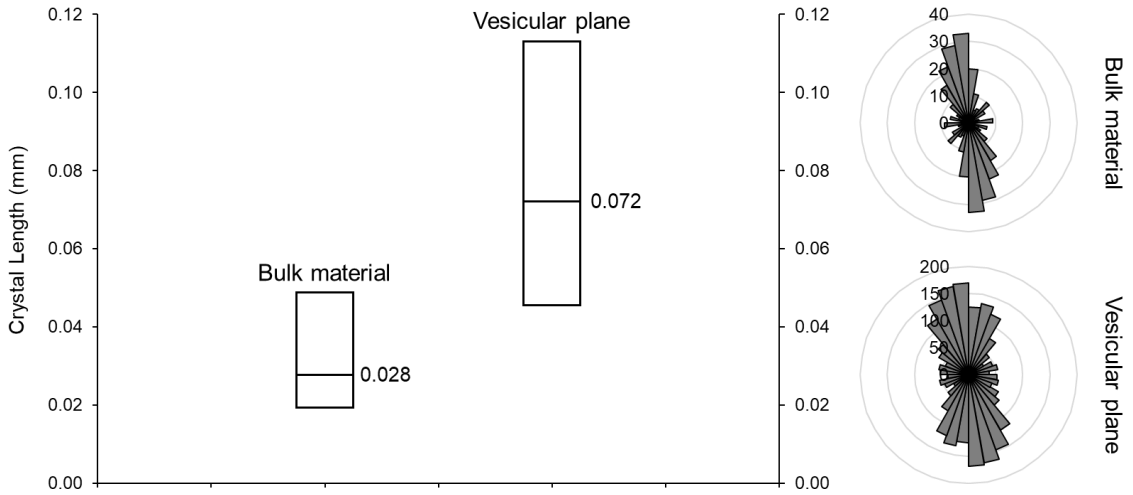

Figure 5.17. Distribution of crystal lengths (25th percentile, median, 75th percentile) for the bulk material versus the material in the vesicular planes, and corresponding distribution of crystal orientations measured relative to the margin.

Another intriguing texture within D1 is the contact between the intermediate and central layers. By eye, this is a thin, black line with black, dendritic crystals stemming from it. Under the microscope, the contact is confirmed to be a chilled margin, displayed as a drop in groundmass grain size moving inwards. The median length of plagioclase microlites drops by 21% across the contact (Figure 5.18).

The boundary appears straight by eye, but under the microscope, it undulates at the length scale of individual microlites (Figure 5.19). Many small, black, oxide crystals branch inwards from this boundary, and these are the most likely cause of the dark line seen by eye. These are typically around 0.04 mm in length, growing perpendicular to the chilled margin even around the small-scale undulations.

However, the most striking feature of the chilled margin is the presence of large, branching crystal structures, which have cores of clinopyroxene and smaller, outer branches of oxide (Figure 5.20). The concentration of dendritic oxides is higher on the NE-facing surfaces of the clinopyroxene cores. By eye, the branching structures never reached further than around 10 mm from the contact. Under the microscope, ascertaining their length is difficult because the structures have a complex, three-dimensional shape outside the plane of the thin section.

One of the most intriguing characteristics of the branching crystal structures is their relation to the surrounding groundmass. The plagioclase microlites, which are aligned with a strong preferred orientation beyond the reach of the branching structures, form curving waves of alignment around the branches, looking as if the clinopyroxene dendrites have pushed them aside (Figure 5.20). Similar branching structures are present within D2 and D5, and a detailed discussion of the processes behind their formation and their interaction with the microlites is presented in Section 5.5.5.

A final thin section from D1 comes from the offshoot shown in Figure 5.8. In the field, the offshoot has dark, glassy margins but is mostly aphanitic, with bands of vesicles running parallel to its margins. In thin section, the offshoot looks similar to the outer layer where it originates, and the bands are associated with a variation in phenocryst content and vesicularity, the same as the marginal bands. However, the banding in the offshoot is less regular than in the margins.

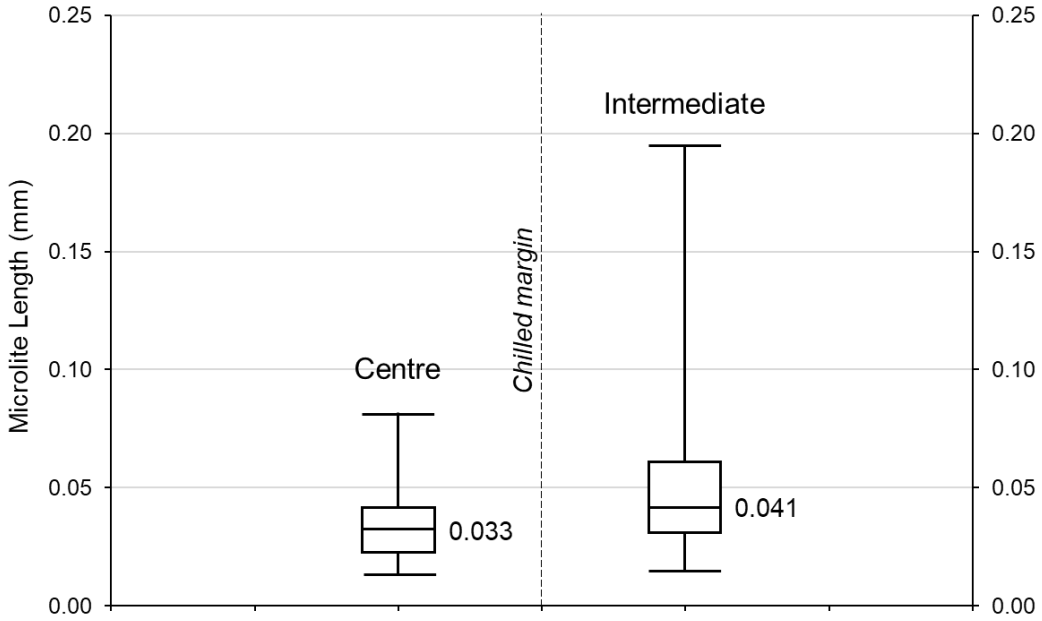

Figure 5.18. Distribution of crystal lengths (minimum, 25th percentile, median, 75th percentile, maximum) for the groundmass of the intermediate and central layers of D1, within 5 mm of the contact separating them.

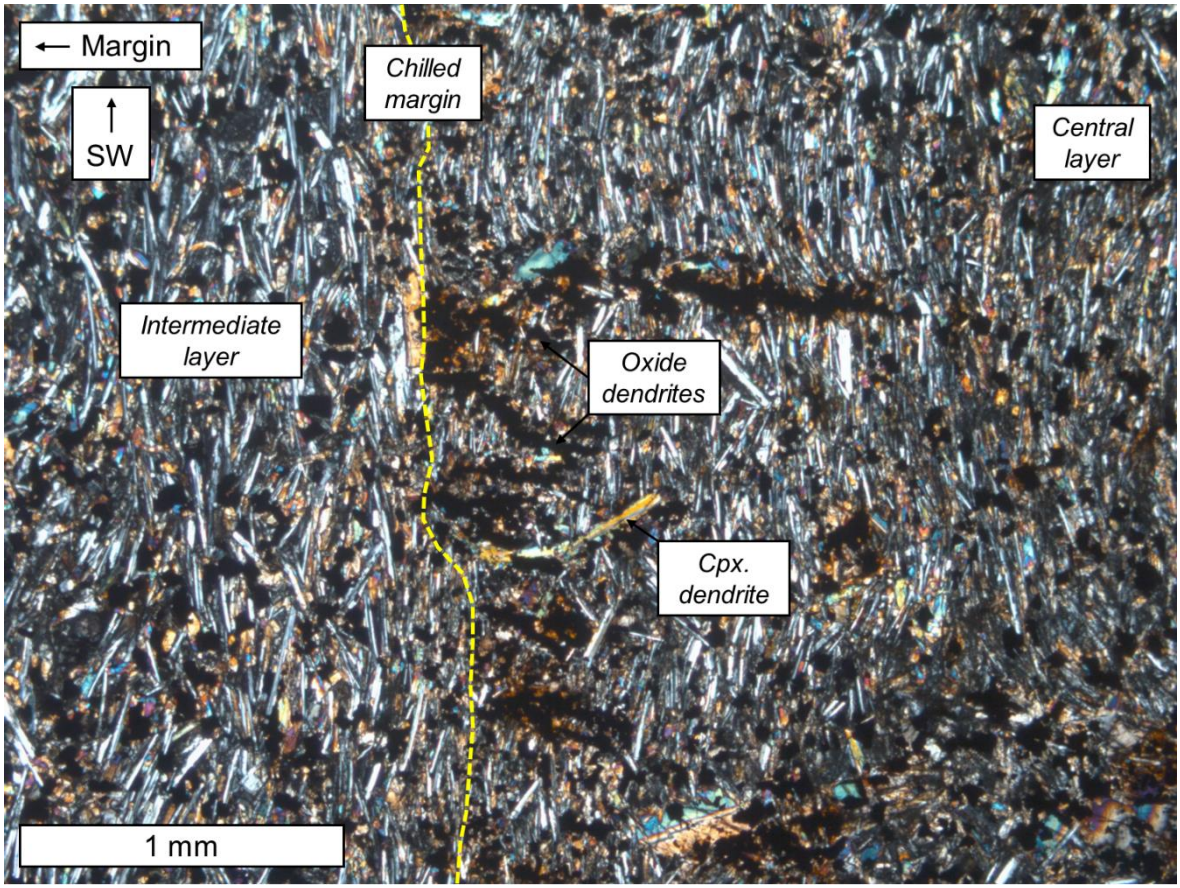

Figure 5.19. Chilled margin (yellow dashed line) separating the intermediate (left) and central (right) layers of D1. The boundary is marked by a drop in groundmass grain size moving towards the dyke centre and is lined with black, dendritic oxides branching inwards. Image is in the horizontal plane.

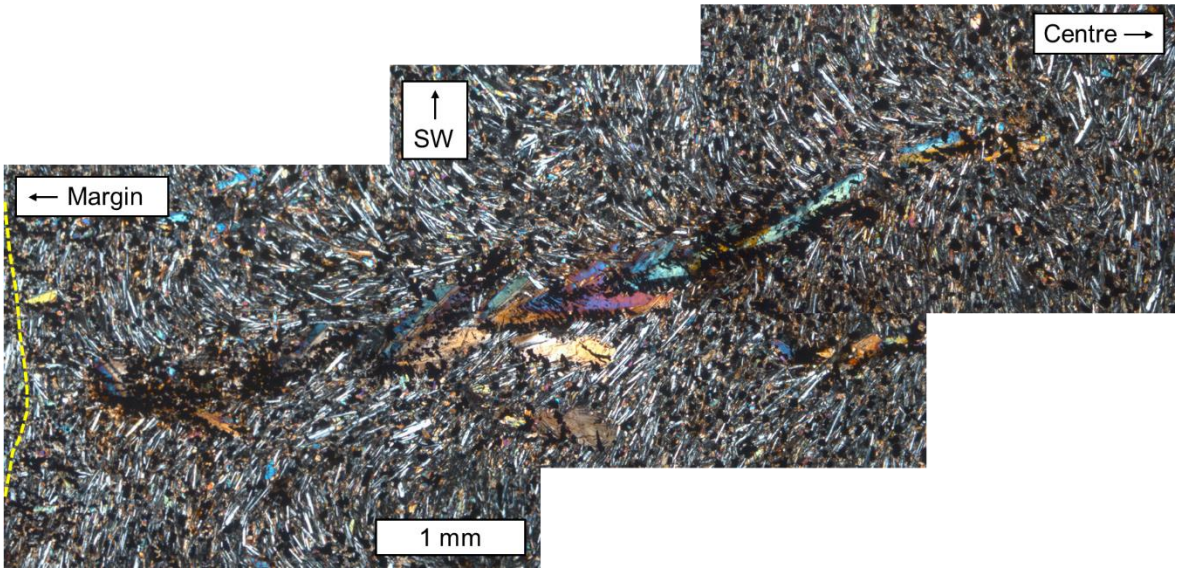

Figure 5.20. Dendritic crystal structure branching inwards from the chilled margin (yellow dashed line) towards the dyke centre. The core of the structure is clinopyroxene, but this core has smaller, secondary dendritic oxides growing from its surface. Image is in the horizontal plane.

5.4.2 D2

D2 strikes at a more north-easterly angle than most other dykes along the Carrizales Ridge, at around 030° (Figure 5.3). It is predominantly vertical, but locally it can dip either north or south. The dyke is distinguished by a lack of vesicles and by prominent cooling joints perpendicular to the dyke margins, and it is around 0.5 m wide with no obvious layering. It cuts across D1, D3 and D4.

D2 segmentation and offshoots

D2 is exposed in two sections for a total of ~150 m. To the east, it follows the path on the northern side of the ridge, where it intersects D4 and D1. It then becomes inaccessible on the steep slopes, before reappearing on the ridge, where it has a relay between two segments and intersects D3 (Figure 5.3; Figure 5.21). The relay is 12 m long, and the segments run parallel for around 10 m before their tips curve towards the opposite segment. Both segment tips taper to points and start narrowing around 3 m from their apparent termination. The relay is exposed on an almost horizontal surface, where the dyke dips northwest (Figure 5.21). No offshoots were found on D2.

D2 layering

D2 contains no obvious layering. It has weathered uniformly across its width, and its distinctive cooling joints commonly stretch from one margin to the other without interruption (Figure 5.22). However, in some sections, a thin, dark line can be seen around 5-8 cm from the margin, sometimes with a spiked appearance pointing towards the dyke centre. This is especially the case approaching the intersection with D4, where the dark line contains sub-millimetre black, dendritic crystals, like those in the internal chilled margin on D1. However, if this is an internal chilled margin, it is not consistent nor obvious enough for categorising layers within D2.

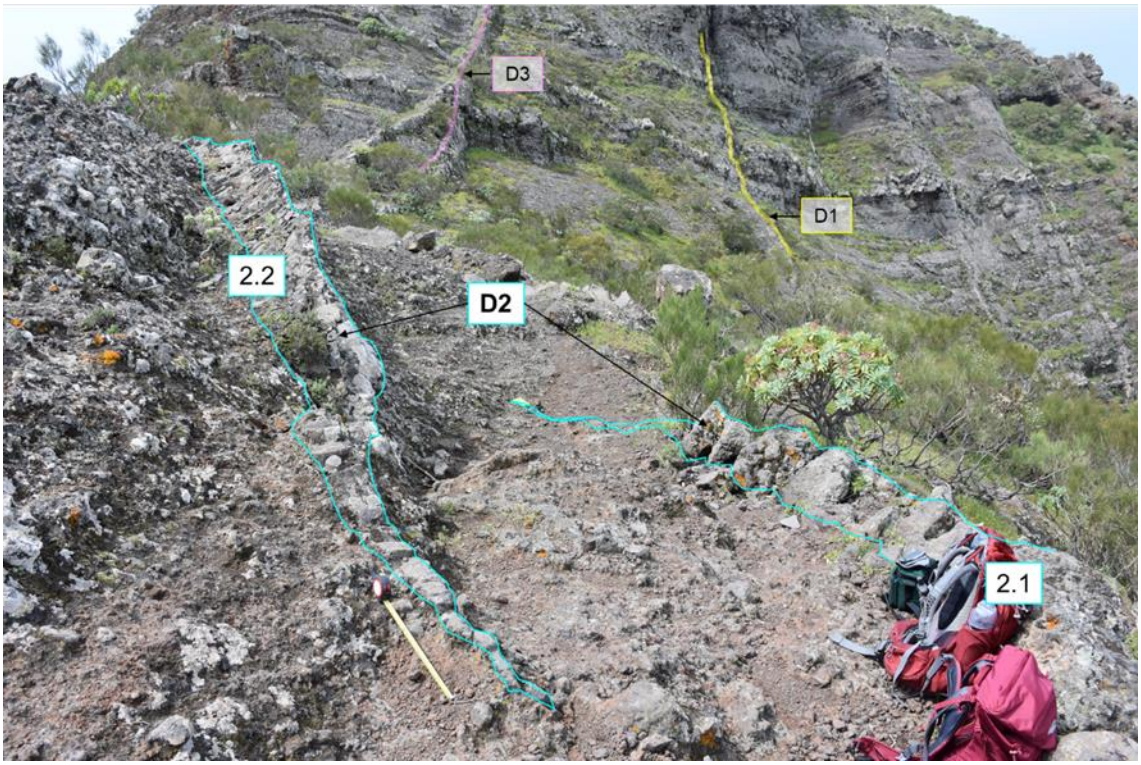

Figure 5.21. Relay between two segments on D2. The relay is 12 m long. Both segments have tapering tips, which curve slightly towards the other segment.

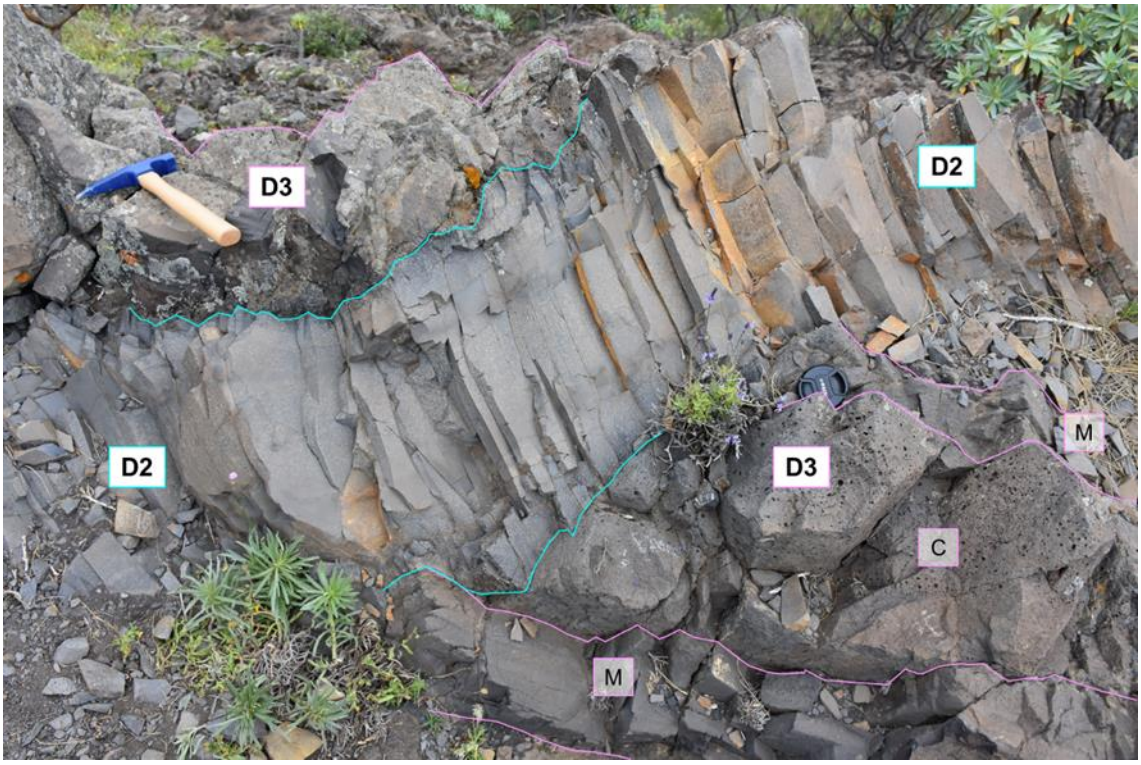

Figure 5.22. Dyke D2 cutting across D3. D2 has distinctive cooling joins stretching across its width, and a symmetric variation in plagioclase phenocryst content. D3 has two clear layers: banded margins (M) and a highly vesicular core (C).

D2 macro-textural features

Although it contains no obvious compositional layering or internal chilled margins, D2 shows a clear, systematic variation in plagioclase phenocryst concentration across its width. Its phenocrysts are up to 2 mm long, and they appear equant or irregular in shape, with no obvious preferred orientation. From a distance, the dyke has obvious textural symmetry, with darker, phenocryst-free regions around 2-4 cm wide lying either side of a central, lighter-coloured phenocryst-rich region, around 10-15 cm wide (Figure 5.22). A second phenocryst-free zone, only 5 mm wide, lies just 5-6 cm in from the margin where D2 intersects D3 (Figure 5.23). These phenocryst-defined sub-layers vary in width over tens of centimetres, and they are not consistent enough over long distances to be true layers by our definition (Section 5.3.3).

Figure 5.23. Sub-layering defined by a variation in plagioclase phenocryst content within D2, where p+ denotes phenocryst-rich and p- denotes phenocryst-poor regions. These regions varied in width and could never be traced more than a few tens of centimetres along the dyke.

D2 micro-textural features

Thin sections were taken in three orthogonal planes across the dark line suspected to be an internal chilled margin. Under the microscope, the dark line is revealed to be a high concentration of dendritic oxide crystals, which appear to have grown inwards towards the centre of the dyke (Figure 5.24). There are also dendritic clinopyroxene crystals growing inwards from this contact, although there are fewer of them compared to those on the internal contact in D1 (Section 5.4.1), and they are generally shorter (< 0.1 mm). The clinopyroxene crystals have secondary oxide dendrites growing on their surface, with a higher concentration of oxides on their NE-facing side (Figure 5.24). There is no obvious compositional or textural change across this internal boundary.

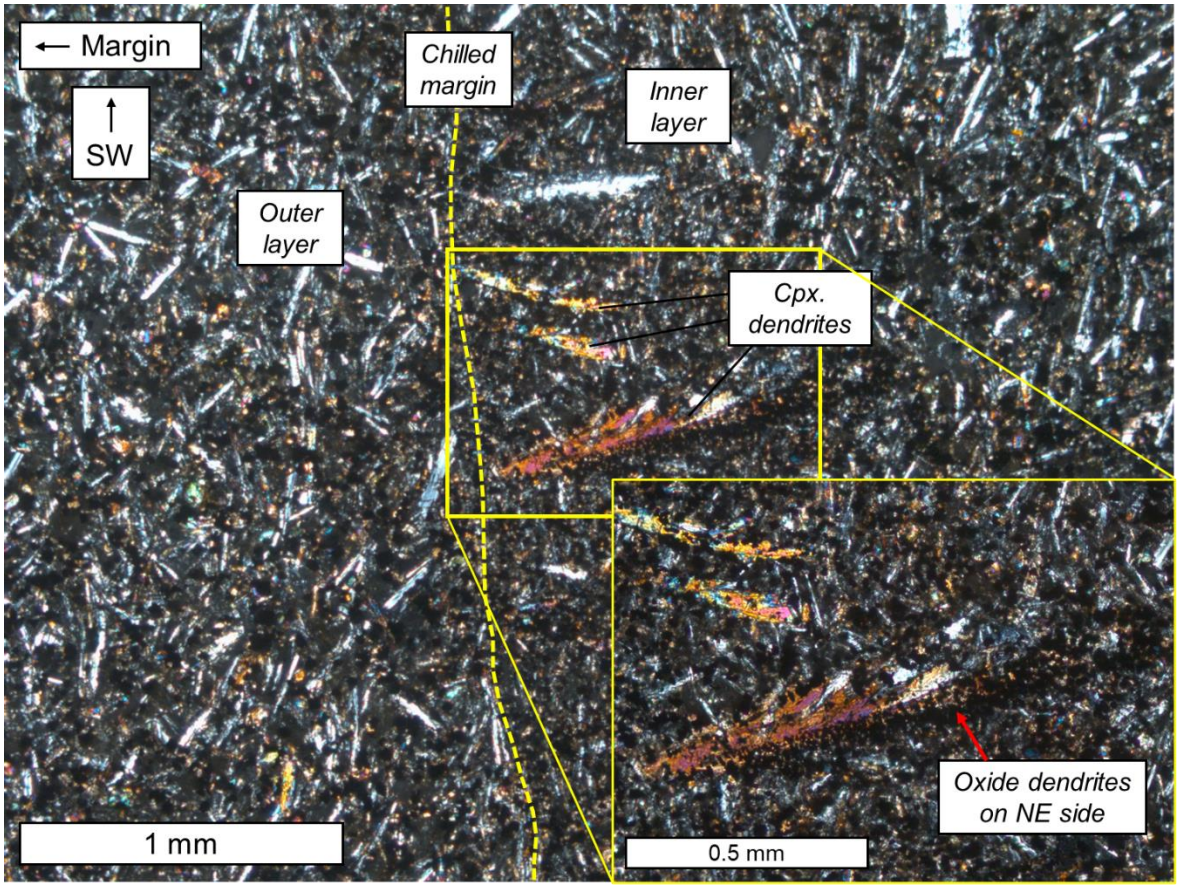

Figure 5.24. Internal chilled margin within D2, marked by a high concentration of oxides (dashed yellow line shows approximate position). Dendritic clinopyroxenes grow inwards from this contact towards the dyke centre, hosting a higher concentration of oxides on their north-east side.

5.4.3 D3

D3 runs parallel to D1, striking at ~060° (Figure 5.3), and it contains two distinct layers: an outer region ~12 cm wide containing marginal bands, and a highly vesicular inner core ~40 cm wide, with large, elongated vesicles up to 2 cm long (Figure 5.22). The dyke is vertical, not dipping significantly north or south (Figure 5.7a; Figure 5.9).

D3 segmentation and offshoots

D3 is split into two segments along the studied section, with a relay exposed on a northeast-facing slope (Figure 5.25). Both segments have the same layered structure and textures. Narrow offshoots from the marginal layer are found around the relay zone, and these are < 10 cm wide, sometimes as narrow as 3 cm, and can be up to tens of metres in length (Figure 5.26). Some offshoots form isolated islands of material, just a few centimetres wide and < 30 cm long, but they are aligned with neighbouring sections of offshoots, suggesting they are or were connected outside the plane of observation. All offshoots originate in the banded margins.

D3 layering

D3 has an outer layer 12 cm wide containing marginal bands, and a highly vesicular core around 40 cm wide. The layering here is less obvious than on D1, as there is no compositional difference, but in many sections the layers are distinguished by differential weathering. However, there is no obvious contact or chilled margin between them, only a sudden inwards increase in vesicle size.

D3 macro-textural features

Vesicles are abundant in both layers of D3, but are larger towards the centre, where maximum diameters commonly exceed 20 mm. The large, central vesicles are typically elongated, forming a V-shape across the dyke, symmetrical about the centre, most obvious on horizontal or gently sloping surfaces. The elongation of vesicles is a result of bubble deformation by flowing magma, and the V-shape points in the direction in which magma flowed (Chapter 3). Where exposure is poor, there is usually a strong preferred orientation of vesicles exposed in at least one half of the dyke, and this is enough to determine the flow direction. However, we can be more confident in our interpretation of the flow direction when both halves of the dyke are visible and form an obvious V-shape.

The orientations of thousands of vesicles were collected from outlines in photos. Vesicle preferred orientations show frequent reversals in recorded flow direction along the length of the dyke, at a scale of several metres (Figure 5.27). Due to poor exposure, the precise tipping point between two opposing directions was never found, although in one case, it was narrowed down to a 3 m section. No change in dyke width, orientation or layering is associated with the vesicle orientations.

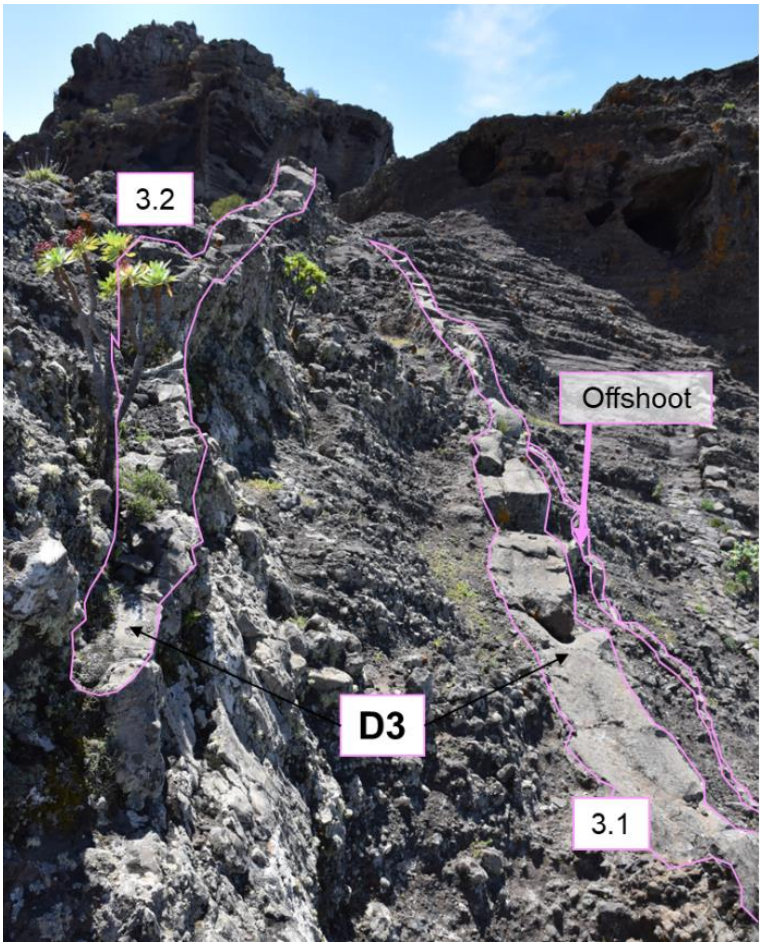

Figure 5.25. Relay between two segments on dyke D3. A narrow offshoot also runs parallel to the relay. The section labelled 3.1 is approximately 64 cm wide. Photo is facing SW. The path is on the right of the image.

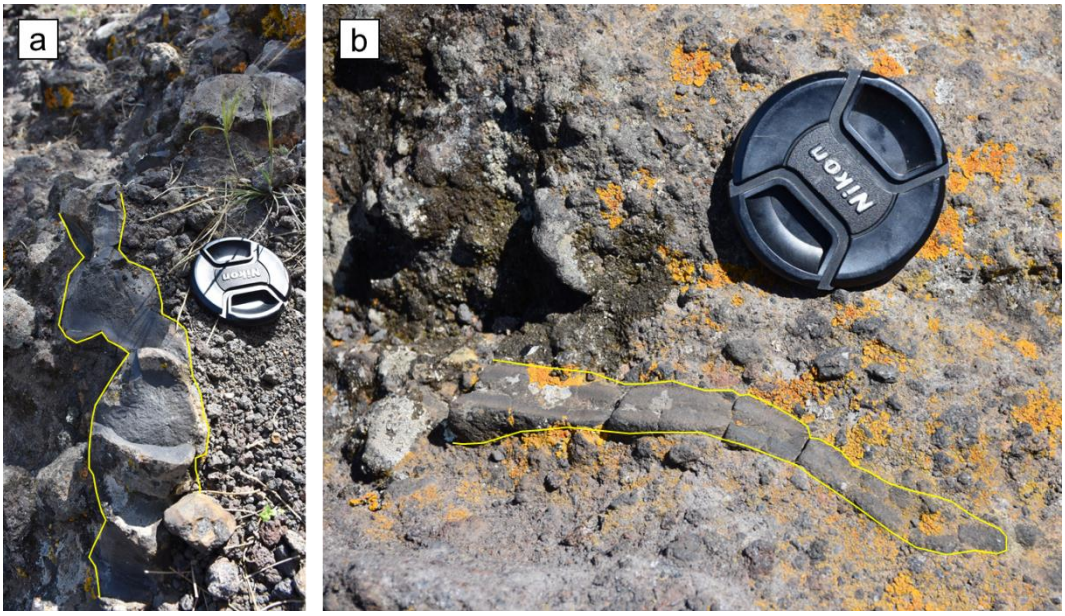

Figure 5.26. Narrow offshoots from D3, which originate in the banded margins. Camera lens cap is 6.5 cm in diameter.

In most cases, the dyke was so heavily weathered that only the large vesicles in the central layer were visible. However, at one location, the marginal vesicles were also well preserved. Here, the preferred orientation of vesicles at the margin opposed the preferred orientation from the dyke core (see the box in Figure 5.27), showing that there was a change in magma flow direction over time at this point in the dyke. The margins show that the initial magma flow was SW, whereas the central vesicles record later magma flow to the NE.

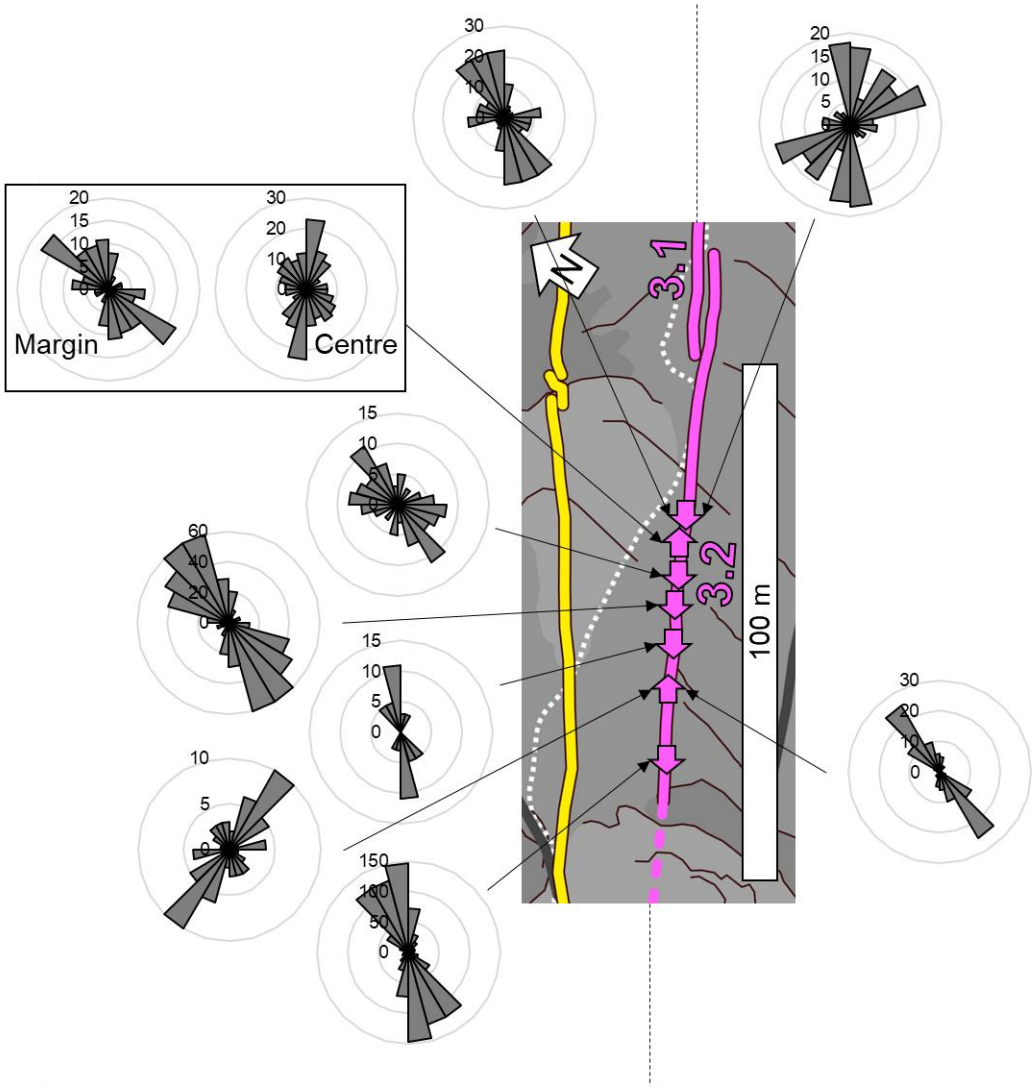

Figure 5.27. Preferred orientations of elongated vesicles along D3, split on either side of the dyke centre. Each site forms a V-shape, but the direction of this V varies along the dyke. The box highlights a site where recorded flow direction differs between the margins and the centre.

5.4.4 Other notable dykes

Intersection between D2 and D4

D2 has generally uniform textures along its length, but this uniformity breaks down where it intersects D4 (Figure 5.3; Figure 5.28). D4 has a similar width to D2, at 0.5 m, and is a composite dyke with two distinct layers: banded margins, and a highly vesicular core containing clinopyroxene phenocrysts. It is only exposed close to where it intersects D2, and so it was not studied in detail. Its layers are relatively uniform in width, but like D2, all uniformity is lost where the dykes intersect.

The intersection is just over 5 m long, and neither dyke cuts cleanly through the other. Instead, the dykes appear to have merged for this short stretch. Outside the intersection, each dyke has a consistent width of 0.5 m, but their intersection is 1.5 m wide, and contains no evidence of the perpendicular cooling joints of D2 or the banded margins of D4. The intersection is very weathered (Figure 5.29), but most of its textures are consistent with D2, showing no vesicles and an abundance of plagioclase phenocrysts. However, highly vesicular streaks, as well as streaks of material with clinopyroxene phenocrysts up to 10 mm in diameter, are also present, and these are consistent with the textures from D4. It appears that the magma within the two dykes mingled when one cut across the other. The margins of the intersection are glassy and contain plagioclase phenocrysts, similar to D2, and so it is likely that D2 was emplaced first.

The most intriguing aspect of this intersection are two regions of dendritic crystals (Figure 5.29). These regions are up to 80 mm wide, with individual crystal branches up to 10 mm long (Figure 5.30). One region is near the northern margin, while the other, mirrored region is just north of the central axis of the intersection. Both regions have a very sharp, straight contact against a layer rich in plagioclase phenocrysts, where the dendritic crystals appear to have been truncated.

The dendrites appear to be much larger versions of the branching structures seen at the internal boundaries of D1 and D2. In fact, the internal chilled margins in D2 become more pronounced within 10 m of the intersection, with a greater number of sub-millimetre, black, dendritic crystals protruding towards the dyke centre. However, the area is so extensively weathered that these internal margins cannot be traced into the intersection, and it is unknown whether they are connected to the larger dendrite zones.

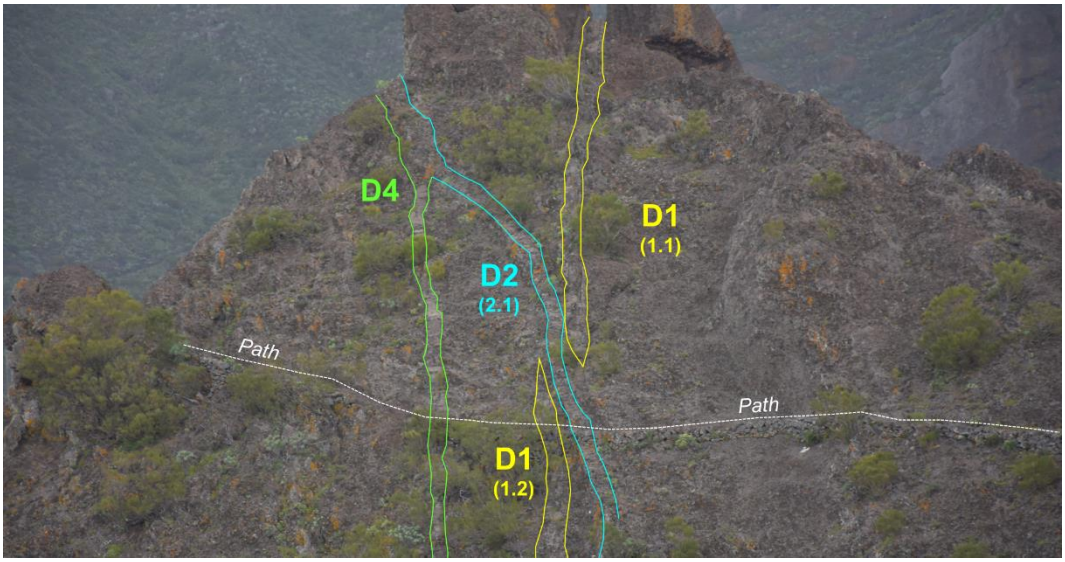

Figure 5.28. Intersection of D2 with D4 and D1 viewed from 240 m away, facing NE from the site shown in Figure 5.8. D1 is approximately 1 m wide, whereas D2 and D4 are both approximately 50 cm wide.

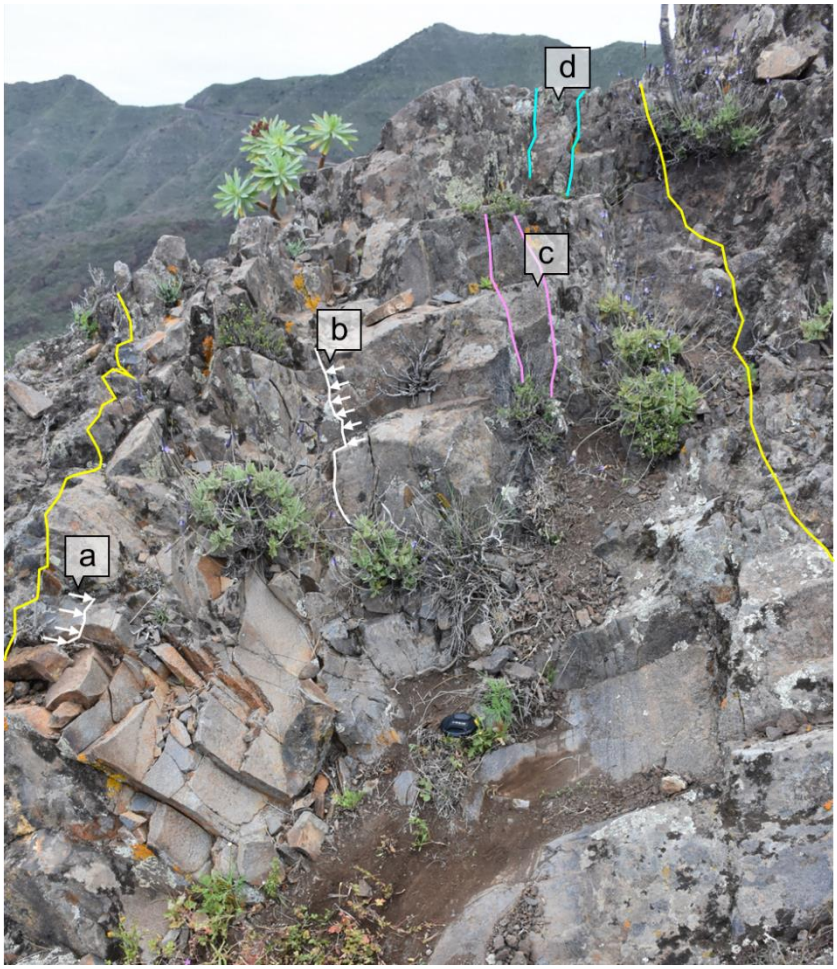

Figure 5.29. Intersection between D2 with D4, facing NE: a) dendrites growing inwards from near the northern margin; b) dendrites growing near centre of intersection; c) highly vesicular region; d) region with large clinopyroxene phenocrysts. The width between the margins, shown in yellow, is 1.5 m.

Figure 5.30. Dendritic crystals at the intersection of D2 and D4, near the northern margin, labelled "a" in Figure 5.29. The dendrites grow inwards towards the centre, but are truncated by a sharp boundary with a region rich in plagioclase phenocrysts.

A thin section was taken across the northern dendrite region (Figure 5.30). Under the microscope, the dendrites are revealed to be clinopyroxene, with long branches stretching inwards towards the dyke centre, curving to the SW. The SW side of each branch houses shorter, stubbier sub-branches, while the NE side is smooth. The NE surfaces of the clinopyroxene crystals house a high concentration of small oxide dendrites, which appear to have grown to the NE, like the branching structures in D1 and D2. However, the dendritic clinopyroxenes have not nucleated solely on an internal contact between two dyke layers. Here, they have nucleated specifically on clusters of plagioclase phenocrysts, not only within the contact, but within material away from the contact (Figure 5.31). Finally, the sharp boundary at the end of the dendrite region is just as clear under the microscope as by eye, where the curving dendrites appear to have been truncated (Figure 5.32). However, there is no clear compositional or textural change in the groundmass associated with this truncation.

The implications of these dendrites, in terms of using them as indicators of flow direction or cooling conditions, are discussed further in Section 5.5.5.

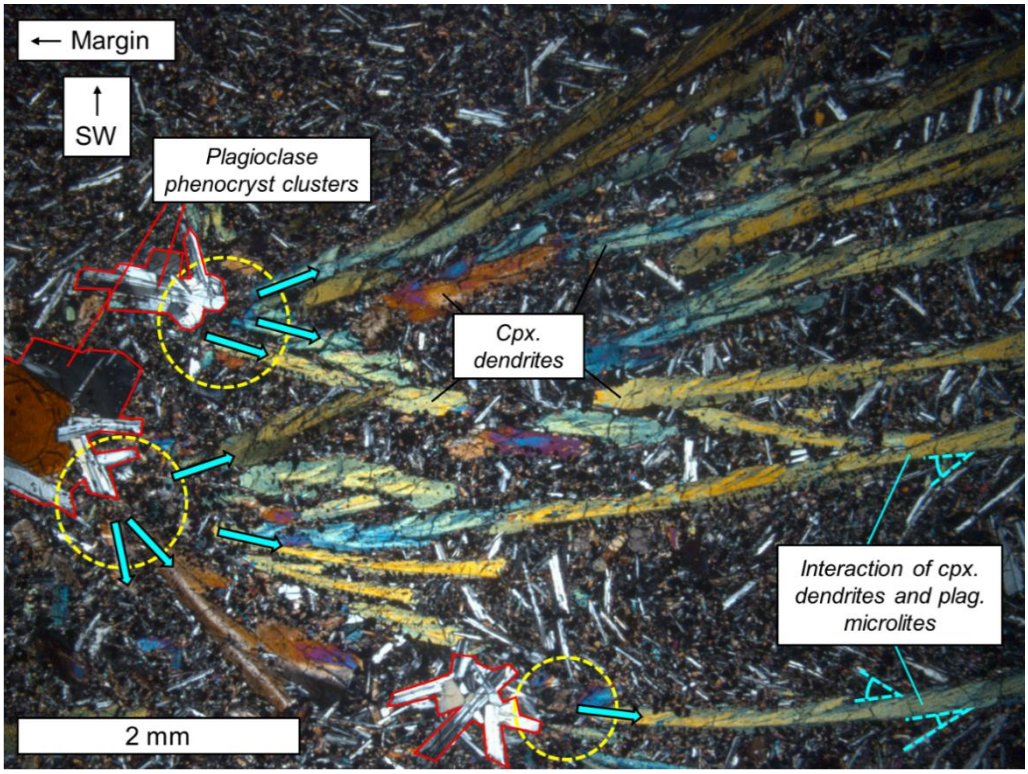

Figure 5.31. Clinopyroxene dendrites from the intersection between D2 and D4. The dendrites have nucleated on clusters of plagioclase phenocrysts (highlighted in dashed yellow circles), then grown inwards towards the dyke centre (growth direction shown by cyan arrows). The orientation of plagioclase microlites is deflected in the vicinity of the clinopyroxene dendrites.

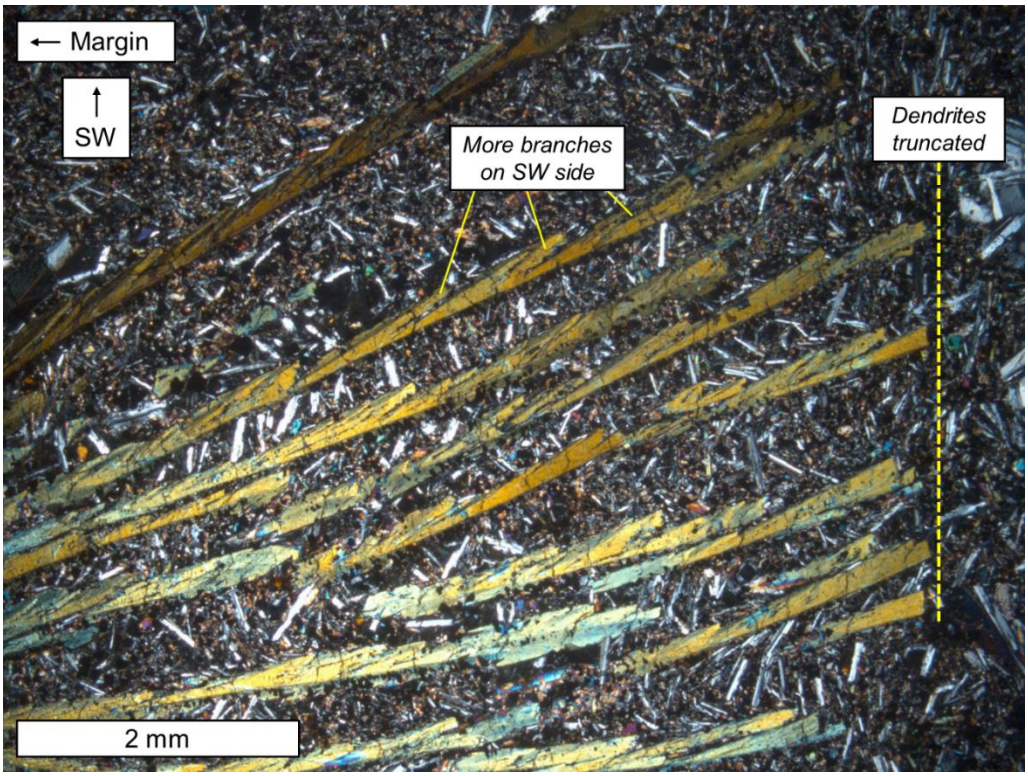

Figure 5.32. Clinopyroxene dendrites at the intersection between D2 and D4. The dendrites curve to the SW, but they reach an abrupt end (yellow dashed line). There is no clear compositional or textural boundary in the groundmass here, but the next layer is richer in plagioclase phenocryst clusters.

Segmentation and offshoots in other dykes

Most dykes along the Carrizales Ridge strike at around 060°, parallel to D1 and to the ridge itself, and are up to 1 m wide. Cliff exposures reveal that it is common for dykes to be segmented in the vertical plane (Figure 5.9; Figure 5.33), and segmentation occurs in dykes of any width. Segment length does not appear to depend on the dyke width; for example, dykes 1 m wide can have segments < 10 m long, while dykes < 0.5 m wide can extend > 50 m without segments (e.g., Figure 5.9; Figure 5.25; Figure 5.33).

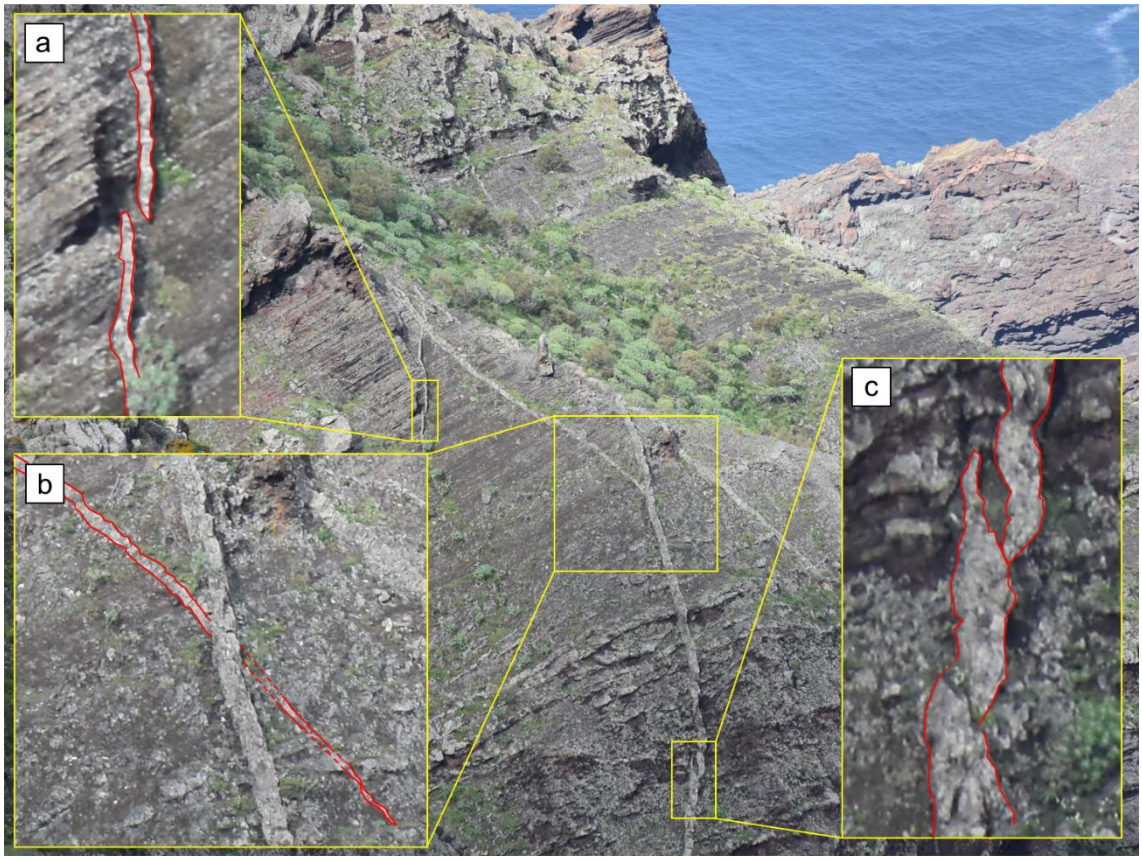

Figure 5.33. Examples of segmentation in near-vertical cliff faces on the NE/SW trending dykes along the Carrizales Ridge. Segment length does not depend on dyke width. These dykes are < 1 m wide.

Another set of dykes cut across the ridge with a more N/S strike. Some of these are much wider than the NE/SW-striking dykes, with the widest being 2.5 m. These dykes are only exposed for small distances with limited vertical exposure. However, although they cannot be traced far, many of these dykes also show evidence of segmentation on vertical cliff faces.

In the Carrizales Valley, north of the ridge, the dykes intrude heavily altered scoria cones and layered lava flows (Figure 5.34). In this vicinity, dykes have very sinuous paths, and their widths, strikes and dips are locally highly variable. Segmentation is common, but segment morphology shows huge variation, both in terms of scale and organisation. Segments can be aligned or offset, discontinuous or overlapping, in contact or separated by a screen of host rock. The tips of segments are usually tapered, but some are blunt. Offshoots are common near the segment tips, with some dykes branching into several offshoots at their termination. However, the sinuous paths of the dykes make it difficult to determine whether one branched from another, or whether neighbouring dykes are in fact segments of the same dyke.

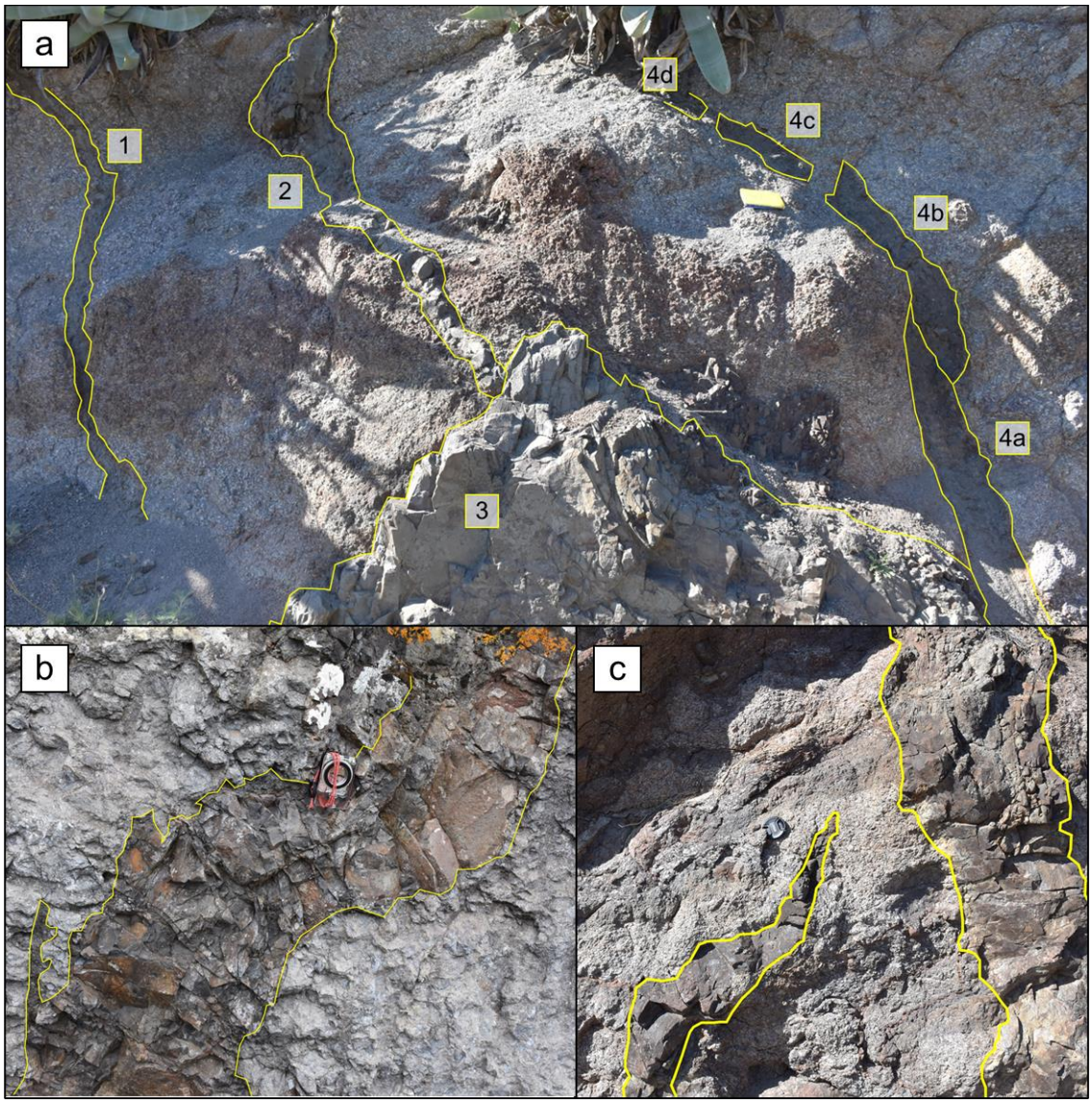

Figure 5.34. Dykes striking N/S across the ridge, with limited exposure: a) highly segmented dykes intruding a lava flow in the Carrizales Valley, consisting of four separate bodies, which may be different dykes or segments of the same dyke; b) likely coalescence of two segments on the Carrizales Ridge; c) a sinuous, tapering dyke segment intruding a lava flow in the Carrizales Valley.

Macro-textural features in other dykes

Several dykes in the region contain interesting textural features, but their limited exposure means that their textures cannot be related to dyke geometry or segmentation, which makes them less useful for understanding the evolution of magma pathways during dyke emplacement. That being said, isolated textures can still help to illuminate general processes operating within dykes. For example, several dykes on the Carrizales Ridge display marginal bands, either as clear variations in colour and vesicularity, like D1 and D3, or as weathered ridges, and the prevalence of this texture supports our prediction that pulsatory propagation at the tip of dykes is a very common process (Chapter 4).

Many dykes on the ridge also displayed a variation in phenocryst content across their width, but without chilled margins to define true layers. For example, one N/S-striking dyke at the eastern end of the ridge shows significant variations in phenocryst size, type and abundance (Figure 5.35). The contacts between these sub-layers are relatively sharp, but there is no sign of any internal chilled margins, or any change in the groundmass between layers. This variation in phenocryst type or concentration echoes the findings from D1 and D2, and once again demonstrates that the processes driving these variations in phenocryst content are widespread within dykes.

Another notable texture was found in a dyke at the far, southwest end of the ridge. Only the tip of this dyke is exposed, with a maximum width of 30 cm, tapering out over a metre. The dyke contains highly vesicular bands, which get wider and less distinct towards the dyke centre. They follow the dyke margins closely, like most cases of marginal banding. However, unlike most cases, these bands pinch out in concentric U-shapes just short of the dyke tip (Figure 5.36). This is the only example of such a texture, as most segment tips have been weathered extensively. As such, it provides a valuable insight into the relationship between marginal banding and dyke geometry.

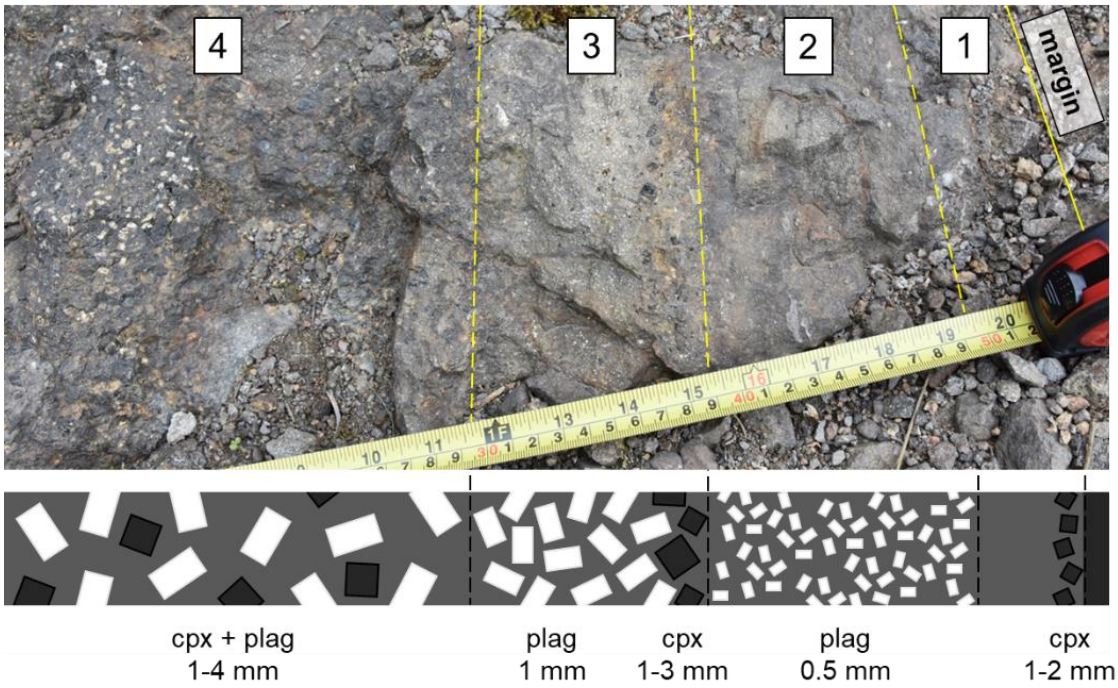

Figure 5.35. Dyke at the eastern end of the Carrizales Ridge with limited exposure, displaying layering defined by a variation in phenocryst type, size and abundance. The schematic shows pyroxene phenocrysts as dark squares, and plagioclase phenocrysts as white rectangles.

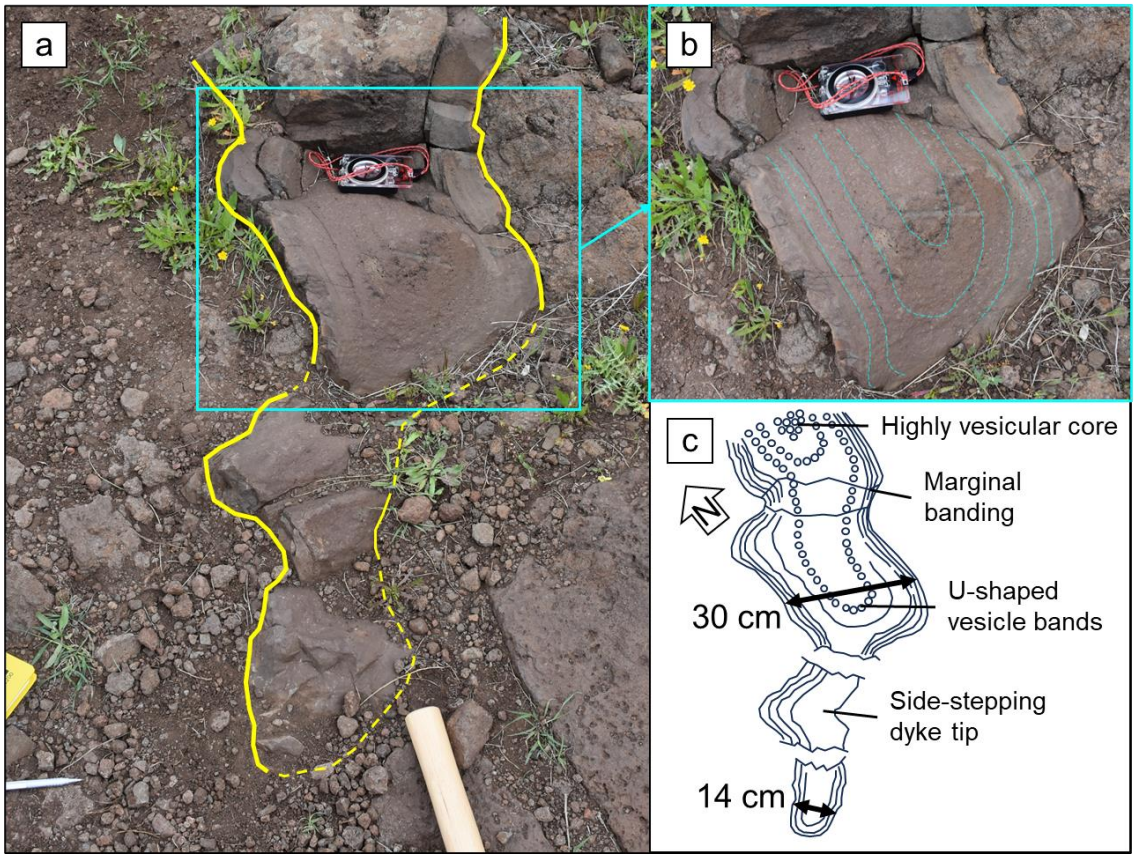

Figure 5.36. a) Dyke at the western end of the Carrizales Ridge with limited exposure, with banding defined by a variation in vesicularity. Several of these bands form concentric U-shapes ahead of the dyke tip; b) close-up of U-shaped vesicle bands; c) sketch emphasizing key features of outcrop.

5.5. Interpretation

5.5.1 Relative ages of dykes on the Carrizales Ridge

Before discussing the emplacement history of the dykes on the Carrizales Ridge, we should determine their relative ages. This will help us understand how the dykes might have influenced one another, in terms of their structure and internal textures.

The dykes D1, D3 and D4 run roughly parallel to the ridge with a strike of ~060°. However, D2 has a strike of 030° and cuts across all three, which provides some insight into their relative ages (Figure 5.3). Starting in the east, D2 intersects D4 (Figure 5.28), and we infer that their magma mingled within this intersection (Section 5.4.4). This suggests that they were emplaced in rapid succession, and although it is unclear which is older, the marginal textures are most similar to D2, making it most likely to have arrived first.

Moving west, D2 crosses D1 between segments 1.1 and 1.2, where the two dykes do not share a contact and remain separated by 20-cm-wide screens of host rock (Figure 5.28). The most likely explanation for this relationship is that D2 was emplaced first, and that D1 was prompted to split into segments due to the stress barrier that D2 created. It seems unlikely that D1 was emplaced first, as there is no significant deflection to the strike of D2 in this vicinity.

To the SW, D2 intersects D3. This is a simple cross-cutting relationship that proves D2 to be younger (Figure 5.22). In fact, the glassy margins on D2 within D3 prove that D3 must have cooled to be a similar temperature to the host rock, meaning that it precedes D2 by months or years, at least. As such, the relative age of dykes along the Carrizales Ridge, from oldest to youngest, is D3, D2, D4, then D1.

5.5.2 Across-width variations in texture

Many dykes in the region show variations in texture across their width. We investigated small-scale marginal banding in Chapter 4, interpreting the bands to be the result of pulsatory propagation at the dyke tip, at timescales of tens of minutes. By contrast, large-scale layering defined by sudden changes in composition, jointing patterns, or internal chilled margins is likely to form through discrete injections of magma with a significant time gap between them (Huppert and Sparks, 1989; Gudmundsson, 1984). However, between small-scale marginal bands and large-scale layers, we still see across-width textural variations in phenocryst and vesicle content, and these sub-layers must form on timescales somewhere in between.

When interpreting across-width variations in texture, we face a conundrum: did these textures exist in this formation while the dyke was actively flowing, or have they been produced by progressive inwards solidification capturing changes over time? Active flow processes such as flow differentiation can drive phenocrysts away from dyke margins, creating across-width variations in phenocryst

content that can persist until solidification (Chapter 4). However, the same texture can develop if the magma flowing through the dyke experiences an increase in phenocryst content over time. Both scenarios are plausible; indeed, they may have occurred simultaneously. To separate their effects, and to get a sense of timescales, we must consider the abruptness of across-width variations, and the existence or absence of internal chilled margins.

A chilled margin is a clear indication of a change in flow conditions. A reduction in grain size can only be produced if the dyke has been allowed to fully solidify, and an internal glassy margin can only be produced if the dyke cools to 278 °C (Section 4.6.3). Using the thermal model introduced in Section 1.6, we calculate the likely cooling timescales for the layers of D1. The outer layers of D1 are both 12 cm wide, and require intervals of a few days between injections in order to produce chilled margins on the next layer (Figure 5.37). These values are underestimates, because the model does not account for advection, which would delay dyke cooling and enhance host rock warming. It is therefore clear that a significant time gap is required between magma injections to develop internal chilled margins. Any fluctuations in flow that occur on shorter timescales should not be expected to leave a textural signature unless they involve a change in composition, or enhance flow differentiation.

We interpret chilled margins as evidence of a discrete magma injection episode, occurring after a significant time interval. Across-dyke textural variations that occur in the absence of chilled margins are therefore the result of fluctuations that occurred within a discrete injection episode.

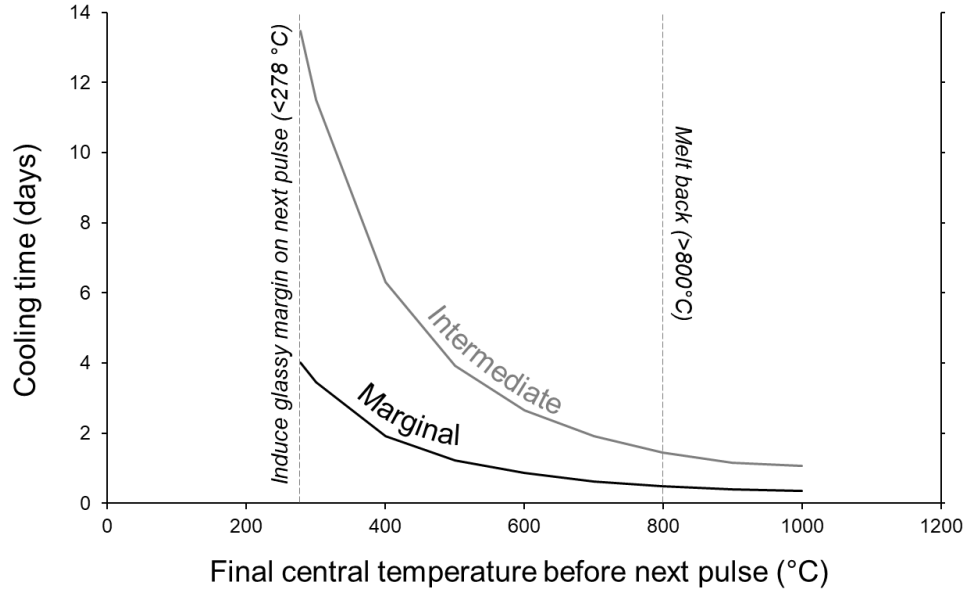

Figure 5.37. Estimating the cooling times of the outer layers of D1 (marginal and intermediate, both 12 cm wide) using the cooling model outlined in Section 1.6. Final central temperatures < 278 °C induce a chilled margin on the next layer, whereas temperatures > 800 °C cause melt back (Section 4.6.3).

Active flow textures may be distinguished from time-series textures by considering the variation in phenocryst size and concentration, and the abruptness of changes. For example, some sections of the central layer of D1 display sub-layering, oscillating from a high abundance of large phenocrysts to no phenocrysts, then to a lower abundance of small phenocrysts (Figure 5.12). This variation in phenocryst size could not have developed through flow differentiation alone, so the phenocryst content of the magma must have varied over time. Due to the lack of chilled margins between these sub-layers, we know that these variations occurred within a single injection episode, and due to the abrupt transitions between sub-layers, we know that the magma composition also changed abruptly during emplacement.

The distinction between active flow textures and time-series textures is most difficult when textural variations are gradual. For example, there are no or few clinopyroxene phenocrysts within 1-2 cm of the internal margin of the central layer of D1. The lack of phenocrysts at the margins could have been caused by flow differentiation (e.g., Gibb, 1968; Komar 1976), or the first magma to enter the fracture may have carried fewer phenocrysts.

In D2, the textures oscillate between phenocryst-rich and phenocryst-poor moving inwards from the margins, over distances of a few millimetres (Figure 5.23). Despite the lack of chilled margins, it is still possible that flow differentiation caused these variations. The solidification front would have been migrating inwards over time, and a sudden increase in magma flow rate would have driven phenocrysts away from this front. The alternative explanation is that the phenocryst content of the magma showed abrupt variations through time, from phenocryst-rich to phenocryst-poor.

Any across-width variation in textures is likely to result from pulsatory magma flow. Episodes of flow differentiation require fluctuations in magma flow rates, whereas abrupt changes in phenocryst content require a sudden change in the suspended phenocryst load, perhaps due to tapping a new source region. Both textures imply sudden changes, indicative of pulsatory flow through the dyke system. These pulses occur on timescales short enough to avoid producing a chilled margin, and we consider them to be fluctuations during a discrete magma injection episode.

5.5.3 Along-dyke variations in texture

As well as seeing variations across the widths of dykes, we see variations in texture along the strike of dykes. In these cases, the same question persists: were these variations present in this formation within the active system, or have they been created by a variation in solidification rates, controlling how long certain sections were active?

D1 shows a variation in sub-layering along the length of segment 1.4 (Figure 5.10). However, the sub-layering is only present for approximately 20 m of the 120 m segment, so the magma pulses responsible for the sub-layers must have passed only through this narrow region. This suggests that other regions of the segment had already cooled and sealed off before the pulses arrived. It is worth

noting that this 20 m section does not contain chilled margins or dendrite crystals at the edge of its central layer; in fact, the intermediate layer also contains clinopyroxene phenocrysts, suggesting that there might have been mingling between the central and intermediate layers here. We therefore infer that this section was active for the longest, and the lack of chilled margins and dendrite crystals implies that the higher advective flux caused it to remain hotter for longer than other regions.

Along-dyke variations in sub-layering provide compelling evidence for flow localisation during dyke emplacement. A segment is unlikely to cool at a uniform rate along its length, due to spatial variations in its width and flow rate. The balance between conduction and advection leads to positive feedback, where wider, hotter areas flow faster and cool more slowly, which causes flow to localise into these regions, meaning that they remain active for longer. We therefore conclude that this 20 m section of segment 1.4, containing additional sub-layering, is a place where flow localised. The full implications in the context of the wider dyke system will be discussed further in Section 5.6.

Another intriguing along-dyke variation is found towards the northern end of segment 1.4, where the clinopyroxene phenocrysts gradually decrease in size and abundance before vanishing entirely a few metres from the segment tip. This variation in phenocryst content may have resulted from gravitational settling as the magma flowed upwards through the dyke system.

Lateral variations in phenocryst content can be produced by gravitational settling wherever there is a lateral component to magma flow. Samples collected from the centre of segment 1.4 show that flow had a strong SW component, but also a downwards component (Section 5.4.1). Downwards flow would result in a net migration of phenocrysts to the NE, the opposite to what we see. An upwards component of flow is required to generate a net migration to the SW. However, flow near the tip of segment 1.4 may well have had an upwards component, and upwards flow is likely to be dominant in the dyke system as a whole. Indeed, the crystals may have settled and segregated in this manner before entering the segment.

We estimate the rate of phenocryst settling using Stokes Law. By approximating our clinopyroxene phenocrysts as spheres, their terminal velocity is given by

$$v_T = \frac{2}{9}\frac{\Delta\rho}{\mu_m} gR^2 \qquad \text{Eq. 5.1}$$

where $\Delta\rho$ is the density difference between the phenocryst and the melt (kg m^{-3}), μ_m is the viscosity of the melt (Pa s), g is gravitational acceleration (m s^{-2}) and R is the radius of the phenocryst (m). Assuming that clinopyroxene has a density of 3200-3600 kg m^{-3} (Deer et al., 2013) and that the melt has a density of 2700-3000 kg m^{-3} (Lesher and Spera, 2015), $\Delta\rho$ is between 200 and 900 kg m^{-3}. The viscosity of molten basalt at 1200 °C is likely to be around 10-100 Pa s (Lesher and Spera, 2015), and we approximate our clinopyroxene phenocrysts to have radii between 1 and 10 mm. The smallest crystals with the lowest density difference at the highest viscosity have a negligible settling velocity

(0.004 mm/s). However, the largest crystals with the highest density difference in the lowest viscosity magma have a settling velocity of 20 mm/s.

If we assume a magma flow rate of 0.5 m s^{-1} (Delaney and Pollard, 1982), at an angle of θ_m degrees from the horizontal, the resultant phenocryst velocity v_r will depend on the vertical component of magma flow v_{mV} minus the settling rate v_s. From the trajectory of settling phenocrysts, described by the angle from the horizontal θ_r, we calculate the distance s_m that magma must flow for the phenocrysts to migrate 1 m (Figure 5.38a). If

$$\theta_r = \operatorname{atan}\left(\frac{v_{mV} + v_s}{v_{mH}}\right) \quad \text{Eq. 5.2}$$

$$\Delta\theta = \theta_m - \theta_r, \quad \text{Eq. 5.3}$$

and

$$\theta_1 = 180 - \theta_m, \quad \text{Eq. 5.4}$$

we can use these angles to calculate the distance that the crystal has travelled

$$s_r = \frac{\sin\theta_1}{\sin\Delta\theta} \quad \text{Eq. 5.5}$$

and the lateral component of that distance

$$s_H = s_r \cos\theta_r. \quad \text{Eq. 5.6}$$

From this, we can find the distance that magma has flowed in order to drive 1 m of lateral phenocryst migration, where

$$s_m = \frac{s_H}{\cos\theta_m}. \quad \text{Eq. 5.7}$$

The rate of lateral migration is simply v_m/s_m. Figure 5.38b shows the calculated distances for a range of magma flow rates and inclinations, based on the highest settling rate of 20 mm/s. We find that it takes 4—2900 m of magma flow for crystals to migrate 2 m at flow angles from 1 to 89°. When flow is upwards, crystals migrate in same direction as the lateral component of magma flow, and they migrate faster as the flow direction approaches the horizontal. However, close to the horizontal or in downwards magma flow, the migration direction reverses. To generate the lack of phenocrysts near the northern tip of segment 1.4, flow must have had an upwards component, either within the segment, or prior to entering the segment. This along-dyke variation in phenocryst content is therefore likely to have been present within the active system.

(a)

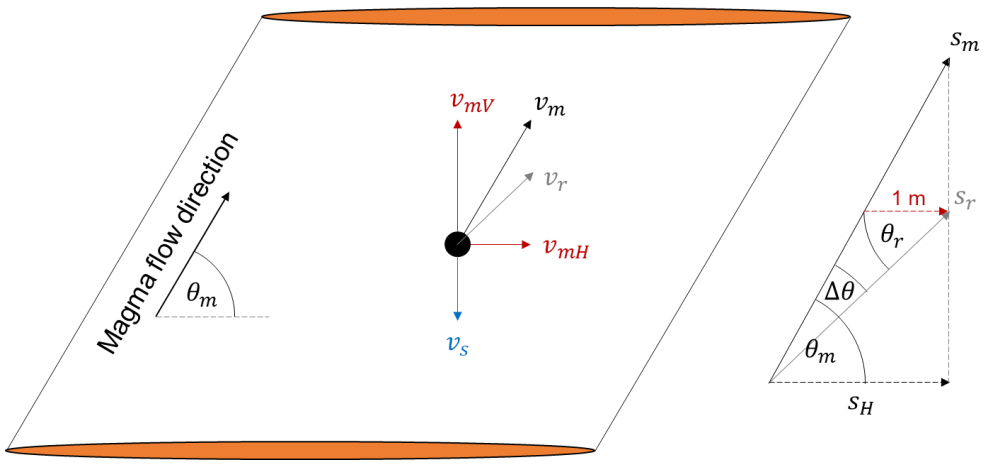

(b)

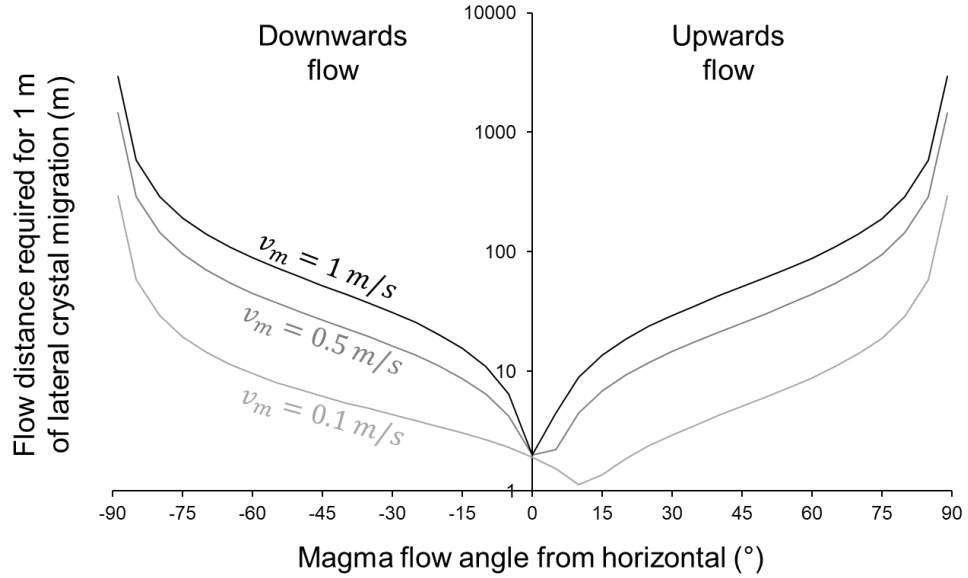

Figure 5.38. Demonstrating the feasibility of crystal settling in driving a lateral variation in phenocryst content: a) crystal settling during diagonal, upwards magma flow leads to a lateral component of phenocryst migration. Magma must flow distance s_m for crystals to migrate 1 m laterally; b) the flow distance required for various angles of magma flow to generate 1 m of phenocryst migration, based on the maximum calculated settling rate of 20 mm/s.

Dyke D3 also contained variations in textures along its length, in the vesicles in its central layer. We interpret the variations in vesicle orientations as a reflection of flow conditions in the final stages dyke emplacement. The central layer is likely to have taken days or weeks to solidify, and so the textures captured here reflect late-stage flow processes immediately prior to the dyke sealing shut. Reversals in recorded flow direction along the dyke are most likely to originate from late-stage convection currents once upwards flow ended, and the implications of this within the larger dyke system are discussed further in Section 5.6.

A final example of along-dyke variations in texture are the vesicle bands described in Section 5.4.4 (Figure 5.36). These are likely to be extensions of the marginal bands, but here we can see their relationship to the dyke tip. Each vesicular band represents a pressure drop associated with a magma pulse, but the concentric pattern shows that these pulses never breached previously solidified regions. Previously, we viewed magma pulses as a product of the dyke stalling temporarily, with each new pulse breaking through solidified material to let propagation continue. However, the textures at this tip suggest that here, the pulses did not provide the impetus for propagation to continue in a lateral, southwest direction. Each vesicle band moving inwards was likely associated with a magma pulse driving vertical propagation elsewhere in the segment, but here, lateral propagation had stalled. This demonstrates the extent of spatial and temporal variability in flow directions during the early stages of dyke emplacement.

5.5.4 Vesicle planes

The vesicle planes are a feature present only within the intermediate layer of D1 (Section 5.4.1). Previous studies into dykes on Tenerife and the nearby island of La Palma have reported similar features, where large, flattened vesicles are concentrated into narrow planes running parallel to the dyke margin (Delcamp et al., 2012; Thiele et al., 2021). It is not clear whether these are more like our vesicle planes or marginal bands (Chapter 4). Marginal bands get wider and less distinct towards the centre, whereas the vesicle planes occur further in from the margins, have an uneven spacing, and have sharp contacts with the surrounding material (Figure 5.16). As such, we infer that the vesicle planes have formed through a different process, at a later stage of dyke emplacement.

There is a stark textural difference between the vesicle planes and surrounding material, and a sharp contact between them. These contacts appear to have exerted control over the shape of the largest vesicles, which implies that the contacts acted as barriers while vesicles were growing. The material on either side of the planes must have been solid enough to resist bubble expansion, while material within the plane was molten enough to permit it. The planes and their surroundings must have been a similar temperature, as the planes are only a few millimetres wide, and the intermediate layer has intruded into pre-warmed surroundings, resulting in a shallower thermal gradient. It therefore appears that two melt compositions existed side-by-side, with the bulk material being much more viscous and

immovable than the material within the planes. For this to have occurred, we infer that the bulk material had a higher liquidus temperature than the planes, meaning that it started crystallising first. The difference in liquidus temperature is likely due to differences in volatile content, with the volatile-rich planes having a lower liquidus than the bulk material. As the dyke cooled, the vesicle planes remained molten longer than their surroundings, allowing the growing vesicles to press against solid walls (Figure 5.39).

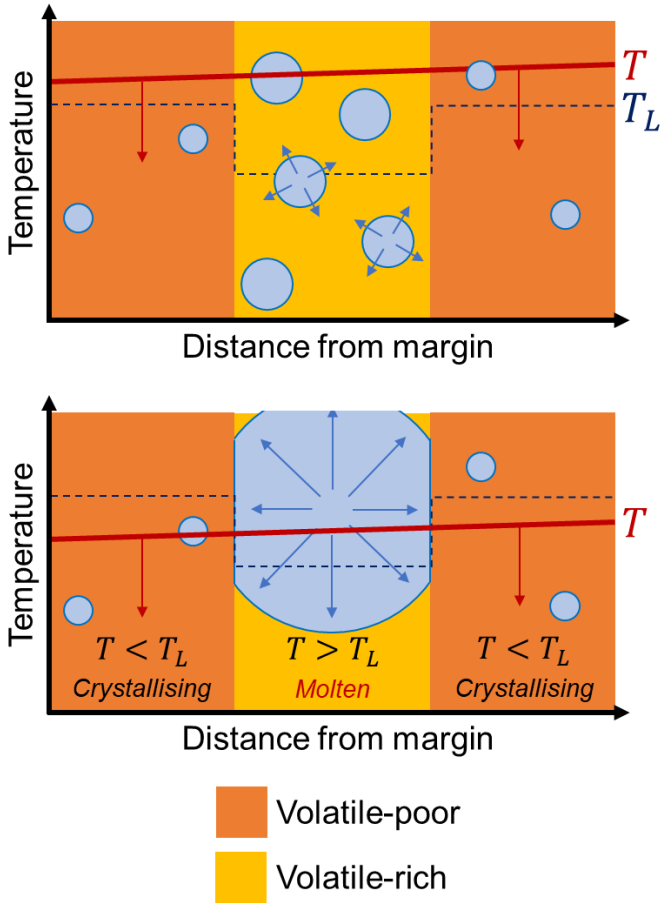

Figure 5.39. Vesicle plane formation schematic. Two magma compositions exist side-by-side without mingling under laminar flow conditions. At this distance from the margin, the thermal gradient is minimal. The volatile-poor magma starts to crystallise first as it has a higher liquidus temperature T_L, and this creates narrow planes of molten, volatile-rich material where bubble growth is restricted.

The source of these co-existing magma compositions is uncertain. In laminar flow, it is possible that "blobs" of magma with a slightly different composition could be streaked out parallel to the margins. Alternatively, the compositional difference was generated in situ by processes associated with flow or solidification. Our favoured explanation is that crystallisation at the solidification front excludes volatiles, which are largely incompatible with the crystal phase (Wallace and Anderson, 2000). As such, there is an increase in volatile concentration ahead of the solidification front, in a narrow boundary layer. As the volatile concentration in the boundary layer increases, its liquidus temperature decreases. Eventually, the magma will reach a temperature where material ahead of the boundary

layer starts to crystallise, while the boundary layer itself remains molten. Vesicles nucleating in the boundary layer press up against solidifying, highly viscous material on either side, resulting in compressed shapes constrained within the vesicle planes. The material within the plane experiences a smaller undercooling than the bulk material, which is why the crystals there are larger.

However the volatiles ended up concentrated within these highly localised regions, the vesicle planes indicate stable, laminar flow within the intermediate layer of D1. These narrow, planar features would have been disrupted if flow had been highly irregular or pulsatory. Therefore, we interpret the vesicle planes as evidence of steady magma flow within an established pathway.

5.5.5 Dendritic crystal layers

The internal chilled margins of D1, D2 and D4 contain black, dendritic crystals growing outwards from the margin towards the dyke centre. The dendrite crystals have two potential uses for interpreting the emplacement history of dykes, as they are indicators of flow direction and host rock temperature. The dendrites are inclined to the southwest, the same as other flow indicators, and they are only ever seen at internal margins, implying that they only grow in warmer environments, in a temperature window from which we can estimate the timings of magma pulses.

Crystals with a similar description to the dendrites have previously been called “comb crystals” and are often associated with comb layering at intrusion margins and around xenoliths (Katz and Keller, 1981; Breiter et al., 2005; McCarthy and Müntener, 2016). Comb crystals are feathery and elongated, and grow perpendicular to a contact, although they are often curved, and can be several millimetres to several decimetres long (Donaldson, 1977). Comb layers are typically found in plutons, but they have been seen in dykes (Taubeneck and Poldervaart, 1960; Moore and Lockwood, 1973; Kile, 1993) and sills (Dawson and Hawthorne, 1973), and pillow lavas (Lofgren and Donaldson, 1975). The comb crystals in the cited examples are formed from a range of minerals, including plagioclase, hornblende, pyroxene, calcite, quartz or olivine. From here, we use the term dendrites rather than comb crystals.

Dendritic crystals grow via heterogenous nucleation, using existing contacts within an intrusion. They grow parallel to the thermal gradient, and their growth is strongly related to cooling conditions (Donaldson, 1977). With significant undercooling, magma will crystallise rapidly via homogenous nucleation, and with even greater undercooling, it will form a glass. Therefore, dendrites can only form in relatively warm environments. Our observations support this, as we only found dendrites on internal contacts rather than the outermost chilled margins of dykes. Clearly, cooling rates at these internal contacts were slow enough to avoid producing glass.

We can estimate a likely range of emplacement timescales using our cooling model and magma properties outlined in Section 1.6. Taking the average width of the marginal layer of D1 to be 12 cm, it would take 4 days of cooling to induce a glassy margin on the intermediate layer. Anything less than 11.5 hours leads to melt back upon the arrival of the intermediate layer, and so the intermediate layer

was probably emplaced a day or so after the marginal layer (Figure 5.37). The intermediate layer also has an average width of 12 cm, but it takes longer to cool due to the warmth of the marginal layer. It would take around 13.5 days of cooling to induce a glassy margin on the central layer, whereas any time less than 1.5 days would lead to melt back. Therefore, it is likely that the central layer was emplaced a several days after the intermediate layer, and the dendritic crystals are likely to have grown in an environment with initial wall temperatures of 300-800 °C. Unfortunately, limited experimental data on dendrite growth means that we cannot narrow this window any further.

A deeper insight into the growth conditions for the dendrites can be ascertained from their relationship with the plagioclase microlites. The microlites appear to have been shunted aside by the encroaching dendrites, which strongly suggests that the plagioclase microlites grew first. We can validate this crystallisation sequence using MELTS (Gualda and Ghiorso, 2015), with a typical Teno alkali basalt composition (Thirlwall et al., 2000) and an estimated water content of 0.8-1.5 wt.% based on magma from neighbouring islands of La Palma and El Hierro (Weis et al., 2015). We find that plagioclase can crystallise before clinopyroxene at pressures < 5 MPa (Figure 5.40), and as such, it is possible that the clinopyroxene dendrites grew into a mushy zone of plagioclase microlites. However, it should be noted that the modelled differences in temperatures are minimal, and the dendrites clearly grew in non-equilibrium conditions.

Dendritic crystals in comb layers are often observed to be curved (Taubeneck and Poldervaart, 1960; Dawson and Hawthorne, 1973; Kile, 1993). This curvature has been observed to point upstream, towards the magma source (Moore and Lockwood, 1973), due to the flow-induced supersaturation gradient favouring growth on the upstream side of crystals (Lofgren and Donaldson, 1975). This may well be true for the oxide crystals in our Teno samples, as they always grow on the inferred upstream side of the clinopyroxene dendrites. However, the dendrites themselves show the opposite trend, curving southwest to point the same direction as other macroscopic flow indicators. It is possible that flow led to mechanical deformation and bending. Similar behaviour has been observed in metal casting, where dendrites can curve downstream due to mechanical deformation causing misorientations within the crystal lattice (Dragnevski et al., 2002). Whatever the cause of dendrite bending within our dykes, the dendrites are a useful flow indicator, as their curvature is more obvious than the preferred orientation of the groundmass or phenocrysts.

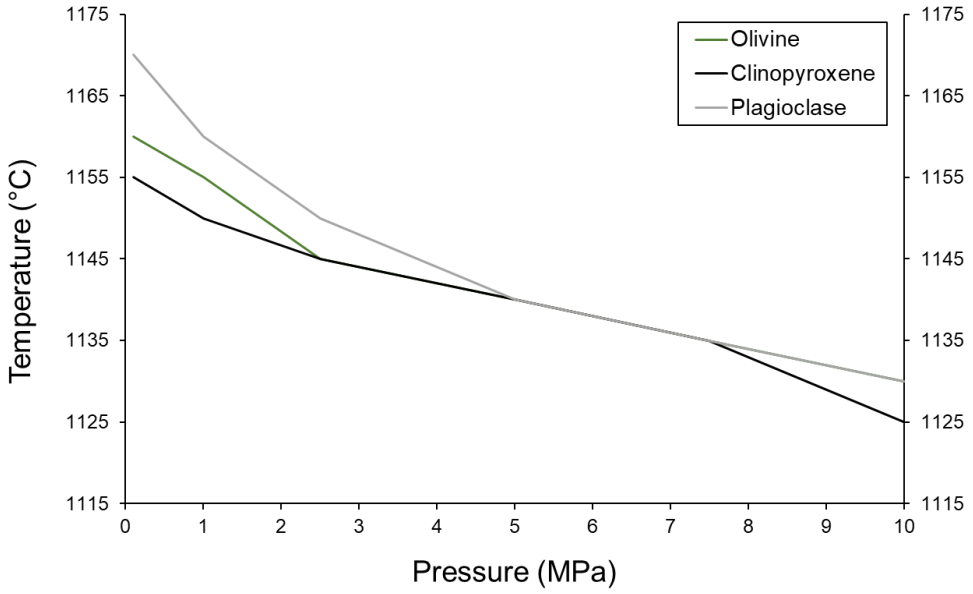

Figure 5.40. Results from MELTS, showing the temperatures and pressures at which mineral phases first appear. Plagioclase crystallises before clinopyroxene at pressures < 5 MPa.

5.6. Discussion

Dyke emplacement history is recorded at a range of scales, from large-scale segmentation patterns to small-scale rock textures. Combining the evidence from a range of scales allows us to infer a comprehensive story from initial crack propagation, to an established magma flow pathway, to the cessation of flow, within the context of the larger system.

5.6.1 Propagation directions

Dyke segmentation is very common in the Teno Massif region, and occurs at a variety of scales, from centimetre-wide offshoots (Figure 5.26; Figure 5.34) to metre-wide, kilometre-long dykes (Figure 5.9; Figure 5.33). Segmentation is commonly observed in dykes around the world, and it is now seen as the rule, not the exception (e.g., Pollard et al., 1975; Baer and Reches, 1987; Jolly and Sanderson, 1995; Airoldi et al., 2011). However, segmentation is usually only seen on either horizontal (e.g., MacDonald et al., 1988; Weinberger et al., 2000; Ray et al., 2007; Kiyosugi et al., 2012) or vertical exposures (e.g., Gudmundsson et al., 1999; Clemente et al., 2007), not both. The Carrizales Ridge therefore provides a valuable opportunity to study dykes along significant lateral distances and over a range of elevations. D1 is segmented in both horizontal and vertical planes, revealing a highly complex 3D structure consisting of segments limited in both horizontal and vertical extent.

Most observations of dyke segmentation are limited to the horizontal plane, and it is commonly inferred that individual segments connect back to a larger, continuous parent body at depth (Pollard et al., 1975; Galindo and Gudmundsson, 2012; Magee et al., 2019). As such, it is inferred that the dyke split into segments at its leading edge as it propagated upwards (e.g., MacDonald et al., 1988;

Weinberger et al., 2000; Airoldi et al., 2011; Ruz et al. 2020). The three-dimensional structure of D1 reveals that this could not have been the case along the Carrizales Ridge, as segments are limited in both their horizontal and vertical extents.

A key inference from dyke segmentation is the direction of magma flow. Clearly, if segments are separated in the plane of observation, the dominant magma flow direction was perpendicular to the plane. In other words, if we see segments on a horizontal surface, magma flow was dominantly vertical at the level of observation, and vice versa. In D1, we see segmentation on both horizontal and vertical surfaces, showing that magma flow directions varied along the dyke. In some areas (e.g., Figure 5.9) flow must have been dominantly lateral, whereas in other areas, flow must have been dominantly vertical (e.g., Figure 5.8). This suggests that the flow pathways between segments were tortuous and convoluted, rather than a simple conduit straight to the surface.

5.6.2 Dyke tip conditions

Dyke segmentation occurs at the leading edge of the active intrusion. Two main causes of segmentation are outlined by Pollard et al. (1975). Firstly, the leading edge of the propagating dyke may encounter pre-existing weaknesses in the host rock, such as faults, which can cause local variations in the speed and/or direction of propagation. Secondly, the narrow leading edge may develop instabilities due to cooling, which could promote segmentation (Pollard et al., 1975; Touvet et al., 2011). A third cause for flow-front instabilities is given by Baer and Reches (1987), who note that a dyke is likely to vary in width along its length, and that wider sections will flow faster and cool more slowly, advancing ahead of narrower sections and promoting segmentation.

Segmentation is often observed to show an en-echelon pattern, where each segment is offset in the same direction, at the same orientation. These patterns are commonly explained by a rotation of the regional stress field in the direction of propagation (Pollard et al., 1975). Dykes align perpendicular to the minimum principal stress direction, so a changing stress field can twist the orientation of the leading edge, and break the long, linear feature into offset segments with the same strike (e.g., Delaney and Pollard 1981; Hoek et al., 1991; Galindo and Gudmundsson, 2012; Magee et al., 2019).

The alignment of segments can reveal the processes controlling dyke propagation pathways. In an en-echelon arrangement, where segments have been oriented by the regional stress field, all segments will have the same strike, and there will be a consistent offset direction between them (Pollard et al., 1975). However, if the dominant control on segmentation was weaknesses in the host rock, such as faults, this consistency is less likely (Magee et al., 2019). In this case, segments may have different strikes, and offsets may be in either direction.

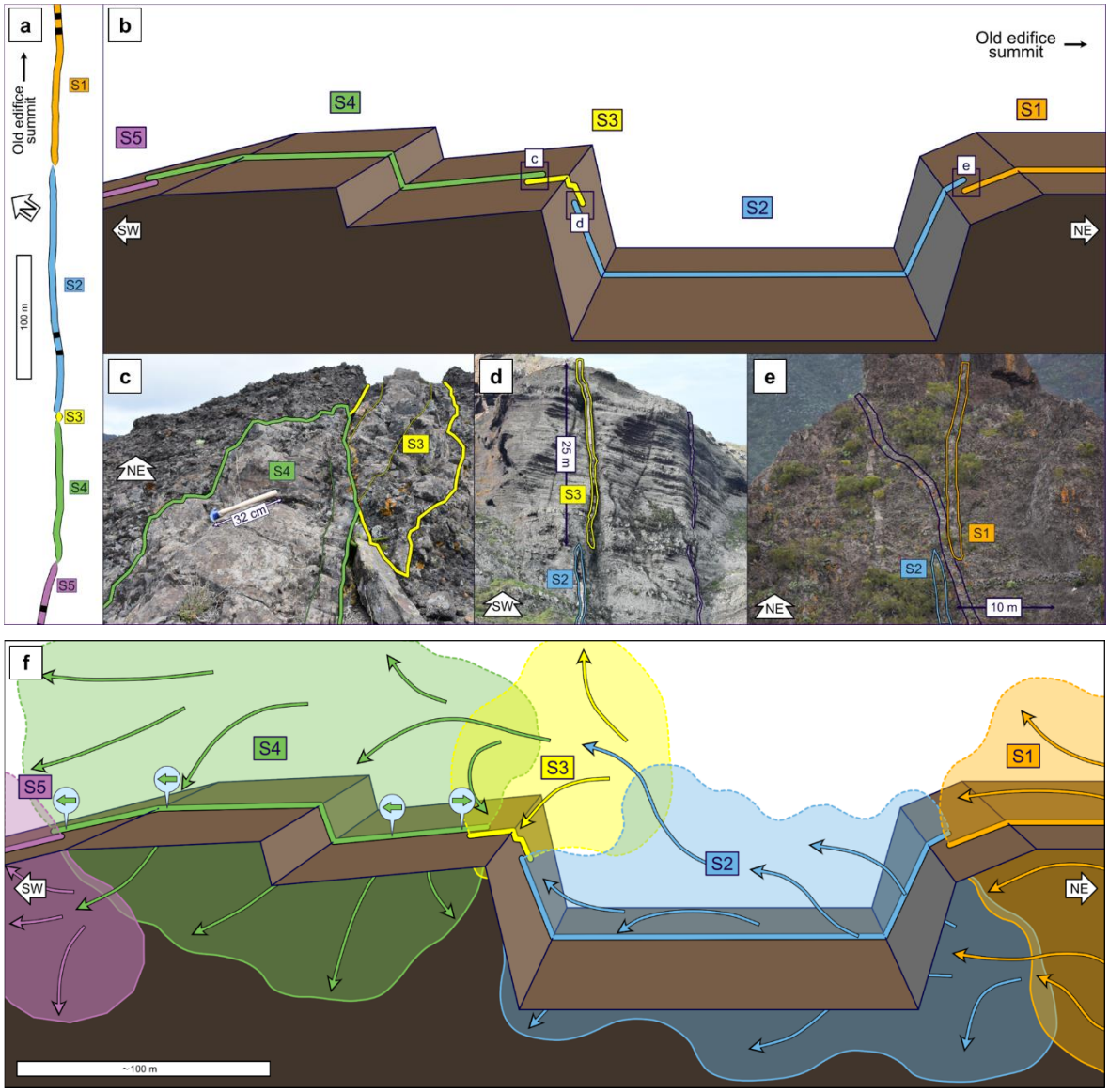

Figure 5.41. Layout of segments on D1: a) map of D1 segments; b) schematic representation of D1 segments; c) relay between S1.3-S1.4, facing NE; d) relay between S1.2-S1.3, facing SW; e) relay between S1.1-S1.2, facing NE; f) potential organisation of segments and flow directions in D1.

Numerical models for dyke propagation often overlook faults as a mechanism for guiding propagation, with most models focussing on regional stress fields (e.g., Muller et al., 2001; Watanabe et al., 2002; Menand et al., 2010; Gaete et al., 2019; Davis et al., 2021; Mantiloni et al., 2021) or lithologic discontinuities (Kavanagh et al., 2006; Maccaferri et al., 2010; 2011). This is despite many field observations of dykes following faults (Jolly and Sanderson, 1995; Valentine and Krogh, 2006; Galindo and Gudmundsson, 2012; Stephens et al., 2017; Mark et al., 2020).

Similarly, many analogue and numerical models overlook the impacts of cooling and solidification on propagation (e.g., Dahm, 2000; Maccaferri et al., 2016; Zia and Lecampion, 2020; Davis et al., 2021). The common justification for this omission is that dykes propagate at around 1-2 km per hour, whereas the time taken to solidify the entire width of the dyke is hours to days, implying that solidification is unlikely to halt or alter propagation (Rivalta et al., 2015). However, we demonstrated

in Chapter 4 that cooling in the narrow dyke tip can lead to pulsatory propagation, which means that instabilities are to be expected along the propagation front. Few numerical (Lister, 1994a; Bolchover and Lister, 1999) or analogue (Taisne and Tait, 2011; Pansino et al., 2019; Pansino et al., 2023) models have attempted to investigate solidification and propagation simultaneously, and so the influence of cooling and solidification on dyke emplacement is relatively unexplored.

All the major dykes studied on the Carrizales Ridge are segmented, and strike at 030-060° (Figure 5.3). However, there is no consistency in their segmentation. Some segments overlap with extensive relays, whereas other segments have no overlap (for example, compare relays in Figure 5.9). Some segments are offset, with various widths of host rock separating them, but other segments are not. These relays and offsets are crucial for determining the cause of segmentation, and the conditions at the propagating dyke tip.

On D1, the offset direction between segments is inconsistent (Figure 5.42), so segmentation was not dominated by a rotation of the stress field (Magee et al., 2019). Indeed, a consistent rotation in the stress field cannot explain the existence of segmentation in both horizonal and vertical cross-sections. The segmentation on D1 was therefore most likely controlled by host rock weaknesses. However, we found no evidence of D1 intruding faults. In one case, D1 appears to have segmented due to the presence of D2 (Figure 5.28), but in most cases, we infer that segmentation was driven by weaknesses that are no longer evident.

It may at first seem unlikely that segmentation could be driven by weaknesses that were so small they could be overwritten by subsequent inflation and deformation. However, we propose that the effects of these minor weaknesses are enhanced by cooling-induced positive feedback at the narrow dyke tip. Propagation pathways are established at the leading edge, which is highly susceptible to cooling, as we established in Chapter 4. This narrow crack, millimetres to centimetres in width, is likely to be influenced by small weaknesses within the host rock, even at a scale between individual clasts. These weaknesses exert the first control over the propagation pathway, and each one of these instabilities has the potential to cascade via positive feedback into the complex, three-dimensional structure we see today.

5.6.3 Creation and stability of segments

Our conceptual model for dyke segmentation is as follows. As the narrow crack fractures the host rock, following the path of least resistance, highly localised propagation directions will develop along the leading edge. The crack always opens against the minimum principal stress, which may show considerable variation at a clast-to-clast scale. As the leading edge propagates further ahead, the regions behind it start to inflate. Inflation prompts small segments to coalesce into a larger feature, which becomes increasingly influenced by regional or topographic stresses, rather than small-scale host rock heterogeneities. This results in a roughly planar feature oriented perpendicular to the

regional minimum stress direction, or aligned with large-scale weaknesses such as faults. Such a process is evidenced by the way that the outermost marginal bands follow the irregular, wavy margins very closely, but the bands become increasingly linear moving inwards, showing an evolution from an irregular to a linear morphology over time.

The small instabilities at the propagation front have the potential to cascade and influence the final dyke morphology, due to the amplification driven by thermal feedback. If a segment remains isolated for long enough that its edges cool and solidify, it is less likely to coalesce with neighbouring segments. There is probably a balance between the thickness of the solidifying walls and the internal pressures driving inflation and coalescence.

It is likely that certain rock types will lend themselves to segmentation more than others. Indeed, previous authors have noted differences in dyke morphology based on the host rock composition, and the presence of cleavage planes or fractures (Baer and Reches, 1987; Hoek, 1991; Jolly and Sanderson, 1995; Airoldi et al., 2011). The coarse, volcaniclastic rocks on the Carrizales Ridge are particularly likely to have led to irregular segmentation patterns, especially if the dykes intruded at a relatively shallow depth between large, poorly consolidated clasts.

The host rock also determines the mode of propagation. Where host rocks are unconsolidated, there is the potential for non-brittle deformation to occur, rather than a traditional brittle elastic fracture. These modes can be distinguished based on segment morphology, with non-brittle deformation leading to shorter segments with finger-like forms or blunt ends (Magee et al., 2019). These characteristics were particularly common in the Carrizales Valley, where dykes are sinuous with variable widths and blunt ends (e.g., Figure 5.34). These dykes exist within heavily altered scoria deposits, and it is likely that some amount of non-brittle deformation (e.g., fluidisation, melting or physical erosion of unconsolidated material) was involved in their emplacement.

The largest dykes on the Carrizales Ridge show no morphological evidence of non-brittle deformation. However, the narrow offshoots on D3 have sinuous, blunted forms (Figures 5.25 and 5.26), even though the main body of D3 does not. Given that all dykes start narrow and then inflate, it is worth considering whether the leading edge can intrude via non-brittle processes, then transition to traditional elastic fracture mechanics as the dyke inflates. If this is the case, evidence of non-brittle propagation at the dyke tip would always be overwritten by subsequent inflation.

We propose that segmentation can be driven by small-scale host rock weaknesses and non-brittle propagation processes, but the evidence is lost to subsequent inflation and deformation. However, the key factor in amplifying instabilities and allowing segmentation to persist beyond the leading edge is cooling in the narrow dyke tip. Wider areas flow faster and cool slower, so they are likely to propagate ahead of their surroundings and remain active for longer. As such, thermal feedbacks are crucial in

amplifying existing variations at the leading edge and allowing small instabilities to grow into segments.

5.6.4 The evolution of flow pathways

At any given time, the dyke is likely to be advancing on multiple fronts, establishing multiple segments. The three-dimensional architecture of D1 shows that propagation directions at the flow front were highly variable, and the result is a complex, branching structure with convoluted flow pathways between segments (Figure 5.41). However, not all pathways would have reached the surface. The segments are in natural competition, with thermal feedbacks always prompting the magma to localise from narrow, cold, slow-moving regions into wider, hotter, faster-moving regions.

We propose that the emplacement of the dykes on the Carrizales Ridge was analogous to the emplacement of a pahoehoe flow field (e.g., Hon et al., 1994; Peterson et al., 1994). The flow is always advancing on multiple fronts, but over time, preferential flow pathways will develop, as cooler, slower-moving regions seal off, and hotter, faster-flowing regions remain open. The process will be much slower in dykes compared to lava flows, due to differences in cooling rates. However, the same feedbacks will operate, just on longer timescales. Indeed, a similar idea has been applied to mafic sills, which have been shown through seismic reflection surveys to have a segmented structure and preferential flow pathways (Thomson and Hutton, 2004; Hansen and Cartwright, 2006). The architecture of these sills is remarkably similar to the Carrizales Dyke, but on a larger scale.

By contrast, the propagation model of Pollard et al. (1975) predicts that segments will eventually coalesce into a larger sheet. However, on the Carrizales Ridge we found limited evidence of segments coalescing. Segment coalescence is recorded by kinks or jogs along a dyke, and by protrusions close to these bends (Magee et al., 2019). No such features were found on the main dykes studied, and although sharp bends were observed in other dykes with limited exposure (e.g., Figure 5.34), it is difficult to distinguish whether these bends formed due to coalescence, or the original crack shape.

The lack of apparent coalescence implies that the segments remained separate and stable for the lifetime of the dyke. We can read further into the variations in flow conditions by examining the textures both across the width and along the length of segments. By our definition, layers are defined by internal chilled margins (e.g., Huppert and Sparks, 1989), cooling joints (e.g., Wada, 1992; Ray et al., 2007), or a sudden change in composition (e.g., Eriksson et al., 2011), and are typically centimetres to metres wide, whereas bands and sub-layers are defined by changes in phenocryst or vesicle size and abundance, with no chilled margins (e.g., Platten, 2000), and are typically millimetres to centimetres wide. We make this distinction due to the timescales involved. To develop a chilled margin, fresh magma can only arrive days or months after the previous layer finished solidifying, defining a separate injection episode. By contrast, bands and sub-layers are emplaced in rapid

succession, and are likely to result from perturbations within the same injection episode; for example, due to pulsatory flow in the dyke tip (Chapter 4).

The three layers within D1 suggest that each segment acted as a stable conduit for three separate injection episodes, around several days apart (Section 5.5.2). The solidified margins appear to have restrained the segments from coalescing into a larger sheet, which is at odds with the Pollard et al. (1975) model. Our dykes appear to have formed cold, solid margins quickly enough to restrict any further coalescence from occurring.

Within D1, variations in sub-layers along the length of segment 1.4 reveal the location of a preferential flow pathway. The region with additional sub-layering (Figure 5.10) is likely to have remained active for longer, and in the broader context of segmentation, this is probably where magma flow became focussed, feeding the leading edge while the rest of the segment sealed shut.

Sub-layering is not just a record of the longevity of flow pathways, but a reflection of a pulsatory propagation process. The evolution of segments is likely to promote pulsatory flow, as well as changes in flow rates and flow directions through time, both of which will result in textural sub-layers. The variations in phenocryst content and internal margins are both likely to result from fluctuations in magma flow rate related to the opening and closing of segments and flow pathways.

5.6.5 Late-stage circulation and cessation of flow

We infer that the dykes along the Carrizales Ridge were emplaced at relatively shallow depths, and so it is likely that some of them reached the surface and fed fissure eruptions. In the context of our conceptual model of propagation and segmentation, the localisation of fissure eruptions (e.g., Richter et al., 1970) is the surface expression of preferential flow pathway development. It is possible that the overall structure of the magmatic plumbing system, resulting from complex segmentation, might impact the behaviour of the eruption, both in terms of the longevity of fissures, and in the distribution of volatiles throughout the system.

Once an eruption ends, or dyke propagation stalls, a large volume of liquid magma remains in the dyke system. This will eventually solidify to form the core of the dyke, and so textures in the dyke centre are likely to represent late-stage processes, captured over the longest times. In many cases, the dykes on the Carrizales Ridge have markedly different textures in their centre compared to their edges, but contain no internal chilled margin separating their sub-layers. This is found in D3 and D4, and in numerous other dykes in the region. The lack of internal chilled margins suggests that these dykes formed in one injection episode, but experienced a change in behaviour, most likely associated with the dyke system sealing shut when the eruption ended, or when propagation stalled. The central vesicles are much larger than those in the margins because they had longer to coalesce at the point of observation once flow ended.

Within D3, vesicles have captured local variations in magma flow direction (Figure 5.27), which can oscillate over distances of several metres. These flow reversals are likely to reflect late-stage convection within the dyke system once the segment had sealed off, leaving a stagnant, self-contained pocket of magma. By contrast, the flow directions indicated by the preferred orientations of clinopyroxene phenocrysts in D1 show no such reversals. In D1, it appears that the flow direction through the segment remained constant until it sealed shut, implying that the segment gradually closed while magma continued to flow through the system. This is possibly due to the central layer of D1 being emplaced through an established, insulated flow pathway, allowing it to remain active for longer. The difference between the centres of D1 and D3 suggests that a dyke intruding through the centre of another recently emplaced dyke is more stable, and may be more likely to reach the surface. By contrast, D3 established its own pathway through cold host rock, and it presumably contained narrower sections vulnerable to sealing shut.

5.7. Dyke emplacement model

Our model for dyke emplacement adds a new level of complexity to existing models (e.g., Pollard et al., 1975; Poland et al., 2008; Townsend et al., 2017). Propagation is guided by processes in the narrow dyke tip, where segmentation is influenced by host rock weaknesses, then amplified and reinforced by thermal feedbacks. We predict a dynamic interplay between segments and flow localisation, with cooling and flow rates controlling the longevity of channels and their ability to supply further propagation. The dyke will propagate on multiple flow fronts, in natural competition, and this will lead to the development of preferential flow pathways, meaning that flow directions vary spatially and temporally.

The planar nature of the dyke will materialise as it self-organises towards energy efficiency. As the dyke inflates, it transitions from a regime controlled by small-scale, local stresses within the host rock to a regime controlled by regional stresses or large-scale host rock weaknesses such as faults. Over time, the dyke will adopt an orientation perpendicular to the minimum principal regional stress direction, and evidence of small-scale weaknesses may be overwritten by deformation and segment coalescence. However, planar features are not thermally efficient, so magma flow should be expected to localise into wider, faster-flowing sections.

Preferential flow pathways through the dyke system can remain stable and active for a long time, as evidenced by the multiple injection events through D1. Dyke margins will progressively cool and thicken, reinforcing segments against coalescence. As such, a dyke can maintain a segmented structure for long enough that it can be reused by multiple magma injections. We predict a balance between cooling rates and segment stability; perhaps, at great depths where dykes cool more slowly, coalescence into a contiguous sheet is favoured. However, in the shallow subsurface where cooling is

faster and host rocks are unconsolidated and heterogenous, segment formation and stability will have a significant impact on the transport of magma towards fissure eruptions, and on the behaviour of the eruption itself. Our model is outlined in Figure 5.42.

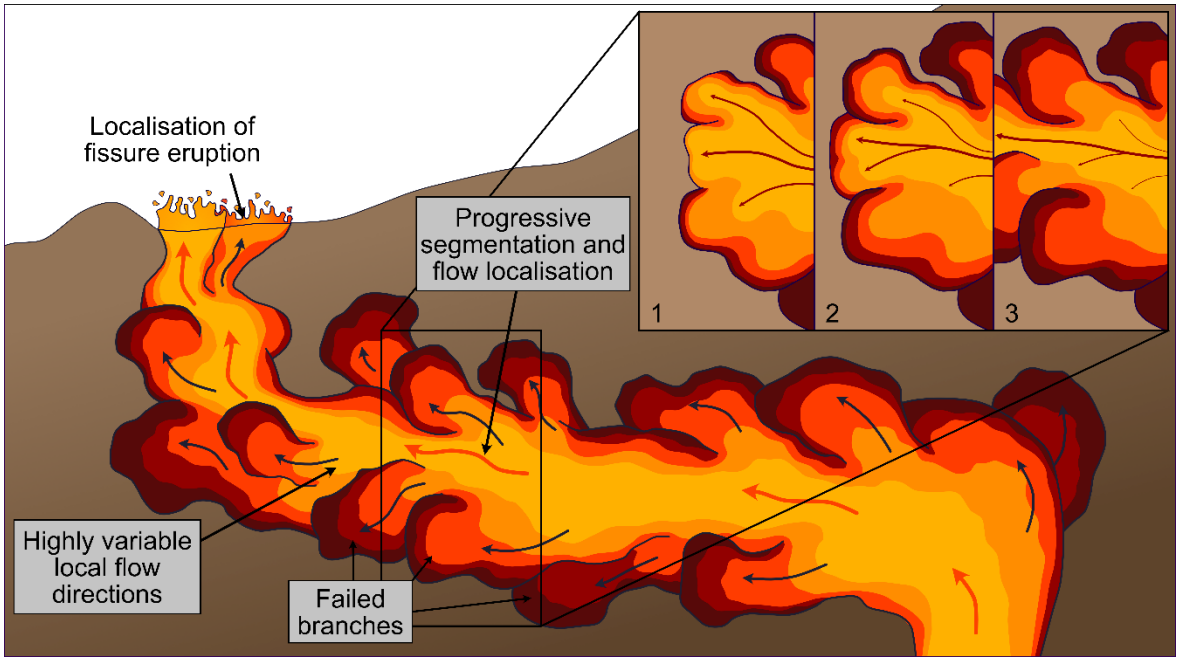

Figure 5.42. Our model for dyke emplacement. At the largest scale, dyke propagation is guided by the regional stress field. Along the narrow leading edge, interactions between host rock weaknesses and thermal feedbacks lead to segmentation. Flow localises naturally, forming preferential pathways through the dyke system and leaving behind failed branches.

5.8. Conclusion

The dykes on the Carrizales Ridge demonstrate the complexity of the magmatic plumbing systems feeding fissure eruptions. Dykes in the shallow subsurface have a complex three-dimensional architecture, and show variations in flow rates and directions with distance and time. The reality appears to be very different from the common understanding of dykes, which are often drawn as simplistic, planar features. Instead, we see a more convoluted network of flow pathways, which experience pulsatory magma flow as sections open up or seal shut.

Our model for dyke propagation via preferential flow pathways has numerous implications. Firstly, when interpreting dyke segments in the field, it should be appreciated that segments may be limited in their vertical as well as their horizontal extent, and that flow directions within segments may have varied spatially and temporally. This should also inform the interpretation of rock fabrics, as flow direction will depend on the position of a sample relative to the ends of a segment, and across the width of the dyke. Our model also provides additional context for interpreting seismicity during dyke emplacement. Previous studies of seismicity have suggested that propagation may occur on multiple fronts, at different rates, involving stalling and restarting (White et al., 2011; Woods et al., 2019), and the architecture of the Carrizales Dyke shows that this is likely to be the case.

Finally, this style of propagation and flow localisation, analogous to the emplacement of pahoehoe lava fields, is likely to influence the behaviour of fissure eruptions at the surface. The localisation of fissure eruptions is the surface expression of flow localisation occurring at depth. Additionally, the structure of the flow pathway may influence the way magma degasses, by controlling the transport of bubbles and gas slugs.

With our model of dyke emplacement, we want to challenge the common conception of dykes, especially the oversimplification to a single, planar structure, and the overlooking of thermal feedback in guiding propagation. Future analogue and numerical studies could investigate the effects of simultaneous propagation and cooling, while studies of seismicity during dyke emplacement will shed light on the active process.

Chapter 6

Summary and conclusions

6.1. Introduction

This thesis has explored various lines of evidence for interpreting dyke emplacement processes, from the small-scale development of crystal and vesicle textures to the large-scale evolution of dyke segments. The main aim of this thesis was to relate dyke textures to magma flow conditions, then use this to build a conceptual model for dyke emplacement, from initial crack propagation through to the cessation of magma flow. In this chapter I will summarise the findings in the context of the thesis aims, then explore their implications and potential applications. I will also identify questions raised during the course of this work, and highlight opportunities for further research.

6.2. Summary of findings

6.2.1 Crystal alignment as a strain-rate indicator

Elongated, non-interacting particles within simple shear flow show a greater degree of alignment when they are captured by a migrating solidification front, compared to when they are observed under isothermal conditions (Section 2.5). The additional alignment caused by solidification is predicted by a characteristic strain, which balances the length of particles, the strain rate ahead of the solidification front, and the migration rate of the solidification front (Eq. 2.24). This relationship was established in analogue experiments, where mica flakes (volume fraction < 0.01) were suspended within molten sugar as an analogue for phenocrysts suspended within magma. The sample was sheared as it progressively solidified, mimicking the capture of textures within an actively flowing dyke. The link between particle alignment and characteristic strain (Figure 2.25) demonstrates the potential for relating the degree of phenocryst alignment to magma strain rates within dykes, where the thermal history can be inferred.

6.2.2 Vesicle shape as a product of flow history

The shapes and orientations of vesicles are a product of flow history. However, vesicle shapes cannot be assumed to represent flow conditions in the molten channel, or immediately prior to solidification (Section 3.5). Bubbles within magma are out of equilibrium with the flow conditions by the time they are captured as vesicles, and the extent to which they are out of equilibrium depends on the rate of change in flow rate, and the rate of solidification. These findings come from analogue experiments on progressively solidifying molten sugar containing steam bubbles, and may be summarised as follows:

- Spherical vesicles can form at the margins of dykes even if strain rates are high, as they solidify so rapidly that they don't have sufficient opportunity to deform.
- If strain rates are *increasing* ahead of the solidification front, then bubbles are in a constant state of stretching. This may occur if the channel narrows but driving pressures remain high.
- If strain rates are *decreasing* ahead of the solidification front, then bubbles are in a constant state of relaxing towards spheres. This will occur as the magma cools and viscosity increases, dampening strain rates ahead of the solidification front.
- Spherical vesicles can be captured within an actively flowing dyke if the balance between solidification rate and shear stress allows them to relax before capture. Spherical vesicles do not necessarily indicate stagnant magma.

6.2.3 Marginal textures reveal propagation processes

Dyke margins solidify in the dyke tip, so they are a record of dyke tip flow processes associated with propagation. Banded textures in dyke margins indicate pulsatory flow, suggesting that the tip propagates in a stepwise manner, likely driven by a cycle of cooling, stalling and rupturing (Section 4.6). These banded textures are relatively common, found in volcanic settings around the world, but our work focusses on two examples: one from the Teno Massif, Tenerife, and one from the Columbia River Basalt Province. Dyke margins have been largely underutilised as a means for investigating dyke tip processes, but they provide crucial evidence for the shape of the initial crack and the flow of magma within it. We use a 1D conduction model to estimate that magma pulses occur on timescales of tens of minutes, from which we infer that the narrow dyke tip is highly susceptible to thermal feedback, with implications for the evolution of the dyke system (Section 4.6.3).

6.2.4 Textural layering in the context of dyke structure reveals large-scale flow processes

Dyke textures reveal the most about dyke emplacement processes when they are interpreted in the context of the larger, segmented dyke structure. Dykes in the Teno Massif, Tenerife, contain textural layering and sub-layering that indicates pulsatory flow, and the frequency of pulses can be estimated based on the presence of internal chilled margins. On one dyke, the number of sub-layers varies with distance along the segment, indicating that some regions witnessed more magma pulses than others. We interpret these variations in layering as evidence of the duration of flow, from which we infer progressive flow localisation within the segment (Section 5.5). Through a combination of textures and structural evidence, we develop a conceptual model for dyke emplacement, where segmentation is driven by host rock weaknesses and thermal feedback, and where flow is continually localising into stable, long-lived channels, analogous to the emplacement of a pahoehoe lava field (Section 5.7).

6.3. Implications, potential applications, further research

6.3.1 Interpreting textures: macroscopic, microscopic, AMS

Crystal alignment and vesicle orientations are commonly used as indicators of magma flow direction, but the experiments presented in Chapters 2 and 3 demonstrate their potential as indicators of strain rate where thermal history can be estimated. Our conceptual model for phenocryst alignment also suggests that the balance between strain rate and solidification front advance should influence the angle of crystal imbrication in the absence of collisions, although we found no evidence for this in our experiments (Section 2.4).

Using the angle of imbrication to infer strain rates would be a game-changer for dyke studies. This could be used to interpret shape preferred orientations measured in thin sections, and also the comparatively rapid AMS measurements used as a proxy for crystal alignment. There are reports of imbrication angles increasing away from dyke margins (e.g., Shelley, 1985; Ross, 1986) or depending on dyke width (e.g., Knight and Walker, 1988), which suggests that cooling and strain rate are having an influence. Our conceptual model predicts that imbrication angles will be higher and the degree of alignment will be lower at smaller characteristic strains, when magmatic strain rates are low, or when the advance rate of the solidification front is high (Section 2.5). This could be tested in further experiments, to determine if imbrication can develop in the absence of particle collisions.

Future studies into the effects of solidification on particle alignment should account for particle interactions. Our experiments are at such low volume fractions (< 0.01) that particles rarely interact, either physically or hydrodynamically, and although this may be analogous to phenocrysts, it cannot describe the conditions experienced by groundmass crystals, which grow and rotate in close proximity. In order to fully understand the imbrication angles seen in groundmass textures or AMS, the effects of crystal collisions must be explored. This has been done in fluids that were sheared then rapidly solidified (e.g., Vona et al., 2011; Arbaret et al., 2013), but not in fluids that progressively solidify as they are sheared.

Finally, our analogue experiments with vesicles demonstrate that vesicle shape is a product of flow history (Section 3.4). Vesicles are more complicated than phenocrysts, because while particles maintain their alignment when flow stops, bubbles relax back to spheres. However, this is not to say that vesicles cannot be interpreted. Numerical models such as the one presented by Ohashi et al. (2018) show great promise for inferring bubble deformation histories if they can be modified to include a viscosity that increases over time. Any single vesicle shape may have been created by a range of possible flow and cooling conditions, but in theory the dyke flow history can be narrowed down by considering the shapes of neighbouring vesicles, which have experienced the same conditions but responded differently due to their sizes. Our analogue experiments show great promise for investigating vesicle shapes. Further work should cover a greater range of flow and cooling

conditions, and the same method could be used on other solidifying fluids such as molten glass, which has properties similar to magma.

6.3.2 Sampling dykes: consider position and age

A central concept of this thesis is that dyke textures should be read as a time-series. Textures in the margins capture flow processes within the propagating dyke tip, when cooling is significant and the solidification front migrates inwards rapidly. Moving towards the dyke centre, it becomes harder to estimate the age of textures because the migration rate of the solidification front depends on the advection rate. Many AMS studies take samples within 10 cm of the dyke margin, following Tauxe et al. (1998). These textures capture the initial flow direction at a given position within the dyke system; however, our conceptual model suggests that initial flow directions may be highly localised before the dyke inflates into a wider, planar feature (Section 5.6). As such, multiple samples should always be taken along the lengths of dykes to capture the general propagation direction, and samples collected near segment terminations should be treated with particular caution.

For studies that examine variations across the widths of dykes, rather than focussing on the margins, we still recommend that, where possible, transects are recorded at multiple positions along the length of the dyke, paying particular attention to segmentation. This may provide more insight into the flow dynamics of the system; for example, if there was any progressive flow localisation.

6.3.3 Dyke tip processes: the first control on propagation dynamics

In Chapter 4 we used banded textures in dyke margins to infer pulsatory magma flow through the dyke tip, driven by a cycle of cooling, stalling and rupturing. Field evidence suggests that dyke tips are very narrow, sometimes only millimetres to centimetres. This is reflected in narrow dykes which failed to inflate, and in the irregular margins of wider dykes, which suggest that the initial crack followed a narrow and convoluted route around clasts in the host rock. These findings provide crucial evidence for dyke tip processes, which are integral to models of dyke propagation.

Most current dyke propagation models operate in the framework of LEFM, and they assume relatively simple crack shapes filled with isothermal fluids. However, because the dyke tip is always cooling rapidly, it has a variable viscosity and is prone to solidification (Section 4.6.3). This must influence the way that magma pressures are imparted on the host rock. There have been few studies on the propagation of solidifying fluids, and none have focussed on the efficacy of stress transfer from the fluid to its surroundings. This is a key area for further research. If solidification is having a significant impact, propagation models may need to use a “modified” or “apparent” fracture toughness, for example, to capture the combined effects of host rock and solidification resisting fracture.

It could be argued that small-scale perturbations in the dyke tip are insignificant in the context of the larger-scale propagation captured by models. However, current models cannot capture the apparent bursts in propagation captured by seismic signals (e.g., Woods et al., 2019), and neither can they

reproduce morphological features such as segmentation. Only analogue experiments in granular materials (e.g., Galland et al., 2006) or using solidifying fluids (e.g., Taisne and Tait, 2011) have captured these characteristics. Therefore, it would seem that the next step in refining dyke propagation models is to establish the significance of thermal feedback and non-brittle intrusion mechanisms operating at the dyke tip. Current propagation models may be successful in forecasting potential pathways based on regional stress fields, but dyke-tip dynamics may be crucial to determining whether a dyke will reach the surface.

6.3.4 Relating solid products to active processes: dyke width

Dyke propagation models are based on our mental image of dyke structure. Within LEFM, the shape and dimensions of a crack control its fracturing capability, and cracks are commonly assumed to have simple, elliptical shapes, which broadly resemble the tapering dyke geometries often seen in the field. However, this raises a key question: how closely do solidified dykes resemble the shapes of active, magma-filled cracks? Dyke textures provide some clues.

As discussed in Section 4.6, all dykes must inflate, growing in width as the dyke tip moves further from the point of observation. Marginal material solidifies relatively rapidly, but once the dyke insulates itself with thick margins within warmed host rock, and once it has inflated and increased the advection of heat through its centre, the solidification front will advance at a much slower rate. In Section 3.6, we proposed that if the rate of advance of the solidification front matched the rate of inflation, the dyke could accumulate material while retaining a molten channel of a constant width (Figure 3.18). It is almost impossible to estimate the width of the molten channel relative to the final width of the solidified dyke. If the dyke kept inflating, then the channel was always narrower than the final width, but we must also consider that the dyke may have deflated (e.g., Kavanagh and Sparks, 2011), in which case the channel may have been wider.

This discrepancy between active dykes and solidified dykes is a critical problem for the interpretation of dyke geometry. It complicates the calculation of magma pressures from dyke widths (e.g., Daniels et al., 2012), and the use of conduction models to estimate cooling times (e.g., Honour et al., 2019). The approximate widths of active dyke intrusions have been estimated from ground deformation (e.g., Montgomery-Brown et al., 2011; Smittarello et al., 2019) – but how do these estimates relate to the final, solid width that may be exposed at the surface in millions of years? Numerical and analogue models justify their crack dimensions and scaling against field measurements of solidified intrusions, but the reality is that we know very little about the shapes of propagating cracks, despite this being crucial to fracturing and cooling dynamics.

Parallels can be drawn between the emplacement of thick dykes and the emplacement of thick lava flows. The debate as to whether thick lava flows were emplaced at once as enormous, turbulent flows, or over time, as repeated, smaller-volume injections eventually tipped in favour of the latter argument

(Wolff et al., 2015). However, the debate around wide dykes has not been so energetic. Some authors have proposed that wide dykes were emplaced as wide, molten cracks hosting turbulent flow (e.g., Macdonald et al., 1988), but wide, composite dykes are always assumed to have formed through multiple injections (e.g., Eriksson et al., 2011). Interpretations vary based on perceptions of active dyke structures and processes. There is a clear need for us to understand the potential widths of active intrusions, and crystal and vesicle textures could provide some of the answers. Even in the absence of obvious layers defined by composition or cooling joints, textures can be used to indicate magma pulses, providing some insight into the rate of dyke emplacement.

The marginal bands in Chapters 4 and 5 allow us to infer the shape of the dyke tip and the rate of dyke inflation. Most dyke margins in the Teno Massif are irregular, suggesting that the initial crack was narrow and convoluted, deflected around individual clasts in the host rock. Where bands are present, they become straighter towards the dyke centre (Figure 4.1). We estimate that each of these bands formed on timescales of tens of minutes; therefore, the transition from dyke tip to dyke body, which occurs via several magma pulses, takes several tens of minutes. Further work on dyke margins and segment terminations could reveal more about the width of the dyke tip region. There is even the potential to relate the behaviour observed at the onset of fissure eruptions (i.e., the rate at which cracks appear, gas emissions increase, and lava starts to erupt) to the shape of a propagating dyke.

6.3.5 Dyke architecture: influencing eruption likelihood and behaviour

Our conceptual model proposes that segmentation is triggered by host rock weaknesses, then amplified and stabilised by cooling and thermal feedback (Section 5.7). These dynamics control dyke structure, which then influences the propagation pathway and the likelihood and behaviour of eruptions. We introduce the term “architecture” to imply some level of creation and design, because the dyke both responds to its surroundings and builds its own plumbing network. The initial interpretations of seismicity and ground deformation during active emplacement are based on the concept of dyke structure. Therefore, interpretations could be improved by a better understanding of dyke architecture, and by considering the dynamics involved in dyke segmentation.

Our conceptual model is analogous to a pahoehoe flow field, and we envisage dyke segments as lobes extruding from a flow front, or as breakouts from upstream. High-resolution seismic datasets could reveal whether the number or spatial distribution of segments at the flow front is related to the overall rate of propagation, or to the likelihood that the dyke reaches the surface. For example, if a dyke is consistently producing segments at the flow front, its path will look very different to a dyke which often produces “breakout” segments further upstream. In an ideal world, this could be established from seismicity during dyke emplacement, and we might have a better gauge of eruption likelihood, perhaps even the eruption duration, and how earlier dykes may interact with later intrusions.

Reference List

Abbott, J.R., Tetlow, N., Graham, A.L., Altobelli, S.A., Fukushima, E., Mondy, L.A., and Stephens, T.S., (1991) Experimental observations of particle migration in concentrated suspensions: Couette flow. *Journal of Rheology*, 35(5), 773-795. https://doi.org/10.1122/1.550157

Allgood, C., Llewellin, E.W., Humphreys, M.C.S., Mathias, S.A., Brown, R.J. and Vye-Brown, C. (2024) Banding in the margins of basaltic dykes indicates pulsatory propagation during emplacement. *Journal of Geophysical Research: Solid Earth*, 129(4), p.e2023JB028007. https://doi.org/10.1029/2023JB028007

Allgood, C., and Mathias, S.A. (2023) Banding in the margins of basaltic dykes indicates pulsatory propagation during emplacement [dataset]. *Durham University Collections*. http://doi.org/10.15128/r2sb397832j

Airoldi, G., Muirhead, J.D., White, J.D. and Rowland, J. (2011) Emplacement of magma at shallow depth: insights from field relationships at Allan Hills, south Victoria Land, East Antarctica. *Antarctic Science*, 23(3), 281-297. https://doi:10.1017/S0954102011000095

Ancochea, E., Fuster, J., Ibarrola, E., Cendrero, A., Coello, J., Hernan, F., Cantagrel, J.M. and Jamond, C. (1990) Volcanic evolution of the island of Tenerife (Canary Islands) in the light of new K-Ar data. *Journal of Volcanology and Geothermal Research*, 44(3-4), 231-249. https://doi.org/10.1016/0377-0273(90)90019-C

Ancochea, E., Hernán, F., Huertas, M.J., Brändle, J.L. and Herrera, R. (2006) A new chronostratigraphical and evolutionary model for La Gomera: implications for the overall evolution of the Canarian Archipelago. *Journal of Volcanology and Geothermal Research*, 157(4), 271-293. https://doi.org/10.1016/j.jvolgeores.2006.04.001

Arbaret, L., Diot, H. and Bouches, J-L. (1996) Shape fabrics in low concentration suspensions: 2D analogue experiments and application to tiling in magma. *Journal of Structural Geology*, 18(7), 941-950. https://doi.org/10.1016/0191-8141(96)00011-9

Arbaret, L., Bystricky, M. and Launeau, P. (2019) Crystal clustering in magmas: Insights from HP–HT experiments. *Comptes Rendus Géoscience*, 351, 574-585. https://doi.org/10.1016/j.crte.2019.10.004

Arbaret, L., Launeau, P., Diot, H. and Sizaret, S. (2013) Magnetic and shape fabrics of magnetite in simple shear flows. *Journal of Volcanology and Geothermal Research*, 249, 25-38. https://doi.org/10.1016/j.jvolgeores.2012.09.003

Arbaret, L., Mancktelow, N.S. and Burg, J-P. (2001) Effect of shape and orientation on rigid particle rotation and matrix deformation in simple shear flow. *Journal of Structural Geology*, 23, 113-125. https://doi.org/10.1016/S0191-8141(00)00067-5

Arbaret, L., Mystricky, M. and Champallier, R. (2007) Microstructures and rheology of hydrous synthetic magmatic suspensions deformed in torsion at high pressure. *Journal of Geophysical Research: Solid Earth*, 112, B10208. https://doi.org/10.1029/2006JB004856

Atkinson, B.K. (1984) Subcritical crack growth in geological materials. *Journal of Geophysical Research: Solid Earth*, 89(B6), 4077-4114. https://doi.org/10.1029/JB089iB06p04077

Atkinson, B.K., and Meredith, P.G. (1987) Experimental fracture mechanics data for rocks and minerals. In: Atkinson, B.K. (Ed.) *Fracture mechanics of rock*. London: Elsevier Academic Press.

Aubele, J.C., Crumpler, L.S. and Elston, W.E. (1988) Vesicle zonation and vertical structure of basalt flows. *Journal of Volcanology and Geothermal Research*, 35(4), 349-374. https://doi.org/10.1016/0377-0273(88)90028-5

Aubourg, C., Tshoso, G., Le Gall, B., Bertrand, H., Tiercelin, J.-J., Kampunzu, A.B., Dyment, J. and Modisi, M. (2008) Magma flow revealed by magnetic fabric in the Okavango giant dyke swarm, Karoo igneous province, northern Botswana. *Journal of Volcanology and Geothermal Research*, 170 (3–4), 247-261. https://doi.org/10.1016/j.jvolgeores.2007.10.013

Baer, G. and Reches, Z. (1987) Flow patterns of magma in dikes, Makhtesh Ramon, Israel. *Geology*, 15(6), 569-572. https://doi.org/10.1130/0091-7613(1987)15<569:FPOMID>2.0.CO;2

Bagnold, R.A. (1954) Experiments on a gravity-free dispersion of large solid spheres in a Newtonian fluid under shear. *Proceedings of the Royal Society A*, 225, 49-63. https://doi.org/10.1098/rspa.1954.0186

Balme, M.R., Rocchi, V., Jones, C., Sammonds, P.R., Meredith, P.G., and Boon, S. (2004) Fracture toughness measurements on igneous rocks using a high-pressure, high-temperature rock fracture mechanics cell. *Journal of Volcanology and Geothermal Research*, 132(2-3), 159-172. https://doi.org/10.1016/S0377-0273(03)00343-3

Baragar, W.R.A. (1960) Petrology of basaltic rocks in part of the Labrador Trough. *Geological Society of America Bulletin*, 71(11), 1589-1644. https://doi.org/10.1130/0016-7606(1960)71[1589:POBRIP]2.0.CO;2

Barrière, M. (1976) Flowage differentiation: limitation of the "Bagnold effect" to the narrow intrusions. *Contributions to Mineralogy and Petrology*, 55(2), 139-145. https://doi.org/10.1007/BF00372223

Battaglia, J., Ferrazzini, V., Staudacher, T., Aki, K., and Cheminée, J.L. (2005) Pre-eruptive migration of earthquakes at the Piton de la Fournaise volcano (Réunion Island). *Geophysical Journal International*, 161(2), 549-558. https://doi.org/10.1111/j.1365-246X.2005.02606.x

Benn, K. and Allard, B. (1989) Preferred mineral orientation related to magmatic flow in ophiolite layered gabbros. *Journal of Petrology*, 30, 925-946. https://doi.org/10.1093/petrology/30.4.925

Bernard, P. (2015) *Fluid Dynamics*. Cambridge: Cambridge University Press. https://doi:10.1017/CBO9781107785281.023

Bhattacharji, S. (1967) Mechanics of flow differentiation in ultramafic and mafic sills. *The Journal of Geology*, 75, 101-112. https://doi.org/10.1086/627234

Bhattacharji, S. and Smith, C.H. (1964) Flowage differentiation. *Science*, 145, 150-153. https://doi.org/10.1126/science.145.3628.150

Blanchard, J.P., Boyer, P. and Gagny, C. (1979) Un nouveau critere de sens de mise en place dans une caisse filonienne: Le "pincement" des minéraux aux epontes: Orientation des minéraux dans un magma en écoulement. *Tectonophysics*, 53(1-2), 1-25. https://doi.org/10.1016/0040-1951(79)90352-4

Bolchover, P. and Lister, J.R. (1999) The effect of solidification on fluid–driven fracture, with application to bladed dykes. *Proceedings of the Royal Society of London. Series A: Mathematical, Physical and Engineering Sciences*, 455, 2389-2409. https://doi.org/10.1098/rspa.1999.0409

Breiter, K., Müller, A., Leichmann, J. and Gabašová, A. (2005) Textural and chemical evolution of a fractionated granitic system: the Podlesí stock, Czech Republic. *Lithos*, 80(1-4), 323-345. https://doi.org/10.1016/j.lithos.2003.11.004

Bretherton, F.P. (1962) The motion of rigid particles in a shear flow at low Reynolds number. *Journal of Fluid Mechanics*, 14(2), 284-304. https://doi.org/10.1017/S002211206200124X

Brouxel, M. (1991) Geochemical consequences of flow differentiation in a multiple injection dyke (Trinity ophiolite, N. California). *Lithos*, 26, 245-252. https://doi.org/10.1016/0024-4937(91)90031-F

Bruce, P.M. and Huppert, H.E. (1989) Thermal control of basaltic fissure eruptions. *Nature*, 342, 665-667. https://doi.org/10.1038/342665a0

Bruce, P.M. and Huppert, H.E. (1990) Solidification and melting along dykes by the laminar flow of basaltic magma, in: Ryan, M.P. (ed.) *Magma transport and storage*. London: John Wiley & Sons, pp. 87-101.

Burnard, P., 1999. Eruption dynamics of "popping rock" from vesicle morphologies. *Journal of Volcanology and Geothermal Research*, 92(3-4), 247-258. https://doi.org/10.1016/S0377-0273(99)00057-8

Cañón-Tapia, E. (2004) Anisotropy of magnetic susceptibility of lava flows and dykes: a historical account, in: Hernandez, M., Luneburg, C.M., Auborg, C. and Jackson, M. (eds.) *Magnetic fabric: methods and applications*. London: Geological Society, London, Special Publications, pp. 205-225. https://doi.org/10.1144/GSL.SP.2004.238.01.14

Cañón-Tapia, E. and Chávez-Álvarez, M.J. (2004) Rotation of uniaxial ellipsoidal particles during simple shear revisited: the influence of elongation ratio, initial distribution of a multiparticle system and amount of shear in the acquisition of a stable orientation. *Journal of Structural Geology*, 26 (11), 2073-2087. https://doi.org/10.1016/j.jsg.2004.03.004

Cañón-Tapia, E. and Coe, R. (2002) Rock magnetic evidence of inflation of a flood basalt lava flow. *Bulletin of Volcanology*, 64(5), 289-302. https://doi.org/10.1007/s00445-002-0203-8

Cañón-Tapia, E. and Pinkerton, H. (2000) The anisotropy of magnetic susceptibility of lava flows: an experimental approach. *Journal of Volcanology and Geothermal Research*, 98, 219-233. https://doi.org/10.1016/S0377-0273(99)00155-9

Cañón-Tapia, E., Walker, G.P. and Herrero-Bervera, E. (1996) The internal structure of lava flows—insights from AMS measurements I: near-vent a'a. *Journal of Volcanology and Geothermal Research*, 70(1-2), 21-36. https://doi.org/10.1016/0377-0273(95)00050-X

Carracedo, J.C., Troll, V.R., Day, J.M., Geiger, H., Aulinas, M., Soler, V., Deegan, F.M., Perez-Torrado, F.J., Gisbert, G., Gazel, E. and Rodriguez-Gonzalez, A. (2022) The 2021 eruption of the Cumbre Vieja Volcanic Ridge on La Palma, Canary Islands. *Geology Today*, 38(3), 94-107. https://doi.org/10.1111/gto.12388

Castro, J.M., and Feisel, Y. (2022) Eruption of ultralow-viscosity basanite magma at Cumbre Vieja, La Palma, Canary Islands. *Nature Communications*, 13, 3174. https://doi.org/10.1038/s41467-022-30905-4

Chanceaux, L. and Menand, T. (2014) Solidification effects on sill formation: An experimental approach. *Earth and Planetary Science Letters*, 403, 79-88. https://doi.org/10.1016/j.epsl.2014.06.018

Clark, S. P. (1966) Thermal conductivity. *GSA Memoirs*, 97, 459–482. https://doi.org/10.1130/MEM97-p459

Clemente, C.S., Amorós, E.B. and Miguel Garcés Crespo, M.G. (2007) Dike intrusion under shear stress: effects on magnetic and vesicle fabrics in dikes from rift zones of Tenerife (Canary Islands). *Journal of Structural Geology*, 29, 1931-1942. https://doi.org/10.1016/j.jsg.2007.08.005

Colucci, S., Battaglia, M., and Trigila, R. (2016) A thermodynamical model for the surface tension of silicate melts in contact with H2O gas. *Geochimica et Cosmochimica Acta*, 175, 113-127. https://doi.org/10.1016/j.gca.2015.10.037

Coward. M.P. (1980) The analysis of flow profiles in a basaltic dyke using strained vesicles. *Journal of the Geological Society*, 137, 605-615. https://doi.org/10.1144/gsjgs.137.5.060

Currie, K.L. and Ferguson, J. (1970) The mechanism of intrusion of lamprophyre dikes indicated by "offsetting" of dikes. *Tectonophysics*, 9(6), 525-535. https://doi.org/10.1016/0040-1951(70)90003-X

Dahm, T. (2000) On the shape and velocity of fluid-filled fractures in the Earth. *Geophysical Journal International*, 142, 181-192. https://doi.org/10.1046/j.1365-246x.2000.00148.x

Daniels, K.A., Kavanagh, J.L., Menand, T., and R. Stephen, J.S. (2012) The shapes of dikes: Evidence for the influence of cooling and inelastic deformation. *GSA Bulletin*, 124(7-8), 1102-1112. https://doi.org/10.1130/B30537.1

Das, A. and Mallik, J. (2020) Applicability of AMS technique as a flow fabric indicator in dykes: insight from Nandurbar-Dhule Deccan dyke swarm. *International Journal of Earth Sciences*, 109(3), 933-944. https://doi.org/10.1007/s00531-020-01841-9

Davis, T., Bagnardi, M., Lundgren, P. and Rivalta, E. (2021) Extreme curvature of shallow magma pathways controlled by competing stresses: insights from the 2018 Sierra Negra eruption. *Geophysical Research Letters*, 48(13), 2021GL093038. https://doi.org/10.1029/2021GL093038

Dawson, J.B. and Hawthorne, J.B. (1973) Magmatic sedimentation and carbonatitic differentiation in kimberlite sills at Benfontein, South Africa. *Journal of the Geological Society*, 129(1), 61-85. https://doi.org/10.1144/gsjgs.129.1.0061

Deer, W.A., Howie, R.A., and Zussman, J. (2013) *An Introduction to the Rock Forming Minerals*. London: The Mineralogical Society.

Delaney, P.T., and Pollard, D.D. (1981) Deformation of host rocks and flow of magma during growth of minette dikes and breccia-bearing intrusions near Ship Rock, New Mexico. *USGS Professional Paper 1202*. https://doi.org/10.3133/pp1202

Delaney, P.T and Pollard, D.D. (1982) Solidification of basaltic magma during flow in a dike. *American Journal of Science*, 282, 856-885. https://doi.org/10.2475/ajs.282.6.856

Delcamp, A., Troll, V.R., Van Wyk de Vries, B., Carracedo, J.C., Petronis, M.S., Pérez-Torrado, F.J. and Deegan, F.M. (2012) Dykes and structures of the NE rift of Tenerife, Canary Islands: a record of stabilisation and destabilisation of ocean island rift zones. *Bulletin of Volcanology*, 74(5), 963-980. https://doi.org/10.1007/s00445-012-0577-1

Donaldson, C.H. (1977) Laboratory duplication of comb layering in the Rhum pluton. *Mineralogical Magazine*, 41(319), 323-336. https://doi.org/10.1180/minmag.1977.041.319.03

Dragnevski, K., Mullis, A.M., Walker, D.J. and Cochrane, R.F. (2002) Mechanical deformation of dendrites by fluid flow during the solidification of undercooled melts. *Acta Materialia*, 50(14), 3743-3755. https://doi.org/10.1016/S1359-6454(02)00186-6

Drever, H. I., and Johnston, R. (1959) The Petrology of Picritic Rocks in Minor Intrusions - a Hebridean Group. *Earth and Environmental Science Transactions of The Royal Society of Edinburgh*, 63(3), 459-499. https://doi.org/10.1017/S0080456800003112

Durham, W.B., Mirkovich, V.V., and Heard, H.C. (1987). Thermal diffusivity of igneous rocks at elevated pressure and temperature. *Journal of Geophysical Research: Solid Earth*, 92(B11), 11615–11634. https://doi.org/10.1029/JB092iB11p11615

Einarsson, P., and Brandsdóttir, B. (1980) Seismological evidence for lateral magma intrusion during the July 1978 deflation of the Krafla volcano in NE-Iceland. *Journal of Geophysics*, 47, 160-165.

Eriksson, P.I., Riishuus, M.S., Sigmundsson, F. and Elming, S.Å. (2011) Magma flow directions inferred from field evidence and magnetic fabric studies of the Streitishvarf composite dike in east Iceland. *Journal of Volcanology and Geothermal Research*, 206, 30-45. https://doi.org/10.1016/j.jvolgeores.2011.05.009

Ernst, R.E. and Baragar, W.R.A. (1992) Evidence from magnetic fabric for the flow pattern of magma in the Mackenzie giant radiating dyke swarm. *Nature*, 356, 511-513. https://doi.org/10.1038/356511a0

Féraud, G., Giannérini, G., Campredon, R. and Stillman, C.J. (1985) Geochronology of some Canarian dike swarms: contribution to the volcano-tectonic evolution of the archipelago. *Journal of Volcanology and Geothermal Research*, 25(1-2), 29-52. https://doi.org/10.1016/0377-0273(85)90003-4

Féménias, O., Diot, H., Berza, T., Gauffriau, A. and Demaiffe, D. (2004) Asymmetrical to symmetrical magnetic fabric of dikes: Paleo-flow orientations and Paleo-stresses recorded on feeder-bodies from the Motru Dike Swarm (Romania). *Journal of Structural Geology*, 26(8), 1401-1418. https://doi.org/10.1016/j.jsg.2003.12.003

Fernandez, A. and Laporte, D. (1991) Significance of low symmetry fabrics in magmatic rocks. *Journal of Structural Geology*, 13, 337-347. https://doi.org/10.1016/0191-8141(91)90133-4

Fialko, Y.A. and Rubin, A.M. (1999) Thermal and mechanical aspects of magma emplacement in giant dike swarms. *Journal of Geophysical Research: Solid Earth*, 104(B10), 23033-23049. https://doi.org/10.1029/1999JB900213

Fischer, T., Hrubcová, P., Salama, A., Doubravová, J., Agústsdóttir, T., Gudnason, E.Á., Horálek, J. and Hersir, G.P. (2022) Swarm seismicity illuminates stress transfer prior to the 2021 Fagradalsfjall eruption in Iceland. *Earth and Planetary Science Letters*, 594, 117685. https://doi.org/10.1016/j.epsl.2022.117685

Forsberg, C.H. (2020) *Heat Transfer Principles and Applications*. London: Elsevier Academic Press.

Fuller, R.E. (1939) Gravitational accumulation of olivine during the advance of basaltic flows. *The Journal of Geology*, 47(3), 303-313. https://doi.org/10.1086/624779

Gaete, A., Kavanagh, J.L., Rivalta, E., Hazim, S.H., Walter, T.R. and Dennis, D.J. (2019) The impact of unloading stresses on post-caldera magma intrusions. *Earth and Planetary Science Letters*, 508, 109-121. https://doi.org/10.1016/j.epsl.2018.12.016

Galindo, I. and Gudmundsson, A. (2012) Basaltic feeder dykes in rift zones: geometry, emplacement, and effusion rates. *Natural Hazards and Earth System Sciences*, 12(12), 3683-3700. https://doi.org/10.5194/nhess-12-3683-2012

Galland, O., Cobbold, P.R., Hallot, E., de Bremond d'Ars, J. and Delavaud, G. (2006) Use of vegetable oil and silica powder for scale modelling of magmatic intrusion in a deforming brittle crust. *Earth and Planetary Science Letters*, 243(3-4), 786-804. https://doi.org/10.1016/j.epsl.2006.01.014

Galland, O., Burchardt, S., Hallot, E., Mourgues, R. and Bulois, C. (2014) Dynamics of dikes versus cone sheets in volcanic systems. *Journal of Geophysical Research: Solid Earth*, 119(8), 6178-6192. https://doi.org/10.1002/2014JB011059

Geshi, N. (2008) Vertical and lateral propagation of radial dikes inferred from the flow-direction analysis of the radial dike swarm in Komochi Volcano, Central Japan. *Journal of Volcanology and Geothermal Research*, 173, 122-134. https://doi.org/10.1016/j.jvolgeores.2008.01.001

Geshi, N., Kusumoto, S., and Gudmundsson, A. (2010) Geometric difference between non-feeder and feeder dikes. *Geology*, 38(3), 195-198. https://doi.org/10.1130/G30350.1

Geshi, N. and Neri, M. (2014) Dynamic feeder dyke systems in basaltic volcanoes: the exceptional example of the 1809 Etna eruption (Italy). *Frontiers in Earth Science*, 2, 13-24. https://doi.org/10.3389/feart.2014.00013

Gibb, F.G. (1968) Flow differentiation in the xenolithic ultrabasic dykes of the Cuillins and the Strathaird Peninsula, Isle of Skye, Scotland. *Journal of Petrology*, 9(3), 411-443. https://doi.org/10.1093/petrology/9.3.411

Giordano, D., Nichols, A.R., and Dingwell, D.B. (2005) Glass transition temperatures of natural hydrous melts: a relationship with shear viscosity and implications for the welding process. *Journal of Volcanology and Geothermal Research*, 142, 105-118. https://doi.org/10.1016/j.jvolgeores.2004.10.015

Giordano, D., Russell, J.K. and Dingwell, D.B. (2008) Viscosity of magmatic liquids: a model. *Earth and Planetary Science Letters*, 271(1-4), 123-134. https://doi.org/10.1016/j.epsl.2008.03.038

Grace, H.P. (1982) Dispersion phenomena in high viscosity immiscible fluid systems and application of static mixers as dispersion devices in such systems. *Chemical Engineering Communications*, 14(3-6), 225-277. https://doi.org/10.1080/00986448208911047

Gualda, G.A. and Ghiorso, M.S. (2015) MELTS _ Excel: A Microsoft Excel-based MELTS interface for research and teaching of magma properties and evolution. *Geochemistry, Geophysics, Geosystems*, 16, 315-324. https://doi.org/10.1002/2014GC005545

Gudmundsson, A. (1984) Formation of dykes, feeder-dykes, and the intrusion of dykes from magma chambers. *Bulletin Volcanologique*, 47(3), 537-550. https://doi.org/10.1007/BF01961225

Gudmundsson, A., Marinoni, L.B. and Marti, J. (1999) Injection and arrest of dykes: implications for volcanic hazards. *Journal of Volcanology and Geothermal Research*, 88(1-2), 1-13. https://doi.org/10.1016/S0377-0273(98)00107-3

Guido, S., Greco, F. and Villone, M. (1999) Experimental determination of drop shape in slow steady shear flow. *Journal of Colloid and Interface Science*, 219(2), 298-309. https://doi.org/10.1006/jcis.1999.6458

Guillou, H., Carracedo, J.C., Paris, R. and Torrado, F.J.P. (2004) Implications for the early shield-stage evolution of Tenerife from K/Ar ages and magnetic stratigraphy. *Earth and Planetary Science Letters*, 222(2), 599-614. https://doi.org/10.1016/j.epsl.2004.03.012

Hanley, E.J., Dewitt, D.P., and Roy, R.F. (1978) The thermal diffusivity of eight well-characterized rocks for the temperature range 300–1000 K. *Engineering Geology*, 12, 31–47. https://doi.org/10.1016/0013-7952(78)90003-0

Hansen, D.M. and Cartwright, J. (2006) The three-dimensional geometry and growth of forced folds above saucer-shaped igneous sills. *Journal of Structural Geology*, 28(8), 1520-1535. https://doi.org/10.1016/j.jsg.2006.04.004

Hargraves, R.B., Hohnson, D. and Chan, C.Y. (1991) Distribution anisotropy: the cause of AMS in igneous rocks? *Geophysical Research Letters*, 18, 2193-2196. https://doi.org/10.1029/91GL01777

Harker, A. (1904) The Tertiary igneous rocks of Skye. *Memoirs of the Geological Survey of Great Britain* (1904), 1-481.

Hartel, R.W., Ergun, R. and Vogel, S. (2011) Phase/state transitions of confectionery sweeteners: Thermodynamic and kinetic aspects. *Comprehensive Reviews in Food Science and Food Safety*, 10, 17-32. https://doi.org/10.1111/j.1541-4337.2010.00136.x

Hastie, W.W., Watkeys, M.K. and Aubourg, C. (2011) Significance of magnetic and petrofabric in Karoo-feeder dykes, northern Lebombo. *Tectonophysics*, 513(1-4), 96-111. https://doi.org/10.1016/j.tecto.2011.10.008

Hastie, W.W., Watkeys, M.K. and Aubourg, C. (2013) Characterisation of grain-size, shape and orientation of plagioclase in the Rooi Rand dyke swarm, South Africa. *Tectonophysics*, 583, 145-157. https://doi.org/10.1016/j.tecto.2012.10.035

Hayashi, Y. and Morita, Y. (2003) An image of a magma intrusion process inferred from precise hypocentral migrations of the earthquake swarm east of the Izu Peninsula. *Geophysical Journal International*, 153, 159-174. https://doi.org/10.1046/j.1365-246X.2003.01892.x

Healy, D., Rizzo, R., Duffy, M., Farrell, N.J., Hole, M. J., and Muirhead, D. (2018) Field evidence for the lateral emplacement of igneous dykes: Implications for 3D mechanical models and the plumbing beneath fissure eruptions. *Volcanica*, 1(2). https://doi.org/10.30909/vol.01.02.85105

Helfrich, K.R. (1995) Thermo-viscous fingering of flow in a thin gap: a model of magma flow in dikes and fissures. *Journal of Fluid Mechanics*, 305, 219-238. https://doi.org/10.1017/S0022112095004605

Hinch, E.J. and Acrivos, A. (1980) Long slender drops in a simple shear flow. *Journal of Fluid Mechanics*, 98(2), 305-328. https://doi.org/10.1017/S0022112080000171

Hintz, A.R. and Valentine, G.A. (2012) Complex plumbing of monogenetic scoria cones: New insights from the Lunar Crater Volcanic Field (Nevada, USA). *Journal of Volcanology and Geothermal Research*, 239, 19-32. https://doi.org/10.1016/j.jvolgeores.2012.06.008

Hoek, J.D. (1991) A classification of dyke-fracture geometry with examples from Precambrian dyke swarms in the Vestfold Hills, Antarctica. *Geologische Rundschau*, 80(2), 233-248. https://doi.org/10.1007/BF01829363

Holness, M.B. and Humphreys, M.C.S. (2003) The Traigh Bhan na Sgurra Sill, Isle of Mull: flow localization in a major magma conduit. *Journal of Petrology*, 44(11), 1961-1976. https://doi.org/10.1093/petrology/egg066

Hon, K., Kauahikaua, J., Denlinger, R. and Mackay, K. (1994) Emplacement and inflation of pahoehoe sheet flows: Observations and measurements of active lava flows on Kilauea Volcano, Hawaii. Geological Society of America Bulletin, 106(3), 351-370. https://doi.org/10.1130/0016-7606(1994)106<0351:EAIOPS>2.3.CO;2

Honour, V., Holness, M., and Stock, M. (2019) The effect of cooling rate on immiscible silicate liquid microstructure: An example from the Palaeogene dykes of Northeast England. *Mineralogical Magazine*, 83(6), 809-820. https://doi.org/10.1180/mgm.2019.71

Hoyer, L. and Watkeys, M.K. (2017) Using magma flow indicators to infer flow dynamics in sills. *Journal of Structural Geology*, 96, 161-175. https://doi.org/10.1016/j.jsg.2017.02.005

Hrčka, R. and Babiak, M. (2017) Wood thermal properties. In: Concu. G. (ed.) *Wood in Civil Engineering*, pp.25-43. http://dx.doi.org/10.5772/65805

Hrouda, F., Buriánek, D. and Krejčí, O. (2020) Effect of post-magmatic processes on magnetic fabric of teschenite association rocks of the Outer Western Carpathians. *Journal of Structural Geology*, 133, 104003. https://doi.org/10.1016/j.jsg.2020.104003

Hrouda, F., Faryard, S.W., Kubínová, Š., Verner, K. and Chlupáčová, M. (2019) Simultaneous free flow and forcefully driven movement of magma in lamprophyre dykes as indicated by magnetic anisotropy: case study from the Central Bohemian Dyke Swarm, Czech Republic. *Geosciences*, 9, 104. https://doi.org/10.3390/geosciences9030104

Huppert, H.E. and Sparks, R.S.J. (1989) Chilled margins in igneous rocks. *Earth and Planetary Science Letters*, 92, 397-405. https://doi.org/10.1016/0012-821X(89)90063-0

Ildefonse, B., Arbaret, L., Diot, H. (1997) Rigid Particles in Simple Shear Flow: Is Their Preferred Orientation Periodic or Steady-State? in: Bouchez, J.L., Hutton, D.H.W., Stephens, W.E. (eds.) *Granite: From Segregation of Melt to Emplacement Fabrics. Petrology and Structural Geology*, 8. Dordrecht: Springer, pp.177-185. https://doi.org/10.1007/978-94-017-1717-5_11

Ildefonse, B. and Fernandez, A. (1988) Influence of the concentration of rigid markers in a viscous medium on the production of preferred orientations: an experimental contribution. I: Non-coaxial strain. *Bulletin of the Geological Institution of the University of Upsala*, 14, 55-60.

Ildefonse, B., Launeau, P., Bouchez, J-.L. and Fernandez, A. (1992) Effect of mechanical interactions on the development of shape preferred orientations: a two-dimensional approach. *Journal of Structural Geology*, 14, 73-83. https://doi.org/10.1016/0191-8141(92)90146-N

Ildefonse, B. and Mancktelow, N.S. (1993) Deformation around rigid particles: the influence of slip at the particle/matrix interface. *Tectonophysics*, 221(3-4), 345-359. https://doi.org/10.1016/0040-1951(93)90166-H

Jammalamadaka, S.R. and SenGupta, A. (2001) *Topics in Circular Statistics*. Singapore: World Scientific.

Jeffery, G.B. (1922) The motion of ellipsoidal particles immersed in a viscous fluid. *Proceedings of the Royal Society A*, 102, 161-179. https://doi.org/10.1098/rspa.1922.0078

Jolly, R.J.H. and Sanderson, D.J. (1995) Variation in the form and distribution of dykes in the Mull swarm, Scotland. *Journal of Structural Geology*, 17, 1543-1557. https://doi.org/10.1016/0191-8141(95)00046-G

Jones, T.J. and Llewellin, E.W. (2021) Convective tipping point initiates localization of basaltic fissure eruptions. *Earth and Planetary Science Letters*, 553, 116637. https://doi.org/10.1016/j.epsl.2020.116637

Karnis, A., Goldsmith, H.L. and Mason, S.G. (1963) Axial migration of particles in Poiseuille flow. *Nature*, 200, 159-160. https://doi.org/10.1038/200159a0

Katz, K. and Keller, J. (1981) Comb-layering in carbonatite dykes. *Nature*, 294(5839), 350-352. https://doi.org/10.1038/294350a0

Kavanagh, J.L., Burns, A.J., Hazim, S.H., Wood, E.P., Martin, S.A., Hignett, S. and Dennis, D.J. (2018) Challenging dyke ascent models using novel laboratory experiments: implications for reinterpreting evidence of magma ascent and volcanism. *Journal of Volcanology and Geothermal Research*, 354, 87-101. https://doi.org/10.1016/j.jvolgeores.2018.01.002

Kavanagh, J.L., Menand, T. and Sparks, R.S.J. (2006) An experimental investigation of sill formation and propagation in layered elastic media. *Earth and Planetary Science Letters*, 245, 799-813. https://doi.org/10.1016/j.epsl.2006.03.025

Kavanagh, J.L. and Sparks, R.S.J. (2011) Insights of dyke emplacement mechanics from detailed 3D dyke thickness datasets. *Journal of the Geological Society*, 168, 965-978. https://doi.org/10.1144/0016-76492010-137

Kile, A. (1993) Investigations into a macrosegregated, differentiated dolerite dyke, northern Skye, Scotland (MSc Thesis) Retrieved from St. Andrews Research Repository (https://research-repository.st-andrews.ac.uk/handle/10023/21844) UK: University of St. Andrews.

Kissel, C., Laj, C., Sigurdsson, H. and Guillou, H. (2010) Emplacement of magma in Eastern Iceland dikes: insights from magnetic fabric and rock magnetic analyses. *Journal of Volcanology and Geothermal Research*, 191, 79-92. https://doi.org/10.1016/j.jvolgeores.2009.12.008

Kiyosugi, K., Connor, C.B., Wetmore, P.H., Ferwerda, B.P., Germa, A.M., Connor, L.J. and Hintz, A.R. (2012) Relationship between dike and volcanic conduit distribution in a highly eroded monogenetic volcanic field: San Rafael, Utah, USA. *Geology*, 40(8), 695-698. https://doi.org/10.1130/G33074.1

Kjøll, H.J., Galland, O., Labrousse, L. and Andersen, T.B. (2019) Emplacement mechanisms of a dyke swarm across the brittle-ductile transition and the geodynamic implications for magma-rich margins. *Earth and Planetary Science Letters*, 518, 223-235. https://doi.org/10.1016/j.epsl.2019.04.016

Knight, M.D. and Walker, G.P. (1988) Magma flow directions in dikes of the Koolau Complex, Oahu, determined from magnetic fabric studies. *Journal of Geophysical Research: Solid Earth*, 93(B5), 4301-4319. https://doi.org/10.1029/JB093iB05p04301

Komar, P.D. (1972) Mechanical interactions of phenocrysts and flow differentiation of igneous dikes and sills. *Geological Society of America Bulletin*, 83(4), 973-988. https://doi.org/10.1130/0016-7606(1972)83[973:MIOPAF]2.0.CO;2

Komar, P.D. (1976) Phenocryst interactions and the velocity profile of magma flowing through dikes or sills. *Geological Society of America Bulletin*, 87(9), 1336-1342. https://doi.org/10.1130/0016-7606(1976)87<1336:PIATVP>2.0.CO;2

Lanzafame, G., Iezzi, G., Mancini, L., Lezzi, F., Mollo, S. and Ferlito, C. (2017) Solidification and turbulence (non-laminar) during magma ascent: insights from 2D and 3D analyses of bubbles and minerals in an Etnean dyke. *Journal of Petrology*, 58(8), 1511-1533. https://doi.org/10.1093/petrology/egx063

Launeau, P. and Cruden, A.R. (1998) Magmatic fabric acquisition mechanisms in a syenite: results of a combined anisotropy of magnetic susceptibility and image analysis study. *Journal of Geophysical Research: Solid Earth*, 103(B3), 5067-5089. https://doi.org/10.1029/97JB02670

Lecampion, B. and Garagash, D.I. (2014) Confined flow of suspensions modelled by a frictional rheology. *Journal of Fluid Mechanics*, 759, 197-235. https://doi.org/10.1017/jfm.2014.557

Lee, J.W., Thomas, L.C., and Schmidt, S.J. (2011) Investigation of the heating rate dependency associated with the loss of crystalline structure in sucrose, glucose, and fructose using a thermal analysis approach (part I). *Journal of Agricultural and Food Chemistry*, 59(2), 684-701. https://doi.org/10.1021/jf1042344

Leighton, D., and Acrivos, A. (1987) Measurement of shear-induced self-diffusion in concentrated suspensions of spheres. *Journal of Fluid Mechanics*, 177, 109-131. https://doi.org/10.1017/S0022112087000880

Leonhardt, R., and Soffel, H.C. (2006) The growth, collapse and quiescence of Teno volcano, Tenerife: New constraints from paleomagnetic data. *International Journal of Earth Sciences*, 95(6), 1053-1064. https://doi.org/10.1007/s00531-006-0089-3

Lesher, C.E., and Spera, F.J. (2015). Thermodynamic and transport properties of silicate melts and magma, in: Sigurdsson, H., Houghton, B., McNutt, S., Rymer, H., and Stix, J. (eds.) *Encyclopedia of volcanoes* (2nd ed.). London: Academic Press, pp.113-142.

Liss, D., Hutton, D.H. and Owens, W.H. (2002) Ropy flow structures: A neglected indicator of magma-flow direction in sills and dikes. *Geology*, 30, 715-718. https://doi.org/10.1130/0091-7613(2002)030<0715:RFSANI>2.0.CO;2

Lister, J.R. (1990) Buoyancy-driven fluid fracture: the effects of material toughness and of low-viscosity precursors. *Journal of Fluid Mechanics*, 210, 263-280. https://doi.org/10.1017/S0022112090001288

Lister, J.R. (1994a) The solidification of a buoyancy-driven flow in a flexible-walled channel. Part 1. Constant-volume release. *Journal of Fluid Mechanics*, 272, 21-44. https://doi.org/10.1017/S0022112094004362

Lister, J.R. (1994b) The solidification of buoyancy-driven flow in a flexible-walled channel. Part 2. Continual release. *Journal of Fluid Mechanics*, 272, 45-66. https://doi.org/10.1017/S0022112094004374

Lister, J.R. and Dellar, P.J. (1996) Solidification of pressure-driven flow in a finite rigid channel with application to volcanic eruptions. *Journal of Fluid Mechanics*, 323, 267-283. https://doi.org/10.1017/S0022112096000912

Lister, J.R. and Kerr, R.C. (1991) Fluid-mechanical models of crack propagation and their application to magma transport in dykes. *Journal of Geophysical Research: Solid Earth*, 96(B6), 10049-10077. https://doi.org/10.1029/91JB00600

Llewellin, E.W., Mader, H.M. and Wilson, S.D.R. (2002) The rheology of a bubbly liquid. *Proceedings of the Royal Society of London. Series A: Mathematical, Physical and Engineering Sciences*, 458(2020), 987-1016. https://doi.org/10.1098/rspa.2001.0924

Lofgren, G.E. and Donaldson, C.H. (1975) Curved branching crystals and differentiation in comb-layered rocks. *Contributions to Mineralogy and Petrology*, 49(4), 309-319. https://doi.org/10.1007/BF00376183

Longpré, M.A., Troll, V.R., Walter, T.R., and Hansteen, T.H. (2009) Volcanic and geochemical evolution of the Teno massif, Tenerife, Canary Islands: Some repercussions of giant landslides on ocean island magmatism. *Geochemistry, Geophysics, Geosystems*, 10(12), Q12017. https://doi.org/10.1029/2009GC002892

Maccaferri, F., Bonafede, M., and Rivalta, E. (2010) A numerical model of dyke propagation in layered elastic media. *Geophysical Journal International*, 180(3), 1107-1123. https://doi.org/10.1111/j.1365-246X.2009.04495.x

Maccaferri, F., Bonafede, M. and Rivalta, E. (2011) A quantitative study of the mechanisms governing dike propagation, dike arrest and sill formation. *Journal of Volcanology and Geothermal Research*, 208, 39-50. https://doi.org/10.1016/j.jvolgeores.2011.09.001

Maccaferri, F., Rivalta, E., Passarelli, L. and Aoki, Y. (2016) On the mechanisms governing dike arrest: Insight from the 2000 Miyakejima dike injection. *Earth and Planetary Science Letters*, 434, 64-74. https://doi.org/10.1016/j.epsl.2015.11.024

MacCarthy, D.A. and Fabre, N. (1989) Thermal conductivity of sucrose, in: Singh, R.P. and Medina, A.G. (eds.) *Food Properties and Computer-Aided Engineering of Food Processing Systems*. Dordrecht: Springer, pp. 105-111.

MacDonald, R., Wilson, L., Thorpe, R.S. and Martin, A. (1988) Emplacement of the Cleveland Dyke: evidence from geochemistry, mineralogy, and physical modelling. *Journal of Petrology*, 29, 559-583. https://doi.org/10.1093/petrology/29.3.559

Maeda, K., Tsunetsugu, Y., Miyamoto, K. and Shibusawa, T. (2021) Thermal properties of wood measured by the hot-disk method: comparison with thermal properties measured by the steady-state method. *Journal of Wood Science*, 67, 1-14. https://doi.org/10.1186/s10086-021-01951-1

Magee, C., O'Driscoll, B., Petronis, M.S. and Stevenson, C.T.E. (2016) Three-dimensional magma flow dynamics within subvolcanic sheet intrusions. *Geosphere*, 12(3), 842-866. https://doi.org/10.1130/GES01270.1

Magee, C., Muirhead, J., Schofield, N., Walker, R.J., Galland, O., Holford, S., Spacapan, J., Jackson, C.A. and McCarthy, W. (2019) Structural signatures of igneous sheet intrusion propagation. *Journal of Structural Geology*, 125, 148-154. https://doi.org/10.1016/j.jsg.2018.07.010

Mantiloni, L., Davis, T., Gaete Rojas, A.B. and Rivalta, E. (2021) Stress inversion in a gelatin box: testing eruptive vent location forecasts with analog models. *Geophysical Research Letters*, 48(6), 2020GL090407. https://doi.org/10.1029/2020GL090407

Marinoni, L.B. and Gudmundsson, A. (2000) Dykes, faults and palaeostresses in the Teno and Anaga massifs of Tenerife (Canary Islands). *Journal of Volcanology and Geothermal Research*, 103(1-4), 83-103. https://doi.org/10.1016/S0377-0273(00)00217-1

Mark, N.J., Holford, S.P., Schofield, N., Eide, C.H., Pugliese, S., Watson, D.A. and Muirhead, D. (2020) Structural and lithological controls on the architecture of igneous intrusions: examples from the NW Australian Shelf. *Petroleum Geoscience*, 26, 50-69. https://doi.org/10.1144/petgeo2018-067

Martin, S.A., Kavanagh, J.L., Biggin, A.J. and Utley, J.E.P. (2019) The origin and evolution of magnetic fabric in mafic sills. *Frontiers in Earth Science*, 7, 64. https://doi.org/10.3389/feart.2019.00064

Martin, V.M., Pyle, D.M., and Holness, M.B. (2006) The role of crystal frameworks in the preservation of enclaves during magma mixing. *Earth and Planetary Science Letters*, 248(3-4), 787-799. https://doi.org/10.1016/j.epsl.2006.06.030

Martins, M.J.N., Augusto, P.E.D., Telis-Romero, J. and Polachini, T.C. (2021) Transport properties of saturated sucrose and maltitol solutions as affected by temperature. *Journal of Molecular Liquids*, 336, 116254. https://doi.org/10.1016/j.molliq.2021.116254

Mathieu, L., De Vries, B.V.W., Holohan, E.P. and Troll, V.R. (2008) Dykes, cups, saucers and sills: Analogue experiments on magma intrusion into brittle rocks. *Earth and Planetary Science Letters*, 271(1-4), 1-13. https://doi.org/10.1016/j.epsl.2008.02.020

MathWorks, Inc. (2020) MATLAB version: 9.9.0 (R2020b) [01.11.23]. Available: https://www.mathworks.com

MathWorks, Inc. (2024) *MATLAB eig*. MATLAB Documentation [online] https://uk.mathworks.com/help/matlab/ref/eig.html [Accessed: 24.01.24]

Maude, A.D. and Whitmore, R.L. (1956) The wall effect and the viscometry of suspensions. *British Journal of Applied Physics*, 7(3), 98-104. https://doi.org/10.1088/0508-3443/7/3/305

McCarthy, A. and Müntener, O. (2016) Comb layering monitors decompressing and fractionating hydrous mafic magmas in subvolcanic plumbing systems (Fisher Lake, Sierra Nevada, USA). *Journal of Geophysical Research: Solid Earth*, 121(12), 8595-8621. https://doi.org/10.1002/2016JB013489

Menand, T., Daniels, K.A. and Benghiat, P. (2010) Dyke propagation and sill formation in a compressive tectonic environment. *Journal of Geophysical Research: Solid Earth*, 115(B8). https://doi.org/10.1029/2009JB006791

Menand, T. and Phillips, J.C. (2007) Gas segregation in dykes and sills. *Journal of Volcanology and Geothermal Research*, 159(4), 393-408. https://doi.org/10.1016/j.jvolgeores.2006.08.003

Menand, T. and Tait, S.R. (2002) The propagation of a buoyant liquid-filled fissure from a source under constant pressure: An experimental approach. *Journal of Geophysical Research: Solid Earth*, 107(B11), ECV16. https://doi.org/10.1029/2001JB000589

Mollo, S., Lanzafame, G., Masotta, M., Iezzi, G., Ferlito, C. and Scarlato, P. (2011) Cooling history of a dike as revealed by mineral chemistry: a case study from Mt. Etna volcano. *Chemical Geology*, 288(1-2), 39-52. https://doi.org/10.1016/j.chemgeo.2011.06.016

Montalbano, S., Diot, H. and Bolle, O. (2016) Asymmetrical magnetic fabrics in the Egersund doleritic dike swarm (SW Norway) reveal sinistral oblique rifting before the opening of the Iapetus. *Journal of Structural Geology*, 85, 18-39. https://doi.org/10.1016/j.jsg.2016.01.006

Montgomery-Brown, E.K., Sinnett, D.K., Larson, K.M., Poland, M.P., Segall, P. and Miklius, A. (2011) Spatiotemporal evolution of dike opening and décollement slip at Kīlauea Volcano, Hawai'i. *Journal of Geophysical Research: Solid Earth*, 116(B3). https://doi.org/10.1029/2010JB007762

Moore, J.G. and Lockwood, J.P. (1973) Origin of comb layering and orbicular structure, Sierra Nevada Batholith, California. *Geological Society of America Bulletin*, 84, 1-20. https://doi.org/10.1130/0016-7606(1973)84<1:OOCLAO>2.0.CO;2

Mostafa, M.S., Afify, N., Gaber, A., and Zaid, E.A. (2004). Investigation of thermal properties of some basalt samples in Egypt. *Journal of Thermal Analysis and Calorimetry*, 75, 179–188. https://doi.org/10.1023/b:jtan.0000017340.19830.45

Mueller, S., Llewellin, E.W, and Mader, H.M. (2010) The rheology of suspensions of solid particles. *Proceedings of the Royal Society A*, 466, 1201-1228. https://doi.org/10.1098/rspa.2009.0445

Mulchrone, K.F., Grogan, S. and De, P. (2005) The relationship between magmatic tiling, fluid flow and crystal fraction. *Journal of Structural Geology*, 27(2), 179-197. https://doi.org/10.1016/j.jsg.2004.10.007

Muller, J.R., Ito, G. and Martel, S.J. (2001) Effects of volcano loading on dike propagation in an elastic half-space. *Journal of Geophysical Research: Solid Earth*, 106(B6), 11101-11113. https://doi.org/10.1029/2000JB900461

Müller-Fischer, N., Tobler, P., Dressler, M., Fischer, P. and Windhab, E.J. (2008) Single bubble deformation and breakup in simple shear flow. *Experiments in Fluids*, 45, 917-926. https://doi.org/10.1007/s00348-008-0509-1

Muñoz, V., Walter, T.R., Zorn, E.U., Shevchenko, A.V., González, P.J., Reale, D. and Sansosti, E. (2022) Satellite radar and camera time series reveal transition from aligned to distributed crater arrangement during the 2021 eruption of Cumbre Vieja, La Palma (Spain). *Remote Sensing*, 14(23), 6168. https://doi.org/10.3390/rs14236168

Munteanu, M., Wilson, A.H., Costin, G., Yao, Y., Lum, J.E., Jiang, S.Y., Jourdan, F., Chunnett, G. and Cioacă, M.E. (2017) The Mafic–Ultramafic Dykes in the Yanbian Terrane (Sichuan Province, SW China): Record of Magma Differentiation and Emplacement in the Emeishan Large Igneous Province. *Journal of Petrology*, 58(3), 513-538. https://doi.org/10.1093/petrology/egx025

Neal, C.A., Brantley, S.R., Antolik, L., Babb, J.L., Burgess, M., Calles, K., Cappos, M., Chang, J.C., Conway, S., Desmither, L. and Dotray, P. (2019) The 2018 rift eruption and summit collapse of Kīlauea Volcano. *Science*, 363(6425), 367-374. https://doi.org/10.1126/science.aav7046

Ohashi, M., Ichihara, M. and Toramaru, A. (2018) Bubble deformation in magma under transient flow conditions. *Journal of Volcanology and Geothermal Research*, 364, 59-75. https://doi.org/10.1016/j.jvolgeores.2018.09.005

Olson, J.E. (2003) Sublinear scaling of fracture aperture versus length: an exception or the rule? *Journal of Geophysical Research: Solid Earth*, 108(B9). https://doi.org/10.1029/2001JB000419

Pansino, S., Emadzadeh, A. and Taisne, B. (2019) Dike channelization and solidification: time scale controls on the geometry and placement of magma migration pathways. *Journal of Geophysical Research: Solid Earth*, 124, 9580-9599. https://doi.org/10.1029/2019JB018191

Pansino, S., Emadzadeh, A. and Taisne, B. (2023) Magma flow patterns in dikes: Observations from analogue experiments. *Journal of Geophysical Research: Solid Earth*, 128(3), p.e2022JB025463. https://doi.org/10.1029/2022JB025463

Petcovic, H.L. and Dufek, J.D. (2005) Modeling magma flow and cooling in dikes: Implications for emplacement of Columbia River flood basalts. *Journal of Geophysical Research: Solid Earth*, 110(B10). https://doi.org/10.1029/2004JB003432

Peterson, D.W., Holcomb, R.T., Tilling, R.I. and Christiansen, R.L. (1994) Development of lava tubes in the light of observations at Mauna Ulu, Kilauea Volcano, Hawaii. *Bulletin of Volcanology*, 56, 343-360. https://doi.org/10.1007/BF00326461

Petford, N., and Koenders, M.A. (1998) Granular flow and viscous fluctuations in low Bagnold number granitic magmas. *Journal of the Geological Society*, 155(5), 873-881. https://doi.org/10.1144/gsjgs.155.5.0873

Phillips, R.J., Armstrong, R.C., Brown, R.A., Graham, A.L., and Abbott, J.R. (1992) A constitutive equation for concentrated suspensions that accounts for shear-induced particle migration. *Physics of Fluids A: Fluid Dynamics*, 4, 30-40. https://doi.org/10.1063/1.858498

Philpotts, A.R. and Asher, P.M. (1994) Magmatic flow-direction indicators in a giant diabase feeder dike, Connecticut. *Geology*, 22, 363-366. https://doi.org/10.1130/0091-7613(1994)022<0363:MFDIIA>2.3.CO;2

Philpotts, A.R. and Philpotts, D.E. (2007) Upward and downward flow in a camptonite dike as recorded by deformed vesicles and the anisotropy of magnetic susceptibility (AMS). *Journal of Volcanology and Geothermal Research*, 161, 81-94. https://doi.org/10.1016/j.jvolgeores.2006.11.006

Picard, D., Arbaret, L., Pichavant, M., Champallier, R. and Launeau, P. (2011) Rheology and microstructure of experimentally deformed plagioclase suspensions. *Geology*, 39, 747-750. https://doi.org/10.1130/G32217.1

Pinel, V. and Jaupart, C. (2004) Magma storage and horizontal dyke injection beneath a volcanic edifice. *Earth and Planetary Science Letters*, 221, 245-262. https://doi.org/10.1016/S0012-821X(04)00076-7

Platten, I.M. (2000) Incremental dilation of magma filled fractures: evidence from dykes on the Isle of Skye, Scotland. *Journal of Structural Geology,* 22, 1153-1164. https://doi.org/10.1016/S0191-8141(00)00024-9

Poland, M.P., Moats, W.P. and Fink, J.H. (2008) A model for radial dike emplacement in composite cones based on observations from Summer Coon volcano, Colorado, USA. *Bulletin of Volcanology*, 70(7), 861-875. https://doi.org/10.1007/s00445-007-0175-9

Pollard, D.D. (1973) Derivation and evaluation of a mechanical model for sheet intrusions. *Tectonophysics*, 19(3), 233-269. https://doi.org/10.1016/0040-1951(73)90021-8

Pollard, D.D., Muller, O.H. and Dockstader, D.R. (1975) The form and growth of fingered sheet intrusions. *Geological Society of America Bulletin*, 86, 351-363. https://doi.org/10.1130/0016-7606(1975)86<351:TFAGOF>2.0.CO;2

Prousevitch, A.A., Sahagian, D.L., and Anderson, A.T. (1993) Dynamics of diffusive bubble growth in magmas: Isothermal case. *Journal of Geophysical Research: Solid Earth*, 98(B12), 22283-22307. https://doi.org/10.1029/93JB02027

Raposo, M.I.B. (2020) Emplacement of dike swarms from the island of Ilhabela (SE Brazil) and its relationship with the South Atlantic Ocean opening revealed by magnetic fabrics. *Physics of the Earth and Planetary Interiors*, 301, 106471. https://doi.org/10.1016/j.pepi.2020.106471

Rallison, J.M. (1981) A numerical study of the deformation and burst of a viscous drop in general shear flows. *Journal of Fluid Mechanics*, 109, 465-482. https://doi.org/10.1017/S002211208100116X

Rallison, J.M. (1984) The deformation of small viscous drops and bubbles in shear flows. *Annual Review of Fluid Mechanics*, 16, 45-66. https://doi.org/10.1146/annurev.fl.16.010184.000401

Ray, R., Sheth, H.C., and Mallik, J. (2007) Structure and emplacement of the Nandurbar-Dhule mafic dyke swarm, Deccan Traps, and the tectonomagmatic evolution of flood basalts. *Bulletin of Volcanology*, 69(5), 537-551. https://doi.org/10.1007/s00445-006-0089-y

Rees, A.I. (1968) The production of preferred orientation in a concentrated dispersion of elongated and flattened grains. *The Journal of Geology*, 76(4), 457-465. https://doi.org/10.1086/627343

Richter, D.H., Eaton, J.P., Murata, K.J., Ault, W.U. and Krivoy, H.L. (1970) Chronological narrative of the 1959-60 eruption of Kilauea volcano, Hawaii. *USGS Professional Paper*, 537-E. https://doi.org/10.3133/pp537E

Rivalta, E., Taisne, B., Bunger, A.P., and Katz, R.F. (2015) A review of mechanical models of dike propagation: Schools of thought, results and future directions. *Tectonophysics*, 638, 1-42. https://doi.org/10.1016/j.tecto.2014.10.003

Roberts, J.L., and Sanderson, D.J. (1971) The intrusive form of some basalt dykes showing flow lineation. *Geological Magazine*, 108(6), 489-499. https://doi.org/10.1017/S0016756800056697

Robertson, E.C., and Peck, D.L. (1974) Thermal conductivity of vesicular basalt from Hawaii. *Journal of Geophysical Research*, 79(32), 4875–4888. https://doi.org/10.1029/JB079i032p04875

Rogan, W., Blake, S., and Smith, I. (1996) In situ chemical fractionation in thin basaltic lava flows: examples from the Auckland volcanic field, New Zealand, and a general physical model. *Journal of Volcanology and Geothermal Research*, 74(1-2), 89-99. https://doi.org/10.1016/S0377-0273(96)00059-5

Roper, S.M. and Lister, J.R. (2007) Buoyancy-driven crack propagation: the limit of large fracture toughness. *Journal of Fluid Mechanics*, 580, 359-380. https://doi.org/10.1017/S0022112007005472

Ross, M.E. (1983) Chemical and mineralogic variations within four dikes of the Columbia River Basalt Group, southeastern Columbia Plateau. *Geological Society of America Bulletin*, 94(9), 1117-1126. https://doi.org/10.1130/0016-7606(1983)94<1117:CAMVWF>2.0.CO;2

Ross, M.E. (1986) Flow differentiation, phenocryst alignment, and compositional trends within a dolerite dike at Rockport, Massachusetts. *Geological Society of America Bulletin*, 97(2), 232-240. https://doi.org/10.1130/0016-7606(1986)97<232:FDPAAC>2.0.CO;2

Rust, A.C. and Cashman, K.V. (2007) Multiple origins of obsidian pyroclasts and implications for changes in the dynamics of the 1300 BP eruption of Newberry Volcano, USA. *Bulletin of Volcanology*, 69, 825-845. https://doi.org/10.1007/s00445-006-0111-4

Rust, A.C. and Manga, M. (2002) Bubble shapes and orientations in low Re simple shear flow. *Journal of Colloid and Interface science*, 249(2), 476-480. https://doi.org/10.1006/jcis.2002.8292

Rust, A.C., Manga, M. and Cashman, K.V. (2003) Determining flow type, shear rate and shear stress in magmas from bubble shapes and orientations. *Journal of Volcanology and Geothermal Research*, 122(1-2), 111-132. https://doi.org/10.1016/S0377-0273(02)00487-0

Ruz, J., Browning, J., Cembrano, J., Iturrieta, P., Gerbault, M. and Sielfeld, G. (2020) Field observations and numerical models of a Pleistocene-Holocene feeder dyke swarm associated with a fissure complex to the east of the Tatara-San Pedro-Pellado complex, Southern Volcanic Zone, Chile. *Journal of Volcanology and Geothermal Research*, 404, 107033. https://doi.org/10.1016/j.jvolgeores.2020.107033

Schindelin, J., Arganda-Carreras, I., Frise, E., Kaynig, V., Longair, M., Pietzsch, T., Preibisch, S., et al. (2012) Fiji: an open-source platform for biological-image analysis. *Nature Methods*, 9(7), 676-682. https://doi.org/10.1038/nmeth.2019

Schofield, N.J., Brown, D.J., Magee, C. and Stevenson, C.T. (2012) Sill morphology and comparison of brittle and non-brittle emplacement mechanisms. *Journal of the Geological Society*, 169(2), 127-141. https://doi.org/10.1144/0016-76492011-078

Sehlke, A., Hofmeister, A. M., and Whittington, A. G. (2020) Thermal properties of glassy and molten planetary candidate lavas. *Planetary and Space Science*, 193, 105089. https://doi.org/10.1016/j.pss.2020.105089

Shampine, L.F., and Reichelt, M.W. (1997) The MATLAB ODE suite. *SIAM Journal on Scientific Computing*, 18, 1-22. https://doi.org/10.1137/S1064827594276424

Shampine, L.F., and Thompson, S. (2001) Solving DDEs in MATLAB. *Applied Numerical Mathematics*, 37(4), 441-458. https://doi.org/10.1016/S0168-9274(00)00055-6

Shelley, D. (1985) Determining paleo-flow directions from groundmass in the Lyttleton radial dykes, New Zealand. *Journal of Volcanology and Geothermal Research*, 25, 69-79. https://doi.org/10.1016/0377-0273(85)90005-8

Shishkina, T.A., Botcharnikov, R.E., Holtz, F., Almeev, R.R., and Portnyagin, M.V. (2010) Solubility of H2O-and CO2-bearing fluids in tholeiitic basalts at pressures up to 500 MPa. *Chemical Geology*, 277, 115-125. https://doi.org/10.1016/j.chemgeo.2010.07.014

Sigmundsson, F., Hooper, A., Hreinsdóttir, S., Vogfjörd, K.S., Ófeigsson, B.G., Heimisson, E.R., Dumont, S., Parks, M., Spaans, K., Gudmundsson, G.B. and Drouin, V. (2015) Segmented lateral dyke growth in a rifting event at Bárðarbunga volcanic system, Iceland. *Nature*, 517, 191-195. https://doi.org/10.1038/nature14111

Sigurdsson, H. (1999) Volcanic episodes and rates of volcanism, in: Sigurdsson, H., Houghton, B., McNutt, S., Rymer H., and Stix, J. (eds.) *Encyclopedia of Volcanoes* (1st ed.). London: Academic Press, pp. 271–279.

Silva, P.F., Marques, F.O., Henry, B., Madureira, P., Hirt, A.M., Font, E. and Lourenco, N. (2010) Thick dyke emplacement and internal flow: a structural and magnetic fabric study of the deep-seated dolerite dyke of Foum Zguid (southern Morocco). *Journal of Geophysical Research*, 115, B12108. https://doi.org/10.1029/2010JB007638

Smittarello, D., Cayol, V., Pinel, V., Peltier, A., Froger, J.L. and Ferrazzini, V. (2019) Magma propagation at Piton de la Fournaise from joint inversion of InSAR and GNSS. *Journal of Geophysical Research: Solid Earth*, 124(2), 1361-1387. https://doi.org/10.1029/2018JB016856

Soriano, C., Beamud, E., Garcés, M. and Ort, M.H. (2016) 'Anomalous' magnetic fabrics of dikes in the stable single domain/superparamagnetic threshold. *Geophysical Journal International*, 204(2), 1040-1059. https://doi.org/10.1093/gji/ggv495

Spence, D.A. and Turcotte, D.L. (1985) Magma-driven propagation of cracks. *Journal of Geophysical Research*, 90 (B1), 575-580. https://doi.org/10.1029/JB090iB01p00575

Staudigel, H., Tauxe, L., Gee, J.S., Bogaard, P., Haspels, J., Kale, G., Leenders, A., Meijer, P., Swaak, B., Tuin, M. and Van Soest, M.C. (1999) Geochemistry and intrusive directions in sheeted dikes in the Troodos ophiolite: Implications for mid-ocean ridge spreading centers. *Geochemistry, Geophysics, Geosystems*, 1, 1999GC000001. https://doi.org/10.1029/1999GC000001

Stephens, T.L., Walker, R.J., Healy, D., Bubeck, A., England, R.W. and McCaffrey, K.J. (2017) Igneous sills record far-field and near-field stress interactions during volcano construction: Isle of Mull, Scotland. *Earth and Planetary Science Letters*, 478, 159-174. https://doi.org/10.1016/j.epsl.2017.09.003

Stover, C.A., Koch, D.L. and Cohen, C. (1992) Observations of fibre orientation in simple shear flow of semi-dilute suspensions. *Journal of Fluid Mechanics*, 238, 277-296. https://doi.org/10.1017/S002211209200171X

Svenningsen, O.M. (1994) The Baltica–Iapetus passive margin dyke complex in the Sarektjåkkå Nappe, northern Swedish Caledonides. *Geological Journal*, 29(4), 323-354. https://doi.org/10.1002/gj.3350290403

Taisne, B. and Jaupart, C., (2009) Dike propagation through layered rocks. *Journal of Geophysical Research: Solid Earth*, 114(B9). https://doi.org/10.1029/2008JB006228

Taisne, B. and Tait, S. (2011) Effect of solidification on a propagating dike. *Journal of Geophysical Research: Solid Earth*, 116, B01206. https://doi.org/10.1029/2009JB007058

Taisne, B. and Gonnermann, H. (2015) Magma transport in dikes, in: Sigurdsson, H., Houghton, B., McNutt, S., Rymer, H., and Stix. J. (eds.) *Encyclopedia of Volcanoes* (2nd ed.). London: Academic Press, pp. 271–279.

Taracsák, Z., Hartley, M.E., Burgess, R., Edmonds, M., Iddon, F., and Longpre, M.A. (2019) High fluxes of deep volatiles from ocean island volcanoes: Insights from El Hierro, Canary Islands. *Geochimica et Cosmochimica Acta*, 258, 19-36. https://doi.org/10.1016/j.gca.2019.05.020

Taubeneck, W.H. and Poldervaart, A. (1960) Geology of the Elkhorn Mountains, Northeastern Oregon: Part 2. Willow Lake intrusion. *Geological Society of America Bulletin*, 71(9), 1295-1322. https://doi.org/10.1130/0016-7606(1957)68[181:GOTEMN]2.0.CO;2

Tauxe, L., Gee, J.S. and Staudigel, H. (1998) Flow directions in dikes from anisotropy of magnetic susceptibility data: the bootstrap way. *Journal of Geophysical Research: Solid Earth*, 103(B8), 17775-17790. https://doi.org/10.1029/98JB01077

Taylor, G.I. (1934) The formation of emulsions in definable fields of flow. *Proceedings of the Royal Society of London, Series A*. 146(858), 501-523. https://doi.org/10.1098/rspa.1934.0169

ThermoFisher Scientific (2022) Avizo version: 2022.1 [01.09.23] Available: https://www.thermofisher.com/uk/en/home/electron-microscopy/products/software-em-3d-vis/avizo-software.html

Thiele, S.T., Cruden, A.R., Zhang, X., Micklethwaite, S., and Matchan, E.L. (2021) Reactivation of magma pathways: Insights from field observations, geochronology, geomechanical tests, and numerical models. *Journal of Geophysical Research: Solid Earth*, 126(5), e2020JB021477. https://doi.org/10.1029/2020JB021477

Thirlwall, M.F., Singer, B.S. and Marriner, G.F. (2000) 39Ar-40Ar ages and geomchemistry of the basaltic shield stage of Tenerife, Canary Islands, Spain. *Journal of Volcanology and Geothermal Research*, 103, 247-297. https://doi.org/10.1016/S0377-0273(00)00227-4

Thomson, K. and Hutton, D. (2004) Geometry and growth of sill complexes: insights using 3D seismic from the North Rockall Trough. *Bulletin of Volcanology*, 66, 364-375. https://doi.org/10.1007/s00445-003-0320-z

Thorarinsson, S., Steinthorsson, S., Einarsson, T., Kristmannsdóttir, H. and Óskarsson, N. (1973) The eruption on Heimaey, Iceland. *Nature*, 241, 372-375. https://doi.org/10.1038/241372a0

Thordarson, T., and Self, S. (1996) Sulfur, chlorine and fluorine degassing and atmospheric loading by the Roza eruption, Columbia River Basalt Group, Washington, USA. *Journal of Volcanology and Geothermal Research*, 74, 49-73. https://doi.org/10.1016/S0377-0273(96)00054-6

Tomé, C.R., Bitencourt, M.dF., Raposo, M.I.B., and Savian, J.F. (2020) Magnetic fabric data on interactive syntectonic magmas of contrasting composition in composite dikes from south Brazil. *Journal of Geodynamics*, 138, 101754. https://doi.org/10.1016/j.jog.2020.101754

Touvet, T., Balmforth, N.J., Craster, R.V. and Sutherland, B.R. (2011) Fingering instability in buoyancy-driven fluid-filled cracks. *Journal of Fluid Mechanics*, 672, 60-77. https://doi.org/10.1017/S0022112010005860

Townsend, M.R., Pollard, D.D. and Smith, R.P. (2017) Mechanical models for dikes: a third school of thought. *Tectonophysics*, 703, 98-118. https://doi.org/10.1016/j.tecto.2017.03.008

Turcotte, D.L. and Schubert, G. (2002) *Geodynamics*. Cambridge: Cambridge University Press.

Valentine, G.A. and Krogh, K.E. (2006) Emplacement of shallow dikes and sills beneath a small basaltic volcanic center – The role of pre-existing structure (Paiute Ridge, southern Nevada, USA). *Earth and Planetary Science Letters*, 246(3-4), 217-230. https://doi.org/10.1016/j.epsl.2006.04.031

Varga, R.J., Gee, J.S., Staudigel, H. and Tauxe, L. (1998) Dike surface lineations as magma flow indicators within the sheeted dike complex of the Troodos Ophiolite, Cyprus. *Journal of Geophysical Research: Solid Earth*, 103(B3), 5241-5256. https://doi.org/10.1029/97JB02717

Vona, A., Romano, C., Dingwell, D.B. and Giordano, D. (2011) The rheology of crystal-bearing basaltic magmas from Stromboli and Etna. *Geochimica et Cosmochimica Acta*, 75(11), 3214-3236. https://doi.org/10.1016/j.gca.2011.03.031

Wada, Y. (1992) Magma flow directions inferred from preferred orientations of phenocryst in a composite feeder dike, Miyake-Jima, Japan. *Journal of Volcanology and Geothermal Research*, 49(1-2), 119-126. https://doi.org/10.1016/0377-0273(92)90008-2

Wadsworth, F.B., Kennedy, B.M., Branney, M.J., von Aulock, F.W., Lavallée, Y. and Menendez, A. (2015) Exhumed conduit records magma ascent and drain-back during a Strombolian eruption at Tongariro volcano, New Zealand. *Bulletin of Volcanology*, 77, 71-81. https://doi.org/10.1007/s00445-015-0962-7

Walker, G.P. (1987) The dike complex of Koolau volcano, Oahu: internal structure of a Hawaiian rift zone, in: Decker, R.W., Wright, T.L., and Stauffer, P.H. (eds.) *USGS Professional Paper 1350* (Vol. 2). Washington: United States Government Printing Office, pp. 961-993.

Walker, G.P. (1989) Spongy pahoehoe in Hawaii: a study of vesicle-distribution patterns in basalt and their significance. *Bulletin of Volcanology*, 51(3), 199-209. https://doi.org/10.1007/BF01067956

Walker, G.P., and Eyre, P.R. (1995) Dike complexes in American Samoa. *Journal of Volcanology and Geothermal Research*, 69(3-4), 241-254. https://doi.org/10.1016/0377-0273(95)00041-0

Wallace, P. and Anderson, A.T. (1999) Volatiles in magmas, in: Sigurdsson, H., Houghton, B., McNutt, S.R., Rymer, H. and Stix, J. (eds.) *Encyclopedia of Volcanoes* (1st ed.). London: Academic Press, pp.149-170.

Walter, T. and Schmincke, H.U. (2002) Rifting, recurrent landsliding and Miocene structural reorganization on NW-Tenerife (Canary Islands). *International Journal of Earth Sciences*, 91(4), 615-628. https://doi.org/10.1007/s00531-001-0245-8

Watanabe, T., Masuyama, T., Nagaoka, K. and Tahara, T. (2002) Analog experiments on magma-filled cracks: Competition between external stresses and internal pressure. *Earth, Planets and Space*, 54(12), 1247-1261. https://doi.org/10.1186/BF03352453

Watson, G.S. (1966) The statistics of orientation data. *The Journal of Geology*, 74(5), 786-797.

Weinberger, R., Lyakhovsky, V., Baer, G. and Agnon, A. (2000) Damage zones around en echelon dike segments in porous sandstone. *Journal of Geophysical Research: Solid Earth*, 105(B2), 3115-3133. https://doi.org/10.1029/1999JB900361

Weis, F.A., Skogby, H., Troll, V.R., Deegan, F.M., and Dahren, B. (2015) Magmatic water contents determined through clinopyroxene: Examples from the Western Canary Islands, Spain. *Geochemistry, Geophysics, Geosystems*, 16(7), 2127-2146. https://doi.org/10.1002/2015GC005800

Weisstein, E.W. (2024) *Euler Differential Equation*. MathWorld – A Wolfram Web Resource [online] https://mathworld.wolfram.com/EulerDifferentialEquation.html [Accessed: 16.01.24]

Weisstein, E.W. (2023) *Sphere Point Picking*. Mathworld – A Wolfram Web Resource [online] https://mathworld.wolfram.com/SpherePointPicking.html [Accessed: 03.11.23]

White, R.S., Drew, J., Martens, H.R., Key, J., Soosalu, H., and Jakobsdóttir, S.S. (2011) Dynamics of dyke intrusion in the mid-crust of Iceland. *Earth and Planetary Science Letters*, 304, 300-312. https://doi.org/10.1016/j.epsl.2011.02.038

Whitehead, J.A. and Helfrich, K.R. (1991) Instability of flow with temperature-dependent viscosity: a model of magma dynamics. *Journal of Geophysical Research*, 96, 4145-4155. https://doi.org/10.1029/90JB02342

Willis, D.G. (1977) A kinematic model of preferred orientation. *Geological Society of America Bulletin*, 88, 883-894. https://doi.org/10.1130/0016-7606(1977)88<883:AKMOPO>2.0.CO;2

Wolff, J.A., Rampino, M.R., Coffin, M.F., and Self, S. (2015) Large igneous provinces and flood basalt volcanism, in: Sigurdsson, H., Houghton, B., McNutt, S., Rymer, H. and Stix, J. (eds.) *Encyclopedia of Volcanoes* (2nd ed.). London: Academic Press, pp. 271–279.

Woodcock, N.H. (1977) Specification of fabric shapes using an eigenvalue method. *Geological Society of America Bulletin*, 88(9), 1231-1236. https://doi.org/10.1130/0016-7606(1977)88<1231:SOFSUA>2.0.CO;2

Woods, J., Winder, T., White, R.S., and Brandsdóttir, B. (2019) Evolution of a lateral dike intrusion revealed by relatively-relocated dike-induced earthquakes: The 2014–15 Bárðarbunga–Holuhraun rifting event, Iceland. *Earth and Planetary Science Letters*, 506, 53-63. https://doi.org/10.1016/j.epsl.2018.10.032

Wylie, J.J., Helfrich, K.R., Dade, B., Lister, J.R. and Salzig, J.F. (1999) Flow localisation in fissure eruptions. *Bulletin of Volcanology*, 60, 432-440. https://doi.org/10.1007/s004450050243

Yamato, P., Tartese, R., Duretz, T. and May, D.A. (2012) Numerical modelling of magma transport in dykes. *Tectonophysics*, 526, 97-109. https://doi.org/10.1016/j.tecto.2011.05.015

Zhang, Y., Xu, Z., Zhu, M., and Wang, H. (2007) Silicate melt properties and volcanic eruptions. *Reviews of Geophysics*, 45(4). https://doi.org/10.1029/2006RG000216

Zia, H. and Lecampion, B. (2020) PyFrac: A planar 3D hydraulic fracture simulator. *Computer Physics Communications*, 255, 107368. https://doi.org/10.1016/j.cpc.2020.107368

Appendix A

Deriving the equation for the velocity profile of laminar coaxial flow between two cylinders

The Navier-Stokes equation for laminar coaxial flow between two cylinders, for two-dimensional problems where flow along the length of the cylinder is neglected, is

$$\frac{\partial u_\theta}{\partial t} + u_r \frac{\partial u_\theta}{\partial r} + \frac{u_\theta}{r}\frac{\partial u_\theta}{\partial \theta} + \frac{u_r u_\theta}{r} = \frac{1}{\rho r}\frac{-\partial P}{\partial \theta} + \nu\left(\nabla^2 u_\theta - \frac{u_\theta}{r^2} + \frac{2}{r^2}\frac{\partial u_r}{\partial \theta}\right) \quad \text{(A1)}$$

where u_θ is the velocity in the direction of flow, parallel to the circumference of the cylinders, u_r is the velocity in the radial direction, t is time, r is radial position, θ is distance in the direction of flow, ρ is the fluid density, and P is pressure (Bernard, 2015). All the terms on the lefthand side should equal zero, because we assume there is no change in u_θ over time or in the direction of flow, and we assume that there is no component of radial velocity, so $u_r = 0$. On the righthand side, we can ignore the first term, as we assume that there is no pressure gradient in the direction of flow. We can also ignore the last term, because of our assumption $u_r = 0$. This leaves the Laplacian operator, which for two-dimensional flow in cylindrical coordinates is given by (Bernard, 2015)

$$\nabla^2 u_\theta = \frac{1}{r}\frac{\partial}{\partial r}\left(r\frac{\partial u_\theta}{\partial r}\right) + \frac{1}{r^2}\frac{\partial^2 u_\theta}{\partial \theta^2}. \quad \text{(A2)}$$

We can ignore the final term on the righthand side because we have assumed that there is no change in u_θ in the direction of flow. By combining the relevant terms from equations A1 and A2, we find a general equation for flow velocity and radial position:

$$\frac{1}{r}\frac{\partial}{\partial r}\left(r\frac{\partial u_\theta}{\partial r}\right) - \frac{u_\theta}{r^2} = 0. \quad \text{(A3)}$$

By differentiating A3, we find that

$$\frac{\partial^2 u_\theta}{\partial r^2} + \frac{1}{r}\frac{\partial u_\theta}{\partial r} - \frac{u_\theta}{r^2} = 0, \quad \text{(A4)}$$

which is a second order Euler-Cauchy equation (Weisstein, 2024). As such, we can assume a solution where $u_\theta = r^m$. Substituting this into Eq. A4, we find that

$$m(m-1)r^{m-2} + \frac{1}{r}mr^{m-1} - \frac{r^m}{r^2} = 0, \quad \text{(A5)}$$

which can be factorised into

$$(m-1)(m+1)r^{m-2} = 0, \tag{A6}$$

showing that $m = \pm 1$. Euler-Cauchy equations with two real roots can be expressed in the form $y = c_1 x^{m_1} + c_2 x^{m_2}$, and so we can state that

$$u_\theta = c_1 r + c_2 r^{-1}. \tag{A7}$$

We can then find values for c_1 and c_2 by defining the boundary conditions of our problem. We know that the fluid in contact with the outer cylinder, which has internal radius R_o, has a velocity of zero. We also know that the fluid in contact with the inner cylinder (i.e., the stirring rod), has the same velocity as the surface of the cylinder, calculated by ωR_i, where ω is the rotation rate in radians over time, and R_i is the radius of the inner cylinder. Therefore, we have two boundary conditions:

$$c_1 R_o + \frac{c_2}{R_o} = 0 \tag{A8.1}$$

and

$$c_1 R_i + \frac{c_2}{R_i} = \omega R_i. \tag{A8.2}$$

By rearranging and substituting equations A8.1 and A8.2, we find equations for c_1 and c_2 in terms of ω, R_i and R_o:

$$c_1 = -\frac{\omega}{R_o^2\left(\frac{1}{R_i^2} - \frac{1}{R_o^2}\right)} \tag{A9.1}$$

and

$$c_2 = \frac{\omega}{\left(\frac{1}{R_i^2} - \frac{1}{R_o^2}\right)}. \tag{A9.1}$$

Then, by substituting A9.1 and A9.2 back into Eq. A7, we find an expression for velocity as a function of radial position and stirring rate, where

$$u_\theta = -\frac{\omega r}{R_o^2\left(\frac{1}{R_i^2} - \frac{1}{R_o^2}\right)} + \frac{\omega}{r\left(\frac{1}{R_i^2} - \frac{1}{R_o^2}\right)}, \tag{A10}$$

which simplifies to

$$v(r) = \omega\, R_i \left(\frac{\frac{R_o}{r} - \frac{r}{R_o}}{\frac{R_o}{R_i} - \frac{R_i}{R_o}}\right), \tag{A11}$$

presented as Eq. 2.7 in the main text.

Appendix B

Published Work

Allgood, C., Llewellin, E.W., Humphreys, M.C.S., Mathias, S.A., Brown, R.J. and Vye-Brown, C., (2024) Banding in the margins of basaltic dykes indicates pulsatory propagation during emplacement. *Journal of Geophysical Research: Solid Earth*, 129(4), p.e2023JB028007. https://doi.org/10.1029/2023JB028007

JGR Solid Earth

RESEARCH ARTICLE
10.1029/2023JB028007

Banding in the Margins of Basaltic Dykes Indicates Pulsatory Propagation During Emplacement

C. Allgood[1], E. W. Llewellin[1], M. C. S. Humphreys[1], S. A. Mathias[2], R. J. Brown[1], and C. Vye-Brown[3]

[1]Department of Earth Sciences, Durham University, Durham, UK, [2]Department of Engineering, Durham University, Durham, UK, [3]British Geological Survey, Edinburgh, UK

Key Points:

- Banded textures at dyke margins are the result of pulsatory magma flow in the tip of the propagating dyke
- Dyke propagation is not continuous, but occurs in steps via a cycle of cooling, stalling, inflating, rupturing and propagating
- Cooling and solidification of magma in the narrow dyke tip has a strong influence on dyke propagation

Supporting Information:

Supporting Information may be found in the online version of this article.

Correspondence to:

C. Allgood and E. W. Llewellin,
ceri.allgood@durham.ac.uk;
ed.llewellin@durham.ac.uk

Citation:

Allgood, C., Llewellin, E. W., Humphreys, M. C. S., Mathias, S. A., Brown, R. J., & Vye-Brown, C. (2024). Banding in the margins of basaltic dykes indicates pulsatory propagation during emplacement. *Journal of Geophysical Research: Solid Earth*, *129*, e2023JB028007. https://doi.org/10.1029/2023JB028007

Received 6 OCT 2023
Accepted 23 MAR 2024

Author Contributions:

Conceptualization: C. Allgood, E. W. Llewellin, M. C. S. Humphreys, R. J. Brown
Data curation: C. Allgood
Formal analysis: C. Allgood, S. A. Mathias
Investigation: C. Allgood
Methodology: C. Allgood, E. W. Llewellin, S. A. Mathias
Resources: R. J. Brown
Software: C. Allgood, S. A. Mathias
Supervision: E. W. Llewellin, M. C. S. Humphreys, R. J. Brown, C. Vye-Brown
Writing – original draft: C. Allgood

Abstract Basaltic fissure eruptions, which are the most common type of eruption on Earth, are fed by dykes which mediate magma transport through the crust. Dyke propagation processes are important because they determine the geometry of the transport pathway and the nature of any geophysical signals associated with magma ascent. Here, we investigate small-scale (mm–cm wide) banding features at the margins of dykes in the Teno Massif (Tenerife, Spain) and the Columbia River Basalt Province (CRBP) (USA). Similar marginal bands have been reported for dykes in numerous localities around the world. Dyke margins record valuable information about propagation because they are the first material to solidify against the host rock at the propagating dyke tip. We find that the marginal bands are defined by cyclic variations in phenocryst concentration and vesicularity, and we infer that these cyclic variations in texture are a product of cyclic variations in magma flow rates and pressures within the dyke tip. This indicates that dyke emplacement occurs in pulses, with propagation repeatedly hindered by the rapid cooling and solidification of magma in the narrow dyke tip. Using a 1D conduction model, we estimate the time taken for each band to cool and solidify, which provides a timescale of several minutes to tens of minutes for the pulses. The occurrence of similar bands in various volcanic settings suggests that pulsatory propagation is a common, if not ubiquitous, process associated with dyke emplacement.

Plain Language Summary Dykes are cracks in the Earth's crust through which magma rises, sometimes feeding volcanic eruptions. Here, we investigate small-scale banding features that are commonly found in solidified magma in dykes, using examples from the Teno Massif (Tenerife, Spain) and the Columbia River Basalt Province (USA). The bands form at the margin of the dyke, against the crack wall, which means that they record what happened when the dyke first formed; that is, when magma first flowed into the crack. We find that the bands are defined by repeated variations in the amount of crystals and bubbles, which we infer to have resulted from variations in magma flow rates and pressures in the dyke tip. This shows that the dykes formed in steps, rather than all in one go. By calculating the time taken for the bands to cool and solidify, we find that each propagation step lasts several minutes to tens of minutes. The occurrence of similar bands in various volcanic settings around the world suggests that most or all dykes form this way. This is important because the stepwise formation of the cracks might create small earthquakes that can be detected as the magma rises toward the Earth's surface.

1. Introduction

Basaltic feeder dykes are planar conduits that feed fissure eruptions. Flow processes within dykes influence eruptive behavior at the surface, such as the localisation of fissure eruptions (Bruce & Huppert, 1989; Delaney & Pollard, 1982; Jones & Llewellin, 2021). In order to forecast potential propagation pathways and to determine which areas might be most at risk from eruptions, we need an understanding of dyke emplacement, from initial propagation to late-stage flow processes.

Subsurface flow cannot be observed directly, but the rates and overall direction of dyke propagation have been inferred using the migration of seismic activity, with typical time-averaged propagation speeds inferred to be tens of centimeters per second (e.g., Einarsson & Brandsdóttir, 1980; White et al., 2011; Woods et al., 2019). Rock textures from ancient, solidified dykes can complement the geophysical data from active systems as an indirect means to investigate subsurface processes (e.g., Philpotts & Asher, 1994; Philpotts & Philpotts, 2007; Wada, 1992). For example, many studies have used rock textures or magnetic fabrics at dyke margins to infer initial propagation directions (e.g., Baer & Reches, 1987; Staudigel et al., 1999).

Writing – review & editing:
E. W. Llewellin, M. C. S. Humphreys, S. A. Mathias, R. J. Brown, C. Vye-Brown

The margins of a dyke are the first material to solidify against the host rock, so they must originate at the leading edge of a dyke as it propagates through the crust. Marginal textures are therefore intrinsically related to the propagation process, and provide a record from initial crack propagation toward sustained magma flow within the dyke. Numerical models of dyke propagation, whether 2D (e.g., Maccaferri et al., 2010; Taisne & Jaupart, 2009) or 3D (e.g., Davis et al., 2021; Zia & Lecampion, 2020), operate within the framework of linear elastic fracture mechanics (LEFM), where propagation is controlled by the geometry of the dyke tip, and either the fracture toughness of the medium, or viscous losses from the fluid (Gonnermann & Taisne, 2015). However, despite LEFM models requiring a tapered dyke tip geometry to concentrate stress and instigate fracture, most overlook the role of solidification, even though the narrow tip must be prone to rapid cooling. Marginal samples provide information about the role of cooling and solidification at the tip of a propagating dyke, and about the geometry of the tip itself. This provides a framework for interpreting geophysical evidence of dyke propagation, and for informing numerical propagation models.

The aim of this work is to interpret variations in magma flow and dyke propagation from the analysis of dyke margin features, in the context of this dyke propagation framework. We focus on two samples which show banded textures at their margins: one from the Teno Massif (Tenerife, Spain) and one from the Columbia River Basalt Province (CRBP) (USA). We view these textures as a time series, with the oldest material at the dyke wall, and progressively younger material toward the dyke center. The samples therefore provide a record from initial propagation to sustained magma flow, and reveal the dyke tip flow conditions associated with propagation.

2. Background

2.1. Examples of Marginal Banding

Marginal bands have been found in basaltic dykes in numerous settings, including the Canary Islands (Delcamp et al., 2012; Thiele et al., 2021), the CRBP (Thordarson & Self, 1996), Paleogene dykes and sills in northwest Scotland (Drever & Johnston, 1959; Holness & Humphreys, 2003; Kile, 1993; Platten, 2000; Roberts & Sanderson, 1971), the Karoo dyke swarm in Namibia (Coward, 1980), American Samoa (Walker & Eyre, 1995), Koolau Volcano, Hawaii (Walker, 1987), and the San Rafael subvolcanic field in Utah (Kavanagh et al., 2018). Marginal bands (Figures 1–3) show a general trend of getting wider and less distinct toward the intrusion center,

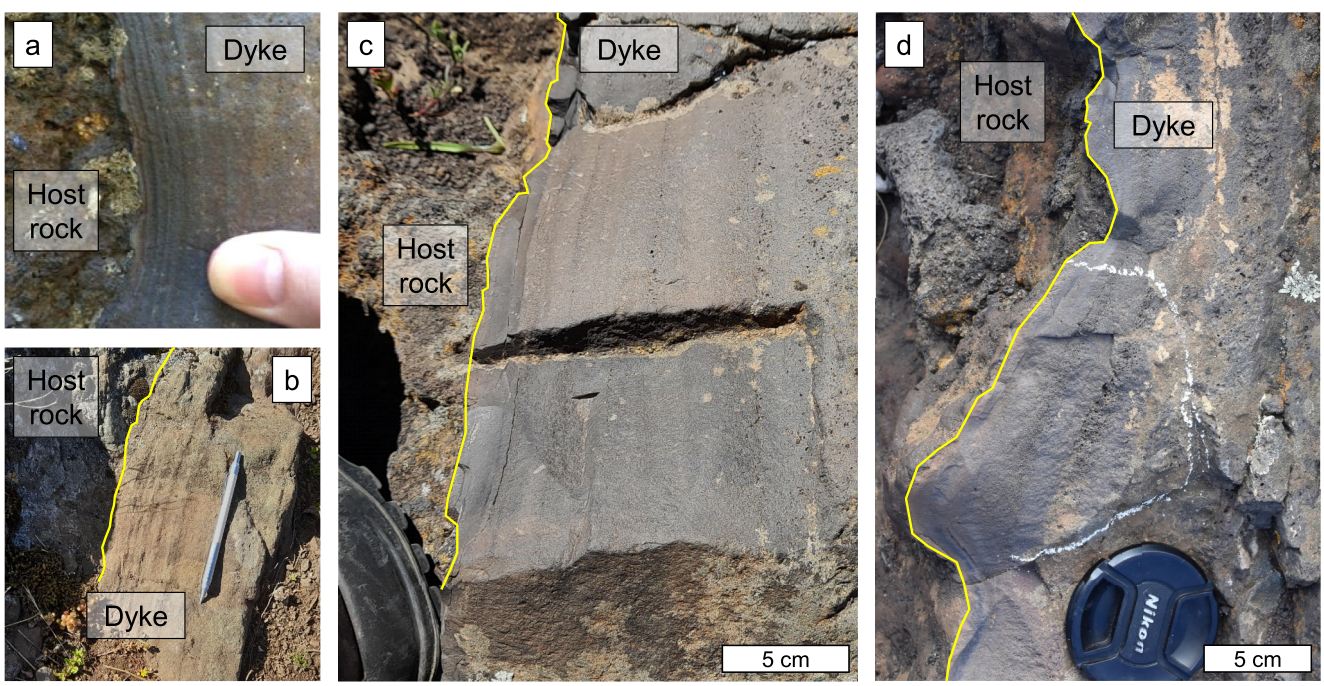

Figure 1. Examples of marginal banding from dykes in the Teno Massif, NW Tenerife. Bands can be found as weathered ridges (a, b), or defined by variation in color and vesicularity (c, d).

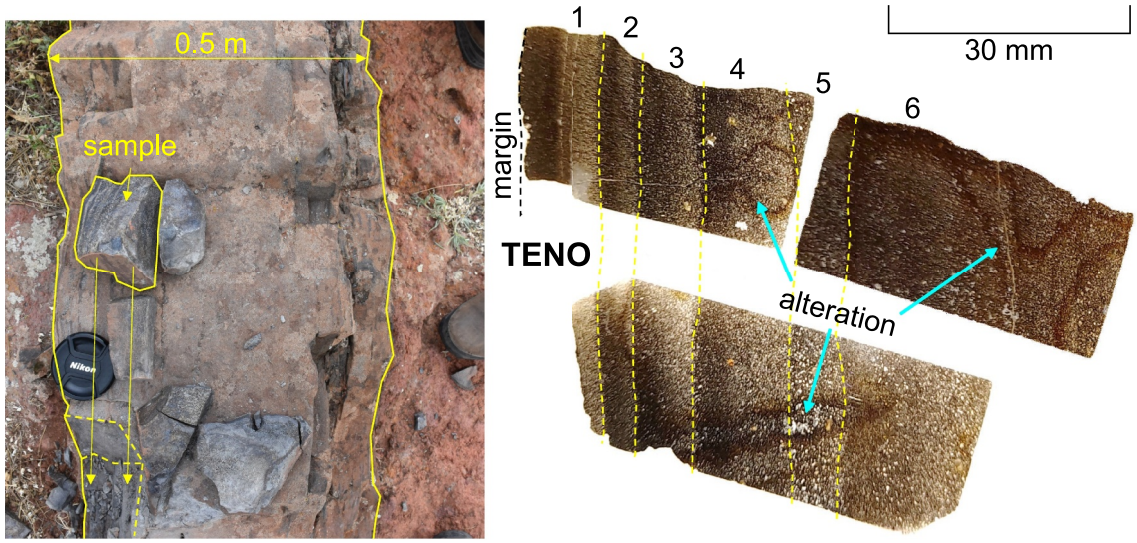

Figure 2. (left) Origin of the Teno sample in the margins of a 0.5-m-wide dyke; (right) three aligned thin sections taken from the sample, showing the first six bands. Heavily altered streaks through the sample are highlighted. The margin indicated is the true margin of the dyke, with no host rock attached.

typically starting at widths of only a few millimeters, and attaining maximum widths of up to several centimeters before becoming indistinct (Kavanagh et al., 2018; Thiele et al., 2021; Thordarson & Self, 1996; Walker & Eyre, 1995).

Marginal bands are typically distinguishable by eye through variations in phenocryst concentration, groundmass grain size, and/or vesicularity. Where bands are defined by phenocryst concentration, they can appear as porphyritic and non-porphyritic zones, sometimes associated with a gradation in phenocryst size (Drever & Johnston, 1959). Alternatively, where bands are defined by groundmass grain size, they appear as a series of discontinuities, involving a drop in grain size moving toward the dyke center (Holness & Humphreys, 2003). Other bands are defined by narrow, highly vesicular or amygdaloidal regions running parallel to the dyke margins (Delcamp et al., 2012; Galindo & Gudmundsson, 2012; Kavanagh et al., 2018; Kile, 1993; Platten, 2000; Thiele et al., 2021; Thordarson & Self, 1996; Walker & Eyre, 1995). Finally, some authors describe platy textures and color variations at dyke margins, the cause of which is uncertain (Coward, 1980; Healy et al., 2018; Roberts & Sanderson, 1971).

Banding is usually restricted to within approximately 15 cm of the dyke margin, especially for bands defined by phenocrysts and groundmass variations (e.g., Drever & Johnston, 1959; Holness & Humphreys, 2003). However, vesicle bands have been observed further toward the centers of intrusions; for example, in the CRBP, highly vesicular bands are present all the way from the margins to the dyke center, increasing in width from 1 to 10 cm (Thordarson & Self, 1996), and vesicular bands have also been observed across the entire widths of dykes in American Samoa (Walker & Eyre, 1995).

2.2. Formation of Bands and Layers Within Dykes

Marginal bands are distinct from the large-scale layering commonly found within dykes, which is often tens of centimeters to several meters wide. The large-scale layers are defined by distinct compositions (Eriksson et al., 2011) or jointing patterns (Gudmundsson, 1984; Ray et al., 2007), or by a textural change between layers, evidenced by chilled margins or melt-back margins. A chilled margin forms when magma cools rapidly against its surroundings, forming a glassy or fine-grained layer (e.g., Brouxel, 1991; Platten, 2000), whereas a melt-back margin forms when magma thermally erodes into older dyke material, then cools slowly, forming a coarser texture (Huppert & Sparks, 1989; Svenningsen, 1994). In either case, a substantial time gap is required between layers. As such, large-scale layering is inferred to form via multiple, discrete injections of magma; for example, where felsic magma has been injected into the center of a pre-existing basaltic dyke (e.g., Eriksson et al., 2011; Tomé et al., 2020). Large-scale layers can therefore be viewed as products of distinct intrusion episodes, with a

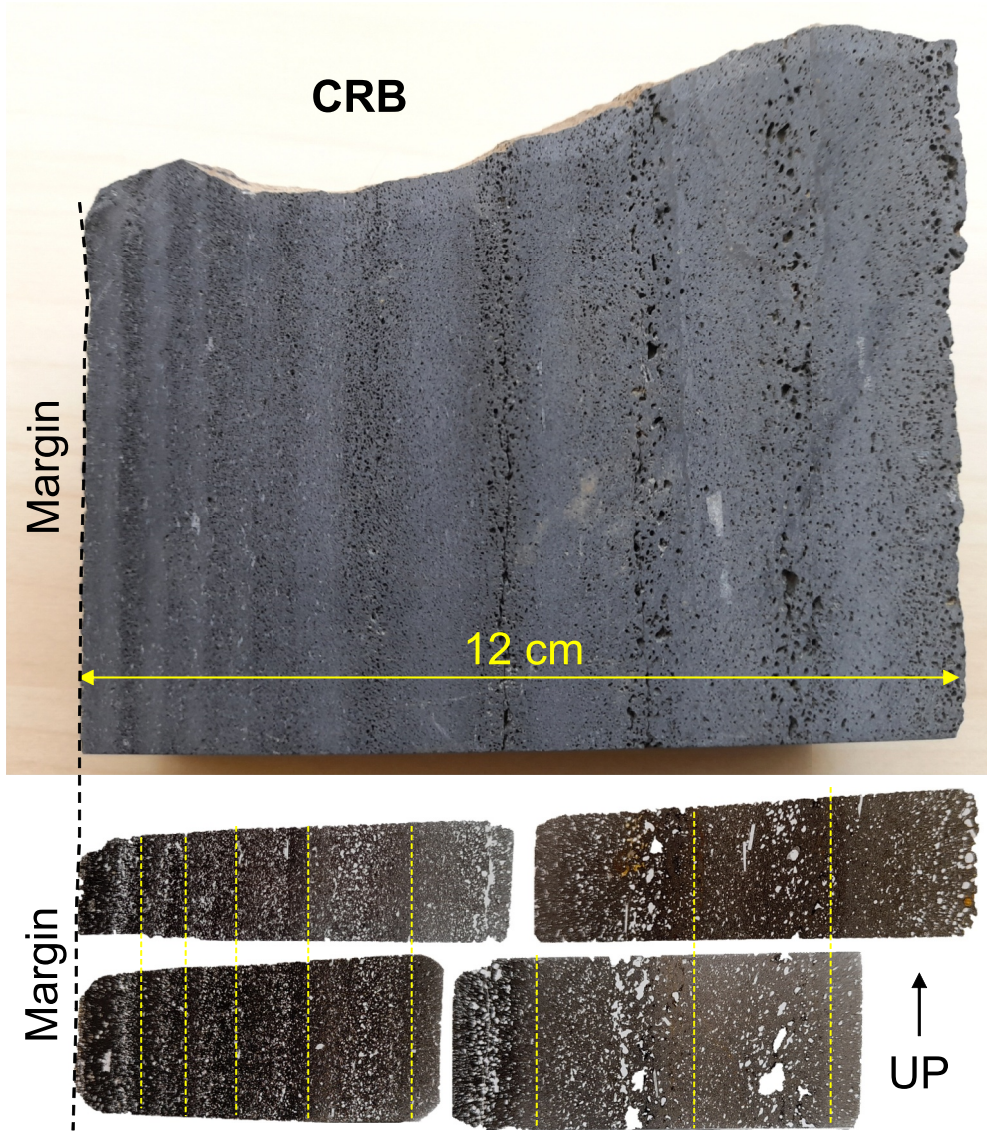

Figure 3. The CRB sample, from the margins of a feeder dyke to the Roza lava flow, with four aligned thin sections taken from the sample in the vertical plane, perpendicular to the margin. Dashed yellow lines on the thin sections show the positions of minimum vesicularity, used to define the bands. The margin indicated is the true margin of the dyke, with no host rock attached.

unique emplacement history for each dyke. This is very different from marginal bands, which always show a general trend of widening and becoming less distinct toward the dyke center. Marginal bands are not, therefore, small-scale versions of a composite dyke.

The most common interpretation of marginal bands is that they represent variations in flow rates within the dyke, attributed to the repeated injection of material (Drever & Johnston, 1959; Platten, 2000). Other explanations of marginal banding include each layer representing a plane of movement at the edge of the dyke (Roberts & Sanderson, 1971). Bands defined by vesicles alone have been interpreted to result from pressure fluctuations and temporal variations in flow (Kavanagh et al., 2018; Kile, 1993; Thiele et al., 2021; Walker & Eyre, 1995), or preferential degassing pathways (Delcamp et al., 2012). However, few reports of marginal banding include observations of internal chilled margins; in fact, their absence has been noted (Platten, 2000). Therefore, although some bands may be defined by drops in grain size short of an internal chilled margin (Holness & Humphreys, 2003; Platten, 2000), it seems that band formation is too rapid to allow long cooling intervals between them.

3. Field Sites and Samples

Two samples displaying prominent marginal banding are investigated to determine the nature of the bands: one from the Teno Massif (Tenerife, Spain); and one from the CRBP (USA). We refer to these samples as the "Teno sample" and the "CRB sample" respectively.

3.1. Teno Sample

The Teno sample comes from a 0.5-m-wide basaltic dyke in the Teno Massif (Figure 2), and comprises the outermost 10 cm of the dyke, with six bands recognizable by eye. Banded margins were seen on several dykes in the immediate area, usually defined by a dark-to-light color variation, and often associated with variations in vesicularity (Figure 1). The Teno Massif is the eroded remains of a basaltic shield volcano active between 5.0 and 6.3 Ma (Leonhardt & Soffel, 2006; Longpré et al., 2009). Most dykes in the region are single intrusions, but multiple and composite intrusions are common, showing large-scale layering with chilled margins and distinct compositions. Dyke tips are commonly exposed, typically tapering into a crack-like geometry (Marinoni & Gudmundsson, 2000).

3.2. CRB Sample

The CRB sample comes from the margins of a 0.95 m wide basaltic dyke in SE Washington State. The dyke is one of many that fed the 14.7 Ma Roza lava flow, which was emplaced over at least 14 years and covers an area of 40,300 km^2 (Thordarson & Self, 1998). The sample comprises the outermost 12 cm of the dyke and contains nine bands distinguishable by eye (Figure 3). Many of the Roza dykes display bands of vesicles at their margins, symmetrical on either side of the dyke, and some contain up to 18 apparent bands. The inferred depth of emplacement is 500 m.

4. Methods

Thin sections were taken from both the Teno sample and the CRB sample, so that their textures could be analyzed from the margins inwards. For the CRB sample, which had a known orientation, thin sections were taken on the vertical plane, perpendicular to the margin. Images were collected at ×5 magnification under a petrological microscope, then stitched together using Inkscape to form image swaths extending across the width of the thin section (Supporting Information S1). Due to the different color and brightness contrasts in the thin section images, plane polarized light images were used for the Teno sample, and cross-polarized light images were used for the CRB sample. Image swaths from separate thin sections from the same sample were aligned using the bands as a guide (Figures 2 and 3), allowing measurements of phenocrysts and vesicles to be given with positions relative to the dyke margin.

Phenocrysts and vesicles were manually outlined in ImageJ (Schindelin et al., 2012). The area, maximum diameter and best-fit ellipse of the outlined features were generated using the internal functions within ImageJ. The best-fit ellipse provided measurements of an object's major and minor axes, aspect ratio and orientation. Two sets of binary images were created using the manual outlines: one set containing phenocrysts, and one set containing vesicles (Figure 4).

To quantify the textural data with distance from the dyke margin, the binary images and raw data were analyzed in strips 1,080 pixels (1 mm) wide, perpendicular to the dyke margin. This bin width was chosen as it was wider than the largest vesicles, and captured enough phenocrysts and vesicles to calculate reliable means, while remaining narrow enough to show changes within individual marginal bands. Medians and interquartile ranges were calculated from the raw data within each strip, for phenocryst and vesicle area, maximum diameter, aspect ratio, long-axis orientation, and circularity. Aspect ratio was defined as major axis/minor axis, while circularity was defined as object perimeter over the circumference of a circle with equal area. For orientation data, circular statistical methods were used to calculate means and standard deviations (Jammalamadaka & SenGupta, 2001).

The binary images were analyzed in MATLAB, where values for phenocryst area fraction and vesicle area fraction were generated based on the proportion of white pixels within a given region of the binary image, and number densities were generated from the number of independent white areas. Vesicle area fraction was calculated as vesicle area/total area, while phenocryst area fraction was calculated as the phenocryst area/(total area—vesicle area), to exclude the vesicles. Phenocryst number densities were calculated as the phenocryst

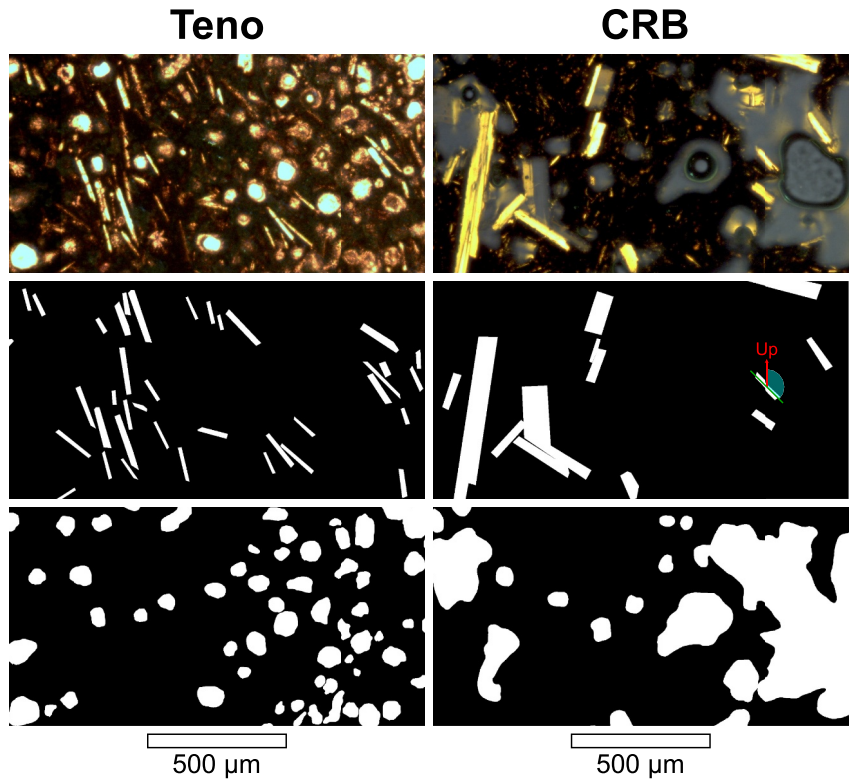

Figure 4. Examples of binary images created from Teno (top left, plane-polarized light) and CRB (top right, cross-polarized light) microscope images. Binary phenocryst images (middle row) and binary vesicle images (bottom row) are created from manual outlines. Angle measurements from the vertical are demonstrated on the CRB phenocrysts. Margin is to the left in both images.

number/(total area—vesicle area), and vesicle number densities were calculated as vesicle number/(total area—vesicle area).

For the CRB sample, groundmass and microlites were investigated using a Zeiss Evo scanning electron microscope with 15.00 kV beam at the GJ Russell Microscopy Facility, Durham University. Three rows of isolated images were captured at 400× magnification, with each row containing images at intervals of 0.5 mm, from the margin into the sixth apparent band. At such high magnification, it was not feasible to create continuous image swaths across the sample. Within each image, plagioclase microlites were outlined manually, and oxides were captured automatically via thresholding in ImageJ.

Within the Teno sample, phenocrysts are 0.02–0.45 mm long (median 0.10 mm) within a dark groundmass, which is glassy within 5 mm of the margin, but becomes progressively more crystalline toward the dyke center. Within the CRB sample, there is a greater range in crystal size; phenocrysts are arbitrarily defined as crystals longer than 0.1 mm (up to a maximum of 4.28 mm), and anything shorter than this is considered a microlite. Additionally, there are two vesicle populations within the CRB sample: angular diktytaxitic voids, all <30 μm, which were only seen using the SEM; and large, rounded, primary magmatic vesicles. The diktytaxitic voids are discussed in more detail later, in Section 5.2.

5. Results

5.1. Teno Sample

Six bands are present within the Teno thin sections (Figure 5). By eye, the bands appear to be defined by dark, glassy material on their marginal side, transitioning into lighter-colored material toward the dyke center, before a relatively sharp boundary with the next band (Figure 2). The bands and their boundaries generally become wider and less distinct toward the dyke center. Here, we focus on the first four bands, which have the most distinct edges.

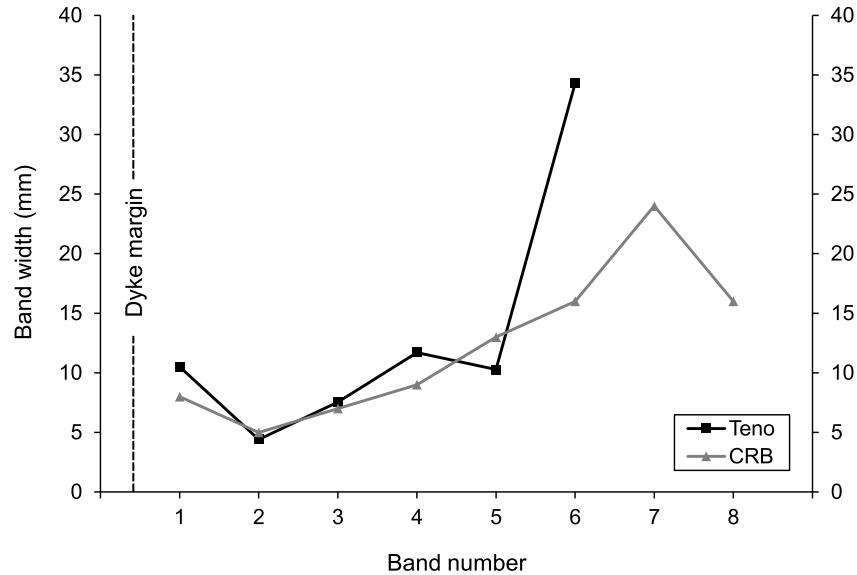

Figure 5. Widths of bands in the Teno and CRB samples. Teno bands were measured based on color variations by eye, later found to be caused by changes in phenocryst concentration. Teno band 6 overran the end of the thin section, making the value plotted a minimum estimate. CRB bands are based on distances between troughs in vesicularity. Absolute measurement error is ±1 mm for each sample, but the edges of bands are subjective.

5.1.1. Teno Phenocrysts

Binary image analysis reveals that the bands are defined by variations in the concentration of phenocrysts, which are dominantly plagioclase. Nearer the dyke margin, the bands contain fewer phenocrysts than the side nearer the center, as shown by the variation in number density, which ranges from 30 to 70 mm^{-2}. The onset of each band is defined by a sharp drop in phenocryst area fraction (Figure 6a) and number density (Figure 6b).

The size of phenocrysts increases gradually toward the dyke center, with mean lengths increasing from around 0.1–0.15 mm across the 9 cm region studied, but there is no relation to the bands (Supporting Information S1). As such, the increase in phenocryst crystallinity within each band is predominantly controlled by the phenocryst number density, not size. There is also a general increase in the crystallinity of the groundmass, which is glassy at the margin, but becomes more crystalline toward the dyke center.

Phenocryst aspect ratio shows no significant variation across the sample and no relation to the bands (Supporting Information S1). The mean orientation of phenocrysts is constant across the bands at around −10°, measured from the dyke margin. The standard deviation shows a gradual increase from around 30° near the dyke margin to values exceeding 50° nearer the dyke center, indicating a reduction in the strength of the shape preferred orientation (SPO) (Supporting Information S1).

5.1.2. Teno Vesicles

Binary image analysis reveals that vesicularity is generally highest near the centers of bands compared with their edges (Figure 6a). This is most evident in the first band, where the peak value of 0.22 in the band interior contrasts with values below 0.05 at the band edges, but this pattern is less distinct in other bands. In all cases, the peak vesicularity does not fall exactly in the band center, but is slightly skewed toward the dyke center. Although vesicle size increases away from the dyke margin, with mean maximum diameters increasing from 0.05 to 0.32 mm across the studied section, vesicle size shows no trend within the bands themselves. The circularity of vesicles decreases toward the dyke center, with no relation to the bands (Supporting Information S1). The mean orientation of vesicles is −10°, the same as the phenocrysts, but the strength of their SPO is lower, with a circular standard deviation of 60° (Supporting Information S1). Vesicle orientation shows no relation to the bands.

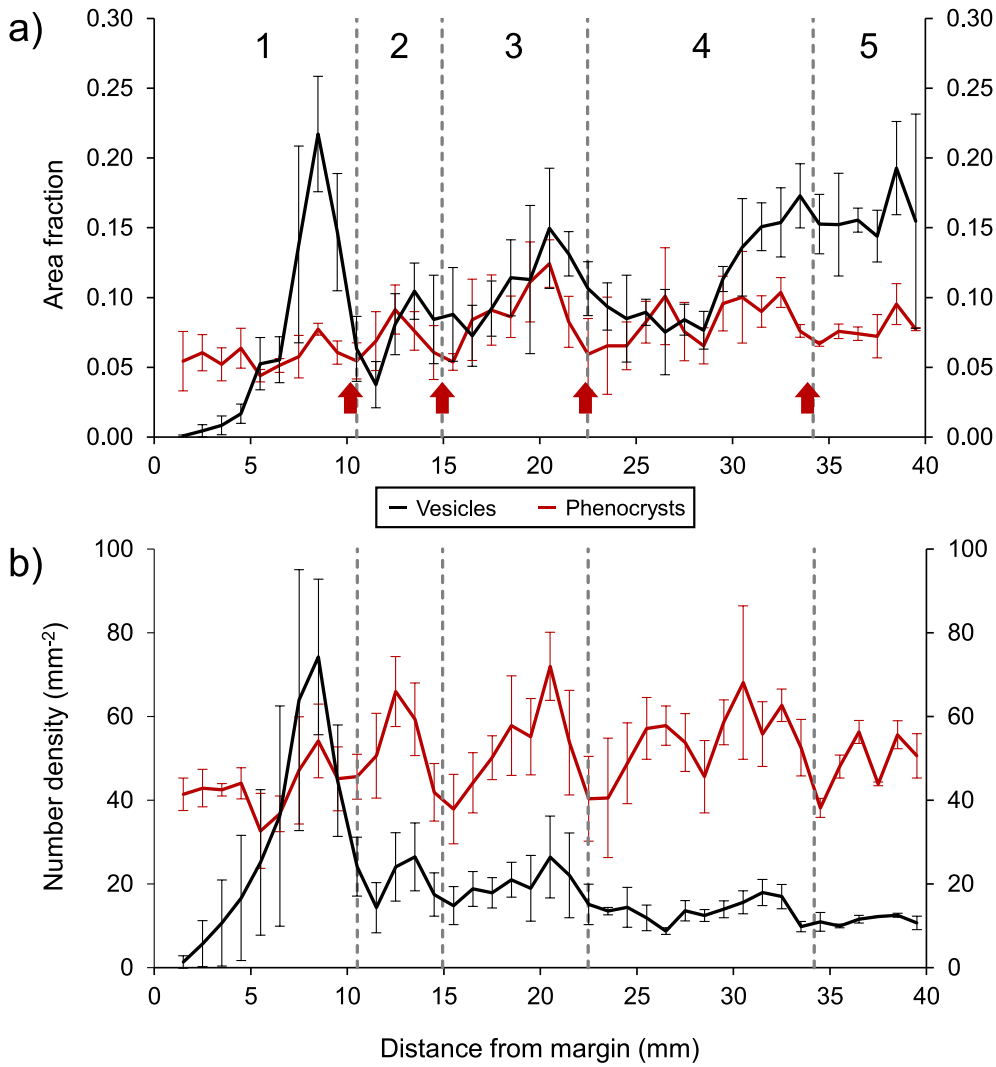

Figure 6. (a) Variation in vesicularity (vesicle area fraction) and phenocryst area fraction across the Teno sample; (b) number densities of vesicles and phenocrysts across the Teno sample. Dashed lines show the positions of the bands determined by eye, based on color variations. Band edges coincide with drops in the phenocryst area fraction (highlighted with red arrows in panel (a)) and number density.

5.2. CRB Sample

Eight bands were identified in the CRB thin sections (Figure 5). By eye, the bands appear to be defined by a variation in vesicularity, but unlike the Teno sample, there are no sharp, color-defined boundaries between bands (Figure 3). By analogy with the Teno sample, we assume that vesicularity peaks in the centers of bands, and define band edges as the regions with the lowest vesicularity. The bands become wider and less distinct toward the dyke center.

5.2.1. CRB Phenocrysts

Binary image analysis reveals no relationship between the bands and any of the measured phenocryst characteristics. Area fraction is shown in Figure 7, and other characteristics (number density, length, aspect ratio and orientation) are presented in the Supporting Information S1. The mean orientation of phenocrysts is $13 \pm 41°$ from the dyke margin, in the vertical plane.

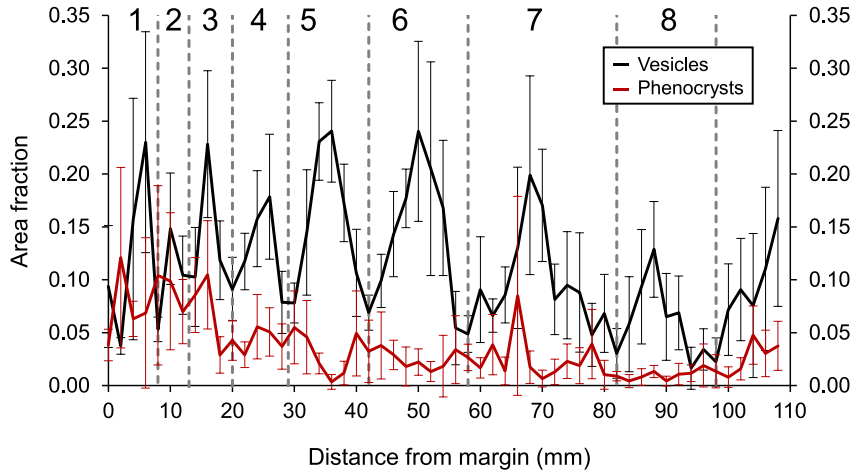

Figure 7. Variation in vesicularity (vesicle area fraction) and phenocryst area fraction across the CRB sample. Gray dashed lines have been placed at troughs in vesicularity. Bands are defined purely by variation in vesicularity, and show no relation to the phenocrysts.

5.2.2. CRB Vesicles

Binary image analysis reveals a clear peak in vesicularity near the center of each band (Figure 7). Peak vesicularity is typically between 0.15 and 0.25, while the lows in vesicularity, taken as the boundaries between bands, have values of 0.01–0.10. Vesicle size increases toward the dyke center, with mean maximum diameters increasing from 0.02 to 0.3 mm, and vesicle size fluctuates across each band, with peaks in maximum size coinciding with peaks in vesicularity (Supporting Information S1). Minimum vesicle circularity coincides with maximum vesicle size, but mean circularity decreases toward the dyke center. The mean orientation of vesicles is constant across the sample, with an overall mean of 24 ± 55° from the dyke margin within the vertical plane (Supporting Information S1). Vesicle orientation shows no relation to the bands.

We note that there are two populations of vesicles present in the CRB sample. In the SEM images, it is apparent that the smallest vesicles (<30 μm) form a diktytaxitic texture (Figure 8). These small voids have angular shapes with straight edges, often completely filling the space between plagioclase microlites. In some cases, the diktytaxitic voids have curved edges on their contact with the groundmass, but they always have at least one angular edge. The size distribution from small, diktytaxitic voids to large, rounded vesicles is not continuous, so they are separate populations. The diktytaxitic textures are only seen in SEM images, and there is no evidence of them connecting with the large, rounded vesicles that were observed under the petrological microscope at lower magnification. The vesicle measurements derived from binary image analysis, presented above, only apply to the larger, primary magmatic vesicle population.

5.2.3. CRB Microlites

SEM analysis of the CRB sample reveals the presence of plagioclase and oxide microlites. Plagioclase microlites have a median length of around 20 μm and a modal aspect ratio of 5, which are both constant across the studied region (Figure 9). No aspect of the plagioclase microlites showed any relation to the bands. Oxide microlites show a gradual increase in maximum diameter from ∼6 to 10 μm across the studied region, and a relatively sharp increase in circularity from 0.3 to 0.5 between 20 and 30 mm from the dyke margin, associated with a change from skeletal, dendritic shapes toward more equant forms (Figure 8). However, no change in oxide size or shape showed any relation to the bands (Figure 9).

6. Discussion

6.1. Conceptual Framework for a Band-Formation Model

We first use the primary field and textural observations to create a conceptual framework for marginal band formation, based on the overall similarities between the two samples, and other examples of marginal bands from

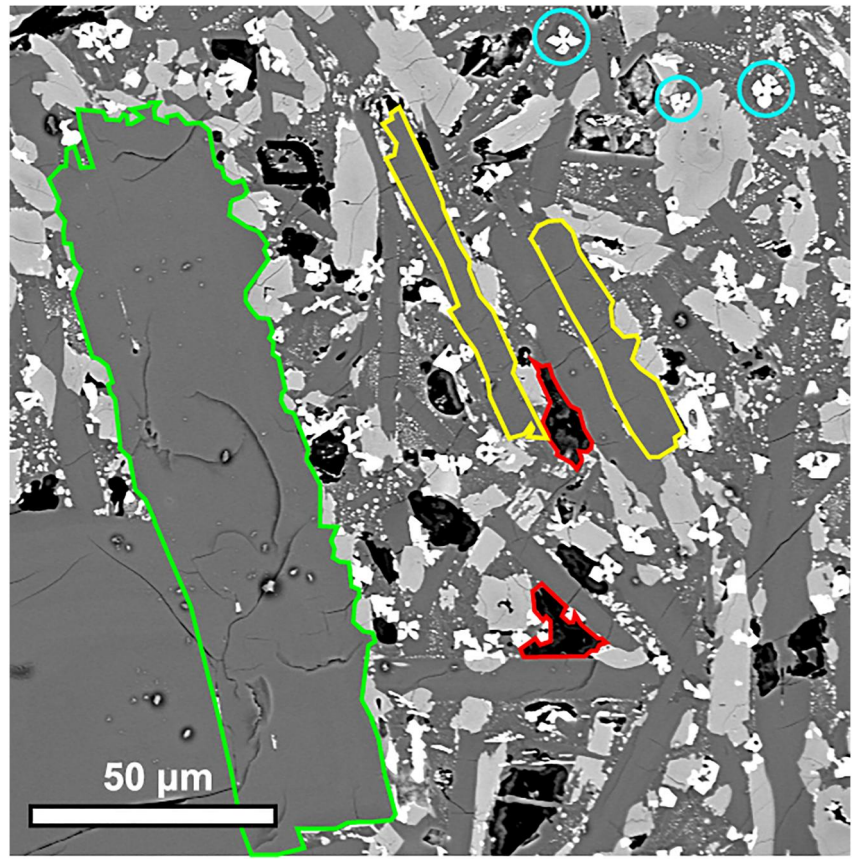

Figure 8. SEM image of the CRB sample. Examples of plagioclase microlites are outlined in yellow, diktytaxitic voids in red, and oxide microlites have been circled in cyan. The large plagioclase crystal on the left side of the image, outlined in green, is 0.15 mm in length, so is classed as a phenocryst.

the literature. The key similarities between the bands in the Teno and CRB samples are their millimeter to centimetre widths, and their tendency to grow wider and less distinct toward the dyke center (Figures 1–3, 5). The bands in the Teno sample are defined by variations in phenocryst number density and vesicularity, with vesicularity peaking near the center of these bands. Banding in the CRB sample comprises cyclic variations in vesicularity only, with no clear way to define the edges of individual bands. Both sets of banding are indicative of a repetitive process.

This repetitive process is significant because dyke margins comprise the earliest material to solidify within the fracture at the dyke tip, meaning that their textures are intrinsically related to propagation. The cyclical textures of the marginal bands indicate a repetitive dyke-tip process, and their prevalence within dykes across diverse volcanic settings (Brouxel, 1991; Delcamp et al., 2012; Drever & Johnston, 1959; Galindo & Gudmundsson, 2012; Holness & Humphreys, 2003; Kavanagh et al., 2018; Platten, 2000; Thiele et al., 2021; Thordarson & Self, 1996; Walker, 1987; Walker & Eyre, 1995) suggests that this process is common.

We propose that the most likely cause of marginal band formation is repeated cooling, solidification and refracturing of magma within the dyke tip. Therefore, we interpret the bands to represent sequential pulses of magma through the narrow dyke tip region, where cooling and solidification is rapid. We propose that each pulse occurs as the dyke propagates a step further, causing repeated widening of the dyke further back from the tip (Figure 10). The similarity in the banding pattern wherever these textures are found along the dyke suggests that the timescales associated with each magma pulse are likely to be roughly constant.

The marginal bands accumulate as follows. Consider a fixed point of observation, initially positioned just ahead of the dyke tip. A new crack forms in the country rock, and a very thin sheet of magma is injected at our point of observation. This is the first pulse, and it cools rapidly to form band one. Propagation stalls, causing pressure

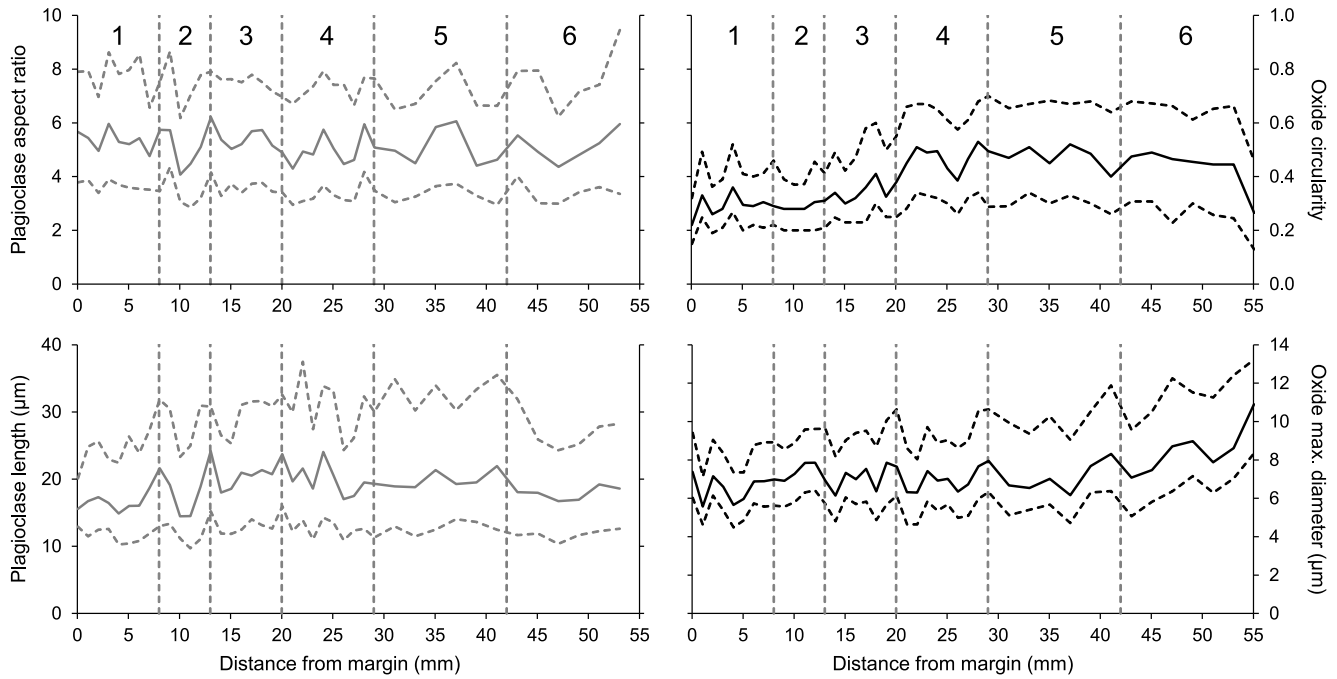

Figure 9. Variation in plagioclase microlite length and aspect ratio, and oxide circularity and maximum diameter across the first six bands of the CRB sample. The solid line shows the median value, and the dashed lines show the interquartile range.

to build behind the solidified tip until it rises high enough to fracture the tip and the host rock beyond, allowing the dyke to propagate another step. This is pulse two, and at our point of observation, this forms the second band. It differs from the first in two key ways: firstly, the dyke tip has advanced further away, and so the magma-filled crack is wider at our point of observation; secondly, the magma has been injected against the previous band, which is warmer than the host rock. As such, band two is wider than band one and lacks a glassy margin. The consistent time interval between pulses is sufficiently long for band two to solidify fully, despite being wider.

This process repeats, and the bands build up. Pulse three cracks through band two, and pulse four cracks through band three. Each new pulse intrudes the center of the last, because this is where material is warmest and therefore weakest (Gudmundsson, 1984). As the tapered dyke tip propagates further, the magma-filled crack gets wider, but the interval between pulses is long enough for each band to fully solidify, despite them getting wider. However, as the tip moves further from the point of observation, pressure drops and fluctuations in flow rate become less pronounced, causing bands to become less texturally distinct. Eventually, magma pulses will be wide enough that they will not solidify to their centers before the next pulse arrives. From then on, no more bands will be produced at the point of observation. Magma flow may still be pulsatory, reflecting the rhythmic propagation of the now-distant crack tip, but this will not be recorded.

Finally, it is interesting to note that, at each step of propagation, the magma pulse responsible will form a first band at the dyke tip, a second band immediately behind the dyke tip, a third band behind that, and so on. This means that each band could, in principle, eventually be traced to the outermost dyke margin, although the extremely high aspect ratio of bands combined with the often poor and patchy exposure of most dyke margins means that this would be very challenging to test in practice.

In the remainder of this section, we explore the feasibility of this model in the context of the data presented in Section 5.

6.2. Band Widths and Dyke Geometry

If we read each band as a pulse of magma that propagated the dyke a step further, then the increase in band width toward the dyke center (Figure 5) provides us with information about the geometry of the dyke tip. The first band

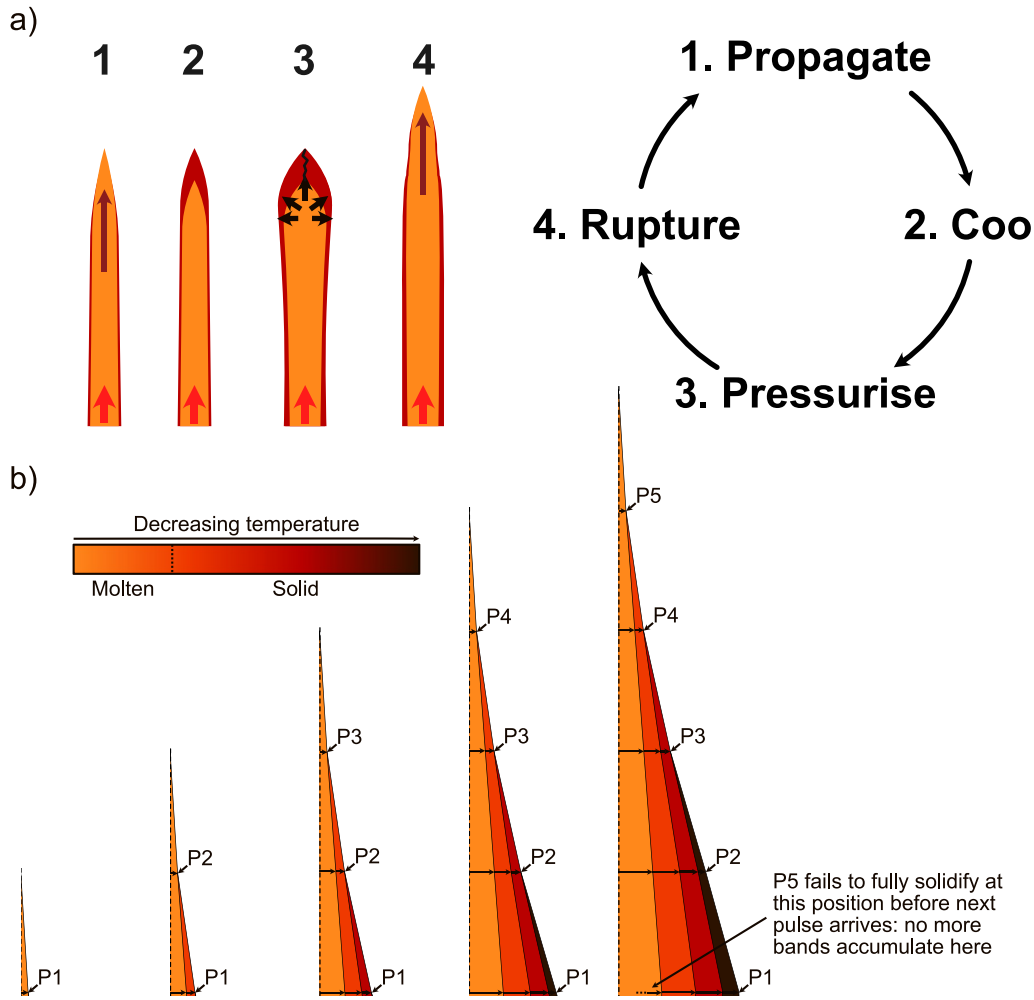

Figure 10. Schematic representation of our conceptual framework: (a) the cooling-driven cycle that leads to pulsatory propagation of the dyke tip; (b) gradual accumulation of bands. Each band represents a pulse of magma through the dyke tip, causing the dyke to propagate a step further, and to inflate further upstream. Note that once a sufficient number of bands have accumulated, a pulse will not fully solidify, causing it to mingle with the next pulse. At this point, the band formation mechanism is lost.

represents the half-width of the first pulse, from the very tip of the dyke, while each subsequent band formed as the tip migrated a step further beyond the point of observation, demonstrating that the molten width of the dyke increased with distance from the tip. We can therefore infer that the dyke tip was tapered, which is concordant with field observations (Figure 11; Clemente et al., 2007; Geshi et al., 2010; Healy et al., 2018; Marinoni & Gudmundsson, 2000; Stephens et al., 2017).

The band widths demonstrate that the tip of the propagating dyke was very narrow. Dyke exposures are sometimes found to be less than a few centimeters wide (Jolly & Sanderson, 1995; Marinoni & Gudmundsson, 2000; Stephens et al., 2017), so it is feasible for a narrow tip region to exist. Indeed, the propagation of fluid-filled, pressurized cracks in the framework of LEFM requires a crack to have a tapering point in order to concentrate stress and instigate fracturing (Rivalta et al., 2015). Our conceptual model does not require dyke tips to have a specific shape (i.e., concave or convex), only that they narrow to a point.

In our framework, the width of each band reflects the tapering dyke tip geometry, not the duration of each magma pulse. The increase in band width toward the dyke center does not indicate longer intervals between magma pulses, as this would manifest as an increase in width of successive first bands in the direction of dyke propagation. Instead, the intervals between magma pulses are likely to have been broadly consistent.

Figure 11. The tapering tip of a dyke in the Teno Massif, Tenerife, which narrows to a width of <2 cm. Such narrow dykes were relatively common in the area, and are assumed to come from the leading edge of a magma pulse, stalled through rapid solidification.

6.3. Solidification and Emplacement Timescales

In our conceptual model, each band represents the half-width of an active section of the dyke at the time of emplacement. We can estimate the time required to solidify each band by considering the rate of heat conduction into the adjacent host rock. We construct a simple numerical model in which magma is emplaced instantaneously into a narrow dyke, then cools conductively until the dyke center reaches a temperature that we choose. A fresh pulse of magma is then emplaced instantaneously along the center of the dyke. The temperature profile is advected laterally to accommodate the new pulse, and the system continues to cool conductively. The widths of each magma pulse are defined by the measured widths of our bands. Full details of the model, including relevant equations and numerical scheme are given in Appendix A.

We apply the model to the Teno sample, using the band width data shown in Figure 5. The CRB bands are of very similar widths, resulting in almost identical timescales, and these are provided in the Supporting Information S1. We estimate the time required for each band to solidify and cool to a defined final temperature, which we take to be the band's emplacement time. We generate a lower bound for emplacement times by ignoring the latent heat released during crystallisation, and an upper bound by including latent heat, which delays solidification. The initial magma temperature, T_M, is taken to be 1,200°C, the same as the eruption temperature measured in 2021 La Palma eruption (Carracedo et al., 2022; Castro & Feisel, 2022), with a solidus temperature $T_S = 1{,}000$°C, and an initial host rock temperature $T_0 = 0$°C. We assume a specific heat capacity of $c_p = 1200$ J kg^{-1} K^{-1} (Mollo et al., 2011; Turcotte & Schubert, 2002), a constant density of $\rho = 2{,}700$ kg m^{-3} for the liquid and solidified magma (Lesher & Spera, 2015), a thermal conductivity of $k = 1.3$ W m^{-1} K^{-1} (Sehlke et al., 2020), and where latent heat is included, a latent heat of $L = 4 \times 10^5$ J kg^{-1} (Bruce & Huppert, 1990; Turcotte & Schubert, 2002). Subsequent magma pulses are injected once the center of the last reaches a defined temperature T_f, and we run the model for six different values of T_f: 1,000, 900, 800, 700, 600 and 500°C.

We proposed in Section 6.2 that the increase in band widths toward the dyke center reflects the tapered geometry of the dyke tip, and that the duration of each magma pulse is likely to be consistent, albeit with variability derived from the stochastic nature of tip propagation. Clearly, greater widths of material take longer to solidify, so the cooling timescales of the widest, innermost bands will be the longest, and will reflect the duration of magma pulses most closely. However, estimating cooling timescales for the inner bands requires us to model the emplacement of the earlier, outer bands, as these act as insulation for all subsequent magma pulses. We do not

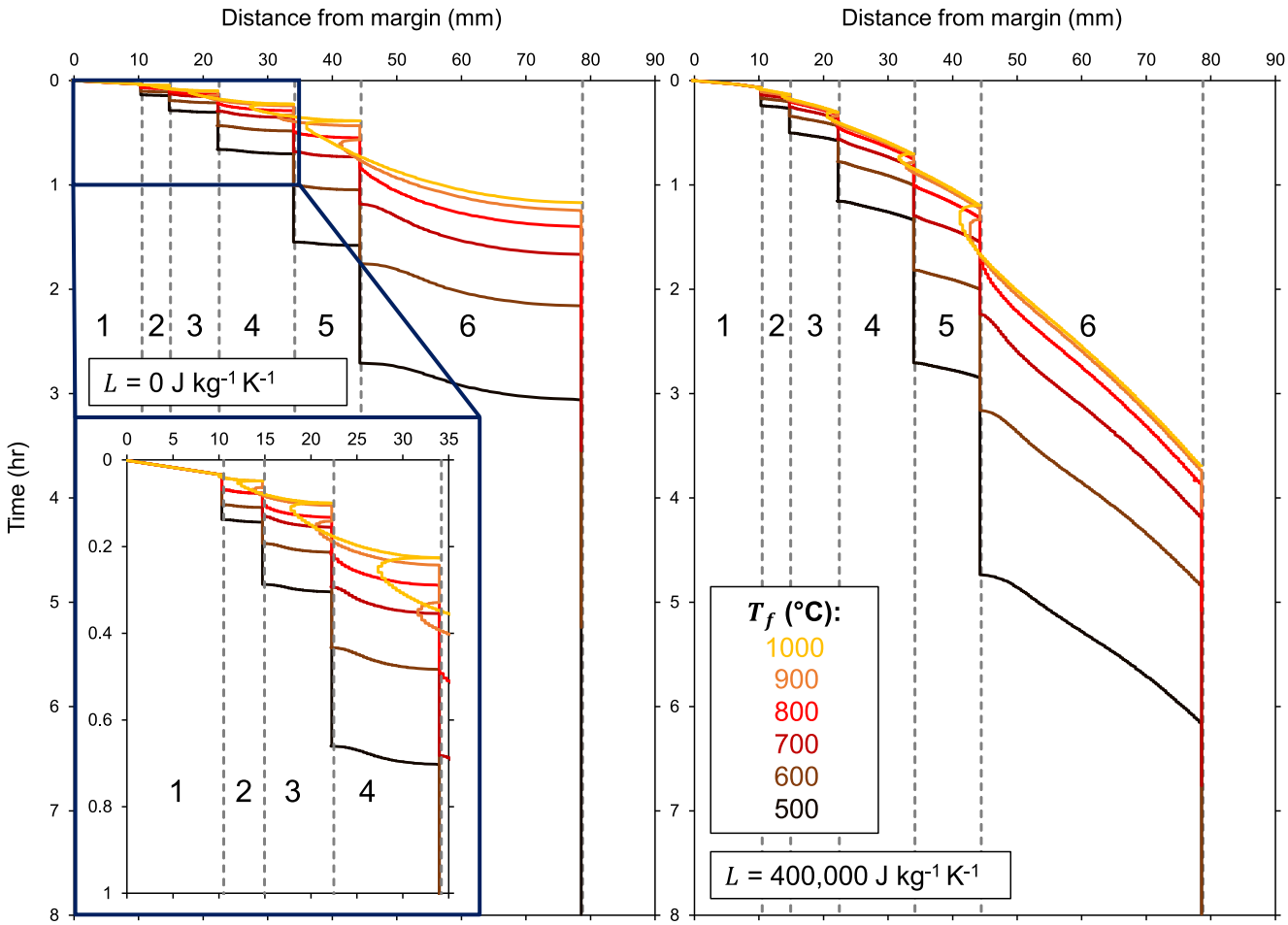

Figure 12. The position of the solidification front (the $T = T_S$ isotherm), moving inwards from the margin, based on the widths of the bands in the Teno sample: (left) latent heat release is neglected; (right) latent heat release is included. T_f is the final temperature at the dyke center before the next magma pulse is emplaced. When the solidification front moves back toward the margin (which is most obvious in the yellow curves), it is melting back previously solidified material.

intend the following solidification timescales for sequential bands to imply that magma pulse duration increased over time. Instead, we view the timescales of the innermost (later-forming) bands as an indicator of potential pulse durations.

We use central temperatures T_f as a constraint on our model because we infer that each band fully solidified before the next pulse arrived. Our samples show sharp, cyclic variations in phenocryst concentration, which would not exist if magma pulses had mingled, or if there had been thermal erosion on the arrival of a new pulse. As such, we know that $T_f \leq T_S$ for each band. Using this temperature constraint, we explore the range of possible magma pulse durations.

We compare the solidification timescales for each band by tracking the position of the solidification front through time, defined as the isotherm within the dyke where $T = T_S$ (Figure 12). Bands solidify faster when the center of the previous band is allowed to cool to a lower temperature before the injection of the next pulse. However, if the next pulse is injected when the center of the last has cooled to only 900°C or 1,000°C, the previous band is melted back. This causes the solidification front to migrate back toward the margin before starting to move toward the dyke center. If pulses are injected with no interval between them (i.e., as soon as the dyke center reaches the solidus, where $T_f = T_S$ = 1,000°C), up to 80% of the previous band can be thermally eroded (see Figure 12, $L = 0$ J kg^{-1} K^{-1}, band 5).

We define the "cooling interval" for a band as the time taken for the dyke center to reach T_f. In all our model runs, $T_f \leq T_S$, so that the cooling interval is always at least as long as the time taken for the band to fully solidify. The cooling intervals for the innermost bands give us a likely timescale for band emplacement.

To put a lower bound on cooling intervals, we must ascertain the maximum temperature T_f to which the dyke center could have cooled prior to the emplacement of the next band. Our modeling suggests that $T_f > 800$°C leads to thermal erosion of the previous band when the next pulse arrives. However, we see no textural evidence for thermal erosion between our bands. Therefore, we conclude that each band cooled to at least 800°C before the next band arrived.

Estimating the upper bound for the cooling interval is more challenging. One line of evidence is the absence of chilled margins between bands. Internal chilled margins are characterized by a drop in groundmass grain size, created where hot magma cools rapidly against cold surroundings (Brouxel, 1991; Huppert & Sparks, 1989; Platten, 2000). Within our samples, the outermost margin is glassy, where the initial magma pulse cooled rapidly against cold host rock, but none of the subsequent bands have particularly glassy outer edges. This implies that magma pulses never cooled close to the initial host rock temperature. To produce a glass, the magma must drop below its glass transition temperature, usually around 739°C for a basaltic melt, depending on cooling rate and concentration of H_2O (Giordano et al., 2005). The first response of material in contact with the wall is to cool to a temperature halfway between the host rock and the magma; therefore, if the initial magma temperature is 1,200°C, the wall must be ≤278°C to induce a chilled margin. As such, we would only expect the bands to have individual glassy margins if the center of the previous band had cooled to 278°C.

We estimate the cooling interval required for the second and third marginal bands to develop a glassy margin by setting $T_f = 278$°C. These bands are the most likely to develop an internal glassy margin, as the first band will have cooled rapidly, and not heated the host rock significantly. We find that for the Teno sample, the first band must cool for 27–45 min to produce a glassy margin on the second band, and the second band must cool for 34–57 min to produce a glassy margin on the third band. For the CRB sample, where the bands are slightly narrower, the first band must cool for 15–26 min, and the second band must cool for 30–50 min. To produce glassy margins on any bands further in, the cooling intervals would be even longer. The fact that we don't see any glassy margins, even on the second and third bands, shows that these bands were being emplaced faster than these estimates, and so we take this value as the upper bound on our emplacement timescales. These timescales are similar to the solidification times of the inner bands, and so we conclude that the intervals between magma pulses were on the scale of tens of minutes.

6.4. Vesicles and Pressure Drops

Within both samples, bands are associated with peaks in vesicularity. Since dykes solidify progressively inwards from their margins, each band can be interpreted as a time series, with the oldest material at the margin, getting progressively younger toward the center. We interpret the peaks and troughs in primary magmatic vesicularity as showing a variation through time, rather than representing the spatial organization of vesicles in the active system. Since vesicularity must depend strongly on pressure, we therefore interpret peaks in vesicularity as periods of low pressure, in which bubbles grew, and troughs in vesicularity as periods of high pressure, in which bubbles shrank.

We propose that the fluctuations in pressure recorded by the vesicles within the dyke margins result from the pressure drops that occur when a new pulse fractures the host rock and causes the dyke to propagate a step further (Figure 10). We draw on extensive previous work on bubble growth in magma (Prousevitch et al., 1993) and on the LEFM of dykes (Menand & Tait, 2002; Rivalta et al., 2015) to assess quantitatively the feasibility of our model. Specifically, we test whether the pressure drop required to produce the cyclic variation in vesicularity is consistent with the pressure drop associated with fracture propagation, and whether the time required for bubble growth is consistent with the time available between magma pulses. A physical framework for this analysis is presented in Appendix B.

According to LEFM, a crack can propagate only when its geometry and internal pressure combine to produce a stress intensity at its tip which exceeds a critical threshold known as the fracture toughness, K_C. We can estimate the internal pressure for fracture propagation P_F via Equation B4, reproduced below:

$$P_F = \left(\frac{K_C^2 \Delta\rho g}{\sqrt{\pi}}\right)^{1/3} \quad (1)$$

where $\Delta\rho$ is the density difference between magma and host rock, and g is gravitational acceleration. Values for fracture toughness are highly uncertain; the literature reports values from 0 to 10^4 MPa $m^{1/2}$, with laboratory measurements (e.g., Atkinson, 1984; Atkinson & Meredith, 1987; Balme et al., 2004) several orders of magnitude smaller than estimates based on dyke geometry (e.g., Daniels et al., 2012; Delaney & Pollard, 1981; Olson, 2003). However, assuming that fracture toughness is in the region of 0–500 MPa $m^{1/2}$, the same as most lab and field values, and that the density difference between magma and its surroundings is between 100 and 500 kg m^{-3} (assuming that magma and host have the same density of 2,700 kg m^{-3}, but magma has a vesicularity up to 0.2), all estimated overpressures are less than 10 MPa. This value is taken to represent the maximum pressure drop that could occur on the instigation of a new fracture in the tip of a temporarily stalled dyke, and this pressure drop would cause the growth of bubbles and the peaks in vesicularity.

Using the estimated value of P_F allows us to calculate a characteristic growth timescale t_R for bubbles within the magma, following the sudden decompression when the fracture propagates a step further. We calculate t_R via Equation B8, reproduced below:

$$t_R = \frac{4\eta(1-\phi)}{P_F}. \tag{2}$$

This equation is valid when the pressure drop is much larger than the Laplace stress arising from surface tension (i.e., when $P_F \gg 2\sigma/R$). Vesicles in our samples typically have $R \gtrsim 10^{-5}$ m, and surface tension of a basaltic melt is typically $\sigma = 0.2$ N m^{-1} (Colucci et al., 2016), hence the Laplace stress is of order 0.1 MPa, which is much smaller than the fracture pressure. Taking a typical viscosity value for basalt of $\eta = 100$ Pa s (Giordano et al., 2008), using the measured values for vesicle fraction ϕ (Section 5), and assuming P_F is between 1 and 10 MPa, all growth timescales are less than 4×10^{-4} s.

We also calculate the diffusional growth timescale t_D for the vesicles in our samples via Equation B9, reproduced below:

$$t_D = \frac{{L_W}^2}{D_{H2O}}, \tag{3}$$

where L_W is the characteristic thickness of the walls between bubbles, and D_{H2O} is the diffusivity of H_2O in the melt. We find that the diffusional timescale for the vesicles in both samples is around 20 s (for detailed calculations, see Appendix B). This is much shorter than the emplacement timescales of the bands (Section 6.3), and so we conclude that bubble size is predominantly controlled by pressure. This makes the vesicularity within the bands a reliable indicator of pressure fluctuations within the dyke tip.

We relate vesicularity to pressure using the equation of Shishkina et al. (2010), which relates the solubility of H_2O in basalt to pressure (Equation B10, reproduced below):

$$S_{H_2O} = 0.2351\ P^{0.5758}, \tag{4}$$

where S_{H2O} is the solubility in wt.%, and P is pressure in MPa. The saturation pressure can be found when S_{H2O} equals the initial H_2O concentration. For any pressures lower than this, it is possible to estimate the total volume of H_2O exsolved per kilogram of magma, which can be expressed as a gas volume fraction. This provides a means to relate pressure to vesicularity (see Appendix B for details). Working the other way around, to get pressure from vesicularity, requires a numerical solution, for which we used the solvers in MATLAB.

For both the Teno and CRB samples, areas of high and low vesicularity were selected within the binary images to provide minimum and maximum vesicularities. For the Teno sample, the maximum vesicularity is 0.22, and the mean value for a vesicularity peak is 0.16, while the minimum vesicularity is 0.04. In the CRB sample, the maximum is 0.24, the mean peak value is 0.20, and the minimum is 0.02. For the Teno basalts, initial water concentrations are likely to be between 0.8 and 1.5 wt.%, based on basalts from La Palma and El Hierro, which are neighboring volcanoes in the early stages of shield evolution, comparable to the setting of the Teno samples (Taracsák et al., 2019; Weis et al., 2015). Saturation pressures are therefore likely to have been between 8.4 and

25 MPa. For the CRB samples, water contents are likely to have been higher, at 1.5–2.0 wt.% (Thordarson & Self, 1996), with saturation pressures of 25–41 MPa.

Assuming a basaltic melt density ρ_m of 2,700 kg m^{-3} and a temperature of 1,200°C, we calculate the equilibrium vesicularity that would result from a given pressure P, below the saturation pressure P_{sat}. For the Teno sample, the maximum pressure drop (from maximum to minimum vesicularity) is 1.5–5.9 MPa, and the mean pressure drop (from mean to minimum vesicularity) is 1.0–1.5 MPa, with the ranges dependent on H_2O concentration. For the CRB sample, the maximum pressure drop is 7.2–13.4 MPa, and the mean pressure drop is 6.1–11.4 MPa. These values are consistent with the ballpark figure for fracture pressure of 10 MPa.

A final point worth mentioning is that within the CRB sample, the smallest vesicles are diktytaxitic voids (Figure 8). This texture has previously been found within dykes and lava flows and is commonly interpreted to result from late-stage degassing driven by crystallisation (Fuller, 1939; Martin et al., 2006; Rogan et al., 1996; Walker, 1989). These voids are a separate population from the larger, rounded vesicles measured under the optical microscope, as the distribution in vesicle size is not continuous. There is no evidence of diktytaxitic voids larger than 30 μm, or of any coalescing into larger, rounded vesicles. As such, it seems likely that they are a late-stage feature related to crystallisation, while the main population of larger, rounded vesicles formed earlier, before the groundmass crystallized.

6.5. Phenocrysts and Flow Differentiation

The bands in the Teno sample are defined by a cyclic variation in the concentration of plagioclase phenocrysts. Bands start with a low concentration of phenocrysts on their marginal side, then increase in concentration toward the dyke center, before a relatively sharp drop in concentration at the beginning of the next band (Figure 6). There is an accompanying variation in vesicularity, which peaks toward the side of the band closer to the dyke center. In the literature, most occurrences of marginal bands fall into one of three categories: phenocryst-defined (Drever & Johnston, 1959); groundmass-defined (Brouxel, 1991; Holness & Humphreys, 2003); or vesicle-defined (Delcamp et al., 2012; Galindo & Gudmundsson, 2012; Kavanagh et al., 2018; Kile, 1993; Platten, 2000; Thiele et al., 2021; Thordarson & Self, 1996; Walker, 1987; Walker & Eyre, 1995). The Teno sample is therefore rare in that it displays cyclic variations in both phenocryst concentration and vesicularity, and this allows us to infer that they form via the same process.

Within the Teno sample, the length of plagioclase crystals shows only a slight increase toward the dyke center (0.1–0.15 mm), with no relation to the bands. Close to the margin, plagioclase is the dominant crystal species within a glassy groundmass. As such, we have classified the plagioclase crystals as phenocrysts, and they likely grew elsewhere before being emplaced at the dyke margin. The gradients in phenocryst concentration are therefore unrelated to cooling rates, and we require another process to explain their presence.

One explanation for the gradients in phenocryst concentration, which we discount, is that there was a cyclic variation in the phenocryst load carried by the magma. The dyke solidifies inwards from its margins, and so a change in the concentration of phenocrysts within the magma flowing through the dyke would lead to a change in the concentration being captured by the solidification front. However, this would require a systematic variation in the phenocryst load over time, for which we see no rationale. An alternative explanation is that each band arrived with the phenocryst gradients already in place, and that these gradients were preserved when the magma solidified. This is in better agreement with the sharp drops in phenocryst concentration at the onset of each band.

We propose that the variation in phenocryst concentration is best explained by flow differentiation, the process by which suspended particles migrate away from steep velocity gradients at the edges of a flow. This phenomenon has previously been observed in analogue laboratory experiments and has been used to explain increased phenocryst concentrations in dyke centers (Barrière, 1976; Bhattacharji, 1967; Bhattacharji & Smith, 1964; Gibb, 1968; Komar, 1972).

Several mechanisms are known to cause lateral particle migration in flows, including wall effects (Maude & Whitmore, 1956) and the Magnus effect (Komar, 1972), but the most widely accepted mechanism for flow differentiation within dykes is caused by particle interactions (Bagnold, 1954), sometimes referred to as the Bagnold effect. When suspended particles collide, they temporarily gain momentum perpendicular to the flow direction. This momentum is higher for particles colliding with a greater velocity difference, prompting a net migration away from steep velocity gradients at the edges of flows, and causing particles to concentrate toward

the flow center (Bagnold, 1954; Petford & Koenders, 1998; Phillips et al., 1992). Laboratory experiments have shown that the rate of lateral migration increases for higher shear rates and higher particle concentrations, both of which increase the frequency of collisions (Abbott et al., 1991; Karnis et al., 1963; Leighton & Acrivos, 1987).

To determine whether flow differentiation could have occurred within the bands of the Teno sample, we calculate a development length L_{dev} using the method of Lecampion and Garagash (2014). This is the characteristic lengthscale traveled by flowing magma over which particles migrate into a steady-state concentration distribution across the channel (the actively flowing part of the dyke). The model is presented in Appendix C.

The model for L_{dev} requires three input parameters: the initial particle fraction ϕ_0; the channel half-width H; and the particle radius a. Initial particle fraction is estimated by taking the total area of phenocrysts within a band, and dividing it by the area of the band excluding vesicles. We determine a mean value of $\phi_0 = 0.07$, with a standard deviation of 0.01, showing that the initial particle fraction is consistent between bands. The channel half-width is taken to be the width of each band (so H ranges from 4.42 to 11.70 mm) and the particle radius is approximated as $a = 0.05$ mm, which is half the median phenocryst length.

Taking a mean value for the width and initial particle concentration of the first four Teno bands, we find that $L_{dev} = 1.4$ km. This value is less than the length of most dykes, demonstrating that flow differentiation can be expected to occur within the narrow tips of dykes. It should also be noted that flow differentiation is an asymptotic process, and most differentiation occurs before L_{dev} is reached.

The development length depends strongly on channel width ($L_{dev} \propto H^3$, Equation C1), such that flows in narrower channels differentiate over shorter distances. This could partly explain why the earliest bands closest to the margin, which formed when the actively flowing width of the dyke was narrowest, are more distinct, with fewer phenocrysts remaining close to their marginal edges.

We infer that flow differentiation is a viable mechanism to produce the systematic increase in phenocryst concentration within each band in the Teno sample. The flow differentiation model presented in Appendix C does not account for the presence of vesicles, which likely affect particle migration. For the Teno sample, there is evidence that vesicles formed after flow differentiation had occurred (Section 6.6). Nonetheless, we caution that the presence of vesicles may be a confounding factor in the analysis above. For the CRB sample, the vesicle fraction greatly exceeds the phenocryst fraction (0.2 and 0.05 respectively), and the order of formation of the two phases is not as clear. Consequently, we do not attempt to analyze flow differentiation for the CRB sample, but we note the lack of textural evidence for it having occurred (Figure 7).

The SPO of phenocrysts within the Teno sample shows no variation toward the dyke center, or within the bands themselves, suggesting that the flow direction for each pulse remained constant (Philpotts & Asher, 1994; Wada, 1992). The degree of SPO is highest closer to the margins, echoing the results of previous studies (Coward, 1980; Das & Mallik, 2020), and the reduction in the degree of preferred orientation toward the dyke center could be due to an increasing groundmass crystallinity within each subsequent pulse, increasing the prevalence of crystal collisions. However, the overall consistency in SPO between the bands suggests that pulses were not substantially different from one another in terms of their fluid dynamics. In the CRB sample, plagioclase phenocrysts also display an SPO which remains constant toward the dyke center, implying the same direction of magma flow throughout the emplacement of the bands.

6.6. Relationship Between Vesicles and Phenocrysts

In the Teno sample, phenocrysts and vesicles have almost identical preferred orientations. Many vesicles are flattened against neighboring phenocrysts, or wrap around the end of a phenocryst (Figure 13). These relationships indicate that the vesicles grew within a pre-existing network of aligned phenocrysts, causing them to elongate in such a way that they attained the same direction of preferred orientation. This implies that, within the Teno sample, the vesicles experienced growth after the phenocrysts had been emplaced, and after the phenocryst textures had been established through flow differentiation. In the CRB sample, phenocrysts and vesicles also have similar preferred orientations, but we do not see textural evidence that allows us to infer whether the vesicles grew constrained by a phenocryst network.

The relationship between phenocryst and vesicle textures provides evidence for the order of events associated with our hypothesis of pulsatory magma flow. We infer that the gradients in phenocryst concentration were

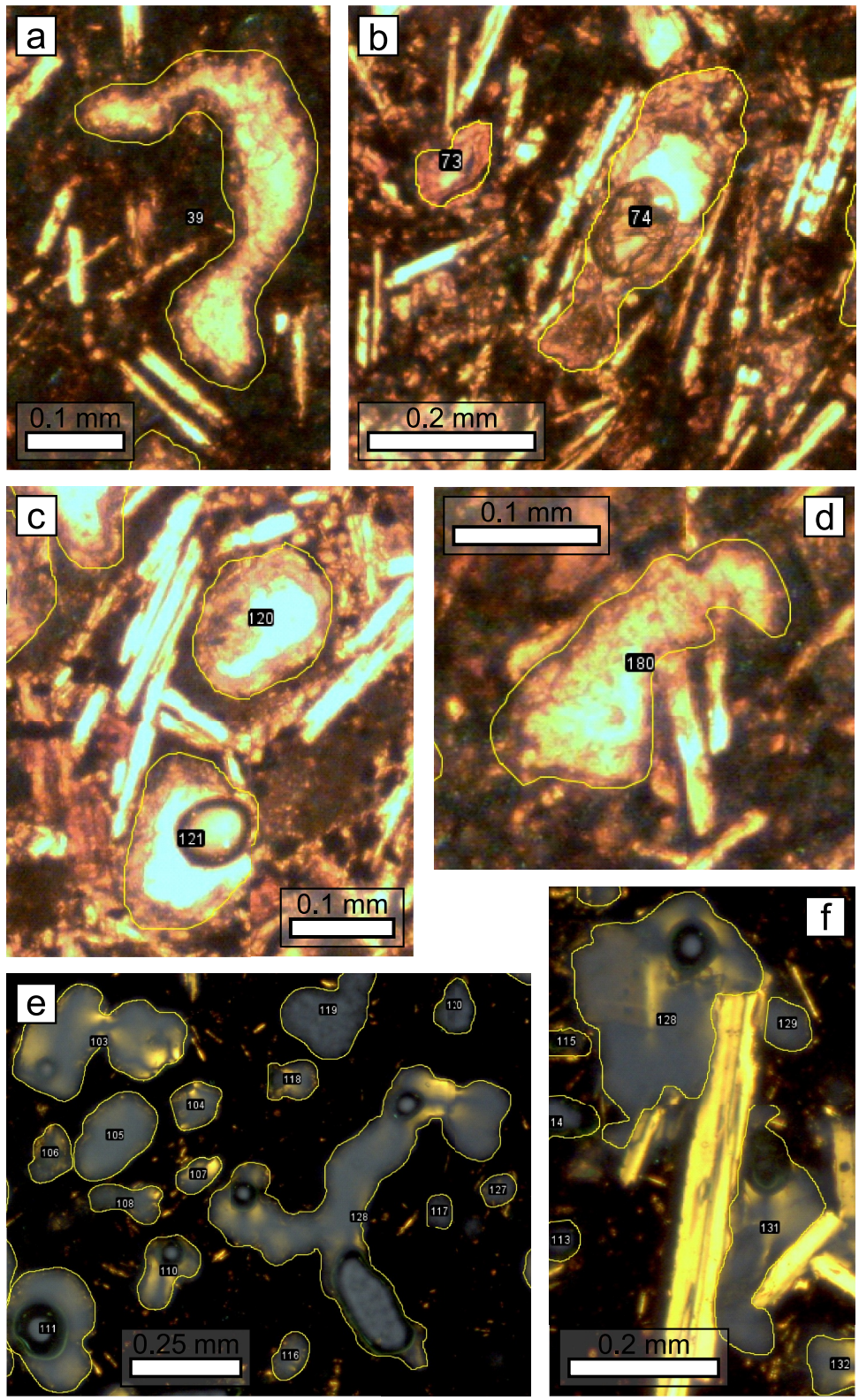

Figure 13. Examples of vesicles within the Teno and CRB samples. Teno: (a) vesicle showing evidence of coalescence; (b, c) vesicle shape and orientation determined by the orientation of surrounding phenocrysts; (d) vesicle enveloping ends of phenocrysts. CRB: (e) highly irregular vesicle shapes in the first band of the CRB sample caused by coalescence; (f) vesicle shapes influenced by neighboring phenocrysts (note that these are rounded, magmatic vesicles, as opposed to the small, angular, diktytaxitic voids that were found using the SEM, which are a separate population (Section 4).

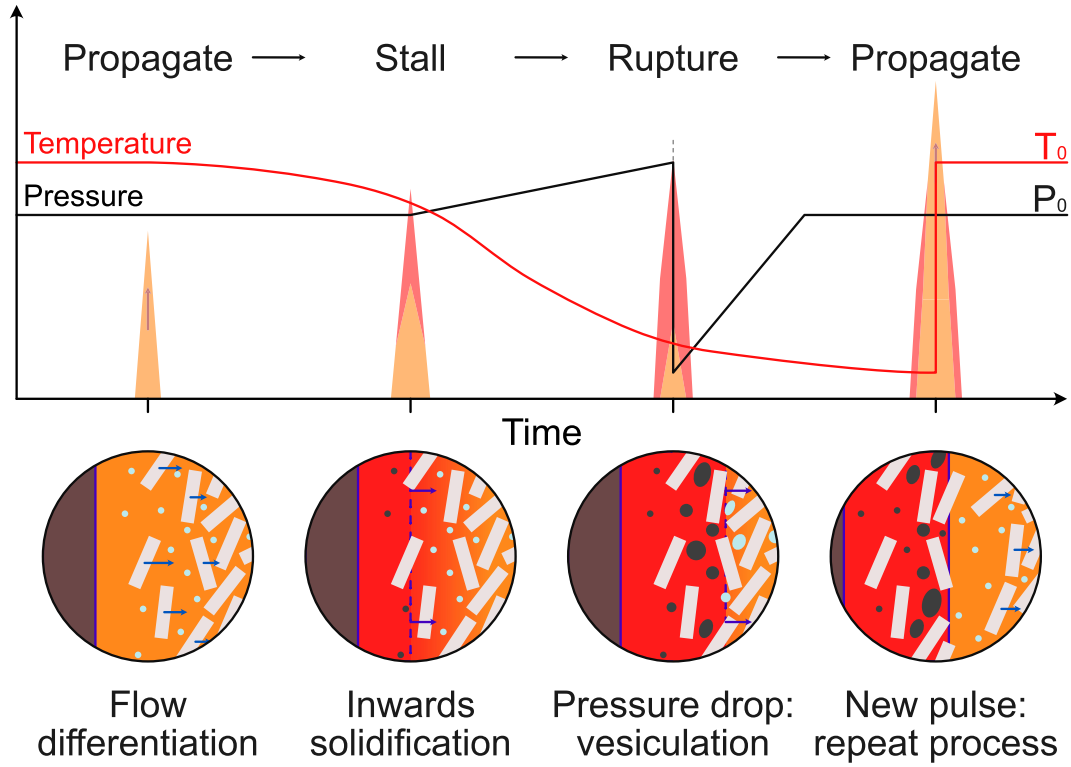

Figure 14. Model for band formation. Each band is a pulse of magma which caused the dyke to propagate another step. Each pulse experienced flow differentiation before cooling and solidifying, capturing the phenocryst gradient. Pressure builds until the dyke tip ruptures, leading to a pressure drop and vesiculation. Propagation resumes with a fresh pulse of magma through the dyke tip.

produced by flow differentiation as the magma pulse was emplaced, and that these concentrations were fixed in place when the pulse cooled and stalled. The vesicles then grew within this existing phenocryst network at the moment that a new fracture formed, when the dyke tip experienced a temporary pressure drop before continuing to advance.

6.7. Band Formation Model

Following the analysis presented in Sections 6.2–6.6, we can refine the model for marginal band formation presented in Section 6.1 as follows:

1. A magma pulse with a tapering geometry propagates through the host rock
2. The narrow tip solidifies rapidly, stalling the progress of the propagating crack
3. Pressure builds behind the blockage until it ruptures
4. A fresh pulse of magma causes the dyke to propagate a step further

This process is cyclic, leading to the progressive build-up of bands along the dyke (Figure 14). The pulsatory flow of magma can create gradients in phenocryst concentration through flow differentiation, while the fluctuation in pressures associated with pulsatory flow and fracturing leads to the variation in vesicularity. The lack of evidence for melt-back or internal chilled margins between bands suggests that the interval between magma pulses is tens of minutes. Bands become wider toward the dyke center because they formed progressively further from the dyke tip, meaning there was a greater width of material available for solidification. The increasing distance to the dyke tip also causes bands to become less distinct toward the dyke center, because the magma becomes progressively insulated by previous bands, allowing melt-back and mixing between pulses, and causing flow and pressure fluctuations to become less severe as the tip propagates further away. Eventually, the dyke tip will be far enough away, and the dyke will be so well-insulated by previous bands, that flow past that point will become steady, and the mechanism for band formation will be lost. As such, we only see these bands at dyke margins.

7. Implications

7.1. Numerical Propagation Models

Dyke propagation models generally fall into two categories: those in which propagation is limited by fracture toughness, and those in which propagation is limited by viscous resistance to flow (Rivalta et al., 2015). In either case, propagation is initiated when the stress intensity at the dyke tip exceeds the fracture toughness of the host material. These models operate in the framework of LEFM, requiring dykes to have a tapering tip to instigate fracturing (e.g., Lister & Kerr, 1991). Once propagation commences, it is continuous: the dyke is arrested only on entering a material with a higher fracture toughness, or by viscous resistance, depending on the model type. Solidification is commonly neglected (e.g., Kavanagh et al., 2006; Maccaferri et al., 2010), and so these models overlook the impact of solidification on dyke propagation.

The omission of solidification is usually justified by comparing propagation rates, indicated by seismicity to be around 1–2 km per hour (e.g., Einarsson & Brandsdóttir, 1980; White et al., 2011), with cooling rates, calculated to be a few days for a molten slab a few meters in width (Rivalta et al., 2015). However, our analysis suggests that using the width of solidified dykes to estimate cooling times is ill-posed; if a dyke has grown by inflation from several pulses, the molten width would always have been less than the final width. If the molten region is narrow, then solidification timescales become comparable to propagation timescales. Furthermore, most propagation models require the dyke tip to taper to a narrow point, which would make it prone to solidification. Even if the main dyke body remains molten, once the tip solidifies, it cannot transmit the fluid pressures required for fracture. This is likely to have a significant impact on propagation, with the potential to stall the dyke's advance at least temporarily. As such, models might consider whether resistance to propagation depends not only on fracture toughness or viscous losses, but also on the efficiency with which the cooling and solidifying dyke tip can exert pressure on its surroundings.

7.2. Experimental and Field Analogs

Analogue models used to explore dyke propagation typically use isothermal fluids (e.g., Kavanagh et al., 2017; Menand & Tait, 2002). However, pulsatory propagation has been observed by injecting paraffin wax into gelatin, as the wax cools and solidifies, leading to stalling and refracturing (Taisne & Tait, 2011). Stalling a interpreted to be caused by solidification reducing the stress intensity at the edge of the wax, meaning it could no longer fracture the gelatin. The paraffin wax intruded through a cycle of stalling, inflating, then rupturing and propagating, the same process we have inferred from the marginal bands in dykes.

Similar pulsatory behavior has also been seen in syrup flowing through chilled tubes, where the balance between cooling, viscosity and local pressures produces unstable flow even for a fixed driving pressure (Whitehead & Helfrich, 1991). This shows that pulsatory flow could occur within the dyke tip even in the absence of complete solidification, due to the effect of cooling on the magma's viscosity.

Finally, pulsatory propagation within dykes could be considered analogous to the emplacement of pahoehoe lava lobes, which propagate by cyclical rupturing, cooling and inflation. Although lava flows lose heat rapidly via radiation, and dykes lose heat slowly via conduction, the same pulsatory processes are likely to be ongoing, albeit on a different timescale.

7.3. Dyke Propagation Inferred From Seismicity

The concept of episodic or pulsatory dyke propagation is not a new idea. One of the few ways to monitor active dyke propagation is through the migration of seismicity, commonly interpreted to originate around the leading edge of the dyke (Einarsson & Brandsdóttir, 1980; White et al., 2011; Woods et al., 2019). However, dyke propagation mapped through seismicity is often seen to happen in bursts at timescales of hours to days, showing that magma transport is not a continuous process, and can occur in pulses. Common interpretations of such behavior include changes in host rock properties, interaction with faults, changing topography on the surface, and variation in pressure at the magma source (Rivalta et al., 2015). For example, two temporary halts in the vertical migration of earthquakes below Piton de la Fournaise were attributed to lithological discontinuities (Battaglia et al., 2005), while bursts in seismicity during the lateral intrusion of a dyke in Iceland were related to caldera subsidence at the magma source (Sigmundsson et al., 2015). However, these events are on a much larger scale than evidenced in the marginal bands, where the timescale for magma pulses and pressure fluctuations is

measured in tens of minutes. Furthermore, these larger-scale processes are unique to each dyke, while marginal bands exhibit the same pattern in every setting and must therefore share a ubiquitous formation process.

Another example of large-scale pulsatory propagation was recorded by the migration of earthquake foci during the Bárðarbunga–Holuhraun rifting event, where rapid lateral growth was interspersed by periods of stalling, lasting hours to days. During stalled periods, earthquake foci migrated backwards from the dyke tip before propagation resumed, interpreted as a result of inflation (Woods et al., 2019). Such behavior was proposed to have arisen due to changes in topography, host rock properties, or source pressure, then exacerbated by solidification around the dyke margins (Woods et al., 2019). Bursts of seismicity related to dyke propagation have previously been interpreted to be a result of solidification and re-fracturing (Hayashi & Morita, 2003; White et al., 2011); however, this occurs on longer timescales than the marginal bands, and must be at a larger scale in order to produce detectable waves of earthquakes.

Our model for pulsatory dyke tip propagation is consistent with the seismic signals from dyke emplacement, in that it indicates the discrete nature of fracturing and dyke advance. Even "smooth" dyke propagation is characterized by a series of discrete earthquakes, each one of which must originate in a distinct fracturing event. The cyclic nature of our propagation model is likely disguised by the fact that the leading edge of the dyke will be segmented, split into regions that propagate in competition with different advance rates. As such, small, systematic, and repetitive bursts of propagation will be hidden by the signals from neighboring sectors, and by larger-scale pulses transiting the system.

7.4. Relation to Dyke Arrest or Eruption Onset

The marginal bands demonstrate that solidification can influence magma flow in the narrow dyke tip. It is therefore feasible that, under the correct conditions (e.g., low magma flux into the tip, highly resistant host rock), solidification could stall propagation for longer, or even entirely. The relation between magma temperature, viscosity and advection rates can lead to positive feedback, meaning that small-scale perturbations in the dyke tip have the potential to cascade into larger events, influencing the behavior of the main dyke body. It is therefore worth considering whether large-scale layering within dykes may not arise from discrete magma pulses from the source, but from pulses generated within the dyke itself due to the influence of solidification. It is interesting to imagine the largest scale on which this behavior might occur; for example, whether centimetre-to meter-scale layering marked by internal chilled margins (e.g., Platten, 2000) or differences in columnar jointing structure (e.g., Das & Mallik, 2020; Gudmundsson, 1984; Ray et al., 2007) could result from large scale, internally generated, solidification-driven magma pulses.

Finally, it is worth noting that although the physical processes discussed here are ubiquitous to propagating batches of solidifying fluids, pulsatory propagation and band formation should not be expected in all dykes. Bands defined by varying vesicularity are more likely in magma with a high volatile content, or at shallower depth, making it more sensitive to pressure drops (Section 6.4). Similarly, variations in phenocryst concentration will only form when flow differentiation is significant, which requires a high volume fraction of phenocrysts with an appropriate size relative to the width of the dyke (Section 6.5). We also predict that, in the shallow subsurface, bands may be removed by thermal erosion if a dyke becomes an established flow pathway feeding eruptions at the surface.

8. Conclusion

Marginal bands are a common feature of basaltic dykes in volcanic settings around the world. They can be defined by a variation in phenocrysts and/or vesicles, and show a general trend of getting wider and less distinct toward the intrusion center. Variations in phenocryst concentration are likely to be caused by flow differentiation, while variations in vesicularity can be caused by pressure fluctuations as the dyke progressively solidifies. Both processes can be explained by pulsatory magma flow.

The margins are the earliest material to solidify, originating in the tip of the dyke, and they therefore hold information on the propagation process. The presence of banding at the margins suggests that pulsatory magma flow is associated with propagation, which is likely to arise from repeated cooling, solidification and re-fracturing of magma in the narrow dyke tip. The millimeter to centimetre widths of the bands implies rapid cooling in tens of minutes, suggesting that the pulses are local and short-lived. Material closer to the dyke center solidified at a

greater distance from the tip, with flow becoming steadier over time, causing bands to become progressively wider and less distinct.

Our analysis does not put any particular constraints on the conditions under which pulsatory propagation due to solidification within the dyke tip can occur, and so we conclude that it is generally applicable, which is consistent with the fact that it can be found in diverse volcanic settings across the world. By contrast, large-scale layering, such as in composite dykes, can be attributed to other processes which will be unique to each dyke, such as fluctuations in magma flow rate from the source. However, it is possible that cooling, blocking and unblocking within the dyke can lead to fluctuations in flow rate, causing larger-scale textural layering. More importantly, the repeated solidifying and re-fracturing of the narrow tip region may have implications for dyke propagation models, especially in the way that magmatic pressures are transmitted to the host rock.

Appendix A: Solidification Model

We estimate solidification timescales based on the widths of the marginal bands, assuming them to be the half-widths of magma pulses through the dyke tip. Following a magma pulse event, heat transport within the dyke is assumed to be purely due to heat conduction normal to the plane of the dyke. We assume that the magma and host rock have the same thermal conductivity, which is reasonable for a basalt dyke intruding layered basaltic lava flows. We then have the option of whether to include or omit the release of latent heat on solidification. Omitting latent heat is justifiable for the first band, where the groundmass is glassy; however, the groundmass becomes more crystalline toward the dyke center, suggesting that latent heat was released as the later bands solidified. We can create a cooling model that accounts for latent heat by considering the enthalpy of the system.

The model boundary condition is that the host rock is held at a fixed temperature T_0 at a distance equal to 10 times the final dyke half-width away from the dyke center, far from the warming effect induced by the dyke on the host rock (we find that the induced warming only extends ∼0.5 m into the host rock). The geometry of the model is shown in Figure A1.

Assuming the magma to be incompressible, the following energy conservation equation applies:

$$\rho \frac{\partial h}{\partial t} = k \frac{\partial^2 T}{\partial x^2} \tag{A1}$$

subjected to the initial condition and boundary conditions:

$$\begin{aligned} T &= T_M \quad 0 \le x \le W \quad t = 0 \\ \frac{\partial T}{\partial x} &\quad x = 0 \quad t > 0 \\ T &= T_0 \quad x = W \quad t > 0 \end{aligned} \tag{A2}$$

where ρ is mass density (kg m^{-3}), h is enthalpy per unit mass (J kg^{-1}), t is time after a magma pulse event (s), k is the thermal conductivity (W m^{-1} K^{-1}), T is temperature within the magma (K), x is distance from the center of the dyke normal to the dyke plane (m), T_M is the temperature of the magma pulse (K), W is the half-width of the dyke (m) and T_0 is the temperature of the host rock (K).

Assuming magma and host rock to have the same specific heat capacity, the relationship between temperature and enthalpy takes the form

$$T = \begin{cases} \dfrac{h}{c_p} & h < c_p T_S \\ T_S & c_p T_S \le h \le c_p T_S + L \\ \dfrac{h - L}{c_p} & h > c_p T_S + L \end{cases} \tag{A3}$$

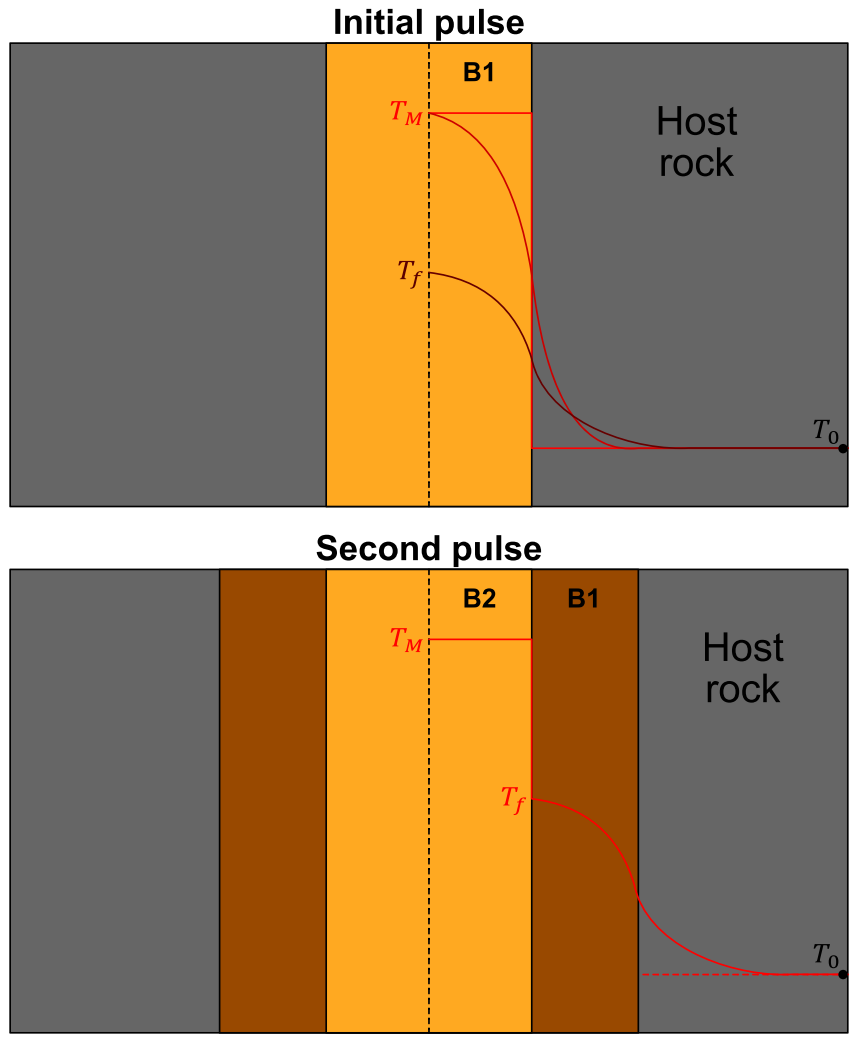

Figure A1. Schematic representation of MATLAB cooling model. A magma pulse is emplaced at T_M in host rock of T_0, and cools following Fourier's law of conduction. When the center reaches a defined final temperature T_f, a new pulse is injected. Old material is shifted sideways to make way, pushing aside host rock that remains un-warmed by the intrusion. The model boundary is held at T_0.

where c_p is specific heat capacity (J kg^{-1} K^{-1}), T_S is the solidification temperature (K) and L is latent heat capacity (J kg^{-1}). Solidification has occurred where $T < T_S$.

A numerical solution (see Allgood & Mathias, 2023) is achieved by discretizing Equation A1 in space using finite differences and solving the resulting set of ordinary differential equations (ODE) with respect to time using MATLAB's stiff ODE solver, ODE15s (Shampine & Reichelt, 1997; Shampine & Thompson, 2001).

A key implicit assumption of the cooling model is that the magma is stationary. Within dykes, the advection of heat through the flow of fresh, uncooled magma through the dyke center can increase cooling times significantly (Fialko & Rubin, 1999; Petcovic & Dufek, 2005). However, for narrow features such as the marginal bands, where solidification is so rapid, the influence of advection is less pronounced. The greatest uncertainty in the model comes from the thermal conductivity, which is poorly constrained (Clark, 1966; Durham et al., 1987; Hanley et al., 1978; Robertson & Peck, 1974; Mostafa et al., 2004). There is additional uncertainty surrounding the release of latent heat within rapidly chilled margins, where the groundmass transitions from glassy to crystalline. This is why we define upper and lower bounds, both neglecting and including the release of latent heat.

Appendix B: Fracture-Induced Pressure Drop and Bubble Growth

According to LEFM, a crack can propagate only when its geometry and internal pressure combine to produce a stress intensity at its tip which exceeds a critical threshold known as the fracture toughness, K_c. For a given crack size (in our case, the vertical length of the crack l), the critical pressure at which this occurs is known as the fracture pressure P_F, which is given by Menand and Tait (2002):

$$P_F = \frac{K_C}{\sqrt{\pi l}}. \tag{B1}$$

For buoyant, self-propagating dykes within the crust, buoyancy pressure P_B is

$$P_B = \Delta\rho g l, \tag{B2}$$

where $\Delta\rho$ is the density difference between magma and host rock and g is gravitational acceleration (Menand & Tait, 2002). For self-propagating dykes, buoyancy is the dominant driving pressure, so $P_F = P_B$ and the length l represents the critical crack length l_C for fracturing. By equating Equation B1 and B2, and by setting $l = l_C$, we find

$$l_C = \left(\frac{K_C}{\sqrt{\pi}\,\Delta\rho g}\right)^{2/3}. \tag{B3}$$

Substituting into Equation B1, we obtain an expression for P_F as a function of fracture toughness and density difference:

$$P_F = \left(\frac{K_C^2 \Delta\rho g}{\pi}\right)^{1/3}. \tag{B4}$$

(Note that Equation B4 is presented as Equation 1 in the main text.)

When the fracture propagates, the magma experiences a pressure drop $\leq P_F$, which causes bubbles in the magma to grow. We estimate a timescale for viscous bubble growth using the model of Prousevitch et al. (1993), where a bubble of radius R grows at a rate given by

$$\frac{dR}{dt} = \frac{P_F - P_L}{4\eta\left(\frac{1}{R} - \frac{R^2}{S^3}\right)} \tag{B5}$$

where $P_L = 2\sigma/R$ is the Laplace pressure arising from surface tension σ for a bubble, η is fluid viscosity, and S is the radius of the melt shell that surrounds the bubble, which is given by

$$S = \left(\frac{R^3}{\phi}\right)^{1/3}. \tag{B6}$$

We take a value for surface tension $\sigma = 0.2$ N m^{-2} (Colucci et al., 2016), and so $P_F \gg P_L$. We therefore neglect P_L, and combining Equations B5 and B6 gives

$$\frac{dR}{dt} = \frac{RP_F}{4\eta(1-\phi)}. \tag{B7}$$

The characteristic viscous growth timescale, t_V, is therefore given by

$$t_V = \frac{R}{\frac{dR}{dt}} = \frac{4\eta(1-\phi)}{P_F}. \tag{B8}$$

(Note that Equation B8 is presented as Equation 2 in the main text).

In response to the pressure drop instigated by fracturing, bubbles will also grow by diffusive degassing of H_2O from the melt. The timescale for diffusive bubble growth can be approximated as

$$t_D = \frac{{L_W}^2}{D_{H2O}}, \tag{B9}$$

where L_W is the characteristic thickness of the walls between bubbles, and D_{H2O} is the diffusivity of H_2O in the melt (Note that Equation B9 is presented as Equation 3 in the main text). For the Teno basalts, initial water concentrations are likely to have been between 0.8 and 1.5 wt.%, based on basalts from La Palma and El Hierro, which are neighboring volcanoes in the early stages of shield evolution, comparable to the setting of the Teno samples (Taracsák et al., 2019; Weis et al., 2015). For the CRB samples, water contents are likely to have been higher, at 1.5–2.0 wt.% (Thordarson & Self, 1996). Using these water contents, we estimate D_{H2O} to be 3.6–5.3^{-10} m^2 s^{-1} for the Teno sample, and 5.3–6.7^{-10} m^2 s^{-1} for the CRB sample, based on the equations of Zhang et al. (2007). Based on average vesicle area, and the average groundmass area per vesicle, we find $L_W = 0.09$ mm in the Teno sample, and $L_W = 0.11$ mm in the CRB sample. The timescale for diffusive bubble growth is therefore around 20 s for both samples. This is much shorter than the emplacement times of the bands (Section 6.3), and so vesicle growth is predominantly controlled by the pressure drops, making vesicularity within the bands a reliable indicator of pressures changing through time.

The variation in vesicularity in the bands can be used to estimate the magnitude of the pressure drops occurring within the dyke tip. We relate vesicularity to pressure using the equation of Shishkina et al. (2010), which relates the solubility of H_2O in basalt to pressure, so that

$$S_{H_2O} = 0.2351\, P^{0.5758}. \tag{B10}$$

where S_{H2O} is the solubility in wt.%, and P is pressure in MPa (Note that Equation B10 is presented as Equation 4 in the main text). The saturation pressure can be found when S_{H_2O} equals the initial water concentration. For any pressures lower than this, it is possible to estimate the total volume of water exsolved per kilogram of magma, thereby providing a means to relate pressure to vesicularity. We can therefore estimate the pressures associated with the peaks and the troughs in vesicularity within our samples. The difference between these pressures gives us the pressure drop associated with each step of pulsatory propagation.

We can calculate the equilibrium vesicularity that would result from a given pressure P, below the saturation pressure P_{sat}. The difference in wt.% between the initial H_2O content S_0 and the solubility S_P at a given pressure can be used to calculate the mass of H_2O exsolved per cubic meter of magma m_{H2O}, where

$$m_{H2O} = \rho_m (S_0 - S_P)/100. \tag{B11}$$

This volume of this exsolved mass of H_2O can be calculated from the ideal gas law, $PV = nRT$, where P is pressure in Pa, V is volume in m^3, n is the number of moles of H_2O, R is the universal gas constant 8.3145 J mol^{-1} K^{-1}, and T is 1473 K. Using the volume of H_2O exsolved per cubic meter of magma, we can calculate the vesicularity ϕ as

$$\phi = \frac{V_{H2O}}{V_{H2O} + 1}. \tag{B12}$$

To get pressure from a given vesicularity, the steps outlined in Equation B10–B12 must be followed in reverse, which requires the use of a numerical solver (e.g., in Excel or MATLAB).

Appendix C: Flow Differentiation Model

To determine whether flow differentiation could have occurred within the bands of the Teno sample, we can calculate a development length L_{dev} using the method of Lecampion and Garagash (2014). This is the distance that magma is required to flow within the dyke for particles to migrate into a steady-state concentration distribution

across the channel (i.e., the actively flowing part of the dyke). The development length depends on the initial, uniform particle fraction within the channel ϕ_0, the particle radius a, and the channel half-width H, so

$$L_{dev} = \frac{H^3}{a^2}\,\frac{I(\phi_0)\,S(\phi_0)}{\kappa(\phi_0)}, \tag{C1}$$

where I is the dimensionless viscous number, S is the dimensionless inelastic storage coefficient, and κ is the dimensionless permeability. The viscous number depends on the maximum particle volume fraction, ϕ_m, so that

$$I(\phi_0) = \left(\frac{\phi_m}{\phi_0} - 1\right)^2. \tag{C2}$$

The inelastic storage coefficient S is controlled by the dimensionless friction coefficient μ, which can be calculated via

$$\mu = \mu_1 + \frac{\phi_m}{\beta}\left(1 - \frac{\phi}{\phi_m}\right) + \left[I(\phi) + \left(\frac{5}{2}\phi_m + 2\right)I(\phi)^{1/2}\right]\left(1 - \frac{\phi}{\phi_m}\right)^2, \tag{C3}$$

where μ_1 is the value of μ at ϕ_m, and β is a dimensionless compressibility coefficient. The value of S can then be calculated using

$$S(\phi_0) = -\frac{\mu}{\phi_0}.\frac{d\phi_0}{d\mu}. \tag{C4}$$

By differentiating Equation C3 with respect to ϕ, we find $d\mu/d\phi$, the reciprocal of which is

$$\frac{d\phi}{d\mu} = \left(-\frac{1}{\beta} - I(\phi)\left(\frac{2}{\phi} + \frac{5}{2}\right) - \frac{2}{\phi_m}\left[I(\phi) + \left(\frac{5}{2}\phi_m + 2\right)I(\phi)^{\frac{1}{2}}\right]\left[1 - \frac{\phi}{\phi_m}\right]\right)^{-1} \tag{C5}$$

which we can then substitute into Equation C4 to find S. The dimensionless permeability is calculated as

$$\kappa(\phi_0) = \frac{2(1-\phi_0)^{\alpha}}{9\phi_0}, \tag{C6}$$

where α is a constant. The constants used by Lecampion and Garagash (2014) have been experimentally verified for suspensions of hard spheres, but reliable empirical relationships do not exist for tabular shapes. Therefore, we must proceed by treating the phenocrysts as spherical; the constants for spheres are: $\phi_m = 0.585$, $\mu_1 = 0.3$, $\beta = 0.158$ and $\alpha = 5.1$.

The development length is then

$$L_{dev} = \frac{H^3}{a^2}\,\frac{I(\phi_0)\,S(\phi_0)}{6\kappa(\phi_0)}. \tag{C7}$$

Taking a mean value for the width and initial particle concentration of the first four Teno bands, we find that $L_{dev} = 1.4$ km. However, the development length is highly sensitive to the channel width, and so band 2, at only 4.44 mm width, has a development length of only 70 m, while band 3, at 18.06 mm, has a development length of 3.9 km. These are still feasible values for flow differentiation to occur, in that they are shorter than the lengths of most dykes. It should also be noted that flow differentiation is an asymptotic process, and most differentiation occurs before L_{dev} is reached.

Data Availability Statement

Raw data from phenocryst and vesicle outlines (size, shape, area fractions etc.), and the MATLAB script of the 1D cooling model are available from the Durham University Data Repository via http://doi.org/10.15128/r2sb397832j (Allgood & Mathias, 2023).

Acknowledgments
This research was funded by NERC (NE/S007431/1). We thank Fabian Wadsworth for useful discussions on flow differentiation.

References

Abbott, J. R., Tetlow, N., Graham, A. L., Altobelli, S. A., Fukushima, E., Mondy, L. A., & Stephens, T. S. (1991). Experimental observations of particle migration in concentrated suspensions: Couette flow. *Journal of Rheology*, *35*(5), 773–795. https://doi.org/10.1122/1.550157

Allgood, C., & Mathias, S. A. (2023). Banding in the margins of basaltic dykes indicates pulsatory propagation during emplacement [Dataset]. *Durham University Collections*. https://doi.org/10.15128/r2sb397832j

Atkinson, B. K. (1984). Subcritical crack growth in geological materials. *Journal of Geophysical Research*, *89*(B6), 4077–4114. https://doi.org/10.1029/JB089iB06p04077

Atkinson, B. K., & Meredith, P. G. (1987). Experimental fracture mechanics data for rocks and minerals. In B. K. Atkinson (Ed.), *Fracture mechanics of rock*. Elsevier Academic Press.

Baer, G., & Reches, Z. (1987). Flow patterns of magma in dikes, Makhtesh Ramon, Israel. *Geology*, *15*(6), 569–572. https://doi.org/10.1130/0091-7613(1987)15<569:FPOMID>2.0.CO;2

Bagnold, R. A. (1954). Experiments on a gravity-free dispersion of large solid spheres in a Newtonian fluid under shear. *Proceedings of the Royal Society of London, Series A*, *225*, 49–63. https://doi.org/10.1098/rspa.1954.0186

Balme, M. R., Rocchi, V., Jones, C., Sammonds, P. R., Meredith, P. G., & Boon, S. (2004). Fracture toughness measurements on igneous rocks using a high-pressure, high-temperature rock fracture mechanics cell. *Journal of Volcanology and Geothermal Research*, *132*(2–3), 159–172. https://doi.org/10.1016/S0377-0273(03)00343-3

Barrière, M. (1976). Flowage differentiation: Limitation of the "Bagnold effect" to the narrow intrusions. *Contributions to Mineralogy and Petrology*, *55*(2), 139–145. https://doi.org/10.1007/BF00372223

Battaglia, J., Ferrazzini, V., Staudacher, T., Aki, K., & Cheminée, J. L. (2005). Pre-eruptive migration of earthquakes at the Piton de la Fournaise volcano (Réunion Island). *Geophysical Journal International*, *161*(2), 549–558. https://doi.org/10.1111/j.1365-246X.2005.02606.x

Bhattacharji, S. (1967). Mechanics of flow differentiation in ultramafic and mafic sills. *The Journal of Geology*, *75*(1), 101–112. https://doi.org/10.1086/627234

Bhattacharji, S., & Smith, C. H. (1964). Flowage differentiation. *Science*, *145*(3628), 150–153. https://doi.org/10.1126/science.145.3628.150

Brouxel, M. (1991). Geochemical consequences of flow differentiation in a multiple injection dyke (Trinity ophiolite, N. California). *Lithos*, *26*(3–4), 245–252. https://doi.org/10.1016/0024-4937(91)90031-F

Bruce, P. M., & Huppert, H. E. (1989). Thermal control of basaltic fissure eruptions. *Nature*, *342*(6250), 665–667. https://doi.org/10.1038/342665a0

Bruce, P. M., & Huppert, H. E. (1990). Solidification and melting along dykes by the laminar flow of basaltic magma. In M. P. Ryan (Ed.), *Magma transport and storage* (pp. 87–101). John Wiley & Sons.

Carracedo, J. C., Troll, V. R., Day, J. M., Geiger, H., Aulinas, M., Soler, V., et al. (2022). The 2021 eruption of the Cumbre Vieja volcanic ridge on La Palma, Canary Islands. *Geology Today*, *38*(3), 94–107. https://doi.org/10.1111/gto.12388

Castro, J. M., & Feisel, Y. (2022). Eruption of ultralow-viscosity basanite magma at Cumbre Vieja, La Palma, Canary Islands. *Nature Communications*, *13*(1), 3174. https://doi.org/10.1038/s41467-022-30905-4

Clark, S. P. (1966). *Thermal conductivity* (Vol. 97, pp. 459–482). GSA Memoirs.

Clemente, C. S., Amorós, E. B., & Miguel Garcés Crespo, M. G. (2007). Dike intrusion under shear stress: Effects on magnetic and vesicle fabrics in dikes from rift zones of Tenerife (Canary Islands). *Journal of Structural Geology*, *29*(12), 1931–1942. https://doi.org/10.1016/j.jsg.2007.08.005

Colucci, S., Battaglia, M., & Trigila, R. (2016). A thermodynamical model for the surface tension of silicate melts in contact with H_2O gas. *Geochimica et Cosmochimica Acta*, *175*, 113–127. https://doi.org/10.1016/j.gca.2015.10.037

Coward, M. P. (1980). The analysis of flow profiles in a basaltic dyke using strained vesicles. *Journal of the Geological Society*, *137*(5), 605–615. https://doi.org/10.1144/gsjgs.137.5.0605

Daniels, K. A., Kavanagh, J. L., Menand, T., & R. Stephen, J. S. (2012). The shapes of dikes: Evidence for the influence of cooling and inelastic deformation. *GSA Bulletin*, *124*(7–8), 1102–1112. https://doi.org/10.1130/B30537.1

Das, A., & Mallik, J. (2020). Applicability of AMS technique as a flow fabric indicator in dykes: Insight from Nandurbar-Dhule Deccan dyke swarm. *International Journal of Earth Sciences*, *109*(3), 933–944. https://doi.org/10.1007/s00531-020-01841-9

Davis, T., Bagnardi, M., Lundgren, P., & Rivalta, E. (2021). Extreme curvature of shallow magma pathways controlled by competing stresses: Insights from the 2018 Sierra Negra eruption. *Geophysical Research Letters*, *48*(13), e2021GL093038. https://doi.org/10.1029/2021GL093038

Delaney, P. T., & Pollard, D. D. (1981). Deformation of host rocks and flow of magma during growth of minette dikes and breccia-bearing intrusions near Ship Rock, New Mexico. USGS Professional Paper 1202.

Delaney, P. T., & Pollard, D. D. (1982). Solidification of basaltic magma during flow in a dike. *American Journal of Science*, *282*(6), 856–885. https://doi.org/10.2475/ajs.282.6.856

Delcamp, A., Troll, V. R., Van Wyk de Vries, B., Carracedo, J. C., Petronis, M. S., Pérez-Torrado, F. J., & Deegan, F. M. (2012). Dykes and structures of the NE rift of Tenerife, Canary Islands: A record of stabilisation and destabilisation of ocean island rift zones. *Bulletin of Volcanology*, *74*(5), 963–980. https://doi.org/10.1007/s00445-012-0577-1

Drever, H. I., & Johnston, R. (1959). The Petrology of Picritic rocks in minor intrusions - A Hebridean Group. *Earth and Environmental Science Transactions of The Royal Society of Edinburgh*, *63*(3), 459–499. https://doi.org/10.1017/S0080456800003112

Durham, W. B., Mirkovich, V. V., & Heard, H. C. (1987). Thermal diffusivity of igneous rocks at elevated pressure and temperature. *Journal of Geophysical Research: Solid Earth*, *92*(B11), 11615–11634. https://doi.org/10.1029/JB092iB11p11615

Einarsson, P., & Brandsdóttir, B. (1980). Seismological evidence for lateral magma intrusion during the July 1978 deflation of the Krafla volcano in NE-Iceland. *Journal of Geophysics*, *47*, 160–165.

Eriksson, P. I., Riishuus, M. S., Sigmundsson, F., & Elming, S. Å. (2011). Magma flow directions inferred from field evidence and magnetic fabric studies of the Streitishvarf composite dike in east Iceland. *Journal of Volcanology and Geothermal Research*, *206*(1–2), 30–45. https://doi.org/10.1016/j.jvolgeores.2011.05.009

Fialko, Y. A., & Rubin, A. M. (1999). Thermal and mechanical aspects of magma emplacement in giant dike swarms. *Journal of Geophysical Research*, *104*(B10), 23033–23049. https://doi.org/10.1029/1999JB900213

Fuller, R. E. (1939). Gravitational accumulation of olivine during the advance of basaltic flows. *The Journal of Geology*, *47*(3), 303–313. https://doi.org/10.1086/624779

Galindo, I., & Gudmundsson, A. (2012). Basaltic feeder dykes in rift zones: Geometry, emplacement, and effusion rates. *Natural Hazards and Earth System Sciences*, *12*(12), 3683–3700. https://doi.org/10.5194/nhess-12-3683-2012

Geshi, N., Kusumoto, S., & Gudmundsson, A. (2010). Geometric difference between non-feeder and feeder dikes. *Geology*, *38*(3), 195–198. https://doi.org/10.1130/G30350.1

Gibb, F. G. (1968). Flow differentiation in the Xenolithic ultrabasic dykes of the Cuillins and the Strathaird Peninsula, Isle of Skye, Scotland. *Journal of Petrology*, *9*(3), 411–443. https://doi.org/10.1093/petrology/9.3.411

Giordano, D., Nichols, A. R., & Dingwell, D. B. (2005). Glass transition temperatures of natural hydrous melts: A relationship with shear viscosity and implications for the welding process. *Journal of Volcanology and Geothermal Research*, *142*(1–2), 105–118. https://doi.org/10.1016/j.jvolgeores.2004.10.015

Giordano, D., Russell, J. K., & Dingwell, D. B. (2008). Viscosity of magmatic liquids: A model. *Earth and Planetary Science Letters*, *271*(1–4), 123–134. https://doi.org/10.1016/j.epsl.2008.03.038

Gonnermann, H., & Taisne, B. (2015). Magma transport in dikes. In H. Sigurdsson, B. Houghton, S. R. McNutt, H. Rymer, & J. Stix (Eds.), *Encyclopedia of volcanoes* (2nd ed., pp. 215–224). Elsevier Science & Technology.

Gudmundsson, A. (1984). Formation of dykes, feeder-dykes, and the intrusion of dykes from magma chambers. *Bulletin Volcanologique*, *47*(3), 537–550. https://doi.org/10.1007/BF01961225

Hanley, E. J., Dewitt, D. P., & Roy, R. F. (1978). The thermal diffusivity of eight well-characterized rocks for the temperature range 300–1000 K. *Engineering Geology*, *12*, 31–47. https://doi.org/10.1016/0013-7952(78)90003-0

Hayashi, Y., & Morita, Y. (2003). An image of a magma intrusion process inferred from precise hypocentral migrations of the earthquake swarm east of the Izu Peninsula. *Geophysical Journal International*, *153*(1), 159–174. https://doi.org/10.1046/j.1365-246X.2003.01892.x

Healy, D., Rizzo, R., Duffy, M., Farrell, N. J., Hole, M. J., & Muirhead, D. (2018). Field evidence for the lateral emplacement of igneous dykes: Implications for 3D mechanical models and the plumbing beneath fissure eruptions. *Volcanica*, *1*(2), 85–105. https://doi.org/10.30909/vol.01.02.85105

Holness, M. B., & Humphreys, M. C. S. (2003). The Traigh Bhan na Sgurra Sill, Isle of Mull: Flow localization in a major magma conduit. *Journal of Petrology*, *44*(11), 1961–1976. https://doi.org/10.1093/petrology/egg066

Huppert, H. E., & Sparks, R. S. J. (1989). Chilled margins in igneous rocks. *Earth and Planetary Science Letters*, *92*(3–4), 397–405. https://doi.org/10.1016/0012-821X(89)90063-0

Jammalamadaka, S. R., & SenGupta, A. (2001). *Topics in circular statistics*. World Scientific.

Jolly, R. J. H., & Sanderson, D. J. (1995). Variation in the form and distribution of dykes in the Mull swarm, Scotland. *Journal of Structural Geology*, *17*(11), 1543–1557. https://doi.org/10.1016/0191-8141(95)00046-G

Jones, T. J., & Llewellin, E. W. (2021). Convective tipping point initiates localization of basaltic fissure eruptions. *Earth and Planetary Science Letters*, *553*, 116637. https://doi.org/10.1016/j.epsl.2020.116637

Karnis, A., Goldsmith, H. L., & Mason, S. G. (1963). Axial migration of particles in Poiseuille flow. *Nature*, *200*(4902), 159–160. https://doi.org/10.1038/200159a0

Kavanagh, J. L., Burns, A. J., Hazim, S. H., Wood, E. P., Martin, S. A., Hignett, S., & Dennis, D. J. C. (2018). Challenging dyke ascent models using novel laboratory experiments: Implications for reinterpreting evidence of magma ascent and volcanism. *Journal of Volcanology and Geothermal Research*, *354*, 84–101. https://doi.org/10.1016/j.jvolgeores.2018.01.002

Kavanagh, J. L., Menand, T., & Sparks, R. S. J. (2006). An experimental investigation of sill formation and propagation in layered elastic media. *Earth and Planetary Science Letters*, *245*(3–4), 799–813. https://doi.org/10.1016/j.epsl.2006.03.025

Kavanagh, J. L., Rogers, B. D., Boutelier, D., & Cruden, A. R. (2017). Controls on sill and dyke-sill hybrid geometry and propagation in the crust: The role of fracture toughness. *Tectonophysics*, *698*, 109–120. https://doi.org/10.1016/j.tecto.2016.12.027

Kile, A. (1993). Investigations into a macrosegregated, differentiated dolerite dyke, northern Skye, Scotland (MSc Thesis) St. Andrews research repository. UK: University of St. Andrews. https://research-repository.st-andrews.ac.uk/handle/10023/21844

Komar, P. D. (1972). Mechanical interactions of phenocrysts and flow differentiation of igneous dikes and sills. *Geological Society of America Bulletin*, *83*(4), 973–988. https://doi.org/10.1130/0016-7606(1972)83[973:MIOPAF]2.0.CO;2

Lecampion, B., & Garagash, D. I. (2014). Confined flow of suspensions modelled by a frictional rheology. *Journal of Fluid Mechanics*, *759*, 197–235. https://doi.org/10.1017/jfm.2014.557

Leighton, D., & Acrivos, A. (1987). Measurement of shear-induced self-diffusion in concentrated suspensions of spheres. *Journal of Fluid Mechanics*, *177*, 109–131. https://doi.org/10.1017/S0022112087000880

Leonhardt, R., & Soffel, H. C. (2006). The growth, collapse and quiescence of Teno volcano, Tenerife: New constraints from paleomagnetic data. *International Journal of Earth Sciences*, *95*(6), 1053–1064. https://doi.org/10.1007/s00531-006-0089-3

Lesher, C. E., & Spera, F. J. (2015). Thermodynamic and transport properties of silicate melts and magma. In H. Sigurdsson, B. Houghton, S. McNutt, & H. Rymer (Eds.), *Encyclopedia of volcanoes*. Elsevier Science & Technology.

Lister, J. R., & Kerr, R. C. (1991). Fluid-mechanical models of crack propagation and their application to magma transport in dykes. *Journal of Geophysical Research*, *96*(B6), 10049–10077. https://doi.org/10.1029/91JB00600

Longpré, M. A., Troll, V. R., Walter, T. R., & Hansteen, T. H. (2009). Volcanic and geochemical evolution of the Teno massif, Tenerife, Canary Islands: Some repercussions of giant landslides on ocean island magmatism. *Geochemistry, Geophysics, Geosystems*, *10*(12), Q12017. https://doi.org/10.1029/2009GC002892

Maccaferri, F., Bonafede, M., & Rivalta, E. (2010). A numerical model of dyke propagation in layered elastic media. *Geophysical Journal International*, *180*(3), 1107–1123. https://doi.org/10.1111/j.1365-246X.2009.04495.x

Marinoni, L. B., & Gudmundsson, A. (2000). Dykes, faults and palaeostresses in the Teno and Anaga massifs of Tenerife (Canary Islands). *Journal of Volcanology and Geothermal Research*, *103*(1–4), 83–103. https://doi.org/10.1016/S0377-0273(00)00217-1

Martin, V. M., Pyle, D. M., & Holness, M. B. (2006). The role of crystal frameworks in the preservation of enclaves during magma mixing. *Earth and Planetary Science Letters*, *248*(3–4), 787–799. https://doi.org/10.1016/j.epsl.2006.06.030

Maude, A. D., & Whitmore, R. L. (1956). The wall effect and the viscometry of suspensions. *British Journal of Applied Physics*, *7*(3), 98–104. https://doi.org/10.1088/0508-3443/7/3/305

Menand, T., & Tait, S. R. (2002). The propagation of a buoyant liquid-filled fissure from a source under constant pressure: An experimental approach. *Journal of Geophysical Research*, *107*(B11), 2306. https://doi.org/10.1029/2001JB000589

Mostafa, M. S., Afify, N., Gaber, A., & Zaid, E. A. (2004). Investigation of thermal properties of some basalt samples in Egypt. *Journal of Thermal Analysis and Calorimetry*, *75*, 179–188. https://doi.org/10.1023/b:jtan.0000017340.19830.45

Mollo, S., Lanzafame, G., Masotta, M., Iezzi, G., Ferlito, C., & Scarlato, P. (2011). Cooling history of a dike as revealed by mineral chemistry: A case study from Mt. Etna volcano. *Chemical Geology*, *288*(1–2), 39–52. https://doi.org/10.1016/j.chemgeo.2011.06.016

Olson, J. E. (2003). Sublinear scaling of fracture aperture versus length: An exception or the rule? *Journal of Geophysical Research*, *108*(B9). https://doi.org/10.1029/2001JB000419

Petcovic, H. L., & Dufek, J. D. (2005). Modeling magma flow and cooling in dikes: Implications for emplacement of Columbia River flood basalts. *Journal of Geophysical Research*, *110*(B10). https://doi.org/10.1029/2004JB003432

Petford, N., & Koenders, M. A. (1998). Granular flow and viscous fluctuations in low Bagnold number granitic magmas. *Journal of the Geological Society*, *155*(5), 873–881. https://doi.org/10.1144/gsjgs.155.5.0873

Phillips, R. J., Armstrong, R. C., Brown, R. A., Graham, A. L., & Abbott, J. R. (1992). A constitutive equation for concentrated suspensions that accounts for shear-induced particle migration. *Physics of Fluids A: Fluid Dynamics*, *4*(1), 30–40. https://doi.org/10.1063/1.858498

Philpotts, A. R., & Asher, P. M. (1994). Magmatic flow-direction indicators in a giant diabase feeder dike, Connecticut. *Geology*, *22*(4), 363–366. https://doi.org/10.1130/0091-7613(1994)022<0363:MFDIIA>2.3.CO;2

Philpotts, A. R., & Philpotts, D. E. (2007). Upward and downward flow in a camptonite dike as recorded by deformed vesicles and the anisotropy of magnetic susceptibility (AMS). *Journal of Volcanology and Geothermal Research*, *161*(1–2), 81–94. https://doi.org/10.1016/j.jvolgeores.2006.11.006

Platten, I. M. (2000). Incremental dilation of magma filled fractures: Evidence from dykes on the Isle of Skye, Scotland. *Journal of Structural Geology*, *22*(8), 1153–1164. https://doi.org/10.1016/S0191-8141(00)00024-9

Prousevitch, A. A., Sahagian, D. L., & Anderson, A. T. (1993). Dynamics of diffusive bubble growth in magmas: Isothermal case. *Journal of Geophysical Research*, *98*(B12), 22283–22307. https://doi.org/10.1029/93JB02027

Ray, R., Sheth, H. C., & Mallik, J. (2007). Structure and emplacement of the Nandurbar-Dhule mafic dyke swarm, Deccan Traps, and the tectonomagmatic evolution of flood basalts. *Bulletin of Volcanology*, *69*(5), 537–551. https://doi.org/10.1007/s00445-006-0089-y

Rivalta, E., Taisne, B., Bunger, A. P., & Katz, R. F. (2015). A review of mechanical models of dike propagation: Schools of thought, results and future directions. *Tectonophysics*, *638*, 1–42. https://doi.org/10.1016/j.tecto.2014.10.003

Roberts, J. L., & Sanderson, D. J. (1971). The intrusive form of some basalt dykes showing flow lineation. *Geological Magazine*, *108*(6), 489–499. https://doi.org/10.1017/S0016756800056697

Robertson, E. C., & Peck, D. L. (1974). Thermal conductivity of vesicular basalt from Hawaii. *Journal of Geophysical Research*, *79*(32), 4875–4888. https://doi.org/10.1029/JB079i032p04875

Rogan, W., Blake, S., & Smith, I. (1996). In situ chemical fractionation in thin basaltic lava flows: Examples from the Auckland volcanic field, New Zealand, and a general physical model. *Journal of Volcanology and Geothermal Research*, *74*(1–2), 89–99. https://doi.org/10.1016/S0377-0273(96)00059-5

Schindelin, J., Arganda-Carreras, I., Frise, E., Kaynig, V., Longair, M., Pietzsch, T., et al. (2012). Fiji: An open-source platform for biological-image analysis. *Nature Methods*, *9*(7), 676–682. https://doi.org/10.1038/nmeth.2019

Sehlke, A., Hofmeister, A. M., & Whittington, A. G. (2020). Thermal properties of glassy and molten planetary candidate lavas. *Planetary and Space Science*, *193*, 105089. https://doi.org/10.1016/j.pss.2020.105089

Shampine, L. F., & Reichelt, M. W. (1997). The MATLAB ODE suite. *SIAM Journal on Scientific Computing*, *18*, 1–22. https://doi.org/10.1137/s1064827594276424

Shampine, L. F., & Thompson, S. (2001). Solving DDEs in MATLAB. *Applied Numerical Mathematics*, *37*(4), 441–458. https://doi.org/10.1016/S0168-9274(00)00055-6

Shishkina, T. A., Botcharnikov, R. E., Holtz, F., Almeev, R. R., & Portnyagin, M. V. (2010). Solubility of H_2O-and CO_2-bearing fluids in tholeiitic basalts at pressures up to 500 MPa. *Chemical Geology*, *277*(1–2), 115–125. https://doi.org/10.1016/j.chemgeo.2010.07.014

Sigmundsson, F., Hooper, A., Hreinsdóttir, S., Vogfjörd, K. S., Ófeigsson, B. G., Heimisson, E. R., et al. (2015). Segmented lateral dyke growth in a rifting event at Bárðarbunga volcanic system, Iceland. *Nature*, *517*(7533), 191–195. https://doi.org/10.1038/nature14111

Staudigel, H., Tauxe, L., Gee, J. S., Bogaard, P., Haspels, J., Kale, G., et al. (1999). Geochemistry and intrusive directions in sheeted dikes in the Troodos ophiolite: Implications for mid-ocean ridge spreading centers. *Geochemistry, Geophysics, Geosystems*, *1*(1). https://doi.org/10.1029/1999GC000001

Stephens, T. L., Walker, R. J., Healy, D., Bubeck, A., England, R. W., & McCaffrey, K. J. (2017). Igneous sills record far-field and near-field stress interactions during volcano construction: Isle of Mull, Scotland. *Earth and Planetary Science Letters*, *478*, 159–174. https://doi.org/10.1016/j.epsl.2017.09.003

Svenningsen, O. M. (1994). The Baltica–Iapetus passive margin dyke complex in the Sarektjåkkå Nappe, northern Swedish Caledonides. *Geological Journal*, *29*(4), 323–354. https://doi.org/10.1002/gj.3350290403

Taisne, B., & Jaupart, C. (2009). Dike propagation through layered rocks. *Journal of Geophysical Research*, *114*(B9), B09203. https://doi.org/10.1029/2008JB006228

Taisne, B., & Tait, S. (2011). Effect of solidification on a propagating dike. *Journal of Geophysical Research*, *116*(B1), B01206. https://doi.org/10.1029/2009JB007058

Taracsák, Z., Hartley, M. E., Burgess, R., Edmonds, M., Iddon, F., & Longpre, M. A. (2019). High fluxes of deep volatiles from ocean island volcanoes: Insights from El Hierro, Canary Islands. *Geochimica et Cosmochimica Acta*, *258*, 19–36. https://doi.org/10.1016/j.gca.2019.05.020

Thiele, S. T., Cruden, A. R., Zhang, X., Micklethwaite, S., & Matchan, E. L. (2021). Reactivation of magma pathways: Insights from field observations, geochronology, geomechanical tests, and numerical models. *Journal of Geophysical Research: Solid Earth*, *126*(5), e2020JB021477. https://doi.org/10.1029/2020JB021477

Thordarson, T., & Self, S. (1996). Sulfur, chlorine and fluorine degassing and atmospheric loading by the Roza eruption, Columbia River Basalt Group, Washington, USA. *Journal of Volcanology and Geothermal Research*, *74*(1–2), 49–73. https://doi.org/10.1016/S0377-0273(96)00054-6

Thordarson, T., & Self, S. (1998). The Roza Member, Columbia River Basalt Group: A gigantic pahoehoe lava flow field formed by endogenous processes? *Journal of Geophysical Research*, *103*(B11), 27411–27445. https://doi.org/10.1029/98JB01355

Tomé, C. R., Bitencourt, M. d. F., Raposo, M. I. B., & Savian, J. F. (2020). Magnetic fabric data on interactive syntectonic magmas of contrasting composition in composite dikes from south Brazil. *Journal of Geodynamics*, *138*, 101754. https://doi.org/10.1016/j.jog.2020.101754

Turcotte, D. L., & Schubert, G. (2002). *Geodynamics*. Cambridge University Press.

Wada, Y. (1992). Magma flow directions inferred from preferred orientations of phenocryst in a composite feeder dike, Miyake-Jima, Japan. *Journal of Volcanology and Geothermal Research*, *49*(1–2), 119–126. https://doi.org/10.1016/0377-0273(92)90008-2

Walker, G. P. (1987). The dike complex of Koolau Volcano, Oahu: Internal structure of a Hawaiian rift zone. In R. W. Decker, T. L. Wright, & P. H. Stauffer (Eds.), *USGS professional paper 1350* (Vol. 2, pp. 961–993). United States Government Printing Office.

Walker, G. P. (1989). Spongy pahoehoe in Hawaii: A study of vesicle-distribution patterns in basalt and their significance. *Bulletin of Volcanology*, *51*(3), 199–209. https://doi.org/10.1007/bf01067956

Walker, G. P., & Eyre, P. R. (1995). Dike complexes in American Samoa. *Journal of Volcanology and Geothermal Research*, *69*(3–4), 241–254. https://doi.org/10.1016/0377-0273(95)00041-0

Weis, F. A., Skogby, H., Troll, V. R., Deegan, F. M., & Dahren, B. (2015). Magmatic water contents determined through clinopyroxene: Examples from the Western Canary Islands, Spain. *Geochemistry, Geophysics, Geosystems*, *16*(7), 2127–2146. https://doi.org/10.1002/2015GC005800

White, R. S., Drew, J., Martens, H. R., Key, J., Soosalu, H., & Jakobsdóttir, S. S. (2011). Dynamics of dyke intrusion in the mid-crust of Iceland. *Earth and Planetary Science Letters*, *304*(3–4), 300–312. https://doi.org/10.1016/j.epsl.2011.02.038

Whitehead, J. A., & Helfrich, K. R. (1991). Instability of flow with temperature-dependent viscosity: A model of magma dynamics. *Journal of Geophysical Research*, *96*(B3), 4145–4155. https://doi.org/10.1029/90JB02342

Woods, J., Winder, T., White, R. S., & Brandsdóttir, B. (2019). Evolution of a lateral dike intrusion revealed by relatively-relocated dike-induced earthquakes: The 2014–15 Bárðarbunga–Holuhraun rifting event, Iceland. *Earth and Planetary Science Letters*, *506*, 53–63. https://doi.org/10.1016/j.epsl.2018.10.032

Zhang, Y., Xu, Z., Zhu, M., & Wang, H. (2007). Silicate melt properties and volcanic eruptions. *Reviews of Geophysics*, *45*(4). https://doi.org/10.1029/2006RG000216

Zia, H., & Lecampion, B. (2020). PyFrac: A planar 3D hydraulic fracture simulator. *Computer Physics Communications*, *255*, 107368. https://doi.org/10.1016/j.cpc.2020.107368